Modelling of stress development and fault slip in and around a producing gas reservoir

Modelling of stress development and fault slip in and around a producing gas reservoir

Proefschrift

ter verkrijging van de graad van doctor
aan de Technische Universiteit Delft,
op gezag van de Rector Magnificus prof.dr.ir. J.T. Fokkema,
voorzitter van het College voor Promoties,
in het openbaar te verdedigen

op woensdag 3 december 2003 te 10.30 uur

door

Franciscus Matheus Marie MULDERS

Diplom-Geologe (mijnbouwkundig ingenieur), RWTH Aachen, Duitsland
geboren te Maasbree

Dit proefschrift is goedgekeurd door de promotoren:
Prof.dr.ir. J.T. Fokkema
Prof.dr. A.K. Turner

Samenstelling promotiecommissie:

Rector Magnificus, voorzitter	
Prof.dr.ir. J.T. Fokkema	Technische Universiteit Delft, promotor
Prof.dr. A.K. Turner	Colorado School of Mines, promotor
Prof.dr. R.M. Holt	SINTEF Petroleum Research
Prof.dr. S.A.P.L. Cloetingh	Vrije Universiteit Amsterdam
Prof.dr. P.K. Currie	Technische Universiteit Delft
Ir. C.J. Kenter	Shell International Exploration & Production BV
Ir. J.P.A. Roest	Staatstoezicht op de Mijnen

Published and distributed by: DUP Science

DUP Science is an imprint of
Delft University Press
P.O. Box 98
2600 MG Delft
The Netherlands
Telephone: +31 15 27 85 678
Telefax: +31 15 27 85 706
E-mail: info@library.tudelft.nl

ISBN 90-407-2454-7

Keywords: 3

Printed in the Netherlands

TABLE OF CONTENTS

SUMMARY

Modelling of stress development and fault slip in and around a producing gas reservoir

Many gas fields are currently being produced in the northern Netherlands. Induced seismicity related to gas production has become a growing problem in the Netherlands in the past two decades. To date, a few hundred induced seismic events occurred. Induced seismicity is generally assumed to be the result of induced reactivation of discontinuities in the subsurface. Field data of the Groningen and Annerveen gas fields as well as other Rotliegend gas fields in the Netherlands are analysed. A large amount of seismic cross sections through seismic events is studied. It is very likely that the seismic events are the result of reactivation of existing discontinuities (like faults) in or near the reservoirs.

The objective of the research presented in this dissertation is to obtain a better understanding of the mechanisms of gas production induced reactivation of faults by means of 3D geomechanical modelling of gas reservoirs. It is a step towards future assessment of expected seismic energy release when (further) developing gas fields in the Netherlands.

Furthermore, attention is given to the development of several quantification methods, used for the analysis of the calculation results. Quantification methods include relative shear displacements, seismic moment, stress paths, mobilised shear capacity and total stress changes per unit depletion.

The geomechanical models represent the geometries found in the seismic cross sections. The models contain a disk-shaped gas reservoir in an extensional stress regime. A steeply dipping normal fault plane intersects the reservoir and divides it into two compartments: a footwall and a hanging wall reservoir compartment. Stress development and fault slip during gas depletion are analysed.

Gas depletion can lead to both normal and reverse fault slip on the same fault plane. In the given setting of a steeply dipping normal fault in an extensional stress regime, normal fault slip due to differential reservoir compaction is the dominant mechanism, rather than reverse fault slip. The effect of differential reservoir compaction is most pronounced for a configuration, where the top of the hanging wall reservoir compartment is positioned exactly opposite to the bottom of the footwall reservoir compartment, resulting in a relatively large amount of fault slip over a narrow area.

Normal fault slip is supported by equal depletion of both reservoir compartments. Reverse fault slip is supported by differential pore pressure development due to reservoir compartmentalisation. Especially the combination of a relatively stiff surrounding rock and differential pore pressure development due to reservoir compartmentalisation can result in relatively large amounts of reverse fault slip.

Both normal and reverse fault slip are promoted by a Young's modulus or Poisson's ratio of the surrounding rock larger than those of the reservoir rock ($E^{sur} > E^{res}$ or $\nu^{sur} > \nu^{res}$). The initial state of stress is relatively closer to the failure line than in case of a smaller stiffness contrast. $E^{sur} < E^{res}$ and $\nu^{sur} < \nu^{res}$ oppose the reactivation of the fault. Values of ν^{sur} lower than 0.2 seem to have no significant influence on the calculated maximum normal fault slip. Calculations indicated that the Young's modulus of the surrounding rock is a more important parameter influencing gas depletion induced fault slip than the Poisson's ratio of the surrounding rock.

Calculations with a 3D anisotropic tectonic stress field show a strong dependency of the amount of calculated fault slip on the direction of the maximum horizontal stress with respect to the fault strike direction. Most normal fault slip occurs when the maximum horizontal stress is directed parallel to the fault strike. Minimum normal fault slip is calculated for a maximum horizontal stress direction perpendicular to the strike direction of the fault. A larger horizontal stress component parallel to the azimuth of the fault has a limiting effect on the fault slip.

Total fault slip can consist of a dip slip and a strike slip component. In case of a horizontal reservoir, no significant strike slip is observed when the fault strike direction is a principal stress direction. A certain amount of strike slip is observed for calculations with an angle between the maximum horizontal stress direction and the fault strike direction of 31^o, 45^o and 59^o. Strike slip contributes to both normal and reverse fault slip.

F.M.M. Mulders Delft, 3rd December 2003

ACKNOWLEDGEMENTS

First of all I would like to thank God. Without His help, I would not have been able to finish this PhD to a successful end. He is always there to listen and to take care.

At this place I would also like to thank a number of people for their support to this research. I thank my promotor Jacob Fokkema for the opportunity to carry out this challenging PhD-research at Delft University of Technology. I am especially thankful for his support, encouragement and enthusiasm during these years. I also want to thank my co-promotor Keith Turner for his support, encouragement and interest, which even continued from across the Atlantic. I am thankful to my supervisor Hans Roest for the numerous discussions over the years on both technical and social level. I had the privilege to enjoy a great collegial atmosphere and to improve my political insights in the years that we shared the office room. I also had the privilege to have a great technical support in numerous meetings and discussions from a Steering Committee. I am particularly grateful for the scientific contribution from and the informal open door policy in different institutions. I would like to sincerely thank –in no particular order-: Dirk Doornhof, Alice Post, Harm Frikken, René Frijhoff and Marcel Bouts from NAM, Cor Kenter from Shell Exploration & Production, Berend Scheffers and Rob van Eijs from TNO-NITG, Torild van Eck and Hein Haak from KNMI and Jan van Herk from SodM. Special thanks go also to the members of the PhD commission Rune Holt, Sierd Cloetingh and Peter Currie.

Special thanks I owe to NAM for the opportunity to make use of their extensive data base. I have especially good memories to the days that I spent at the NAM offices for gathering data. Special thanks go to Robert Gmelig-Meyling, Hermann Priebe, Jeanette Boon, David Wann, Jan van de Sande, John Sutherland and Koos Pipping.

My colleagues at the former section Engineering Geology of DUT and ITC and my colleagues from TNO-NITG are particularly thanked for the great working atmosphere and support. This also includes the roommates I have had during the past years at DUT. Special thanks go to the former MSc-students Markus Glab, Yufei Dong, Abdelkader Mahi, Aung Zaw Moe and Erik Kirkemo for their co-operation and scientific contribution to this research work and friendship.

For financial support for printing this thesis I thank the Faculty of Civil Engineering and Geosciences of Delft University of Technology as well as Shell Exploration & Production BV in Rijswijk and NAM (Nederlandse Aardolie Maatschappij) BV in Assen.

Warm thanks go to my wife Camelia, for her understanding, support and never letting me down, especially in the last phase of my research throughout the long absences and long working hours. Thanks go also to my family for their patience, understanding and encouraging advises. Special thanks to Ari and Camelia for the design of the cover of this book.

SHORT CV

Born in 1972 in Maasbree, the Netherlands.

Schooled in Heerlen, the Netherlands.

Studied Engineering Geology, with specialisation in rock- and soil mechanics, at Aachen University of Technology (RWTH Aachen, Germany) and finished in 1997. The MSc-thesis is carried out at Delft University of Technology, Netherlands, in co-operation with the Research Centre Sand-lime bricks Industry ('Research Centrum Kalkzandsteen Industrie').

Worked from 1997 to 1998 as Associate Researcher at Delft University of Technology, Department of Applied Earth Sciences, Section Engineering Geology, to co-operate in a research project for investigating possible causes of seismicity in a depleting anticline-shaped gas reservoir.

Worked from 1998 to 2003 as PhD Researcher at Delft University of Technology, Department of Applied Earth Sciences, Section Engineering Geology; research in co-operation with NAM, Shell Exploration & Production, TNO-NITG, KNMI and State Supervision of Mines.

Works since July 2003 at the Netherlands Institute of Applied Geoscience – National Geological Survey (TNO-NITG), Department of Geo-Energy, as geological engineer.

LIST OF SYMBOLS

Latin symbols

A	Area	m^2
$[B]$	Differential matrix	-
c	Cohesion	Pa
c^f	Cohesion of the fault	Pa
c_r	Cohesion of the rock	Pa
$c^{res,sur}$	Cohesion of the reservoir, surrounding rock	Pa
C_u	Uniaxial compressive strength	Pa
D	Reservoir depth	m
$[D]$	Rheological matrix	Pa
D_n	Fault normal stiffness	Pa/m
D_s	Fault shear stiffness	Pa/m
e	Aspect ratio of the reservoir (= thickness / width)	-
E	Young's modulus	Pa
$E^{res,sur}$	Young's modulus of the reservoir, surrounding rock	Pa
$\{F\}$	Nodal force vector	N
$\{F^{ext}\}$	External load vector	N
F_i	Force vector	N
$\{F^{int,i}\}$	Internal force vector at increment i	N
$F(\sigma'_1, \sigma'_3, c, \phi)$	Yield function	Pa
G	Shear modulus	Pa
g_i	Gravity acceleration vector	m/s^2
h	Fault thickness	m
$I_{1,2,3}$	First, second and third stress invariant	Pa
$J_{1,2,3}$	First, second and third deviatoric stress invariant	Pa
K	Bulk modulus	Pa
$[K]$	Stiffness matrix	Pa
K_0	Effective stress ratio for isotropic stress field ($\sigma'_H = \sigma'_h$)	-
K_{0H}	Effective stress ratio ($= \sigma'_H / \sigma'_v$) for anisotropic stress field	-
K_{0h}	Effective stress ratio ($= \sigma'_h / \sigma'_v$) for anisotropic stress field	-
K_{fr}	Bulk modulus of the framework of the rock	Pa
K_s	Bulk modulus of the solid	Pa
M_0	Seismic moment	Nm
M_0^{normal}	Seismic moment for normal fault slip	Nm
$M_0^{reverse}$	Seismic moment for reverse fault slip	Nm
MSC	Mobilised shear capacity for fault	-
MSC^{3D}	Mobilised shear capacity for rock volume	-
n_1, n_2, n_3	Direction cosines	-
n_i	Surface normal vector	-
$\{o^i\}$	Out-of-balance force vector at increment i	N
p	Pore pressure	Pa
p_{ini}	Initial pore pressure	Pa

p_{ini}^{fault}	Initial pore pressure in fault	Pa
$p_{ini}^{res,sur}$	Initial pore pressure in reservoir, surrounding rock	Pa
RSD	Relative shear displacement	m
RSD_{min}	Minimum relative shear displacement (largest reverse fault slip)	m
RSD_{max}	Maximum relative shear displacement (largest normal fault slip)	m
S	Surface area	m^2
s_{ij}	Deviatoric stress tensor	Pa
s_i^p	Principal deviatoric stress vector	Pa
S_{ijkl}	Eshelby shape factors	-
$s(\eta)$	Inner product of the out-of-balance force with the iterative displacement increment	Nm
s,t,n	Relative displacement on the fault in strike, down/up dip, normal direction	m
T_i	Traction vector	Pa
$\{u\}$	Vector of nodal degrees of freedom	m
$u_{1,2,3}$	Displacement	m
V	Volume	m^3
x_1,x_2,x_3	Spatial co-ordinates (rectangular)	m
x,y,z	Spatial co-ordinates (rectangular)	m
z	Depth (negative in downward direction)	m

Greek symbols

α	Biot's poroelastic constant	-
β	Fault dip angle	^{o}
β_{crit}	Critical fault dip angle ($=45^o + \frac{1}{2}\phi^f$)	^{o}
γ	Total stress change per unit depletion ($= \Delta\sigma / \Delta p$)	-
$\gamma_{v,H,h}$	Total stress change per unit depletion in the direction of vertical, maximum horizontal, minimum horizontal stress	-
$\gamma_{x,y,z}$	Total stress change per unit depletion in x,y,z-direction	-
Γ	Shear strain	-
δ_{ij}	Kronecker delta	-
$\Delta\sigma'$	Effective stress change ($= \sigma'^{\,after} - \sigma'^{\,before}$)	Pa
$\Delta\sigma$	Total stress change ($= \sigma^{\,after} - \sigma^{\,before}$)	Pa
Δp	Pore pressure change ($= p^{\,after} - p^{\,before}$)	Pa
$\Delta p^{res,sur}$	Pore pressure change in reservoir, surrounding rock	Pa
Δp^{fault}	Pore pressure change in fault	Pa
$\{\varepsilon\}$	Strain vector	-
$\{\varepsilon_0\}$	Initial strain vector	-
ε_{ij}	Strain tensor	-
ε_v	Volumetric strain	-

η	Scaling value	-
θ	Haigh-Westergaard stress co-ordinate	^{o}
λ	Clockwise angle between fault strike direction and direction of the maximum horizontal stress	^{o}
ν	Poisson's ratio	-
$\nu^{res,sur}$	Poisson's ratio of reservoir, surrounding rock	-
ξ	Haigh-Westergaard stress co-ordinate	Pa
ρ	Haigh-Westergaard stress co-ordinate	Pa
ρ_{bulk}	Bulk density	kg/m^3
$\rho_{bulk}^{res,sur}$	Bulk density of reservoir, surrounding rock	kg/m^3
$\rho_{pore\ fluid}$	Density of the pore fluid	kg/m^3
ρ_0	Haigh-Westergaard stress co-ordinate ρ for $\xi = 0$	Pa
ρ_{fail}	Haigh-Westergaard stress co-ordinate ρ at failure	Pa
ρ^*	Projection of the Haigh-Westergaard stress co-ordinate ρ on the deviatoric plane	Pa
ρ^*_{fail}	Projection of the Haigh-Westergaard stress co-ordinate ρ at failure on the deviatoric plane	Pa
σ	Stress (positive for compression)	Pa
$\overline{\sigma}$	Mean stress	Pa
$\{\sigma\}$	Stress vector	Pa
$\{\sigma_0\}$	Initial stress vector	Pa
σ_{ij}	(Total) stress tensor	Pa
σ'_{ij}	Effective stress tensor	Pa
$\overline{\sigma}_{ij}$	Mean stress tensor	Pa
$\overline{\sigma}_{i}$	Mean stress vector	Pa
σ^p	Principal stress	Pa
σ^p_i	Principal stress vector	Pa
$\sigma^*_1, \sigma^*_2, \sigma^*_3$	Projections of the principal stress vector on the deviatoric plane	Pa
$\sigma_{1,2,3}$	Maximum, intermediate and minimum (total) principal stress	Pa
$\sigma'_{1,2,3}$	Maximum, intermediate and minimum effective principal stress	Pa
$\sigma'_{v,H,h}$	Vertical, maximum horizontal and minimum horizontal effective stress	Pa
$\sigma'_{x,y,z}$	Effective stress in x,y,z-direction	Pa
σ_n	(Total) normal stress	Pa
σ'_n	Effective normal stress	Pa
$\sigma'_{n,failure}$	Effective normal stress at failure	Pa
τ	Shear stress	Pa
$\tau_{failure}$	Shear stress at failure	Pa
τ_{max}	Maximum shear stress	Pa
τ_s	Shear stress in strike direction of the fault	Pa
τ_t	Shear stress in down / up-dip direction of the fault	Pa
ϕ	Friction angle	^{o}
ϕ^f	Friction angle of the fault	^{o}
ϕ_r	Friction angle of the rock	^{o}

ϕ^*_r	Projection of the friction angle of the rock on the rendulic plane	^{o}
$\phi^{res,sur}$	Friction angle of reservoir, surrounding rock	^{o}
φ	Porosity	-
ψ	Dilatancy angle	^{o}
$\psi^{res,sur}$	Dilatancy angle of reservoir, surrounding rock	^{o}
$\Psi_{1,2}$	Shear deformation angle	^{o}

1 INTRODUCTION

1.1 Gas production in the Netherlands

Natural gas is, when compared to other fossil fuels, an environmentally relatively clean source for energy supply in both winning and usage per energy unit (kWh). For environmental and economical reasons, the share of natural gas in the energy supply grows within the EU and worldwide. Dutch natural gas has, with more than 50% of the EU gas reserves on a central geographical position, an excellent basis for giving an important contribution to the future demand of natural gas within the EU.

Many gas fields are currently being produced in the northern Netherlands (187 fields at January 1 2003, from which 79 fields are positioned on-shore and 108 fields off-shore (Ministry of Economic Affairs 2003). Up to January 1 2003, 353 gas fields are identified in the Netherlands (153 fields on-shore and 200 fields off-shore). 20 of these 353 gas fields are abandoned.

The gas in the Netherlands is dominated by the giant Groningen gas field with an initial total capacity of approximately $2800 \cdot 10^9$ m^3 gas. In the Netherlands, $2622 \cdot 10^9$ m^3 gas has been produced in total since the first production in 1947. An estimation of the expected remaining gas reserves amounts $1689 \cdot 10^9$ m^3 (all values valid for January 1 2003).

1.2 Gas production induced seismicity

The gas is in most cases captured in sandstone rocks from the Rotliegend Formation, at a depth of approximately -3000 m, as is the case for the giant Groningen field. The production of these gas fields causes changes in the effective stress field in the reservoir and its surroundings, resulting in compaction of the reservoir rock. This in turn leads in most cases to subsidence at the earth's surface and in some cases to induced seismicity.

Induced seismicity is basically the result of reactivation of pre-existing geological fault planes in or near the producing reservoirs. When gas is produced from the reservoir, the reduction in pore pressure and effective stress changes can cause shear stresses along the fault plane to change, eventually creating slip conditions and fault movement during gas extraction. As stated by Pennington *et al*. (1986), continuous movement can cause stresses to accumulate on slip resistant regions at some parts of the fault. When these highly stressed regions, which are termed asperities, ultimately yield, energy is released seismically. The accumulated energy may also be released aseismically through slow visco-plastic deformation (creep) of the asperity, but there is no generally accepted method for determining whether slip on a given fault will be seismic or aseismic.

Gas production induced seismicity has become a growing problem in the Netherlands in the past two decades. The first registered seismic event in the northern Netherlands associated to gas production occurred in the city of Assen in 1986. After this event, KNMI (Royal Dutch Meteorological Institute) extended and refined the existing detection network in the northern Netherlands. Intensive observation of the region is carried out nowadays with 11 downhole seismometers and 10 accelerometers, besides the existing surface seismometer network (Figure 1.1). To date, a few hundred events have been registered in this area (Figure 1.2). Approximately 40 events are recorded annually, from which 5 to 10 are sensed by the public. The occurrence of these small events near producing gas fields in historically aseismic regions, as well as their shallow hypocentres (-800 to -3500 m depth) indicate that most earthquakes in these parts of the Netherlands are non-tectonic (induced). The induced seismic events are with less than 3.8 on the Richter scale relatively small in magnitude (Haak *et al.* 2001). From 1989 on, induced seismic events are also registered near gas fields in the west of the Netherlands near Purmerend and Alkmaar. The largest induced seismic event to date took place on 9th September 2001 near the city of Alkmaar with a magnitude of 3.5 on the Richter scale. In few cases, induced seismicity has lead to slight damage on buildings, such as damaged plaster, small cracks and the widening of existing cracks. So far, induced seismicity has not lead to structural damage to the construction of buildings.

In Figure 1.3, a map of the Netherlands and surrounding is shown with seismic events as measured by KNMI. The relatively large earthquakes in the south of the Netherlands (largest magnitude to date: 5.8 on Richter scale) are the result of tectonic movements of the Rhein Graben. Earthquakes occur in this region at a depth of -5 to –30 km.

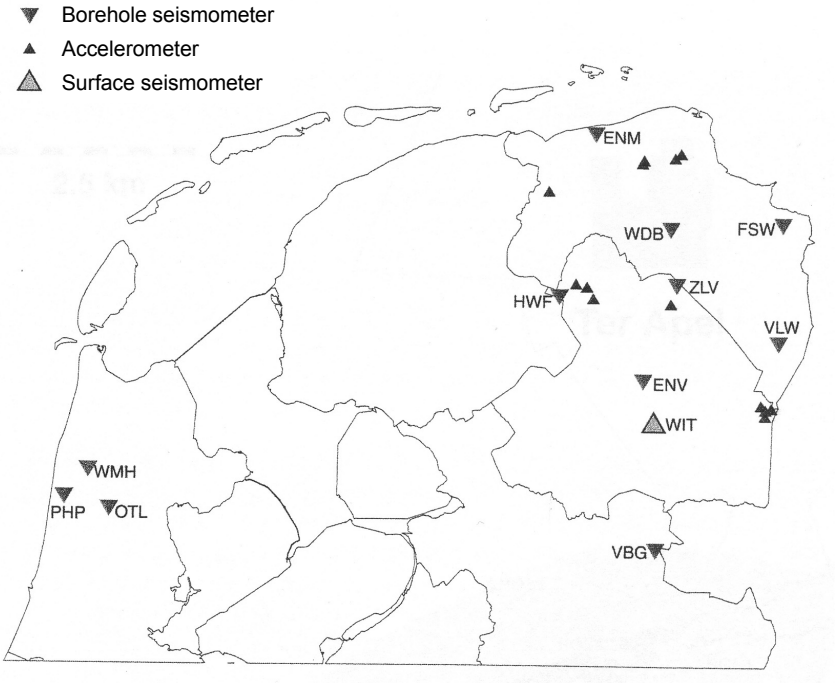

Figure 1.1. Present locations of seismometers and accelerometers in the northern Netherlands (after Dost 2000).

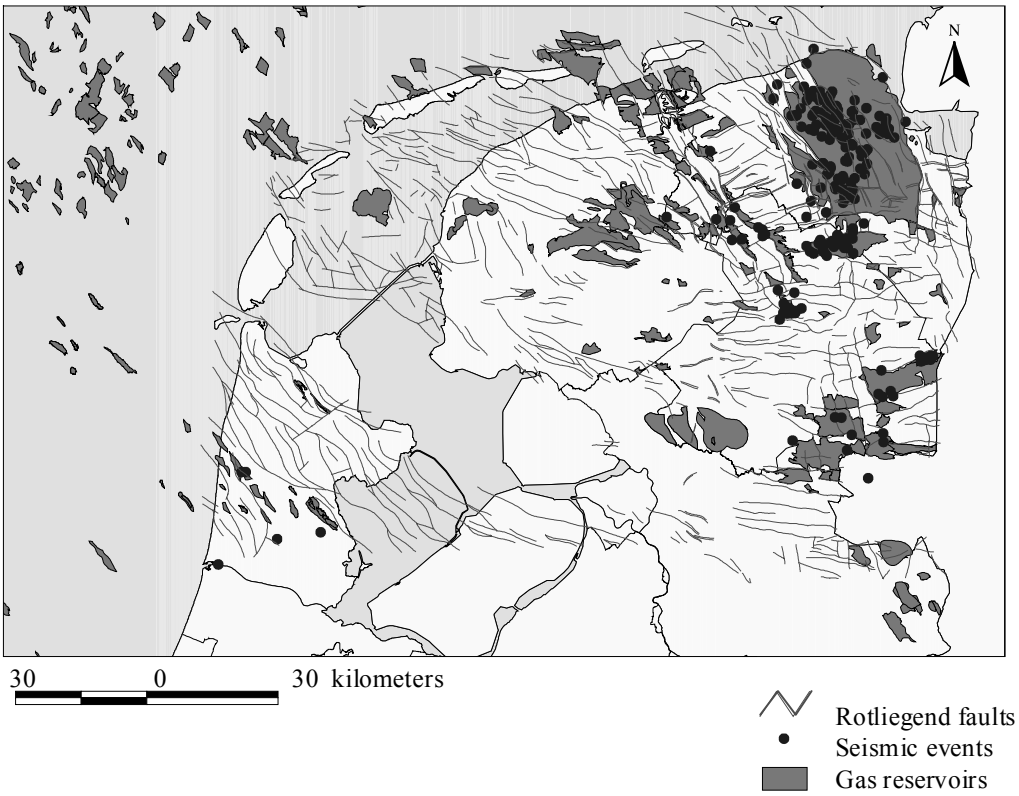

Figure 1.2. Map of the northern Netherlands showing the geographical locations of gas reservoirs, Rotliegend faults (at reservoir level) and seismic events. Source: TNO-NITG, KNMI. See Appendix 2 for this figure in colour.

1.3 Gas production and the environment

There exists an increasing awareness about environmental and social consequences of gas production and mining activities in general, not only because of induced seismicity but also because of subsidence at the earth's surface. A new Mining Act has been installed since January 2003. It makes an extraction plan compulsory for every new field that is (going to be) produced, including among others a seismic risk analysis. Five components are asked: a hazard analysis of expected induced seismic events, the expected size and type of damage, proposed measures concerning reduction of seismic events, proposed measures concerning reduction of damage by seismic events and the set-up of a monitoring plan. Research after the mechanisms and possibilities of gas production induced seismicity may give additional value to the first component.

Currently, a system for probabilistic seismic hazard analysis (PSHA) is being set-up by several governmental and industrial parties. Based on statistical data, such analysis could assess the probability that a certain peak ground acceleration and velocity may occur (and the resulting damage); amplification effects in the shallow soil are taken into account.

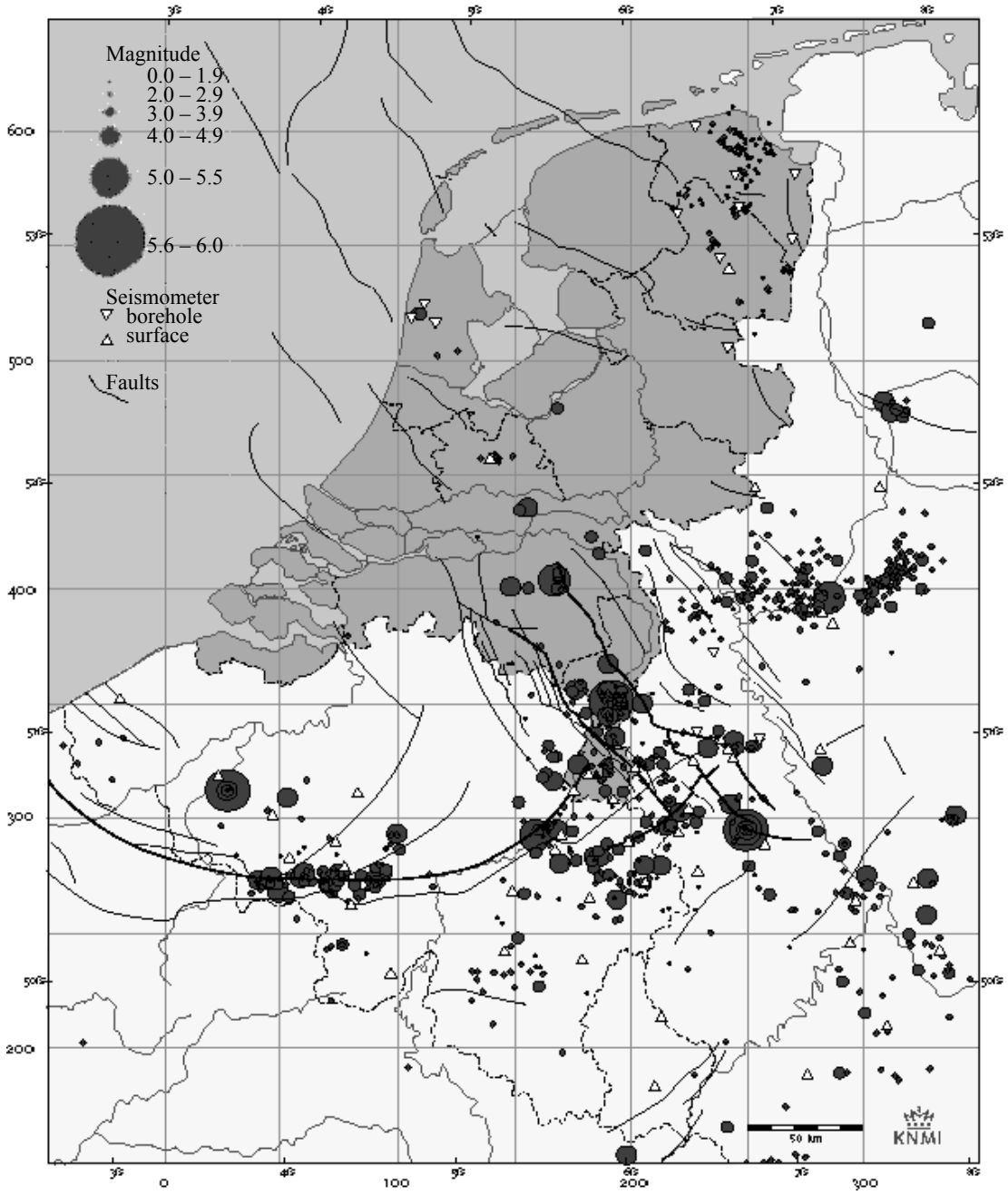

Figure 1.3. Map of the Netherlands and surrounding countries with registered earthquakes from 1905 to 1996. Source: KNMI. See Appendix 2 for this figure in colour.

1.4 Research objective

Approximately ten years of research have helped increase the knowledge and understanding of the mechanisms of gas production induced seismic events. Nevertheless, the exact causes of the events are still not completely clear. For instance, faults intersecting a producing reservoir with normal fault geometry are very prone to differential reservoir compaction and normal fault reactivation (Roest & Kuilman 1994). Such fault geometry is shown in Figure 1.4 for the Bergermeer gas field and is representative for most of the gas fields in the northern Netherlands. Four relatively large events took place along this fault in 1994 and 2001. Fault plane solutions by KNMI revealed however reverse reactivations of this fault (Haak *et al.* 2001).

The objective of the research presented in this dissertation is to obtain a better understanding of the mechanisms of gas reservoir production induced fault reactivation by means of 2D- and 3D-geomechanical modelling of gas reservoirs, using the finite element software package DIANA. Geomechanical modelling has been found to be an efficient tool in evaluating the causal relationships of gas production and fault reactivation.

The study focuses on the influence of several geomechanical parameters on stress development and fault slip in and around a disk-shaped gas reservoir intersected by a normal fault. Attention is given to the development, implementation and visualisation of several quantification methods in DIANA, used for the analysis of the calculation results. Quantification methods include relative shear displacements, seismic moment, stress paths, mobilised shear capacity and arching. Parameters include reservoir geometry (ellipsoid and disk), reservoir size, -depth and -tilt angle, reservoir and surrounding rock properties (Young's modulus and Poisson's ratio), initial reservoir overpressure, throw along fault, reservoir compartmentalisation and 3D-isotropic and anisotropic initial tectonic stress fields.

The geomechanical models incorporate a geometry which is based on field data analysis and representative for most of the Rotliegend gas fields in the Netherlands, in particular the Groningen and Annerveen gas fields but also the Bergermeer gas field. For a proper evaluation of the influence of the parameters on stress development and fault slip, the models are kept basic and generic. The volume surrounding the reservoir is assumed to consist of one homogeneous isotropic rock mass in order to keep the model free from any additional effects eventually produced by a layered geological structure.

The study focuses on seismic events at reservoir level, since field data analysis revealed that the far majority of all events is located at reservoir level.

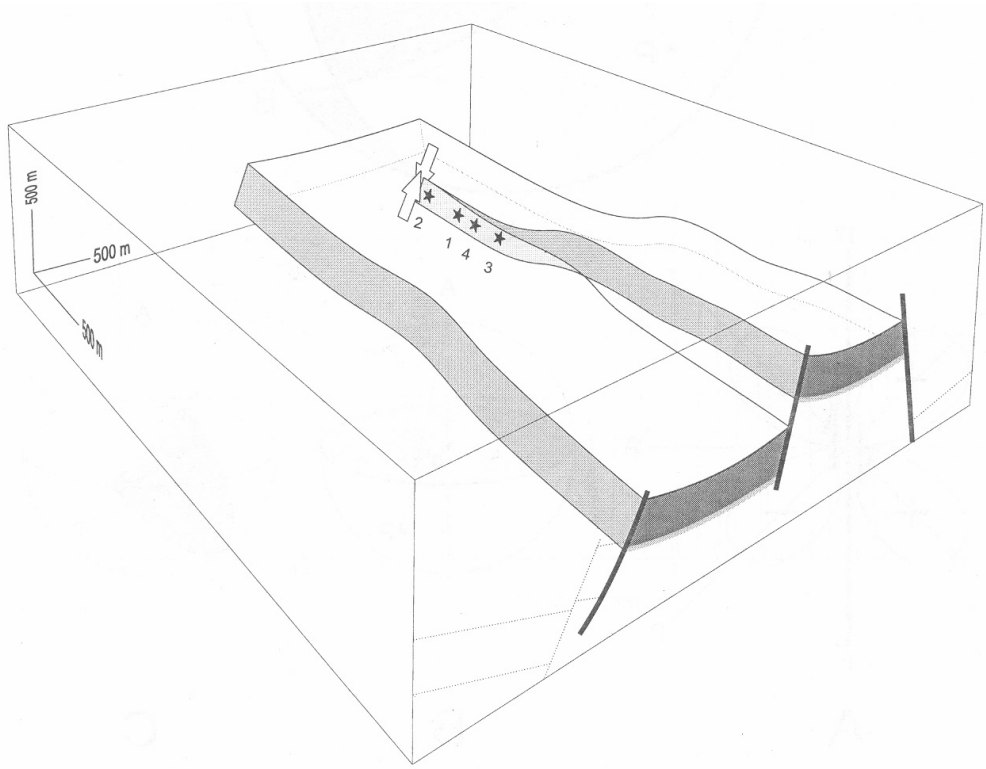

Figure 1.4. Schematic representation of the fault in the Bergermeer gas field in the Netherlands, along which four seismic events are observed (after Haak et al. 2001). The fault represents a normal fault. According to fault plane solutions of KNMI, the deformation mechanism of the seismic events is reverse fault slip.

1.5 Outline

This dissertation is organised as follows:

Chapters 2-5 give a general introduction in subjects needed for the understanding of the work presented in this dissertation, such as stress/strain behaviour, plasticity and the finite element method. Chapter 2 gives a general introduction to the theoretical concepts of stress, infinitesimal strain, linear elasticity, poroelasticity and the effective stress principle. The Haigh-Westergaard stress co-ordinates are introduced here, which are needed for the derivation of an expression to calculate the mobilised shear capacity in rock volumes. Chapter 3 deals with the theoretical concepts of fault reactivation and rock failure in producing hydrocarbon reservoirs, based on the Mohr-Coulomb failure criterion. Chapter 4 presents the results of a finite element calculation, illustrating the stress concentrations around an asperity on a previously cut fault plane through a rock sample. The calculation is performed in the framework of a research proposal for identification of stress concentrations in the subsurface by means of 4D-time lapse seismic, requiring laboratory experiments to monitor such stress concentrations in rock samples by acoustic measurements. Chapter 5 describes the theoretical background of finite element calculations for geomechanical modelling.

The results of a literature study on hydrocarbon reservoir induced seismicity are summarised in Chapter 6.

Chapter 7 gives a description of the geologic setting and characteristics of the Groningen and Annerveen gas fields in the northern Netherlands. It presents the conclusions of a field data analysis of seismic cross sections through the hypocentres of the seismic events within the boundaries of the fields. The geomechanical models used for the calculations in this study are based on the geology as described in Chapter 7. Their model set-up is presented in Chapter 8 together with the results of some preliminary calculations, performed in order to choose appropriate boundary conditions and values for certain geomechanical parameters: initial pore pressure and pore pressure development on the fault plane, normal- and shear stiffness of the fault plane and model size.

Chapter 9 describes the development, implementation and visualisation of several quantification methods in DIANA, used for the analysis of the calculation results. Quantification methods include relative shear displacements, seismic moment, stress paths, mobilised shear capacity and total stress changes per unit depletion. Newly developed formulas for mobilised shear capacity, in order to express the proximity of a (principal) state of stress on a fault plane or in a rock volume to the Mohr-Coulomb failure criterion, are successfully applied.

The results of 2D- and 3D-geomechanical calculations are presented and discussed in Chapters 10 and 11. Chapter 10 gives an overview of stress development in generic basic models of ellipsoidal and disk-shaped gas reservoirs without fault. Existing analytical solutions as well as numerical modelling results are presented and discussed. Differences in stress development between ellipsoidal and disk-shaped gas reservoirs are analysed. Chapter 10 zooms furthermore in on disk-shaped gas reservoirs and discusses the influence of several parameters on the stress development in and around the gas reservoir: reservoir rock properties, surrounding rock properties and reservoir tilting. Chapter 11 describes stress development and fault slip on steeply dipping normal faults intersecting a disk-shaped gas reservoir as a function of several parameters: surrounding rock properties, initial reservoir pore pressure, throw along the fault plane, differential pore pressure development due to reservoir compartmentalisation and initial tectonic stress field.

Conclusions are summarised and discussed in Chapter 12. Recommendations for further research are given as well.

2 THEORETICAL CONCEPTS OF STRESS, INFINITESIMAL STRAIN, LINEAR ELASTICITY AND POROELASTICITY

The following explanations about stress, strain and poroelasticity are mainly based on Brady & Brown 1993, Chen & Han 1988, Fjaer *et al.* 1992, Oertel 1996 and Ranalli 1995. For the theoretical background of stress, infinitesimal strain, linear elasticity and poroelasticity in Chapter 2, subscript notation for (Cartesian) vectors and tensors is used, whereby the subscripts are to be assigned the values 1, 2 and 3. A point in space is then defined by the orthogonal Cartesian coordinates x_1, x_2 and x_3 with respect to a given orthogonal Cartesian reference frame with origin O and the three mutually perpendicular unit vectors $\underline{i}_1$, $\underline{i}_2$ and $\underline{i}_3$ (Figure 2.1a). In the given order, $\underline{i}_1$, $\underline{i}_2$ and $\underline{i}_3$ form a right-handed system. For repeated subscripts, the summation convention holds.

However, although being very convenient for theoretical calculations, this notation is not practical for the finite-element calculation purposes of this thesis. Therefore, all chapters in this thesis other than 2 refer to an x,y,z-coordinate system for two reasons: first, it is in accordance with the coordinate system in the finite-element software DIANA used for this research work. Calculation output is in terms of stresses and displacements in x-, y- and z-directions. Second, it is commonly used in rock mechanics. A point in space is then located by employing the orthogonal Cartesian coordinates x, y and z with respect to a given orthogonal Cartesian reference frame with origin O and the three mutually perpendicular unit vectors $\underline{i}_x$, $\underline{i}_y$ and $\underline{i}_z$ (Figure 2.1b). In the given order, the x-, y- and z-axes form a right-handed system. The subscripts x, y and z represent the 1, 2 and 3 of the subscript notation, respectively.

In rock mechanics it is common practice to use different symbols for the diagonal and nondiagonal terms of the stress tensor: σ_{ij} for i=j and τ_{ij} for i≠j. The same applies to the infinitesimal strain tensor: ε_{ij} for i=j and Γ_{ij} for i≠j. Such different notation is used throughout this thesis except for Chapter 2, since this chapter deals with theoretical calculations using subscript notation. Note that in this thesis, like in rock mechanics, compressional stress is defined as a positive stress, whereas tensional stress is negative. It is important to remember that some other sciences involving elasticity use the opposite sign convention. SI-units are used throughout.

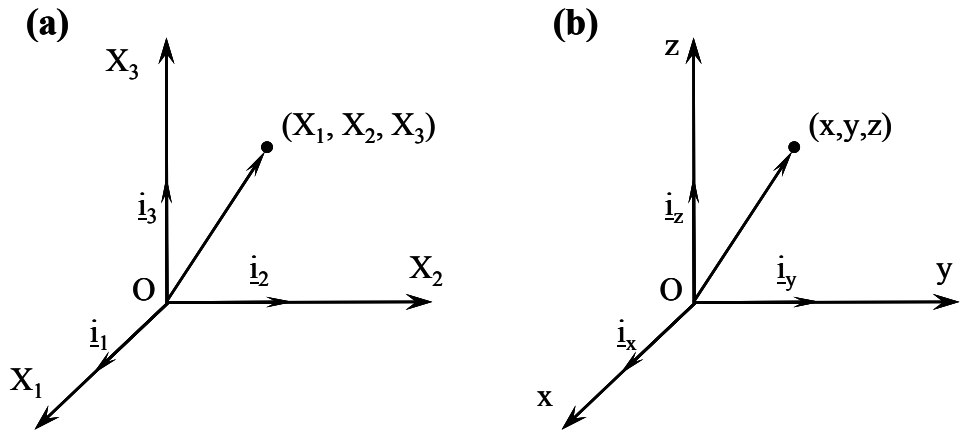

Figure 2.1. Definition of a point in space by orthogonal Cartesian coordinates with respect to a given orthogonal Cartesian reference frame with origin O and three mutually perpendicular unit vectors, (a) for the theoretical calculations and background theory background of stress, infinitesimal strain, linear elasticity and poroelasticity in Chapter 2 and (b) for all chapters in this thesis but Chapter 2. Note that the z-axis is upward directed and that depth in this thesis has a negative value.

2.1 Stress

2.1.1 Definition of stress: the stress tensor

The simplest definition of stress is that of average stress, which is defined as being force per surface through which the force is acting. However, the total force may not be equally divided over that surface area. Suppose that the area is subdivided into an infinite number of subsections, through which an infinitely small part of the total force is acting. The part of the total force may vary from one subsection to another.

Stress can therefore at best be defined by way of Euler's principle. Stress is a tensor quantity that describes the mechanical force density (force per unit area) on the complete surface of a domain inside a material body. A stress exists wherever one part of a body exerts a force on neighbouring parts. This definition of stress depends on the concept of a continuum. A continuum is an idealized material whose physical attributes are continuous functions of position. A continuum cannot have gaps or jumps (discontinuities) in its properties. Real materials are never continua. They are discontinuous at the atomic scale, and often at larger scales as well. The notion of a continuum is, therefore, only a macroscopic approximation, but it allows useful mathematical approaches to the treatment of real phenomena.

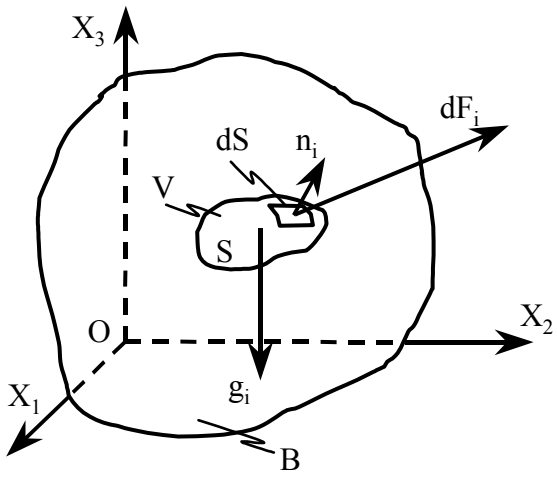

Figure 2.2. Euler's stress principle. The continuous body B contains an element of volume V surrounded by the closed surface S. An element dS on that surface has the outward normal n_i and upon it the surrounding material exerts the force dF_i. Body force g_i acts on volume V.

Consider a continuous body B (Figure 2.2). Let V be an element of volume inside it, bounded by the closed surface S. Two kinds of forces act on this volume element: body forces and surface forces. Body force g_i represents the weight of volume element V per unit mass. It is equal to the gravity acceleration. The surface forces result from Newton's third law of motion: whenever two objects interact with each other, they exert forces upon each other. Let dS be a small surface element on surface S with outward normal unit vector n_i. dF_i is the surface force that the part of body B outside S, on the positive side of n_i, exerts on the part inside through dS. This force is a function of both the size and the orientation of dS. Assume that as dS goes to zero, any moment of force or torque acting about any point on the surface dS vanishes in the limit. Then the ratio dF_i/dS tends to a finite limit:

$$T_i^n = \lim_{dS \to 0} \frac{dF_i}{dS}, \tag{2.1}$$

where the vector T_i^n is termed the traction. It represents the force per unit area acting on dS with orientation specified by n_i. Its dimension is $[ml^{-1}t^{-2}]$ or Pa. It is clear that T_i^n depends on the orientation of the surface element dS. Stress at some point completely defines the tractions for all orientations of n_i at that point by means of a stress tensor σ_{ij}:

$$\sigma_{ij} = \begin{pmatrix} \sigma_{11} & \sigma_{12} & \sigma_{13} \\ \sigma_{21} & \sigma_{22} & \sigma_{23} \\ \sigma_{31} & \sigma_{32} & \sigma_{33} \end{pmatrix}. \tag{2.2}$$

In fact, the stress tensor gives a complete description of the state of stress at a point by identifying the stresses related to three surfaces of a small parallelepiped in an orthogonal coordinate system, as shown in Figure 2.3. The dimensions of the

parallelepiped are that small, that the parallelepiped should be considered as a point-sized cube or a cube with finite size inside a region subject to a homogeneous stress. Note that the direction of the stress components is valid for the sign convention that compressive stresses are positive. The tractions that act on the concealed faces are antiparallel to those shown.

The indices i and j indicate the orientation of the single stress components: the first subscript denotes the direction of the normal to the surface on which the stress is acting and the second subscript denotes the direction of the traction. For a cube at rest, meaning that there is no net translational or rotational force acting on it, $\sigma_{ij}=\sigma_{ji}$. This reduces the number of independent components of the stress tensor to six.

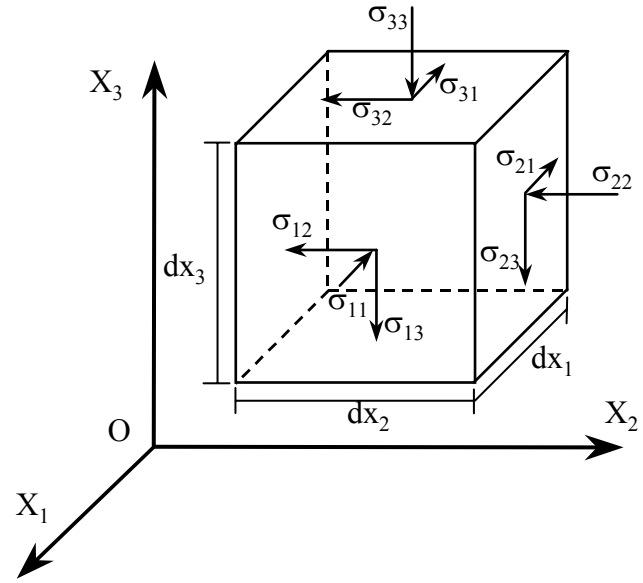

Figure 2.3. Stress components on three faces of infinitesimal parallelepiped of volume $dx_1dx_2dx_3$ for the sign convention that compressive stresses are positive.

2.1.2 Definition of normal stress and shear stress

If the stress state at a point is known, then it is possible to derive the traction across any surface with unit normal n_i passing through that point. Consider the small tetrahedron OABC inside a continuous body of Figure 2.4. Three surfaces of this tetrahedron are each parallel to two coordinate axes. Traction T_i of the fourth surface ABC with outer unit normal $n_i = \cos\alpha_i$ is searched. n_1, n_2 and n_3 are the so-called direction cosines. Note that $n_1^2 + n_2^2 + n_3^2 = 1$. Since the stress is homogeneous and the size differences of the four bounding surfaces are irrelevant because tractions are normalised to unit area, it can be stated that:

$$T_i = \sigma_{ij}n_j. \tag{2.3}$$

Eq. (2.3) is referred to as Cauchy's formula. It relates the traction across any surface within a continuous body with the stress tensor. T_i can be decomposed into a component σ_n normal to the surface and a component τ tangential to the surface.

These two components are referred to as normal- and shear stress vector, respectively. They can be calculated in terms of Cauchy's formula according to:

$$\sigma_n = \sigma_{ij}\, n_j\, n_{i,} \tag{2.4a}$$
$$\tau = \sigma_{ij}\, n_j\, t_{i,} \tag{2.4b}$$

where t_i is a unit tangent to the surface. Note that the shear stress depends on the direction of t_i. With eq. (2.4), the normal- and shear stress can be calculated for any surface passing through a point, if the stress state is known at that point.

The diagonal terms of the stress tensor are often referred to as normal stresses, since their direction is normal to the respective reference surfaces of the parallelepiped. The nondiagonal terms are often described as shear- or tangential stresses because of their tangential orientation with respect to the reference surfaces of the parallelepiped.

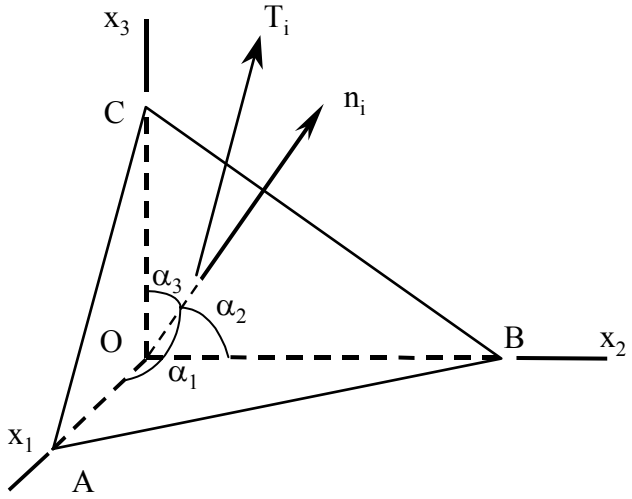

Figure 2.4. Tractions on the front face of a tetrahedron with outward normal n_i of unit length and traction T_i.

2.1.3 Principal stress

For certain orientations of the paralleleppiped of Figure 2.3 in the three-dimensional stress system, the nondiagonal terms of the stress tensor vanish, so that the stress tensor becomes particularly simple:

$$\sigma_{ij} = \begin{pmatrix} \sigma_1 & 0 & 0 \\ 0 & \sigma_2 & 0 \\ 0 & 0 & \sigma_3 \end{pmatrix}. \tag{2.5}$$

In Chapter 2.1.1 it is already shown, that the resultant stress on any surface in a body can be expressed in terms of a normal stress component and a shear stress component (Figure 2.4 and eq. (2.4)). A principal plane is defined as one on which the shear stress components vanish. The normal stress acting on such a plane is then a principal

stress, which acts in the direction of the principal stress axis. Since there are, in any specification in a state of stress, three reference directions to be considered, there are three principal stress axes. There are thus three principal stresses and their orientations to be determined to define the principal state of stress at a point. Suppose that in Figure 2.4, the cutting plane ABC is oriented such that the resultant traction T_i on the plane acts normal to it, in the direction of the outward normal to the plane n_i, and has a magnitude σ^p. The traction components on ABC are then defined by:

$$T_i = \sigma^p n_i \,. \tag{2.6}$$

The traction components on plane ABC are through eq. (2.3) also related to the stress tensor and the orientation of the plane. Subtracting eq. (2.6) from eq. (2.3) results in:

$$(\sigma_{ij} - \sigma^p \delta_{ij})\, n_j = 0, \tag{2.7}$$

where δ_{ij} is the Kronecker delta: $\delta_{ij}=1$ for $i=j$ and $\delta_{ij}=0$ for $i\neq j$. The matrix eq. (2.7) represents a set of three simultaneous, homogeneous, linear equations in n_i:

$$(\sigma_{11} - \sigma^p) n_1 + \sigma_{12} n_2 + \sigma_{13} n_3 = 0 \,, \tag{2.8a}$$
$$\sigma_{21} n_1 + (\sigma_{22} - \sigma^p) n_2 + \sigma_{23} n_3 = 0 \,, \tag{2.8b}$$
$$\sigma_{31} n_1 + \sigma_{32} n_2 + (\sigma_{33} - \sigma^p) n_3 = 0 \,, \tag{2.8c}$$

which is a classic eigenvalue problem with σ^p being the eigenvalue and n_i the eigenvector. In order to find the three values of σ^p, which are the three principal stress magnitudes, the homogeneous eq. (2.7) has to be solved. $n_i = 0$ is a trivial solution, but from the theory of eigenvectors, n_i has to be a nonzero vector. In the theory of matrices (e.g. Kreyszig 1988) it is proved that eq. (2.7) has a non-trivial (or nonzero) solution if and only if its coefficient matrix is noninvertible. The coefficient matrix is noninvertible if and only if its determinant is equal to zero:

$$\left\| \sigma_{ij} - \sigma^p \delta_{ij} \right\| = -{\sigma^p}^3 + I_1 {\sigma^p}^2 + I_2 \sigma^p + I_3 = 0 \,, \tag{2.9}$$

where I_1, I_2 and I_3 are the first, second and third stress invariant respectively:

$$I_1 = \sigma_{11} + \sigma_{22} + \sigma_{33,} \tag{2.10a}$$
$$I_2 = -(\sigma_{11}\sigma_{22} + \sigma_{22}\sigma_{33} + \sigma_{33}\sigma_{11}) + \tau_{12}^2 + \tau_{23}^2 + \tau_{31}^2, \tag{2.10b}$$
$$I_3 = \sigma_{11}\sigma_{22}\sigma_{33} + 2\tau_{12}\tau_{23}\tau_{31} - \sigma_{11}\tau_{23}^2 + \sigma_{22}\tau_{31}^2 + \sigma_{33}\tau_{12}^2. \tag{2.10c}$$

Eq. (2.9) is the so-called 'characteristic equation' of σ_{ij}. Solution of this characteristic equation yields the three principal stresses σ_1, σ_2 and σ_3, where by convention $\sigma_1 \geq \sigma_2 \geq \sigma_3$. The principal directions are then obtained by solving eq. (2.8) for n_1, n_2 and n_3, successively for the case $\sigma^p=\sigma_1$, $\sigma^p=\sigma_2$ and $\sigma^p=\sigma_3$. The stress invariants are those combinations of stress components whose values do not change under transformation of coordinates. Stress invariants become important when making use

of Haigh-Westergaard stress co-ordinates (Chapter 2.1.5). In terms of principal stress they become:

$$I_1 = \sigma_1 + \sigma_2 + \sigma_3, \tag{2.11a}$$
$$I_2 = -(\sigma_1\sigma_2 + \sigma_2\sigma_3 + \sigma_3\sigma_1), \tag{2.11b}$$
$$I_3 = \sigma_1\sigma_2\sigma_3. \tag{2.11c}$$

2.1.4 Mean stress and deviatoric stress

A stress tensor consists actually of two components: an isotropic and a deviatoric component. The isotropic stress, often referred to as mean stress, is defined as:

$$\overline{\sigma}_{ij} = \begin{pmatrix} \overline{\sigma} & 0 & 0 \\ 0 & \overline{\sigma} & 0 \\ 0 & 0 & \overline{\sigma} \end{pmatrix} = \tfrac{1}{3}\sigma_{kk}\delta_{ij} = \tfrac{1}{3}I_1\delta_{ij}\,. \tag{2.12}$$

The mean stress $\overline{\sigma}$ equals one third of the trace of the stress tensor, which is one third of the first stress invariant. The mean stress remains unaltered during any change of the coordinate axes. The deviatoric stress tensor s_{ij} is defined by:

$$s_{ij} = \sigma_{ij} - \overline{\sigma}_{ij}\,. \tag{2.13}$$

The deviatoric stress (some literature sources speak about stress deviator or stress deviation) is thus what is left of the stress once the isotropic part has been removed. It is clear that the mean stress causes uniform compression or extension. Deviatoric stress causes distortion. Similar to the stress invariants defined by eq. (2.11), invariants of stress deviation J_1, J_2 and J_3 can be defined by:

$$J_1 = s_1 + s_2 + s_3 = 0, \tag{2.14a}$$
$$J_2 = -(s_1s_2 + s_2s_3 + s_3s_1), \tag{2.14b}$$
$$J_3 = s_1s_2s_3. \tag{2.14c}$$

Note that $J_1 = 0$. This is because the mean stress is subtracted three times from a value which is equal to three times the mean stress.

2.1.5 Haigh-Westergaard stress co-ordinates

Assume now an arbitrary state of stress in a 3-dimensional principal stress space, i.e. a stress space whereby the coordinate axes are principal stress directions. The stress tensor σ_{ij} can then be described by a principal stress vector σ_i^p:

$$\sigma_i^p = \begin{pmatrix} \sigma_1 \\ \sigma_2 \\ \sigma_3 \end{pmatrix}. \tag{2.15}$$

According to eq. (2.13), a stress tensor can be described by the sum of its mean and deviatoric stress tensor. Similarly, the principal stress vector σ_i^p can be described by the sum of its mean stress vector $\overline{\sigma}_i$ and principal deviatoric stress vector s_i^p (see Figure 2.5):

$$\sigma_i^p = \begin{pmatrix} \overline{\sigma}_1 \\ \overline{\sigma}_2 \\ \overline{\sigma}_3 \end{pmatrix} + \begin{pmatrix} s_1 \\ s_2 \\ s_3 \end{pmatrix} = \begin{pmatrix} \overline{\sigma} \\ \overline{\sigma} \\ \overline{\sigma} \end{pmatrix} + \begin{pmatrix} s_1 \\ s_2 \\ s_3 \end{pmatrix} = \overline{\sigma}_i + s_i^p, \tag{2.16}$$

where $\overline{\sigma}_i$ is located in the direction of the isotropic axis, for which $\sigma_1 = \sigma_2 = \sigma_3$, while s_i^p is always located in a deviatoric plane, i.e. a plane perpendicular to the isotropic axis. A state of stress in a 3-dimensional principal stress space can be described by the Haigh-Westergaard stress co-ordinates ξ, ρ and θ (Chen & Han 1988). They are indicated in Figures 2.5 and 2.6. Figure 2.6a is a deviatoric plane view. σ_1^*, σ_2^* and σ_3^* are the projections of the principal stress axes on the deviatoric plane. $\underline{i}_1^*$, $\underline{i}_2^*$ and $\underline{i}_3^*$ are the unit vectors in the respective directions. Figure 2.6b shows the state of stress in a rendulic plane, i.e. a plane containing all three vectors σ_i^p, $\overline{\sigma}_i$ and s_i^p. Note that for the condition that $\sigma_1 \geq \sigma_2 \geq \sigma_3$, a possible state of stress only can occur in a restricted area within the principal stress space, indicated in Figure 2.6a by the shaded area.

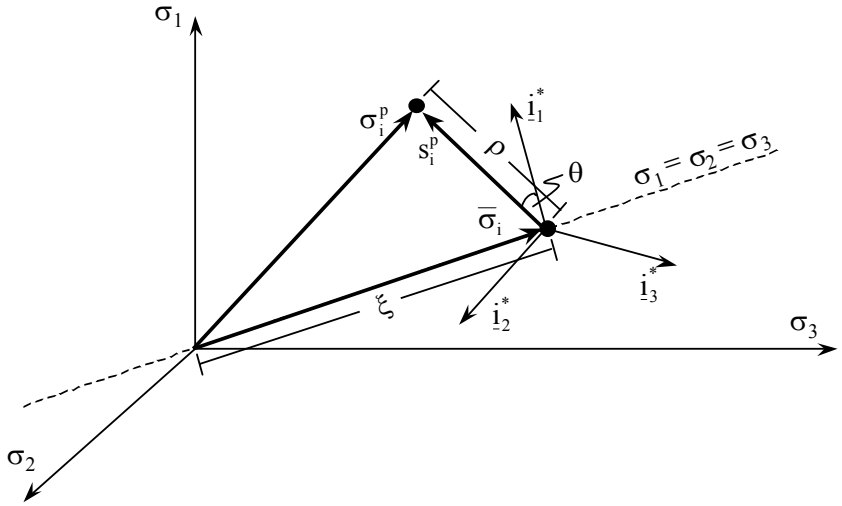

Figure 2.5. Graphical representation of principal stress vector σ_i^p, mean stress vector $\overline{\sigma}_i$, principal deviatoric stress vector s_i^p and Haigh-Westergaard stress co-ordinates ξ, ρ and θ in a 3-dimensional principal stress space. Vectors $\underline{i}_1^*$, $\underline{i}_2^*$ and $\underline{i}_3^*$ are unit vectors in the direction of the projections of the three principal stress axes onto the deviatoric plane σ_1^*, σ_2^* and σ_3^* (see Figure 2.6a). Vectors $\underline{i}_1^*$, $\underline{i}_2^*$ and $\underline{i}_3^*$ and s_i^p all lay in the same plane, which is oriented normal to the mean stress vector $\overline{\sigma}_i$.

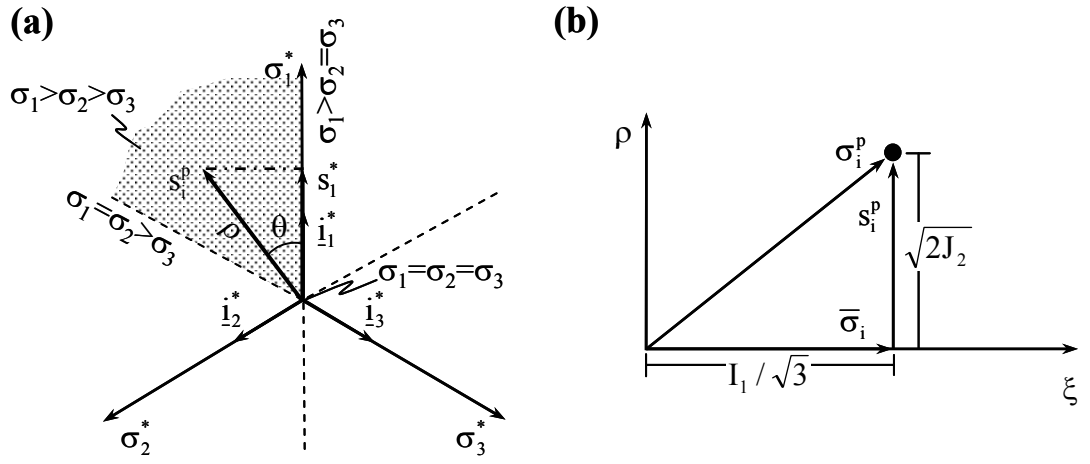

Figure 2.6. Haigh-Westergaard stress co-ordinates and stress vectors in (a) deviatoric plane view and (b) rendulic plane view. σ_1^*, σ_2^* and σ_3^* are the projections of the principal stress axes on the deviatoric plane. $\underline{i}_1^*$, $\underline{i}_2^*$ and $\underline{i}_3^*$ are the unit vectors in the respective directions. Possible states of stress under the condition that $\sigma_1 \geq \sigma_2 \geq \sigma_3$ occur in the shaded area of figure (a) only.

ξ is equal to the magnitude of the mean stress vector:

$$\xi = \sqrt{3}\bar{\sigma}_1 = \sqrt{3}\bar{\sigma}_2 = \sqrt{3}\bar{\sigma}_3 = \sqrt{3}\bar{\sigma} = I_1/\sqrt{3}\,. \tag{2.17}$$

ρ is equal to the magnitude of the deviatoric stress vector:

$$\rho = \sqrt{s_1^{\,2} + s_2^{\,2} + s_3^{\,2}}\,. \tag{2.18}$$

Making use of eq. (2.13) this becomes in terms of principal stresses:

$$\rho = \sqrt{(\sigma_1 - \bar{\sigma})^2 + (\sigma_2 - \bar{\sigma})^2 + (\sigma_3 - \bar{\sigma})^2}\,. \tag{2.19}$$

Multiplying both right hand- and left hand side of eq. (2.14b) by a factor 2 and adding formally the value of $J_1^{\,2}$, which equals zero, one obtains:

$$2J_2 = -\,2s_1s_2 - 2s_2s_3 - 2s_3s_1 + (s_1 + s_2 + s_3)^2 = s_1^{\,2} + s_2^{\,2} + s_3^{\,2} \tag{2.20}$$

and therefore:

$$\rho = \sqrt{2J_2}\,. \tag{2.21}$$

θ is defined as the angle between the projected vertical principal stress axis and the deviatoric stress vector and is positive counter clockwise (see Figures 2.5 and 2.6a). It can be determined by:

$$\cos\theta = \frac{\left|s_1^*\right|}{\rho}, \tag{2.22}$$

where $\left|s_1^*\right|$ is the magnitude of the projection of vector s_i^p onto the σ_1^*-axis, equal to the scalar product of vectors $\underline{s}^p$ and $\underline{i}_1^*$:

$$\left|s_1^*\right| = \underline{s}^p \cdot \underline{i}_1^* . \tag{2.23}$$

The vector $\underline{i}_1^*$ can be easily determined from Figure 2.7. Assume that the state of stress in point P is defined by the principal stress vector OP={1,1,1}. Vector OQ is then {0,1,1), meaning that distance OQ is $\sqrt{2}$ and QP is 1. Vector RP lies in the deviatoric plane through point P in the direction of the σ_1^*-axis. Its unit vector is the required vector $\underline{i}_1^*$. Since

$$\tan\zeta = \frac{QP}{OQ} = \frac{QR}{QP} = \tfrac{1}{2}\sqrt{2}, \tag{2.24}$$

it follows that QR=$\frac{1}{2}\sqrt{2}$. This means that vector OR=(0,1½,1½). Subtracting vector OR from vector OP results in vector RP=(1,-½,-½). The unit vector in the direction of the σ_1^*-axis becomes then:

$$\underline{i}_1^* = \frac{1}{\sqrt{6}}\begin{pmatrix} 2 \\ -1 \\ -1 \end{pmatrix}. \tag{2.25}$$

Analogously the other two unit vectors can be found:

$$\underline{i}_2^* = \frac{1}{\sqrt{6}}\begin{pmatrix} -1 \\ 2 \\ -1 \end{pmatrix}, \tag{2.26a}$$

$$\underline{i}_3^* = \frac{1}{\sqrt{6}}\begin{pmatrix} -1 \\ -1 \\ 2 \end{pmatrix}. \tag{2.26b}$$

Substituting eq. (2.25) into eq. (2.23) and noting from eq. (2.14a) that $s_2+s_3=-s_1$ and rewriting, we obtain:

$$\left|s_1^*\right| = \sqrt{\tfrac{3}{2}}s_1 . \tag{2.27}$$

It follows then from eqs. (2.21) and (2.22) that:

$$\cos\theta = \frac{\sqrt{3}s_1}{2\sqrt{J_2}}. \tag{2.28}$$

In order to express θ solely in terms of invariants, the goniometric identity $\cos3\theta = 4\cos^3\theta - 3\cos\theta$ is substituted into eq. (2.28), yielding:

$$\cos 3\theta = \frac{3\sqrt{3}}{2J_2\sqrt{J_2}}\left(s_1{}^3 - s_1 J_2\right). \tag{2.29}$$

From the expressions for the invariants of stress deviation (eq. (2.14)) it can be derived that $(s_1{}^3 - s_1J_2) = J_3$, so that:

$$\theta = \frac{1}{3}\arccos\left(\frac{3\sqrt{3}J_3}{2\left(\sqrt{J_2}\right)^3}\right). \tag{2.30}$$

The function f(x) = arccos(x) has a minimum of 0 and a maximum of π, so that:

$$0 \le \theta \le \frac{\pi}{3}. \tag{2.31}$$

On first sight, this definition of θ seems to be insufficient, since Figure 2.6a suggests that θ should vary between 0 and 2π in order to cover the full stress space. This fact is accounted for when the principal stress vector is expressed in terms of the Haigh-Westergaard stress coordinates ξ, ρ and θ. This is the next step to be taken. From eq. (2.16) it is known that the principal stress vector is the sum of the mean stress vector and the principal deviatoric stress vector. The mean stress vector in terms of Haigh-Westergaard stress coordinates can be found by combining eqs. (2.16) and (2.17):

$$\overline{\sigma}_i = \frac{1}{\sqrt{3}}\begin{pmatrix}\xi\\ \xi\\ \xi\end{pmatrix}. \tag{2.32}$$

For the principal deviatoric stress vector $s^p{}_i$, the term s_1 is known from eq. (2.28):

$$s_1 = \frac{2}{\sqrt{3}}\sqrt{J_2}\cos\theta. \tag{2.33}$$

The other two terms s_2 and s_3 can be found in a similar way as term s_1. Expressions similar to eq. (2.22) can be defined for $\left|s_2^*\right|$ and $\left|s_3^*\right|$, see Figure 2.6a, with $\left|s_2^*\right|$ and $\left|s_3^*\right|$ being the magnitudes of the projection of vectors $s^p{}_i$ onto the $\sigma_2{}^*$- and $\sigma_3{}^*$-axis, respectively:

$$\cos\left(\tfrac{2\pi}{3}-\theta\right)=\frac{\left|s^{2*}{}_i\right|}{\rho}, \tag{2.34a}$$

$$\cos\left(\tfrac{2\pi}{3}+\theta\right)=\frac{\left|s^{3*}{}_i\right|}{\rho}. \tag{2.34b}$$

As in eq. (2.23), $\left|s_2^*\right|$ and $\left|s_3^*\right|$ are equal to the scalar products of vector $s^p{}_i$ and the unit vectors $\underline{i}_2^*$ and $\underline{i}_3^*$, respectively:

$$\left|s_2^*\right| = s_i^p \cdot \underline{i}_2^*, \tag{2.35a}$$

$$\left|s_3^*\right| = s_i^p \cdot \underline{i}_3^*. \tag{2.35b}$$

Combining the eqs. (2.34), (2.35) and (2.26) and knowing that $s_1 + s_2 + s_3 = 0$ results in:

$$s_2 = \frac{2}{\sqrt{3}}\sqrt{J_2}\cos\left(\tfrac{2\pi}{3}-\theta\right), \tag{2.36a}$$

$$s_3 = \frac{2}{\sqrt{3}}\sqrt{J_2}\cos\left(\tfrac{2\pi}{3}+\theta\right). \tag{2.36b}$$

The principal stress vector can now be expressed in terms of Haigh-Westergaard stress coordinates by substituting eqs. (2.32), (2.33) and (2.36) into eq. (2.16):

$$\sigma_i^p = \frac{1}{\sqrt{3}}\begin{pmatrix}\xi\\ \xi\\ \xi\end{pmatrix} + \sqrt{\tfrac{2}{3}}\rho\begin{pmatrix}\cos\theta\\ \cos\left(\theta-\frac{2\pi}{3}\right)\\ \cos\left(\theta+\frac{2\pi}{3}\right)\end{pmatrix}. \tag{2.37}$$

The expression of a state of stress at a point in terms of Haigh-Westergaard coordinates becomes important when we deal with Mobilised Shear Capacity, i.e. the proximity of a stress state in a rock volume to failure, in Chapter 9.

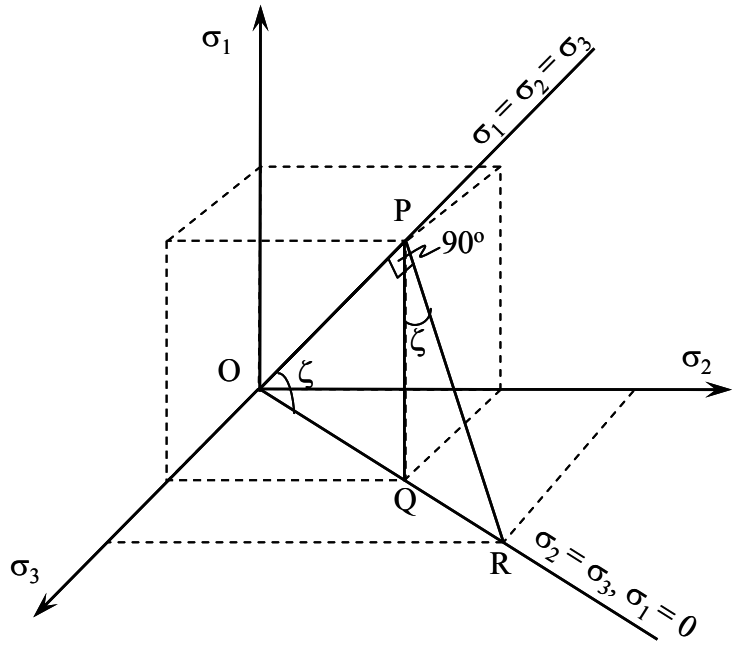

Figure 2.7. Geometrical relations in the 3-dimensional principal stress space.

2.2 Infinitesimal strain

Consider the situation shown in Figure 2.8, where a stress σ_{33} is acting on top of a rock sample, which in turn is supported by the ground. Suppose now that the stress pushes on the rock to such an extent, that the rock deforms as shown in Figure 2.8.
The stress causes the height L of the sample to be reduced to L'. Because the sample is unconfined at its lateral sides, σ_{33} causes the width D of the sample to be increased to D'. If the relative position of the particles within a sample are changed, so that the new positions cannot be obtained simply by a rigid translation and/or rotation of the sample, the sample is said to be strained. There exist two kinds of strain: elongation, often referred to as normal strain or simply 'strain', and shear strain. Normal strain is the change in length per unit length. It is the type of strain shown in Figure 2.8:

$$\varepsilon_{33} = \frac{L - L'}{L}, \tag{2.38b}$$

$$\varepsilon_{11} = \varepsilon_{22} = \frac{D - D'}{D}. \tag{2.38b}$$

Note that the definitions according to eq. (2.38) bring about that normal strain is positive for contraction and negative for expansion, which is in accordance with the sign convention for stresses.

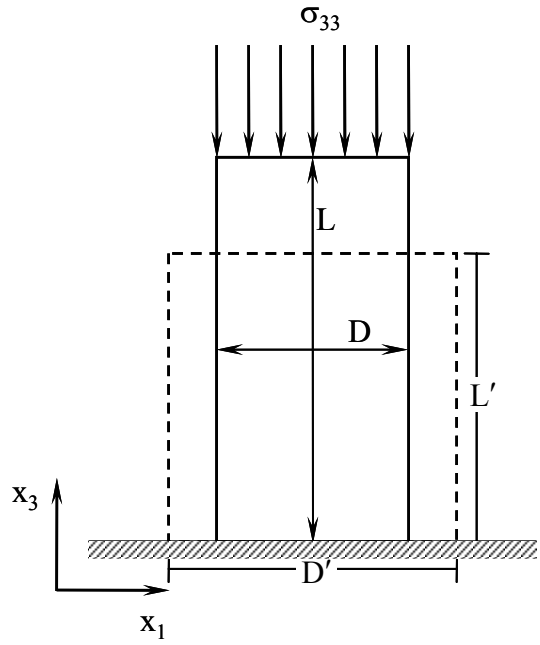

Figure 2.8. Deformation (dashed line) of an unconfined sample with height L and width D under uniaxial load σ_{33}.

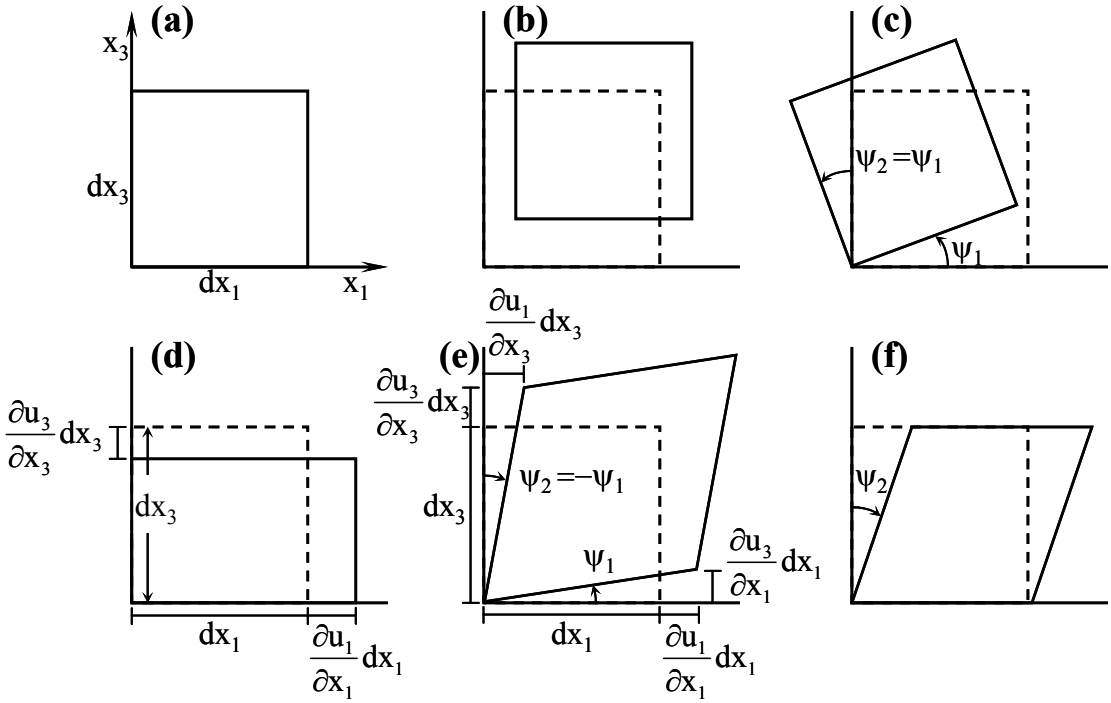

Figure 2.9. Examples of different types of deformation: (a) undeformed, this stage is shown in the other five figures by dotted lines; (b) translation; (c) rotation; (d) normal strain; (e) pure shear strain; (f) simple shear strain.

Figure 2.9 shows examples of different types of deformation. Figures 2.9b and c show two kinds of strainless (rigid body) deformation: translation and rotation. Figure 2.9d illustrates normal strain. The situation is similar as that shown in Figure 2.8, but now the so-called infinitesimal strain is introduced in order to arrive at the infinitesimal

strain tensor ε_{ij}. Consider the normal strain in the x_1-direction ε_{11}. In accordance to eq. (2.38) it follows that:

$$\frac{du_1}{dx_1} \rightarrow \frac{\partial u_1}{\partial x_1} \equiv \varepsilon_{11} \text{ as } dx_1 \rightarrow 0. \tag{2.39}$$

Infinitesimal strain means that derivatives such as eq. (2.39) are small relative to one, so their products are very small and can be ignored. In practice this means that displacements of contiguous particles differ only by an infinitesimal amount, so that the absolute distance from the origin of the coordinate system does not affect the displacement gradients such as expressed in eq. (2.39). Although infinitesimal strain is a mathematical approximation, it is much more amenable to sophisticated mathematical treatment (e.g. in the theory of elasticity) than finite strain, in which the analysis of strain is concerned with the change of distance between pairs of points. the assumption of ignorance of products of displacement derivatives is justified since many important geologic deformations are small over short time frames. Rewriting eq. (2.39) leads to:

$$du_1 \equiv \frac{\partial u_1}{\partial x_1} dx_1. \tag{2.40}$$

This relation is indicated in Figures 2.9d and e. Figure 2.9e illustrates shear strain. Shear strain Γ is defined by:

$$\Gamma = \tfrac{1}{2}\Psi = \tfrac{1}{2}(\Psi_1 - \Psi_2), \tag{2.41}$$

with Ψ being the angle change between two initially orthogonal directions. Ψ is positive counter clockwise. In the case that $\Psi_2 = -\Psi_1$, pure shear strain applies: there is no rotation. In the case that $\Psi_2 = \Psi_1$, there is only rotation without shear strain (Figure 2.9c). Note that eq. (2.41) indeed results in a shear strain of zero for this case. In fact, it averages the two angles Ψ_1 and Ψ_2, so that the rotational component is filtered out from the deformation and the shear strain remains. Note that simple shear strain, as shown in Figure 2.9f, is a combination of pure shear strain and rotation. From Figure 2.9e it follows that:

$$\tan \Psi_1 = \frac{\partial u_3}{\partial x_1} dx_1 \Bigg/ \left(dx_1 + \frac{\partial u_1}{\partial x_1} dx_1 \right), \tag{2.42}$$

which simplifies to:

$$\tan \Psi_1 = \frac{\partial u_3}{\partial x_1 + \partial u_1}. \tag{2.43}$$

Infinitesimal strain implies, although not shown in Figure 2.9e, that du_i is actually much smaller than dx_i. Considering that the same holds for ∂u_1 and ∂x_1 and that for small angles the tangent of an angle equals the angle itself in radians, it is:

$$\Psi_1 \approx \tan \Psi_1 = \frac{\partial u_3}{\partial x_1}. \tag{2.44}$$

Analogously one finds for Ψ_2:

$$\Psi_2 = \frac{\partial u_1}{\partial x_3}. \tag{2.45}$$

From eqs. (2.41), (2.44) and (2.45), the shear strain can be defined as:

$$\Gamma_{31} = \Gamma_{13} = \varepsilon_{31} = \varepsilon_{13} = \tfrac{1}{2}\left(\frac{\partial u_3}{\partial x_1} + \frac{\partial u_1}{\partial x_3}\right). \tag{2.46}$$

With similar conditions and procedures for the third dimension, the infinitesimal stress tensor becomes:

$$\varepsilon_{ij} = \begin{pmatrix} \varepsilon_{11} & \varepsilon_{12} & \varepsilon_{13} \\ \varepsilon_{21} & \varepsilon_{22} & \varepsilon_{23} \\ \varepsilon_{31} & \varepsilon_{32} & \varepsilon_{33} \end{pmatrix} = \begin{pmatrix} \dfrac{\partial u_1}{\partial x_1} & \tfrac{1}{2}\left(\dfrac{\partial u_1}{\partial x_2} + \dfrac{\partial u_2}{\partial x_1}\right) & \tfrac{1}{2}\left(\dfrac{\partial u_1}{\partial x_3} + \dfrac{\partial u_3}{\partial x_1}\right) \\ \tfrac{1}{2}\left(\dfrac{\partial u_2}{\partial x_1} + \dfrac{\partial u_1}{\partial x_2}\right) & \dfrac{\partial u_2}{\partial x_2} & \tfrac{1}{2}\left(\dfrac{\partial u_2}{\partial x_3} + \dfrac{\partial u_3}{\partial x_2}\right) \\ \tfrac{1}{2}\left(\dfrac{\partial u_3}{\partial x_1} + \dfrac{\partial u_1}{\partial x_3}\right) & \tfrac{1}{2}\left(\dfrac{\partial u_3}{\partial x_2} + \dfrac{\partial u_2}{\partial x_3}\right) & \dfrac{\partial u_3}{\partial x_3} \end{pmatrix}, \tag{2.47}$$

or shortly:

$$\varepsilon_{ij} = \left(\frac{\partial u_i}{\partial x_j} + \frac{\partial u_j}{\partial x_i}\right). \tag{2.48}$$

2.3 Elasticity and elastic moduli

Consider again the situation in Figure 2.8, where σ_{33} causes a contractional strain in the corresponding direction ε_{33} and an expansion $\varepsilon_{11} = \varepsilon_{22}$ in the two horizontal directions. Assume now that the loaded material behaves as a homogeneous, isotropic, solid continuum and that there exists a linear relation between the applied stress σ_{33} and the normal strain in the corresponding direction ε_{33}. The rock is then said to behave linear elastically according to:

$$\sigma_{33} = E \cdot \varepsilon_{33}. \tag{2.49}$$

Eq. (2.49) is known as Hooke's law. E is termed Young's modulus or E-modulus. It represents the stiffness of a material, i.e. the resistance against compression under uniaxial loading conditions such as shown in Figure 2.8. The ratio

$$\nu = -\frac{\varepsilon_{11}}{\varepsilon_{33}} = -\frac{\varepsilon_{22}}{\varepsilon_{33}}, \tag{2.50}$$

with $0 \leq \nu \leq 0.5$, is the Poisson's ratio. It is a measure of lateral expansion relative to longitudinal contraction. A Poisson's ratio of 0.5 means that $\varepsilon_{33} = -2\varepsilon_{11} = -2\varepsilon_{22}$, i.e. the expansion of the sample is equal to its contraction. It is valid for the theoretical case of incompressible materials and is often assumed for fluids or to model a hydrostatic state of stress in salt layers/structures.

Note that eqs. (2.49) and (2.50) are valid for unconfined samples, i.e. samples where $\sigma_{33} \neq 0$ and $\sigma_{11} = \sigma_{22} = 0$. In reality, rocks in the subsurface are not unconfined such as in the previous example, but confined. In the case that the sample is confined and no horizontal strain is allowed, a horizontal stress builds up, whereby its magnitude depends on the Poisson's ratio of the sample. The Poisson's ratio is then a measure of the translation of the vertical stress into the horizontal direction. A horizontal stress build up, on the other hand, is being 'translated' again via the Poisson's ratio into the vertical direction. Summarized, eq. (2.49) becomes, fulfilling eq. (2.50), in terms of stress and strain tensor:

$$\varepsilon_{ij} = \frac{1}{E}[(1+\nu)\sigma_{ij} - \nu\sigma_{kk}\delta_{ij}]. \tag{2.51}$$

In terms of stress this becomes:

$$\sigma_{ij} = \lambda\varepsilon_{kk}\delta_{ij} + 2\mu\varepsilon_{ij}, \tag{2.52}$$

where λ and μ are Lamé's parameters:

$$\lambda = \frac{E\nu}{(1+\nu)(1-2\nu)}, \tag{2.53a}$$

$$\mu = \frac{E}{2(1+\nu)} \equiv G. \tag{2.53b}$$

Note that eqs. (2.51) and (2.52) are valid for a homogeneous, solid material. When dealing with a poroelastic material, i.e. a porous and permeable medium where the pores are completely filled (saturated) with pore fluid, the mentioned stress tensors are in terms of effective stresses (see Chapter 2.4).

Eq. (2.53) introduces the shear modulus G, which is a measure of the sample's resistance against shear deformation. Another important elastic modulus is the bulk modulus K. It is a measure of the sample's resistance against hydrostatic compression. In accordance to eq. (2.49) it is defined as the ratio of isotropic or mean stress $\overline{\sigma}$

relative to the volumetric strain ε_v (note that $\overline{\sigma} = \sigma_{11} = \sigma_{22} = \sigma_{33}$ and $\sigma_{12} + \sigma_{23} + \sigma_{31} = 0$):

$$K = \frac{\overline{\sigma}}{\varepsilon_v} = \lambda + \tfrac{2}{3}\mu, \tag{2.54}$$

where

$$\varepsilon_v = \varepsilon_{kk}. \tag{2.55}$$

2.4 Total and effective stress and poroelasticity

The general relations between stresses and strains according to eq. (2.52) are valid for isotropic homogeneous solid materials without pore volume. However, rocks are generally composite materials incorporating a pore volume, which influences not only their elastic response, but also their yield stresses etc. Especially when dealing with hydrocarbon reservoirs, the effective stress concept, introduced first by Terzaghi (1943), has to be considered. The effective stress, rather than the total stress, determines whether the rock fails or not due to the external load. The theory of poroelasticity, introduced by Biot (1962), refines this effective stress concept. According to the theory of poroelasticity, where the material considered is a porous and permeable medium and the pores are saturatedly filled with fluid, the effective stress concept can be expressed as (Biot 1962):

$$\sigma_{ij} = \sigma'_{ij} + \alpha p \delta_{ij}, \tag{2.56}$$

with

$$\alpha = 1 - \frac{K_{fr}}{K_s}, \tag{2.57}$$

where K_{fr} and K_s are the bulk modulus of the framework of the rock and solid rock particles, respectively. α is termed the Biot-constant. The physical meaning of eq. (2.56) is that a total external stress σ_{ij} acting on a porous rock saturated with fluid is subdivided into two parts: an effective stress σ'_{ij}, working on the framework of the rock sample, and a part $\alpha p \delta_{ij}$, carried by the fluid. The remaining part of the pore pressure, $(1-\alpha)p\delta_{ij}$, is counteracted by internal stresses in the solid. In view of this effective stress principle, eqs. (2.51) and (2.52) have to read:

$$\varepsilon_{ij} = \frac{1}{E}[(1+\nu)\sigma'_{ij} - \nu\sigma'_{kk}\delta_{ij}], \tag{2.58}$$

$$\sigma'_{ij} = \lambda\varepsilon_{kk}\delta_{ij} + 2\mu\varepsilon_{ij}. \tag{2.59}$$

The upper limit for K_{fr} is the so-called Voigt bound $(1-\varphi)K_s$ (Watt *et al.* 1976). The lower limit for K_{fr} is zero, so that $\varphi \leq \alpha \leq 1$. For weak rocks, α is close to 1. Laboratory

measurements on Slochteren Sandstone, in which the Groningen gas is captured, give a value for α of 0.9 ± 0.1 (Hettema *et al.* 1998). In order to avoid the time consuming process of fully coupled mechanical-fluid flow finite element calculations, a value of 1.0 is assumed in the geomechanical models for this study. For more details on the application of effective stress principles on geomechanical modelling see Chapter 3.

3 GENERAL CONCEPTS OF FAULT REACTIVATION AND ROCK FAILURE IN PRODUCING HYDROCARBON RESERVOIRS

Generally it is assumed, that seismic events associated with pore pressure changes in hydrocarbon reservoirs are the result of reactivation of existing faults or joints in or near the reservoir (see Chapter 6 for more background on this assumption). Faults and joints in rocks are the result of in-situ stress conditions which exceed the strength of the rock, so that the rock yields and deforms irreversibly. The rock is said to deform plastically. Irreversible rock deformation can be the result of shear failure, tensile cracking or pore collapse. Shear failure on pre-existing geological faults is the most common failure mechanism in producing hydrocarbon reservoirs and occurs when the development of shear stress on a fault plane exceeds its shear resistance. This chapter describes the conceptual background of fault reactivation and rock failure as a result of stress changes due to production in hydrocarbon reservoirs. First the general concepts of failure mechanics are introduced (Chapter 3.1), in particular the Mohr-Coulomb failure criterion, since this criterion is widespread in rock mechanics and used in the finite-element calculations for this thesis. Subsequently the effects of hydrocarbon production on the subsurface stress field and their implication on failure are discussed. A brief overview of stress regimes and associated types of faulting in the subsurface is given in Chapter 3.2. Starting from the theory of poroelasticity (see Chapter 2.4), the general concept of differential stress development in hydrocarbon reservoirs and its implication on fault reactivation is discussed in Chapters 3.3 and 3.4, respectively.

3.1 General concepts of failure mechanics: the Mohr-Coulomb failure criterion

As explained in Chapter 2.1.2, it is possible to derive the shear- and normal stress across any surface passing through a point if the stress state at that point is known. This means that the stress state in the subsurface results in shear- and normal stresses on the fault planes present in the subsurface. When the shear stress along such a fault plane is too large, the fault will slip or reactivate and shear failure occurs. In accordance to Mohr, the failure could be described by a failure criterion, in general expressed by function f:

$$|\tau| = f(\sigma'_n), \tag{3.1}$$

where τ is the shear stress magnitude along the plane and σ'_n is the effective normal stress magnitude across the plane. Note the use of effective stresses when dealing with rock failure, since rocks are generally composite materials incorporating a pore volume. As explained in Chapter 2.4, an external total stress acting on a porous rock

saturated with pore content is subdivided into two parts: an effective stress, working on the framework of the rock sample, and a pore pressure, carried by the fluid (internal stresses in the solid are neglected for simplicity, which is the same as assuming a Biot-coefficient equal to 1.0). Since failure occurs between particles of the rock and therefore concerns failure of the framework of the rock, the effective stress, rather than the total stress, determines whether the rock fails or not due to the external load.

Consider the situation as shown in Figure 3.1a. Note that, according to definition, $\sigma'_1 > \sigma'_3$. From force equilibrium it can be derived that:

$$\sigma'_n = \tfrac{1}{2}(\sigma'_1 + \sigma'_3) + \tfrac{1}{2}(\sigma'_1 - \sigma'_3)\cos 2\beta, \tag{3.2a}$$
$$\tau = \tfrac{1}{2}(\sigma'_1 - \sigma'_3)\sin 2\beta. \tag{3.2b}$$

Note that, when inserting the expression $\sigma' = \sigma - \alpha p$ into eqs. (3.2a) and (3.2b), only the normal stress is affected: we can speak in terms of total normal stress or effective normal stress. A shear stress is unaffected by a pore pressure. Plotting the corresponding values of σ'_n and τ according to eq. (3.2) in a diagram results in the so-called Mohr's circle, which' radius is equal to the maximum shear stress τ_{max}. The latter stress is the largest shear stress possible on the fault plane and occurs in case that the orientation of the fault is under an angle of 45^o towards the direction of the largest principal stress. Note that the situation analysed in Figure 3.1a is in fact a 2-dimensional situation for the principal stress combination σ'_1 and σ'_3 (plane stress assumption). The more complicated Mohr's construction in three dimensions is not treated in detail here, but its basic features are shown in Figure 3.1c. As is visible, similar principles in defining the Mohr's circles occur for the other two principal stress combinations. The shaded region contains all possible combinations of τ and σ'_n for the given effective principal stresses.

In Figure 3.1, possible Mohr functions according to eq. (3.1) are shown: linear functions according to the Mohr-Coulomb failure criterion, defined by the two parameters c (cohesion) and ϕ (angle of internal friction or simply called 'friction angle'):

$$|\tau| = c + \sigma'_n \tan\phi. \tag{3.3}$$

The term '$\tan\phi$' is often referred to as 'coefficient of internal friction', described by the symbol μ. The cohesion of pre-existing faults is often assumed to be zero. Eq. (3.3) defines graphs that separate a safe region from a failure region. Failure occurs when a state of stress is located at the failure line. Note that for intact rock this is as soon as Mohr's circle touches the failure line.

Failure for a pre-existing fault plane requires a combination of normal effective- and shear stress such that it results in a location on the failure line. This depends on the fault dip angle β. From Figure 3.1a it follows, that the most critical angle for β is:

$$\beta_{crit} = 45^o + \phi/2. \tag{3.4}$$

This angle β_{crit} is defined with respect to the direction of the smallest principal stress σ'_3. The angle between the most critical failure plane and the direction of the largest principal stress σ'_1 is 45º - ϕ/2. When a state of stress on intact rock exceeds the rock strength, the orientation of the failure plane is under this angle. The strike direction of the failure plane will be in the direction of the intermediate principal stress. Figure 3.1b shows the state of failure and associated Mohr's circle for a fault dip angle different from the most critical angle. For a fault orientation such that one of the principal stress directions is normal to the fault plane, no shear stress is present. Failure is then only possible when this normal principal stress exceeds the tensile strength of the fault. Assuming a cohesion of zero for the fault this is for the situation in Figure 3.1b when $\sigma'_3 = 0$.

By inserting the equations for τ and σ'_n (eq. (3.2)) into eq. (3.3), using the relation given by eq. (3.4) and rearranging, the Mohr-Coulomb failure criterion can be expressed in terms of principal stresses instead of normal effective- and shear stress:

$$\sigma'_1 = \frac{2c\cos\phi}{1-\sin\phi} + \sigma'_3 \frac{1+\sin\phi}{1-\sin\phi}. \tag{3.5}$$

Note that eq. (3.5) is only valid for intact rock at failure or for existing failure planes with an orientation of 45º - ϕ/2 with respect to the largest principal stress direction. Eq. (3.5) is plotted graphically in Figure 3.2. Note that for $\sigma'_3 = 0$, the uniaxial compressive strength C_u of a rock is obtained:

$$C_u = \frac{2c\cos\phi}{1-\sin\phi}. \tag{3.6}$$

Note from eq. (3.5), that pure shear failure, as defined by Mohr's hypothesis, depends only on the minimum and maximum principal effective stresses and not on the intermediate stress (remember the assumption that $\sigma'_1 \geq \sigma'_2 \geq \sigma'_3$). This principle is graphically illustrated in Figure 3.1b, where the shaded region contains all possible combinations of τ and σ'_n for the given effective principal stresses.

Figure 3.3 shows the Mohr-Coulomb failure surface in a 3-dimensional stress space. Figure 3.2 is in fact a projection of this failure surface onto the σ'_1, σ'_3-plane and contains also the Mohr-Coulomb failure line in accordance to eq. (3.5) for the case that $\sigma'_1 < \sigma'_2 < \sigma'_3$. Note the symmetry about $\sigma'_1 = \sigma'_3$. σ'_2 is the intermediate stress for both failure lines. Projections similar to Figure 3.2 are obtained for the cases that σ'_1 and σ'_3 are intermediate. Combining these projections results in the hexagonal pyramidal shape of the Mohr-Coulomb failure surface in a 3-dimensional stress space as shown in Figure 3.3a. The principal effective stress vector, the mean effective stress vector and the principal deviatoric stress vector as well as the Haigh-Westergaard stress coordinates (see Chapter 2.1.5) are shown for reference.

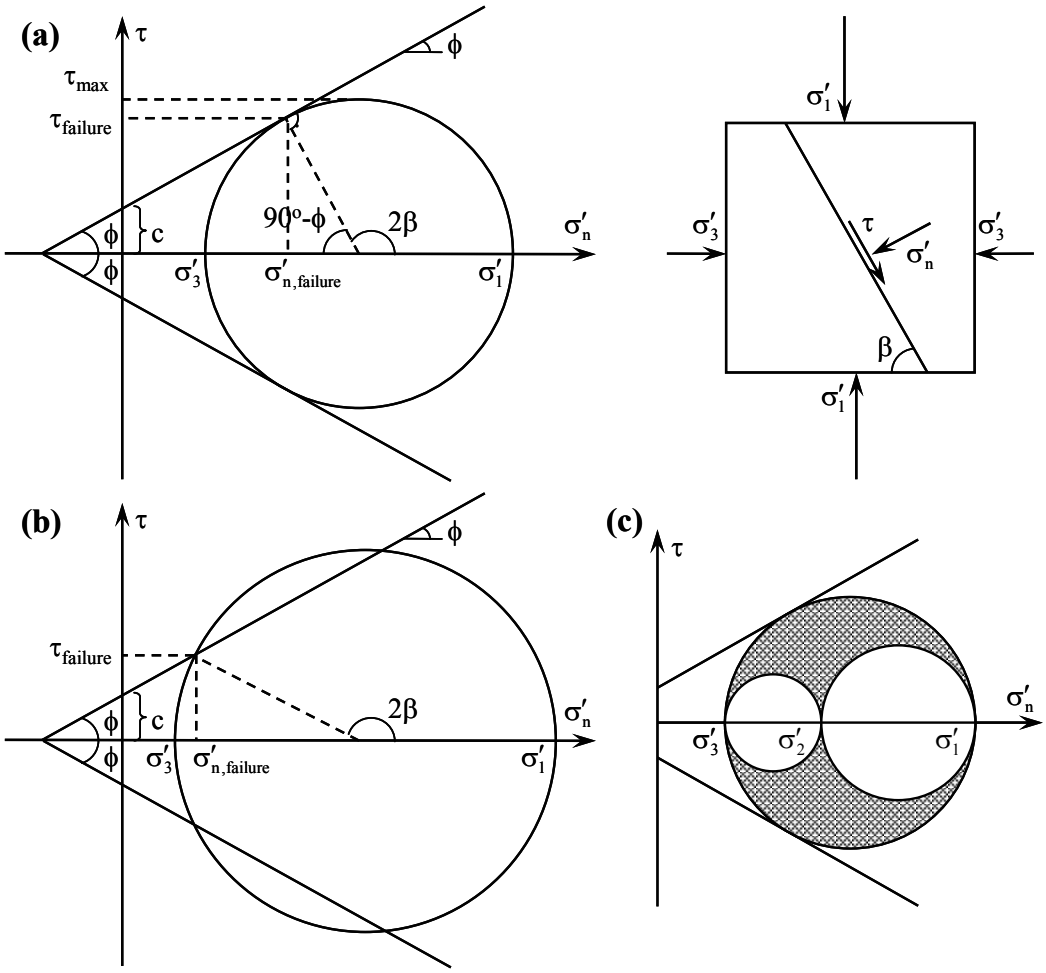

Figure 3.1. *(a) Shear- and normal effective stress on a plane in dependency of its orientation relative to the maximum and minimum principal effective stresses shown by a Mohr's circle. The straight lines in the shear stress / normal effective stress diagram indicate a Mohr-Coulomb failure criterion. The figure indicates failure of intact rock or of a pre-existing fault plane with the most critical dip angle $\beta_{crit}=45^o+\phi/2$ (see eq. (3.4)). (b) Same as Figure (a), with the difference that the figure indicates failure of a fault plane with a dip angle different from the most critical dip angle. (c) Mohr's circles for a 3-dimensional anisotropic principal stress state and Mohr-Coulomb failure criterion.*

Figure 3.3 also shows the Mohr-Coulomb failure criterion in deviatoric and rendulic plane view, respectively. A deviatoric plane is a plane perpendicular to the hydrostatic axis. In Figure 3.3 it is chosen such that it contains the principal deviatoric stress vector. A rendulic plane is a plane containing the hydrostatic axis. Deviatoric planes are often referred to as π-planes, although a π-plane is actually a deviatoric plane through the point $(\sigma'_1,\sigma'_2,\sigma'_3)=(0,0,0)$. Any possible state of stress in a rock volume or on a fault plane lies within the hexagonal pyramid (elastic deformation) or at the hexagonal pyramid (plastic deformation). A stress state can theoretically never be outside of the pyramid. For the condition that $\sigma'_1 \geq \sigma'_2 \geq \sigma'_3$, a possible state of stress only can occur in a restricted area within the principal stress space, indicated in the rendulic plane view by the shaded area.

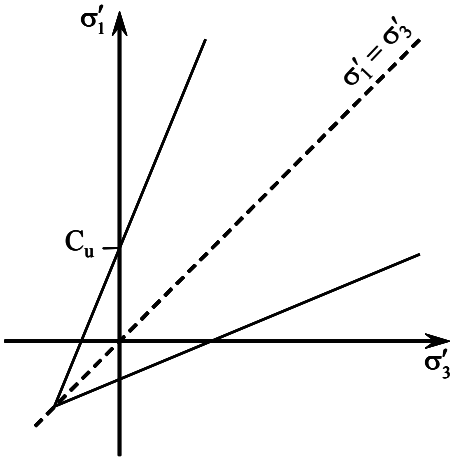

Figure 3.2. Failure lines in on the σ'_1, σ'_3-plane for the cases $\sigma'_1 > \sigma'_3$ and $\sigma'_1 < \sigma'_3$.

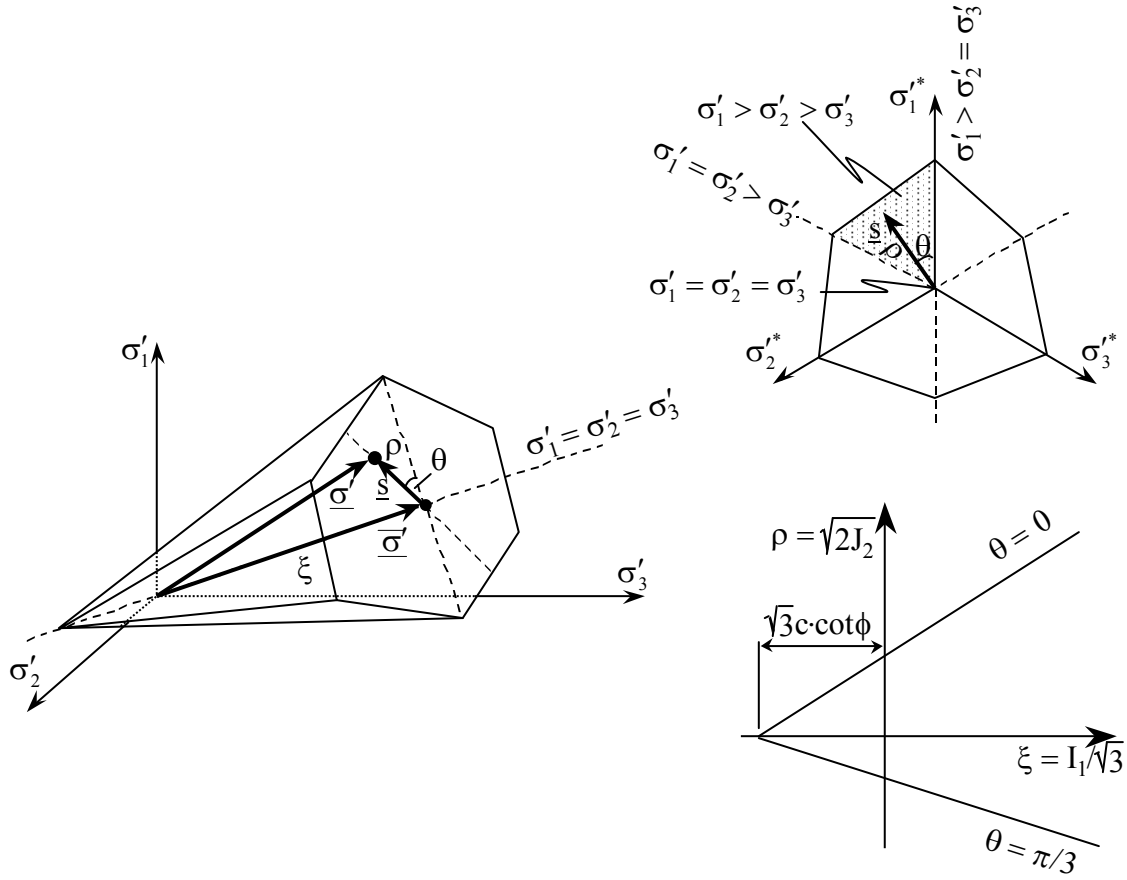

Figure 3.3. The Mohr-Coulomb failure surface in 3-dimensional principal stress space with indication of an effective stress vector, a mean effective stress vector and a deviatoric stress vector. Top right figure: deviatoric plane view. Bottom right figure: rendulic plane view. ξ, ρ and θ are Haigh-Westergaard stress coordinates (see Chapter 2.1.5). For the condition that $\sigma'_1 \geq \sigma'_2 \geq \sigma'_3$, a possible state of stress only can occur in a restricted area within the principal stress space, indicated in the rendulic plane view by the shaded area.

The Mohr-Coulomb failure criterion may also be presented in the form of a so-called yield function $F(\sigma'_1, \sigma'_3, c, \phi)$ which takes on values less than zero for states of stress within the hexagonal pyramid and zero on the failure surface itself:

$$F(\sigma'_1, \sigma'_3, c, \phi) = \tfrac{1}{2}\sigma'_1(1 - \sin\phi) - \tfrac{1}{2}\sigma'_3(1 + \sin\phi) - c\cos\phi. \qquad (3.7)$$

The yield function becomes important in the derivation of the Mobilised Shear Capacity for rock volumes. This is further explained in Chapter 9.

3.2 Stress regimes and fault types in the subsurface

Figure 3.4 gives a possible classification of stresses in the subsurface (after Amadei & Stephansson 1997). Stresses in rock can be divided into initial or virgin stresses and induced stresses. Initial stresses mainly originate from gravity and present-day or past tectonic activity. This is also the case for the Northern Netherlands. In addition, halokinesis plays a role in this region. Induced stresses are associated with artificial disturbance such as mining activities or are induced by changes in natural conditions (drying, swelling, consolidation etc.). In the northern Netherlands, gas production and storage and salt mining are the main sources of induced stresses.

A 3-dimensional stress field in the subsurface is often described by the three stress components σ_v, σ_H and σ_h and the pore pressure p, where σ_v is the vertical total stress, σ_H is the maximum horizontal total stress and σ_h is the minimum horizontal total stress. This description has to be seen in the perspective of the often made assumption, that the vertical stress is a principal stress. σ_H and σ_h are then automatically principal stresses as well.

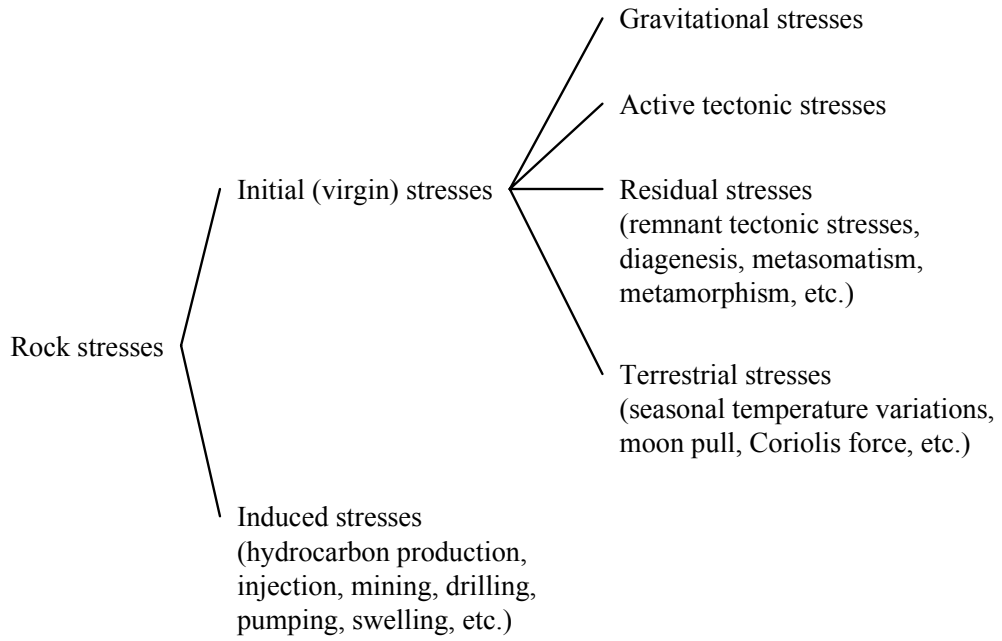

Figure 3.4. Possible classification of rock stresses (after Amadei & Stephansson 1997).

Horizontal and vertical stresses are often described by the so-called effective stress ratio K_0. Because later in this thesis it is dealt with 3-dimensional anisotropic stress fields, two distinct effective stress ratios K_{0H} and K_{0h} are introduced as:

$$K_{0H} = \frac{\sigma'_H}{\sigma'_v}, \tag{3.8}$$

$$K_{0h} = \frac{\sigma'_h}{\sigma'_v}, \tag{3.9}$$

with σ'_v, σ'_H and σ'_h being the vertical, maximum horizontal and minimum horizontal effective stress, respectively. In most cases, vertical stress at a certain depth originates solely from the gravitational weight of the overlying formations. If the density varies with depth, the vertical total stress due to gravity becomes:

$$\sigma_v = \int_z^0 \rho(z) g_i dz\,. \tag{3.10}$$

In here, g_i is the gravity acceleration, z is the depth whereby the z-axis is pointing vertically upwards and $\rho(z)$ is the rock density as a function of the depth. The horizontal gravitational stresses are usually determined under the assumption that the rocks are laterally constrained, so that $\varepsilon_h = 0$. The rock can then deform solely vertically and the horizontal stress results then from the 'translation' of the vertical stress into the horizontal directions via the Poisson's ratio. From eq. (2.73) it follows with $\sigma'_H = \sigma'_h = \sigma'_{11} = \sigma'_{22}$, $\varepsilon_h = \varepsilon_{11} = \varepsilon_{22} = 0$ and $\sigma'_v = \sigma'_{33}$ that:

$$\sigma'_H = \sigma'_h = \frac{\nu}{1-\nu}\sigma'_v\,. \tag{3.11}$$

For instance for $\nu = 0.2$, this results in $K_{0H} = K_{0h} = 0.25$. It has to be mentioned here that eq. (3.11) is used to determine horizontal gravitational stresses. It should in general not be used to estimate present horizontal stresses in a formation. No sediment will be exposed to perfectly elastic conditions with constant rock properties over millions of years, but tectonic activity and other geological processes have very likely put its stamp on the initial in-situ state of stress. K_0-values can vary significantly, from 0.2 to 1.5 at larger depths (deeper than approximately 1500m) (Fjaer *et al.* 1992).

According to the theories of shear failure (e.g. Mohr-Coulomb), fracturing or faulting will take place in one or both of a pair of conjugate planes which are parallel with the direction of the intermediate principal stress, and are both at equal angles of less than 45^o to the direction of the greatest principal stress (see Chapter 3.1). Under the assumption that the vertical stress is a principal stress, this means for the case $\sigma'_v > \sigma'_H > \sigma'_h$, that normal faulting occurs, whereby the faults have dip angles greater than 45^o (see Figure 3.5). The stress regime is said to be extensional. In the case that the horizontal stresses are high, such that the vertical stress is the smallest principal stress ($\sigma'_H > \sigma'_h > \sigma'_v$), thrust or reverse faulting occurs, whereby the fault dip angle

is less than 45°. A compressional stress regime occurs. If the intermediate principal stress is vertical ($\sigma'_H > \sigma'_v > \sigma'_h$), vertical failure planes are created incorporating strike-slip and a strike-slip stress regime occurs. The above descriptions are based on the well-known Anderson's fault classification (Anderson 1951). Stress regimes whereby two of the three principal stresses are equal are indicated by different names. The stress regimes with $\sigma'_1 > \sigma'_2 = \sigma'_3$ or $\sigma'_1 = \sigma'_2 > \sigma'_3$ are termed radial extension and radial compression, respectively. The consequences of these two stress regimes on the shape of the 3-dimensional Mohr-Coulomb failure surface and Mobilised Shear Capacity in rock volumes are discussed in Chapter 9. A stress regime where all three principal stresses are equal ($\sigma'_1 = \sigma'_2 = \sigma'_3$) is an isotropic stress regime. The assumption that the vertical stress is a principal stress is reasonable in areas which have not been exposed to tectonic activity or are relaxed in the sense that there are no remnant stresses from previous tectonic activity. The principal stress directions might be significantly different near fault zones or near zones with different rock properties.

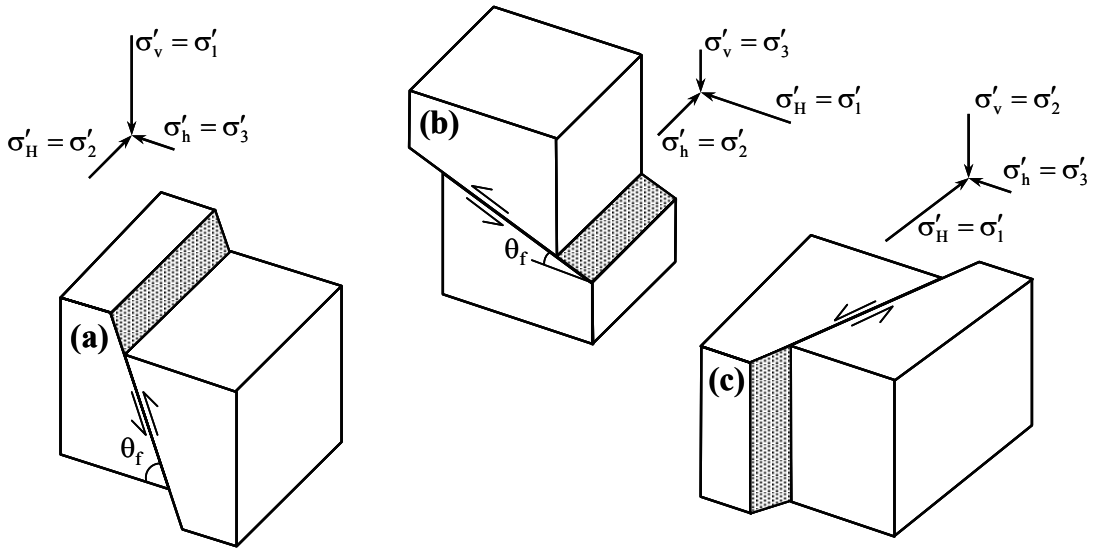

Figure 3.5. Fault types and stress regimes: (a) normal fault, extensional stress regime; (b) thrust fault, compressive stress regime; (c) strike-slip fault, strike-slip stress regime. θ_f is the fault dip angle. It is assumed that the vertical stress is a principal stress. Note that $\sigma'_1 > \sigma'_2 > \sigma'_3$.

3.3 General concepts of stress development in hydrocarbon reservoirs

Depletion of a hydrocarbon reservoir causes a reduction of the initial reservoir pore pressure. This in turn leads to changes in both total and effective stresses in the reservoir and surrounding rock. Generally, effective stresses increase inside of the reservoir causing reservoir compaction. Figure 3.6 shows typical compaction behaviour of a disk-shaped gas reservoir in cross-sectional view. Depending on the reservoir geometry, rock properties of reservoir and surrounding rock, initial stress field and pore pressure development, stress concentrations and zones with relatively small stresses can develop simultaneously during hydrocarbon production in different parts of the reservoir.

Figure 3.6. Typical compaction behaviour of a disk-shaped gas reservoir in cross-sectional view, from elastic 2D axisymmetrical finite-element calculations. The left side is the reservoir centre, the right side is the lateral reservoir edge. Reservoir radius and thickness are 1500m and 150m, respectively. Deformations are magnified by a factor 200. The rocks surrounding the reservoir have a somewhat higher Young's modulus than the reservoir rock.

The effective stress change $\Delta\sigma'$ is related to the pore pressure change Δp and the total stress change $\Delta\sigma$ according to eq. (2.58). In terms of vertical and horizontal stresses this equation becomes:

$$\Delta\sigma_v = \Delta\sigma'_v + \alpha\Delta p, \tag{3.12a}$$
$$\Delta\sigma_H = \Delta\sigma'_H + \alpha\Delta p, \tag{3.12b}$$
$$\Delta\sigma_h = \Delta\sigma'_h + \alpha\Delta p. \tag{3.12c}$$

In this thesis, a change in stress/pressure is defined as the stress/pressure after hydrocarbon production minus the stress/pressure before production:

$$\Delta\sigma' = \sigma'^{\,\text{after}} - \sigma'^{\,\text{before}}. \tag{3.13}$$

This means that a stress increase during hydrocarbon production has a positive sign and a stress decrease has a negative sign. Note that $\Delta p < 0$ for production.

The change in total stress in relation to the pore pressure change is termed arching and can be expressed by the ratio γ:

$$\gamma_v = \Delta\sigma_v / \Delta p, \tag{3.14a}$$
$$\gamma_h = \Delta\sigma_h / \Delta p. \tag{3.14b}$$

There exists usually a distinction between vertical and horizontal arching, whereby the horizontal arching depends on the direction considered. Basically one could make a distinction between γ_H and γ_h, but this is not common practice. More often, γ is referred to the co-ordinate system used, so that for instance for an x,y,z-co-ordinate system the terms γ_x, γ_y and γ_z would apply.

γ-values can be calculated for the reservoir rock itself but also for the rock formations surrounding the reservoir. In both cases, Δp is the pore pressure change in the reservoir, regardless eventual pore pressure changes in the surrounding rocks. γ expresses then always the total stress change per unit depletion at a certain location. The value of γ depends on the rock properties of the reservoir and surrounding rock,

the reservoir geometry and the geological setting in which the reservoir is placed. Values of γ are characteristic for a hydrocarbon reservoir. They are not constant throughout the reservoir but are location dependent.

In general, for reservoirs with a lateral extension larger than the thickness, $\gamma_h > \gamma_v$ inside of the reservoir. Or, in terms of effective stress changes, $\Delta\sigma'_h < \Delta\sigma'_v$. Such direction-dependent (effective) stress development in hydrocarbon reservoirs is a common phenomenon and is termed differential stress development. This differential stress development in the reservoir, whereby the vertical effective stress increase is larger than the horizontal effective stress increase, is of extensional character and therefore promotes normal faulting (see Chapter 3.4). This is in line with field observations (e.g. Segall 1989), numerical calculations (see Chapters 10 and 11 of this thesis) and analytical solutions (Rudnicki 1999 and Segall & Fitzgerald 1998). In the theoretical case of a spherical elastic reservoir in an elastic full space, $\gamma_h = \gamma_v$. Of course a hydrocarbon reservoir will not be infinitely wide or spherical. For small reservoirs consisting of weak rocks, a value for γ_v of 0.5 is quite common. For large reservoirs such as the Groningen and Annerveen gas reservoirs, γ_v is very close to zero.

3.4 Basic concept of fault reactivation / rock failure by differential stress development in a horizontal hydrocarbon reservoir with infinite lateral extension

Mechanisms of fault reactivation in producing hydrocarbon reservoirs are manifold and are discussed based on a literature study in Chapter 6. The consequences of differential stress development on fault reactivation inside of a reservoir are illustrated here for the theoretical case of a horizontal reservoir with infinite lateral extension, depleting over its entire infinite width. The reservoir compaction in this case is of uniaxial nature. Such uniaxial conditions hold also for smaller, realistic reservoir sizes (see for more details Chapter 10). It has to be noted here that differential stress development alone is in most cases not enough to reactivate existing faults. Geometrical anisotropy and differential compaction behaviour on either side of a fault are usually necessary to trigger a substantial reactivation of faults.

In the case of a horizontal reservoir with infinite lateral extension, the overburden rock keeps on pushing its own weight (σ_v) on the reservoir rock, without being restricted by a less or not compacting sideburden, so that $\Delta\sigma_v = 0$. Under the assumption that the vertical stress is a principal stress it follows from eq. (3.12) that

$$\Delta\sigma'_v = -\alpha\Delta p\,. \tag{3.15}$$

For $\alpha = 1.0$, this means that the amount of vertical effective stress increase is equal to the amount of pore pressure decrease. The part Δp of the vertical total stress, previously carried by the pore filling, is entirely loaded to the framework of the

reservoir rock. It is then said that no vertical load is arched away. Indeed $\gamma_v = 0$ according to eq. (3.14).

The uniaxial compaction behaviour of the lateral infinitely extended reservoir requires that there is no strain in horizontal directions: $\varepsilon_h = 0$. Writing eq. (2.58) for ε_h in terms of $\Delta\sigma'_h$, $\Delta\sigma'_H$ and $\Delta\sigma'_v$ results in:

$$\varepsilon_h = \frac{1}{E}[(1+\nu)\Delta\sigma'_h - \nu(\Delta\sigma'_h + \Delta\sigma'_H + \Delta\sigma'_v)] = 0\,. \tag{3.16}$$

Substituting eq. (3.12) into eq. (3.16) and assuming for the laterally infinite reservoir that $\Delta\sigma_H = \Delta\sigma_h$ results in:

$$\Delta\sigma_h = \frac{\nu}{1-\nu}\Delta\sigma_v + \left(\frac{1-2\nu}{1-\nu}\right)\alpha\Delta p\,, \tag{3.17}$$

which is the same as:

$$\Delta\sigma'_h = \frac{\nu}{1-\nu}\Delta\sigma'_v\,. \tag{3.18}$$

Knowing that $\Delta\sigma_v = 0$ it follows then from eqs. (3.14) and (3.17) that in case of a laterally infinite extending reservoir with solely elastic deformation:

$$\gamma_h = \alpha\left(\frac{1-2\nu}{1-\nu}\right). \tag{3.19}$$

For instance under the condition that $\alpha = 1.0$ and $\nu = 0.2$, this means a γ_h-value or horizontal arching of 0.75. From combination of eqs. (3.12) and (3.14) it follows that:

$$\Delta\sigma'_h = -(\alpha - \gamma_h)\Delta p\,. \tag{3.20}$$

From eq. (3.20) it is clear, that the horizontal effective stress increase is less than the vertical effective stress increase by an amount of $\gamma\Delta p$. This means for the example mentioned above that only 25% of the total horizontal load Δp, previously carried by the pore filling, is loaded to the framework of the reservoir rock. 75% of the horizontal load is said to be arched away, expressed by a γ_h-value of 0.75.

The differential stress development given by eqs. (3.15) and (3.20) is of extensional character and can therefore promote normal faulting, such as illustrated in Figure 3.7 for the case of uniaxial reservoir compaction in an extensional stress regime ($\Delta\sigma'_v > \Delta\sigma'_H > \Delta\sigma'_h$), with the vertical stress being a principal stress.

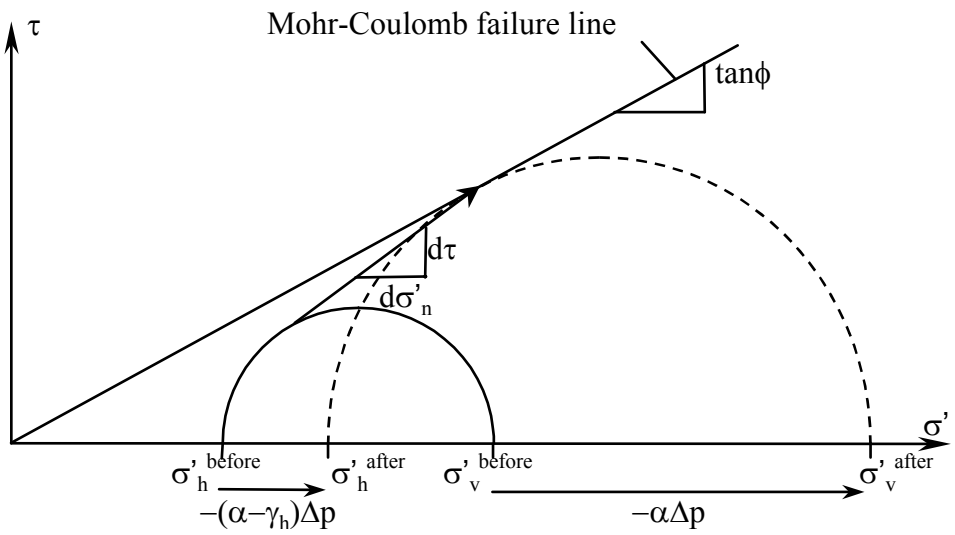

Figure 3.7. General concept of fault reactivation as a result of differential stress development during hydrocarbon extraction, shown by Mohr circles for uniaxial reservoir compaction in an extensional stress regime ($\sigma'_v > \sigma'_H > \sigma'_h$), with the vertical stress being a principal stress. The solid and dotted Mohr circles denote the state of stress before and after gas depletion, respectively. The Mohr-Coulomb failure line is of a cohesionless fault. The stress path belongs to a fault with the most critical fault dip angle of $45^o+\phi/2$. The gradient of the stress path is the ratio of the shear stress change and the change in normal effective stress on the fault.

4 FAULT SLIP, ASPERITIES AND SEISMICITY

4.1 General mechanisms of seismic and aseismic deformation

When gas is produced from the reservoir, the reduction in pore pressure causes compaction and due to differential stress development and differential compaction, shear stresses along the fault plane can increase rapidly, creating slip conditions during gas extraction. As stated by Pennington *et al.* 1986, continuous movement causes stresses to accumulate on slip resistant regions at some parts of the fault. When these highly stressed regions, often referred to as asperities, ultimately yield, energy is released seismically. The accumulated energy may also be released aseismically through slow visco-plastic deformation (creep) of the asperity, but there is no generally accepted method for determining whether slip on a given fault will be seismic or aseismic (Nagelhout & Roest 1997, Scholtz 1990).

4.2 Finite element modelling of stresses around an asperity

In order to get an idea of stress concentrations around an asperity as described above, this section describes the results of a preliminary numerical calculation, which is performed in the context of a research project for testing the possibility of identification of stress concentrations in the subsurface by means of 4D-time lapse seismic. Part of the mentioned research project were laboratory experiments for monitoring such stress concentrations in rock samples by acoustic measurements. The idea was to create such a stress concentration around an asperity on a previously cut fault plane through a rock sample. For an overview of the relation between the applied load, the magnitude of the stress concentration around such an asperity and the rock properties, preliminary numerical calculations were required. The numerical calculation results are described in this section in order to illustrate stress concentrations around an asperity.

4.2.1 Finite element model set-up

The model geometry is shown in Figure 4.1. It represents a square with dimensions 20 x 20 cm and is cut from top to bottom by a fault plane with a dip angle of 60º from the horizontal. The model consists of an isotropic, homogeneous and ideal elastoplastic rock mass with a Mohr-Coulomb failure criterion. Material properties are those measured by Hettema (1996) for Felser Sandstone (Table 4.1). The dilatation angle is chosen to be 10^{o} (Charlier 2000). The fault is modelled assuming Coulomb-friction with negligible cohesion. The fault has zero thickness. Normal- and shear stiffness are based on rules of thumb provided by TNO Building and Construction Research (eqs. (8.1) and (8.2), see Chapter 8.3.2.1). In the middle of the fault an asperity is modelled by assigning a very large cohesion of 1.0 GPa to the two interface elements in the centre of the fault plane. Its size is 1.867 cm measured along the fault plane.

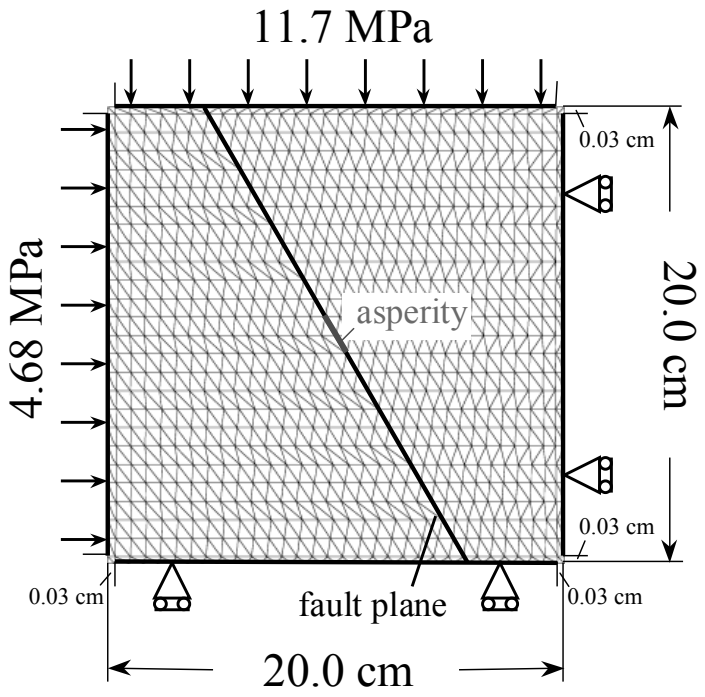

Figure 4.1. Applied load- and boundary conditions. No loads are applied in a distance of less than 0.03 cm of the edge of the model.

Table 4.1. Material properties.

Young's modulus	8.1 GPa
Poisson's ratio	0.22
Density	2070 kg/m^3
Cohesion	5.0 MPa
Friction angle	45º
Dilatancy angle	10º
Fault normal stiffness	9.24 GPa/m
Fault shear stiffness	3.32 GPa/m
Fault friction angle	30º
Fault dilatancy angle	10º
Fault cohesion (except asperity)	1.0 Pa
Fault cohesion (asperity)	1.0 GPa

The element type used for the rock mass is CT30E (triangular plane strain element with 15 nodes). This element is based on fourth-order interpolation and area integration. The fault is modelled by structural interface elements CL20I (linear, 5+5 nodes). The model consists of 1690 elements and 13650 nodes.

A vertical load of 11.7 MPa is applied perpendicular on top of the model, whereas a horizontal load of 0.4 times the vertical load (4.68 MPa) is applied to the left side (Figure 4.1). These loads are 25% of a stress field with σ_v = 46.8 MPa and σ_h = 18.72 MPa, which would occur at 3km depth in case that the vertical stress is gravitational with an average rock density of 1590 kg/m^3 and a K_0-value of 0.4 applies (see Chapter 3 for background). Application of 100% of the field load results in a divergence of the finite element calculation, meaning that no equilibrium can be reached. This is most

probably due to the large stress differences and concentrations in the model. The loads are applied statically to the model in ten equal steps. No gravity forces are applied, since these are negligible compared to the applied loads. A pore pressure is not modelled.

To take into account the very stiff aluminium platens used in the laboratory experiments, the nodes at the top edge of the model are defined to have the exactly the same vertical displacements during loading. Their horizontal displacements can differ from each other. The same is done for the left edge of the model: the horizontal displacements are the same during loading, whereas the vertical displacements can vary. To check whether the boundary condition of the same vertical and horizontal displacements at the top and the left edge of the model is appropriate, a calculation is performed without these restrictions in displacements, so with only a load perpendicular to the top and left edge of the model without any additional conditions, or in other words, with a load on the top edge remains constant even though the fault moves. This calculation diverged.

The boundary conditions on the model are such, that the bottom and the right side of the model cannot have displacements in vertical and horizontal direction, respectively. The boundary conditions take into account the 'free' zones at the edges of the rock sample, which are not covered by the platens in the triaxial cell and therefore are not loaded. No boundary conditions or loads are applied to a distance of 0.3cm from all four model corners in both x- and y-direction.

The advantage of the modelled experimental set-up is, that it incorporates the fault dip angle most sensitive for shear stress built-up: $\beta_{crit} = 45^o + \phi^f/2$, with β_{crit} being the critical fault dip angle and ϕ^f being the friction angle of the fault, which is 30º in our calculations. The disadvantage of the experimental set-up is the fact that peak stresses do not only build up at the asperity in the middle of the fault, but also at the edges of the fault at the top and bottom of the model (see Figure 4.2). This could disturb the acoustic measurements.

4.2.2 Calculation results

As is clear from Figure 4.2, both the vertical and horizontal stress distribution in the model is as good as symmetrical. Stress peaks occur at the asperity and at the edges of the fault at the top and bottom of the model. The maximum horizontal stress at the asperity is 80.0 MPa, the maximum vertical stress at the asperity is 62.7 MPa. Note that this is a local maximum. The absolute vertical stress maximum is about twice as high and occurs at the edges of the fault at the top of the model. This clearly shows the disadvantage of the modelled experimental set-up for acoustic measurements.

Vector plots of principal stresses in the view plane (Figure 4.3) show a clear concentration of stress trajectories in the zone around the asperity. A zone with high stresses can be observed more or less perpendicular to the asperity. The weaker neighbouring zones on the fault plane are unloaded and show even tensile stresses. An

unloading effect is present along the whole fault in the entire model (except for the asperity), characterised by tensile stresses (white zones in Figure 4.2). Normal- and shear stresses on the fault (Figure 4.4) show a clear concentration at the asperity, whereas the rest of the fault is unloaded. Stresses of almost zero magnitude reflect the tensile stresses which can be seen in the contour plots of Figure 4.2. Peak stresses occur at the ends of the asperity.

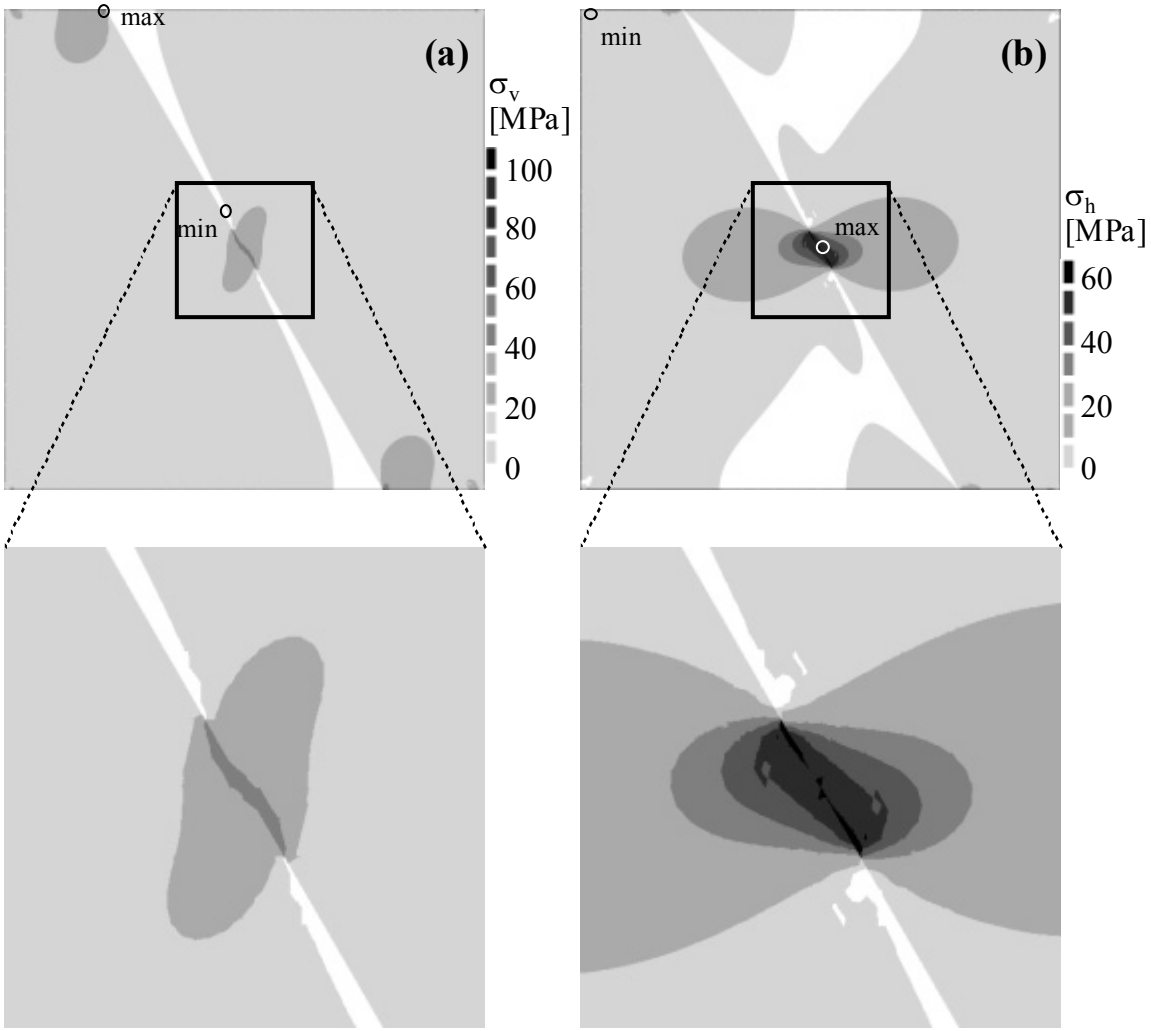

Figure 4.2. Calculated stresses after loading. (a) Vertical stress; max. value: 115 MPa; min. value: -7.0 MPa. (b) Horizontal stress; max. value: 66.5 MPa; min. value: -6.7 MPa. Positive stress values denote compression. Contour shapes indicate the location of the fault and the asperity. Location of maximum and minimum value is indicated. See Appendix 2 for this figure in colour.

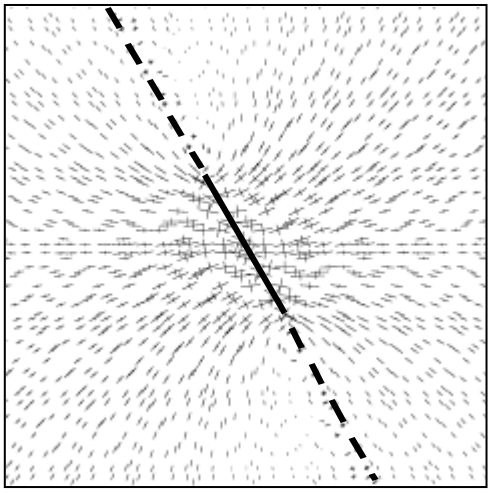

Figure 4.3. Vector plot of calculated principal stresses after loading. The locations of the fault and the asperity are indicated by the dashed and solid black lines, respectively. The zoom factor is the same as in Figure 4.2. See Appendix 2 for this figure in colour.

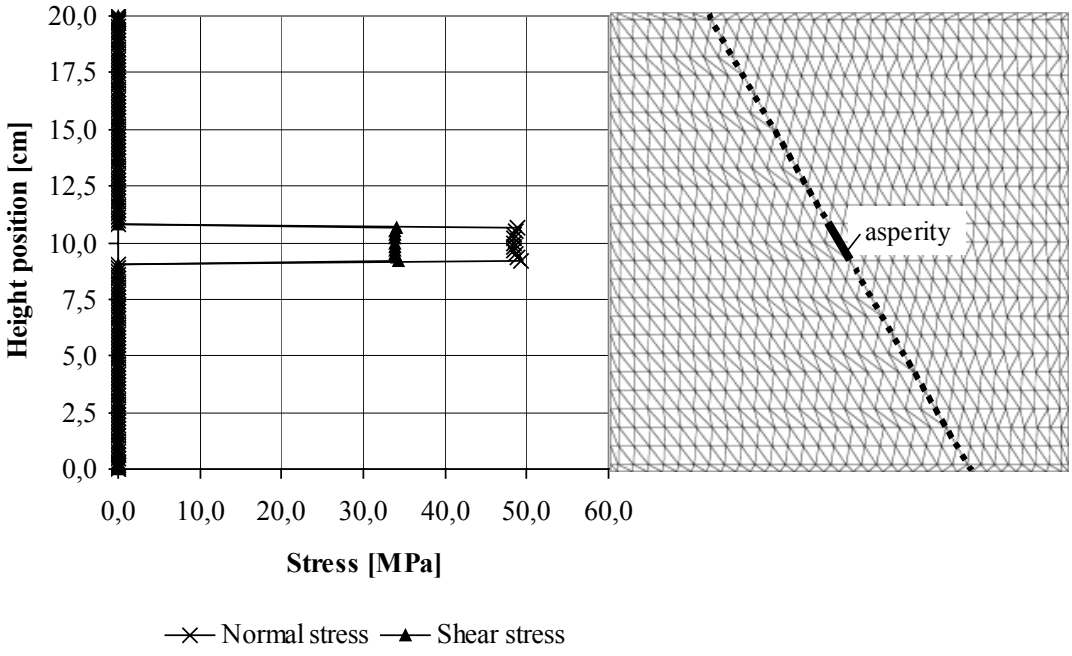

Figure 4.4. Normal- and shear stresses on the fault after loading. The fault and the asperity are indicated by the dotted and the solid thick lines, respectively. Peak stresses occur at the ends of the asperity, where also stress contour plots show local peak values. Stresses of almost zero magnitude on the rest of the fault reflect the tensile stresses which can be seen in the contour plots of Figure 4.2.

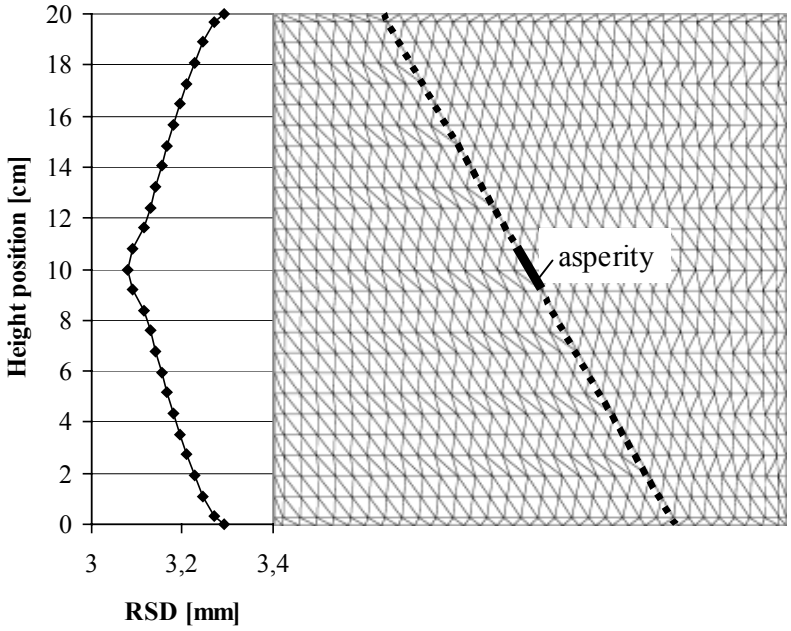

Figure 4.5. Calculated relative shear displacements (RSD) on the fault during loading. The fault and the asperity are indicated by the dotted and the solid thick lines, respectively. RSD in the asperity is the result of elastic deformation. The rest of the fault is irreversibly slipping but is hold back by the asperity.

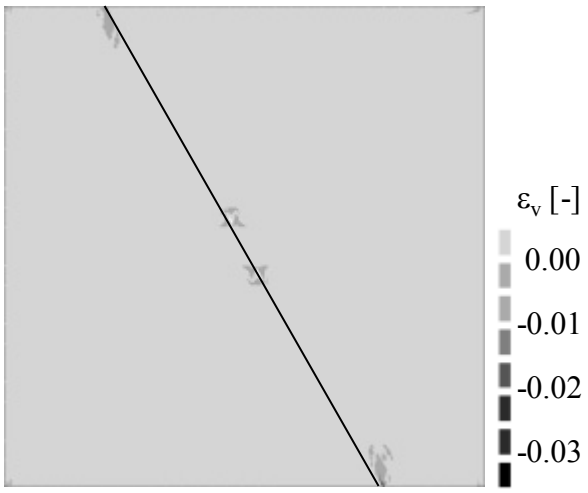

Figure 4.6. Calculated vertical plastic strain after loading.

Displacements in the model are negligible small with maximum values of less than 0.4 mm. Calculated fault slip or relative shear displacement (see Chapter 9.1.1 for background) is with a maximum value of 3.3 mm also very small (Figure 4.5). According to the DIANA calculation output file, no plastic fault slip occurred in the asperity. Relative shear displacements in the asperity are the result of elastic deformation. The rest of the fault, on the other hand, slips plastically but is hold back by the asperity.

A contour plot of vertical plastic strains (Figure 4.6) shows that plastic deformation occurs in the model at the peak stress locations, i.e. at both ends of the asperity and at the both ends of the fault at the top and bottom of the model. The direction of the contours indicates a tendency for cracking in these regions, whereby the cracks dip more or less with the same angle as the fault plane (60º) but in opposite direction.

4.2.3 Discussion and conclusions

The numerical calculation results show that the chosen rock samples and loading conditions generally provide a satisfying experimental set-up for tests on acoustic monitoring of stress concentrations around an asperity. However, a few improvements could still be achieved. This is described in the following.

In the modelled experimental set-up, peak stresses do not only build up at the asperity in the middle of the fault, but also at the edges of the fault at the top and bottom of the model. The vertical stress at the edge of the fault at the top of the model is about 1.5 times as high as at the asperity. This could disturb the acoustic measurements. A model could be designed, in which the fault plane cuts the rock from the top left to the bottom right corner. The combination with the unloaded zones at the edges of the model would make the asperity the only factor which prevents the fault from slipping. Stress build-up is then only present at the asperity. Care has then to be taken that the loading of the asperity does not get too large, since free sliding along the fault and hardly controlled failure could occur if the stress build-up would become too high and the asperity would fail.

An unloading effect is present along the whole fault in the entire model (except for the asperity), characterised by tensile stresses. There exists a clear concentration of stresses in the zone around the asperity. The fault tends to slip irreversibly but is hold back by the asperity. There exists a tendency for cracking at the peak stress locations. Considering all this, it seems best to measure beforehand the physical strength of the asperity in the laboratory. Loads on the rock sample don’t need to be high. It is expected that a small loading achieves sufficient stress concentration around the asperity for good acoustic measurements.

5 THEORETICAL BACKGROUND OF GEOMECHANICAL MODELLING BY MEANS OF FINITE ELEMENT CALCULATIONS

Geomechanical modelling techniques are developed in order to simulate physical processes such as stress/strain behaviour, fluid flow, heat transfer and dynamic loading in complex situations. They are often used to estimate the effects of mining activities on stress/strain behaviour of rocks and environmental issues. Many techniques have been developed such as the finite element, finite difference, distinct element and boundary element methods. For this thesis the finite element is chosen by means of the software code DIANA (DIsplacement ANAlyser), developed by TNO Building and Construction Research, since this code is mainly used in the Netherlands for geomechanical modelling of subsurface gas reservoirs. In this chapter, the theoretical background the finite element method (FEM) is presented. Chapter 5.1 describes the basic concepts of FEM by linear elastic calculation procedures. Chapter 5.2 deals with nonlinearity due to plasticity. Chapter 5.3 gives an overview of the different element types in DIANA used for this thesis.

5.1 General concepts of FEM: linear static analysis

5.1.1 General solution procedure

In the finite element method, the domain of the problem – a line segment, a planar region or a volume, depending on whether the problem is one-, two- or three-dimensional – is divided into smaller sub-regions or elements. The elements can have any shape. They are assumed to be connected to each other by nodal points or nodes on the element boundaries. A rock volume for instance can be divided into several solid elements such as shown in Figure 5.1. Such elements are assumed to represent continua. Finite element calculations are therefore continuous calculations. Discontinua, such as a geological fault, are modelled by interface elements (see Chapter 5.3).

Consider the four-node, three dimensional, solid pyramidal (tetrahedral) element as shown in Figure 5.1. Nodal forces act at the nodes of the element. This results in a distortion of the element, expressed by nodal displacements (and/or rotations as the case may be). For the element to be in equilibrium, the nodal displacements cause internal stresses or body forces to be present within the element which counteract the nodal forces such, that the resultant of body and nodal forces and the resultant moment around any axis vanish (Newton's third law). Since the element represents a continuum, the internal stresses are present at any arbitrarily chosen point throughout the whole element. The stresses can be related to the displacements u, v and w at any arbitrarily chosen point within the element and therefore to the nodal displacements and the nodal forces.

In practice, the nodal or external forces are applied to a finite element mesh by defining loads such as gravitational loads, surface pressures, pore pressures, excavations etc. From these external loads, the displacements and in turn the internal stresses are calculated, depending on the chosen rheologies and geometries of the elements. Information on the specific rheology and geometry of a single element is captured in the so-called element stiffness matrix $[K]^{el}$. The superscript ^{el} denotes that the displacements are for element 'el' only. The connection of all elements within a finite element mesh via their nodes makes that they all interact. This interaction gives rise to the so-called system stiffness matrix [K], which is constructed through the superposition of the element stiffness matrices $[K]^{el}$. It allows the set-up of a system of equations which has to be solved:

$$[K]\{u\} = \{F\}. \tag{5.1}$$

In here {u} is a vector of the nodal degrees of freedom (displacements and rotations) and {F} is the vector of nodal forces corresponding with the degrees of freedom {u}. In practice, {u} are the unknowns and {F} are known. Eq. (5.1) represents in fact a system of n equations with n unknowns. The construction of [K] to solve for the unknowns {u} in terms of {F} is basically what the finite element method (as applied to elastic problems) is all about.

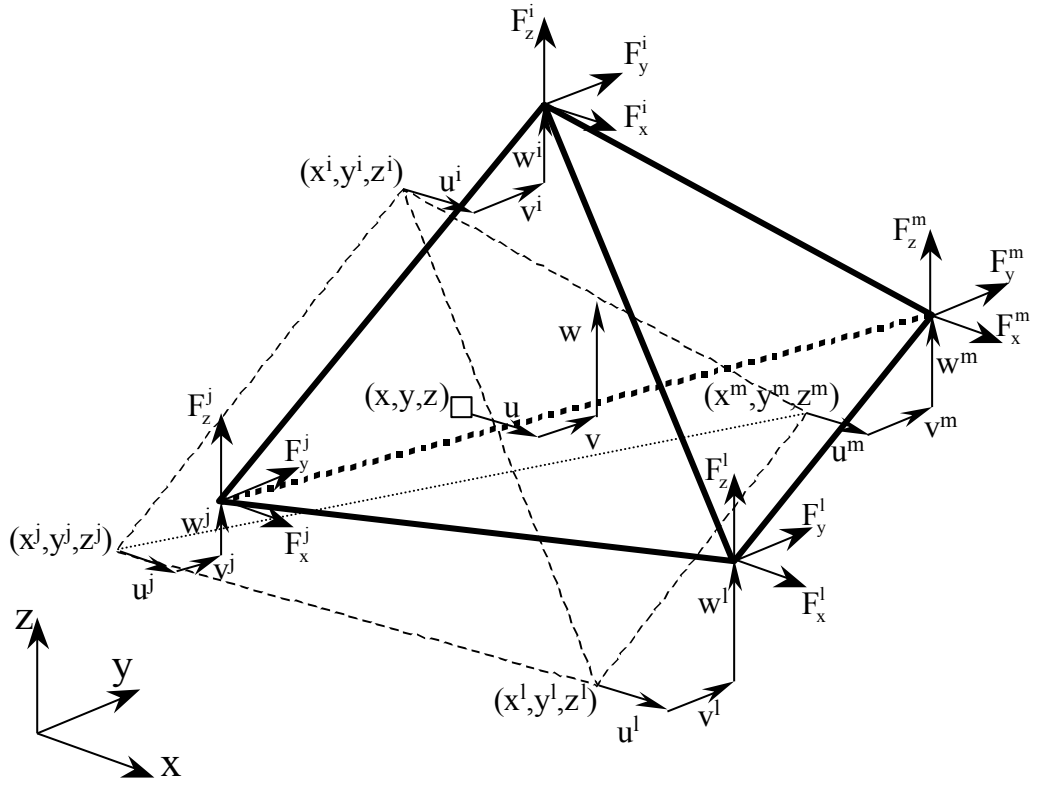

Figure 5.1. Displacements and forces within a four-node, three-side solid pyramid element. u, v and w are displacement vector components in an arbitrarily chosen point (x,y,z) within the element. $(u,v,w)^{i,j,l,m}$ *are the nodal displacements at nodes i, j, l and m.* $(F_{x,y,z})^{i,j,l,m}$ *are the nodal forces.*

The solution procedure as described above is based on the equations of equilibrium and applies to most finite element packages, among others DIANA. Eq. (5.1) requires an implicit calculation scheme, meaning that the system of equations is solved simultaneously. The term 'implicit' comes from the fact, that the necessary force/displacement relationship is defined indirectly: an interpolation is done in order to obtain the elemental displacements from the nodal displacements as a function of the element geometry. The implicit solution procedure requires eq. (5.1) to incorporate a linear relation between the applied forces and the displacements and is therefore very suited for linear static (elastic) calculations. Nonlinear relations as is the case with plasticity require additional features such as iterating (see Chapter 5.2). When stresses are changing rapidly, for instance in seismic wave propagation, accelerations come into play and the equations of motion must be considered. DIANA is based on a Lagrangian calculation scheme: during each calculation step incremental displacements are added to renew the position of given nodes. The Lagrangian approach makes this code well suited to describe large distortions of a restricted number of nodes.

5.1.2 Calculation of stress and strain in solid 3D-finite elements

Figure 5.1 shows an example of a finite element (four-node, three-side solid pyramid) with the (nodal) force- and displacement vectors. Its code name in DIANA is TE12L and is mainly used for the calculations in this thesis. In Chapter 5.1.1 it is explained, that external forces applied at the nodes of a finite element $\{F\}$ are balanced by internal stresses within the element $\{\sigma\}$ via the nodal displacements $\{u\}$.

In order to set up the system stiffness matrix [K] and solve eq. (5.1), the element stiffness matrices of each single element $[K]^{el}$ have to be determined first. To do so, the principle of work is invoked. This principle states that if a structure is in equilibrium, the work done by the external forces $\{F\}^{el}$ through a set of displacements $\{u\}^{el}$ must equal the work done by internal stresses $\{\sigma\}$ through the strains $\{\varepsilon\}$ caused by the displacements. Applying this principle results in the expression:

$$\{u\}^{el\,T}\{F\}^{el} = \int_V \{\varepsilon\}^T\{\sigma\}dV\,. \tag{5.2}$$

The superscript ^{el} indicates that only one element is considered. Integration of the right-hand side of eq. (5.10) is performed over the volume of the element V. $\{u\}^{el}$ and $\{F\}^{el}$ are vectors containing the nodal displacements and the nodal external forces of the considered element, respectively. For an element as shown in Figure 5.1, $\{u\}^{el}$ and $\{F\}^{el}$ would look like:

$$\{u\}^{el} = \{u^i, v^i, w^i, u^j, v^j, w^j, u^l, v^l, w^l, u^m, v^m, w^m\}, \tag{5.3a}$$

$$\{F\}^{el} = \{F_x^i, F_y^i, F_z^i, F_x^j, F_y^j, F_z^j, F_x^l, F_y^l, F_z^l, F_x^m, F_y^m, F_z^m\}. \tag{5.3b}$$

Strains are the result of displacements (see Chapter 2.2). The strains $\{\varepsilon\}$can be formally linked to the nodal displacements $\{u\}^{el}$ via the so-called differential matrix [B]:

$$\{e\} = [B]\{u\}^{el}. \tag{5.4}$$

[B] contains constants and/or expressions, which depend on the size and shape of the chosen elements. They can be seen as a way of interpolating the nodal displacements to strains at a certain position within the element. For the four-node, three-side solid pyramid element of Figure 5.1, [B] is a 6x12-matrix solely containing constants, so that stress and strain are constant throughout the element. This type of element is therefore called a constant-strain element. Varying strain and stress in the element require more nodes in the finite element (e.g. midside nodes) for a numerical solution. For simplicity, [B] is not shown here in detail. More extensive descriptions can be found in e.g. Zienkiewicz (1971), Pande *et al.* (1990) and Wittke (1990).

Substituting eq. (5.4) into eq. (5.2) results in:

$$\{F\}^{el} = \int_V [B]^T \{\sigma\} dV . \tag{5.5}$$

Stresses $\{\sigma\}$ can be expressed in terms of strains $\{\varepsilon\}$ via the rheological matrix [D]:

$$\{\sigma\} = [D]\{\varepsilon\}. \tag{5.6}$$

Matrix [D] contains the stress-strain relation of the material modelled and is in this thesis a function of the Young's modulus and the Poisson's ratio. It is for 3-dimensional conditions:

$$[D] = \frac{E(1-\nu)}{(1-2\nu)(1+\nu)} \begin{bmatrix} 1 & \nu/(1-\nu) & \nu/(1-\nu) & 0 & 0 & 0 \\ \nu/(1-\nu) & 1 & \nu/(1-\nu) & 0 & 0 & 0 \\ \nu/(1-\nu) & \nu/(1-\nu) & 1 & 0 & 0 & 0 \\ 0 & 0 & 0 & (1-2\nu)/(2(1-\nu)) & 0 & 0 \\ 0 & 0 & 0 & 0 & (1-2\nu)/(2(1-\nu)) & 0 \\ 0 & 0 & 0 & 0 & 0 & (1-2\nu)/(2(1-\nu)) \end{bmatrix}. \tag{5.7}$$

For other element types such as plane strain or axisymmetric elements and for other rheologies such as orthotropic elasticity, [D] becomes somewhat different. This is not explained in detail here but can be found in Zienkiewicz (1971). Substituting eq. (5.6) into eq. (5.5) leads to:

$$\{F\}^{el} = \int_V [B]^T [D][B]\{u\}^{el} dV = [K]^{el}\{u\}^{el}, \tag{5.8}$$

with

$$[K]^{el} = \int_V [B]^T [D][B] dV \,. \tag{5.9}$$

$[K]^{el}$ contains constants depending on the rheological properties and shape of the element. Summarising for all the nodal forces and nodal displacements results in a solvable system of algebraic equations as given by eq. (5.1). Initial strains $\{\varepsilon_0\}$ and stresses $\{\sigma_0\}$ are accounted for by defining the stress vector as

$$\{\sigma\} = [D]\{\varepsilon\} - [D]\{\varepsilon_0\} + \{\sigma_0\}. \tag{5.10}$$

For simplicity they are not included in the above derivations. Doing so results in:

$$\{R\}^{el} = [K]^{el}\{u\}^{el}, \tag{5.11}$$

where

$$\{R\}^{el} = \{F\}^{el} + \int_V [B]^T [D]\{\varepsilon_0\} dV - \int_V [B]^T \{\sigma_0\} dV \,. \tag{5.12}$$

5.2 Nonlinear material behaviour: plasticity

The implicit calculation scheme as described in Chapter 5.1 requires a linear relation between the applied force vector {F} and the displacement vector {u} and is therefore very suited for linear static (elastic) calculations. In case of nonlinear analysis (as is the case with plasticity) the original relationship (system stiffness matrix) becomes time- and path-dependent. Therefore the external loads can no longer be combined at once with the internal loads to govern the nodal forces, as is done during an elastic analysis. In order to determine the state of equilibrium, the nonlinear problems are not only made discrete in space (by finite elements, see Chapter 5.1) but also in time with increments. Note that for the static calculations in this thesis this time discretisation is virtual, only used to describe a sequence of situations. A purely incremental method usually leads to inaccurate solutions in nonlinear analysis, unless very small step sizes are used. An iterative solution algorithm is therefore used in order to achieve equilibrium at the end of the increment. This procedure is termed an incremental-iterative solution procedure.

5.2.1 Iterative procedures

An example of an incremental-iterative procedure is shown in Figure 5.2. Assume that a nonlinear relation between {F} and {u} exists as shown. The external load ${}^t\{F^{ext}\}$, applied at the virtual time t, is the first increment. In the second increment, the applied load is increased to ${}^{t+\Delta t}\{F^{ext}\}$. For the situation at the start of each increment, the system stiffness matrix is determined and solved. If only one increment is considered, the time increment Δt and the situation at the start of the increment are fixed (e.g. for the increment $t+\Delta t$ this would be ${}^t\{F^{ext}\}$ and ${}^t\{u\}$). The equilibrium equation within

the increment then only depends on ${}^{t+\Delta t}\{\Delta u\}$. The nonlinear problem can then be written as: find ${}^{t+\Delta t}\{\Delta u\}$ such that

$$ {}^{t+\Delta t}\{u\} = {}^{t}\{u\} + {}^{t+\Delta t}\{\Delta u\} \tag{5.17} $$

and, with $\{o^i\}$ as the out-of-balance force vector for iteration i,

$$ \{o^i\} = {}^{t+\Delta t}\{F^{ext}\} - \{F^{int,\,i}\} = 0, \tag{5.18} $$

where $\{F^{int,\,i}\}$ is the calculated internal force vector at increment i. The general procedure of an iteration process is shown in Figure 5.3. In all procedures, the total displacement increment $\{\Delta u\}$ is adapted iteratively by iterative increments $\{\delta u\}$ until equilibrium is reached, up to a prescribed tolerance.

Various iterative solution algorithms are available in DIANA. Their difference is the way in which $\{\delta u\}$ is determined. Figure 5.2 shows the Modified Newton-Raphson method. It evaluates the system stiffness matrix only at the start of each increment. The system stiffness matrix can also be evaluated each iteration, as is the case with the Regular Newton-Raphson method. It means that Modified Newton-Raphson usually converges slower to equilibrium than Regular Newton-Raphson. On the other hand, it is not necessary to set up a new stiffness matrix for each iteration. The Modified Newton-Raphson method usually needs more iterations, but every iteration is faster than in Regular Newton-Raphson. It is up to the user of the software to determine the optimal iterative procedure.

For our calculations, a combination of Constant Stiffness and Modified Newton-Raphson iterative procedures is used. The Constant Stiffness method uses the stiffness matrix left behind by the previous increment. If the Constant Stiffness method is used since the first increment, it uses the linear stiffness matrix from the previous linear static analysis and equals then the Linear Stiffness method.

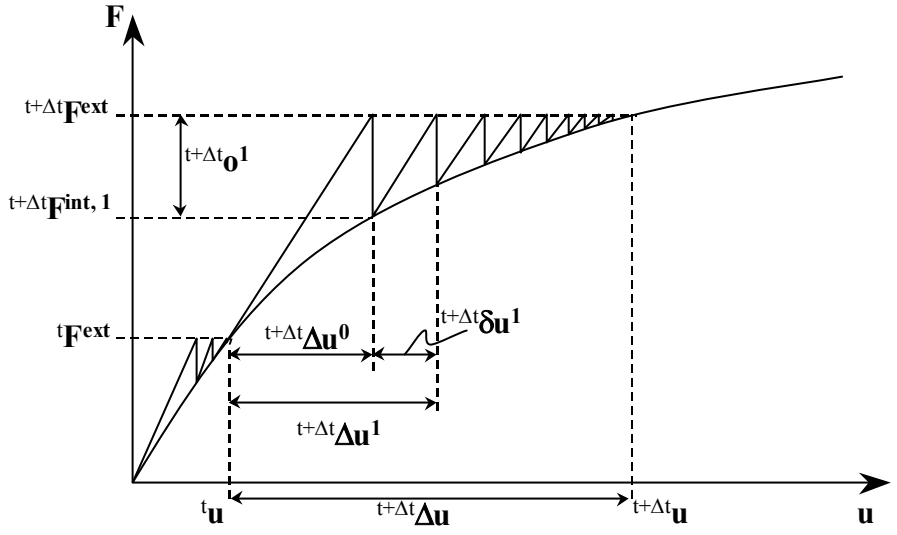

Figure 5.2. Example of an incremental-iterative solution procedure for nonlinear analyses in DIANA: Modified Newton-Raphson method.

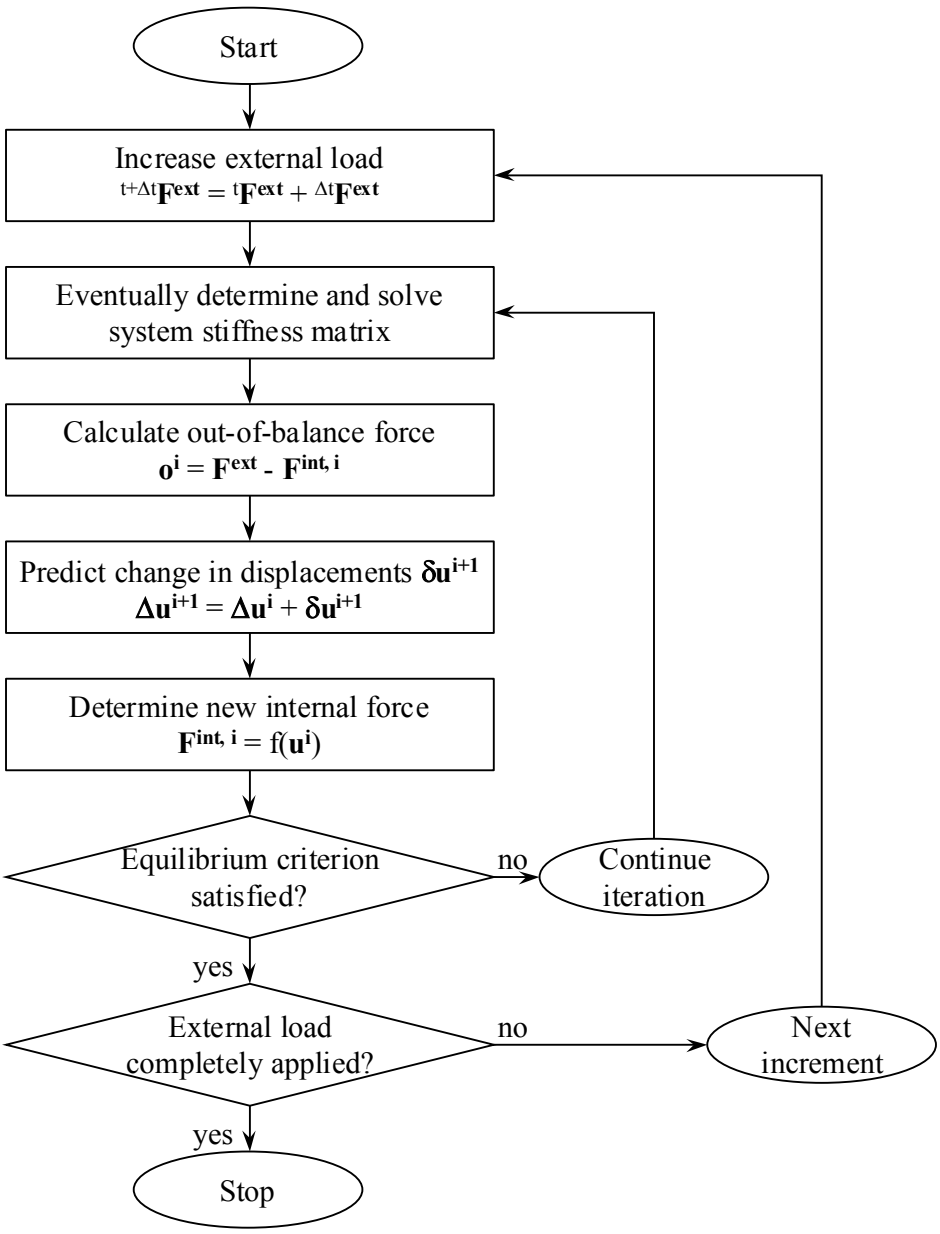

Figure 5.3. Flow diagram of a general incremental-iterative solution procedure for nonlinear analyses in DIANA.

5.2.2 Line Search algorithm

The iteration methods described before are based on a reasonable prediction, so that the iteration process converges to the 'exact' numerical solution. However, if the prediction is too far from equilibrium the iteration process will not converge. The Line Search algorithm can increase the convergence rate and is used in the calculations in this thesis. It uses a prediction of the iterative displacement increment $\{\delta u\}$ as obtained by one of the ordinary iteration algorithms and scales this vector by a value η as follows:

$$\{\Delta u^{i+1}\} = \{\Delta u^{i}\} + \eta\{\delta u^{i+1}\}. \tag{5.19}$$

i is the iteration number. See Figure 5.2 for reference of the used symbols in eq. (5.19). The value η is determined such that

$$s(\eta) = \{o(\eta)\}^{T} \cdot \{\delta u\} = 0. \tag{5.20}$$

Eq. (5.20) means in words, that the inner product $s(\eta)$ of the out-of-balance force with the iterative displacement increment should be equal to zero. $s(\eta)$ is first calculated for the out-of-balance force at the start (η_0=0) and at the end (η_1=1) of the iteration. $\eta_{2,3,...}$ are then determined as shown in Figure 5.4, until the absolute value of $s(\eta)$ is less than 0.8 times the value s(0). The value of 0.8 can be adjusted manually in DIANA. If both values s(0) and s(1) have the same sign, extrapolation is used to determine a new value for η, whereby DIANA bounds η between an upper and lower bound (default values 1 and 0.1, respectively).

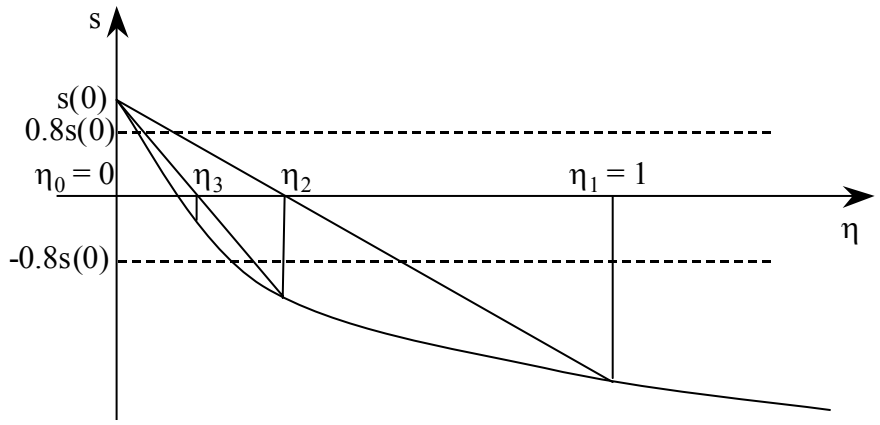

Figure 5.4. Line Search iteration.

5.2.3 Convergence criteria

The iteration process must be stopped if the results are satisfactory. The iteration process can be stopped if a specified maximum number of iterations has been reached, or if a certain tolerance, prescribed by one of the convergence norms, has been reached. For the calculations in this thesis, the iteration process is stopped if a specified maximum number of iterations has been reached. In order to ensure a good quality of the calculation results, it is then checked if convergence occurs during the iteration process of each increment and if the out-of-balance force is below an acceptable tolerance after each iteration process. For this check, the force norm is used, which is defined as (see Figure 5.5 for reference):

$$\text{Relative out-of-balance force} = \frac{\sqrt{\{o^{i}\}^{T}\{o^{i}\}}}{\sqrt{\{o^{0}\}^{T}\{o^{0}\}}}. \tag{5.21}$$

The relative out-of-balance force compares the out-of-balance force after iteration i with the initial unbalance $\{o^0\}$. As is visible in Figure 5.5, the initial unbalance is equal to the applied incremental load, which is equal to ${}^{t+\Delta t}\{F^{ext}\} - {}^{t}\{F^{ext}\}$. The relative out-of-balance force basically expresses how much unbalance is allowed in terms of applied incremental load. For instance a value of 0.01 means that an unbalance of 1% of the applied incremental load is tolerated. Figure 5.5 also indicates the other two convergence norms offered by DIANA: the displacement norm and the energy norm. They are determined in a way analogous to eq. (5.21). For this thesis, only the force norm is used. For more details about number of iterations chosen in the calculations and the accepted tolerance in the numerical calculations for this thesis see Chapter 8.

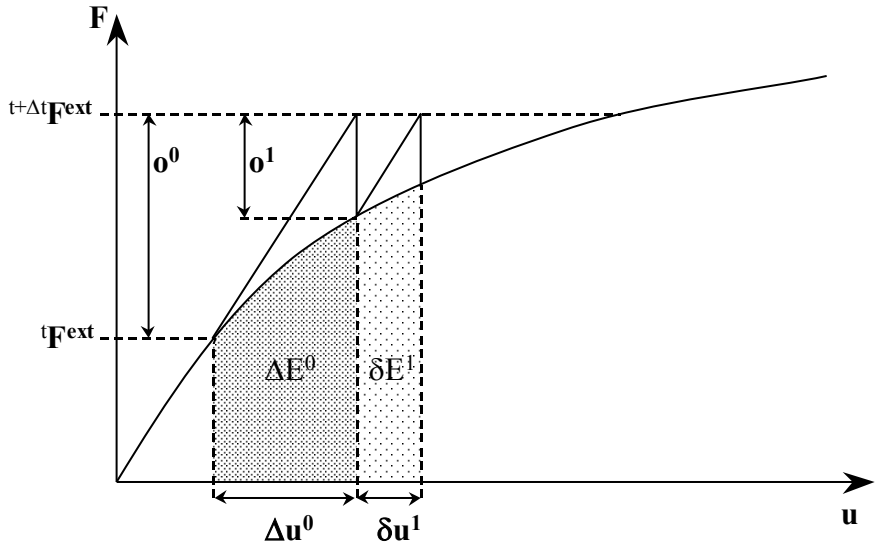

Figure 5.5. Norm items for convergence criteria in DIANA.

5.3 Element types used for the FE-calculations

The finite element method is a continuous calculation method. The structural solid elements are assumed to be continua. A geological fault plane is a discontinuous structure along which frictional behaviour can occur. This is modelled by interface elements. Interface elements consist of two sides, each with a certain number of corresponding nodes. These two sides are allowed to move relative to each other. Interface elements relate the tractions $\{t\}=\{t_n,t_s,t_t\}$ and the relative displacements $\{\Delta u\}=\{\Delta u_n,\Delta u_s,\Delta u_t\}$ across the interface. The amount of relative displacements depends on the constitutive behaviour and the strength properties of the elements, which are defined by the user. For the fault plane and thus the interface elements in this thesis, Coulomb frictional behaviour is assumed.

The types of elements used in the finite element models in this thesis are shown in Figure 5.7. The 3D-geomechanical models in this thesis consist of the DIANA element types TE12L and T18IF. TE12L are structural solid pyramids with three sides and four nodes used to model the rock volume. T18IF are structural triangular

interface elements with two times three nodes to model a fault plane. The four-noded pyramid elements are based on linear interpolation of the nodal displacements and incorporate therefore a constant strain and stress distribution over the element volume (see Chapter 5.1). This element type is chosen for two reasons. First, the 3D-models in this thesis are built making use of so-called 'general bodies' in the DIANA-pre-processor 'iDIANA', i.e. volumes bounded by multiple structural surfaces. These general bodies require the use of pyramidal solid elements and do not allow the use of wedge- and brick-shaped elements. Second, the use of the elements is limited by the hardware capacity. Higher-order midside noded pyramidal elements required for the relatively large geomechanical 3D models too much calculation capacity. Because of the use of the three side four node pyramidal elements, triangular two time three noded interface elements are used to model the fault plane. These elements relate the tractions $\{t\}=\{t_n,t_s,t_t\}$ and the relative displacements $\{\Delta u\}=\{\Delta u_n,\Delta u_s,\Delta u_t\}$ across the interface. The local axes along the surface are {n}, {t} and {s}, with {n} perpendicular to the plane and {t} and {s} in the plane. The element is based on linear interpolation.

Calculations of 2D finite element models, both plane strain and axisymmetric, are performed for this thesis as well. Plane strain elements are characterized by the fact that their thickness is equal to unity and that the strain components perpendicular to the element face are zero (Figure 5.6). Note that this condition results in a reaction stress in this direction. Plane strain models therefore theoretically represent cross sections through structures which are infinitely long in the direction perpendicular to the cross sectional plane. They are very suited to model cross sections through large structures. The plane strain DIANA-elements used in this thesis are T6EPS (triangle, 3 nodes) and CT12E (triangle, 6 nodes), in combination with the interface elements L8IF (line, 2 + 2 nodes) and CL12I (line, 3 + 3 nodes), respectively (Figure 5.7).

Axisymmetric models are considered to contain an axis of rotational symmetry at one of the model boundaries (Figure 5.6). Each axisymmetric element therefore models a ring. Such models are often referred to as '2½D models'. They are very suited to model axisymmetric structures such as ellipsoidal and disk-shaped gas reservoirs without faults. The axisymmetric DIANA-elements used in this thesis are T6AXI (triangle, 3 nodes) and CT12A (triangle, 6 nodes), see Figure 5.7.

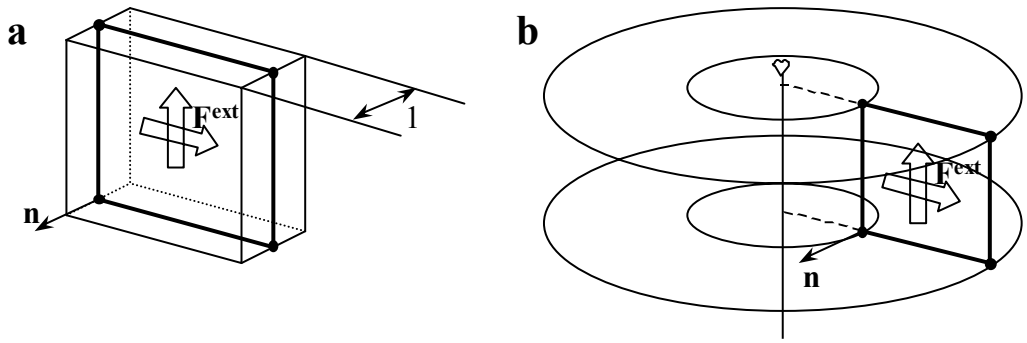

Figure 5.6. Characteristics of a) plane strain elements and b) axisymmetric elements.

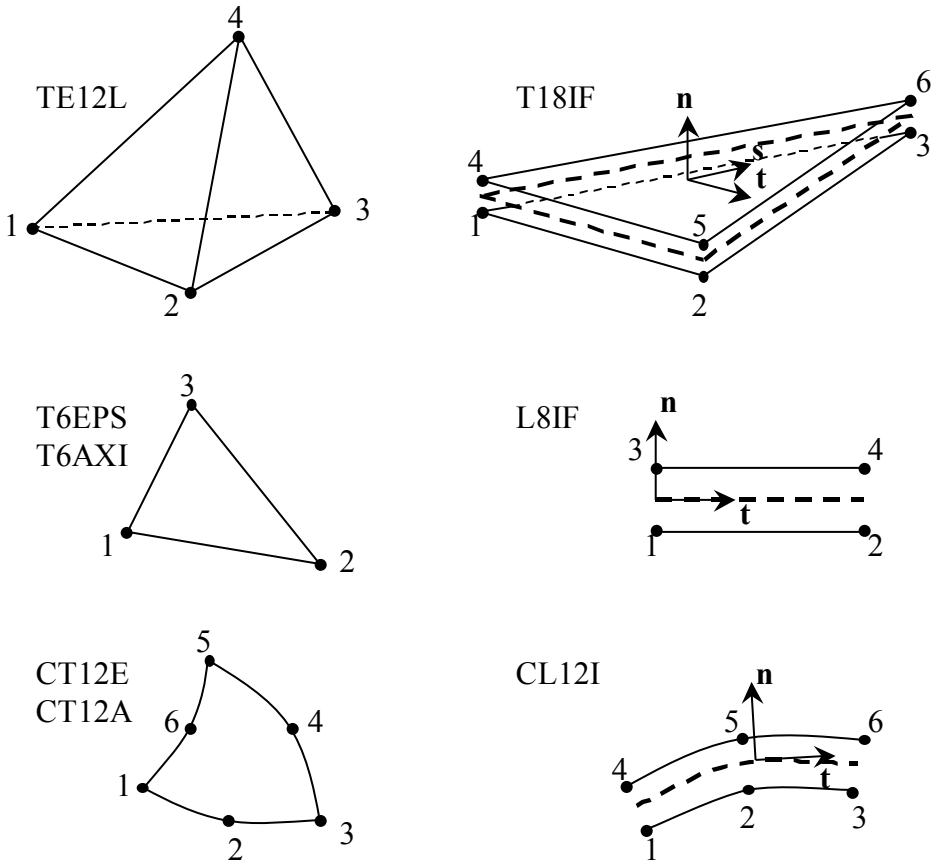

Figure 5.7. DIANA element types used for the calculations in this thesis.

6 LITERATURE STUDY ON HYDROCARBON RESERVOIR INDUCED SEISMICITY

The phenomenon of man-induced seismicity due to several types of engineering developments, sometimes referred to as IS, is well known. Numerous literature resources refer to one or more specific cases. Induced seismicity can be related with the impounding of water reservoirs at the earth's surface (dam constructions), the construction of mines and quarries, fluid or gas injection, extraction of hydrocarbons and steam and nuclear underground explosions. Such engineering developments are not the sole cause of earthquakes, but they merely induce seismic activity by altering stress regimes, so failure occurs (Baranova *et al.* 1999). Hydrocarbon reservoir induced seismicity (HRIS) is a term used for induced seismicity related to water injection for enhanced oil recovery and hydrocarbon extraction. Note that the term 'Reservoir Induced Seismicity' (RIS) refers to seismicity associated with water reservoirs at the earth's surface.

Induced seismicity associated with hydrocarbon extraction have been reported for numerous cases. A list of 24 hydrocarbon fields and sedimentary basins where hydrocarbon recoveries induced earthquakes with magnitudes larger than 3 on Richter scale can be found in Grasso (1992). It is not a complete listing of all fields worldwide where induced seismicity occurred, but it gives a good overview of the most remarkable fields. It is unknown how many basins contain active faults which are aseismic (below the resolution of the seismic recording equipment) or go unrecognized due to an absence of historical data (Bungum *et al.* 1991 in Addis *et al.* 1996, Davis & Pennington 1989). According to Grasso (1992) "there is no evidence for a minimum of 80% of commercially productive basins worldwide for earthquakes with magnitudes larger than or equal to a magnitude of 3 on Richter scale". Magnitudes of most of the induced seismic events in the northern Netherlands fall within the range of 1.5 – 2.0 on Richter scale (KNMI 2003a). A few larger events occurred in the Roswinkel, Bergermeer and Groningen gas fields. The largest induced event in the northern Netherlands to date took place in the Bergermeer field near the city of Alkmaar with a magnitude of 3.5 on Richter scale (Haak *et al.* 2001).

Generally it is assumed that induced seismicity is a result of slip on pre-existing surfaces that are optimally oriented for frictional sliding (Segall *et al.* 1994, Grasso 1992, Segall & Fitzgerald 1998, Roest & Kuilman 1994 and Nagelhout & Roest 1997). Basically three mechanisms for extraction-induced earthquakes are known from literature: triggering of discontinuities within the reservoir by poroelastic stress development (Chapter 6.1), triggering of discontinuities associated with reservoir contraction (Chapter 6.2) and mass transfer or isostasy (Chapter 6.3).

Fluid or gas extraction can also cause faults that previously were slipping aseismically to lock up for periods of time before slipping seismically. Such mechanism has been

reported by Grasso (1992) for the Grozny field, where six years of gas production (Δp = -30 MPa) stabilised the tectonic seismic instabilities. Stresses seem to be enhanced at the "locked" portions of the fault. After six years seismicity occurs as shear strength is at its maximum.

Table 6.1. Hydrocarbon fields and sedimentary basins where hydrocarbon extraction induced earthquakes with a magnitude equal to or larger than 3 on Richter scale (from Grasso 1992 with additions).

Sedimentary Basin	**Area or Field**	**Reference**
Alberta, Canada	Snipe Lake Field	Milne 1970
Alberta, Canada	Strachan Field	Wetmiller 1986
Appalachian, Canada	Gobles Field	Mereu *et al.* 1986
Aquitaine, France	Lacq Field	Rothé 1977; Grasso & Wittlinger 1990
Aquitaine, France	Meillon Field	Grasso 1992
Los Angeles, CA, USA	Wilmington Field	Richter 1958, in Kovach 1974
Los Angeles, CA, USA	Orcutt Field	Kanamori & Hauksson 1991
Los Angeles, CA, USA	Montebello Field	McGarr 1991
San Joaquin, CA, USA	Coalinga Field	McGarr 1991
San Joaquin, CA, USA	Kettleman Field	McGarr 1991
Caucasus, Tchetcheny	Grozny Field	Smirnova *et al.* 1977
Central Asia, Uzbekistan	Gasli Field	Simpson & Leith 1985
Russia	Starogroznenskoye Field	Kouznetsov *et al.* 1994
Turkmenistan, Russia	Barsa-Gelmes-Vishka Field	Kouznetsov *et al.* 1994
Midcontinent, OK, USA	El Reno Field	Nicholson 1992
Netherlands	Roswinkel Field	De Crook *et al.* 1998
Rotliegendes, Netherlands	Groningen Field	KNMI 2003b
Rotliegendes, Netherlands	Bergermeer Field	Haak *et al.* 2001
Rotliegendes, Germany	Salzwedel Field	Leydecker 1992
North Sea, Norway	Ekofisk Field	Grasso 1990
North Sea, Denmark	Dan Field	Grasso 1990
Po Valley, Italy	Caviaga Field	Calloi *et al.* 1956
Rocky Mountains, USA	Rangely Field	Raleigh *et al.* 1972
West Texas, TX, USA	Fashing Field	Pennington *et al.* 1986
West Texas, TX, USA	Imogine Field	Pennington *et al.* 1986
West Texas, TX, USA	Cogdell Field	Davis & Pennington 1989
West Texas, TX, USA	War-Wink Field	Doser *et al.* 1991, 1992
West Texas, TX, USA	Kermit-Keystone Fields	Doser *et al.* 1992
Southern Alabama, AL, USA	Big Escambia Creek, Little Rock and Sizemore Creek Fields	Gromberg & Wolf 1999
Kuwait	Minagish/Umm Gudair Fields	Bou-Rabee 1994
Williston, NE, USA	Sleepy Hollow Field	Rothé & Lui 1983

6.1 Triggering of discontinuities within the reservoir by poroelastic stress development

Triggering of discontinuities within the reservoir by poroelastic stress development is basically the result of differential stress development: effective stresses within the reservoir increase due to the pore pressure reduction, whereby the vertical effective stress increase is in most cases larger than the horizontal effective stress increase (see Chapter 3.4 for more details and explanations). In most reservoirs, total horizontal stresses decrease during hydrocarbon extraction whereas total vertical stresses remain as good as equal. Such behaviour has been reported by e.g. Hillis (2001), Hettema *et al.* (1998), Teufel *et al.* (1991), Engelder & Fischer (1994), Santarelli *et al.* (1998), Khan & Teufel (2000) and is supported by numerical modelling (Nagelhout & Roest 1997, Roest & Mulders 2000) and analytical solutions (Segall & Fitzgerald 1998, Rudnicki 1999). Differential stress development is basically the result from the fact, that the reservoir cannot contract as much as it actually wants due to the elastic coupling of the reservoir rock to the surrounding rock. The strains induced by the pore pressure change are different for an imaginary reservoir which is thought to be removed from the earth and for the same reservoir in its in-situ position in the subsurface. The elastic earth holds back the reservoir and inhibits a free deformation of the reservoir, which would take place in the theoretical case that there is no surrounding rock. Differential stress development as described above basically induces a relative horizontal tension within the reservoir (Figure 6.1), promoting frictional sliding on pre-existing normal faults within the reservoir (Segall & Fitzgerald 1998, Rudnicki 1999, Teufel *et al.* 1991). Normal faulting is promoted if the regional stress is extensional and the Biot-coefficient of the reservoir rock is sufficiently large (> 0.85, Segall & Fitzgerald 1998).

6.2 Triggering of discontinuities associated with reservoir contraction

Triggering of discontinuities associated with reservoir contraction can be the result of two submechanisms: triggering of discontinuities outside the reservoir by poroelastic stress transfer associated with reservoir contraction and triggering of discontinuities inside or outside a reservoir by differential reservoir compaction. The first submechanism, triggering of discontinuities outside the reservoir by poroelastic stress transfer associated with reservoir contraction, results from contraction of the reservoir and the elastic coupling of the reservoir rock to the surrounding rock. Figure 6.1 shows the relative stress regimes that develop around a reservoir undergoing hydrocarbon extraction. Contraction of the reservoir stresses the surrounding rock and induces a relative horizontal compression above and below the reservoir and a relative horizontal extension in the sideburden, at the lateral reservoir edges. Figure 6.2 shows a summary by Segall (1989) of observed faulting associated with hydrocarbon extraction. He explained by calculations with simple geometries stress perturbations that are consistent with observed earthquake locations and focal mechanisms. Note that not all of the faults are developed in any given setting: the style of faulting depends on the ambient stress state. The modelled stress changes outside of the

reservoir are with ~1 MPa typically small (Segall 1992, Baranova *et al.* 1999, Wu *et al.* 1998, Glowacka & Nava 1996, Grasso 1992 and Maillot *et al.* 1999). According to Grasso (1992), the magnitudes of these stress changes are independent of the tectonic setting and earthquakes with magnitudes of smaller than 5 on Richter scale can occur either above or below the reservoir and seismic instabilities can be triggered at distances of more than 20 km from the reservoir.

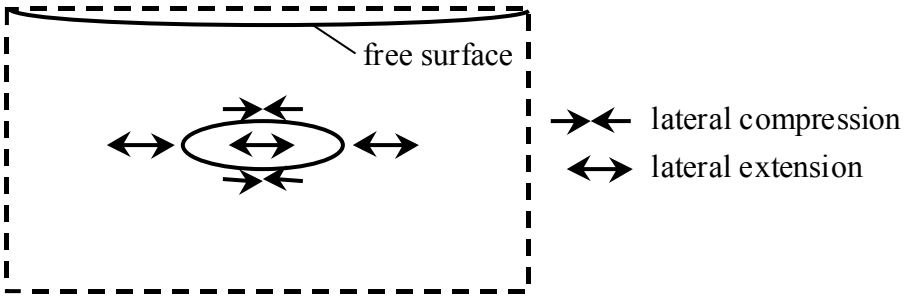

Figure 6.1. Illustration of relative stress changes inside and outside an ellipsoidal inhomogeneity undergoing pore pressure decrease (after Segall & Fitzgerald 1998).

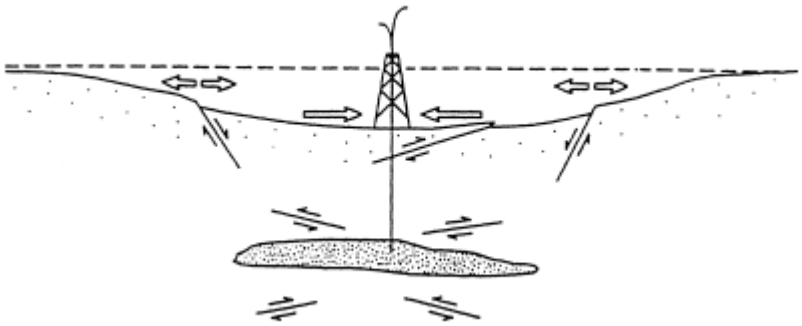

Figure 6.2. Schematic cross section summarising surface deformation and faulting associated with fluid withdrawal (from Segall 1989).

Fracturing and normal faulting are always promoted, in extensional environments, near the edge of the reservoir or in regions of high pore pressure gradient (Segall & Fitzgerald 1998, Rudnicki 1999). The maximum shear stress is strongly concentrated near the reservoir, and in particular near the edge. If the prior stress is spatially uniform the model thus predicts that seismicity would be concentrated near the margin of the reservoir, at depths both above and below the reservoir (Segall 1992). This is in agreement with the geomechanical modelling results of Brignoli *et al.* (1997) and Roest & Kuilman (1994). From the study of Roest & Kuilman (1994) it follows that slip on a vertical reservoir boundary fault occurs in particular at the top of a reservoir and to a lesser extent at the bottom of a reservoir (Figure 6.3a). The dip of a fault was found to be a major control on local fault activation. If the fault dips towards the reservoir, locally normal slip along the fault occurs at the top of the reservoir (Figure 6.3b). If the reservoir is located on the other side of the fault plane, the hanging wall of the fault is above the reservoir (Figure 6.3c). In these two cases reverse slip occurs at a lower level. Normal fault slip is maximum for a fault dip angle

of 60 – 70^{o} with the horizontal. The calculated fault slip as shown in Figures 6.3 b and c superimpose for the normal fault configuration as shown in Figure 6.3e, where the two parts of the reservoir move in opposite directions as result of compaction. Displacements occur in opposite directions on either side of the fault at the same level. This is termed 'differential compaction'. Slip can occur in particular if the prevailing horizontal stresses in the reservoir rock are relatively low. Fault slip at either side of the fault in case of a reverse fault configuration as shown in Figure 6.3d are the same as for a single reservoir and do not reinforce each other. Examples of induced seismicity in the Netherlands due to differential reservoir compaction are the Bergermeer, Eleveld, Groningen and Annerveen gas fields (Roest & Kuilman 1994, Roest & Mulders 2000, this dissertation). A good example is also the Lacq gas field in France, where the deformation mechanism is the lowering of a summital block above the compacting reservoir, whereby the movements are in the reverse direction to the original ones: initial normal faults move as reverse faults and initial reverse faults move as normal faults (Maury *et al.* 1992).

Slip along bedding planes is also mentioned as a possible deformation mechanism, especially at the top and bottom of the reservoir near its lateral edges (Kenter *et al.* 1998, Barends *et al.* 1995 and Roest & Mulders 2000).

Two additional mechanisms reported by Grasso (1992) are stress diffusion, whereby rocksalt acts as a viscoelastic channel for stress changes between a reservoir and overburden rocks, and pore pressure diffusion, whereby reservoir depletion can affect the aquifer pressure of the area. The first mechanism is also suggested by Barends *et al.* (1995).

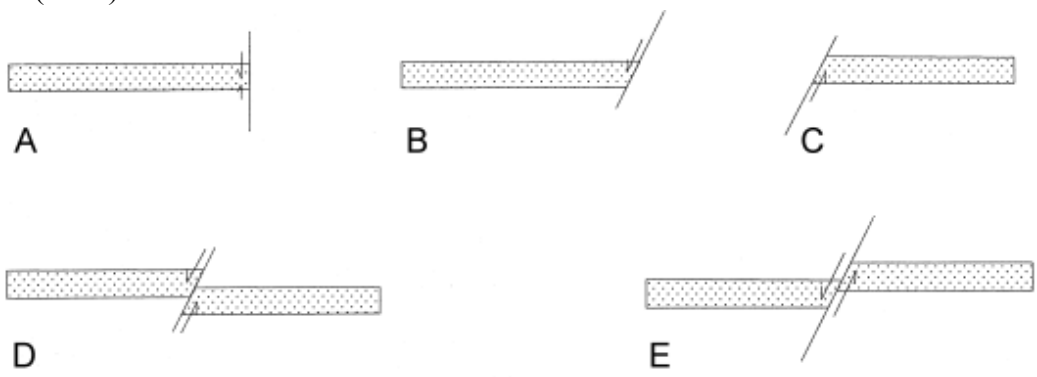

Figure 6.3. Influence of geometrical effects on fault reactivation (after Roest & Kuilman 1994).

6.3 Mass transfer

The third mechanism, mass transfer or isostasy, is related to massive hydrocarbon recovery. The removal of load can disturb the existing stress field and induce larger earthquakes at larger depths (McGarr 1991, Grasso 1992). Examples are the 1983 Coalinga, the 1985 Kettleman and the 1987 Whittier earthquake sequences, where a maximum magnitude of 6.5 on Richter scale was measured. Each occur at depths of the order of 10 km, beneath major producing oil fields. The total seismic deformation was just that required to offset the force imbalance caused by oil production (McGarr 1991).

6.4 Deep well fluid injection

The mechanism of induced seismicity of deep well fluid injection is based on the reduction in effective normal stresses due to the pore pressure increase, which allows faults to slip at ambient levels of shear stress (Healy *et al.* 1968 and Raleigh *et al.* 1976). This causes the Mohr circle in a τ/σ'_n-diagram to move to the left, causing failure in case that the injection pressure is sufficiently large. Hillis (2001) suggests that the poroelastic coupling of Δp and $\Delta\sigma_h$ as illustrated in Figure 3.7 for gas extraction can also play a role for injection activities. Galybin *et al.* (1998) suppose that the pore pressure caused by water injection can propagate down the fault, decreasing its shear resistance until shear stresses initiate propagation of shear fracture. An overview of well-documented examples of earthquakes induced by deep well injection can be found in Nicholson & Wesson (1990).

7 GEOLOGICAL SETTING AND CHARACTERISTICS OF THE GRONINGEN AND ANNERVEEN GAS FIELDS IN THE NORTHERN NETHERLANDS

In order to study the influence of several parameters on the possibility of gas depletion induced fault slip for the Groningen and Annerveen gas fields by means of finite element calculations, it is necessary to obtain a good overview over the geology of the two mentioned fields. A general overview of the geological structural units present in the northern Netherlands is given in Chapter 7.1. Chapters 7.2 and 7.3 deal with stratigraphy and tectonic history and fault systems, respectively, and are mainly based on RGD (1995) and Frikken (1999). Chapter 7.4 describes the current tectonic stress field in the northern Netherlands. The occurrence of seismicity in the Groningen and Annerveen gas fields is given in Chapter 7.5. Chapter 7.6 concludes with a summarising description of the Groningen and Annerveen gas fields for geomechanical modelling purposes of this study (see Chapters 8, 10 and 11).

7.1 Geological structural units

An overview of the Mesozoic structural geology of the Netherlands is shown in Figure 7.1. It is in fact a geological map of the Netherlands where the thick layer of sediments of the Tertiary period, covering the structure, is removed. For a geological time scale see Figures 7.3 and 7.8.

The Mesozoic rocks in the southeast of the Netherlands is affected by a NW-SE striking fault system as spur of fault structures in Germany and Belgium, which formed a number of horst and graben blocks during the Tertiary and Quaternary, such as the Roer Valley Graben and the Peel Horst structures. This fault system shows a high present-day activity and is responsible for a relatively high seismic activity of this area. Earthquakes in this area occur at a depth corresponding to that of the fault structures, around 20 km to a maximum of approximately -30 km. The largest earthquake in the Netherlands to date took place in 1992 to the south of the city of Roermond with a magnitude of 5.8 on Richter scale. Its depth was -17 km. For more descriptions of seismicity in the Netherlands see Chapter 1.

Most tectonic features in the Netherlands developed during the Late Jurassic and Early Cretaceous, such as the N-S oriented Central Graben and the NW-SE oriented Broad Fourteens Basin, West Netherlands Basin, Central Netherlands Basin and Vlieland Basin.

The Northern Netherlands is dominated by the Friesland Platform and the Groningen High (Figure 7.2). In between the Friesland Platform and Groningen High is the

Lauwerszee Trough. It is a Tertiary subsidence area, bounded to the west and east by the NW-SE trending Hantum Fault Zone and West Groningen Fault Zone, respectively. The West Groningen Fault Zone is not as pronounced as the Hantum Fault Zone. It is a narrow zone with only a few faults, the vertical throw of which reaches a maximum value of 300 m. The vertical throw along the Hantum Fault Zone reaches at some places 1100 m. The Hantum Fault Zone is part of a fault system which includes also the Holsloot Fault Zone, the Dalen Graben and the Reutum Fault to the south. To the southeast of the Groningen High and Lauwerszee Trough are the Ems Low and the Lower Saxony Basin.

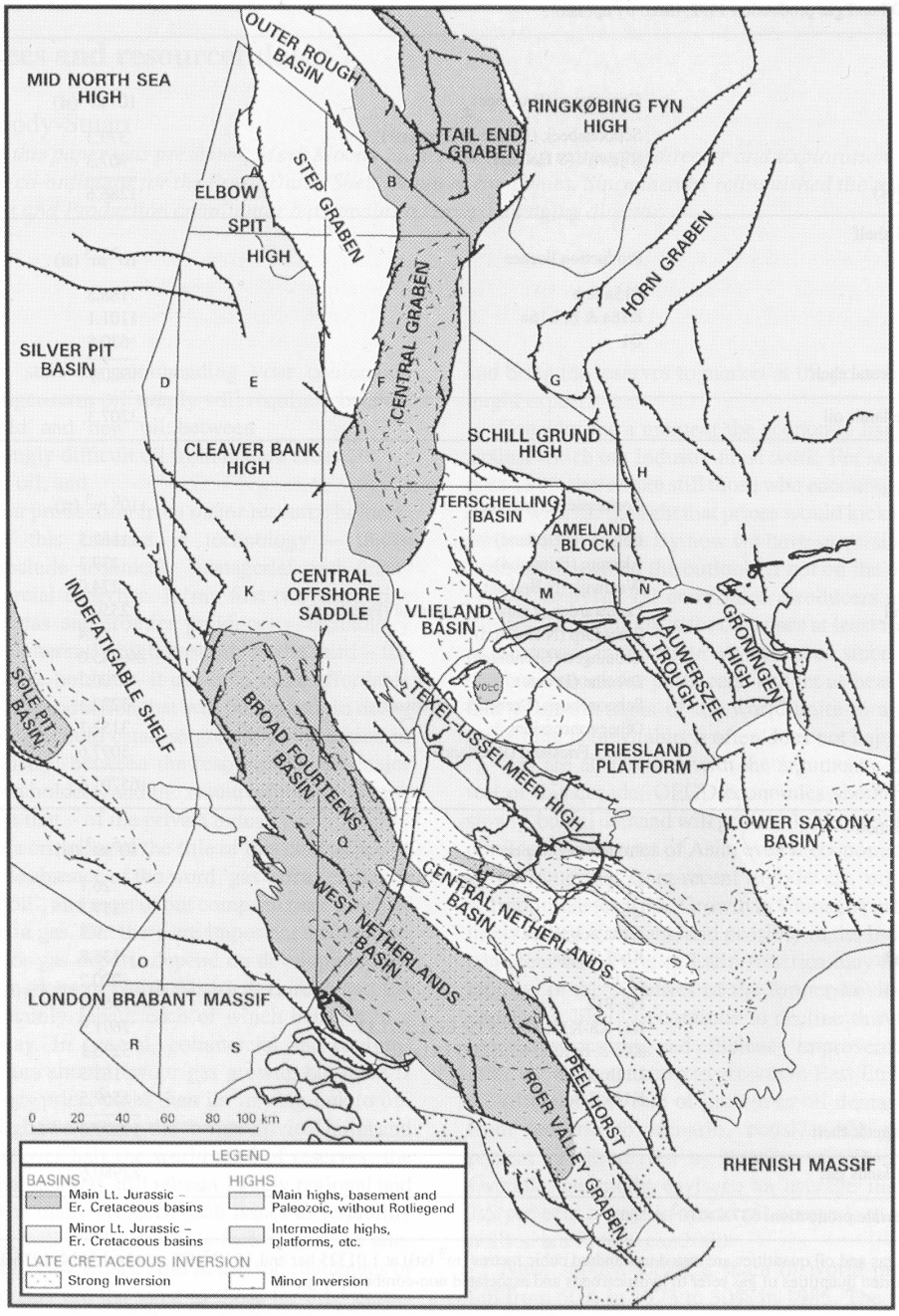

Figure 7.1. Mesozoic structural geology of the on- and offshore Netherlands (from Rondeel et al. 1996). See Appendix 2 for this figure in colour.

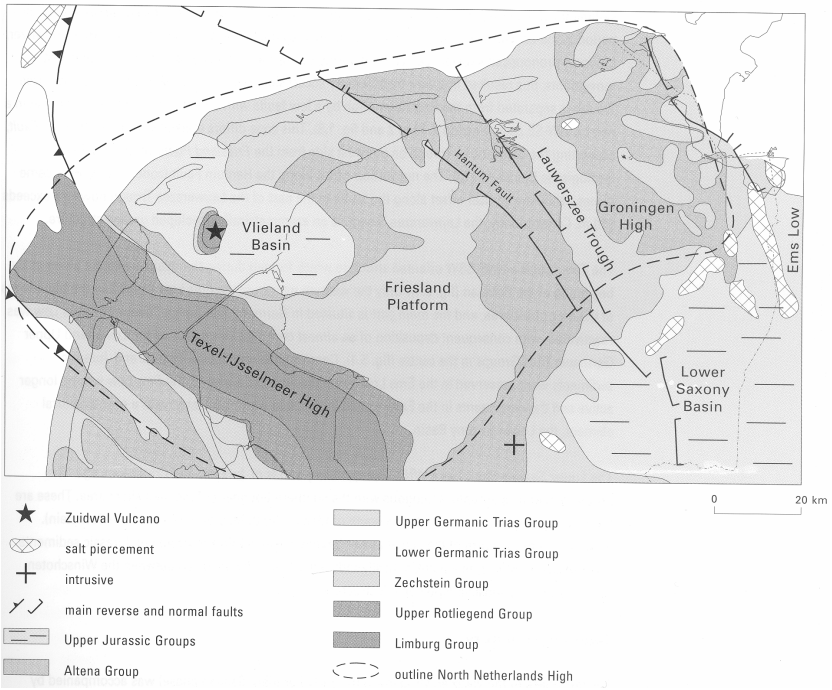

Figure 7.2. Geological map of the northern Netherlands where Cretaceous and Cainozoic formations have been removed (from RGD 1995).

7.2 Stratigraphy

This section describes the lithostratigraphical history and structure of the northern Netherlands. An overview over the lithostratigraphical units for the Groningen High, the Lauwerszee Trough and the Ems Low is shown in Figure 7.3. In Figure 7.4, a geological cross section through the Groningen gas field is displayed, with indication of the lithostratigraphical units.

N-S directed compressive stresses of the Variscan Orogeny (Sudetic phase, Late Carboniferous, see Figures 7.3 and 7.8) led to the evolution of an E-W oriented mountain chain in Europe: the Variscan mountains to the south and southeast of the present Netherlands. In response to the compression and the isostatic load of the Variscan Mountains, a foreland basin was formed to the north of this fold belt. Large quantities of erosional products from the mountain chain were deposited here. A regressional tendency during the Late Carboniferous led to the deposition of marine-influenced delta and pro-delta deposits during the Namurian to paralic and subsequently fluvial deposits during the Westphalian. Large-scale peat formation occurred during the latest Westphalian A and Westphalian B. These deposits, especially the Maurits Formation, form a major source rock for the Dutch natural gas.

In the Early Permian, the Southern Permian Basin came into being to the north of the present Netherlands (Figure 7.5). Sedimentation did not take place in the present northern Netherlands until the Late Permian. Aeolian and fluvial sands and conglomerates of the Upper Rotliegend Group were deposited in arid climate conditions. In a north-westerly direction, the ratio of the fluvial sediments decreased

in favour of aeolian and lacustrine sediments (Figure 7.6). During more humid periods, lacustrine conditions extended more towards the south and resulted in the deposition of the Ameland and Ten Boer Claystones (Figure 7.7).

Graben formation in the North Atlantic/Arctic region combined with a eustatic sea-level rise initiated the forming of an open passage between the Barentz Sea in the north and the Southern Permian Basin. In response to this, a very rapid transgression occurred in the basin, which had already subsided below the palaeo sea-level (Glennie 1986). This initiated the forming of a large inland sea, in which cycles of carbonates and evaporites were deposited, as a result of a combination of the arid climate on the one hand and an alternating influx of sea water on the other.

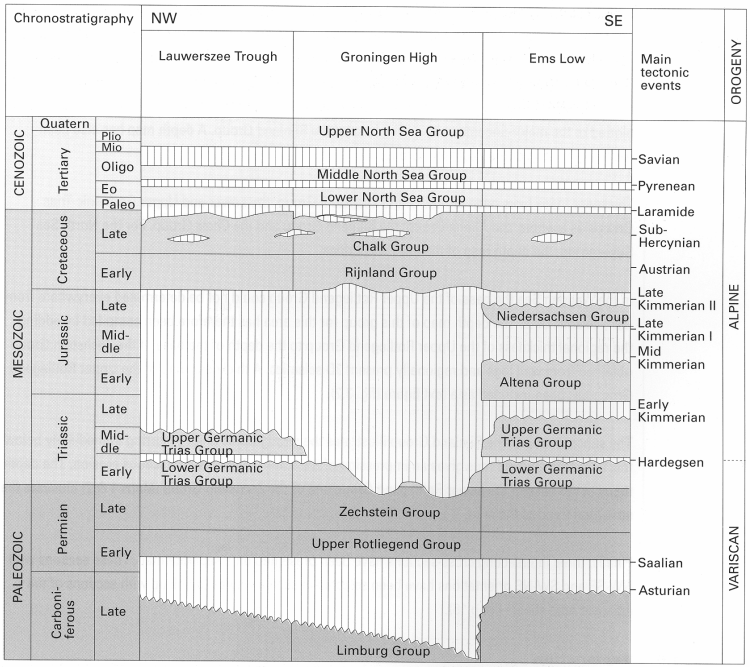

Figure 7.3. Lithostratigraphical units of three important geological structures in the northern Netherlands (from RGD 1995).

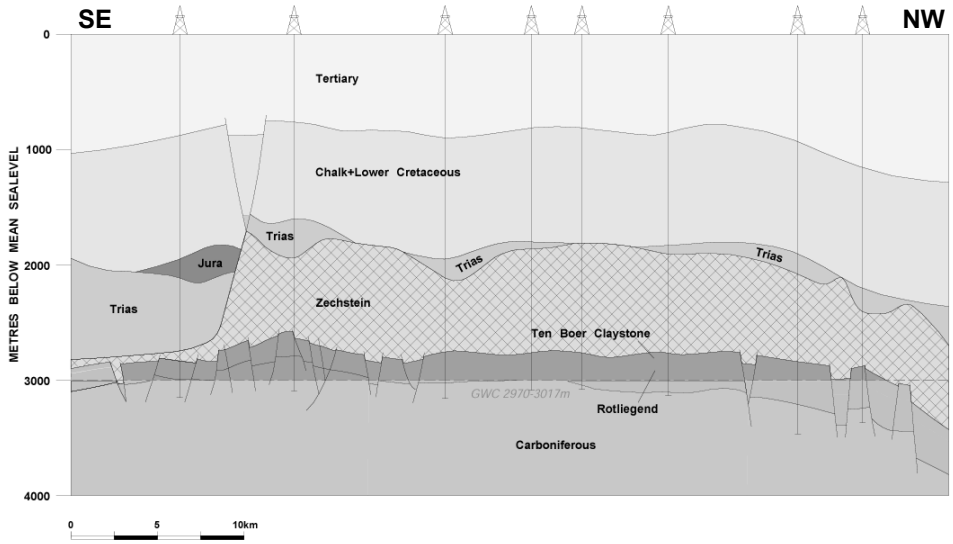

Figure 7.4. Geological cross section through the Groningen gas field (source: NAM). See Appendix 2 for this figure in colour.

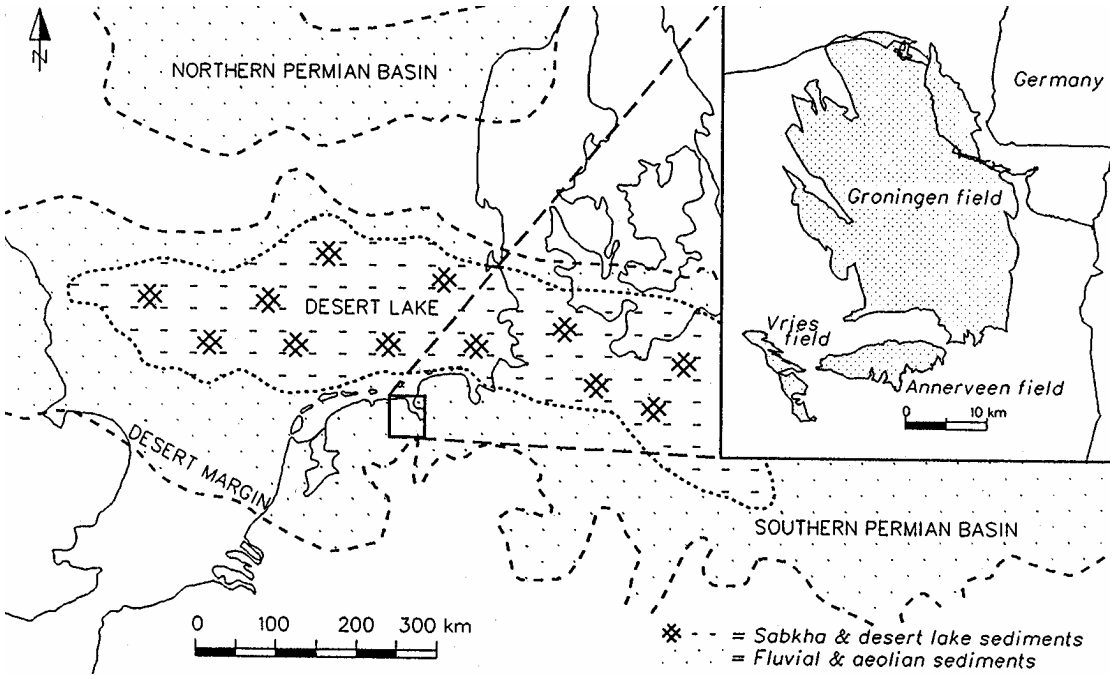

Figure 7.5. Palaeogeography during the Early Permian with present-day location of the Groningen and Annerveen gas fields (from Veenhof 1996).

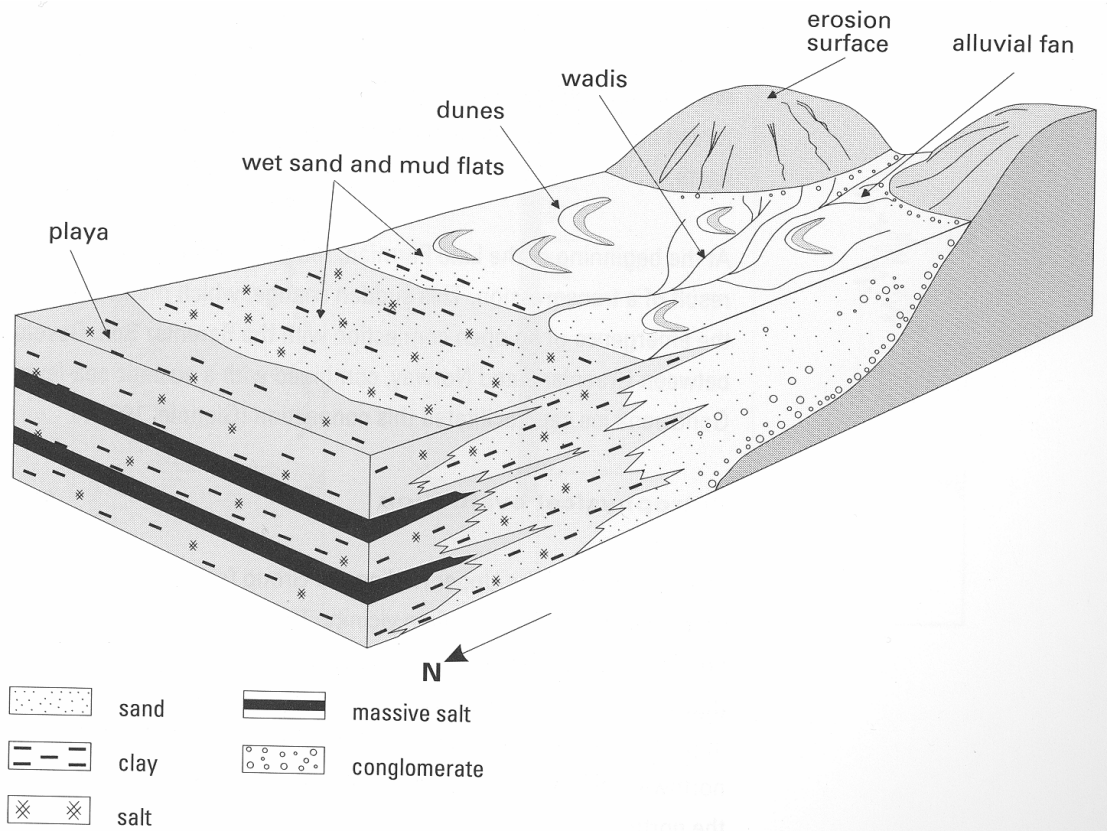

Figure 7.6. Schematic representation of the environment during the sedimentation of the Upper Rotliegend Group during the Late Permian (from RGD 1995).

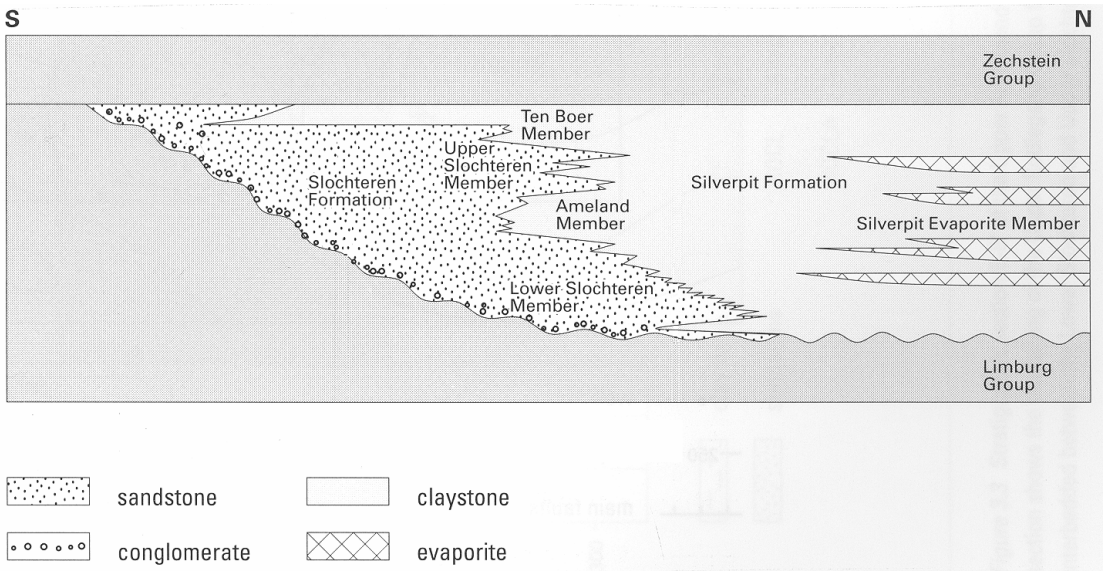

Figure 7.7. Lithostratigraphical overview of the Upper Rotliegend Group sediments, showing the lateral extension of the different formations (from RGD 1995).

The Lower Germanic Trias Group is composed of clastic, continental (fluvial and lacustrine) deposits. The carbonates and evaporites of the Upper Germanic Trias Group reflect an increasing marine influence. Clastic Jurassic sediments show a very limited spreading in the Northern Netherlands due to uplift and erosion. Marine sediments were deposited during the entire Cretaceous. The Rijnland Group and the Chalk Group consist of clastic sediments and carbonates, respectively. The Cainozoic sequence is built up of clastic sediments deposited under varying marine and continental conditions.

The late Palaeozoic, Mesozoic and Cainozoic lithostratigraphy as described above is, together with the tectonic history of the Netherlands and the Continental Shelf, very favourable to capture hydrocarbons. The (stratigraphic) occurrence of oil and gas and productive rock units is shown in the geological time scale of Figure 7.8. In total approximately 190 gas reservoirs are present in this area. In the Groningen and Annerveen gas fields, the gas is captured in the clastic rocks of the Upper Rotliegend Group, as is also the case for some 160 additional fields. The Zechstein evaporites are responsible for the sealing of most gas reservoirs in the northern Netherlands. On burial the Westphalian source rocks generated gas which migrated mainly into the overlying Rotliegend reservoirs. Two main charge phases took place for the Groningen field, which are also applicable to the Annerveen field: Jurassic and Tertiary to Quaternary, before and after Late Kimmerian uplift respectively (Van Wijhe *et al.* 1980). Approximately 25 reservoirs are contained in Zechstein carbonates and Carboniferous fluvial channel sandstones. Some gas and oil occurrences accumulated in reservoir rocks above the Zechstein. This is most probably due to source rocks of Mesozoic age, which are the organic-rich marine Posidonia Shale Formation in the Altena Group and lacustrine source rocks in the Coevorden Formation.

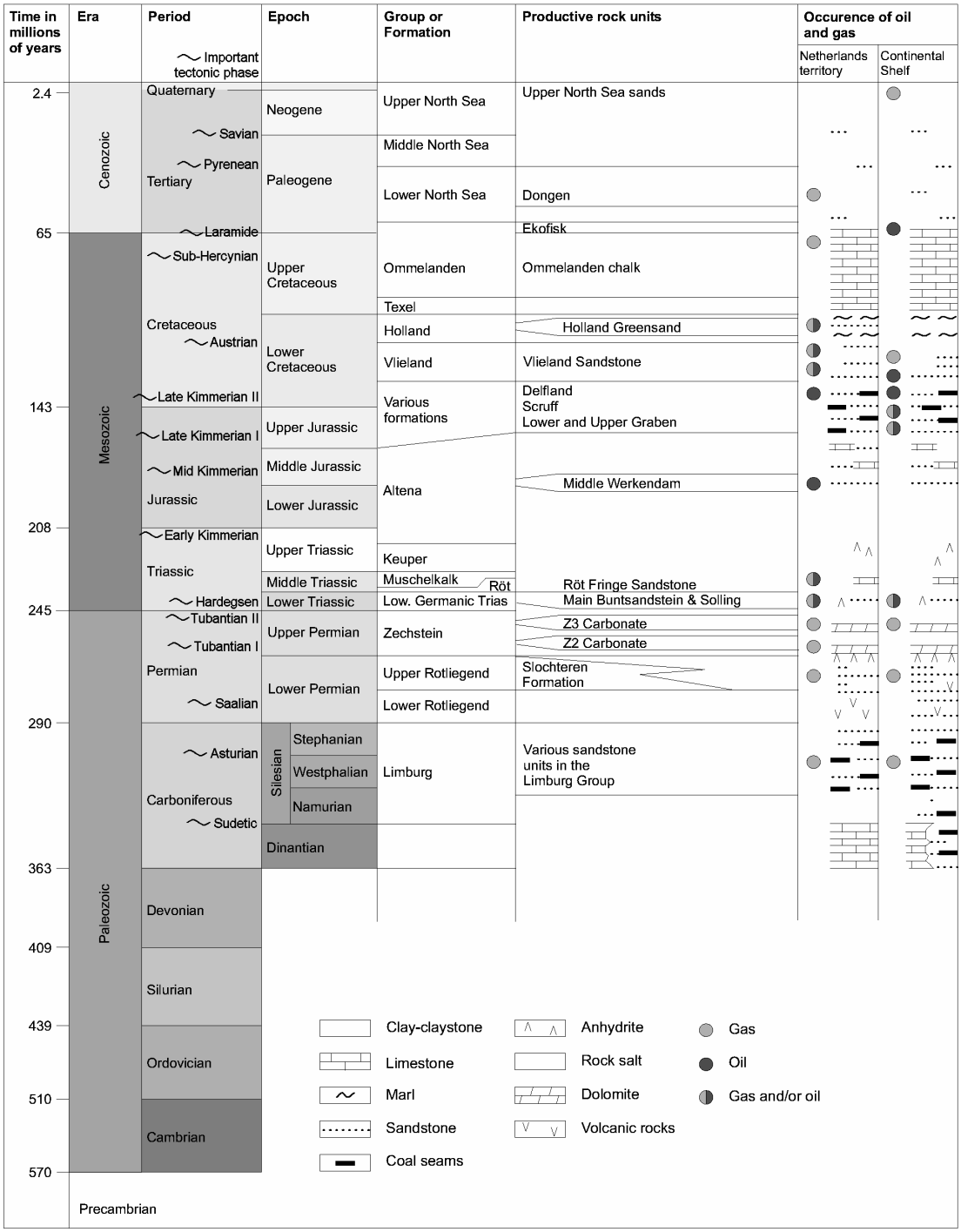

Figure 7.8. Geological time scale with composite stratigraphical column of the Netherlands and the Continental Shelf (after Ministry of Economic Affairs 2001). See Appendix 2 for this figure in colour.

7.3 Tectonic history and fault systems

The different tectonic phases which marked the geologic development of the northern Netherlands are indicated in Figures 7.3 and 7.8. During the Late Carboniferous, the Variscan Orogeny led in the Sudetic phase with N-S directed compressive stresses to the evolution of the Variscan mountains. The compression in the Asturian phase at the end of the Westphalian led to a progression of the Variscan orogenic front towards the north (Lorentz & Nicholls 1976), resulting in folding and thrust faulting in the Carboniferous sediments in the foreland basin.

During the Saalian phase in the Late Carboniferous and Early Permian, a transpressional stress regime developed due to dextral movements of Europe relative to Africa (Arthaud & Matte 1977, Ziegler 1989): the N-S compressional stress regime, characteristic for the Variscan Orogeny, slightly changed into an E-W directed extensional stress regime. Tectonic movements during the Permian are therefore of wrench and extensional nature. They resulted in major subsidence in the Ems Low and pronounced uplift and erosion on the Friesland Platform and the Groningen High. Furthermore, a fault pattern developed in the Variscan foreland with NW-SE trending fault systems, characterised by dextral strike slip, and E-W and N-S trending fault systems. Movements along these fault systems resulted in the coming into being of different horst- and graben structures. The development of the Lauwerszee Trough was initiated but still very premature.

Transtensional movements of the Tubantian I phase (Geluk 1999) at the beginning of the deposition of the Zechstein Group triggered a reactivation of older fault zones. The extensional Tubantian II phase at the end of the Permian initiated relative uplift of the Friesland Platform and Groningen High. It constituted a period of extensional tectonics (Geluk 1999) as a result of the breaking up of Pangaea (Ziegler 1990), which would last until the earliest Cretaceous. These extensional tectonic phases were responsible for the formation of the major structural units in Figure 7.2.

As a result of two phases of extensional tectonics during the Triassic (Hardegsen and Early Kimmerian phases), the Southern Permian Basin was modified and transected by several NNE-SSW trending elements, such as the Central North Sea Graben. Several tectonic elements were reactivated. During the Early Kimmerian phase in the Late Triassic, a N-S oriented complex graben system was formed to the east of the Groningen High as a modification of the Ems Low. Movements took also place along the Holsloot Fault Zone. The above description illustrates the rift-raft structures, in which the Triassic is pulled apart in large blocks.

The Late Jurassic and Early Cretaceous is a period characterised by a number of major tectonic events (Late Kimmerian phases). The ENE-WSW trending extensional stresses resulted in rifting, whereby the subsidence was concentrated in a number of fault-related troughs, such as the Lauwerszee Trough and the Central North Sea Graben. These troughs were separated by highs, such as the Friesland Platform and

the Groningen High. Transtensional dextral strike slip and dip slip occurred along NW-SE trending fault systems such as the Hantum Fault Zone.

The Friesland Platform and the Groningen High became subjected to strong uplift especially during the Late Kimmerian II phase in the Early Cretaceous. Very large displacements have occurred in the Lauwerszee Trough during the Kimmerian phases (maximum vertical throw of 300 m and 1100 m along the West Groningen Fault Zone and the Hantum Fault Zone, respectively, see Chapter 7.1).

During the Sub-Hercynian phase in the Late Cretaceous, a compressive stress field resulting from the collision of Africa and Europe (Ziegler 1982) was responsible for a brief change (inversion) in the direction of movement of the major structural elements. The inversion initiated uplift of the former Upper Jurassic/Lower Cretaceous basins and pronounced subsidence of the former highs (Baldschuhn *et al.* 1991).

The phases during the Tertiary were associated with the Alpine Orogeny. During the Tertiary, active faulting and fault reactivation occurred in a few places only and relates principally to movements related to the Late Kimmerian fault zones, such as the Hantum Fault Zone, the Dalen Graben and the Holsloot Fault Zone (Figure 7.9).

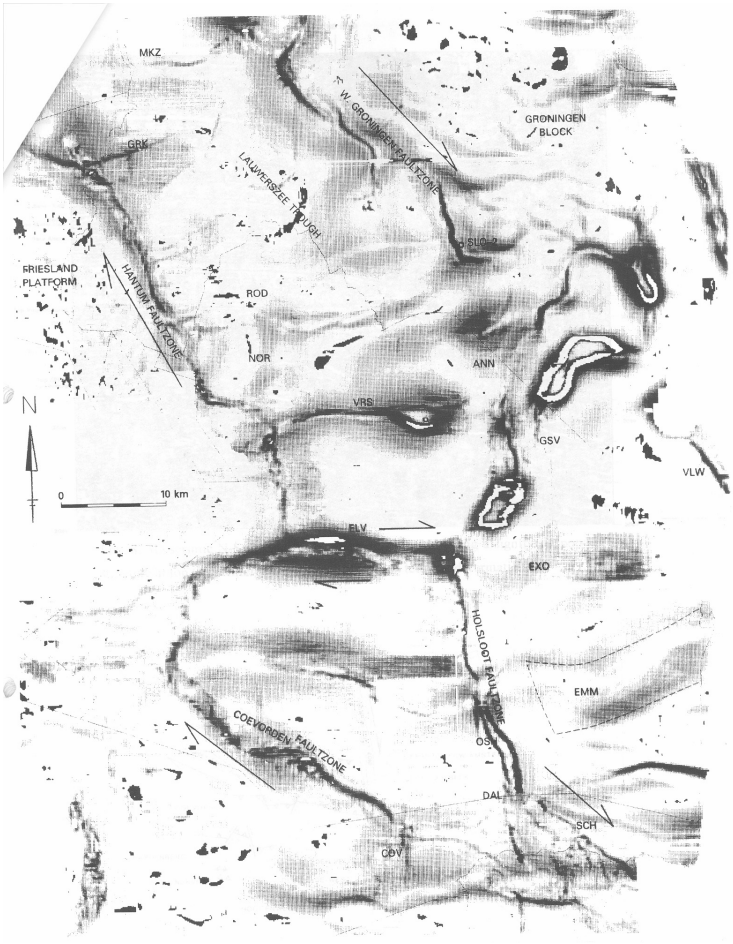

Figure 7.9. Base Tertiary dip-map of the northern Netherlands (from Frikken 1999).

7.4 Current fault pattern in the Groningen and Annerveen gas fields

According to the depth contour map of the top of the Groningen gas reservoir as shown in Figure 7.10, the Groningen gas field is in general bounded by major graben structures on its west, south and east side. This is visually especially pronounced in the birds-eye view of the 3D-Groningen gas reservoir (Figure 7.11). The structure of the Groningen High, which contains the Groningen gas field, is clearly visible. The graben structure on the west side is the NW-SE trending Lauwerszee Trough. The graben structures on the south- and east side are E-W and N-S trending, respectively. Graben systems in the three mentioned directions can be found throughout the entire Groningen gas field. Their distribution is not even, but location-dependent.

Very remarkable are the major NW-SE striking normal faults which cut through the reservoir (Figure 7.11). Their throw can be very large: up to 300 m (see Chapter 7.1). These faults are concentrated in the west part of the field and are related to two major graben structures which cut the field here (Figure 7.10). The southernmost graben structure is part of the West Groningen Fault Zone bounding the Lauwerszee Trough. The NW-SE grabens in the west part of the field are intersected by N-S trending grabens, resulting in a complicated fault pattern in this part of the field. The NW-SE trending grabens are much more pronounced and show a larger throw than the N-S trending grabens (Figures 7.12 and 7.13).

The northernmost major graben structure branches towards the southeast. One branch continues in south-eastern direction and forms the graben structure in which the well clusters Amsweer (AMR) and Schaapbulten (SCB) are located. Another branch runs southwards. The well clusters Overschild (OVS) and Noordbroek (NBR) are located within this N-S trending graben structure. Many N-S striking normal faults, which can incorporate a relatively large throw, are present in this graben structure (Figure 7.14).

The southern major graben structure neighbours the highest part of the Groningen gas field around the well clusters Kooipolder (KPD), Slochteren (SLO) and Froombosch (FRB), which is part of a horst structure that covers a large area in the southern part of the Groningen gas field. Close to the southern major graben, the horst structure is mainly characterised by NW-SE trending normal faults (Figure 7.15). Also N-S and W-E striking normal faults occur frequently. Further to the eastern part of the field, a rhomboidal fault pattern of N-S and E-W striking normal faults becomes very characteristic. NW-SE trending faults are as good as absent here.

The northern part of the Groningen gas field is structural geologically seen a quiet area, as is visible in a seismic cross section through this part of the field (Figure 7.16). Not many faults occur here. The most remarkable are some NW-SE trending grabens in between the well Uithuizermeeden-1A (UHM-1A) and the well cluster ’t Zandt (ZND) and an E-W trending graben structure which is visible to the south of the well clusters ’t Zandt (ZND) and Bierum (BIR). The density of the grabens and the throw along their normal faults is less than in the other parts of the Groningen gas field. The northern boundary of the field is formed by northwards dipping of the reservoir blocks below the gas-water contact level of -2976 m depth.

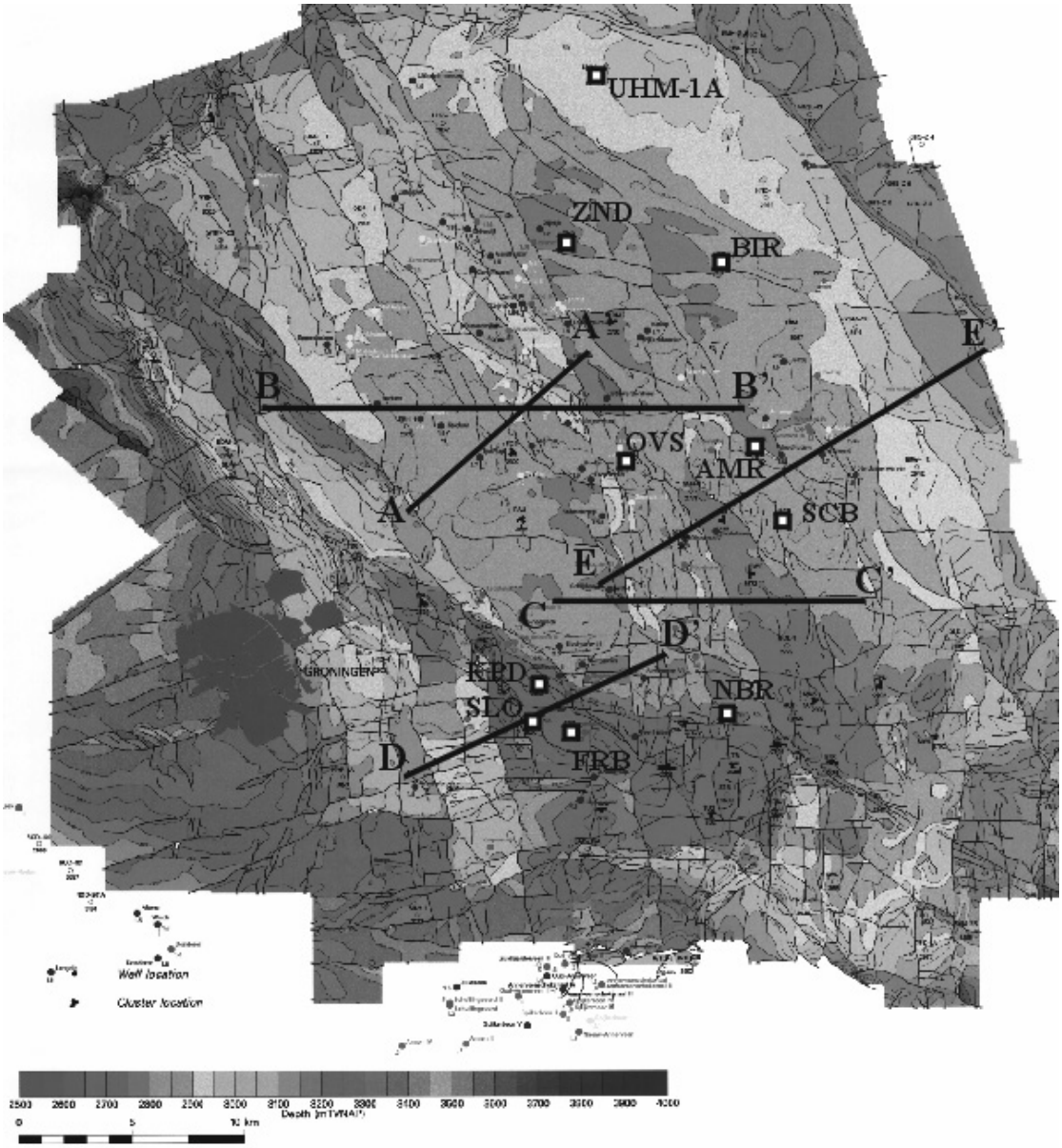

Figure 7.10. Top reservoir depth contour map of the Groningen gas field (source: NAM). White squares denote the location of some well clusters. Coloured dots denote the location of seismic events as determined by KNMI. Profile lines AA', BB', CC', DD' and EE' are shown, corresponding to Figures 7.12 – 7.15 and 7.21. See Appendix 2 for this figure in colour.

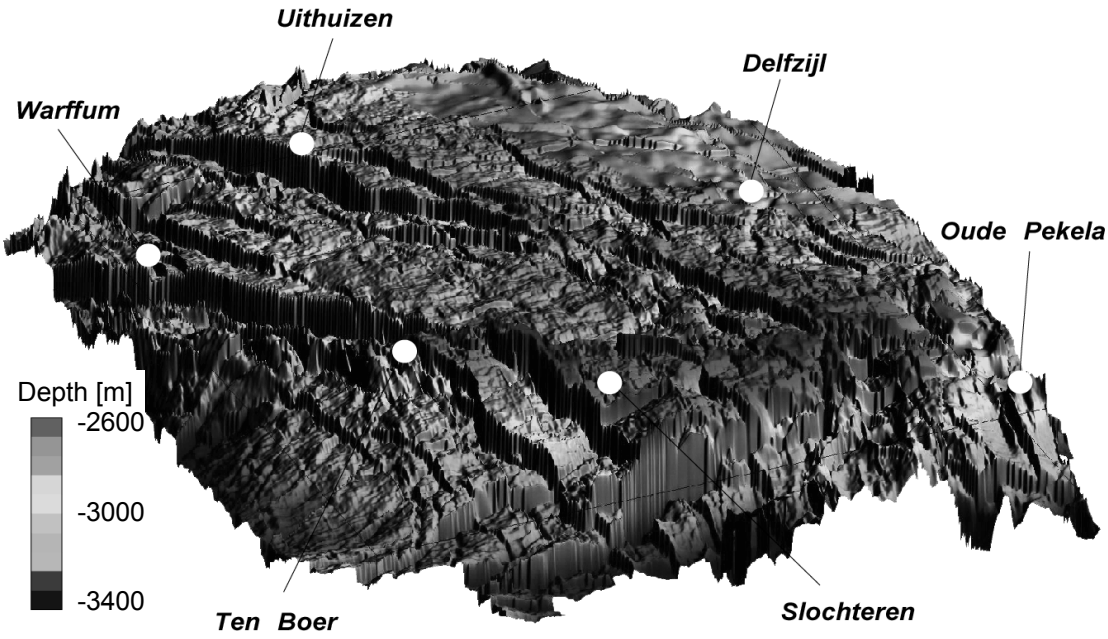

Figure 7.11. Birds-eye view from south-western direction on the Groningen gas field. Contours indicate the top reservoir depth (source: NAM). See Appendix 2 for this figure in colour.

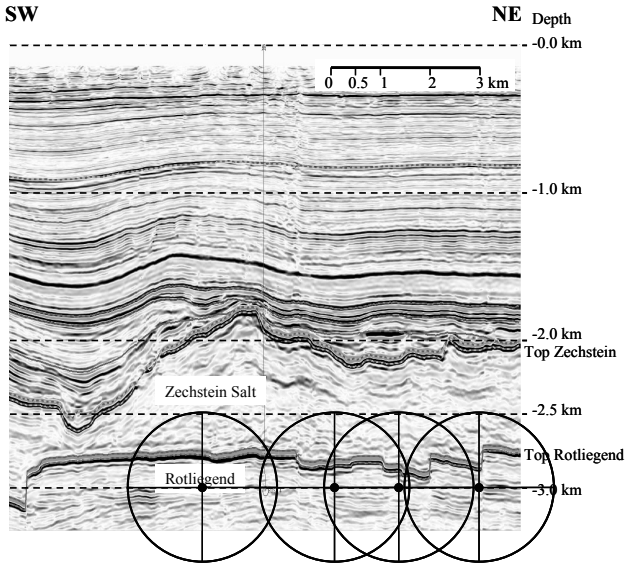

Figure 7.12. Seismic cross section AA' through the Groningen field (for location see Figure 7.10). The vertical scale is three times the horizontal scale. Black dots indicate locations of seismic events as determined by KNMI. A black ellipse around an event denotes the uncertainty in location (source: NAM, KNMI). See Appendix 2 for this figure in colour.

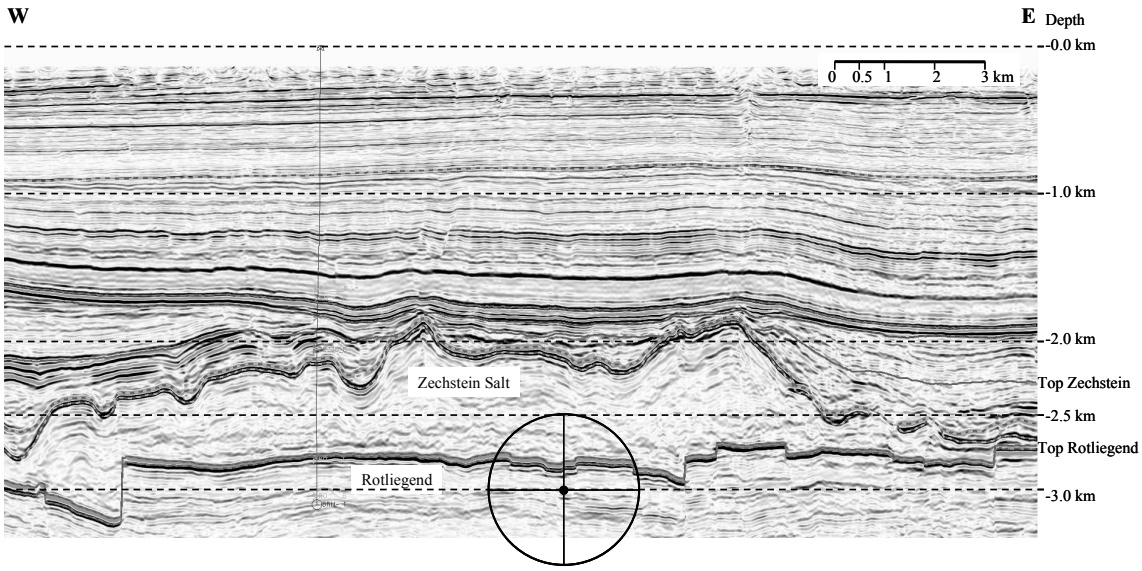

Figure 7.13. Seismic cross section BB' through the Groningen field (for location see Figure 7.10). The vertical scale is three times the horizontal scale. Black dots indicate locations of seismic events as determined by KNMI. A black ellipse around an event denotes the uncertainty in location (source: NAM, KNMI). See Appendix 2 for this figure in colour.

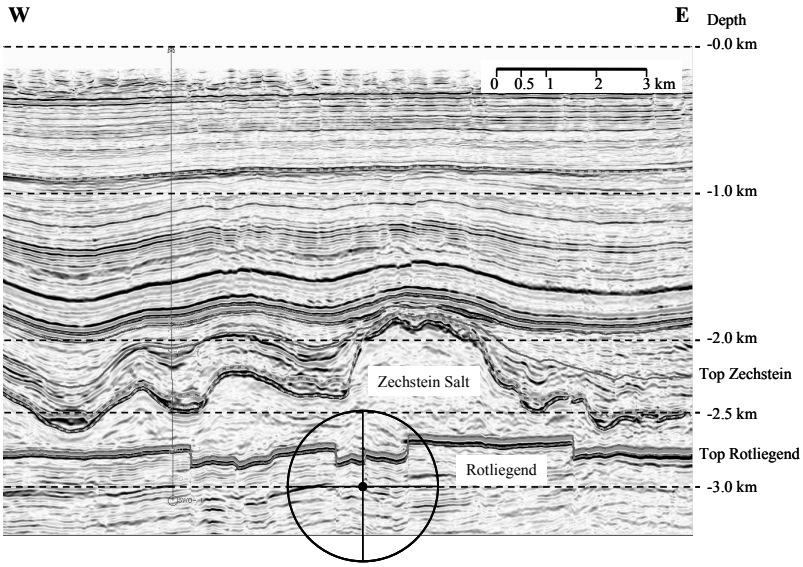

Figure 7.14. Seismic cross section CC' through the Groningen field (for location see Figure 7.10). The vertical scale is three times the horizontal scale. Black dots indicate locations of seismic events as determined by KNMI. A black ellipse around an event denotes the uncertainty in location (source: NAM, KNMI). See Appendix 2 for this figure in colour.

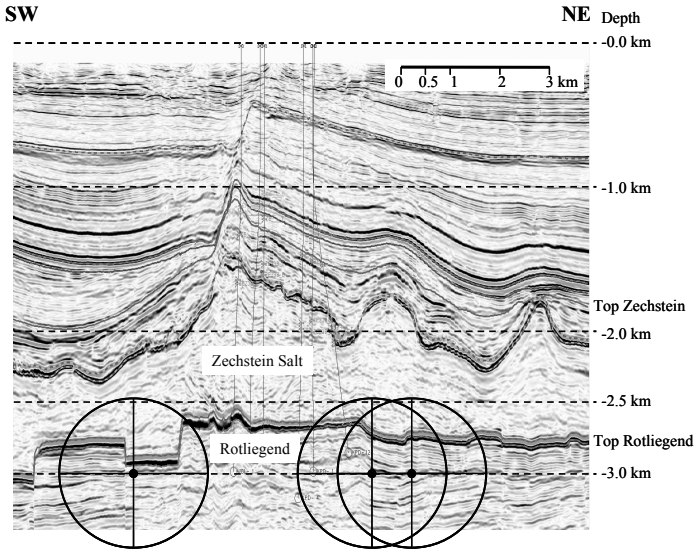

Figure 7.15. Seismic cross section DD' through the Groningen field (for location see Figure 7.10). The vertical scale is three times the horizontal scale. Black dots indicate locations of seismic events as determined by KNMI. A black ellipse around an event denotes the uncertainty in location (source: NAM, KNMI). See Appendix 2 for this figure in colour.

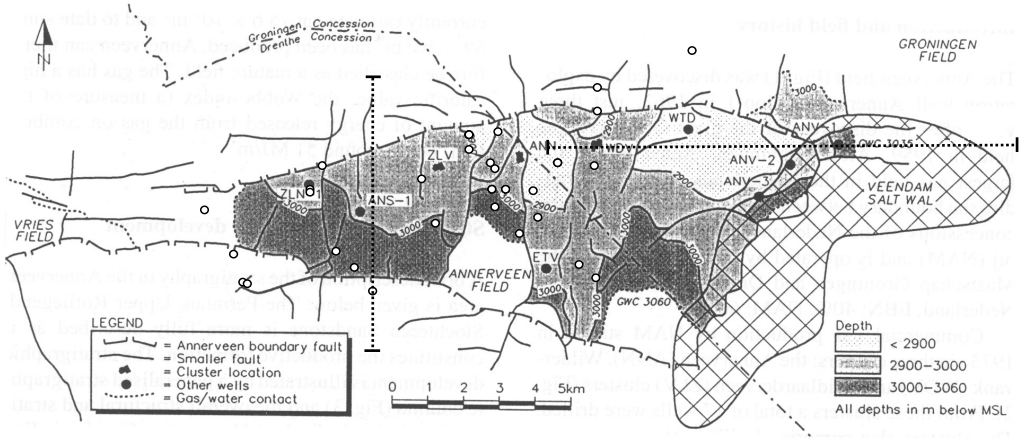

Figure 7.16. Generalised top reservoir depth contour map of the Annerveen gas field (after Veenhof 1996). White dots denote the location of seismic events as determined by KNMI. Profile lines are shown, corresponding to Figures 7.17 and 7.18.

The Annerveen gas field shows a fault pattern which is somewhat different from the Groningen gas field. It consists mainly of N-S trending normal faults (Figure 7.16). None of these N-S trending faults has a large enough throw to completely offset the reservoir. Throws are mostly in the range of 10 – 20 m (Veenhof 1996). These faults may represent older, reactivated Carboniferous lineations (Veenhof 1996). In fact, this trend matches well with the rhomboidal fault pattern characteristic for the southern part of the Groningen gas field. The N-S trending grabens continue to the Annerveen gas field (Figure 7.17; note the effect of the travel time or velocity pull-up, caused by

the Veendam salt wall). The E-W trending graben structures, which bound the Annerveen gas field to the north and south, seem not to have affected the E-W trending elongate horst block in which the Annerveen gas is captured (Figure 7.18). NW – SE trending faults of extensional nature are rare. They are interpreted to be of post-Permian age (probably Late Kimmerian, Stauble & Milius 1970 in Veenhof 1996). The field is dip-closed to the west. Overall, the horst block is tilted towards the south.

Overall in the Groningen and Annerveen gas fields, NE-SW trending structures are virtually absent.

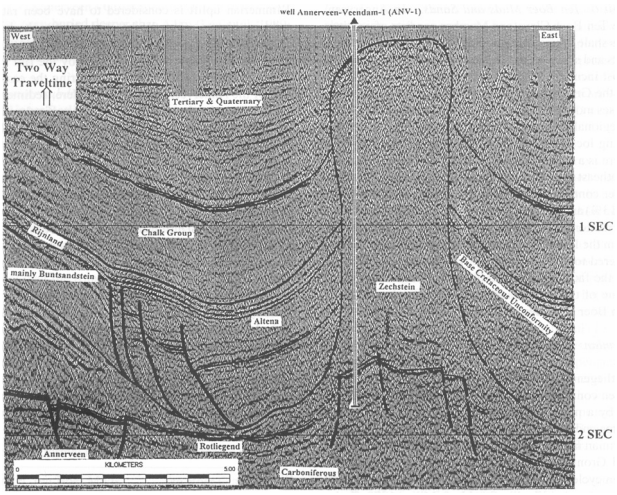

Figure 7.17. Seismic WE cross section through well ANV-1 (for location see Figure 7.16) in the Annerveen field (from Veenhof 1996).

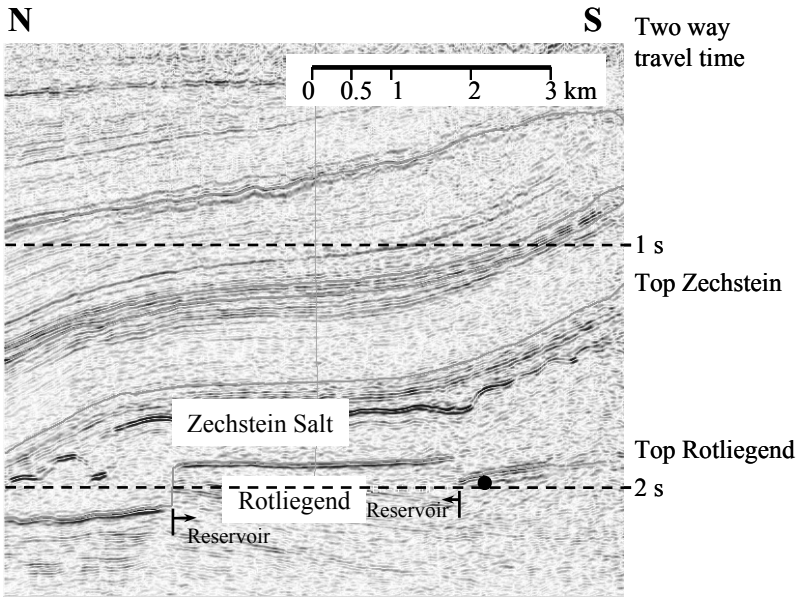

Figure 7.18. Seismic NS cross section through the Annerveen field (for location see Figure 7.16). The vertical scale is in two way travel time in seconds. The black dot indicates the location of a seismic event as determined by KNMI (source: NAM, KNMI). See Appendix 2 for this figure in colour.

7.5 Current tectonic stress field in the northern Netherlands

The rather complex tectonic history with associated fault generation and reactivation of the northern Netherlands is described in Chapter 7.3. It consists of a complex interplay of both compressional and extensional tectonics, including wrench tectonics. The current stress field in the northern Netherlands can be assumed to result mainly from the Tertiary Alpine Orogeny.

The present-day in situ state of stress in the northern Netherlands is not directly measured. Current insights in the in situ stress field are based on borehole breakout studies (Frikken 1999, Frikken 2000, Rondeel & Everaars 1993) and hydraulic fracturing (Frikken 1999). Insights of the intraplate stresses of the area are well documented by the World Stress Map (Zoback *et al.* 1991, Zoback 1992, Müller *et al.* 2000) and are supported by finite element modelling of the recent crustal stress field of Central Europe (Grünthal & Stromeyer 1994).

The World Stress Map shows data (Figure 7.19) in eight locations on the onshore Netherlands: three in the northern Netherlands and five in the southern Limburg area. The latter are derived from earthquake focal mechanisms. The northern Netherlands data are taken from the study from Draxler & Edwards (1984). They observed a very consistent borehole breakout direction in Carboniferous rocks of N050E $\pm$ 10 in the area between Slochteren and Hamburg. Hydraulic fracture propagation in north-western Germany is NNW-SSE. World Stress Map data therefore indicate that the stress field is marked by largest principal horizontal stresses oriented NW-SE, which is supported by earlier studies (Rondeel & Everaars 1993, Gruenthal & Stromeyer 1994, Klein & Barr 1986). Frikken (1999) mentions a wider range for the horizontal maximum principal stress direction, based on borehole breakouts from several Borehole Imaging Logs: NW-SE to N-S, whereby the direction depends on the local stress regime of individual blocks. A rose diagram of hydraulic fracture strike orientation of the Slochteren Sandstone in well BLF-104 (NE-Netherlands) as shown by Frikken (1999) indicates a N28W orientation of the present-day horizontal maximum principal stress on this location (Figure 7.20). Rondeel & Everaars (1993) mention an average orientation of N55W and N20W for Carboniferous rock and rock formations above the Carboniferous, respectively. Conclusions in a report for NAM (Frikken, 2000), based on breakout observations and various assumptions, mention that the orientation of the maximum horizontal stress could range from N8E to N16W.

Although still under discussion it is generally assumed, that the present-day direction of the largest horizontal stresses in the Netherlands is NW-SE. It is very likely that due to geological structures in the subsurface this direction can locally be different.

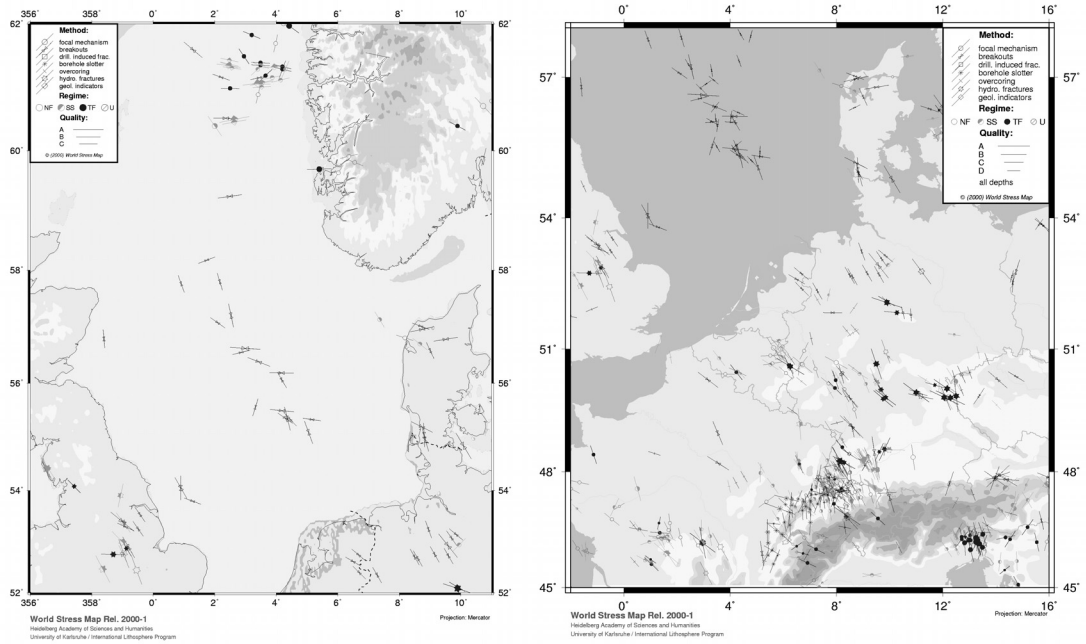

Figure 7.19. Stress maps of the North Sea and central Europe (from Reinecker et al. 2003). Stress symbols display the orientations of the maximum horizontal stress σ_H. The length of the stress symbols represents the data quality, with A as the best quality category. A-quality data are believed to record the orientation of the horizontal tectonic stress field to within $\pm$ 10°-15°, B-quality data to within $\pm$ 15°-20° and C-quality data to within $\pm$ 25°. D-quality data are considered to yield questionable tectonic stress orientations (Zoback 1992). The tectonic regimes are: NF for normal faulting, SS for strike-slip faulting, TF for thrust faulting and U for an unknown regime. See Appendix 2 for this figure in colour.

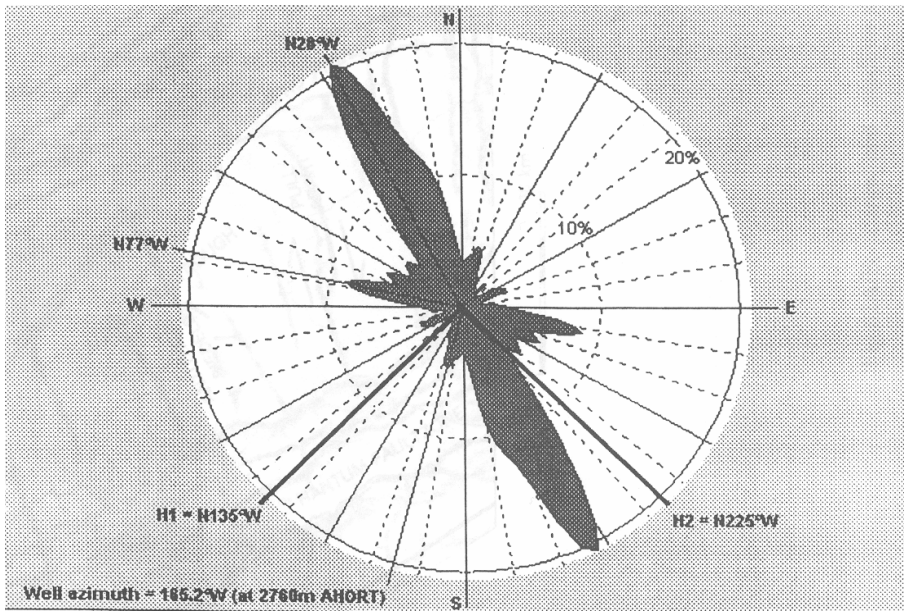

Figure 7.20. Rose diagram of hydraulic fracture strike orientation of the Slochteren Sandstone in well BLF-104, north-eastern Netherlands (from Frikken 1999).

A state of stress is besides the direction of the stress components determined by the magnitude of the components. The vertical stress is generally assumed to be the result of the weight of the rock mass. The magnitudes of the maximum and minimum horizontal stresses in the subsurface of the northern Netherlands are not known in detail. The tectonic setting of the Netherlands suggests an extensional stress regime influenced by the Alpine Orogenesis. In previous research on geomechanical modelling of gas reservoirs in the northern Netherlands, a K_0-value of 0.4 is therefore often assumed (Roest & Kuilman 1993, Nagelhout & Roest 1997, Schreppers 1998, Glab 2001). Frikken (2000) points to the occurrence of both strike slip and dip slip components on regional faults and concludes that the maximum horizontal stress should be close to the vertical stress, meaning that K_{0H} would be close to 1.0.

It has to be mentioned here that the horizontal stress magnitudes are very difficult to estimate and that they are very sensitive to local variations due to geological structures in the subsurface.

7.6 Seismicity in the Groningen and Annerveen gas fields

To date, a few hundred seismic events occurred within the lateral boundaries of the Groningen and Annerveen gas fields. For each event up to January 2001, seismic cross sections are studied by making use of the 3D-seismic database of NAM and the hypocentre data of KNMI. The hypocentre location of each event incorporates an uncertainty in depth of $\pm$ 500 m and a lateral uncertainty of $\pm$ 1500m. This is indicated by the ellipses in Figures 7.12 – 7.15 and 7.21. Despite this uncertainty in location, it is clear from Figures 7.12 – 7.15 and 7.21 that the majority of these events is located in the vicinity of steeply dipping normal faults at reservoir level.

Events are not necessarily always related to reactivation of normal faults at reservoir level. In literature, some examples exist of reactivation of subhorizontal thrust faults just above and/or below the reservoir (Baranova *et al.* 1999), reactivation of faults at shallower levels related to salt structures (Roest & Kuilman 1994, BOA 1993), and reactivation of faults at greater depth by mass transfer (McGarr 1991), see Chapter 6. The latter mechanism can be excluded for the northern Netherlands, since the depth estimation of all events in the Groningen and Annerveen gas fields is at reservoir level (appr. -3 km depth). This depth estimation also makes the mechanism of reactivation of faults at shallow levels related to salt structures very unlikely. An event such as shown in Figure 7.21 could possibly be related to the salt structure above the reservoir but is much more likely to be related to the reservoir boundary. Faults in the Groningen and Annerveen gas fields are predominantly subvertical normal faults, making the mechanism of reactivation of subhorizontal reverse faults unlikely. Furthermore, a compressional stress regime with relatively high K_0-values is needed for reactivation of this type of faults. Such a stress regime is absent in the northern Netherlands (Chapter 7.4).

It can therefore be concluded that the seismic events in the Groningen and Annerveen gas fields are in general related to the reactivation of steeply dipping (subvertical) normal faults at reservoir level. It has to be mentioned here that reactivation of a normal fault does not necessarily mean normal fault movement. A normal fault can also be reactivated by reverse movement. Fault plane solutions of KNMI indicate reverse fault reactivation along steeply dipping faults for some seismic events in the Roswinkel and Bergermeer gas fields. The reactivated fault in the Bergermeer gas field is a normal fault (see Chapter 1).

The majority of the seismic events in the Groningen field is related to the two major NW-SE trending graben structures which intersect the field at its west side (Figure 7.10). Another important group of events occurs in the two NW-SE and N-S trending branches of the northernmost major grabenstructure. Seismic events are virtually absent in the south-eastern part of the field, where the rhomboidal fault structure consisting of N-S and E-W trending faults is present. Seismic events are also virtually absent in the northern part of the field. This is most probably due to the relatively simple geology in this area, consisting of (sub)horizontal layering and low fault density. Seismic events in the Annerveen gas field are restricted to the central and western part of the field (Figure 7.16). Most events occur in the central part. The fault pattern in the Annerveen field indicates that these events are mainly the result of reactivation of N-S trending normal faults. Some seismic events may be related to reactivation of E-W trending reservoir bounding faults.

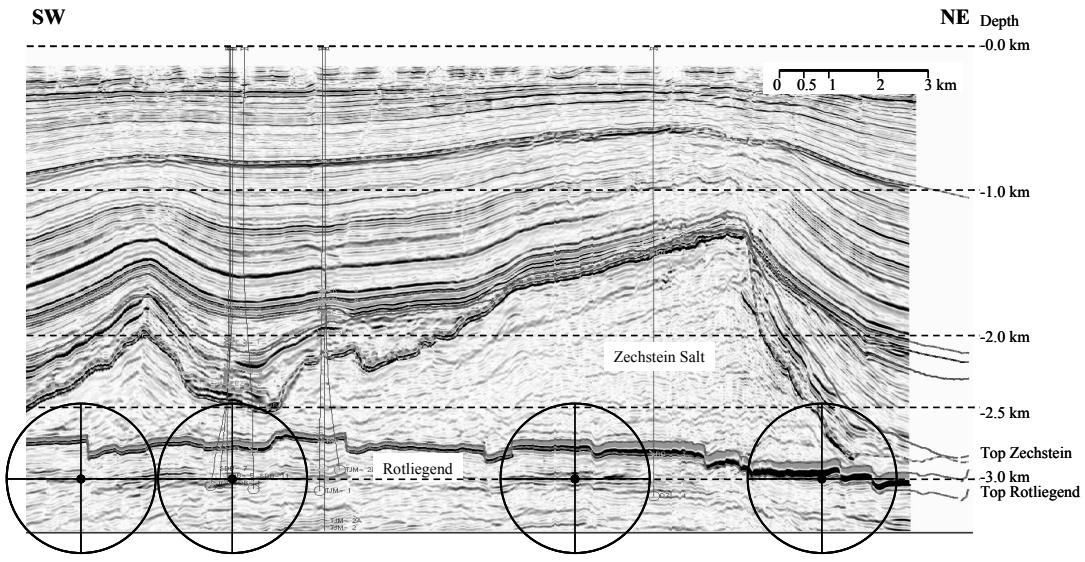

Figure 7.21. Seismic cross section EE' through the Groningen field (for location see Figure 7.10). The vertical scale is three times the horizontal scale. Black dots indicate locations of seismic events as determined by KNMI. A black ellipse around an event denotes the uncertainty in location (source: NAM, KNMI). See Appendix 2 for this figure in colour.

7.7 Summarising description of the Groningen and Annerveen gas fields

In this section, a summarising description of the Groningen and Annerveen gas fields for geomechanical modelling purposes of this study is given. This description forms the bases of the chosen geometry of the finite element models, rock property values and initial pore pressure. The models are described in Chapter 8.

Both Groningen and Annerveen gas fields are very large in size and cut by numerous faults (Groningen field: approximately 900 km^2). It is virtually impossible to make a detailed 3-dimensional geomechanical model of the entire fields including their faults and expect a detailed analysis of fault reactivation and stress development as a result of gas depletion. It is therefore decided to build generic reservoir models which incorporate the basic features of the two fields and study the effects of different parameters on stress development and fault reactivation.

The Groningen block is generally tilting towards the north. NW-SE striking normal faults, which can have large amounts of throw (up to 300 m, see Chapter 7.3), are the dominant trend in Groningen. N-S and E-W trending faults with lesser amounts of throw are also frequent. The horst block capturing the Annerveen gas is overall tilted towards the south. N-S trending normal faults with relatively small amounts of throw, mostly between 10 – 20 m, form the dominant fault type in the Annerveen gas field.

The Annerveen and Groningen gas reservoirs do not consist of a homogeneous rock mass but each is subdivided into several units, as can be for instance seen in the N-S stratigraphical profile through the Upper Rotliegend Group through the Groningen gas field (Figure 7.22). The rocks of the Annerveen and Groningen gas fields are mainly sandstones with intercalations of conglomerates and shales. The upper unit in both Annerveen and Groningen is the Ten Boer Claystone. In Groningen, this unit consists mostly of non-reservoir shales and silts and forms a shaly reservoir seal. In Annerveen, the Ten Boer member shows a clear trend from coarse to fine clastics from southeast to northwest since this region was located closer to the Southern Permian Basin margin. It comprises continuous shale layers with intercalations of fine sandstones, silts and shaly sands, whereby the lower sequences contain reservoir quality sands. The unit represents the southernmost incursion of the Rotliegend desert lake (Figure 7.6). In the northern part of the Groningen field, the relatively thick Ameland Claystone member divides the reservoir sandstones in a lower and an upper part. Some thin Carboniferous (Westphalian) sandstones subcrop locally at the base of the Rotliegend and contribute to gas production.

The thickness of the Slochteren Sandstone, containing most of the Groningen gas field, varies between 70 m in the extreme southeast of the field to 240 m in the northwest. Reservoir thickness of the Annerveen gas field is 100 – 150 m. The Slochteren Sandstone is situated at an average depth of about -2900 m. The Annerveen gas field is located somewhat deeper, but almost at the same level. The average gas-water contact in the Groningen gas reservoir is -2970 m deep. This value

is -3060 m for the Annerveen gas field. All depths mentioned are below MSL (Mean Sea Level). The original average reservoir pore pressure was 34.7 MPa (347 bar) for the Groningen gas field and 34.5 MPa (345 bar) for the Annerveen gas field (Mobach & Gussinklo 1994, Veenhof 1996).

For the finite element models of this research, the following characteristics have been chosen. The chosen reservoir thickness in the models is 150 m, with its top located at a depth of -2900 m. The initial pore pressure is chosen to be 35.0 MPa (350 bar). A less or non-producing intercalation such as the Ameland Claystone and a gas-water contact are not modelled. The reservoir is 3000 m wide, which is in the range of reservoir compartments as observed in the Groningen and Annerveen gas fields. Most of the geomechanical reservoir models incorporate a normal fault intersecting the reservoir with varying amounts of throw. In view of the intended parameter study, the volume surrounding the reservoir is assumed to consist of one homogeneous isotropic rock mass in order to keep the model generic and free from any additional effects eventually produced by a layered geological structure.

Rock property values are based on previous geomechanical compaction and subsidence studies of Rotliegend gas reservoirs (Schreppers 1998, NAM 1998 and NAM 2000). The default reservoir rock properties are: $E = 13.0$ GPa, $\nu = 0.2$, $c = 5$ MPa and $\phi = 30^{o}$. The default rock property values for the surrounding rock are: $E = 18.5$ GPa, $\nu = 0.25$, $c = 5$ MPa and $\phi = 25^{o}$. These values are used in NAM (1998) as average values for the overburden rocks above the Zechstein evaporites. The properties of the surrounding rock can be considered as being representative for the Ten Boer Claystone. The Ten Boer Claystone is usually modelled using a Young's modulus of 18.0 GPa and a Poisson's ratio of 0.25 (NAM 2000). The dilatancy angle ψ is assumed to be 10^{o} for both reservoir and surrounding rocks, a typical value for sandstone rocks at field conditions (Charlier 2000).

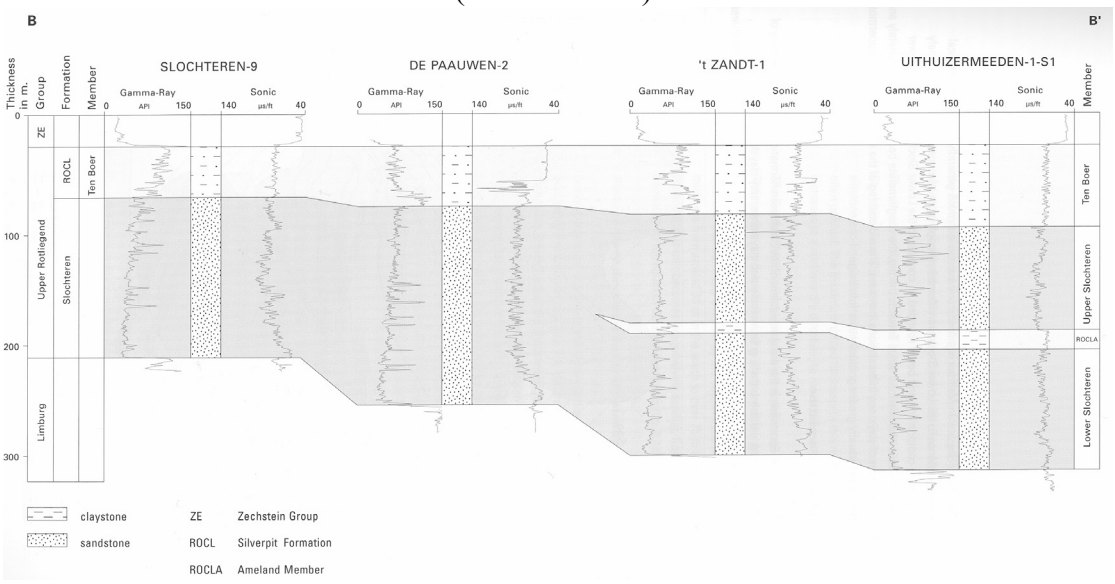

Figure 7.22. Stratigraphical NS profile of the Upper Rotliegend Group through the Groningen field; for location see Figure 7.23 (from RGD 1995).

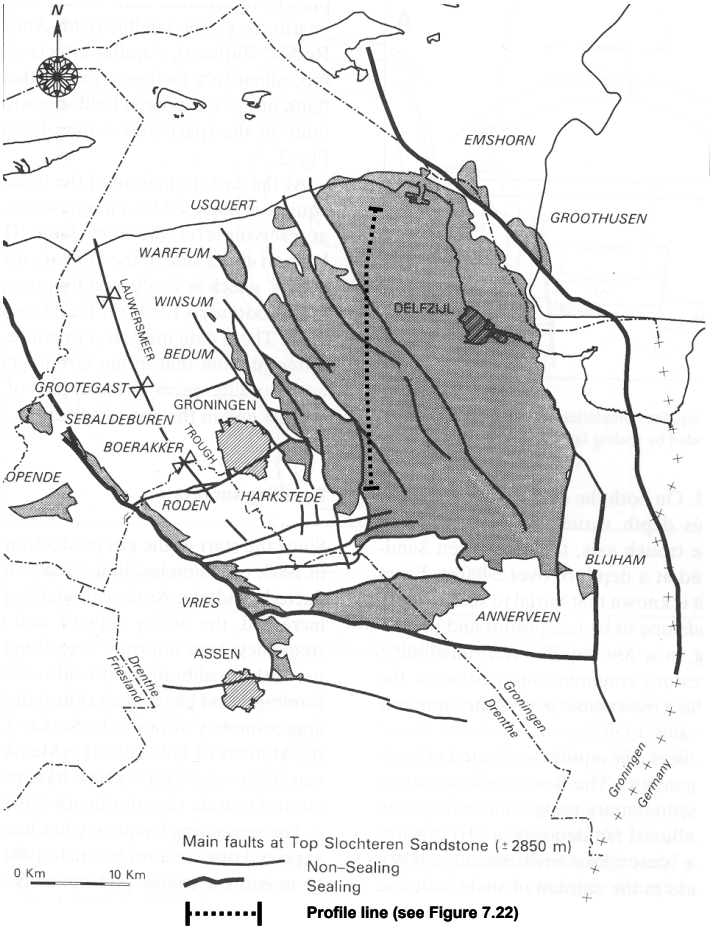

Figure 7.23. Map showing outlines of gas fields and main faults at reservoir level (after Doornhof 1992).

In the geomechanical models for this study, faults are modelled incorporating the same initial pressure as the neighbouring rock formations. During reservoir depletion, the part of the faults in contact to reservoir rock deplete with the same amount as the reservoir rock. This is based on the following. Figure 7.23 shows a map of the Groningen area with indications of the sealing properties of the main faults through the Slochteren Sandstone. Sealing faults are basically restricted to the east and west of the Groningen and Annerveen fields, relatively far outside of the fields. The southern bounding fault of the Annerveen gas field is a sealing fault as well. Faults within this area and thus within the Groningen and Annerveen gas fields are considered to be non-sealing. This is in accordance with the statement of Veenhof (1996), that most of the Annerveen gas field is well drained and that the numerous faults which are mapped in the main field do not form transmissibility barriers. An exception occurs at the eastern flank of the field, where semi-transmissive faults are present. This is clear from the pressure development in the well ANV-1 (Annerveen), which follows the pressure trend of the nearest well in the Groningen field (Zuidwending, ZWD-1), see Figure 7.24. Neighbouring wells in the Annerveen field (Zuidlaren, ZLN-1, and Annerveenschekanaal, ANS-1) follow the Annerveen field depletion trend. Currently the fault or fault zone between ANV-1 and the nearby part of the Annerveen field is holding a pressure differential of more than 10 MPa (100 bar). As the quality of the

seal is difficult to estimate, the risk exists that the fault could be breached once the pressure differential exceeds the faults' sealing capacity. Subsequently, the ANV-1 gas would flow to the Annerveen main field (Veenhof 1996).

The effect of 'aquifer depletion', whereby the pressure in a small associated aquifer will decrease gradually with the pressure in a large gas bearing reservoir, as is the case in the Groningen gas field (Doornhof 1992), is not modelled. The pore pressure in the rock formations surrounding the reservoir are assumed to be initially hydrostatic and to remain constant during depletion of the gas reservoir.

For a detailed description of the finite-element model setup and model properties see Chapter 8.

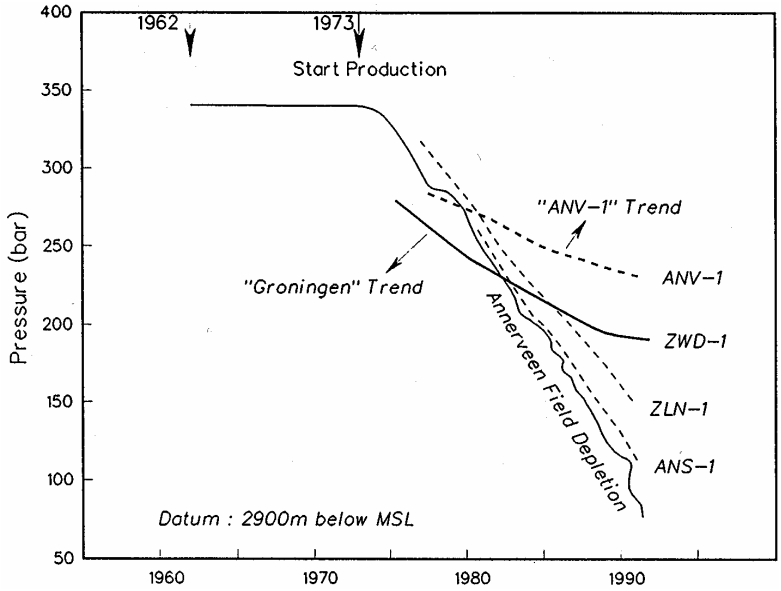

Figure 7.24. Pressure development in time for the Annerveen field and the southern margin of the Groningen field (from Veenhof 1996).

8 MODEL SET-UP

This chapter describes the chosen model geometry and (default) geomechanical properties and loading conditions. The model geometry is chosen based on field data analysis (Chapter 7). The reservoir depth and thickness and the normal fault setting are representative for most of the Rotliegend gas fields in the Netherlands. The size of the reservoir is in the range of reservoir compartments as observed in the Groningen and Annerveen gas fields. The volume surrounding the reservoir is assumed to consist of one homogeneous isotropic rock mass in order to keep the model generic and free from any additional effects eventually produced by a layered geological structure. The generic model character is also the reason for choosing a relatively simple disk-shaped geometry of the reservoir. Rock properties are based on based on previous geomechanical compaction and subsidence studies of Rotliegend gas reservoirs (Schreppers 1998, NAM 1998 and NAM 2000). Initial pore pressure and tectonic stress field are based on field data analysis, literature and personal communication (see Chapters 7.5 and 7.7).

In the following, the geometries of the 3D models and their generation in DIANA's pre-processor 'iDIANA' are described firstly in Chapter 8.1. Subsequently the geometries of the 2D models are described in Chapter 8.2. Chapter 8.3 gives the default geomechanical properties and loading conditions applied to the models and evaluates the applicability of the assumed model size.

8.1 3D-model geometry

The 3D finite element models consist basically of a box of 12,000x12,000x5000m (Figure 8.1). A disk-shaped reservoir is horizontally centred within this box. It is intersected by a fault plane. A Cartesian x,y,z co-ordinate system is applied as shown in Figure 8.1. The x-, y- and z-axes form in the given order a right-handed system. The x-axis points in the dip direction of the fault plane, the y-axis points in the strike direction of the fault plane and the z-axes points vertically upwards. The origin O of the co-ordinate system is positioned horizontally centred at the top of the model.

Chapter 8.1.1 zooms in on a description of nine different reservoir geometries and the nine corresponding 3D finite element models which are built for this thesis. Chapter 8.1.2 describes the details and assumptions on the fault geometry. In Chapter 8.1.3 the total model size as given above and boundary conditions are discussed.

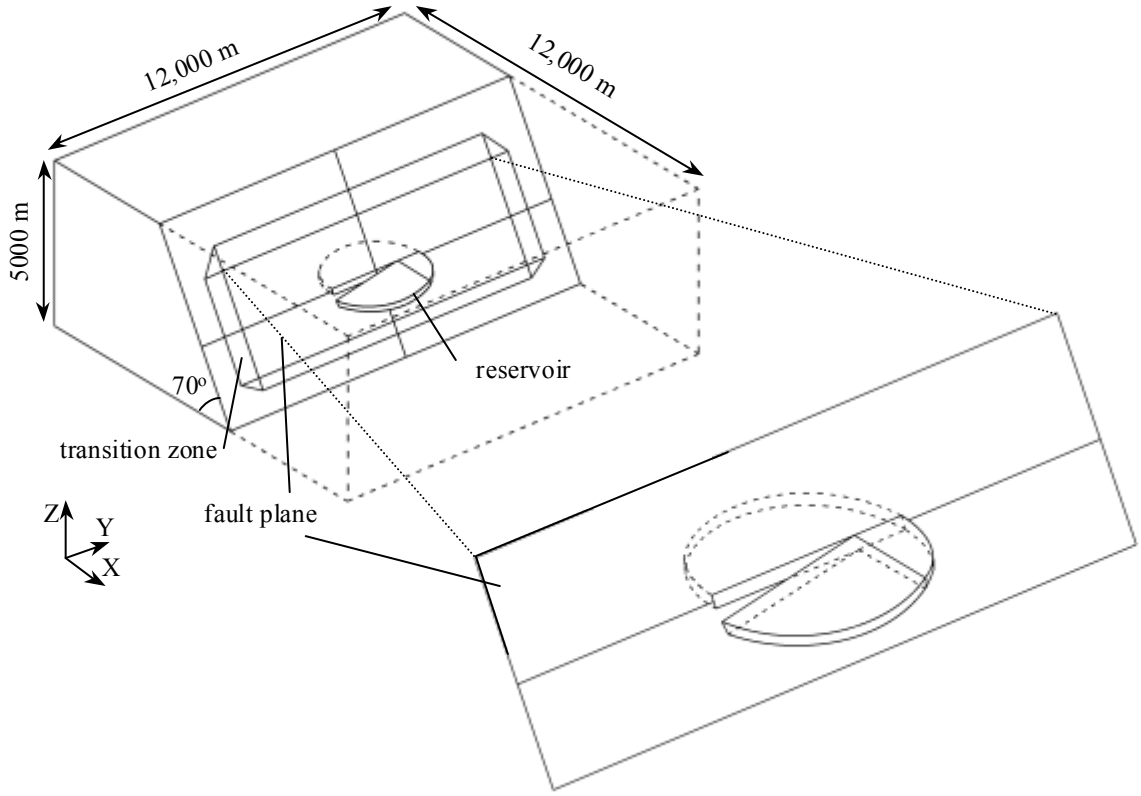

Figure 8.1. Basic geometry of the 3D finite element models, shown by model 'throw_var' (see Chapter 8.1.1.2).

8.1.1 Reservoir geometry

The 3D models incorporate a disk-shaped gas reservoir with a radius of 1500m and a thickness of 150m (see Figures 8.1 and 8.2). The aspect ratio of the disk is thus 0.05. The top of the reservoir is located at a depth of -2900m. The volume surrounding the reservoir is assumed to consist of one homogeneous isotropic rock mass. A fault plane intersects the reservoir through its centre and divides the reservoir in two distinct compartments: a footwall reservoir compartment and a hanging wall reservoir compartment. The fault plane is created such that it runs always through the centre of the disk at a depth of -2975m, through the point (0,0,-2975).

Nine different 3D models are built, each with a different amount of throw (vertical separation) along the fault (Chapters 8.1.1.1 and 8.1.1.2). For values of throw larger than zero, the hanging wall reservoir compartment is located deeper than the footwall reservoir compartment, thus creating a normal fault setting. The top of the footwall reservoir compartment is in all models located at a depth of -2900m. Each model is referred to by a specific name.

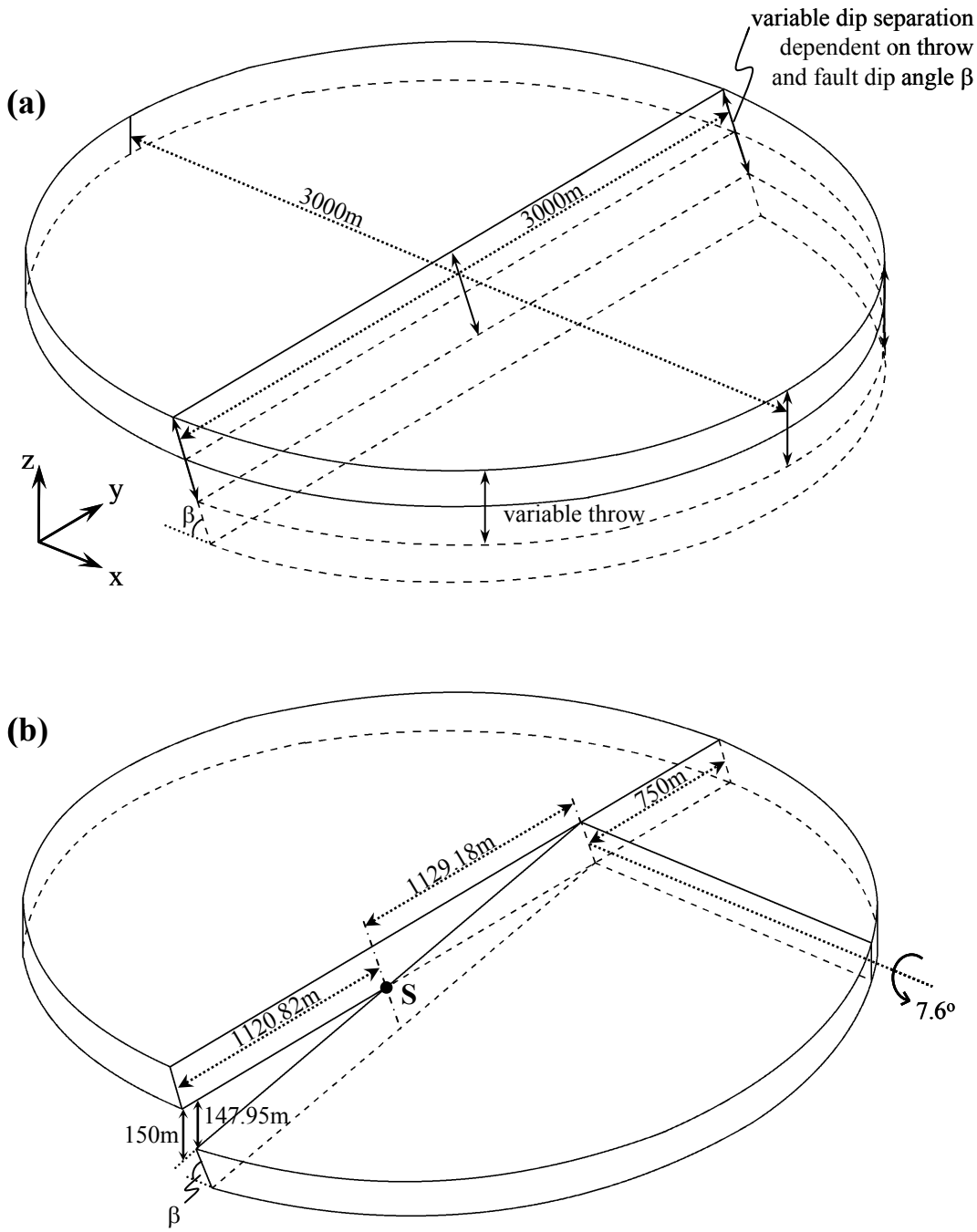

Figure 8.2. Geometry of the disk-shaped gas reservoirs in the 3D models. A fault plane intersects the reservoir through its centre and divides it in a footwall and hanging wall reservoir compartment. (a) Model series 'throw_const_...D'. (b) Model 'throw_var'; point S is the point on the fault plane where the top of the hanging wall reservoir compartment is exactly opposite to the bottom of the footwall reservoir compartment.

8.1.1.1 Model series 'throw_const_...D'

Models 'throw_const_...D' incorporate a throw which is constant along the strike of the fault (Figure 8.2a). D stands for the reservoir thickness, which is not varied and has a constant value of 150m. The number which appears in the model name at the before last position indicates the amount of throw. For instance ½ means that the amount of throw is ½ times the reservoir thickness: 75m. A value of 1 indicates a throw which is equal to the reservoir thickness: 150m. For this specific case, the top of the hanging wall reservoir compartment is located at the same depth as the bottom of the footwall reservoir compartment. The value 0 indicates that there is no throw along the fault plane. Model series 'throw_const_...D' consists in total of eight models (Table 8.1).

Table 8.1. Definition of eight models of model series 'throw_const_...D'.

Model name	*Throw (m)*	*Throw / D (D=150m)*
throw_const_0D	0	0
throw_const_¼D	37.5	¼
throw_const_½D	75	½
throw_const_¾D	112.5	¾
throw_const_1D	150	1
throw_const_1¼D	187.5	1¼
throw_const_1½D	225	1½
throw_const_2D	300	2

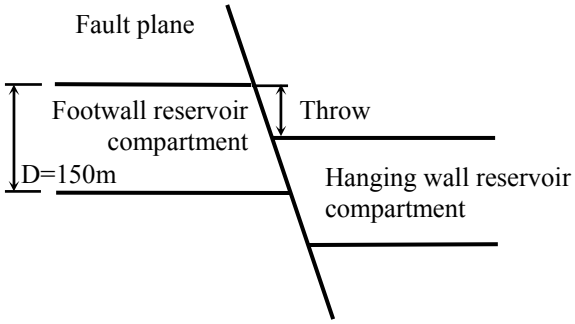

8.1.1.2 Model 'throw_var'

In model 'throw_var', the throw varies along the strike of the fault plane (Figure 8.2b). A clear example of such geometry is situated in the Bergermeer gas field in the Netherlands (see e.g. Roest & Mulders, 2000). Top reservoir depth contour maps of the Groningen gas field, such as shown in Figure 7.10 (Chapter 7.4), indicate that such geometry occurs in the Groningen gas field as well. The throw variation results from a partly dipping of the hanging wall reservoir compartment towards the negative Y-direction of the model, whereas the footwall reservoir compartment remains horizontal. The dipping of the reservoir compartment is defined by an angle around an imaginary rotation axis, which runs perpendicular to the strike of the fault at 2975 m depth, 750 m in positive Y-direction from the reservoir centre (see Figure 8.2b). This rotation angle is chosen to be 7.6^{o}. The reason of this choice is a maximum throw of almost two times the reservoir thickness (297.95m) at the lateral reservoir edge. Note that a part of the hanging wall reservoir compartment is not dipping, making that the two reservoir compartments in this region are located exactly opposite to each other. In fact, model 'throw_var' summarises the eight models of series 'throw_const_...D' in one model.

8.1.2 Fault geometry

The fault plane intersects the reservoir and divides the reservoir in two distinct compartments. The fault plane is positioned such, that it runs through the very centre of the reservoir, through point (0,0,-2975). The fault plane strikes parallel to the model y-axis. The fault dip direction is equal to the model x-axis direction. The default fault dip angle β is 70º. The fault thickness is 0m.

The fault plane does not extend until the model boundaries but has a limited extent (see Figures 8.1 and 8.3). The connection of hanging and footwall by continuous rock volume at the boundaries of the model prevents slipping of the entire hanging wall, which would result in divergence during iterating in the nonlinear analysis.

The fault is modelled using interface elements. As is explained in Chapter 5.3, interface elements consist of two sides, each with a certain number of corresponding nodes. These two sides are allowed to move relative to each other. They are indicated in Figure 8.3b by 'f1' and 'f2', respectively. Note that the physical thickness of the fault plane is 0 m. Figure 8.3 suggests that the fault plane has a physical thickness, but the figure is only imaginary in order to explain the numerical geometry of the fault plane. In the model, planes f1 and f2 coincide initially.

The fault plane is surrounded by a transition zone and an outer edge of continuous surrounding rock. The transition zone connects the pairs of nodes of the interface elements to the solid elements, which are used to model the continuous rock volume. Figure 8.3b shows this concept in cross-sectional view. Figure 8.3c shows the construction of the transition zone at the upper left corner of the fault plane. The fault plane ends with an interface element T18IF, situated in between the footwall and hanging wall rock volumes consisting of TE12L-elements. The pair of nodes at the end of the fault plane has to be reduced to one node for a proper connection of the TE12L-elements in the continuous rock zone. No element is defined for the shaded zone in Figure 8.3b. It represents therewith an empty space. It is important that the shaded zone is bounded solely by three nodes. In case of lower order elements without midside nodes this shaded zone is then bound by one solid element on either side. In case of higher order elements with midside nodes, the shaded zone only continues until the first midside node.

The used technique as described above is based on TNO Building & Construction Research 1999. It is especially justified for the fault thickness of 0 m, since the numerical 'gap' in the transition zone is than physically absent.

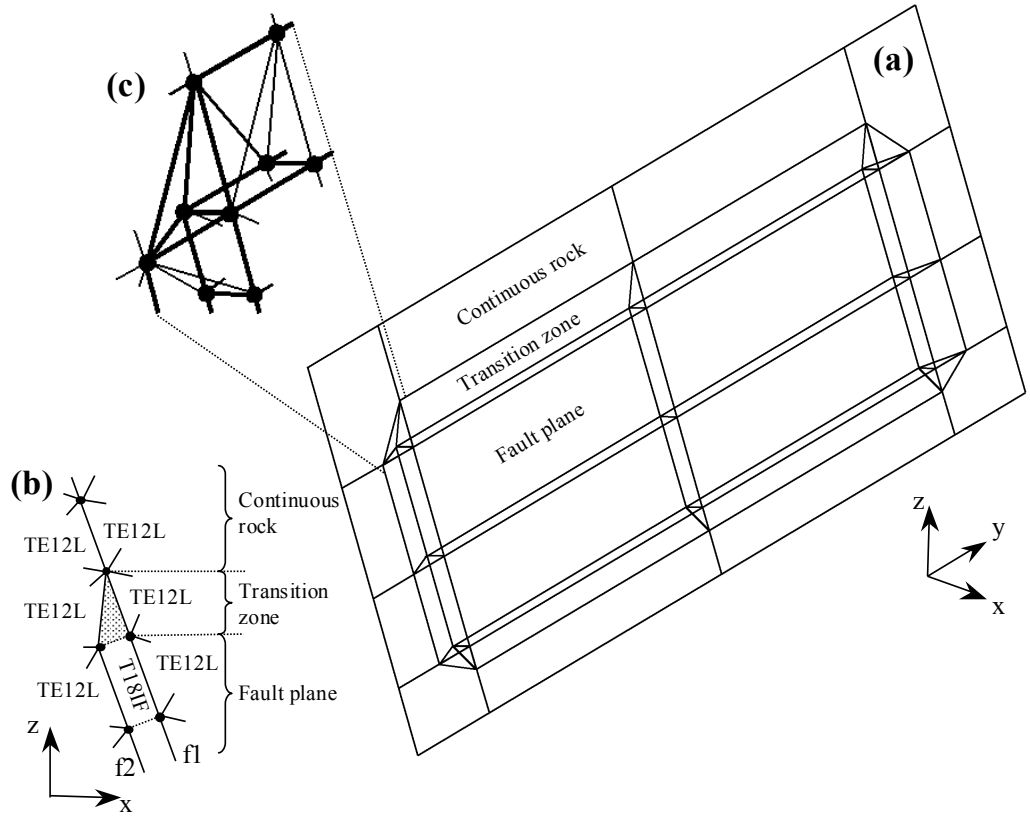

Figure 8.3. *(a) Numerical geometry of the fault plane. Note that the physical thickness is zero. (b) Cross sectional view. Interface elements T18IF are bounded by the two surfaces f1 and f2. The surfaces f1 and f2 coincide initially in the numerical models. TE12L are solid finite elements; the shaded zone, representing the transition zone, is not defined by a finite element. Note that this zone physically vanishes for a fault thickness of 0 m. (c) Detail of the element structure at the top left corner of the fault plane. Note again that the thickness shown in the figure is only imaginary.*

8.1.3 Total model size and boundary conditions

At the four lateral sides of the model, horizontal translations normal to the respective sides are constrained. Vertical translations are constrained at the bottom of the model. The top surface is free from any constraints and represents so with the earth's surface.

As a rule of thumb, a total lateral model size of 3-6 times the size of the reservoir should be taken. For the modelled reservoir with a diameter of 3,000m, this would mean a model size of 9,000 – 18,000m. As described before, the total model size is 12,000x12,000x5,000m, meaning that the lateral boundaries are located at a distance of 6,000m from the centre of the reservoir. It is investigated whether this distance is appropriate and how it affects the calculated fault slip and stress development in and around the reservoir. This investigation is described in Chapter 8.3.8.

8.1.4 Mesh density and element types

The fault plane consists of a large number of hexahedral and triangular prism bodies (a body is a volume surrounded by a closed set of surfaces). This allows the generation of a regular mesh (Figure 8.4) with a consistent node and element numbering, which is indispensable for the production of contour plots of relative shear displacements on the fault plane (see Chapter 9.1.1).

Because of the multiple bodies and thus multiple surfaces on both sides of the fault plane, reservoir and surrounding are built using general bodies. General bodies are volumes bounded by multiple structural surfaces. The use of general bodies generally limits the generation of bad shaped elements. A disadvantage is that besides line divisions no direct control on the element density is possible. Line divisions determine how many nodes and thus elements are created along a specific line. Furthermore, the number of elements which are generated in a general body strongly depends not only on the meshing divisions of the lines bounding the general body, but also on the meshing divisions of other lines elsewhere in the model and on the sequence in which the different bodies are created. Figure 8.5 shows the mesh structure of the reservoir for model 'throw_var'. Table 8.2 gives an overview of the number of elements generated in each of the nine different models. Element types are TE12L (structural solid pyramids with three sides and four nodes) for the rock volume and T18IF (structural triangular interface elements with two times three nodes) for the fault plane, see Chapter 5.3. The number of elements and choice of element type is determined by the hardware provided. 3D-models with higher order elements were not possible.

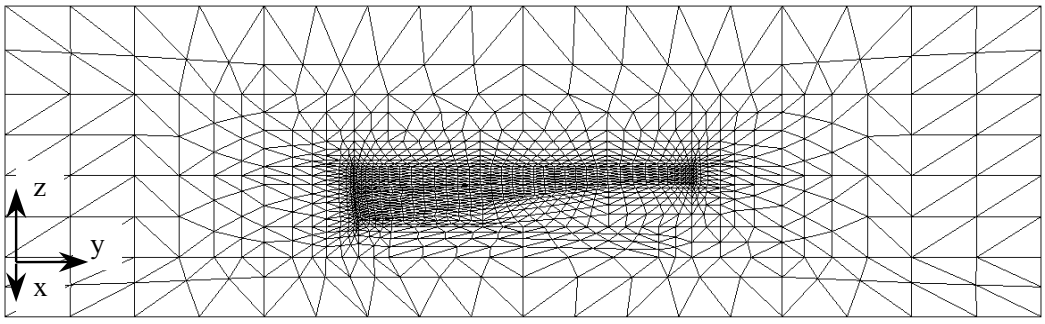

Figure 8.4. Finite element mesh structure on the fault plane, shown for model 'throw_var'. View direction is normal to the fault plane.

Table 8.2. Number of elements and nodes in the 3D models.

Model	*No. of elements*		*No. of nodes*
	TE12L	*T18IF*	
throw_const_0D	44,390	1876	8518
throw_const_¼D	50,005	2048	9545
throw_const_½D	49,934	2228	9618
throw_const_¾D	46,974	2408	9208
throw_const_1D	52,436	2510	10,172
throw_const_1¼D	52,245	2362	10,072
throw_const_1½D	55,399	2550	10,690
throw_const_2D	61,768	2772	11,846
throw_var	57,677	2572	11,051

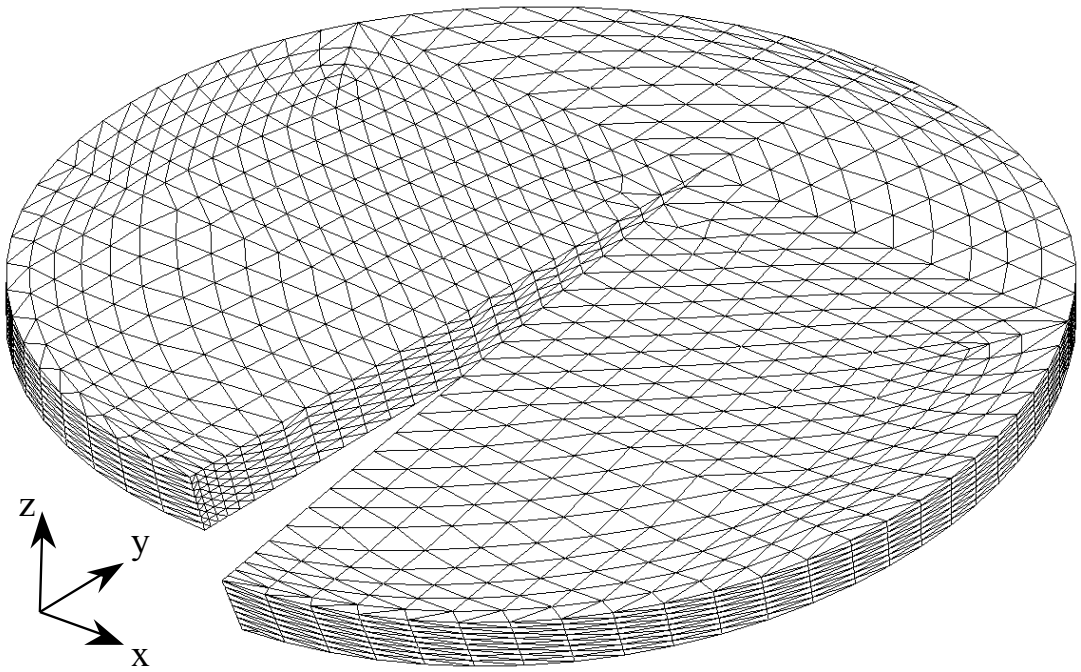

Figure 8.5. Finite element mesh structure of the reservoir, shown for model 'throw_var'.

8.1.5 Creation of model geometry in 'iDIANA'

The models are created in 'iDIANA', DIANA's pre-processor for model generation, by first constructing the necessary shapes in form of planes, cylinders and boxes. With the iDIANA-options 'geometry surface intersect…' and 'geometry point intersect…', the whole model geometry can be built relatively easy. The 'geometry surface intersect...' option creates intersection surfaces on a predefined analytical shape such as a plane or cylinder. The 'geometry point intersect...' option positions an existing point to be on the intersection of up to three shapes. This way allows the creation of various models with different sizes, fault dip angles and reservoir compartment dip angles by simply changing some co-ordinate values in a batch file, which contains all necessary commands for the model set-up.

The fault plane is created by means of the 'geometry sweep…'-option. Its thickness is 0 m. Sweeping a geometry to its location requires the tolerance to be either switched off or set to 0. When a new geometry is generated due to a copy or sweep operation, 'iDIANA' checks if a point already exists within the current tolerance before generating a new point. For the surface intersection option to function, the tolerance must be switched on again or set at its default value, which is a relative tolerance of 0.001. 'Relative' indicates that the tolerance is given as a factor to be applied to the length of the largest diagonal of the workbox.

8.2 2D-model geometry

2D models are built for two reasons. First, stress trajectories cannot be plotted conveniently in DIANA for 3D models. This option becomes important for the analysis of initial state of stress and stress development as a function of surrounding rock properties (see Chapter 11.2). Second, some basic calculations on reservoirs without an intersecting fault can be performed with axisymmetric models (see Chapter 10). An overview of the used geometries is given in this chapter (Figures 8.6 - 8.8). Note that model '2D_throw_½D' represents in fact a cross-section through the 3-dimensional model 'throw_const_½D'.

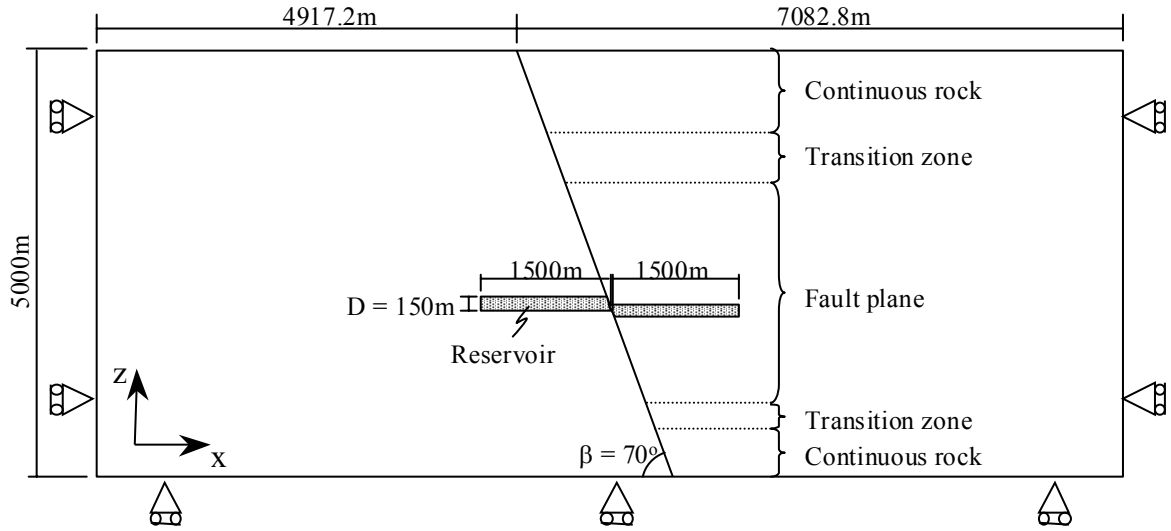

Figure 8.6. Geometry of the 2-dimensional plane strain model '2D_throw_½D'. It represents in fact a cross section through the 3-dimensional model 'throw_const_½D'.

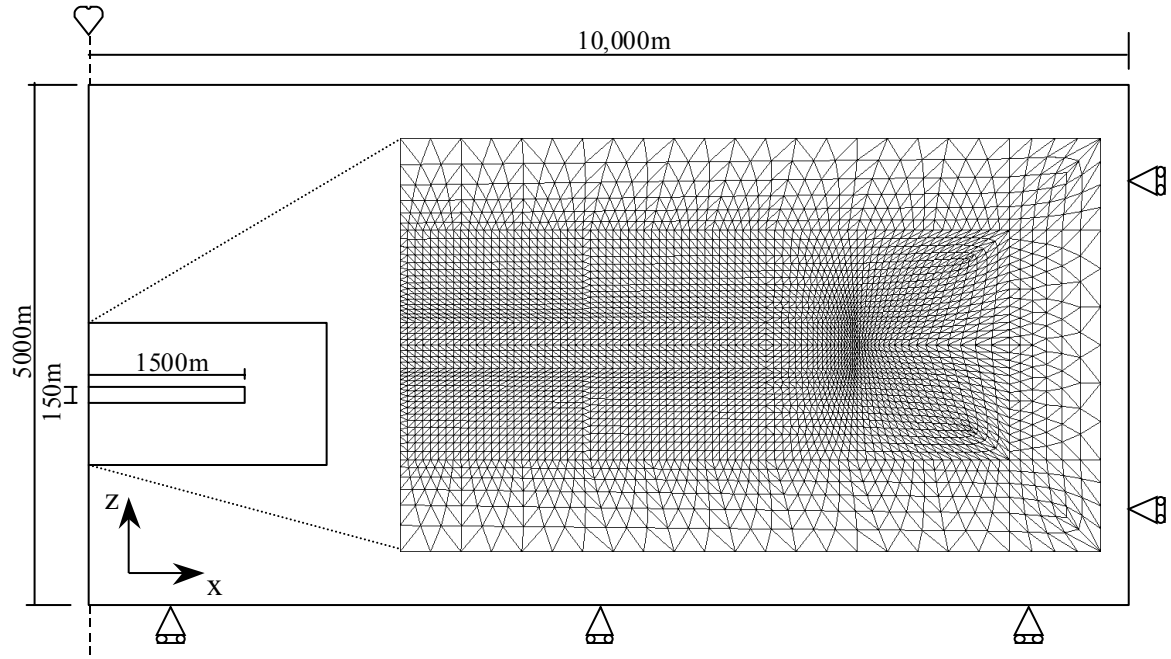

Figure 8.7. Geometry of the 2-dimensional axisymmetric model of a disk-shaped gas reservoir.

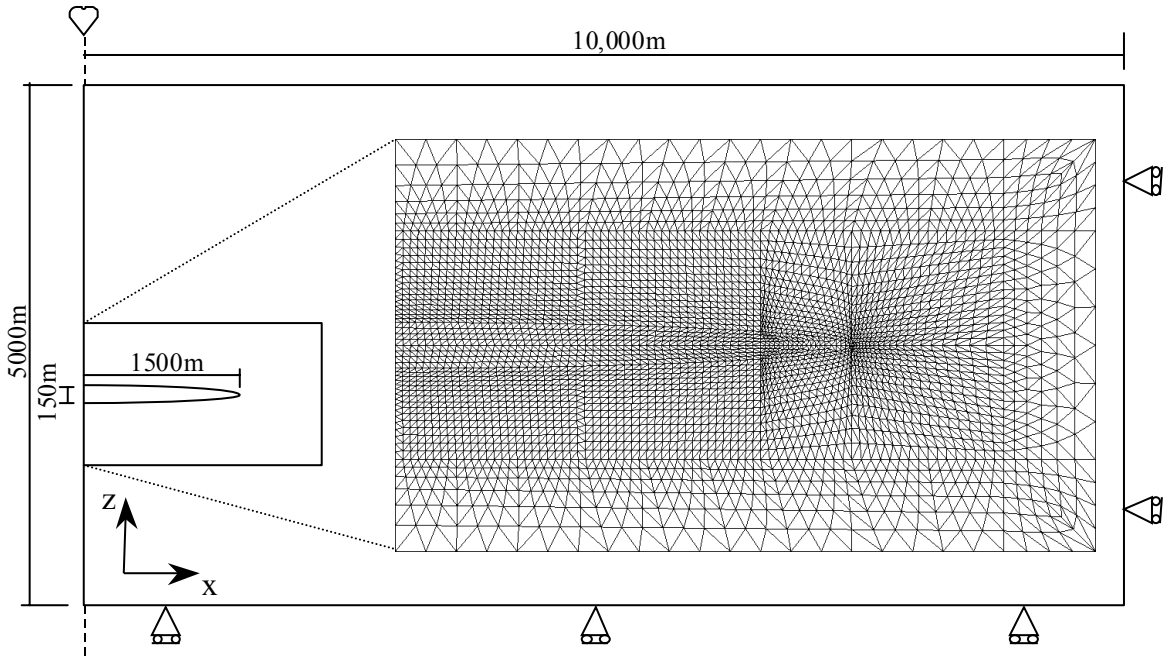

Figure 8.8. Geometry of the 2-dimensional axisymmetric model of an ellipsoidal gas reservoir.

8.3 Default geomechanical properties and loading conditions

8.3.1 Default rock properties

Both reservoir and surrounding rock are assumed to behave elastoplastically with Mohr-Coulomb failure as described in Chapters 2 and 3. No hardening, cracking or other options such as nonlinear elasticity or cap are modelled. Default rock properties of both reservoir and surrounding rock are given in Table 8.3. They are based on previous geomechanical compaction and subsidence studies of Rotliegend gas reservoirs (Schreppers 1998, NAM 1998 and NAM 2000). The default rock property values for the surrounding rock are used in NAM (1998) as average values for the overburden rocks above the Zechstein evaporites. The dilatancy angle ψ is assumed to be 10º, a typical value for sandstone rocks in field conditions (Charlier 2000). The properties of the surrounding rock can be considered as being representative for the Ten Boer Claystone, which forms a shaly reservoir seal above the Groningen and Annerveen gas reservoirs. The Ten Boer Claystone is usually modelled using a Young's modulus of 18.0 GPa and a Poisson's ratio of 0.25 (NAM 2000).

Note that the rock mechanical input parameters as described above represent a generic, idealised situation. Subsurface data are usually obtained by laboratory measurements, indirect (dynamic) measurements and interpretations. This leads to an uncertainty in the assessment of the in-situ geomechanical rock behaviour. Furthermore, the reservoir and surrounding rock are described as isotropic, homogeneous continua. Natural gas fields incorporate variations in lithology, leading to variations in their geomechanical properties. The volume surrounding the reservoir consists in reality consisting of a layered geological structure. Together with the

generic shape of the reservoir (disk or ellipsoid) and surrounding this allows an analysis of the effects of parameter variation on stress development and fault slip in and around the reservoir, free from any additional effects eventually produced by specific, case dependent features.

A less or non-producing intercalation such as the Ameland Claystone in the northern part of the Groningen field, thin producing Carboniferous sandstones and Zechstein evaporites in the overburden (Chapter 7) are not modelled.

Table 8.3. Default geomechanical rock properties used for the FE-calculations in this study. Calculations with different rock properties are explicitly described in the respective chapters.

Rock property		*Reservoir rock*	*Surrounding rock*
Symbol	*Description*		
E	Young's modulus	13.0 GPa	18.5 GPa
ν	Poisson's ratio	0.20	0.25
ρ_{bulk}	Bulk density	2400 kg/m^3	2400 kg/m^3
c_r	Rock cohesion	5.0 MPa	5.0 MPa
ϕ_r	Rock friction angle	30^o	25^o
ψ_r	Rock dilatancy angle	10^o	10^o

8.3.2 Default fault properties

Plastic fault slip on the fault plane is modelled using Coulomb friction. Before plastic slip occurs, the fault deforms elastically, to a degree that is controlled by the normal stiffness (D_n) and shear stiffness (D_s) of the fault. The choice of default values for normal and shear stiffness are described in Chapter 8.3.2.1. Default values for plastic fault properties are given in Chapter 8.3.2.2. Strain softening, displacement weakening, the forming of asperities and time-dependent relaxation of built-up stresses are not included in the modelling of faults.

8.3.2.1 Elastic fault properties

Before slip occurs, the fault deforms elastically, to a degree that is controlled by the normal and shear stiffness of the fault. The shear stiffness D_s of interface elements sets the relation between shear traction and elastic shear relative displacement, before the stress state on this fault reaches its yield criterion. The same applies for the normal stiffness D_n with normal traction and normal relative displacement. The unit of normal and shear stiffness is that of stress per length.

Published data on stiffness properties for rock joints are limited. Summaries of data can be found in Bandis *et al.* (1983), Kulhawy (1975) and Rosso (1976). Values for both shear- and normal stiffness typically range from roughly 10 to 100 MPa/m for weak faults with soft clay in-filling, to over 100 GPa/m for tight joints in granite and basalt (Itasca 1995).

Appropriate values of D_n and D_s are in the range of the elastic properties of the rock formations surrounding the fault. TNO Building & Construction Research (1999) advices the following equations for determining appropriate values in DIANA:

$$D_n = \frac{(1-\nu)E}{(1+\nu)(1-2\nu)h}; \tag{8.1}$$

$$D_s = \frac{E}{2(1+\nu)h}. \tag{8.2}$$

In here E and ν are the Young's modulus and Poisson's ratio of the modelled rock mass surrounding the fault and h is the fault thickness. For a fault thickness smaller than 1 m, a value of 1 m can be used for h in order to avoid extremely large stiffness values. Extremely large stiffness values can in the finite element calculations lead to 'glued' interfaces, i.e. interfaces on which any slip or separation is prevented.

Eqs. (8.1) and (8.2) are the basic expression of Hooke's Law for elastic stress-strain behaviour for normal- and shear strain (see eq. (5.3)). Note that D_s is calculated by dividing the shear modulus of the rock neighbouring the fault by the fault thickness (see also eq. (2.53b)). The seismic moment (see Chapter 9.1.2 for definition) is a function of among others the shear modulus of the rock neighbouring the fault. Calculation of the seismic moment in DIANA uses the shear stiffness of the fault instead for technical reasons, making the use of eq. (8.2) obligatory in this case.

Default fault stiffness values in this study are calculated according to eqs. (8.1) and (8.2). Note that they are not constant along the fault plane for models with differing reservoir and surrounding rock properties. The fault plane can, for the majority of the models as described in Chapters 8.1 and 8.2, be subdivided in three different regions (Figure 8.9):

- region A, where the fault is bounded on both sides by reservoir rock;
- region B, where the fault plane is bounded on one side by reservoir rock and on the opposite side by surrounding rock;
- region C, where the fault plane is bounded on both sides by surrounding rock.

The default fault stiffness values as used in the calculations with default rock properties (Chapter 8.3.1) are listed in Table 8.4. For the calculations of the stiffness values in fault region B, the rock properties of reservoir and surrounding rock are averaged. Note that the value for h in the case of zero fault thickness is 1 m. Calculations with fault stiffness values deviating from the above described procedure are explicitly marked in the respective chapters.

Different values for D_n and D_s can lead to different amounts of fault slip initiated during gas depletion. See Chapter 8.3.7 for results of a calculation series on this topic.

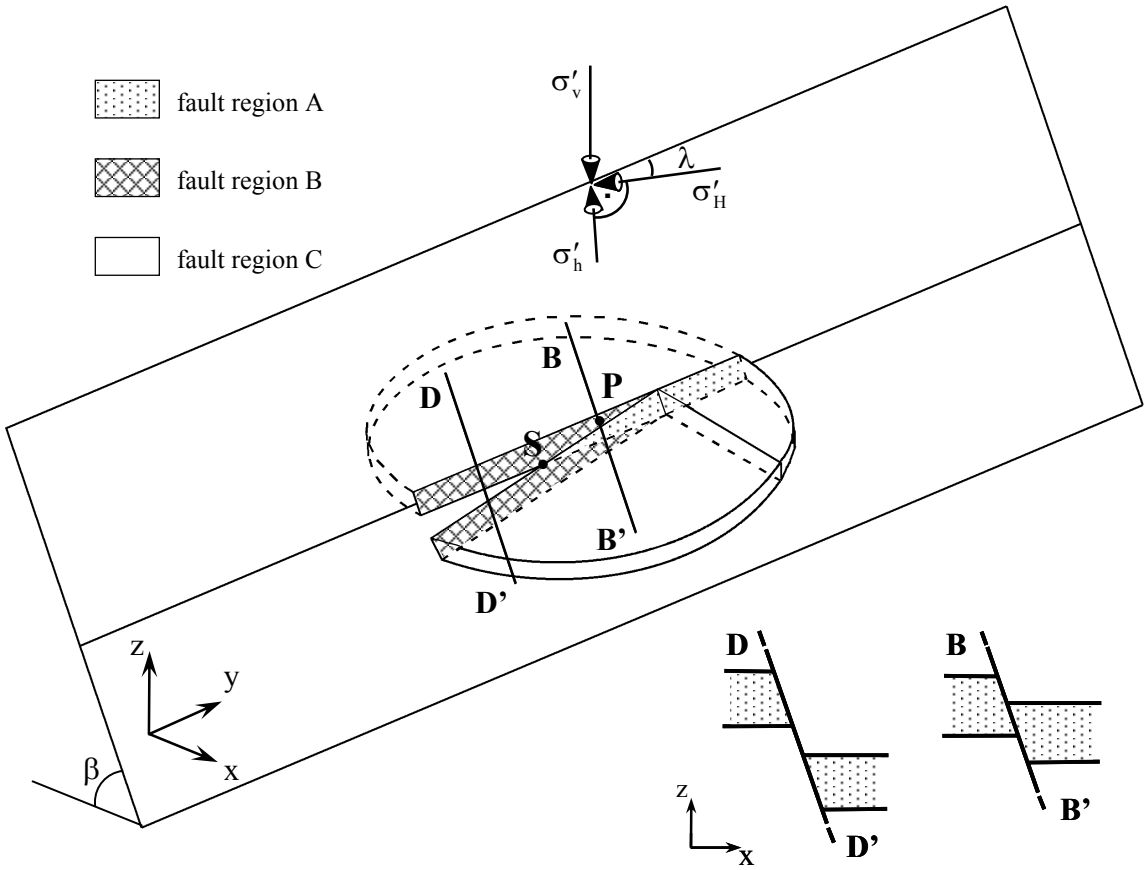

Figure 8.9. Indication of fault regions A, B and C, shown for model 'throw_var', and geometrical definition of the vertical effective stress σ'_v, maximum horizontal effective stress σ'_H and minimum horizontal effective stress σ'_h (see Chapter 8.3.3). The direction of σ'_H is defined by angle λ, i.e. the angle between the strike direction of the fault plane and the direction of σ'_H in clockwise direction. The bottom right figures show the fault plane in cross sectional view with the footwall- and hanging wall reservoir compartments along the observation lines BB' and DD'. Point S is the point on the fault plane where the top of the hanging wall reservoir compartment is exactly opposite to the bottom of the footwall reservoir compartment. Point P is a point along observation line BB' (see Chapter 8.3.4.3).

Table 8.4. Default fault stiffness values for the three fault zones A, B and C as a function of the fault neighbouring rock properties according to eqs. (8.1) and (8.2) for default rock properties as given in Chapter 8.3.1.

Fault region	*Young's modulus neighbouring rock [GPa]*	*Poisson's ratio neighbouring rock [GPa]*	*Normal stiffness [GPa/m]*	*Shear stiffness [GPa/m]*
A	13.00	0.200	14.4	5.4
B	15.75	0.225	18.1	6.4
C	18.50	0.250	22.2	7.4

8.3.2.2 Plastic fault properties

The fault plane is modelled using Coulomb friction. It is difficult to estimate the fault strength parameters in terms of frictional behaviour at depth. Because these parameters will have a major impact on the calculation results, they should be chosen with great care.

The fault plane represents an existing plane of weakness along which failure has occurred. It is therefore assumed to be cohesionless ($c^f = 0$). A fault dilatancy angle ψ_f of 0º is assumed.

Its strength depends only on the fault friction angle ϕ^f. Paterson (1978) suggests that most values for the fault friction coefficient fall within the range of 0.4 – 0.7, meaning fault friction angles of 20º - 35º. According to Goodman (1989), values for fault friction angles typically range between 25° and 35°. When intact rock fails and some movement has taken place along the failure plane, the friction angle on this plane is not equal to that of the intact rock anymore, but basically reduces to a residual friction angle. Considering the default rock properties of Table 8.3, a fault friction angle of 30º is therefore the upper limit.

A too low friction angle can result in an unstable fault, eventually leading to numerical instabilities and divergence during iterating. The fault friction angle should be high enough to ensure numerical stability of the model and convergence to a solution when iterating and to avoid undesired side effects such as a large movement on the entire fault plane adding up to the movements at reservoir level, in which we are actually interested. Assuming that the vertical stress is a principal stress, with $\sigma'_v = \sigma'_1$ and $\sigma'_h = \sigma'_3$, it follows from eqs. (3.1) and (3.3) and Figure 3.1 that plastic fault slip occurs when

$$\sigma'_v = \frac{\sigma'_h\left(\sin(2\beta - \phi^f) + \sin\phi^f\right) + 2c^f\cos\phi^f}{\sin(2\beta - \phi^f) - \sin\phi^f}. \tag{8.3}$$

For a cohesionless fault ($c^f = 0$) this reduces to:

$$\frac{\sigma'_h}{\sigma'_v} = \frac{\sin(2\beta - \phi^f) - \sin\phi^f}{\sin(2\beta - \phi^f) + \sin\phi^f}. \tag{8.4}$$

Note that eq. (8.4) is an expression for the effective stress ratio K_{0h} (see Chapter 3.2, eq. (3.9)). In Chapter 8.3.3 it will be explained that a default tectonic stress regime with $K_{0H} = K_{0h} = 0.4$ will be applied to the models. For a fault dip angle β of 70º, the fault is according to eq. (8.2) at failure for $\phi^f = 22.3$º. For the most critical fault dip angle $\beta_{crit} = 45º + ½\phi^f$, the fault is theoretically at failure for $\phi^f = 25.4$º.

These fault friction angle values based on eq. (8.4) have to be considered with care. Contrasts in the elastic properties of rocks can cause deflection of stress trajectories (Bell & Lloyd 1989, Pourjavad *et al.* 1998 and Chapter 11.2 in this dissertation), affecting the relative orientation of the fault plane with respect to the principal stress directions. They also might affect principal stress vector magnitudes. Elastic rock property contrasts occur in the majority of the models in this dissertation, where the softer reservoir rock of the hanging wall reservoir compartment incorporates a throw within a stiffer surrounding.

Based on the foregoing, a fault friction angle of 28º is chosen.

8.3.3 Initial tectonic stress field

The initial tectonic stresses applied to the numerical models are based on field data analysis, literature and personal communication (see Chapter 7.5).

The effective stress acting in vertical direction is calculated by combining the weight of the rocks, which is calculated by applying the gravity acceleration on the model, with the pore pressure in the rocks and the fault plane (Chapter 8.3.4).

The K_0 –procedure in DIANA is used to impose the initial state of stress onto the model. This procedure initiates the horizontal effective stresses σ'_H and σ'_h into the model from the calculated vertical effective stress σ'_v according to the effective stress ratios $K_{0H} = \sigma'_H / \sigma'_v$ and $K_{0h} = \sigma'_h / \sigma'_v$ (see Chapter 3.2). The effective stress ratios are user-specified. The maximum and minimum horizontal stresses σ'_H and σ'_h are always perpendicular to each other. The direction of σ'_H is user-specified. The horizontal principal stress direction is defined with respect to the fault plane in the finite-element models by angle λ (Figure 8.9). λ is the angle between the strike direction of the fault plane and the direction of σ'_H in clockwise direction. $\lambda = 0^o$ and 90^o mean a direction of σ'_H parallel and perpendicular to the strike of the fault plane, respectively.

Unless explicitly specified, an initial extensional stress field is assumed before gas depletion with effective stress ratios $K_{0H} = K_{0h} = 0.4$. In this case λ does not need to be specified. Further explanations on the initial state of stress for anisotropic tectonic stress fields are given in Chapter 11.6.2.

The explanations given above are valid only for 3D-models. For 2D-models, only one effective stress ratio K_0 can be specified. Its default value is 0.4. During initialisation of the effective stresses in the model, deformation of the model was not allowed. This was required in order to preserve the initial model geometry.

8.3.4 Initial pore pressure and pore pressure development during gas depletion

8.3.4.1 Reservoir and surrounding rock

The initial pore pressure in the surrounding rock is hydrostatic and remains constant throughout gas depletion. The pore fluid density is assumed to be 1000kg/m^3. With a gravity acceleration of 9.81m/s^2 this results for instance in a pore pressure of 28.5 MPa at a depth of -2900m. At the start of depletion, the reservoir is per default slightly overpressured with an initial pore pressure of 35.0 MPa, in accordance to the initial average pore pressures of 34.7 MPa in the Groningen gas field (Mobach & Gussinklo 1994) and 34.5 MPa in the Annerveen gas field (Veenhof 1996), see Chapter 7.7. A theoretical vertical pressure profile through a 150m thick overpressured reservoir with its top at a depth of -2900m is given in Figure 8.10. Calculations with a hydrostatic initial pore pressure in the reservoir are performed as well.

Gas depletion is modelled by decreasing the initial reservoir pore pressure to 0 MPa in several static depletion steps. In the case of a reservoir with a hydrostatic initial pore pressure, the pore pressure is depleted linearly in ten static depletion steps. Note that since the hydrostatic pressure increases with depth, the depletion at the bottom of the reservoir is in this case somewhat higher than at the top of the reservoir. For instance the initial hydrostatic pore pressure at the top and bottom of a 150 m thick reservoir with its top at a depth of -2900 m is 28.5 and 29.9 MPa, respectively (see Figure 8.10). Gas depletion to 0 MPa in ten equal depletion steps results in a pore pressure decrease of 2.85 MPa per depletion step at the top of the reservoir and 2.99 MPa at the bottom of the reservoir.

In the case that the reservoir is initially overpressured (35.0 MPa initial pore pressure in the whole reservoir, see Figure 8.10), the reservoir is depleted to 0 MPa in eleven static depletion steps. The first ten steps are equal to the case of a hydrostatic initial pore pressure as described in the previous paragraph. For the example as shown in Figure 8.10 this would mean for the top and the bottom of the reservoir ten depletion steps each of 2.85 MPa and 2.99 MPa, respectively. The remaining pore pressure, marked by the shaded area in Figure 8.10, is then depleted in a final eleventh step. This is done in order to keep the loading equal for both cases (hydrostatic and overpressured initial pore pressure). Stress paths and fault slip after these ten depletion steps are then comparable. The eleventh depletion step in case of an initially overpressured reservoir is performed in order to study the effect of a depletion to 0 MPa.

No fluid flow is modelled. The pressure drop applies equally to the whole reservoir part which is depleted. No gas/water contact is modelled. Initial pore pressure and depletion scenario are always indicated in the respective chapters on calculation results.

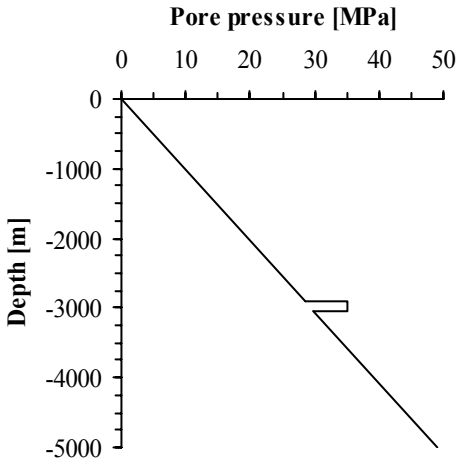

Figure 8.10. Modelled default pore pressure profile through a 150m thick reservoir with a top reservoir depth of -2900m. The reservoir is per default initially overpressured with a pore pressure of 35.0 MPa throughout the whole reservoir. The pore pressure in the surrounding rock is hydrostatic and increases with depth (assumed pore fluid density: 1000 kg/m^3; gravity acceleration: 9.81 m/s^2). Some calculations are performed with a hydrostatic initial reservoir pore pressure.

8.3.4.2 Fault plane

As is the case for the rock volumes in the models, an initial pore pressure and pore pressure development can be defined for the fault plane. A pore pressure in the fault directly affects the normal effective stress acting on the fault. A higher pore pressure means a lower effective normal stress and, since the shear stress remains unaffected, thus a state of stress closer to the failure criterion. Assumptions on the initial pore pressure in the interface elements and its depletion scenario should therefore be taken with great care.

The fault plane in the model can be subdivided in three different regions, as described before in Chapter 8.3.2.1 in relation to the fault shear and normal stiffness (Figure 8.9):

- region A, where the fault is bounded on both sides by reservoir rock;
- region B, where the fault plane is bounded on one side by reservoir rock and on the opposite side by surrounding rock;
- region C, where the fault plane is bounded on both sides by surrounding rock.

It is assumed that over geological times faults in the subsurface basically incorporate the same pore pressure as the neighbouring rock formation. The initial pore pressure in fault region C is therefore chosen to be hydrostatic, in accordance to the initial pore pressure in the surrounding rock. The initial pore pressure in fault region A is

hydrostatic or overpressured, depending whether the initial reservoir pore pressure is hydrostatic or overpressured. An initial overpressure of 35.0 MPa is default (Chapter 8.3.4.1). A question arises for the initial pore pressure in fault region B for the case that the reservoir is initially overpressured whereas the initial pore pressure in the surrounding rock is hydrostatic: overpresured or hydrostatic?

Another question arises from the pore pressure development during gas depletion. Faults within the Groningen and Annerveen gas fields are considered to be non-sealing, meaning that most of the gas fields is well drained and that most of the numerous faults which are mapped do not form transmissibility barriers (see Chapter 7.7). The pore pressure development during gas depletion in fault region A is therefore specified as reservoir-dependent pore pressure development: fault region A is modelled as depleting with the same amount as the reservoir rock. The pore pressure in the surrounding rock and hence in fault region C remains at its initial value during gas depletion. Meanwhile fault region B is bounded on one side by producing reservoir rock and on the opposite side by non-producing surrounding rock. the question is if the pore pressure in fault region B remains constant at its initial value during gas depletion or if it decreases according to the (neighbouring) reservoir depletion?

Since the fault plane has a limited thickness (0 m in the calculations) and the complete reservoir depletion reflects a time of approximately 50 years, the fault is regarded as a drained structure. This has been considered by applying the same initial pore pressure and the same pore pressure depletion to fault region B as to the reservoir. In a realistic setting, a pore pressure gradient would very likely develop. The interface elements in the software require a homogeneous pore pressure for each element. A pore pressure gradient cannot be specified. The above assumptions are in accordance with Van Wees *et al.* (2001), who specified the pore pressure along the faults as reservoir-dependent pore pressure.

The effect of ‘aquifer depletion’, whereby the pressure in a small associated aquifer will decrease gradually with the pressure in a large gas bearing reservoir, as is the case in the Groningen gas field (Doornhof 1992), is not modelled. The pore pressure in the rock formations surrounding the reservoir are assumed to be initially hydrostatic and to remain constant during depletion of the gas reservoir.

8.3.4.3 Evaluation of the assumed initial pore pressure and pore pressure depletion scenario in fault region B of the fault plane

In order to check the validity of the assumptions made in Chapter 8.3.4.2, five different pore pressure scenarios are studied (Table 8.5). 3D-model ‘throw_var’ is used for the calculations with default rock properties and initial reservoir pore pressure of 35.0 MPa as given by Table 8.6, except for the fault dip angle (60^o), the iteration method (Constant Stiffness in depletion phase) and the pore pressure depletion scenario (depletion of the overpressured reservoir in ten equal steps each of

3.5 MPa instead of eleven steps). Figure 8.11 shows for each scenario the stress path in observation point P (see Figure 8.9). For a description of the quantification methods used in the following explanations see Chapter 9.

Scenario 1 is calculated in order to investigate whether the definition of a pore pressure in the fault can be reasonably avoided. The stress path is located very far to the right due to a high effective normal stress. Relative shear displacements are restricted to a relatively small zone around point S. It can be concluded, that for reasonable calculation results in order to study the effects of different parameters on fault reactivation, a pore pressure has to be applied in the interface elements.

The stress paths belonging to depletion scenarios 3, 4 and 5 are for no, half and full depletion of fault zone B, respectively. The initial pore pressure for these scenarios is hydrostatic. No depletion of the fault leads to decreasing normal effective stresses (Figure 8.11, scenario 3). Initially, shear stresses increase but as soon as the stress path hits the yield line they are forced to decrease. In some interface elements the normal effective stress reaches zero.

The difference between full and half depletion is basically reflected in a difference in stress path gradient. The slower depletion in fault region B for scenario 4 leads to higher pore pressures and therefore lower effective normal stresses in fault region B. The slower effective normal stress increase in scenario 4 leads to a steeper stress path and more fault slip than in scenario 5.

The influence of initial pore pressure in fault region B is given by a comparison of scenarios 2 and 5, for a depletion of fault region B in accordance to the reservoir depletion. The basic difference is the initial state of stress. A higher initial pore pressure in fault region B results in a state of stress in this region closer to yielding before the start of gas depletion. The full depletion makes that the stress path gradients are not as steep as for instance for scenario 4. It avoids the development of unrealistically large amounts of fault slip.

Fault slip in observation point P on the fault plane (see Figure 8.9 for location) is plotted in Figure 8.12 for each pore pressure scenario. No pore pressure in the fault (scenario 1) results in only little fault slip due to the high effective normal stress. No depletion of fault region B (scenario 3) leads to an overestimation of the calculated fault slip in fault region B (Figure 8.12b).

Scenario 2 is chosen for further calculations. This is based on the assumption that the fault can be regarded as a drained structure (see Chapter 7.7).

Table 8.5. Fault pore pressure scenarios. Region C always incorporates a hydrostatic pore pressure except for scenario 1 and is never depleted.

Scenario	*Fault region A*		*Fault region B*	
	Initial pressure	*Depletion*	*Initial pressure*	*Depletion*
1	No pressure	-	No pressure	-
2	Overpressured	Full	Overpressured	Full
3	Overpressured	Full	Hydrostatic	No
4	Overpressured	Full	Hydrostatic	Half
5	Overpressured	Full	Hydrostatic	Full

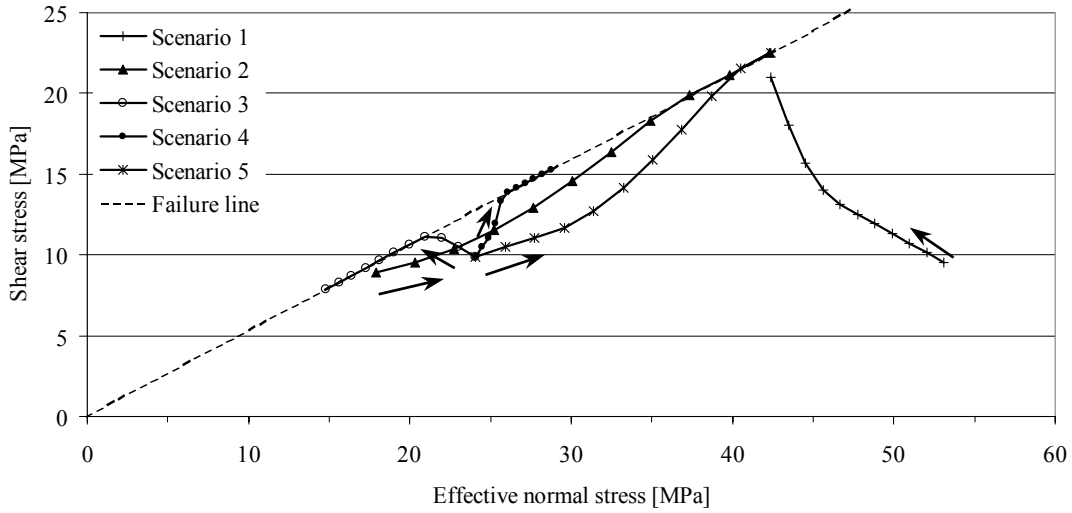

Figure 8.11. Stress paths in observation point P in model 'throw_var' (see Figure 8.9 for location) for different fault pore pressure scenarios (Table 8.5). Arrows indicate the initial stress state and development direction of the stress paths. Calculation with default values as given by Table 8.6, Chapter 8.3.6, except for the fault dip angle (60°), the iteration method (Constant Stiffness in depletion phase) and the pore pressure depletion scenario (depletion of the overpressured reservoir in ten equal steps each of 3.5 MPa instead of eleven steps).

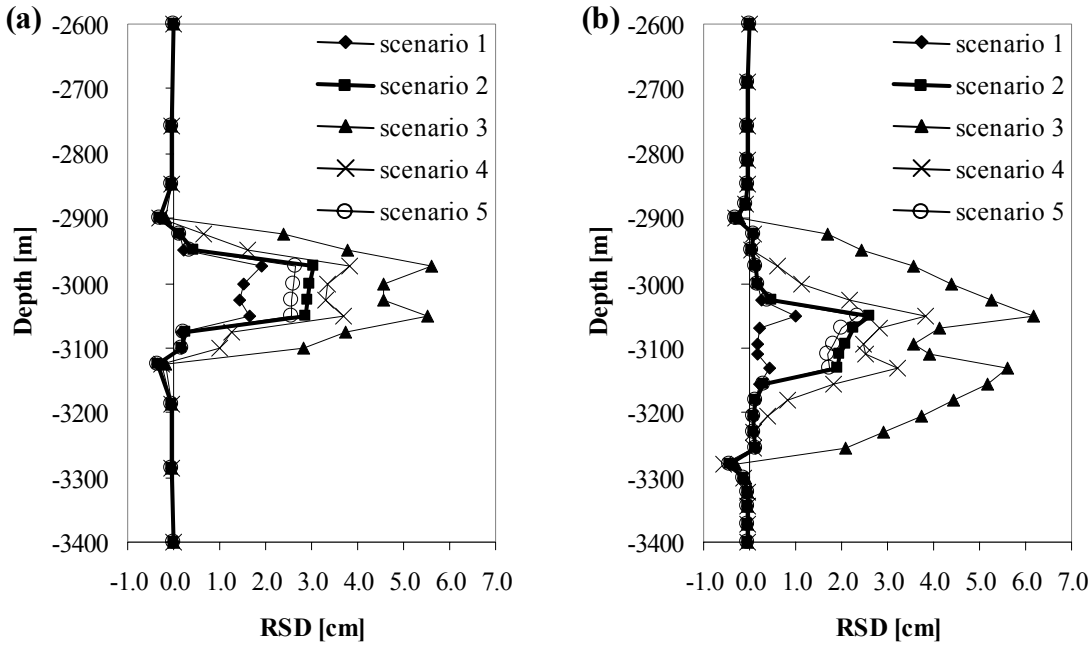

Figure 8.12. Calculated fault slip on the fault plane in model 'throw_var' along (a) observation line BB' and (b) observation line DD' (see Figure 8.9 for location), for different fault pore pressure scenarios (Table 8.5). Calculation with default values as given by Table 8.6, Chapter 8.3.6, except for the fault dip angle (60^o), the iteration method (Constant Stiffness in depletion phase) and the pore pressure depletion scenario (depletion of the overpressured reservoir in ten equal steps each of 3.5 MPa instead of eleven steps).

8.3.5 Incremental-iterative solution procedure

Prior to gas depletion, the model is brought into an initial state of equilibrium to the initially applied gravity, tectonic stress field and pore pressures. The initial loading is applied to the models in two equal steps or increments. This is the consolidation phase. Gas depletion is modelled by reducing the pore pressure in the reservoir and the adjacent and intersecting parts of the fault (fault regions A and B) in 10 static steps or increments to zero. This is the depletion phase.

Prior to a nonlinear analysis, a linear static analysis must be performed in DIANA. The stress field, calculated in the preliminary linear static analysis, is then applied as initial stress field for the nonlinear analysis. In general the internal forces following from initial stresses from the linear static analysis are not in equilibrium with the initial external load at the start of the nonlinear analysis. This is because the material properties have been extended with nonlinear values and the horizontal effective stresses are adjusted according to the effective stress ratios specified (see Chapter 8.3.3). The initial stresses are adapted incrementally in order to reach an equilibrium state in the nonlinear analysis (consolidation phase). During initialisation of the

effective stresses in the model, deformation of the model was not allowed. This was required in order to preserve the initial model geometry. Superposition of displacements and strains during the establishment of the initial equilibrium in the consolidation phase are suppressed for the following depletion phase. Only the stress state is affected.

The initial load of the consolidation phase is applied to the model in two equal increments. This is done since DIANA often indicated plastic fault slip on almost the entire fault plane during iterating in the first load increment, also when the defined initial stress field should result solely in elastic deformation of fault and rock. A relative out-of-balance force (see Chapter 5.2.3 for definition) in the range of 10^{-5} was indicated. For calculations where the initial stress field should not imply plastic deformation, such plastic fault slip was absent in the second increment and the relative out-of-balance force dropped to values in the range of 10^{-16}. The iterative procedure applied to the consolidation phase is the Constant Stiffness method (see Chapter 5.2.1).

A calculation series has been performed in order to distinguish the number of iterations which should be performed for each of the two increments of the consolidation phase. For a description of the quantification methods used in the following explanations see Chapter 9. Figure 8.13a shows the calculated maximum fault slip as a result of gas depletion along the fault plane as a function of the number of iterations during the consolidation phase for the 2D model 'throw_var', with default geomechanical properties as listed in Table 8.6 (Chapter 8.3.6), except for the pore pressure depletion scenario (depletion of the overpressured reservoir in ten equal steps each of 3.5 MPa instead of eleven steps). The graph shows a decreasing trend with increasing number of iterations. Apparently some fault slip occurs during this consolidation, which adds up to the fault slip calculated in the gas depletion phase if the consolidation is not long enough. This means that the longer the consolidation phase, the less is the calculated fault slip during gas depletion. A high number of iterations means a long calculation time. It is therefore decided to keep the number of iterations at five per increment, making a total of ten iterations for the whole consolidation phase.

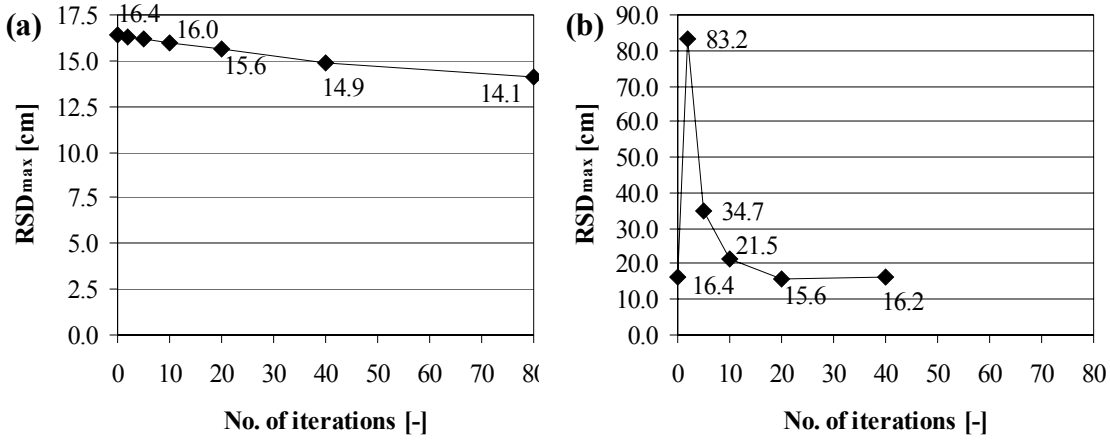

Figure 8.13. Influence of the number of iterations per increment on the calculated maximum fault slip for (a) consolidation phase and (b) depletion phase. Model: throw_var; calculations with default values as given by Table 8.6, Chapter 8.3.6. The number of iterations in the depletion phase for the calculations of figure (a) is 20 per increment. The number of iterations in the consolidation phase for the calculations of figure (b) is 5 per increment.

Gas depletion is modelled by reducing the pore pressure in the reservoir and the adjacent and intersecting parts of the fault (fault regions A and B) in 10 static steps or increments to zero. The iterative procedure for the depletion phase was the Modified Newton-Raphson method (see Chapter 5.2.1). In the same way as for the consolidation phase, a calculation series has been performed in order to distinguish how many iterations should be performed per increment of the depletion phase. The results are plotted in Figure 8.13b. The model, geomechanical properties, loading- and boundary conditions are the same as for the calculation series to distinguish the number of iterations in the consolidation phase. Two regions can be distinguished in the graph: a region where the calculated fault slip is very high for six iterations or less and a region with as good as constant RSD-values for seven iterations and more. As stated before, the number of iterations should be low in order to save calculation time. In view of the very high values for few iterations it is decided to perform twenty iterations per load increment in the depletion phase, making a total of 200 iterations for the whole phase.

A common feature, used in both consolidation and depletion phase, is DIANA's Line Search algorithm (see Chapter 5.2.2). For the calculation procedure it is chosen for a fixed number of iterations per load increment for all calculations rather than iterate until the relative out-of-balance force reaches a predefined convergence criterion. This is done by setting as convergence criterion a relative out-of-balance force of $1.0 \cdot 10^{-20}$ and continuing with the next load increment after the specified maximum number of iterations has been reached. It is checked for each calculation whether the relative out-of-balance force is below a value of $1.0 \cdot 10^{-2}$ after each increment. A value of $1.0 \cdot 10^{-2}$

means that the out-of-balance force is equal to 1% of the applied load increment. It is often used as default value. The development of relative out-of-balance force during a calculation is presented in Figure 8.14. The development is acceptable. The relative out-of-balance force is below a value of $1.0 \cdot 10^{-2}$ at the end of each increment. The development of the relative out-of-balance force as presented in Figure 8.14 is representative for all other calculations.

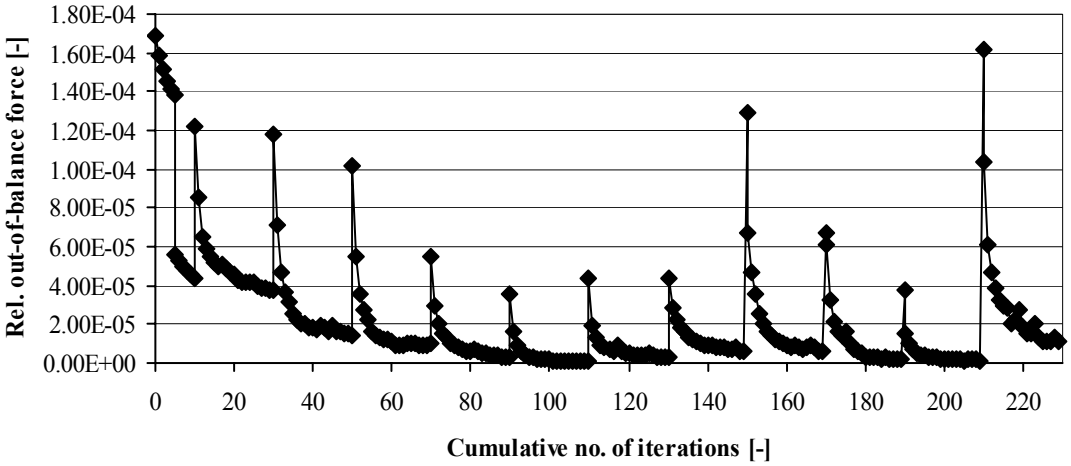

Figure 8.14. Development of relative out-of-balance force during the calculation of model 'throw_var' with default properties (Table 8.6).

8.3.6 Summary: overview geomechanical properties and loading conditions

An overview of the geomechanical properties and loading conditions used for most of the calculations in this dissertation is given in Table 8.6. Two different scenarios are listed:

- surrounding rock properties equal to the reservoir rock properties ($E^{sur} = E^{res} =$ 13.0 GPa; $\nu^{sur} = \nu^{res} = 0.2$; $\phi^{sur} = \phi^{res} = 30^{o}$) and initial hydrostatic reservoir pore pressure;
- default surrounding rock properties ($E^{sur} = 18.5$ GPa; $\nu^{sur} = 0.25$; $\phi^{sur} = 25^{o}$) and initially slightly overpressured reservoir (initial pore pressure 35.0 MPa).

Values in calculations differing from default are explicitly indicated in the respective chapters.

Table 8.6. Geomechanical properties and loading conditions for two different scenarios used for most of the calculations in this dissertation.

General properties					
E^{res}	13.0 GPa	β	70^o	Iteration method	
ν^{res}	0.20	h	0 m	- consol. phase	Constant Stiffness
$c^{res} = c^{sur}$	5.0 MPa	c^f	0 Pa		
ϕ^{res}	30^o	ϕ^f	28^o	- depletion phase	Mod. Newton Raphson
$\psi^{res} = \psi^{sur}$	10^o	ψ^f	0^o		
$\rho^{res}_{bulk} = \rho^{sur}_{bulk}$	2400 kg/m^3	K_{0H}	0.4	No. of iterations	
p^{sur}_{ini}	hydrostatic	K_{0h}	0.4	per increment	
Δp^{sur}	0 Pa	λ	0^o	- consol. phase	5
		$\rho_{pore\ fluid}$	1000 kg/m^3	- depletion phase	20
*surrounding rock properties equal to the reservoir rock properties and initial hydrostatic reservoir pore pressure**					
E^{sur}		13.0 GPa		D_n (fault region A, B, C)	14.4 GPa/m
ν^{sur}		0.20		D_s (fault region A, B, C)	5.4 GPa/m
ϕ^{sur}		30^o		No. of load increments	
p^{res}_{ini}		hydrostatic		- consolidation phase	2
Δp^{res}		-hydrostatic		- depletion phase	10
p^{fault}_{ini} (region A, B, C)		hydrostatic			
Δp^{fault} (region A, B)		-hydrostatic			
Δp^{fault} (region C)		0 Pa			
default rock properties and initial reservoir pore pressure of 35.0 MPa					
E^{sur}		18.5 GPa		D_n (fault)	
ν^{sur}		0.25		- region A	14.4 GPa/m
ϕ^{sur}		25^o		- region B	18.1 GPa/m
p^{res}_{ini}		35.0 MPa		- region C	22.2 GPa/m
Δp^{res}		-35.0 MPa		D_s (fault)	
p^{fault}_{ini} (region A, B)		35.0 MPa		- region A	5.4 GPa/m
p^{fault}_{ini} (region C)		hydrostatic		- region B	6.4 GPa/m
Δp^{fault} (region A, B)		-35.0 MPa		- region C	7.4 GPa/m
Δp^{fault} (region C)		0 Pa		No. of load increments	
				- consolidation phase	2
				- depletion phase	11

** Depth of centre of footwall reservoir compartment is -2975 m, meaning an initial pore pressure of 29.75 MPa. The superscripts ^{res}, ^{sur} and ^{f} refer to reservoir rock, surrounding rock and fault, respectively.*

8.3.7 A short note on fault slip and fault normal- and shear stiffness

Different values for D_n and D_s can lead to different amounts of fault slip initiated during gas depletion. Figure 8.15 shows the maximum relative shear displacement on the fault plane in dependence of shear and normal stiffness. Note that in this calculation series the shear and normal stiffness are equal. Some rock and fault property values differ for this calculation series from the default values: the fault friction and dilatancy angle are 22^o and 10^o, respectively, and the surrounding rock has properties which are equal to the default reservoir rock properties. Furthermore, a Constant Stiffness iteration method is applied to both consolidation and depletion phase, with four iterations per load increment for both phases. The values of other strength and load parameters are default as indicated in Table 8.6. The location of RSD_{max} is in all calculations equal and very close to the point where the two reservoir compartments start to be geometrically separated from each other (point S, see Figures 8.2 and 8.9).

There exists a strong dependence of the amount of relative shear displacement (see Chapter 9.1.1 for definition) on the chosen values of D_s and D_n. Values of RSD increase for decreasing values of D_s and D_n. Especially for lower stiffness values, their influence becomes very significant. Extreme high stiffness values mean glued interfaces, i.e. interfaces on which any slip or separation is prevented. RSD-values are indeed as good as zero for $D_s = D_n = 1000$ GPa/m.

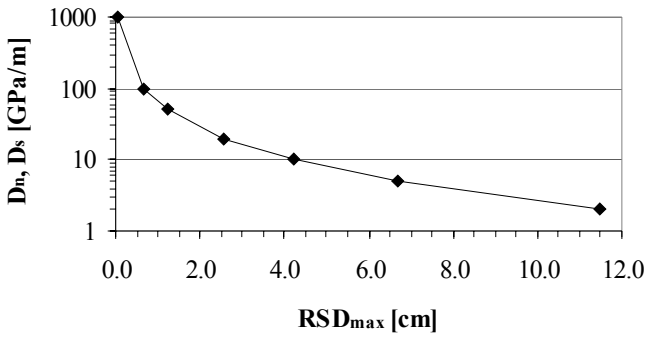

Figure 8.15. Maximum relative shear displacement on the fault plane as a function of shear- and normal stiffness of the interface elements.

8.3.8 Evaluation of model size

At the four lateral sides of the model, horizontal translations normal to the respective sides are constrained. As described before, the total model size is 12,000x12,000x5,000m, meaning that the lateral boundaries are located at a distance of 6,000m from the centre of the reservoir. It is investigated whether this distance is appropriate and how it affects the calculated fault slip and stress development in and around the reservoir.

Eight 2-dimensional plane strain calculations have been performed based on the model '2D_throw_½D', each with identical reservoir and fault geometry and properties but with different model sizes: 8,000, 10,000, 12,000, 14,000, 17,000, 20,000, 30,000 and 100,000m. An overview of the model geometries is given in Figure 8.16. The model with a size of 100,000m is considered to be a reference model with infinitely far model boundaries. Calculation results of the other seven models are compared to those of this reference model.

The mesh consists of the lower-order DIANA-element types T6EPS (plane strain, 3-noded triangular) and L8IF (line interface, 2+2 nodes). Lower-order elements are chosen since the 3D models consist of lower-order pyramidal elements with corresponding interface elements. Furthermore, eventual deviations in the calculation results due to different total model sizes will be most pronounced for lower-order elements. Rock properties and loading conditions are default as listed in Table 8.6.

The mesh is identical for all models up to a distance of 2,300m from the centre of the reservoir. Gas depletion-induced vertical and horizontal effective stress changes are compared along two observation lines as indicated in Figure 8.16. This comparison is done by calculating the deviation of the stress changes in each model from the stress changes in the reference model of size 100,000m according to:

$$\Delta\sigma'^{dev} = \Delta\sigma'^{ref} - \Delta\sigma'^{m}. \tag{8.5}$$

In here, $\Delta\sigma'^{dev}$ is the effective stress change deviation at a certain location on the observation lines, $\Delta\sigma'^{ref}$ is the calculated effective stress change at that location in the reference model (size 100,000m) and $\Delta\sigma'^{m}$ is the calculated effective stress change at that location in one of the other seven models, whereby indices ^{m} can take the values 8,000, 10,000, 12,000, 14,000, 17,000, 20,000 or 30,000. Gas depletion-induced fault slip is compared on analogous way. An overview of the modelling results is given in Figures 8.17 and 8.18 and Table 8.7.

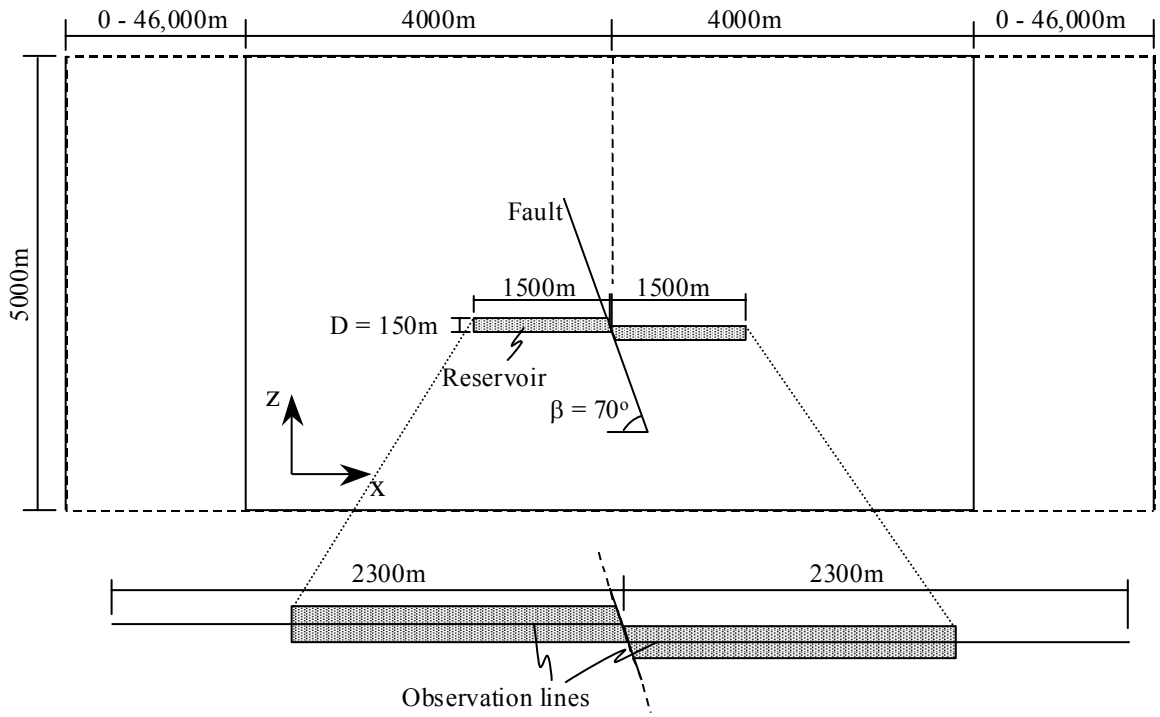

Figure 8.16. Overview of the model geometries used for the boundary distance study, based on the 2-dimensional plane strain model '2D_throw_½D'. Gas depletion-induced calculated effective stress changes along the two observation lines and fault slip along the fault are compared to those of a reference model of 100,000m width.

Deviations in the calculated effective stress changes are relatively small in all models. Largest deviations occur understandable in the smallest models. The largest deviations in the 8000m-wide models are still relatively low: horizontal and vertical effective stress changes in this model deviate at most with 0.22 MPa and 0.25 MPa from the reference model, respectively. For the 12,000m-wide model these values are 0.15 MPa and 0.19 MPa, respectively. An effective stress change deviation of 0.25 MPa is 0.71% of the simulated reservoir pore pressure reduction of 35.0 MPa.

The same can be said for the deviations in calculated relative shear displacement (see Chapter 9.1.1 for definition): deviations are relatively small in all models. The calculated maximum fault slip in the 8000m-wide model (12.9 cm) is 0.1 cm larger than in the 100,000m-wide reference model (12.8 cm). This is a deviation of 0.78% from the reference value. For the 12,000m-wide model, the maximum fault slip is 0.09 cm larger.

Calculated deviations in fault slip and effective stress changes are relatively low for all models. They show the applicability of the chosen model size of 12,000m width. Significant improvement is not accomplished by a larger model size.

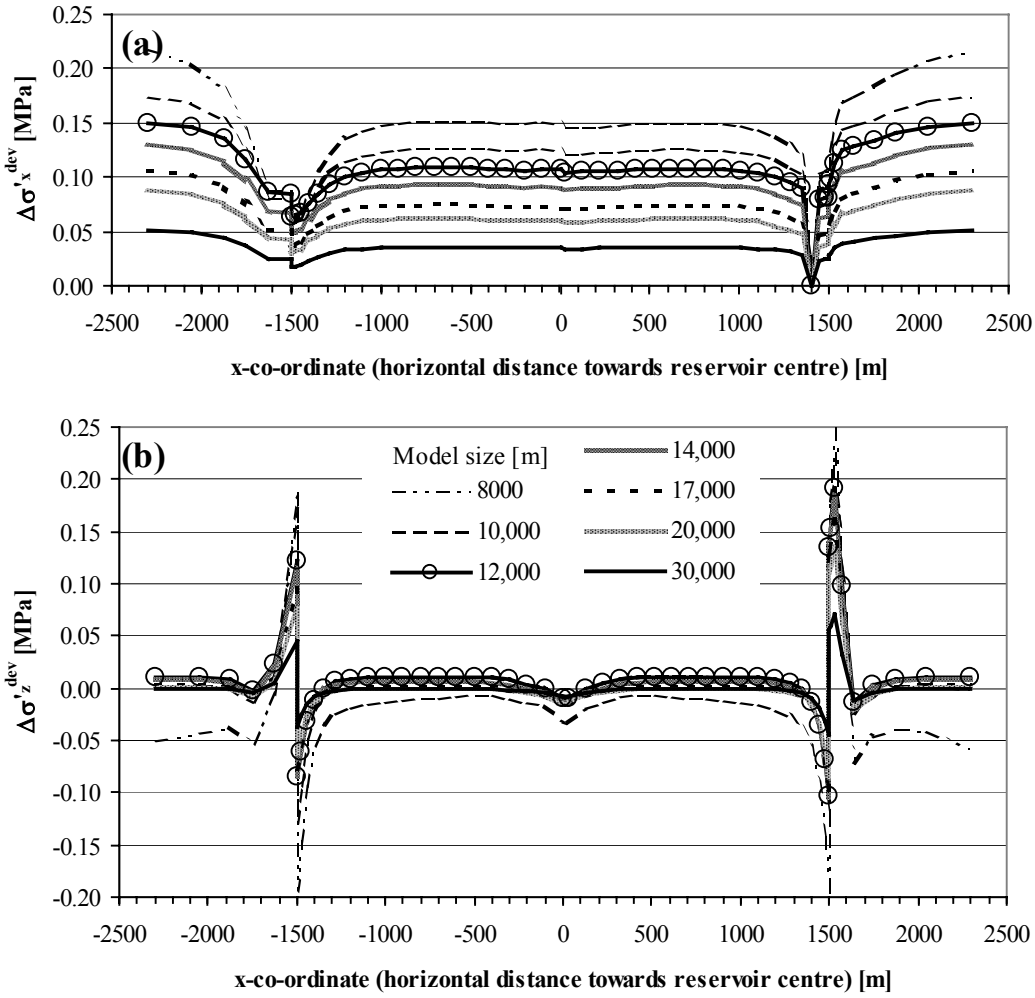

Figure 8.17. Deviations in the calculated (a) horizontal effective stress changes and (b) vertical effective stress changes along the two observation lines (Figure 8.16) for different model sizes. Reference model size is 100,000 m.

Table 8.7. Maximum deviation in horizontal and vertical effective stress changes and in relative shear displacement along the two observation lines (Figure 8.16) for different model sizes. Reference model size is 100,000 m.

Model size [m]	$\lvert \Delta\sigma'^{dev}_x \rvert_{max}$ *[MPa]*	$\lvert \Delta\sigma'^{dev}_z \rvert$ *[MPa]*	$\lvert RSD^{dev} \rvert_{max}$ *[cm]*
8000	0.218	0.249	0.11
10,000	0.175	0.225	0.10
12,000	0.150	0.191	0.09
14,000	0.130	0.185	0.09
17,000	0.106	0.161	0.08
20,000	0.088	0.135	0.07
30,000	0.051	0.072	0.03

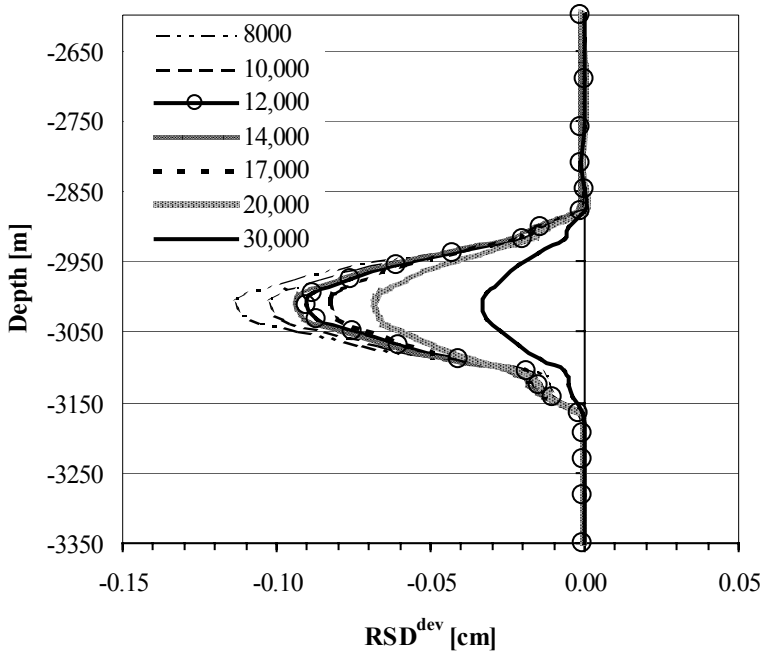

Figure 8.18. Deviations in the calculated relative shear displacements along the fault (Figure 8.16) for different model sizes. Reference model size is 100,000 m.

8.3.9 Comparison of 2D- and 3D-models

In order to check the validity of the 3D models, which make use of lower order elements instead of higher order elements, 3D-calculations of model 'throw_const_½D' with lower order elements (TE12L and T18IF) are compared to calculation results of the 2D model 'throw_½D' for lower order elements (T6EPS and L8IF) and higher order elements (CT12E and CL12I). Calculations are performed for two conditions (see Tables 8.6 and 8.8):

- surrounding rock properties equal to the reservoir rock properties ($E^{sur} = E^{res} =$ 13.0GPa; $\nu^{sur} = \nu^{res} = 0.2$; $\phi^{sur} = \phi^{res} = 30^{o}$) and initial hydrostatic reservoir pore pressure;
- default surrounding rock properties ($E^{sur} = 18.5$GPa; $\nu^{sur} = 0.25$; $\phi^{sur} = 25^{o}$) and initial reservoir pore pressure (35.0 MPa).

For a description of the quantification methods used in the following explanations see Chapter 9. First, stress paths calculated for respective locations on the fault are compared for the three different models for the case that the reservoir and surrounding rock properties are equal (Figure 8.19). For location of observation points 1 – 13 on the fault see Figure 8.19. In the 3D-model, the observation points are located along observation line EE', which runs down dip, parallel to the fault plane through the centre of the reservoir (see Figure 11.1, Chapter 11.1).

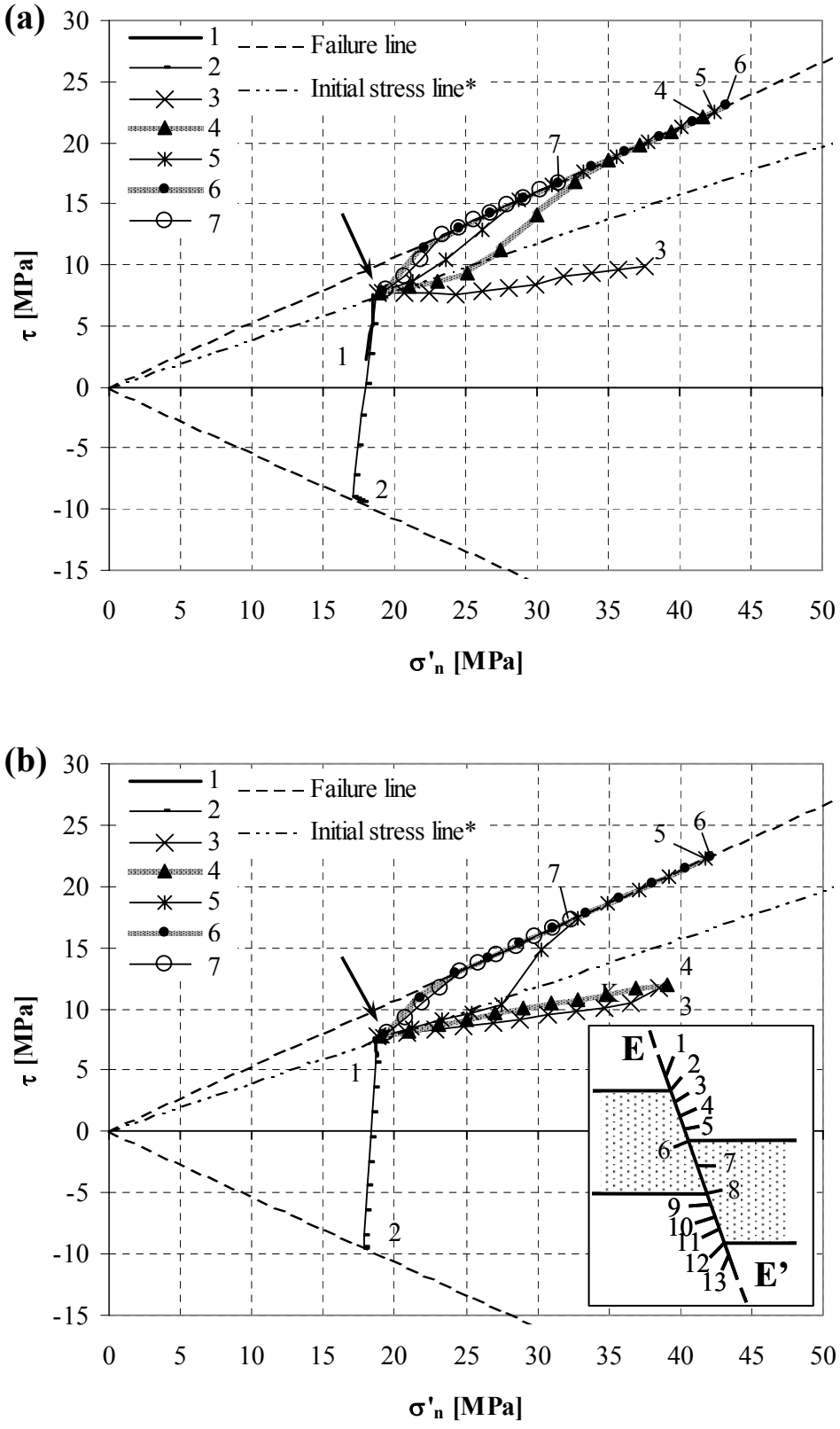

Figure 8.19. Calculated stress paths for different observation points for model '2D_throw_½D' with (a) lower order elements (T6EPS and L8IF) and (b) higher order elements (CT12E and CL12I). For further description see Figure 8.19 (c).

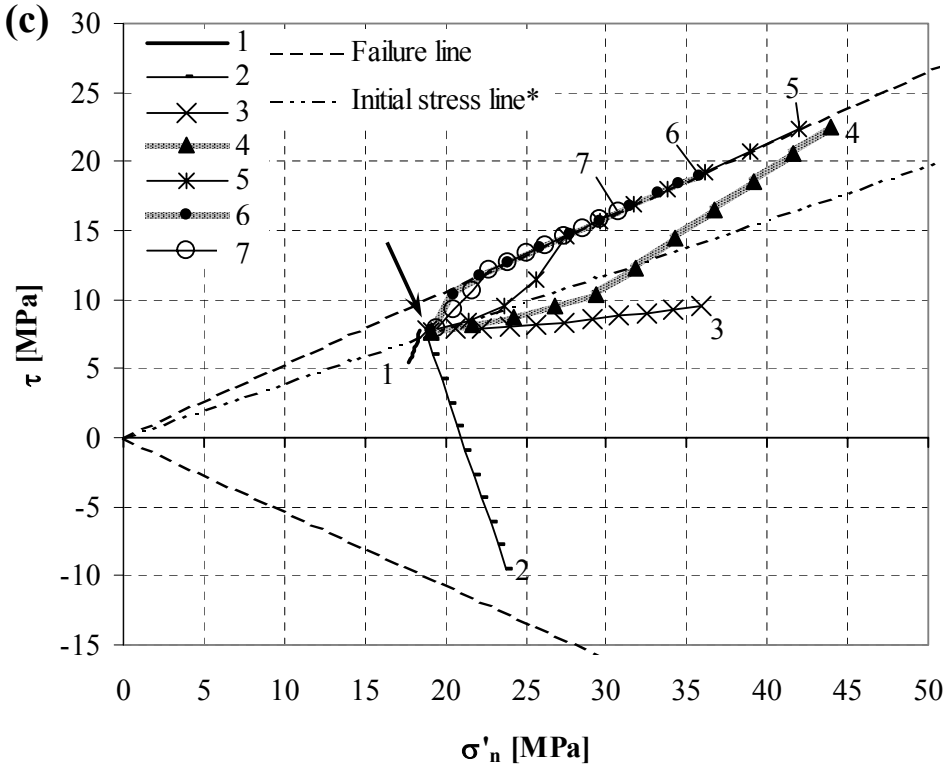

Figure 8.19. *(c) Calculated stress paths for different observation points for the 3D-model 'throw_const_½D' with lower order elements (TE12L and T18IF).*
Surrounding and reservoir rock properties are equal and the initial reservoir pore pressure is hydrostatic (see Table 8.6). The initial state of stress is similar for all stress paths and is indicated by an arrow. The end of the stress paths is marked by the respective observation point letter.
** The 'initial stress line' is calculated according to eqs. (3.2a) and (3.2b), Chapter 3.1.*

Two main differences can be observed between the calculated stress paths of the different models. Firstly, stress paths in observation point D are in the 3D-model and the 2D-model with lower order elements affected by the stress development in point E: the stress path for point D becomes steeper after the stress path in point E has reached the failure line. This is not the case for the 2D-model with higher order elements. As a consequence, calculated normal fault slip is for the 3D-model with a maximum value of 6.7 cm slightly larger than in the higher order 2D-model (6.1 cm), see Figure 8.20a and Table 8.8. The stress path gradient in the first depletion steps in observation points F and G is for the 3D-model somewhat larger than in the higher order 2D-model, suggesting that the stress development is calculated as being more critical in the 3D-model. Secondly, the stress path in observation point B develops in the 3D-model with increasing effective normal stress, whereas σ'_n remains almost equal (slightly decreasing) in both of the 2D-models. Because of this, the stress path in point B does not reach the failure line for the 3D-model, but reaches failure in the

higher order 2D-model just before the complete depletion of the reservoir, during the last (10^{th}) depletion step. Calculated (elastic) reverse fault slip is with -0.4 and -0.5 cm almost equal for the 3D-model and the 2D-model with higher order elements. The 2D-model with lower order elements seems to overestimate the shear stress development in observation point B: failure is reached during the 7^{th} depletion step. As a consequence, a larger reverse fault slip of -1.0 cm is calculated, consisting of an elastic and plastic component.

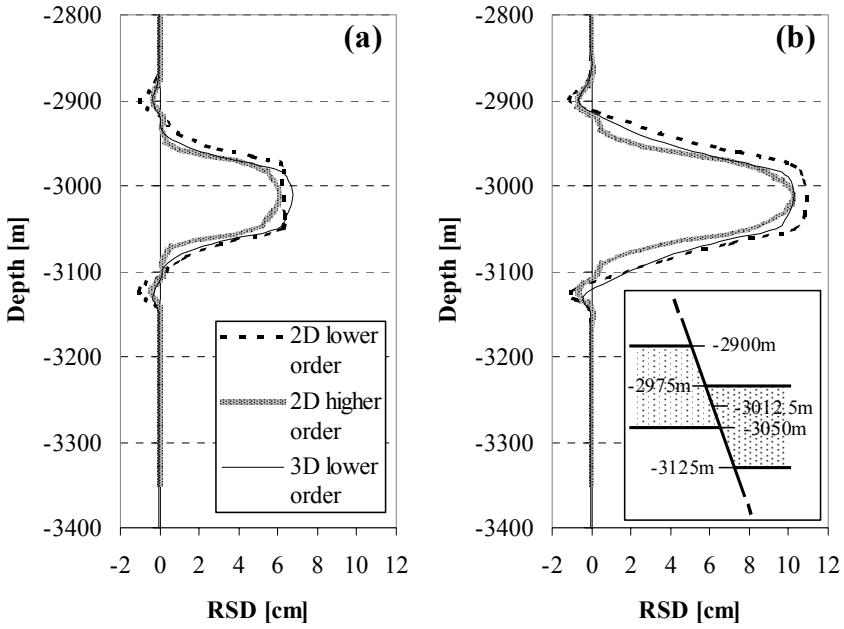

Figure 8.20. Calculated RSD-values along the fault for three different models for (a) equal reservoir and surrounding rock properties and initial hydrostatic reservoir pore pressure and for (b) surrounding rock properties being stiffer as reservoir rock properties and initial reservoir overpressure of 35.0 MPa (see Table 8.6). Pore pressure reduction is for all cases according to an initial hydrostatic reservoir pore pressure (10 depletion steps).

Similar conditions as described above apply for calculations with surrounding rock properties stiffer than the reservoir rock, see Table 8.8 and Figure 8.20.

Because of the symmetry of the 3D-model 'throw_const_½D', the calculated fault slip should be largely the same along a horizontal line in the strike direction of the fault plane. It is checked if this is the case. Calculated RSD-values from the 3D-models are graphically plotted along a horizontal observation line FF' in the strike direction of the fault plane (Figure 8.21). All graphs show a similar pattern with a peak value at the reservoir centre and a local minimum at a distance of 400 m. The difference between these local extremes is with 1.1 cm at it largest for the scenario with stiff surrounding rock, overpressured reservoir and complete depletion. The RSD-graphs along observation line EE', such as shown in Figure 11.2, thus represent a maximum value. The variation is due to an asymmetrical meshing due to the use of the 'general body'-option in DIANA and the use of lower order, constant strain/stress elements.

Table 8.8. Comparison of calculated RSD-values in 2D- and 3D-models for three different scenarios.

*Scenario description****			RSD_{max} *[cm]*			RSD_{min} *[cm]*		
*Surroun-ding rock properties**	p_{ini}^{res} **	Δp^{res}	*2D l.o.*	*2D h.o.*	*3D l.o.*	*2D l.o.*	*2D h.o.*	*3D l.o.*
same	hydrostatic	- hydrostatic	6.3	6.1	6.7	-1.0	-0.5	-0.4
stiff	overpressure	- hydrostatic	10.9	10.2	10.3	-1.1	-0.8	-0.7
stiff	overpressure	- 35.0 MPa	13.4	12.0	12.9	-1.6	-0.9	-1.1

l.o. = lower order; h.o. = higher order

* *relative to reservoir rock properties;*
'same': $E^{sur} = E^{res} = 13.0$ GPa, $\nu^{sur} = \nu^{res} = 0.2$ and $\phi^{sur} = \phi^{res} = 30^o$
'stiff': $E^{sur} = 18.5$ GPa, $\nu^{sur} = 0.25$ and $\phi^{sur} = 25^o$

** *'hydrostatic': p_{ini}^{res} is according to a hydrostatic pore pressure gradient with $\rho_{fluid} = 1000$ kg/m^3*
'overpressure': $p_{ini}^{res} = 35.0$ MPa

*** *Initial pore pressure and pore pressure development in fault regions A and B and fault normal- and shear stiffness change accordingly for the different scenarios.*

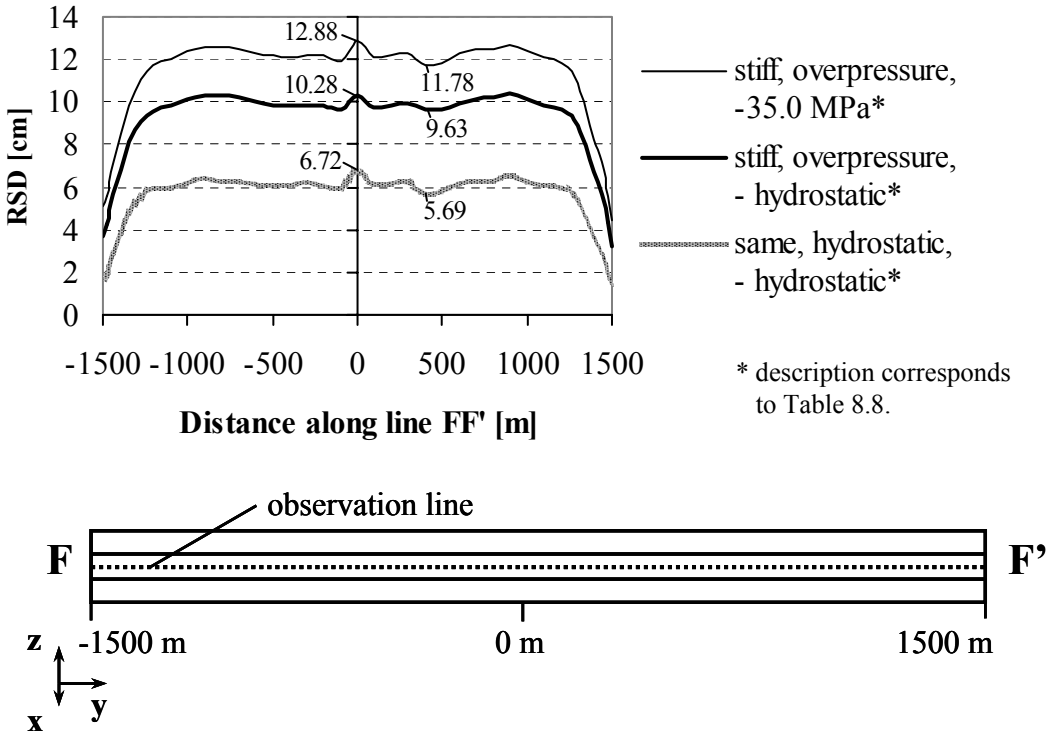

Figure 8.21. Calculated RSD-values for 3D-model 'throw_const_½D' along observation line FF' for different scenario's. The scenario descriptions correspond to Table 8.8. Values indicate the maximum and minimum RSD-values in the central part of the graphs. The lower picture shows the position of line FF'. View direction is normal to the fault plane. Black lines are intersection lines of the two reservoir compartments with the fault plane.

9 QUANTIFICATION OF CALCULATION RESULTS

This chapter describes the quantification methods used for the analysis and comparison of the calculation results. Most of the methods concern the stress development and the movements on the fault plane (Chapter 9.1). Chapter 9.2 deals with methods to quantify the proximity to failure and stress development in the (reservoir) rock volume.

9.1 Fault plane

Three quantitative methods are used to compare the calculation results on the fault plane: relative shear displacement (RSD), stress paths and mobilised shear capacity (MSC). MSC is also applied for rock volumes (MSC^{3D}, Chapter 9.2.1).

Relative shear displacement is used in this dissertation in order to express the amount of fault slip initiated by depletion of a reservoir. Stress paths are used to monitor the initial state of stress and stress development on the fault plane in terms of shear- and effective normal stress. They are especially useful for a detailed analysis of the state of stress throughout depletion at specified locations on the fault plane. Analyses dealing with a large number of stress paths can become rather complex and time consuming. Mobilised shear capacity provides a way to overcome the complexity of an analysis by means of stress paths. Mobilised shear capacity is a scalar quantity which expresses the criticalness of a state of stress in terms of proximity to a given failure criterion. It is especially useful for a quick analysis of the criticalness of a state of stress on a fault plane (MSC) or in a rock volume (MSC^{3D}), but does not provide the details as would be obtained by an analysis by means of stress paths.

9.1.1 Relative shear displacement (RSD)

Relative shear displacement or slip on a fault plane is defined as the differential movement in shear direction of two corresponding nodes on the opposite sides of an interface element.

In this thesis we are interested in the amount of fault slip which develops on a gas reservoir intersecting fault plane during gas depletion. The basic geometry of such a fault plane is shown in Figure 9.1a. The fault plane consists of the two sides f1 and f2. Gas depletion can result in differential movement of the two sides f1 and f2, so that corresponding nodes on either sides of the fault might experience displacements which are different in direction and/or magnitude. Subtracting the displacement vector of a node at plane f2 from the displacement vector of the corresponding node at plane f1 results in a relative displacement vector. Such a relative displacement vector

consists of three components: a normal component n and two tangential components t and s (Figure 9.1b). t and s are defined as being the amount of relative displacement in the down-dip direction and the strike direction of the fault plane, respectively. For the given co-ordinate system in the 3D FE-models of this thesis (see Figure 9.1b and Chapter 8), t, s and n can be calculated according to:

$$t = \Delta x \cos\beta - \Delta z \cos(90^o - \beta), \tag{9.1}$$

$$s = \Delta y, \tag{9.2}$$

$$n = \left|\Delta x \cos(90^o - \beta)\right| - \left|\Delta z \cos\beta\right|, \tag{9.3}$$

with Δx, Δy and Δz being the relative displacements in the global x,y,z-co-ordinate system:

$$\Delta(x, y, z) = (x, y, z)_{f1} - (x, y, z)_{f2}. \tag{9.4}$$

Note that the component t is defined such, that normal fault slip, whereby the hanging wall moves downwards relative to the footwall (Figure 9.1b), has a positive sign and reverse fault slip, whereby the hanging wall moves upwards relative to the footwall, has a negative sign. Positive and negative values for s indicate sinistral (anticlockwise) and dextral (clockwise) movements, respectively.

The relative shear displacement RSD is the resultant of the two components t and s:

$$RSD = \frac{t}{|t|}\sqrt{s^2 + t^2} \quad \text{when } t \neq 0, \tag{9.5a}$$

$$RSD = |s| \quad \text{when } t = 0. \tag{9.5b}$$

Note that the RSD-values are defined as having the same sign as component t. A positive RSD-value denotes normal fault slip, whereby the hanging wall moves downwards relative to the footwall with or without strike slip component. Pure strike slip is positive as well. A negative RSD-value denotes reverse fault slip, whereby the hanging wall moves upwards relative to the footwall, with or without strike-slip component.

Eqs. (9.1) – (9.4) are only valid for the specific relation between the orientation of the fault plane and the co-ordinate system as given in Figure 9.1, whereby $0^o \leq \beta \leq 90^o$. Other equations apply for other geometrical relations, but these can be derived fairly easy.

Note that the interface elements deform elastically prior to failure according to their elastic stiffness properties defined by the normal- and shear stiffnesses D_n and D_s. The calculated fault slip as a result of gas depletion therefore contains an elastic and a plastic component. The plastic fault slip, representing a physical frictional sliding of the two fault surfaces, is responsible for eventual seismicity. In order to give an estimate of the maximum dynamic displacement, the elastic component has actually

to be subtracted from the total calculated amount of fault slip. However, at the time of writing this dissertation, it was technically not possible to distinguish between the elastic and plastic displacement components. Calculated RSD-values as presented in this dissertation consist therefore of both an elastic and plastic fault slip component.

The maximum amount of elastic fault slip in a certain location on the fault plane occurs when the stress path at that location just reaches the failure criterion. Some calculations, where some states of stress on the fault plane were very close to the failure criterion, indicated that the amount of elastic fault slip was in the range of 0.4 cm. Only relative shear displacements larger than 0.4 cm are therefore considered significant in this dissertation.

RSD-contour plots can be made in DIANA's post-processor iDIANA. In iDIANA, calculations on the attributes of result data sets stored in the database can be performed and processed to a new attribute using the option 'results calculate expression…'. However, this option requires the use of results of the same node or integration point. Results of different nodes or integration points of the same attribute cannot be combined. However, RSD-contour plots require this combination. A way to overcome this difficulty is to save the nodal displacements of the interface elements in a iDIANA ASCII file (fvi-file). Via the use of a macro in Excel, the displacement values of corresponding nodes can be subtracted and processed in order to obtain the desired results. These can then be inserted in the fvi-file, which can be imported in iDIANA to create the binary file for making contour plots. Although the procedure is fairly easy, every new model geometry requires the creation of a new macro. This can be a time-consuming process for large models. Furthermore, the importation of the fvi-file requires a special format of this file, which must be maintained.

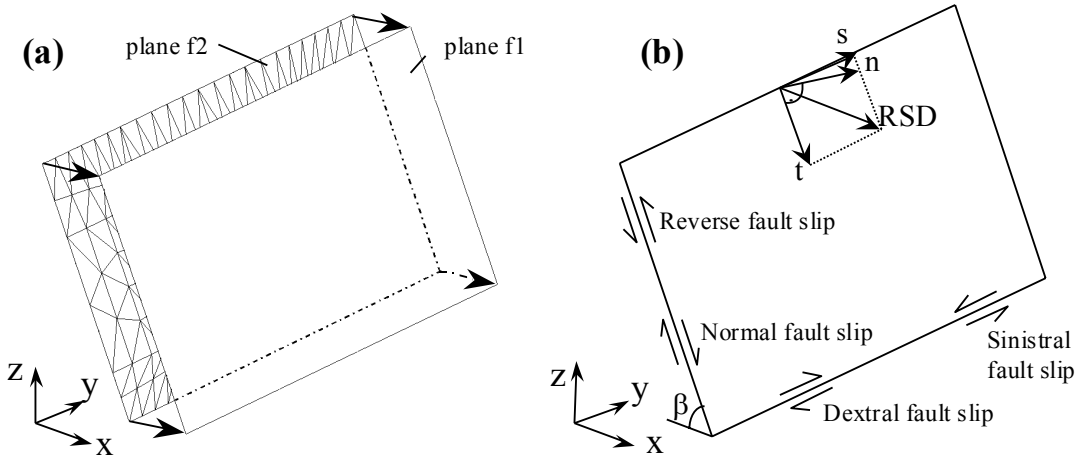

Figure 9.1. *(a) Basic geometry of the fault plane, bounded by the two surfaces f1 (hanging wall side) and f2 (footwall side). (b) Definition of the relative displacement vector components n, t and s for the normal, down-dip and strike direction of the fault plane, respectively. Eqs. (9.1) – (9.4) are only valid for the given relation between the orientation of the fault plane and the co-ordinate system, whereby* $0^o \leq \beta \leq 90^o$.

9.1.2 Seismic moment (M_0)

RSD-values can be very different over the surface area of a fault plane. An example of this is shown in Figure 9.2. Calculated RSD-contours on the fault plane and RSD-graphs for four different observation lines along the fault plane are plotted for model 'throw_var'(Chapter 8.1.1.2 and Figure 11.19, Chapter 11.4) with default properties and loading conditions (Table 8.6, Chapter 8.3.6). For instance, RSD_{max} along observation line CC' is larger than along line BB', but the sharp peak in the graph indicates that fault slip is restricted to a narrower area.

For a good comparison of gas depletion induced fault slip in different calculations with different geometries, the calculated RSD-values should be integrated over the fault plane area in order to come to a single scalar quantity for each calculation. This gives rise to the introduction of the seismic moment M_0. The seismic moment is defined by Aki (1966) as the product of the amount of fault slip (RSD), the area of the fault rupture (A) and the shear modulus of the rock formation through which the fault slip takes place (G), see Figure 9.3:

$M_0^{normal} = G \cdot A \cdot RSD$ when $RSD > 0$, (9.6a)
$M_0^{reverse} = G \cdot A \cdot RSD$ when $RSD < 0$. (9.6b)

Gas depletion induced fault slip often leads to both normal and reverse fault slip (Figure 9.1) on the same fault plane. During the integration of the RSD-values over the fault plane, a dictinction has to be made between negative and positive RSD-values in order to avoid an underestimation of the seismic moment. Integration solely over positive RSD-values leads to a positive seismic moment, M_0^{normal}, representative for normal fault slip. Integration solely over negative RSD-values results in a negative seismic moment, $M_0^{reverse}$, representative for reverse fault slip.

Integration of RSD-values over the fault plane in the numerical models gives the total amount of fault slip produced by gas depletion times the surface area over which the fault slip occurs. The obtained value has then to be multiplied by the shear modulus of the neighbouring rock formations in order to arrive at the seismic moment as given by eqs. (9.6). This latter step is technically complicated in DIANA's postprocessor iDIANA. iDIANA makes therefore use of the shear stiffness D_s of the respective interface elements, which are representative for the shear modulus of the adjacent rock formations as long as they are determined according to the equation (see Chapter 8.3.2.1):

$$D_s = \frac{E}{2(1+\nu)h}, \tag{9.7}$$

where E and ν are the Young's modulus and Poisson's ratio of the adjacent rock formations, respectively, and h is the fault thickness. For a fault thickness smaller than 1 m, a value of 1 m can be used for h in order to avoid extremely large stiffness values. Extremely large stiffness values can in the finite element calculations lead to

'glued' interfaces, i.e. interfaces on which any slip or separation is prevented. It is the user's responsibility to make sure that the input of the fault shear stiffness in the DIANA-calculations is correct and based on eq. (9.7) for a proper determination of the seismic moment. The input of the fault shear stiffness in the FE-models of this dissertation is described in Chapter 8.3.2.1. It is also dealt with the case that two different rock formations with distinct rock properties occur on either sides of the fault plane. E and ν have than to be averaged. The average values are then inserted into eq. (9.7).

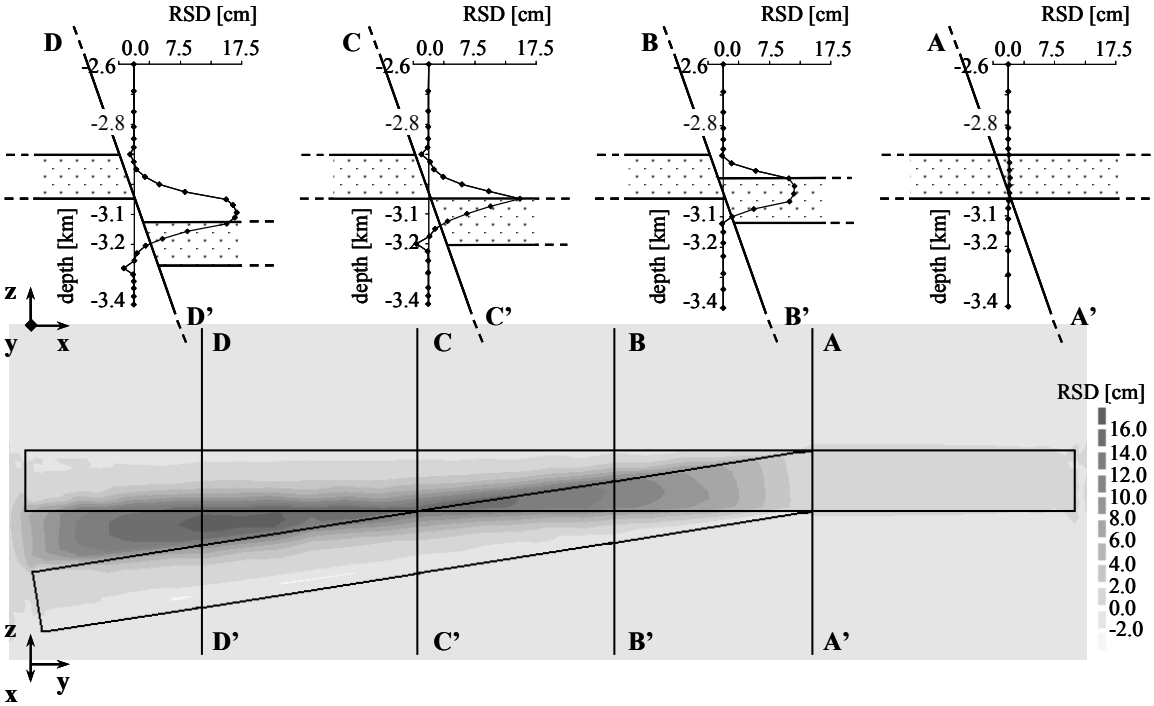

Figure 9.2. Relative shear displacements (RSD) on the fault plane for model 'throw_var' with default properties and loading conditions and full pore pressure reduction (11 depletion steps, see Table 8.6, Chapter 8.3.6). The maximum RSD-value is 16.7 cm, located in between observation lines CC' and DD', close to line DD'. View direction of the contour plot is normal to the fault plane. Intersection lines of the two reservoir compartments with the fault plane are shown. View direction of the cross sections is in strike direction of the fault. Pointed areas denote the reservoir compartments. See Appendix 2 for this figure in colour.

Note that the calculated seismic moments in the numerical models as described above represent an upper limit, a maximum seismic potential for the modelled fault(s) under the applied conditions, since it is assumed that 100% of the gas depletion induced fault slip is translated to those seismic moments. The slip, calculated in the model, may in reality occur either aseismically, or as a seismic event or as a combination of the two (Chapter 4). Aseismic fault slip does not contribute to a seismic moment. Due to the limitations of the method followed, i.e. elastoplastic modelling, it is impossible to establish if asperities will form during depletion and whether built-up stresses will

be released seismically or aseismically. Even if the seismic moment would be known, this seismic energy could be released in one relatively large seismic event or in a series of smaller events. It is therefore not recommendable to translate the calculated seismic moments to magnitudes on Richter scale. The calculations presented in this dissertation can never be a forecast of the magnitude of the events which are going to occur when a reservoir with the type of modelled setting is produced. The calculated seismic moments are just parameters, which express the criticalness of a fault for reactivation under certain circumstances, and which can be used in subsequent research for a probabilistic approach of the problem of induced seismicity.

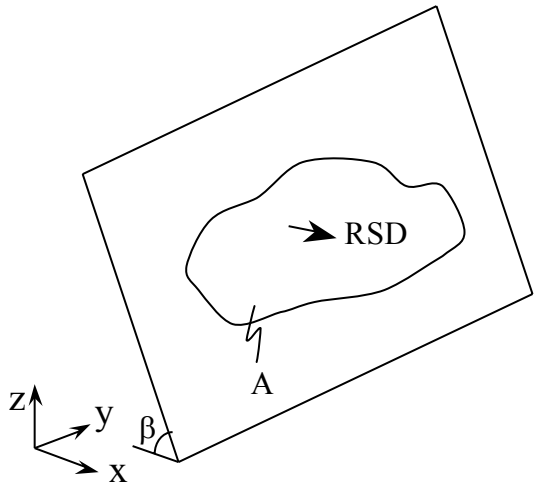

Figure 9.3. Parameters for the definition of the seismic moment M_0 after eq. (9.6).

Because of the integration over the fault plane, the method to calculate the seismic moment as described above is only valid for 3-dimensional numerical models. The option in DIANA to calculate the seismic moment for 3-dimensional interface elements is at the time of writing under construction. For this thesis, a preliminary version is used to calculate the seismic moment. A new output option STRAIN DISSEI will be available. STRAIN DISSEI stands for the product of D_s and RSD on the fault plane. Integration of STRAIN DISSEI over the fault plane results in the seismic moment, whereby a distinction needs to be made between M_0^{normal} and $M_0^{reverse}$. This distinction is made in DIANA's postprocessor iDIANA.

9.1.3 Stress paths and stress path gradient

Stress paths are a good way to study the initial state of stress, prior to gas depletion, and the stress development on the fault plane in detail. Stress paths in this dissertation describe the development of shear- and effective normal stress on the fault plane throughout depletion of the reservoir. Each stress path is valid for a certain location on the fault. Figure 9.4 shows examples of stress paths for different locations on line EE' on the fault plane of model 'throw_const_½D'(Chapter 8.1.1.1 and Figure 11.19, Chapter 11.4) with surrounding rock properties equal to the reservoir rock properties and initial hydrostatic reservoir pore pressure (Table 8.6, Chapter 8.3.6).

Stress paths can be used to determine whether a state of stress on a fault plane converges to, runs parallel to or diverges from the failure line of the fault. When the absolute stress path gradient is larger than the gradient of the failure line, i.e. when $\left|\Delta\tau / \Delta\sigma'_n\right| > \tan\phi^f$, the stress path converges and the stress development is said to be critical. For absolute stress path gradients equal to or smaller than the gradient of the failure criterion ($\left|\Delta\tau / \Delta\sigma'_n\right| \leq \tan\phi^f$), the stress path runs parallel to or diverges from the failure line, respectively. The stress development in these cases is said to be non-critical. The stress path gradient can change during the gas depletion (Figure 9.4, stress paths 4 and 5). Stress paths which are non-critical in the first part of the depletion phase can become critical in a later stage of the depletion and vise versa.

A stress path with a critical gradient does not necessarily need to lead to failure of the fault plane. The initial state of stress plays a major role in this matter as well. Consider the stress paths 2, 4 and 6 in Figure 9.4. The stress paths have an absolute gradient with is larger than the gradient of the failure line. Stress path 6 reaches failure already after 1 depletion step, whereas stress paths 2 and 4 do not reach failure for the given conditions. Complications on stress paths and research results of a parameter study are described by Glab (2001).

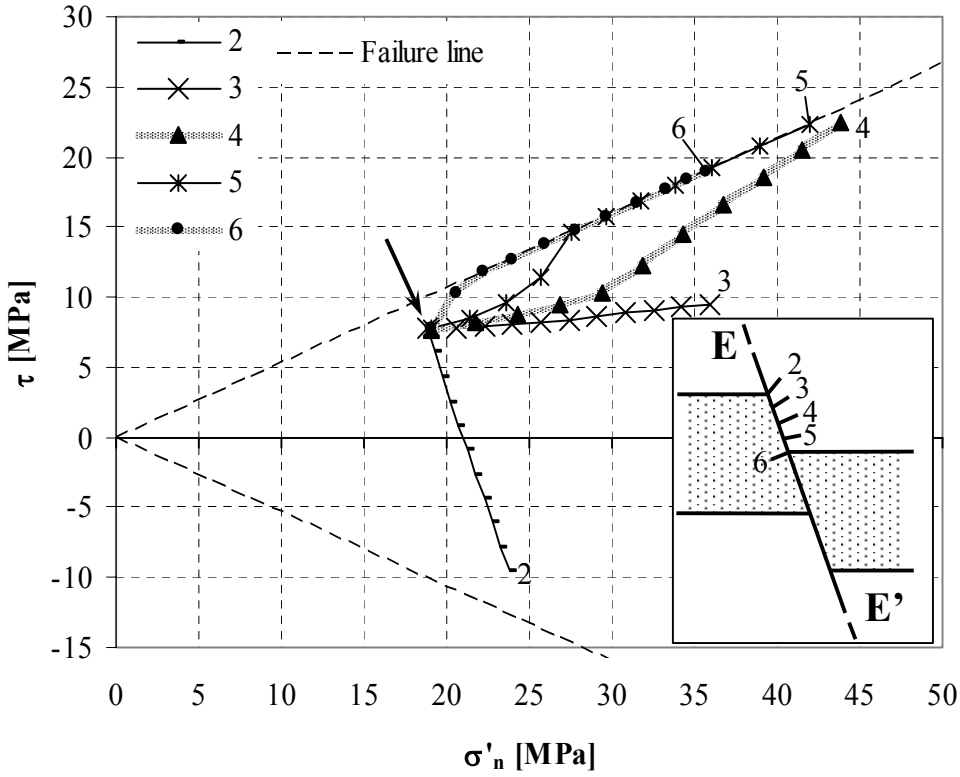

Figure 9.4. Examples of stress paths, calculated for different observation points along observation line EE' in model 'throw_const_½D' (see Figure 11.19, Chapter 11.4) with surrounding rock properties equal to the reservoir rock properties and initial hydrostatic reservoir pore pressure (Table 8.6, Chapter 8.3.6). The initial state of stress is similar for all stress paths and is indicated by an arrow. The end of the stress paths are marked by the respective observation point number.

9.1.4 Mobilised shear capacity on faults (MSC)

Mobilised shear capacity (MSC) on a fault expresses quantitatively the proximity of a state of stress in a certain location on that fault to a predefined failure criterion. Mobilised shear capacity is therefore a function of the shear- and effective normal stress present in that location and the assumed strength properties of the fault. In case of a Mohr-Coulomb failure criterion, the definition becomes as shown in Figure 9.5:

$$\text{MSC} = \text{AC/BC}. \tag{9.8}$$

A is a point reflecting an arbitrary set of effective normal stress σ'^{A}_{n} and shear stress τ^{A}. AB is the shortest distance between the state of stress and a Mohr-Coulomb failure criterion with arbitrary fault friction angle ϕ^{f} and fault cohesion c^{f}. BC is a line through point A perpendicular to the failure line, where C is its intersection point with the effective normal stress axis and B is its intersection point with the failure line. σ'^{B}_{n}, σ'^{C}_{n}, τ^{B} and τ^{C} are effective normal- and shear stresses in points B and C, respectively. MSC-values fall within the range from 0 to 1. An MSC-value of 1 means failure, a value of 0 means that no shear stress is present.

From the geometrical relations as shown in Figure 9.5 the distances AC and BC can be calculated according to:

$$\text{AC} = \sqrt{\left(\sigma'^{C}_{n} - \sigma'^{A}_{n}\right)^2 + \left(\tau^{A}\right)^2}\,, \tag{9.9}$$

$$\text{BC} = \sqrt{\left(\sigma'^{C}_{n} - \sigma'^{B}_{n}\right)^2 + \left(\tau^{B}\right)^2}\,, \tag{9.10}$$

where

$$\sigma'^{C}_{n} = \sigma'^{A}_{n} + \tau^{A} \tan\phi^{f}\,, \tag{9.11}$$

$$\sigma'^{B}_{n} = \frac{\sigma'^{A}_{n} + \left(\tau^{A} - c^{f}\right)\tan\phi^{f}}{\tan^2\phi^{f} + 1}\,, \tag{9.12}$$

$$\tau^{B} = \frac{\sigma'^{A}_{n}\tan\phi^{f} + \left(\tau^{A} - c^{f}\right)\tan^2\phi^{f}}{\tan^2\phi^{f} + 1} + c^{f}\,. \tag{9.13}$$

As stated before, MSC-values are within the range between 0 and 1. An MSC-value of 1 in a certain location on the fault means that the fault fails in that location, whereas a value of 0 indicates that no shear stress is present in that location. Basically one can say that the larger an MSC-value, the closer a state of stress is to failure, but there exists a dependency of the effective normal stress. An increase in mobilised shear capacity does not necessarily imply a critical stress path. Consider the three stress paths A_{2a}, A_{2b} and A_{2c} in Figure 9.6. They all incorporate an increase in mobilised shear capacity, but only stress path A_{2a} converges to the failure line and is therefore critical. Stress paths A_{2b} and A_{2c} are parallel to and diverge from the failure

line, respectively, and are therefore non-critical. In fact, distance AB determines whether a stress path is critical or not, so that:

$$(\mathrm{BC}-\mathrm{AC})_2-(\mathrm{BC}-\mathrm{AC})_1<0:\text{ critical} \tag{9.14a}$$

$$(\mathrm{BC}-\mathrm{AC})_2-(\mathrm{BC}-\mathrm{AC})_1\geq 0:\text{ non-critical} \tag{9.14b}$$

Calculations showed that the maximum attainable MSC-value is exactly 1.0, according to the theory. No values larger than 1.0 are calculated. It shows the correct derivation of the formulas for the calculation of MSC and their proper implementation into the DIANA software. The output attributes in iDIANA related to the state of stress of interface elements are in terms of tractions in direction of the local element co-ordinate system. MSC-values can be directly calculated in iDIANA according to eqs. (9.8) – (9.13) using the option 'results calculate expression…'.

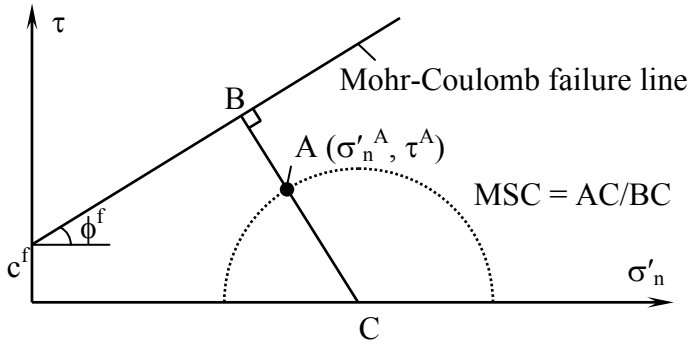

Figure 9.5. Definition of MSC for an arbitrary set of effective normal and shear tractions marked by point A. AC and BC can be calculated from $\sigma_n'^{A}$, τ^A, ϕ^f and c^f (see formulas in text). The dashed half circle is an imaginary Mohr-circle through point A with centre point C.

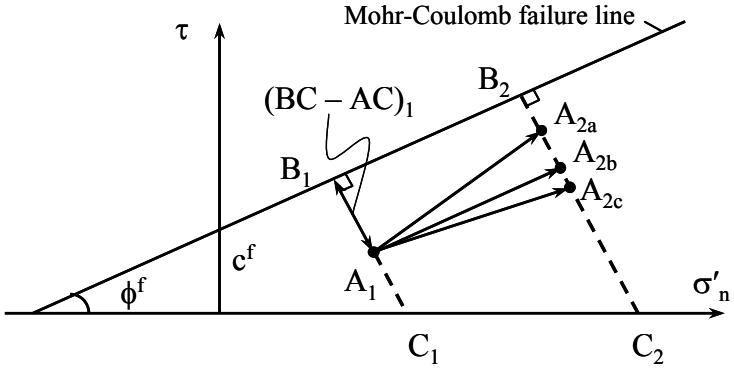

Figure 9.6. Stress paths from stress state A_1 to stress states A_{2a}, A_{2b} and A_{2c} all incorporate an increasing MSC-value, although the stress path to A_{2b} is parallel to and the stress path to A_{2c} is slightly diverging from the failure line.

9.2 Rock volume

9.2.1 Mobilised shear capacity in rock volume (MSC^{3D})

Mobilised shear capacity in a rock volume (MSC^{3D}) is similarly defined as the mobilised shear capacity on a fault (MSC). It expresses quantitatively the proximity of a state of stress in a certain location in that rock volume to a predefined failure criterion. In this study the Mohr-Coulomb failure criterion, defined by the hexagonal pyramid in a 3-dimensional effective principal stress space (Figure 9.7a), is used. The central axis of this pyramid is the hydrostatic axis. This axis is characterised by the fact that the three (effective) principal stresses are equal.

Any possible state of effective stress in a rock volume lies within or at the hexagonal pyramid and can be described by the sum of its mean effective stress vector and deviatoric stress vector (see Chapter 2.1.5, eq. (2.16)) and therefore by the Haigh-Westergaard stress co-ordinates ξ, ρ and θ (Chapter 2.1.5, eq. (2.37)). The mean effective stress vector, with magnitude ξ, lies on the hydrostatic axis. The deviatoric stress vector is always located in a deviatoric plane, i.e. a plane perpendicular to the hydrostatic axis. Its magnitude is equal to ρ. The direction of the deviatoric stress vector is defined by θ, which the angle between the projected vertical (effective) principal stress axis and the deviatoric stress vector and is positive counterclockwise.

A deviatoric plane view of the Mohr-Coulomb failure criterion is shown in Figure 9.7b. The principal stress axes are projected on the deviatoric plane, which is indicated by an asterix. For the condition that $\sigma'_1 \geq \sigma'_2 \geq \sigma'_3$, the possible states of stress reduce to a restricted area within the principal stress space, indicated by the shaded area in Figure 9.7b.

Figure 9.7c shows the state of stress in a rendulic plane, i.e. a plane containing the effective principal stress vector, the mean effective stress vector and the deviatoric stress vector. The mean effective stress vector runs from point O to B, whereas the deviatoric stress vector runs from point B to A. In accordance to eq. (9.8), the mobilised shear capacity in this 3-dimensional stress space (MSC^{3D}) can be defined as:

$$MSC^{3D} = \frac{\rho^*}{\rho^*_{fail}}. \tag{9.15}$$

It is obvious that MSC^{3D} is a function of the Haigh-Westergaard stress co-ordinates and the plastic strength properties of the rock in a certain location of that rock volume. ξ determines the size of the Mohr-Coulomb failure circumference in the deviatoric plane. ρ and θ together determine how close a stress state is located to the failure line in the rendulic plane.

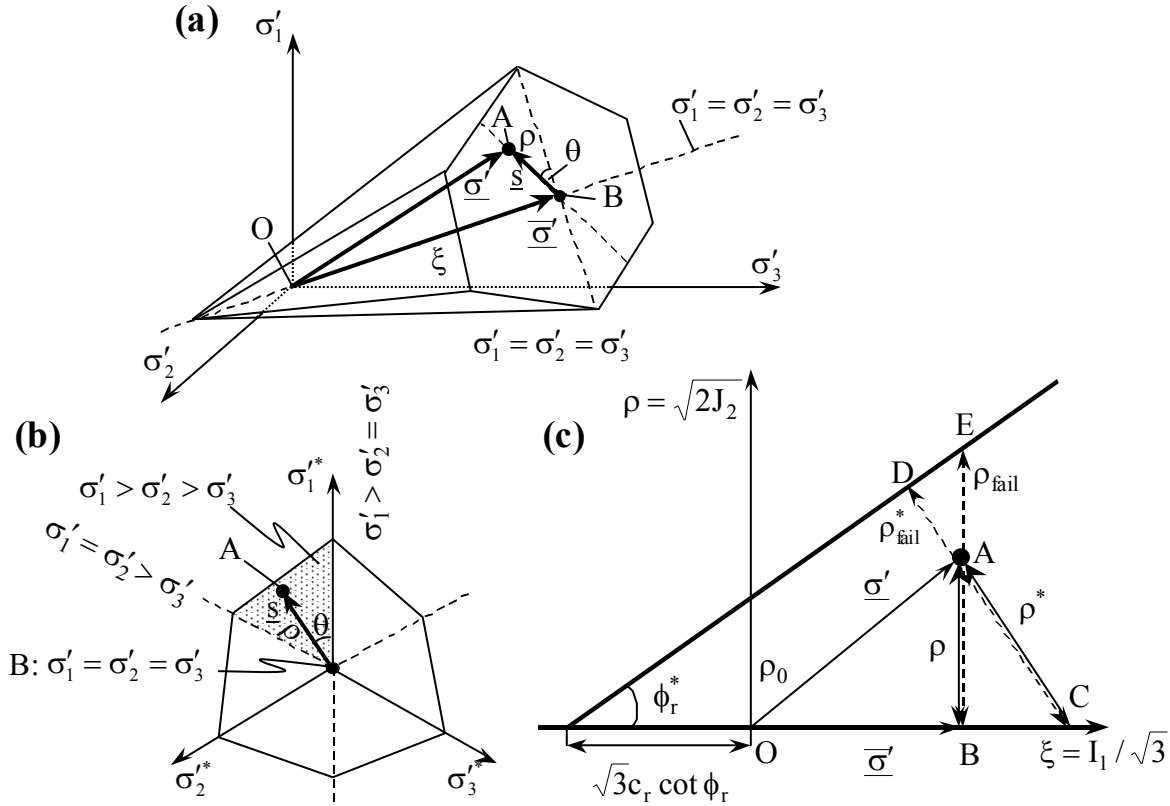

Figure 9.7. *(a) The Mohr-Coulomb failure surface in 3-dimensional effective principal stress space with indication of the Haigh-Westergaard stress co-ordinates. An effective state of stress $\underline{\sigma'}$ marked by point A consists of a mean effective stress vector $\overline{\underline{\sigma'}}$ (marked by point B) and a deviatoric stress vector $\underline{s}$. (b) Deviatoric plane view. For the condition that $\sigma_1' \geq \sigma_2' \geq \sigma_3'$, a possible state of stress only can occur in a restricted area within the effective principal stress space, indicated in the rendulic plane view by the shaded area. (c) Rendulic plane view, containing the three vectors $\underline{\sigma'}$, $\overline{\underline{\sigma'}}$ and $\underline{s}$, for the definition of MSC^{3D}.*

In order to get to an expression for MSC^{3D}, one needs to express a state of stress and the Mohr-Coulomb failure surface in terms of Haigh-Westergaard co-ordinates. In Chapter 3.1, the Mohr-Coulomb failure criterion is presented in the form of a yield function $F(\sigma_1', \sigma_3', c_r, \phi_r)$, which takes on values less than zero for states of stress within the hexagonal pyramid and zero on the failure surface itself (eq. (3.7)). Because MSD^{3D} is defined for rock volume, eq. (3.7) becomes with the correct indices for the cohesion and the friction angle:

$$F(\sigma_1', \sigma_3', c_r, \phi_r) = \tfrac{1}{2}\sigma_1'(1 - \sin\phi_r) - \tfrac{1}{2}\sigma_3'(1 + \sin\phi_r) - c_r \cos\phi_r. \qquad (9.16)$$

The two effective principal stresses can according to eq. (2.37) in Chapter 2.1.5 be expressed as a function of the Haigh-Westergaard stress co-ordinates:

$$\sigma_1' = \frac{\xi}{\sqrt{3}} + \frac{\sqrt{2}\rho}{\sqrt{3}}\cos\theta, \tag{9.17a}$$

$$\sigma_3' = \frac{\xi}{\sqrt{3}} + \frac{\sqrt{2}\rho}{\sqrt{3}}\cos\left(\theta + \tfrac{2\pi}{3}\right). \tag{9.17b}$$

Substituting the expressions for σ_1' and σ_3' of eqs. (9.17a) and (9.17b) into eq. (9.16) and re-arranging, one obtains the yield function F in terms of Haigh-Westergaard coordinates:

$$F(\xi,\rho,\theta,c_r,\phi_r) = -\sqrt{2}\xi\sin\phi_r + \sqrt{3}\rho\sin\left(\theta+\tfrac{\pi}{3}\right) - \rho\sin\phi_r\cos\left(\theta+\tfrac{\pi}{3}\right) - \sqrt{6}c_r\cdot\cos\phi_r. \tag{9.18}$$

Failure occurs when F = 0:

$$\rho_{fail} = \frac{\sqrt{6}c_r\cdot\cos\phi_r + \sqrt{2}\xi\sin\phi_r}{\sqrt{3}\sin\left(\theta+\tfrac{\pi}{3}\right) - \sin\phi_r\cos\left(\theta+\tfrac{\pi}{3}\right)}. \tag{9.19}$$

Note that ρ_{fail} and thus MSC^{3D} depend both on ξ and θ. The dependency on ξ is clear from Figure 9.7a, as the hexagonal pyramid gets wider for larger values of ξ. This effect is similar to the dependency of the mobilised shear capacity on faults (MSC) on the effective normal stress as described in Chapter 9.1.4. The dependency of ρ_{fail} on θ is visible in Figures 9.7b and c. The failure line for $\theta = 0^o$ in the rendulic plane view (Figure 9.7c) is steeper than for $\theta = 60^o$.

For the limit condition that $\theta = 0^o$ the effective principal stresses relate to each other as $\sigma_1' > \sigma_2' = \sigma_3'$ (triaxial compression), and ρ_{fail} becomes then:

$$\rho_{fail}(\theta = 0^o) = \frac{2\sqrt{6}c_r\cdot\cos\phi_r + 2\sqrt{2}\xi\sin\phi_r}{3-\sin\phi_r}. \tag{9.20}$$

For the other limit condition that $\theta = 60^o$ triaxial extension applies with $\sigma_1' = \sigma_2' > \sigma_3'$ and thus:

$$\rho_{fail}(\theta = 60^o) = \frac{2\sqrt{6}c_r\cdot\cos\phi_r + 2\sqrt{2}\xi\sin\phi_r}{3+\sin\phi_r}. \tag{9.21}$$

From eqs. (9.20) and (9.21) it follows, that $\rho_{fail}(\theta = 0^o)$ is larger than $\rho_{fail}(\theta = 60^o)$ and that:

$$\frac{\rho_{fail}(\theta = 60^o)}{\rho_{fail}(\theta = 0^o)} = \frac{3-\sin\phi_r}{3+\sin\phi_r}. \tag{9.22}$$

Because the rock friction angle ϕ_r varies theoretically between 0^o and 90^o, the ratio given by eq. (9.22) varies between 0.5 ($\phi_r = 90^o$) and 1.0 ($\phi_r = 0^o$). Note that for $\phi_r = 0^o$, $\rho_{fail}(\theta = 0^o)$ and $\rho_{fail}(\theta = 60^o)$ become equal and the Mohr-Coulomb criterion reduces to the Tresca criterion.

From goniometric relations in Figure 9.7c, it can be easily derived that:

$$\rho^* = \frac{\rho}{\cos\phi_r^*} \text{ and} \tag{9.23}$$

$$\rho_{fail}^* = \cos\phi_r^*\left(\rho_{fail} - \rho\right) + \frac{\rho}{\cos\phi_r^*}. \tag{9.24}$$

Recalling the definition of MSC^{3D} of eq. (9.15), it then follows that:

$$MSC^{3D} = \frac{\rho\left(1 + \tan^2\phi_r^*\right)}{\rho_{fail} + \rho\tan^2\phi_r^*} \tag{9.25}$$

ρ_{fail} can be calculated with eq. (9.19). ρ can be calculated according to eq. (2.19):

$$\rho = \sqrt{\tfrac{2}{3}\left(\sigma_1'^2 + \sigma_2'^2 + \sigma_3'^2 - \sigma_1'\sigma_2' - \sigma_1'\sigma_3' - \sigma_2'\sigma_3'\right)} \tag{9.26}$$

$\tan\phi_r^*$ follows from Figure 9.7c:

$$\tan\phi_r^* = \frac{\rho_0}{\sqrt{3}c \cdot \cot\phi_r} \tag{9.27}$$

where $\rho_0 = \rho_{fail}(\xi = 0)$:

$$\rho_0 = \frac{\sqrt{6}c \cdot \cos\phi_r}{\sqrt{3}\sin\left(\theta + \frac{\pi}{3}\right) - \sin\phi_r\cos\left(\theta + \frac{\pi}{3}\right)} \tag{9.28}$$

MSC^{3D}-values vary within the range from 0 to 1. When $MSC^{3D} = 0$, the state of stress lies on the hydrostatic axis. For $MSC^{3D} = 1$, the state of stress lies on the failure surface. The maximum value attained in several calculations is exactly 1.0, showing the correctness of the derived formulas and their proper implementation in the DIANA-software.

As stated described before in Chapter 9.1.4 for mobilised shear capacity on faults, an increase in MSC^{3D} does not necessarily imply a stress development towards failure. The same principle as shown in Figure 9.6 applies also for MSC^{3D}, whereby the distance AB has to be thought replaced by $(\rho_{fail}^* - \rho^*)$ (Figure 9.8). In fact, distance $(\rho_{fail}^* - \rho^*)$ determines whether a stress path is develops towards failure (is critical) or not. To judge whether a stress development is critical or not, one should make use of the following criterion:

$$\left(\rho^*_{fail} - \rho^*\right)_2 - \left(\rho^*_{fail} - \rho^*\right)_1 < 0 : \text{critical} \qquad (9.29a)$$

$$\left(\rho^*_{fail} - \rho^*\right)_2 - \left(\rho^*_{fail} - \rho^*\right)_1 \geq 0 : \text{non-critical} \qquad (9.29b)$$

Note that the derivation of the formulas does not take into account tension cut-off or a compression failure surface (cap). They are solely based on the Mohr-Coulomb failure criterion with a cohesion and a friction angle. Values for MSC^{3D} can be directly calculated in iDIANA using the option 'results calculate expression…'. Its application in iDIANA proved to be successful.

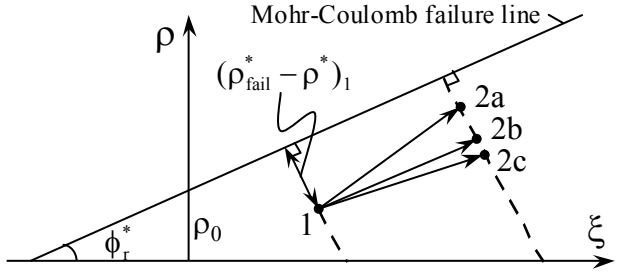

Figure 9.8. Stress paths from stress state 1 to stress states 2a, 2b and 2c all incorporate an increasing MSC^{3D}-value, although the stress path to 2b is parallel to and the stress path to 2c is slightly diverging from the failure line.

9.2.2 Effective and total stress changes per unit depletion

In this thesis, a change in stress/pressure is according to eq. (3.13) defined as the stress/pressure after hydrocarbon production minus the stress/pressure before production:

$$\Delta\sigma' = \sigma'^{\,\text{after}} - \sigma'^{\,\text{before}}. \qquad (9.30)$$

This means that a stress increase during hydrocarbon production has a positive sign and a stress decrease has a negative sign. Note that $\Delta p < 0$ for hydrocarbon production. The effective stress change $\Delta\sigma'$ is related to the total stress change $\Delta\sigma$ and the pore pressure change Δp times Biot-constant α (see Chapter 2.4). In terms of the co-ordinate system in the DIANA-models this becomes according to eq. (3.12):

$\Delta\sigma'_x = \Delta\sigma_x - \alpha\Delta p,$ (9.31a)
$\Delta\sigma'_y = \Delta\sigma_y - \alpha\Delta p,$ (9.31b)
$\Delta\sigma'_z = \Delta\sigma_z - \alpha\Delta p,$ (9.31c)

where z denotes the vertical direction, y denotes the horizontal direction parallel to the strike of the fault plane and x denotes the azimuth of the fault plane.

The change in total stress in relation to the pore pressure change is often termed arching (e.g. Kenter *et al.* 1998) and can be expressed by the ratio γ (Chapter 3.3, eq. (3.14)). Similar to the effective stress changes of eqs. (9.31), γ can be defined for the three distinct main directions in the FE-models:

$\gamma_x = \Delta\sigma_x / \Delta p$, (9.32a)
$\gamma_y = \Delta\sigma_y / \Delta p$, (9.32b)
$\gamma_z = \Delta\sigma_z / \Delta p$. (9.32c)

Hence, γ-values express the total stress change per unit depletion. They can be calculated for the reservoir rock itself but also for the rock formations surrounding the reservoir. In both cases, Δp is the pore pressure change in the reservoir, regardless eventual pore pressure changes in the surrounding rocks. γ expresses then always the total stress change per unit depletion at a certain location. The value of γ depends on the rock properties of the reservoir and surrounding rock, the reservoir geometry and the geological setting in which the reservoir is placed. Values of γ are characteristic for a hydrocarbon reservoir. They are not constant throughout the reservoir but are dependent on rock properties and reservoir geometry.

10 STRESS DEVELOPMENT IN GENERIC BASIC RESERVOIR MODELS WITHOUT FAULT

This chapter gives an overview of stress development in ellipsoidal and disk-shaped hydrocarbon reservoirs. Analytical solutions as well as numerical modelling results are presented and discussed. Existing analytical solutions for calculation of stress changes in hydrocarbon reservoirs due to pore pressure and temperature changes are presented in Chapter 10.1 for ellipsoidal reservoirs (Rudnicki 1999, 2003 and Segall & Fitzgerald 1998) and disk-shaped reservoirs (Geertsma 1973). Differences in stress development between ellipsoidal and disk-shaped reservoirs are analysed in Chapter 10.2. Chapter 10.3 zooms in on disk-shaped reservoirs and discusses the influence of several parameters on the stress development in and around the reservoir: reservoir rock properties, surrounding rock properties, reservoir geometry (depth and aspect ratio) and reservoir tilting.

10.1 Analytical solutions

10.1.1 Ellipsoidal reservoirs

Analytical solutions for the calculation of stress changes as a result of pore pressure and temperature changes in an elastic axisymmetrical ellipsoidal reservoir embedded in an elastic full space are given by Segall & Fitzgerald (1998) and Rudnicki (1999, 2003). These analytical solutions are based on the Eshelby solution to compute elastic strains in an ellipsoidal inclusion in an elastic full space subjected to pore pressure and/or temperature changes (Eshelby 1957). The principle of these solutions is that the reservoir cannot contract as much as it would like due to the elastic coupling to the surrounding rock. There exists a difference in the pore pressure and temperature change induced strains between an imaginary reservoir which is thought to be removed from the earth and the same reservoir in its in-situ position in the subsurface. As there are no stresses applied to the boundary of the reservoir in the first imaginary case, the change in pore pressure and/or temperature would induce a 'stress-free' or 'transformation' strain ε_{ij}^{T}. The elastic earth holds back the reservoir and inhibits a free deformation according to the transformation strain. Eshelby (1957) showed that the resulting strain in the inclusion is given by

$$\varepsilon_{ij}^{\text{inclusion}} = \varepsilon_{ij}^{T} - S_{ijkl}\varepsilon_{kl}^{T}. \tag{10.1}$$

S_{ijkl} are rank four tensors known as the 'Eshelby shape factors' (e.g. Mura 1982). The second term of the right-hand side of eq. (10.1) represents the constraint of the elastic surroundings applied to the reservoir. Note that eq. (10.1) is valid for the sign convention that compression is positive.

Segall & Fitzgerald (1998) and Rudnicki (1999) translate the Eshelby solution into analytical solutions which make it possible to calculate pore pressure and temperature change induced stress changes in the elastic ellipsoidal reservoir as a function of the aspect ratio and rock properties of the reservoir. The aspect ratio e is defined as the ratio of the shortest (vertical) half axis and the longest (horizontal) half axis of the axisymmetric ellipsoid. Segall & Fitzgerald (1998) give additional solutions for stress changes inside and immediate outside of the reservoir. Rudnicki (1999) takes additionally the surrounding rock properties into account.

According to Rudnicki (2003), eq. (32) in Rudnicki (1999) should read

$$\Delta q / \Delta s = \left\{ \frac{2(1-\nu_I)}{\zeta^I (1-2\nu_I)} - 1 \right\}^{-1}. \tag{10.2}$$

For $\zeta^I = 1$, this reduces to $(1-2\nu_I)$. In here ζ^I is the Biot constant (α) of the reservoir rock, ν_I is the Poisson's ratio of the reservoir rock (ν^{res}) and $\Delta q/\Delta s$ is the stress path gradient in a p,q-diagram (note that p is replaced by s in order to avoid confusion with the pore pressure p). In eq. (30) in Rudnicki (1999), g should be replaced by 1+g, which is equal to G_I/G_∞ (G_I and G_∞ being the shear modulus of the reservoir rock (G^{res}) and surrounding rock (G^{sur}), respectively). But, in all the other expressions, $g=G_I/G_\infty-1$ and $k=K_I/K_\infty-1$ (K_I and K_∞ being the bulk modulus of the reservoir rock (K^{res}) and surrounding rock (K^{sur}), respectively). This is easily verified from eq. (11) or eq. (15) in Rudnicki (1999): Setting g = 0 and k = 0 (no elastic mismatch between reservoir and surrounding rock), the reservoir stress and strain are identical to the far field values if the reservoir pore pressure is zero. Furthermore, the numerator of the term to the left of the large bracket in the definition of I(e) (eq. 22 in Rudnicki 1999) should read e rather than e^2.

Horizontal and vertical arching (γ_h and γ_v, see Chapters 3.4 and 9.2.2 for definition) according to the analytical solutions by Rudnicki (1999) are plotted in Figure 10.2 as function of the aspect ratio e of the ellipsoidal reservoir and the Poisson's ratio of the reservoir rock ν^{res}. The graphs in Figure 10.2 are valid for $G^{res}/G^{sur} = 1.0$. Using this expression and the expression $G = E/2(1 + \nu)$, it follows that

$$\frac{E^{res}}{2(1+\nu^{res})} = \frac{E^{sur}}{2(1+\nu^{sur})}. \tag{10.3}$$

For a Poisson's ratio of the surrounding rock ν^{sur} of 0.2 and a Young's modulus of the reservoir rock E^{res} of 13.0 GPa, this results in

$$E^{sur} = \frac{15.6}{(1+\nu^{res})} \text{ [GPa]}. \tag{10.4}$$

Note that for the condition that $G^{res}/G^{sur} = 1.0$, E^{sur} is a function of ν^{res} and varies as ν^{res} varies. The dependency of E^{sur} on the chosen values of ν^{res} for this condition can be seen in Table 10.1.

The analytical solutions for ellipsoidal reservoirs, which are based on the Eshelby (1957) solutions, result in reservoir stress changes (due to pore pressure and temperature changes) which are constant throughout the entire reservoir. Under these conditions, there is one value for the vertical stress changes (and thus for γ_v) and one value for the horizontal stress changes (and thus for γ_h) for the entire reservoir. The analytical solutions are compared to numerical FE-calculations to check the validity of this result (Chapter 10.2).

10.1.2 Disk-shaped reservoirs

Geertsma (1973) derived analytical solutions for both the displacement field and the changes in the stress field for disk-shaped reservoirs in an elastic half-space with a traction-free surface and with uniform deformation properties throughout the entire sedimentary basin, including overburden and basement. These solutions are valid for a uniform pressure drop within the reservoir and apply to the surrounding rock, in which no change in pore pressure is assumed. Stress changes are expressed in terms of γ-values (total stress changes per unit depletion).

For a disk-shaped gas reservoir with a radius of 1960m, a thickness of 150m, a depth of the reservoir centre of 2975m, $E^{res} = E^{sur} = 13.0$ GPa and $\nu^{res} = \nu^{sur} = 0.2$, calculated stress changes outside of the reservoir in terms of γ are as plotted in Figure 10.1. For a definition of γ, see Chapters 3.4 and 9.2.2. For a more detailed explanation about the shape of the γ-graphs as plotted in Figure 10.1, see Chapter 10.2. The work of Geertsma (1973) is extended by Geertsma & Van Opstal (1973), in order to calculate the displacement field at the surface above a compacting reservoir of a complicated 3D-shape and with a given reservoir pressure distribution, based on the linear elastic theory of nuclei of strain in the half space. Segall (1992) presented methods for computing poroelastic stress changes due to fluid extraction for general axisymmetric reservoir geometries, based on the solutions of Geertsma (1973).

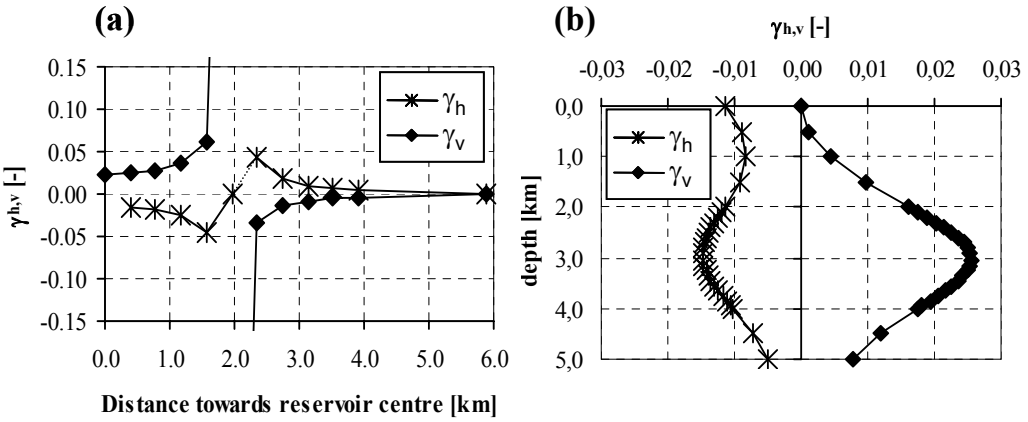

Figure 10.1. Analytically calculated radial (horizontal) and vertical stress changes per unit depletion around a disk-shaped reservoir, outside of the reservoir, according to Geertsma (1973); (a) Along a horizontal line at the top of the reservoir, just outside of the reservoir. The dotted part of the γ_h-graph is not a direct result of Geertsma's formulas but an own interpolation. (b) Along the vertical central axis of the disk-shaped reservoir, outside of the reservoir. The graphs are discontinuous at reservoir level (appr. 3 km depth). Reservoir properties are as follows: radius 1960 m, thickness 150 m, depth of reservoir centre 2975 m, Young's modulus 13.0 GPa, Poisson's ratio 0.2.

10.2 Stress development in ellipsoidal and disk-shaped reservoirs from FE-calculations and comparison with analytical solutions

10.2.1 Calculation series

The analytical solutions for ellipsoidal reservoirs result in reservoir stress changes (due to pore pressure and temperature changes) which are constant throughout the entire reservoir. The analytical solutions as described in Chapter 10.1.1 are compared to numerical calculations in order to check the validity of this result and to see how a pore pressure drop in the reservoir and different reservoir and surrounding rock properties affect stress changes both within and outside of the reservoir.

A series with axisymmetric FE-models is performed, with model geometry according to Figure 8.8 in Chapter 8.2. Element type CT12A (axisymmetric, triangular, 6 nodes) is used for the calculations. The aspect ratio e of the ellipsoidal reservoir and the Poisson's ratio of the reservoir rock ν^{res} are varied. The aspect ratio of the ellipsoidal reservoir is varied by adjusting its width according to Table 10.2. The thickness of the ellipsoidal reservoir is 150 m at its centre in all calculations. Aspect ratios of 0.05, 0.2 and 0.7 are taken. Table 10.1 gives an overview of the used rock properties in the calculations. Note the dependency of E^{sur} on ν^{res} according to eq. (10.4), since the calculations are performed for the condition that $G^{res}/G^{sur} = 1.0$ and thus comparable to the analytical solutions as shown in Figure 10.2.

In order to compare the stress development in disk-shaped and ellipsoidal reservoirs, a series of calculations is performed for disk-shaped reservoirs as well for e = 0.05 (radius 1500 m; thickness 150 m). Rock properties are varied according to Table 10.1. The axisymmetric finite element model as shown in Figure 8.7, Chapter 8.2, is used.

All conditions chosen for the numerical FE-calculations are in accordance to the analytical solution by Rudnicki (1999), except for the finite size and the free movable earth's surface. The analytical solutions are valid for an elastic full space.

Table 10.1. Rock properties used in the calculations.

Calculation code	*00-156*	*01-142*	*02-130*	*03-120*	*04-111*	*049-105*
E^{res} *[GPa]*	13.0	13.0	13.0	13.0	13.0	13.0
ν^{res} *[-]*	0.0	0.1	0.2	0.3	0.4	0.49
E^{sur} *[GPa]*	15.6	14.2	13.0	12.0	11.1	10.5
ν^{sur} *[-]*	0.2	0.2	0.2	0.2	0.2	0.2

Table 10.2. Size of ellipsoidal reservoirs for different aspect ratios.

Calculation code	*e005*	*e02*	*e07*
a [m]	75	75	75
b [m]	1500	375	107
e=a/b [-]	0.05	0.2	0.7

10.2.2 Calculation results and observations

The results of numerical calculations of ellipsoidal reservoirs with different aspect ratios are compared to analytical solutions. Analytically calculated γ_v- and γ_h-values according to Rudnicki (1999) are plotted in Figure 10.2 as a function of the aspect ratio of the ellipsoidal reservoir and its Poisson's ratio ν^{res}. γ_v- and γ_h-values are estimated from this graph for the three aspect ratios 0.05, 0.2 and 0.7. The estimated γ_v- and γ_h-values are listed in Tables 10.4 and 10.5 and compared to the numerical calculation results. The results of the numerical calculations and analytical solutions are virtually equal. In Table 10.3, the values of γ_h and γ_v calculated in the very centre of the reservoir for the different numerical calculations are listed. They are plotted graphically in Figure 10.3. γ/e-graphs in Rudnicki (1999) show curvatures and values similar to the numerical modelling results.

Table 10.3. γ_h and γ_v in the centre of ellipsoidal reservoirs with three different aspect ratios from FE-calculations. E^{res} = 13.0 GPa, ν^{sur} = 0.2.

	E^{sur} *[GPa]*	*15.6*	*14.2*	*13.0*	*12.0*	*11.1*	*10.5*
	ν^{res} *[-]*	*0.0*	*0.1*	*0.2*	*0.3*	*0.4*	*0.49*
e = 0.05	γ_h *[-]*	0.963	0.856	0.722	0.550	0.320	0.038
	γ_v *[-]*	0.073	0.065	0.055	0.042	0.024	0.003
e = 0.2	γ_h *[-]*	0.875	0.778	0.656	0.500	0.292	0.034
	γ_v *[-]*	0.250	0.222	0.187	0.143	0.083	0.010
e = 0.7	γ_h *[-]*	0.716	0.637	0.537	0.409	0.238	0.228
	γ_v *[-]*	0.568	0.506	0.426	0.324	0.189	0.180

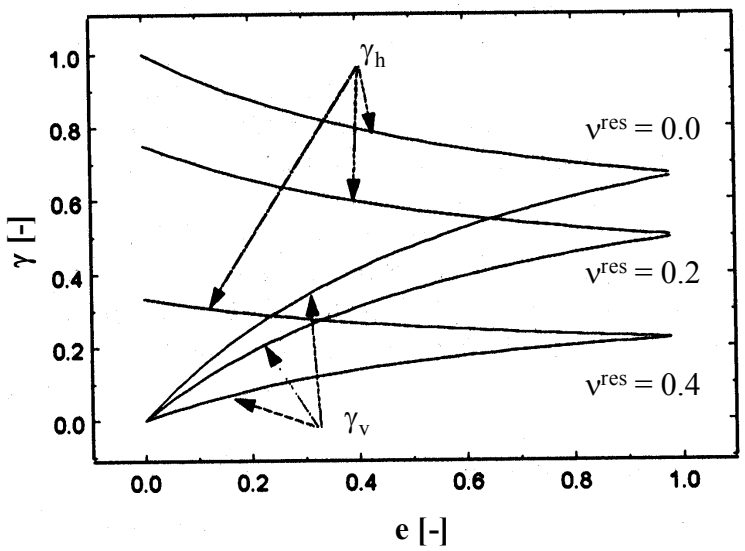

Figure 10.2. Analytically calculated γ_v and γ_h as a function of the aspect ratio e of the ellipsoidal reservoir and its Poisson's ratio ν^{res} for $G^{res}/G^{sur} = 1.0$ (after Rudnicki 1999).

Table 10.4. Comparison between γ_h-values in the reservoir centre for analytical calculations (estimated from Figure 10.2) and numerical calculation results for ellipsoidal reservoirs. $E^{res} = 13.0$ GPa, $\nu^{sur} = 0.2$.

	E^{sur} [GPa]	15.6	14.2	13.0	12.0	11.1	10.5
	ν^{res} [-]	0.0	0.1	0.2	0.3	0.4	0.49
e = 0.05	γ_h analytical [-]	0.967		0.725		0.321	
	γ_h numerical [-]	0.963	0.856	0.722	0.550	0.320	0.038
e = 0.2	γ_h analytical [-]	0.875		0.658		0.288	
	γ_h numerical [-]	0.875	0.778	0.656	0.500	0.292	0.034
e = 0.7	γ_h analytical [-]	0.717		0.525		0.229	
	γ_h numerical [-]	0.716	0.637	0.537	0.409	0.238	0.228

Table 10.5. Comparison between γ_v-values in the reservoir centre for analytical calculations (estimated from Figure 10.2) and numerical calculation results for ellipsoidal reservoirs. $E^{res} = 13.0$ GPa, $\nu^{sur} = 0.2$.

	E^{sur} (GPa)	15.6	14.2	13.0	12.0	11.1	10.5
	ν^{res} [-]	0.0	0.1	0.2	0.3	0.4	0.49
e = 0.05	γ_v analytical [-]	0.079		0.058		0.025	
	γ_v numerical [-]	0.073	0.065	0.055	0.042	0.024	0.003
e = 0.2	γ_v analytical [-]	0.250		0.188		0.083	
	γ_v numerical [-]	0.250	0.222	0.187	0.143	0.083	0.010
e = 0.7	γ_v analytical [-]	0.567		0.425		0.188	
	γ_v numerical [-]	0.568	0.506	0.426	0.324	0.189	0.022

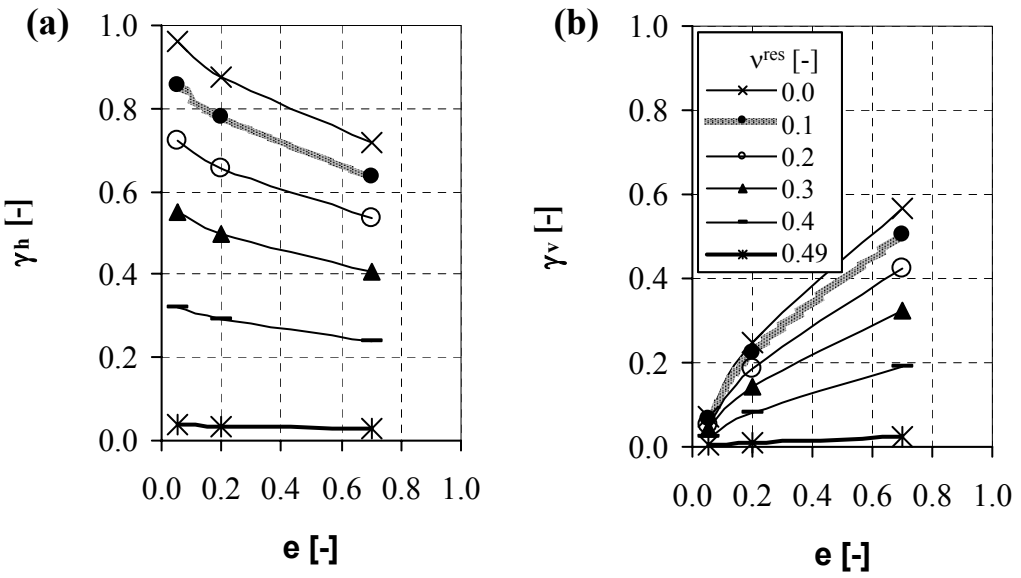

Figure 10.3. Numerically calculated (a) horizontal arching values (γ_h) and (b) vertical arching values (γ_v) as a function of the aspect ratio e of the ellipsoidal reservoir and its Poisson's ratio ν^{res} for G^{res}/G^{sur} = 1.0. Markers indicate the calculation results.

In order to check the validity of the analytical solutions, which incorporate a pore pressure change-induced stress change which is constant throughout an entire ellipsoidal reservoir, numerically calculated arching values and associated effective stress changes are plotted in Figures 10.4a and b, 10.6a and c and 10.7a and c. γ-values are virtually constant throughout the entire ellipsoidal reservoir: the contour plots of Figures 10.4a and b show no significant variation with $0.71 \leq \gamma_h \leq 0.75$ and $0 \leq \gamma_v \leq 0$. The graphs in Figure 10.6a, presenting γ_v- and γ_h-values along a horizontal observation line through the centre of the reservoirs (see Figure 10.5 for configuration), show horizontal lines until the lateral reservoir edge. The same behaviour could be observed in other calculations of the ellipsoidal reservoir with different rock properties and other aspect ratios than the Figures 10.4, 10.6 and 10.7 are valid for. γ_h and γ_v can be assumed constant throughout the reservoir for ellipsoidal reservoirs. This observation is in line with the analytical solutions for ellipsoidal reservoirs.

Comparison of numerical calculation results of the ellipsoidal and disk-shaped reservoirs with e = 0.05 show significant difference in the pattern of calculated stress changes (see Figures 10.4, 10.6 and 10.7 and Tables 10.6 and 10.7). Calculated γ-values and effective stress changes are not constant in disk-shaped reservoirs as is the case for ellipsoidal reservoirs, but show significant variation in a zone at the lateral reservoir edge. Stress development at the lateral side of the reservoir is very influenced by the lateral reservoir boundary. Looking at arching values along a horizontal observation line through the reservoir centre (Figure 10.6b), basically four zones can be distinguished for the disk-shaped reservoir with a radius of 1500 m and a thickness of 150 m (e = 0.05):

Zone A covering most of the (central) reservoir, where γ_h-values are relatively large with negligible variation and where γ_v is as good as zero;

Zone B at the lateral reservoir edge inside of the reservoir, where γ_v-values are relatively large and γ_h-values are relatively small;

Zone C at the lateral reservoir edge outside of the reservoir, where negative γ_v-values with relatively large magnitudes can be observed and γ_h-values are relatively small;

Zone D outside of the reservoir where γ-values approach zero and virtually no stress changes occur.

Graphs in Figure 10.6b show that the size of zone B is approximately 200 m for the current calculations. This is very similar to the zone with a higher risk on shear failure on bedding planes as found in the compaction study of the Shearwater gas field (Kenter *et al.*, 1998). Remarkable is the fact, that zone B is absent in ellipsoidal reservoirs, whereas zones A, C and D occur.

An observation for both ellipsoidal and disk-shaped reservoirs is that γ_h-values within the reservoirs decrease with increasing values of ν^{res} (and in the same time smaller values of E^{sur}), whereas $\Delta\sigma'_h$-values increase with increasing ν^{res} (Figure 10.3a and Tables 10.3, 10.4 and 10.6). γ_v decreases with increasing values of ν^{res} (and in the same time smaller values of E^{sur}), see Figure 10.3b and Tables 10.3, 10.5 and 10.7. These effects are especially pronounced for larger reservoir aspect ratios (Figure 10.3 and Table 10.3) and for γ_v at the lateral edge of the disk-shaped gas reservoirs (Table 10.7). Furthermore, it follows from Figures 10.2 and 10.3 that the horizontal arching decreases with increasing aspect ratio. The vertical arching increases with increasing aspect ratio for both numerical and analytical calculations.

In the surrounding rock just above and below the reservoir at centre location, horizontal effective stresses slightly increase and vertical effective stresses slightly decrease (Figures 10.7c and d). These stress changes are for the modelled conditions not more than a few MPa. γ-values are almost zero.

For the disk-shaped reservoir, two small zones just above and below the lateral reservoir edge can be observed, where γ_v-values are relatively large and γ_h-values become more negative (Figure 10.4).

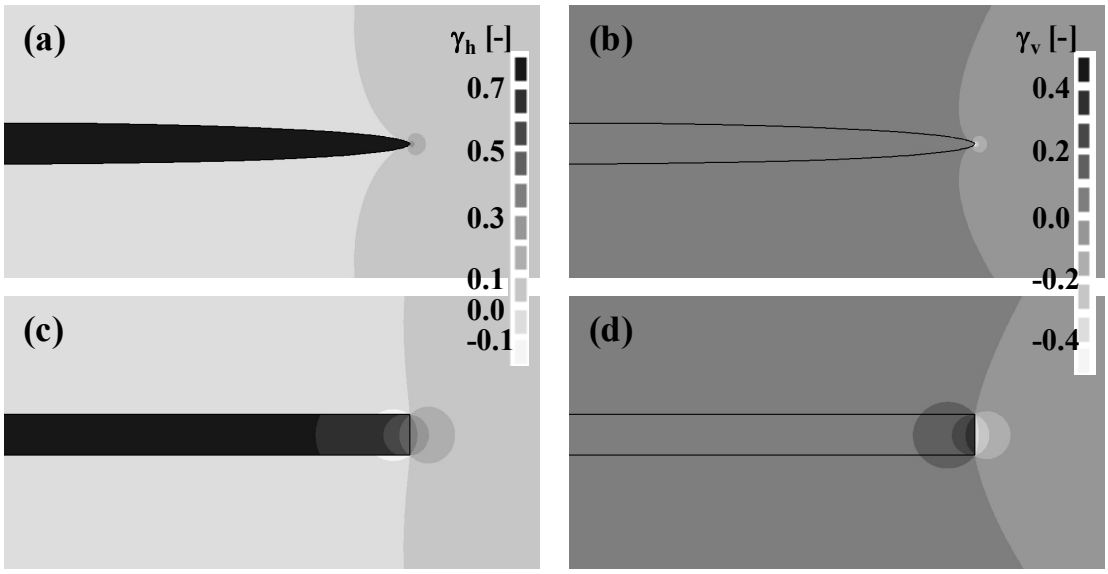

Figure 10.4. Comparison of numerically calculated γ-values in (a) and (b) an ellipsoidal reservoir and (c) and (d) a disk-shaped reservoir. Black lines indicate the circumference of the reservoirs. (a) and (c): γ_h; (b) and (d): γ_v. Reservoir radius: 1500m; reservoir thickness: 150 m (e = 0.05); $\nu^{sur} = \nu^{res} = 0.2$; $E^{sur} = E^{res} = 13.0$ GPa. See Appendix 2 for this figure in colour.

Table 10.6. Calculated γ_h in ellipsoidal and disk-shaped reservoirs. Observation points: reservoir centre (1) and lateral reservoir edge (3), see Figure 10.5. $E^{res} = 13.0$ GPa, $\nu^{sur} = 0.2$.

E^{sur} [GPa]	15.6	14.2	13.0	12.0	11.1	10.5
ν^{res} [-]	0.0	0.1	0.2	0.3	0.4	0.49
Reservoir centre (observation point 1)						
γ_h ellipsoid [-]	0.995	0.884	0.745	0.567	0.330	0.040
γ_h disk [-]	0.975	0.866	0.731	0.556	0.324	0.042
Lateral reservoir edge (observation point 3)						
γ_h ellipsoid [-]	0.946	0.842	0.711	0.540	0.314	0.033
γ_h disk [-]	0.377	0.323	0.257	0.178	0.085	0.004

Table 10.7. Calculated γ_v in ellipsoidal and disk-shaped reservoirs. Observation points: reservoir centre (1) and lateral reservoir edge (2), see Figure 10.5. $E^{res} = 13.0$ GPa, $\nu^{sur} = 0.2$.

E^{sur} [GPa]	15.6	14.2	13.0	12.0	11.1	10.5
ν^{res} [-]	0.0	0.1	0.2	0.3	0.4	0.49
Reservoir centre (observation point 1)						
γ_v ellipsoid [-]	0.046	0.042	0.036	0.026	0.013	-0.003
γ_v disk [-]	0.048	0.043	0.036	0.027	0.016	0.002
Lateral reservoir edge (observation point 3)						
γ_v ellipsoid [-]	0.126	0.114	0.099	0.078	0.047	0.005
γ_v disk [-]	0.569	0.519	0.464	0.384	0.253	0.036

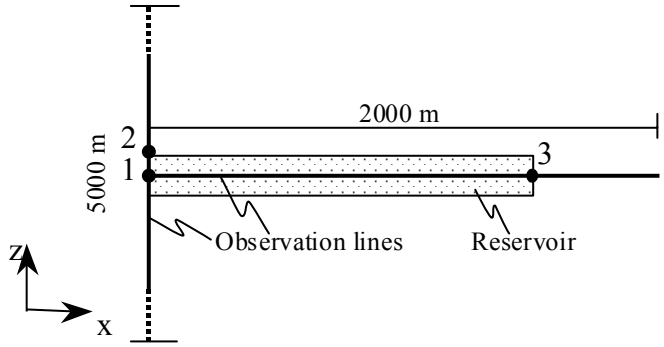

Figure 10.5. Location of observation lines for the graphs in Figures 10.6, 10.7 and 10.11. Both lines run through the reservoir centre. Points 1, 2 and 3 indicate the location of observation for the graphs in Figures 10.8 – 10.10.

10.2.3 Discussion

The observations that γ_h and γ_v decrease for increasing ν^{res} and that for increasing aspect ratio γ_h and γ_v decrease and increase, respectively, could be explained as follows. In case of an infinitely wide reservoir ($e \rightarrow 0$), uniaxial reservoir compaction occurs. In Chapter 3.4 it is already explained, that in this case the overburden rock keeps on pushing its own weight (σ_v) on the reservoir rock, without being limited by a less or not compacting sideburden. This means that the total vertical load does not change during reservoir production ($\Delta\sigma_v = 0$), resulting in a γ_v-value of 0. This result is also obtained by the analytical solutions for all reservoir and surrounding rock properties (Rudnicki 1999, Segall & Fitzgerald 1998). Although not directly calculated, this also seems to be the case for the numerical calculations (Figure 10.3).

Horizontal effective stress changes ($\Delta\sigma'_h$) are in a one-dimensional, uniaxial case ($e = 0$) solely based on the translation of $\Delta\sigma'_v$ via the Poisson's ratio of the reservoir rock:

$$\Delta\sigma'_h = \frac{\nu}{1-\nu}\Delta\sigma'_v . \tag{10.5}$$

A horizontal arching value can then be calculated according to (see Chapter 3.4, eq. (3.18)):

$$\gamma_h = \alpha\left(\frac{1-2\nu^{res}}{1-\nu^{res}}\right) \tag{10.6}$$

The equations to calculate γ_h as presented by Rudnicki (1999 and 2003) reduce to eq. (10.6) for $e \rightarrow 0$. Results of eq. (10.6) under the assumption that $\alpha = 1$ are presented in Table 10.8.

Table 10.8. γ_h for uniaxial reservoir compaction (e = 0.0) according to eq. (10.6) for different ν^{res}, under the assumption that $\alpha = 1.0$.

ν^{res} [-]	0.0	0.1	0.2	0.3	0.4	0.49
γ_h eq. (10.6) [-]	1.000	0.889	0.750	0.571	0.333	0.039

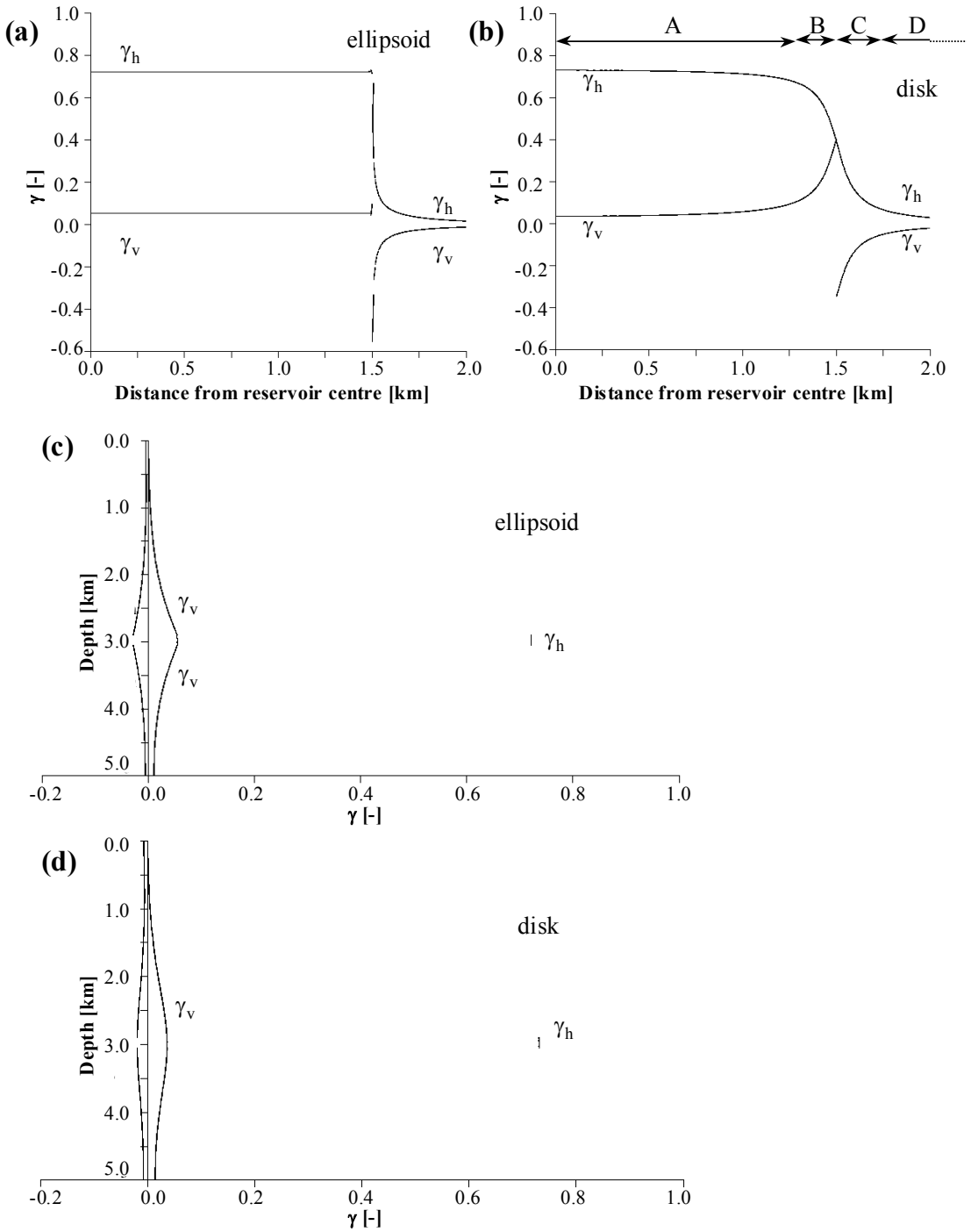

Figure 10.6 *(a) and (b). γ_h and γ_v along a horizontal line through the reservoir centre in (a) an ellipsoidal and (b) a disk-shaped reservoir.*
(c) and (d). γ_h and γ_v along a vertical line through the reservoir centre in (c) an ellipsoidal and (d) a disk-shaped reservoir.
The reservoir radius and thickness are 1500m and 150m, respectively (e = 0.05). For location of the observation lines see Figure 10.5. $\nu^{res} = \nu^{sur} = 0.2$, $E^{res} = E^{sur} = 13.0$ GPa.

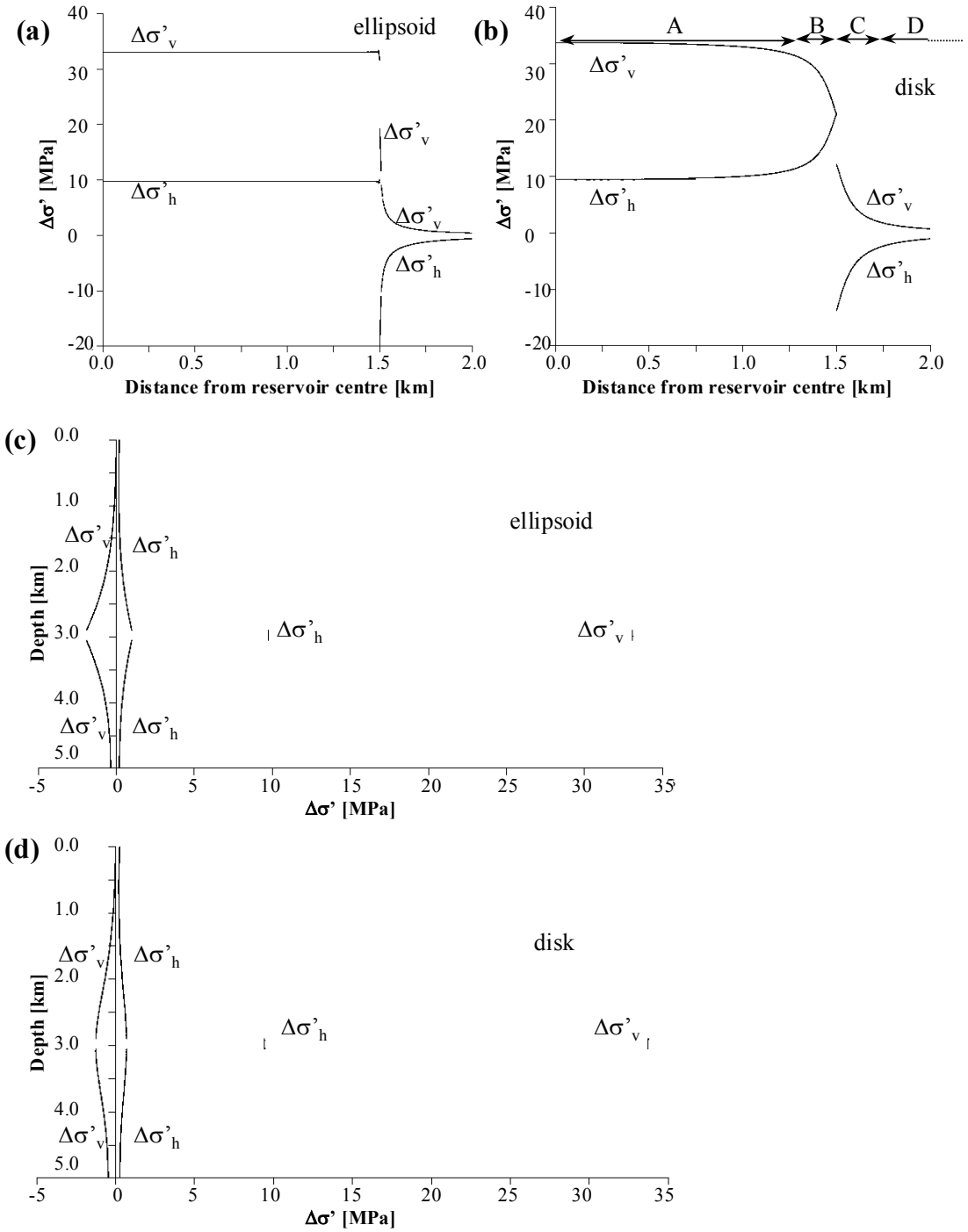

Figure 10.7 (a) and (b). Horizontal and vertical effective stress changes along a horizontal line through the reservoir centre in (a) an ellipsoidal and (b) a disk-shaped reservoir.

(c) and (d). Horizontal and vertical effective stress changes along a vertical line through the reservoir centre in (c) an ellipsoidal and (d) a disk-shaped reservoir.

The reservoir radius and thickness are 1500m and 150m, respectively (e = 0.05). For location of the observation lines see Figure 10.5. $\nu^{res} = \nu^{sur} = 0.2$, $E^{res} = E^{sur} = 13.0$ *GPa.*

Numerically calculated γ_v- and γ_h-values at the centre of both the ellipsoidal and the disk-shaped reservoir match, for the reservoir radius of 1500 m and e = 0.05, the analytical values for uniaxial reservoir compaction conditions very well for all Poisson's ratios of the reservoir rock (Tables 10.6 and 10.7). Stress changes in the reservoir centre are thus, for the specified geometries, as if the reservoir were infinitely wide.

A larger Poisson's ratio of the reservoir rock results in a smaller arching in the reservoir both vertically and horizontally. Smaller γ-values mean a larger built-up of effective stresses. From eq. (10.5) it is clear that a large ν^{res}-value leads to a larger translation of vertical effective stress built-up into horizontal directions. Furthermore, a larger Poisson's ratio means a material with larger bulk stiffness and smaller shear stiffness. Materials with a Poisson's ratio of 0.5 are incompressible. The larger the value of ν^{res}, i.e. the larger the bulk stiffness of the reservoir rock, the less stress is arched away to the surrounding rocks. Effective stress changes are larger for larger values of ν^{res}, whereas γ_h-values are smaller.

As the aspect ratio of the reservoir increases, the reservoir width gets smaller. γ_v increases, due to arching of vertical stresses away from the relatively weak reservoir rock into the stiffer sideburden rock. γ_h decreases, due to an increasing freedom of the reservoir rock to contract laterally. The steepest gradients of the γ/e-graphs for both horizontal and vertical directions occur for small aspect ratio values (see Figures 10.2 and 10.3). γ/e-graphs show smaller gradients for larger aspect ratios. This is probably due to a drastical change of the reservoir width for small changes in small aspect ratio values: as the aspect ratio increases from 0.0 to 0.2, the reservoir width decreases from infinite to 375 m (see Table 10.2). The reservoir shape for e = 0.2 has already a strong spherical character. As the aspect ratio increases from 0.2 to 0.7, the reservoir width decreases from 375 m to 107 m. This change is not so large and γ/e-graphs show smaller gradients in this range. Extrapolating the numerical modelling graphs of Figure 10.3 points to a good match to the analytical solutions for (almost) spherical reservoirs with $e \rightarrow 1$.

Throughout the ellipsoidal reservoir, stress changes and thus arching values are virtually constant. For the disk-shaped reservoirs, this is only the case in zone A (see Figures 10.6 and 10.7). Comparison of Figure 10.6b with Figure 10.7b indicates that the relatively large γ_v-values in zone B of the disk-shaped reservoir are due to a lesser increase in vertical effective stress in this part of the reservoir than in the more central reservoir part. At the edges of the disk-shaped reservoir, the vertical effective stresses tend to be loaded to the non-compacting sideburden rock instead of to the compacting reservoir rock itself, resulting in larger values of γ_v inside of the reservoir at the lateral reservoir edge, but smaller (negative) values of γ_v outside of the reservoir. Stresses are said to be arched away from the reservoir. Negative γ_v-values result from the fact that the total vertical stresses in the sideburden rock increase. The definition of γ as total stress change per unit depletion ($\Delta p < 0$) results then in negative values for γ_v.

Based on eq. (10.5) one could conclude that, due to the lesser increase of the vertical effective stresses in the reservoir at the lateral edge, horizontal effective stresses would increase less at this location as in the reservoir centre, resulting in larger γ_h-values and smaller $\Delta\sigma'_h$-values. However, Figures 10.6 and 10.7 clearly show, that γ_h-values are smaller and $\Delta\sigma'_h$-values are larger in zone B than in the reservoir centre (zone A). The sideburden rock follows the lateral compaction of the reservoir and keeps on pushing on the reservoir rock. Due to this effect, $\Delta\sigma'_h$ is larger in the reservoir at its lateral edge. The pushing effect is enhanced by a relatively large $\Delta\sigma'_v$ in the sideburden rock, which is translated via the Poisson's ratio to a certain amount of $\Delta\sigma'_h$. The more the inside of the reservoir is approached, the less $\Delta\sigma'_h$ gets because of shear stress absorption at the lateral reservoir edge, due to the elastic coupling of the reservoir rock to the surrounding rock. The lateral edge of ellipsoidal reservoirs is not straight but almost follows a spherical shape. Even for the small aspect ratio of 0.05, the largest amount of curvature in the cross-sectional ellipse occurs at its lateral edge. Because of this geometry, arching effects of the vertical stress into the sideburden rock are concentrated and restricted to a very small region only at the very lateral reservoir edge. Horizontal stresses in the sideburden rock, before reservoir depletion counteracted by the pore pressure and horizontal effective stresses in the reservoir at its lateral edge, are during depletion relatively easily arched away from the reservoir into the over- and underburden rock. This results in arching values at the lateral side of the ellipsoidal reservoir which are virtually equal to those in the reservoir centre (Figures 10.4a and b and 10.6a), except for somewhat differing arching values at the very edge of the reservoir in observation point 3 (see Figure 10.6a and Tables 10.6 and 10.7).

Horizontal effective stress changes ($\Delta\sigma'_h$) at the lateral reservoir edge show a very steep gradient for both ellipsoidal and disk-shaped reservoirs (Figures 10.7a and b). Horizontal effective stresses increase during gas depletion within the reservoir due to the pore pressure decrease, but decrease outside of the reservoir at the lateral reservoir edge (zone C) due to the horizontal reservoir contraction.

In the surrounding rock just above and below the reservoir at centre location, horizontal effective stresses slightly increase and vertical effective stresses slightly decrease (Figures 10.7c and d). These stress changes are for the modelled conditions not more than a few MPa. γ-values are almost zero. Induced horizontal effective stress increase in the range of a few MPa are in line with the analytical solutions for induced effective stress changes just above and below ellipsoidal reservoirs according to Segall & Fitzgerald (1998) and the observations in literature sources (Segall 1992, Baranova *et al.* 1999, Wu *et al.* 1998, Glowacka & Nava 1996, Grasso 1992 and Maillot *et al.* 1999).

For the disk-shaped reservoir, two small zones just above and below the lateral reservoir edge can be observed, where γ_v-values are relatively large and γ_h-values become more negative (Figure 10.4). This is in line with the analytical solution of Geertsma (1973), see Figure 10.1a. In these two zones, γ_v-values are relatively large due to unloading of vertical effective stresses, which are arched away to the

sideburden of the reservoir. γ_h-values become more negative and indicate an increase of horizontal effective stresses in the two zones. Due to the pore pressure reduction in the reservoir and the related horizontal reservoir contraction, which is limited by the elastic coupling of the reservoir to over- and underburden, a part of the horizontal total stresses, previously carried by the reservoir rock and pore contents, is arched away in the stiffer over- and underburden.

10.3 Stress development in disk-shaped reservoirs as a function of rock property contrast between reservoir and surrounding rock and reservoir tilting

In order to obtain insight in the influence of rock property contrast between reservoir and surrounding rock and reservoir tilting on the stress development in a disk-shaped reservoir, several calculations using 2D-models are performed. Regarding the rock properties it is distinguished between Young's modulus and Poisson's ratio. The calculations in this chapter are performed in the framework of setting up a stress atlas at Shell Exploration & Production Rijswijk (Netherlands), describing the characteristics of stress development in depleting reservoirs with different geometries and (surrounding) rock properties. The calculated results in form of graphs along horizontal and vertical observation lines as presented for instance in Figure 10.6 are approximated analytically and summarised in an Excel chart named 'StressKader' by Mahi (2003). With this spread sheet, γ-graphs along several observation lines through the disk-shaped reservoir can be easily plotted by simply inserting some parameter values in a master sheet within the ranges of the calculations. The chart is available at Shell International Exploration & Production BV, Rijswijk, Netherlands.

10.3.1 Influence of rock property contrast between reservoir and surrounding rock

For the calculations performed for this Chapter 10.3.1, 2D axisymmetric models are used for the calculations (element type CT12A) with a geometry similar to the model as shown in Figure 8.7, Chapter 8.2, but with different reservoir dimensions: the top reservoir depth is 2925 m, the reservoir thickness is 150 m and the reservoir radius is 500 m. Young's modulus and Poisson's ratio of reservoir and surrounding rock are varied. Materials behave all elastically. No plasticity is incorporated. The initial reservoir pressure is 35.0 MPa, which is reduced to 0 MPa during depletion of the reservoir. No pore pressure is assumed in the surrounding rock formations. The density of all materials is 2400 kg/m^3. The initial stress field in the model is solely gravitational.

10.3.1.1 Young's modulus

In order to study the effects of a contrast in Young's modulus between reservoir and surrounding rock on the stress development within the reservoir, a calculation series is performed with varying E^{res} and E^{sur}, whereas $\nu^{res} = \nu^{sur} = 0.2$. For further description of the models see Chapter 10.3.1.

In Figures 10.8, 10.9 and 10.10, the dependency of γ_h and γ_v on the stiffness contrast between the reservoir and surrounding rock E^{sur}/E^{res} is shown for three different locations: location 1 (reservoir centre), location 2 (top of the reservoir above the centre, just outside of the reservoir) and location 3 (lateral reservoir edge, just inside of the reservoir), see Figure 10.5.

Values for γ_h and γ_v in case of uniaxial reservoir compaction with $\nu^{res} = 0.2$ are theoretically 0.75 and 0.0, respectively (see Chapter 10.2.3). Calculated γ-values in the reservoir centre (location 1, see Figure 10.5) approximate these theoretical values for uniaxial reservoir compaction for almost all calculated scenarios (Figure 10.8). Exceptions can be observed for extremely stiff surrounding rock or soft reservoir rock, leading to relatively large γ_v-values and a slight increase of γ_h-values, and for extremely soft surrounding rock or stiff reservoir rock, leading to relatively small γ_h-values. A slight increase in γ_v and γ_h can be observed for increasing surrounding rock stiffness. Larger γ-values mean a smaller effective stress increase during gas depletion. This means that a tendency exists for the stresses to be arched around the relatively soft depleted reservoir. Note that for the theoretical case that $E^{sur} = 0$, free deformation of the reservoir would apply ($\Delta\sigma'_h = \Delta\sigma'_v = -\alpha\Delta p$). The graph in Figure 10.8b indeed seems to approach $\gamma_h = 0$ for this case, explaining the relatively small γ_h-value as the ratio E^{sur}/E^{res} approaches zero.

Above and below the reservoir centre, in the surrounding rock (location 2), the reservoir contraction generally results in an increase of total horizontal stresses in these locations and thus negative γ_h-values (Figure 10.9). These arching effects are more pronounced for a softer surrounding rock relative to the stiffness of the reservoir rock. For relatively stiff surrounding rocks, γ_h has a positive sign, indicating that the total horizontal stresses decrease during depletion. The transition from an increase to a decrease in $\Delta\sigma'_h$ is for the modelled conditions ($\nu^{res} = \nu^{sur} = 0.2$) approximately for $E^{sur} = 2E^{res}$.

A smaller E^{sur}/E^{res}-ratio results at the lateral reservoir edge, inside of the reservoir rock (location 3), to smaller γ_v- and γ_h-values (Figure 10.10). Note that γ_h- and γ_v-values are (virtually) equal at location 3 (see e.g. Figure 10.6b). In other words, both horizontal and vertical effective stress increase is larger in this location as the surrounding rock is softer relative to the reservoir rock. This behaviour is understandable when recalling the explanation in Chapter 10.2.3 for the zone at the lateral reservoir edge with larger $\Delta\sigma'_h$-values due to the horizontal deformation of the sideburden rock, which pushes at the reservoir rock. This effect is stronger as the deformation of the surrounding rock easier relative to the reservoir rock, or, in other

words, when the surrounding rock is softer relative to the reservoir rock. A softer sideburden rock causes the vertical stresses to be arched to the sideburden rock to a lesser extent. The vertical effective stress increase within the reservoir at the lateral edge becomes larger and thus γ_v smaller. Note that for the theoretical case that $E^{sur}=0$, free deformation of the reservoir would apply. The graph in Figure 10.10 indeed approaches $\gamma_v = \gamma_h = 0$ for this case ($\Delta\sigma'_v = \Delta\sigma'_h = -\alpha\Delta p$).

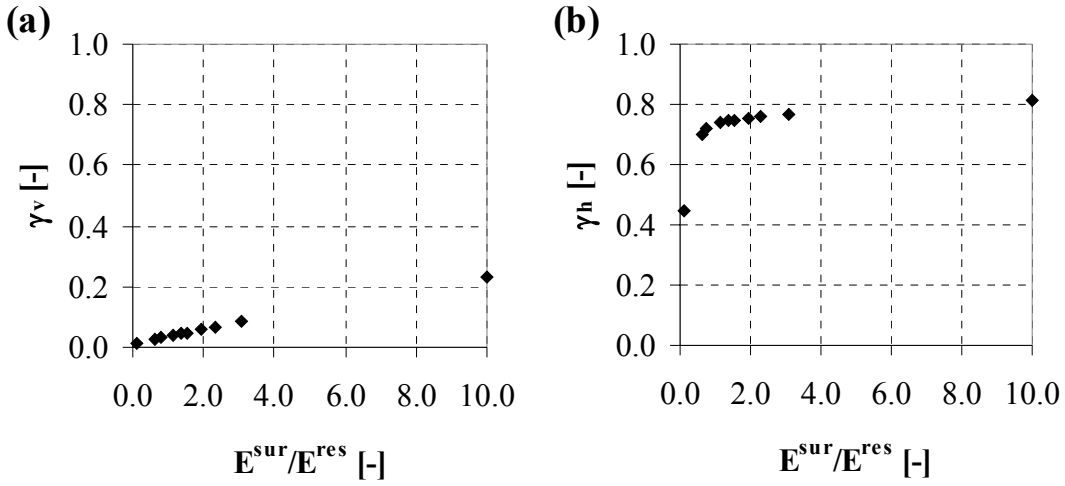

Figure 10.8. γ_h and γ_v at the reservoir centre (observation point 1, see Figure 10.5) as a function of the ratio E^{sur}/E^{res}. For this calculation series E^{res} = 13.0 GPa and E^{sur} varies. $\nu^{res} = \nu^{sur} = 0.2$; top reservoir depth: 2925 m; reservoir radius: 500 m; reservoir thickness: 150 m.

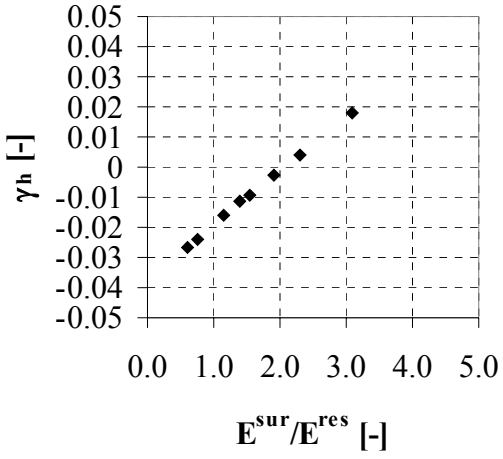

Figure 10.9. γ_h at the top of the reservoir above the centre, just outside of the reservoir (observation point 2, see Figure 10.5) as a function of the ratio E^{sur}/E^{res}. For this calculation series E^{res}=13.0 GPa and E^{sur} varies. $\nu^{res} = \nu^{sur} = 0.2$; top reservoir depth: 2925 m; reservoir radius: 500 m; reservoir thickness: 150 m.

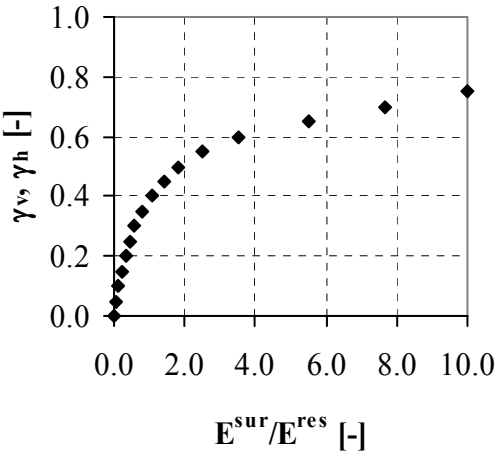

Figure 10.10. $\gamma_v = \gamma_h$ at the lateral reservoir edge, just inside of the reservoir (observation point 3, see Figure 10.5) as a function of the ratio E^{sur}/E^{res}. For this calculation series E^{res}=13.0 GPa and E^{sur} varies. $\nu^{res} = \nu^{sur} = 0.2$; top reservoir depth: 2925 m; reservoir radius: 500 m; reservoir thickness: 150 m.

10.3.1.2 Poisson's ratio

The Poisson's ratio of the reservoir rock influences the stress development within the reservoir since it can be considered as a measure of the translation of the vertical effective stress changes into horizontal directions. Eqs. (10.5) and (10.6) give the amount of such translation for uniaxial reservoir compaction. For the theoretical case that $\nu^{res} = 0.0$, γ_h becomes 1.0 and for the case that $\nu^{res} = 0.5$, γ_h is 0.0. Further explanations and details can be found in Chapter 10.2.

In order to study the effects of the Poisson's ratio of the surrounding rock on the stress development within the reservoir, a calculation series is performed with varying ν^{sur}, whereas $\nu^{res} = 0.2$ and $E^{res} = E^{sur} = 13.0$ GPa. For further description of the models see Chapter 10.3.1.

In Figure 10.11, the influence of the Poisson's ratio of the surrounding rock on the stress development along a horizontal and vertical observation line through the reservoir centre is illustrated. ν^{sur} hardly influences the stress development for the modelled conditions. This result is in agreement with Khan & Teufel (2000). According to these studies, stress development in depleting reservoirs is hardly affected by ν^{sur} for ν^{sur}-values ≤ 0.3.

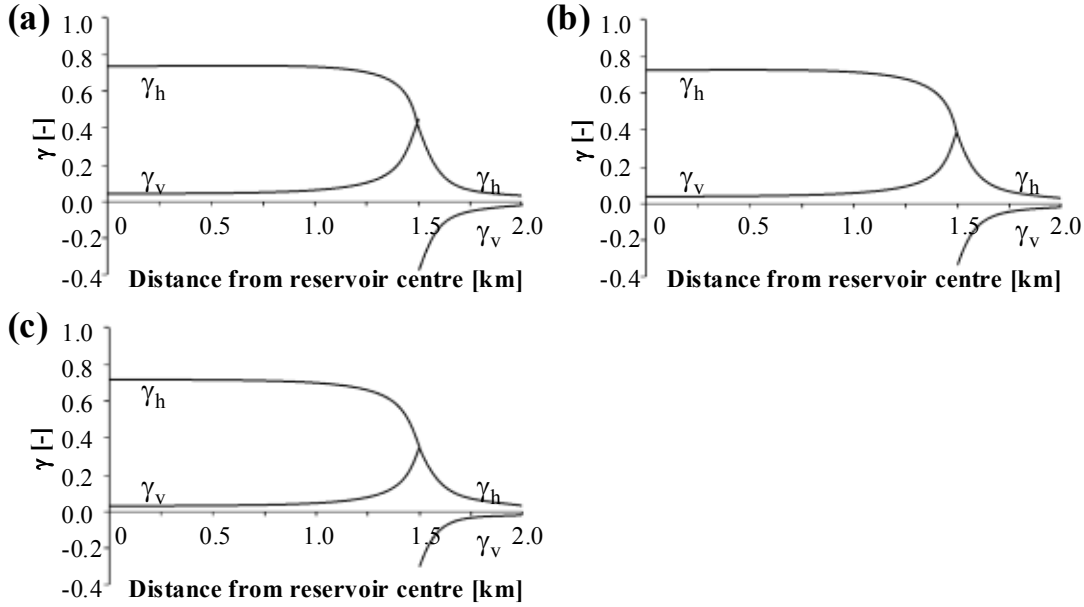

Figure 10.11. γ_h and γ_v along a horizontal line through the reservoir centre in a disk-shaped reservoir for different values of ν^{sur}. (a) ν^{sur} = 0.01, (b) ν^{sur} = 0.25 and (c) ν^{sur} = 0.49. The reservoir radius and thickness are 500 m and 150 m, respectively. For location of the observation lines see Figure 10.6. ν^{res} = 0.2, E^{res} = E^{sur} = 13.0 GPa.

10.3.2 Influence of reservoir tilting

The calculations performed so far for Chapter 10 all incorporate a horizontal reservoir. A series of calculations is therefore performed in order to study the influence of reservoir tilting on the stress development. The tilting makes the use of axisymmetric models impossible. Therefore plane-strain models are built, 20,000m wide and 5000m high with element types CT12E: plane strain, 6-noded triangle (Figure 10.12). Four models are built, each with a different inclination of the reservoir: 0, 7.6, 15 and 30º. The reservoir is 150 m thick and 3000 m wide (representing a radius of 1500 m). It is horizontally centred, with a depth location of the centre of 2975 m in all models. For the reservoir with 0º inclination this means that its top is 2900 m deep. Lateral model boundaries and model bottom are constrained in horizontal and vertical direction, respectively. Rock properties are as follows: $\nu^{sur} = \nu^{res} = 0.2$, $E^{sur} = E^{res} = 13.0$ GPa and density = 2400 kg/m^3. Materials behave all elastically. No plasticity is incorporated. The initial reservoir pore pressure is 35.0 MPa, which is reduced to 0 MPa during depletion of the reservoir. No pore pressure is assumed in the surrounding rock formations. The initial stress field in the model is solely gravitational.

Figure 10.13 shows contour plots of the calculated γ_h- and γ_v-values for a reservoir inclination of 30^o. An overview of observed values is given in Table 10.9. For a reservoir inclination angle of 0^o (horizontal reservoir), results are basically the same as discussed in Chapter 10.2 for a horizontal, disk-shaped reservoir: larger values of γ_v

occur at the lateral side of the reservoir, whereas γ_h-values are smaller at this location. As the reservoir tilts, dipping towards the left, the zone with large γ_h-values and small γ_v-values, respectively, concentrates at the top right and bottom left edges of the reservoir (see Figure 10.12). A zone with small γ_h-values and large γ_v-values, respectively, develops at the bottom right and top left edges of the reservoir.

It is clear that a zone with small γ_h-values develops in the top right corner of the reservoir during hydrocarbon production, since the reservoir is relatively thin in horizontal direction around this location and overburden and sideburden can push from both sides on the reservoir rock. γ_h approaches with a minimum value of only 0.074 in this location almost zero, meaning that the horizontal effective stress increase here is almost equal to the pore pressure decrease. In the bottom right corner of the reservoir develops a zone with a horizontal effective stress shade: the position of the reservoir is very favourable for horizontal effective stresses to arch around the relatively weak reservoir, which is relatively thick around this location. γ_h-values become large in this point, in our calculations even larger than one: 1.02. This means that horizontal effective stresses in this point even decrease instead of increase.

Table 10.9. Calculated γ_v and γ_h in disk-shaped reservoirs with different tilting.

Reservoir tilt angle [^{o}]	*γ_h [-] min**	*max**	*centre*	*γ_v [-] min**	*max**	*centre*
0	0.234	0.724	0.724	0.021	0.442	0.021
7.6	0.188	0.727	0.712	0.033	0.588	0.033
15	0.150	0.850	0.677	0.035	0.726	0.068
30	0.074	1.020	0.548	-0.053	0.954	0.196

** For the location of minimum and maximum values in the cases that the reservoir tilt angle $\geq$ 7.6^o, see Figure 10.13.*

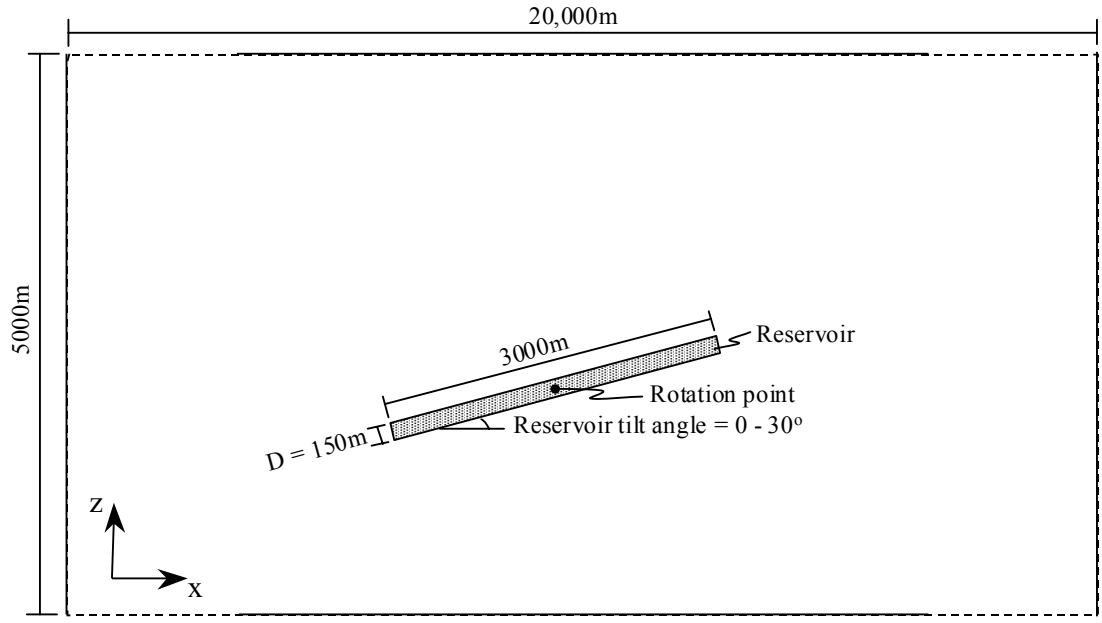

Figure 10.12. Geometry of the 2D plane strain models used for the calculations in Chapter 10.3.2. Lateral boundaries and bottom of the model are constrained in horizontal and vertical direction, respectively.

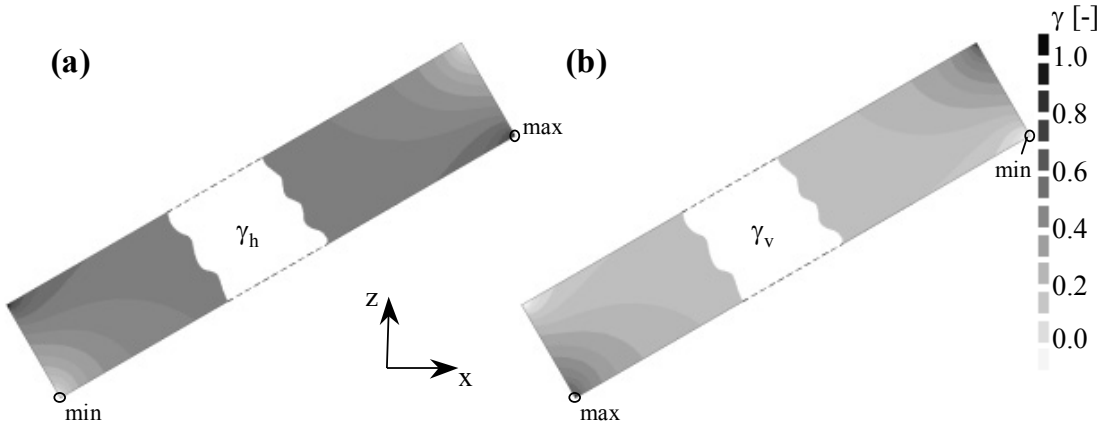

Figure 10.13. Contour plots of calculated (a) γ_h-values and (b) γ_v-values at the reservoir edges for a reservoir tilt angle of 30°. The location of maximum and minimum values for the calculations with a tilt angle $\geq$ 7.6° are indicated. See Appendix 2 for this figure in colour.

Contour plots of the calculated γ_v-values show a pattern similar to those of the γ_h-values, with the difference that a zone with large γ_v-values develops in the top right corner and a zone with small γ_v-values develops in the bottom right corner of the reservoir. Arching of the vertical stresses away from the relatively weak and vertically relatively thick zone of the reservoir rock in the top right corner is favoured by the inclination of the reservoir. Contrarily, the bottom right reservoir corner experiences even negative arching values for a reservoir inclination of 30°, meaning that vertical effective stresses in this point increase even more than the pore pressure decreases.

There exists a symmetry of stress development in the model. A zone with large γ_v-and small γ_h-values occurs in the top right corner and in the bottom left corner of the reservoir. A zone with small γ_v-and large γ_h-values occurs in the bottom right corner and in the top left corner of the reservoir.
γ-values as observed at the centre point of the reservoir show a more general behaviour of arching, valid for most of the reservoir (Figure 10.14). It shows that horizontal arching is decreasing for increasing inclination of the reservoir, whereas vertical arching increases. It is clear that as the reservoir inclines, the sideburden has more area to push sideward on the compacting reservoir rock. This results in a larger increase of horizontal effective stresses and thus less horizontal arching for a larger reservoir inclination. In the theoretical case of an inclination of 90°, γ_h should approach the value of zero.

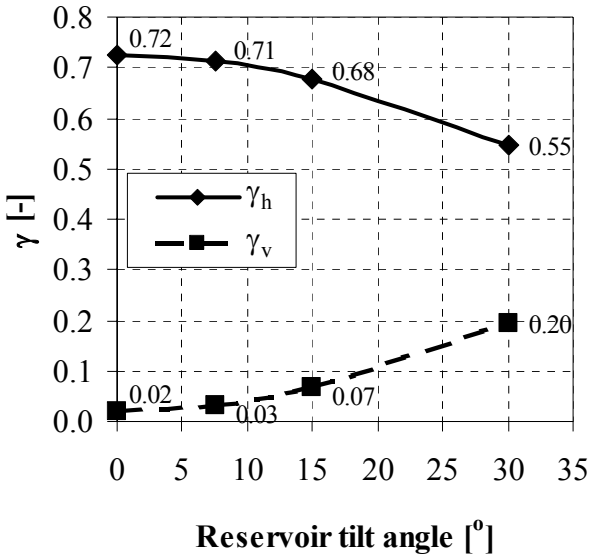

Figure 10.14. Horizontal and vertical arching in the centre of the reservoir as a function of the reservoir tilt angle.

10.4 Implications of modelling results on induced seismicity

In general it is assumed, that seismic events are the result of reactivation of existing discontinuities (like faults) in or near the reservoir (see Chapters 4 and 6). Triggering of faults is basically the result of differential stress development: effective stresses develop in different directions with different amounts. For instance for a reservoir with a horizontal extension larger than the vertical extension, the effective vertical stress increase is larger than the effective horizontal stress increase, since the horizontal reservoir contraction is more constrained than the vertical due to the elastic coupling of the reservoir rock to its surroundings. See Chapter 3.4 for more details and explanations on the concept of critical stress development for the case of a laterally infinitely extended reservoir (uniaxial reservoir compaction).

The following considerations are valid for the calculations as presented in Chapter 10, incorporating reservoirs with a width larger than their thickness in an extensional (gravitational) stress regime.

According to the calculation results, differential stress development, which would promote the reactivation of normal faults, can be observed throughout the entire ellipsoidal reservoirs and throughout most of the disk-shaped reservoirs with exception of the lateral edge of the disk-shaped reservoirs (zone A, see Figures 10.6b and 10.7b). Calculated γ_h-values are larger than calculated γ_v-values, as a result of a smaller horizontal than vertical effective stress increase. Such conditions could lead to a critical stress development as is for instance illustrated in Figure 3.7 (Chapter 3.4) by Mohr circles, promoting the reactivation of normal faults. Reverse faults are stabilised.

At the lateral edge of the disk-shaped reservoirs within the reservoir (zone B), calculated γ_h-values are larger than calculated γ_v-values. The horizontal effective stress increase is larger than the vertical effective stress increase in this region, which would oppose the reactivation of normal faults. Reverse faults in this region should be promoted if a compressional stress regime would apply.

At the lateral edge of both ellipsoidal and disk-shaped reservoirs outside of the reservoir (zone C), vertical effective stresses increase whereas horizontal effective stresses decrease. This would promote the reactivation of normal faults in this region. Reverse fault reactivation in this region should be opposed.

Generally, stress changes just above and below the reservoirs are small, except for two zones just above and below the lateral edge of the disk-shaped reservoir. With $\Delta\sigma'_h > 0$ (increasing horizontal effective stress) and $\Delta\sigma'_v < 0$, normal fault reactivation should be opposed here, but the reactivation of reverse faults should be promoted if a compressional stress regime would apply.

A larger Poisson's ratio of the reservoir rock, a larger reservoir aspect ratio (smaller reservoir width relative to its thickness) and tilting of the reservoir (at least up to a tilt angle of 30^o) counteract differential stress development at the reservoir centre. According to analytical solutions (see Figure 10.2), $\gamma_h = \gamma_v$ when the reservoir width is equal to its thickness (e = 1.0). The difference between horizontal and vertical effective stress increase reduces for increasing values of ν^{res}, e and reservoir tilt angle. Stress paths such as shown in Figure 3.7 therefore become less steep (stabilise), opposing the reactivation of normal faults. Calculations incorporating a tilting reservoir showed large stress concentrations and stress shades around the reservoir corner points (reservoir top and bottom at its lateral edges). γ_h- and γ_v-values show that especially at these locations significant differential stress development occurs, indicating a relatively large potential for fault reactivation at these locations.

The Poisson's ratio of the surrounding rock hardly influences the stress development at the reservoir centre. This is also the case for a contrast in Young's modulus between reservoir and surrounding rock, except for very large or very small values of E^{sur}. The latter two cases stabilise the stress development at the reservoir centre.

11 STRESS DEVELOPMENT AND FAULT SLIP IN GENERIC BASIC DISK-SHAPED RESERVOIR MODELS WITH FAULT

This chapter describes stress development and fault slip on steeply dipping normal faults intersecting a disk-shaped gas reservoir as a function of several parameters: surrounding rock properties, initial reservoir pressure, throw along the fault plane and initial tectonic stress field. In Chapter 11.1, stress development and fault slip on a normal fault intersecting a disk-shaped gas reservoir is illustrated and explained for model 'throw_const_½D' (see Chapter 8). Chapter 11.1 also zooms in on the stress development in the rock volume and identification of areas in and around the disk-shaped reservoir with critical stress development. It illustrates the basic mechanics of fault slip and stress development in a producing gas reservoir and forms the basis for the subsequent Chapters 11.2 – 11.6. These chapters each deal with one of the parameters mentioned above.

11.1 Stress development and fault slip on a normal fault intersecting a disk-shaped gas reservoir (model 'throw_const_½D')

This section illustrates the basic mechanics of fault slip and stress development in a producing disk-shaped gas reservoir intersected by a normal fault on the basis of two calculations of the 3D-model 'throw_const_½D', a commonly observed reservoir geometry (see Figure 8.2, Table 8.1 and Figure 11.1 for model geometry). Making use of the quantification methods developed in Chapter 9, this section forms the basis for the discussions and explanations in the subsequent sections.

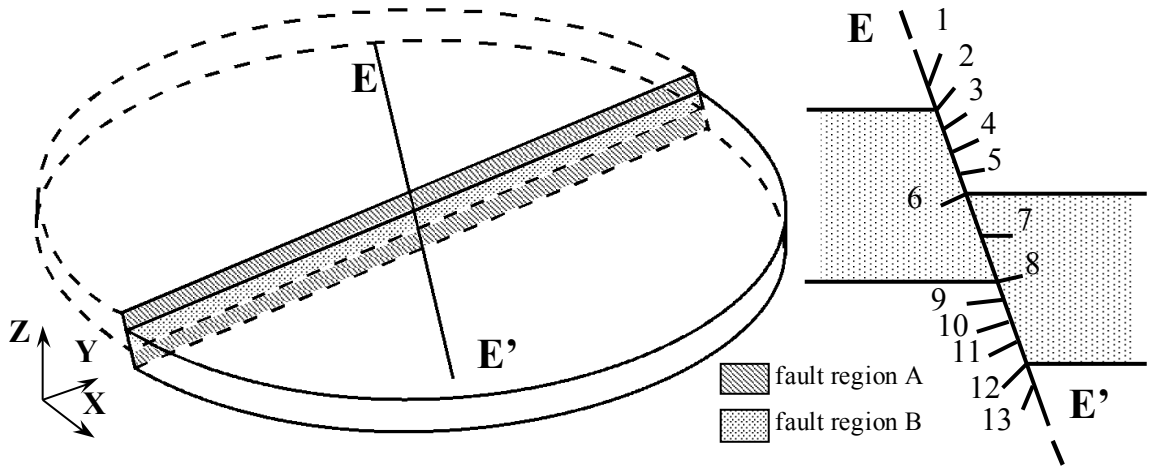

Figure 11.1. Reservoir geometry of model 'throw_const_½D' with indication of observation line EE' and observation points 1 - 13 on line EE'.

Table 11.1. Geomechanical properties and loading conditions for two different scenarios used for most of the calculations in Chapter 11.

General properties					
E^{res}	13.0 GPa	β	70^o	Iteration method	
ν^{res}	0.20	h	0 m	- consol. phase	Constant
$c^{res} = c^{sur}$	5.0 MPa	c^f	0 Pa		Stiffness
ϕ^{res}	30^o	ϕ^f	28^o	- depletion phase	Mod. Newton
$\psi^{res} = \psi^{sur}$	10^o	ψ^f	0^o		Raphson
$\rho^{res}_{bulk} = \rho^{sur}_{bulk}$	2400 kg/m^3	K_{0H}	0.4	No. of iterations	
p^{sur}_{ini}	hydrostatic	K_{0h}	0.4	per increment	
Δp^{sur}	0 Pa	λ	0^o	- consol. phase	5
		$\rho_{pore\ fluid}$	1000 kg/m^3	- depletion phase	20
*surrounding rock properties equal to the reservoir rock properties and initial hydrostatic reservoir pore pressure**					
E^{sur}		13.0 GPa	D_n (fault region A, B, C)		14.4 GPa/m
ν^{sur}		0.20	D_s (fault region A, B, C)		5.4 GPa/m
ϕ^{sur}		30^o	No. of load increments		
p^{res}_{ini}		hydrostatic	- consolidation phase		2
Δp^{res}		-hydrostatic	- depletion phase		10
p^{fault}_{ini} (region A, B, C)		hydrostatic			
Δp^{fault} (region A, B)		-hydrostatic			
Δp^{fault} (region C)		0 Pa			
default rock properties and initial reservoir pore pressure of 35.0 MPa					
E^{sur}		18.5 GPa	D_n (fault)		
ν^{sur}		0.25	- region A		14.4 GPa/m
ϕ^{sur}		25^o	- region B		18.1 GPa/m
p^{res}_{ini}		35.0 MPa	- region C		22.2 GPa/m
Δp^{res}		-35.0 MPa	D_s (fault)		
p^{fault}_{ini} (region A, B)		35.0 MPa	- region A		5.4 GPa/m
p^{fault}_{ini} (region C)		hydrostatic	- region B		6.4 GPa/m
Δp^{fault} (region A, B)		-35.0 MPa	- region C		7.4 GPa/m
Δp^{fault} (region C)		0 Pa	No. of load increments		
			- consolidation phase		2
			- depletion phase		11

** Depth of centre of footwall reservoir compartment is -2975 m, meaning an initial pore pressure of 29.75 MPa. The superscripts ^{res}, ^{sur} and ^{f} refer to reservoir rock, surrounding rock and fault, respectively.*

Geomechanical properties and loading conditions used for the two calculations are as listed in Table 11.1. One calculation is performed for surrounding rock properties equal to the reservoir rock properties and initial hydrostatic reservoir pore pressure. For the model geometry with a reservoir depth between -2900 and -3125 m and a pore fluid density of 1000 kg/m^3, this means an initial reservoir pore pressure around 30 MPa. Note that for these property- and loading conditions solely the effect of a pressure decrease in the reservoir is modelled. The other calculation incorporates default rock properties and initial reservoir pore pressure of 35.0 MPa.

11.1.1 Relative shear displacement (RSD)

Calculated gas depletion-induced RSD-values on the fault plane are shown in Figure 11.2. The graph as presented in Figure 11.2b is along observation line EE' (see Figure 11.1), which runs down dip, parallel to the fault plane through the centre of the reservoir. In the model the maximum RSD-value is 6.7 cm, located in the centre of fault region A, where the two reservoir compartments overlap (at observation point 7). The RSD-values are positive and according to their definition (Chapter 9.1.1) this means normal fault slip, whereby the hanging wall moves downwards relative to the footwall. This is caused by the downward movement of the top of the hanging wall reservoir compartment, whereas the bottom of the footwall reservoir compartment moves upwards (Figure 11.3). This differential compaction behaviour reaches its maximum at observation point 7.

Two local RSD-minima occur at points 2 and 12. The negative values indicate reverse fault slip at these two locations, whereby the hanging wall moves upwards relative to the footwall. Reservoir compaction causes the top of the footwall reservoir compartment to move downwards. The surrounding rock formation on the opposite side of the fault plane moves downwards as well due to the compaction of the hanging wall reservoir compartment, but to a lesser extent since its location is 75 m above the reservoir compartment. The relative movement is therefore of a reverse type. Absolute fault slip values in observation points 2 and 12 are very small when compared to the maximum value in point 7. This behaviour is related to the fact, that the reservoir not only vertically compacts, but also shows a certain amount of horizontal contraction (Figure 11.3). For the geomechanical properties and loading conditions used in this particular calculation, the reverse movements as illustrated in Figure 11.2 fall in the elastic range of fault deformation according to the fault shear- and normal stiffness: stress paths do not reach the failure criterion, as is illustrated in Figure 11.4.

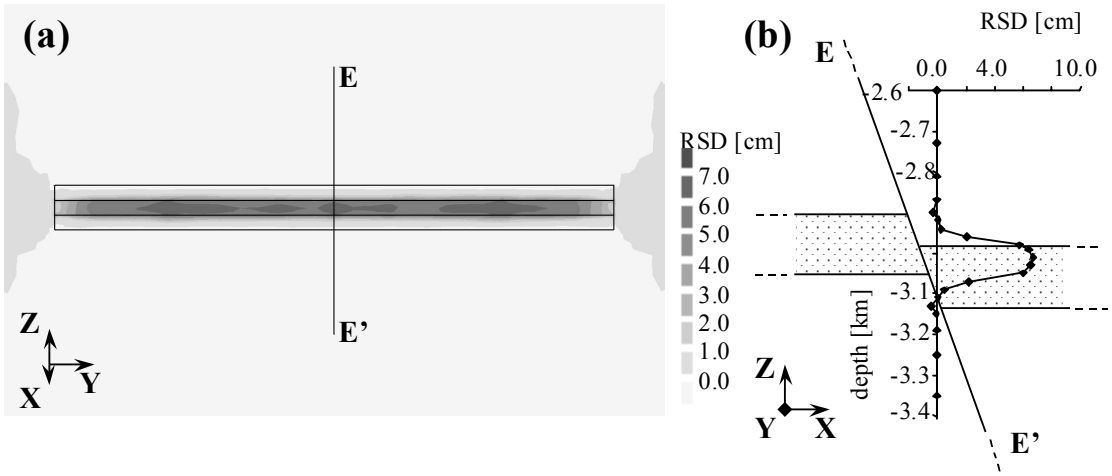

Figure 11.2. Calculated RSD-values as a result of gas depletion for model 'throw_const_½D' with surrounding rock properties being the same as reservoir rock properties and initial hydrostatic reservoir pore pressure. (a) contour plot; view direction is normal to the fault plane. (b) Graphical plot for observation line EE'; dotted areas denote the reservoir compartments. See Appendix 2 for this figure in colour.

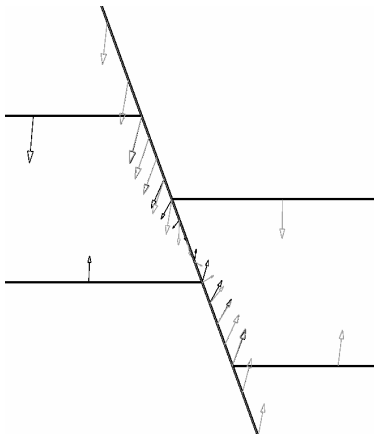

Figure 11.3. Displacement vectors at the fault plane along observation line EE' as a result of gas depletion for model 'throw_const_½D' with properties of surrounding rocks being the same as reservoir rock properties and initial hydrostatic reservoir pore pressure. Black arrows and grey arrows indicate displacements at the footwall and hanging wall, respectively. See Appendix 2 for this figure in colour.

11.1.2 Stress paths on the fault plane

This section characterises the stress development on the fault plane in relation to the observed fault slip as described in the previous section. In this way, a certain initial state of stress and stress development can be judged as promoting or opposing normal or reverse fault slip.

Figures 11.4a and b show calculated stress paths for different observation points along line EE' as they developed during gas depletion. There exists a symmetry between the stress paths of the bottom half (observation points 1 to 7) and the tip half (observation points 7 to 13) of the model. Stress paths in corresponding locations, such as points 1 and 13 or points 2 and 12, are very similar to each other. The slight difference is the result of a different depth location. Because of the symmetry of the bottom half and tip half of the model, only the top half is considered in the further discussions.

Consider first the initial states of stress, marked in Figure 11.4 by the arrow. Their position is at the dotted lines, which indicate the theoretically possible combinations of shear- and effective normal stresses on the fault plane for $K_0 = 0.4$, assuming that the vertical stress is a principal stress (see eqs. (3.2a) and (3.2b), Chapter 3.1). The initial states of stress are represented by this line regardless of the position on the fault for the case that $E^{sur} = E^{res} = 13.0$ GPa, $\nu^{sur} = \nu^{res} = 0.2$ and the initial reservoir pore pressure is hydrostatic.

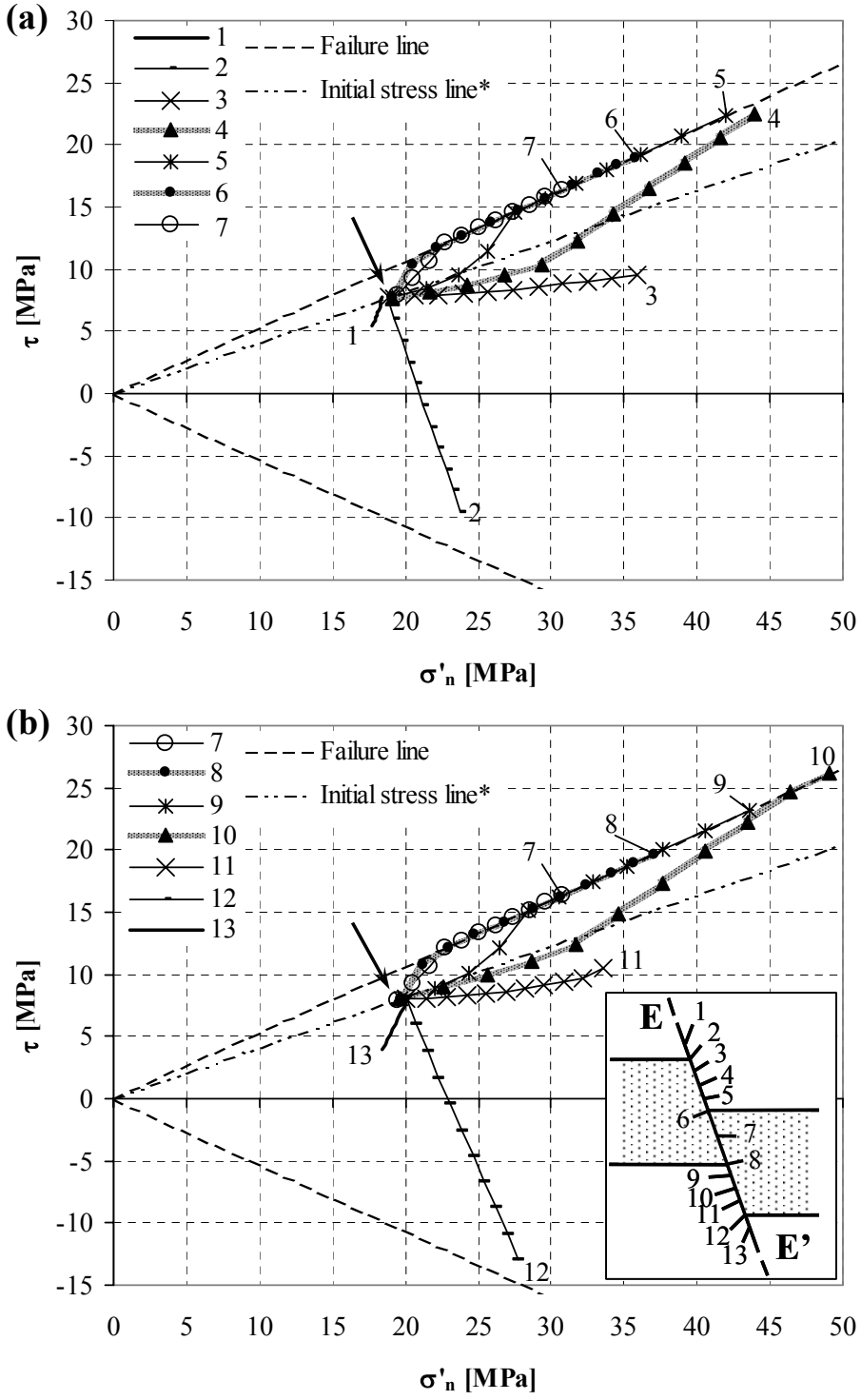

Figure 11.4. Calculated stress paths for different observation points along line EE' for model 'throw_const_½D' with surrounding rock properties being the same as reservoir rock properties and initial hydrostatic reservoir pore pressure (Table 11.1). The initial state of stress is similar for all stress paths and is indicated by an arrow. The end of the stress paths are marked by the respective observation point number.
** The 'initial stress line' is calculated according to eqs. (3.2a) and (3.2b), Chapter 3.1.*

K_0 is defined as the ratio of horizontal and vertical effective stress: $K_0 = \sigma'_h / \sigma'_v = \sigma'_H / \sigma'_v$. $K_0 = 0.4$ means that an extensional stress regime is present: $\sigma'_h = \sigma'_H = 0.4\,\sigma'_v$. Assuming that the vertical stress is a principal stress this is the same as $\sigma'_3 = \sigma'_2 = 0.4\,\sigma'_1$. In Chapter 3 we have adopted the assumption that initial shear stresses are positive for extensional stress regimes. Extensional stress regimes support normal faulting (see Chapter 3.2). A reactivation of the fault in normal sense means that the vertical effective stress increase is larger than the increase of horizontal effective stress: $\Delta\sigma'_v > \Delta\sigma'_h$, meaning that the shear stress will increase. A reactivation of a fault in an extensional stress regime in reverse sense, for which $\Delta\sigma'_v < \Delta\sigma'_h$, is characterised by a decrease of shear stress, followed by an increase of the absolute value.

Stress paths in Figures 11.4a and b show an increase in shear stress during gas depletion for observation points 4 - 10, meaning that the fault tends to be reactivated in a normal sense in these locations. This is in line with the observation of normal fault slip at these locations (Chapter 11.1.1). Stress paths in locations 2 and 12 are characterised by a decreasing shear stress and thus by a tendency of the fault to be reactivated in reverse sense. The observation that calculated RSD-values are negative in these locations and thus reverse fault slip applies support this conclusion. Stress paths of observation points 2 and 12 cross the normal effective stress axis (when σ'_v and σ'_h become equal) and develop straight towards the failure line for negative shear stresses (when σ'_h becomes larger than σ'_v). The stress path in points 3 and 11 are almost horizontal. These stress paths represent the transition point between fault zones with increasing shear stress (normal fault slip) and decreasing shear stress (reverse fault slip).

Reactivation with plastic fault slip occurs only if the stress path reaches the failure criterion of the fault plane. This is the case for observation points 5 - 10. When comparing these stress paths to the calculated RSD-values in Figure 11.2, we see indeed a substantial amount of fault slip in these locations. Plastic fault slip is absent in observation points 2 and 12: stress paths do not reach the failure line. RSD-values are very small and are the result of elastic deformation of the fault according to its elastic parameters D_n and D_s.

The stress development in a certain location on the fault plane can be strongly influenced by the stress development in neighbouring locations. This is illustrated very clearly in observation points 4 and 5 (Figure 11.4a). The stress path in observation point 5, initially slightly diverging from the failure line, starts to converge strongly from the third depletion step onwards and reaches failure during the fourth depletion step. During the second depletion step, the stresses at observation point 6 reach failure and do not build up further. Stress increase is therefore transferred to neighbouring zones, which leads to an increase of the stress path gradient. The same effect propagates along on the fault plane: in point 5, failure is reached during the fourth depletion step, leading to the knick in the stress path in point 4 after the fourth depletion step. The stress development in point 4, initially stabilising (stress path diverging from the failure line), becomes destabilising after the fourth depletion step

because of this propagation effect. The stress path in point 11 (Figure 11.4b) is almost horizontal. Only in the last depletion step, this stress path becomes a bit steeper, due to failure in observation point 10 during the last depletion step.

In the previous paragraph, examples are given of stress paths that become steeper and therefore more destabilising due to the stress development in neighbouring locations. The opposite effect, where stress paths become more stabilising, is also observed and is illustrated in Figure 11.5 for a calculation of model 'throw_const_½D' with default properties of the surrounding rocks and initial reservoir overpressure (see Table 11.1). Stress paths for observation points 3 and 4 develop along the failure line for most of the depletion phase. The stress path in point 2 develops with decreasing shear stresses and reaches failure during the eighth depletion step, initiating plastic reverse fault slip at this location. This causes the state of stress in observation point 3 to develop from a state of failure, causing plastic normal fault slip, to an elastic state of stress: the stress development stabilises and moves away from the failure line after the eighth depletion step.

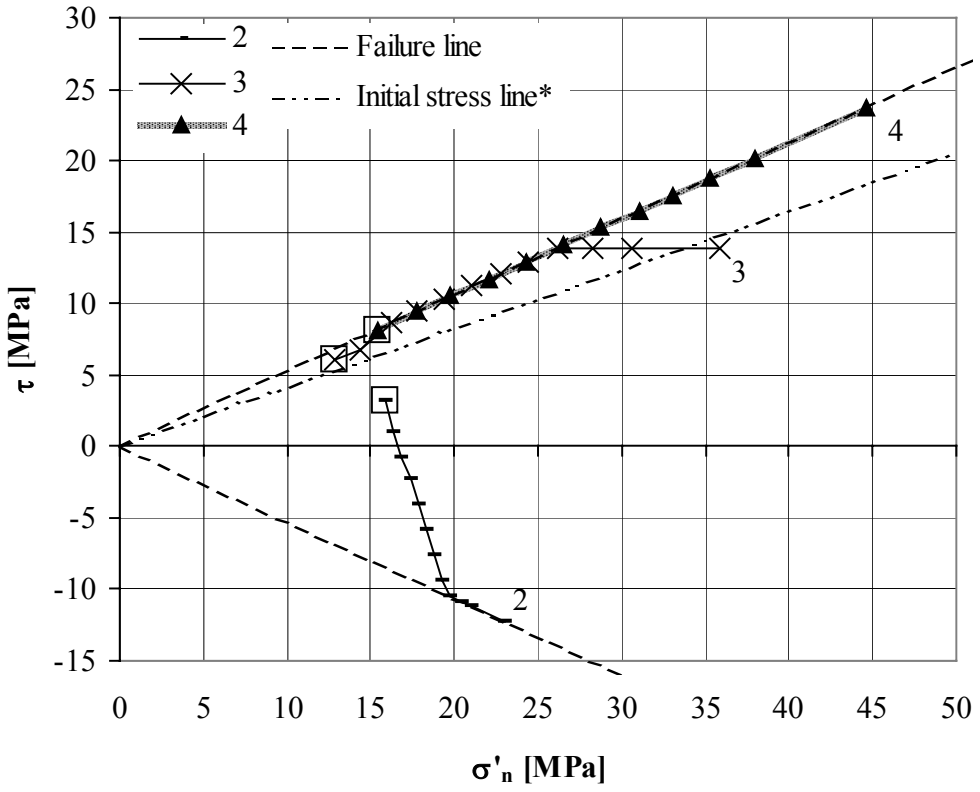

Figure 11.5. Calculated stress paths for different observation points along line EE' for model 'throw_const_½D' with default rock properties and initial reservoir overpressure (see Table 11.1). The initial stress state is marked by an open square. The end of the stress paths are marked by the respective observation point number.
** The 'initial stress line' is calculated according to eqs. (3.2a) and (3.2b), Chapter 3.1.*

11.1.3 Mobilised shear capacity on the fault plane (MSC)

Rather than relatively complicated stress path plots, which give the stress development for specific locations on the fault plane, the criticalness of the state of stress on the entire fault plane can be plotted in one contour plot in terms of MSC-values (Chapter 9).

Contour plots of calculated MSC-values on the fault plane before and after gas depletion are shown in Figure 11.6. MSC values prior to depletion are homogeneous with values around 0.8. This is accordance with the theoretical value of 0.814 for the present conditions ($\beta = 70^o$, $K_0 = 0.4$, $\phi^f = 28^o$ and $c^f = 0$ Pa), which can be calculated using the eqs. (3.2a), (3.2b) and (9.8) – (9.13).

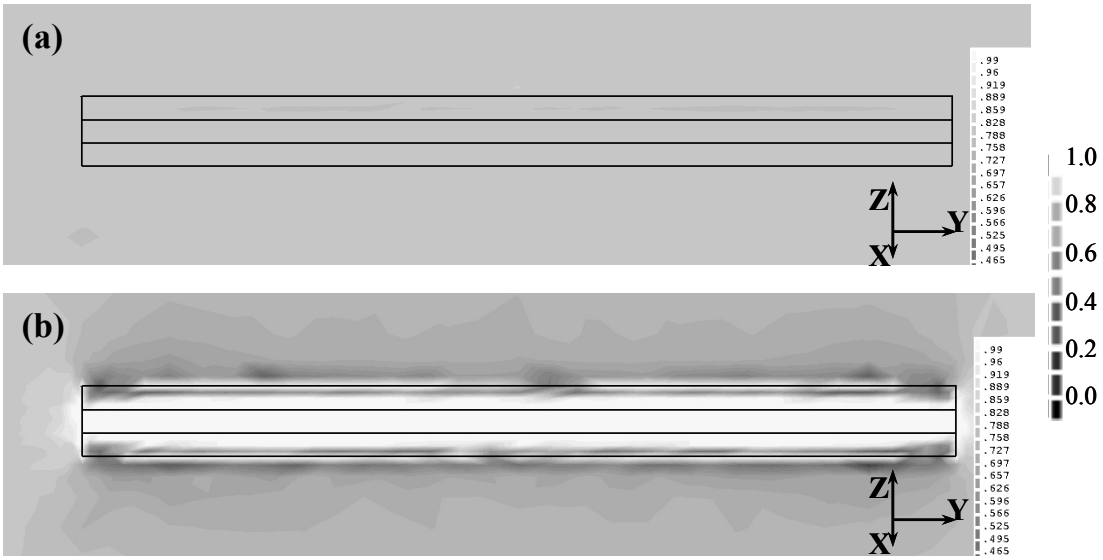

Figure 11.6. Calculated MSC-values on the fault plane, (a) before gas depletion and (b) after gas depletion, for model 'throw_const_½D' with surrounding rock properties being the same as reservoir rock properties and initial hydrostatic reservoir pore pressure. View direction is normal to the fault plane. Black lines indicate the intersection of the reservoir compartments with the fault plane. See Appendix 2 for this figure in colour.

MSC-values on the fault plane vary between 0.23 and 1.00 after gas depletion (Figure 11.6b). Gas depletion causes the MSC-values on most of the fault plane in contact to one or both of the reservoir compartments to be increased to 1.0, meaning that the state of stress in these zones has reached the failure criterion and plastic fault slip occurs. Three zones of critical stress development on the fault plane can be distinguished, where MSC-values become (close to) 1.0 after depletion (light colours in Figure 11.6b): a relatively large region where the footwall and hanging wall reservoir compartments overlap and the fault is bounded on either side by a reservoir compartment, a narrow region at the top of the footwall reservoir compartment and a narrow region at the bottom of the hanging wall reservoir compartment. The latter two regions are bounded by regions with relatively dark colours, indicating small MSC-

values after depletion and a stabilising stress development. This is in accordance to the stress path plots as shown in Figure 11.4. Stress paths in observation points 2, 4 - 10 and 12 represent the three zones with light contours in Figure 11.6b. Note that the stress paths in observation points 2 and 12 develop with decreasing shear stress, crossing the effective normal stress axis. This means that MSC-values decrease in the first instance but increase after the stress path has crossed the effective normal stress axis. The stress paths in observation points 1, 3, 13 and 11 develop away from failure. MSC-values in the corresponding locations are relatively low after gas depletion (Figure 11.6b).

Although the mobilised shear capacity provides a useful tool to express the criticalness of a state of stress on the fault plane relative to a failure criterion, it is not a good tool to analyse in detail the stress development and related fault slip.

11.1.4 Mobilised shear capacity in rock volume (MSC^{3D})

In order to obtain insight in the criticalness of the stress development not only on the fault plane but also in the reservoir rock, the mobilised shear capacity in rock volume (MSC^{3D}) is a useful tool.

Contour plots of calculated MSC^{3D}-values before and after gas depletion are shown in Figure 11.7 for a vertical cross-section through the centre of the reservoir. View direction is in the strike direction of the fault plane. The contour plots express the vicinity of a principal state of stress to the Mohr-Coulomb failure surface. Light colours denote a state of stress close to failure; dark colours denote low deviatoric stress. Before gas depletion, MSC^{3D}-values are in the range of 0.67 – 0.68 at the depth of the reservoir. Contour plots do not show any disturbances near the reservoir or the fault, suggesting that the initial stress field is homogeneous and not affected by the geometrical structures. After gas depletion, zones with high MSC^{3D}-values occur in the surrounding rock directly bounding the lateral reservoir edge. MSC^{3D}-values reach a maximum of 1.0 here, suggesting plastic rock deformation to occur. Similar zones occur in the surrounding rock near the fault plane. MSC^{3D}-values are maximum 0.97 here, indicating solely elastic rock deformation under the modelled circumstances. MSC^{3D}-values after gas depletion are typically around 0.82 within the central parts of the reservoir and decrease to minimum 0.69 at the lateral edge.

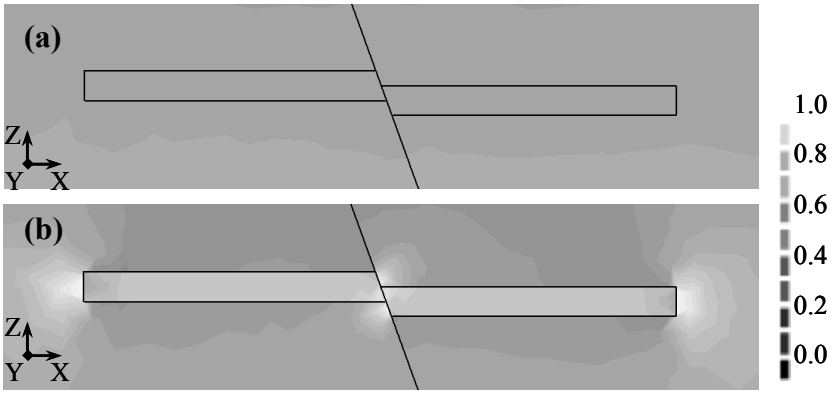

Figure 11.7. Calculated MSC^{3D}-values in the rock volume, (a) before gas depletion and (b) after gas depletion, for model 'throw_const_½D' with surrounding rock properties being the same as reservoir rock properties and initial hydrostatic reservoir pore pressure. View plane is a vertical cross section through the centre of the reservoir, normal to the strike direction of the fault. Black lines indicate the reservoir boundaries and the fault plane. See Appendix 2 for this figure in colour.

An increase in mobilised shear capacity does not necessarily imply a critical stress path. Figure 11.8 shows the regions where the stress development is critical (light colour) and non-critical (dark colour) according to eq. (9.29), Chapter 9.2.1. The lateral parts of the reservoir and most of the surrounding rock above and below the reservoir are stabilising, whereas the main part of the reservoir and the surrounding rock lateral to the reservoir are destabilising. This is in accordance to the observed stress development in disk-shaped reservoirs (Chapter 10). Furthermore, two zones in the surrounding rock near the fault plane above and below the reservoir are destabilising, whereas two zones within the reservoir near the fault plane at the top and bottom of the reservoir stabilise. It is the result of a similar stress development as at the lateral reservoir edges. Note that the calculation is made for an extensional stress regime. It is expected that for a compressive stress regime, these conclusions are exactly inverted.

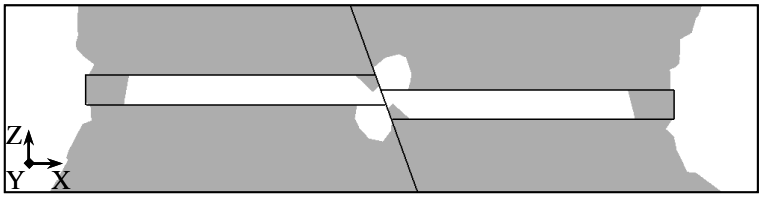

Figure 11.8. Areas with critical stress development (white) and non-critical stress development (grey) according to eq. (9.29) for an extensional stress regime for model 'throw_const_½D' with surrounding rock properties being the same as reservoir rock properties and initial hydrostatic reservoir pore pressure. View plane is a vertical cross section through the centre of the reservoir, normal to the strike direction of the fault. Black lines indicate the reservoir boundaries and the fault plane.

11.2 Influence of surrounding rock properties

This section describes the effects of varying Young's moduli and Poisson's ratios of the surrounding rocks on the initial state of stress, stress development and gas-depletion induced slip on a fault plane. First, the series of calculations is described in Chapter 11.2.1. Subsequently the effects of the young's modulus and the Poisson's ratio are analysed in Chapters 11.2.2 and 11.2.3, respectively. These results are discussed in Chapter 11.2.4.

11.2.1 Calculation series

For the purposes of evaluating the effect of varying Young's modulus and Poisson's ratio, the 2D-model '2D_throw_½D' is used (see Figure 8.6), which represents a cross section through the previously described 3D-model 'throw_const_½D' (Chapter 11.1). 2D models are used because stress trajectories cannot be visualised clearly in DIANA for 3D models. This option becomes important for the analysis of initial states of stress and stress development as a function of surrounding rock properties. The 2D-models make use of higher order elements: 6-noded plane strain triangles for the rock volume (element type CT12E) and 3+3 noded line interface elements for the fault (element type CL12I). Some results of the 2D-models are compared to those of the 3D-models (Chapter 11.2.4) in order to check the compatibility and validity of the higher order 2D and lower order 3D models.

Geomechanical properties and loading conditions are as listed in Table 11.1, with an initial hydrostatic reservoir pore pressure. Young's modulus and Poisson's ratio of the surrounding rock are varied. The following scenarios have been studied: E^{sur} = 8.0, 10.0, 13.0, 15.0, 18.5, 20.0, 25.0, 30.0, and 40.0 GPa and ν^{sur} = 0.0, 0.1, 0.2, 0.25, 0.3, 0.4 and 0.49. In case of variation of E^{sur}, ν^{sur} remains the same at 0.2. When ν^{sur} is varied, E^{sur} remains constant at 13.0GPa. The friction angle of the surrounding rock is taken to be the same as for the reservoir rock: $\phi^{sur} = \phi^{res} = 30^{o}$. Fault normal and shear stiffness are always 14.4 and 5.4 GPa/m, respectively, for the entire fault, regardless of the surrounding rock properties. These property- and loading conditions are chosen so that solely the effects of the two varied parameters are studied, without being disturbed/overlapped by other variations. Note that for a Young's modulus and Poisson's ratio of the surrounding rock equal to the reservoir rock ($E^{sur} = E^{res}$ = 13.0 GPa and $\nu^{sur} = \nu^{res}$ = 0.2), solely the effect of a pressure decrease in the reservoir is modelled. This is considered as a standard case.

11.2.2 Young's modulus

The Young's modulus of the surrounding rock plays an important role for the initial state of stress on the fault. The initial state of stress, in turn, is a very important factor in the development of the amount of fault slip. Critical stress paths are more likely to reach the failure criterion in an earlier stage of depletion when the initial state of stress is closer to failure, eventually leading to more fault slip. Initial states of stress as a function of E^{sur} are plotted in Figure 11.9 for five different locations on the fault.

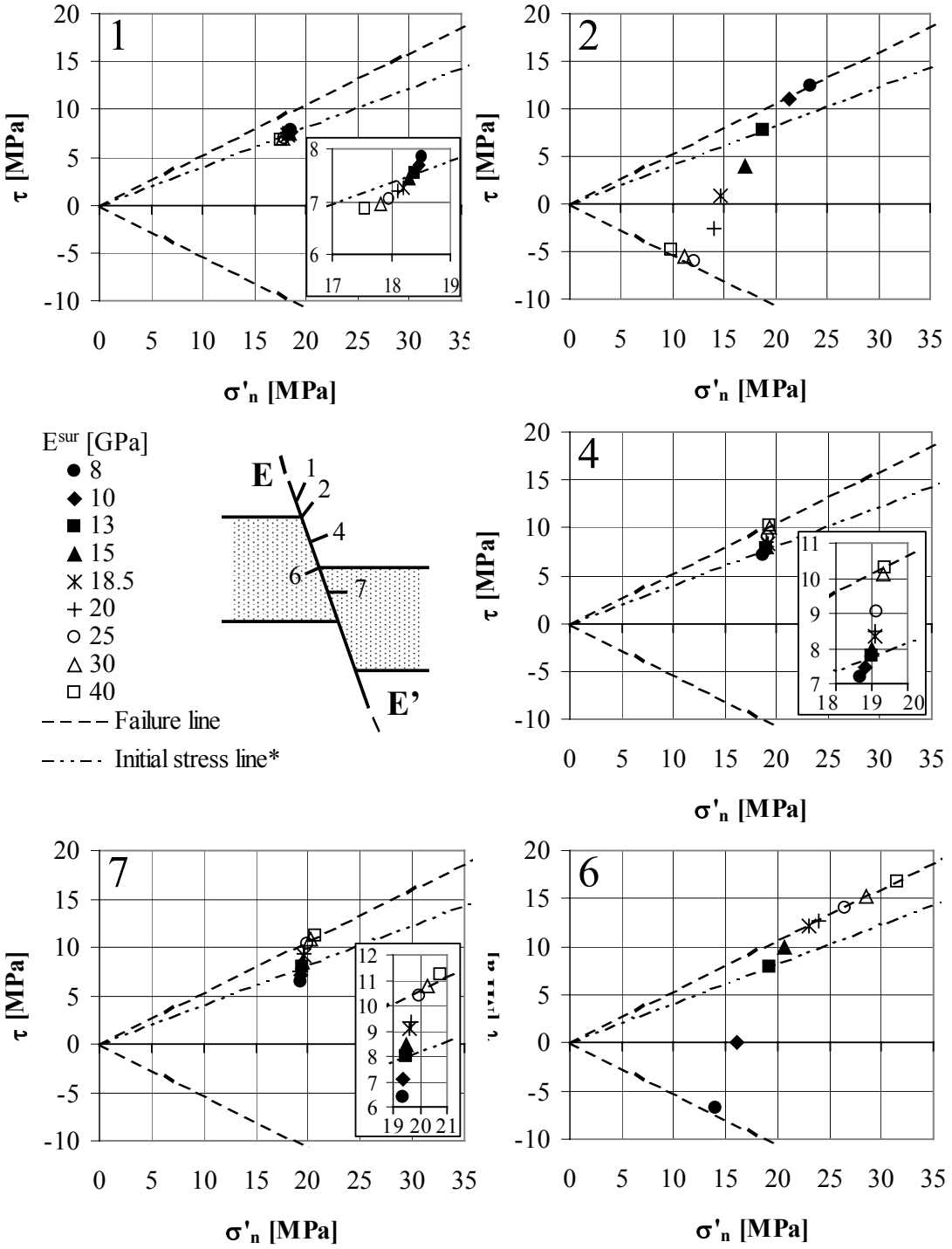

Figure 11.9. Initial states of stress for five different locations on the fault (1, 2, 4, 6 and 7) as a function of the Young's modulus of the surrounding rock (E^{sur}). Calculation results of model '2D_throw_½D' with E^{res} = 13.0 GPa, $\nu^{sur} = \nu^{res} = 0.2$ and initial hydrostatic reservoir pore pressure.
** The 'initial stress line' is calculated according to eqs. (3.2a) and (3.2b), Chapter 3.1.*

Basically two different fault zones can be distinguished: a zone around point 2 (top of the footwall reservoir compartment), where an increasing E^{sur} leads to decreasing shear- and effective normal stresses on the fault, and a zone marked by the points 4, 6 and 7, where an increasing E^{sur} leads to increasing values of τ and σ'_n on the fault.

These observations can be explained as illustrated by the effective principal stress vector plots of Figures 11.10 and 11.11. Effective principal stress vectors for three different cases are shown, for an E^{sur}-value equal to, lower than and larger than the E^{res}-value. For the case that $E^{sur} = E^{res} = 13.0$ GPa (Figure 11.10), a very regular stress pattern applies with the largest principal stress being vertical and the horizontal principal stress determined by the K_0-value of 0.4. For this case, eqs. (3.2a) and (3.2b) of Chapter 3.1 can be used to calculate the shear- and effective normal stresses on the fault plane. Doing so results in the dotted lines in Figure 11.9, which indicate the theoretically possible combinations of shear- and effective normal stresses on the fault plane. As expected, the initial states of stress for the case that $E^{sur} = E^{res} = 13.0$ GPa are positioned on this line regardless of the position on the fault.

The difference between the Young's moduli of reservoir and surrounding rock make that the effective principal stress vectors show variations both in direction and magnitude (Figure 11.11). For a good visualisation the extreme E^{sur}-values of 1.0 and 70.0 GPa are taken. Similar patterns occur for the other values of E^{sur}, but to a lesser extent. The variations of the effective principal stress vectors in direction and magnitude cause the initial states of stress as plotted in Figure 11.9 to differ from the τ/σ'_n-combinations as calculated according to eqs. (3.2a) and (3.2b).

Consider first the fault zone where the two reservoir compartments overlap, around the observation points 4 and 7, for the case that $E^{sur} > E^{res}$. The originally vertical effective principal stress vectors are slightly turned from their originally vertical direction, a bit more perpendicular to the fault (compare Figures 11.10 and 11.11b). The angle between the fault and the subhorizontal effective principal stress is thus somewhat smaller. Recall now the eqs. (3.2a) and (3.2b), used for the calculation of shear and normal stress as a function of magnitude and orientation of the smallest and largest principal stresses. β in these equations represents the fault dip angle but is in fact the angle between the fault and the smallest principal stress direction. This angle, originally 70^o for the standard case (Figure 11.10), decreases now, becoming closer to the most critical angle $\beta_{crit} = 45^o + \frac{1}{2}\phi^f = 59^o$ for the assumed fault friction angle of 28^o. According to eqs. (3.2a) and (3.2b), this leads to an increase in both τ and σ'_n.

Furthermore, the calculations indicated that, in the fault zone around the observation points 4 and 7, the magnitude of the subvertical effective principal stress became somewhat larger whereas the magnitude of the subhorizontal effective principal stress remained more or less equal. Both the mean stress ($\sigma'_1 + \sigma'_3$) and the differential stress ($\sigma'_1 - \sigma'_3$) in eqs. (3.2a) and (3.2b) increase and therefore the values of τ and σ'_n, whereby τ is more affected than σ'_n.

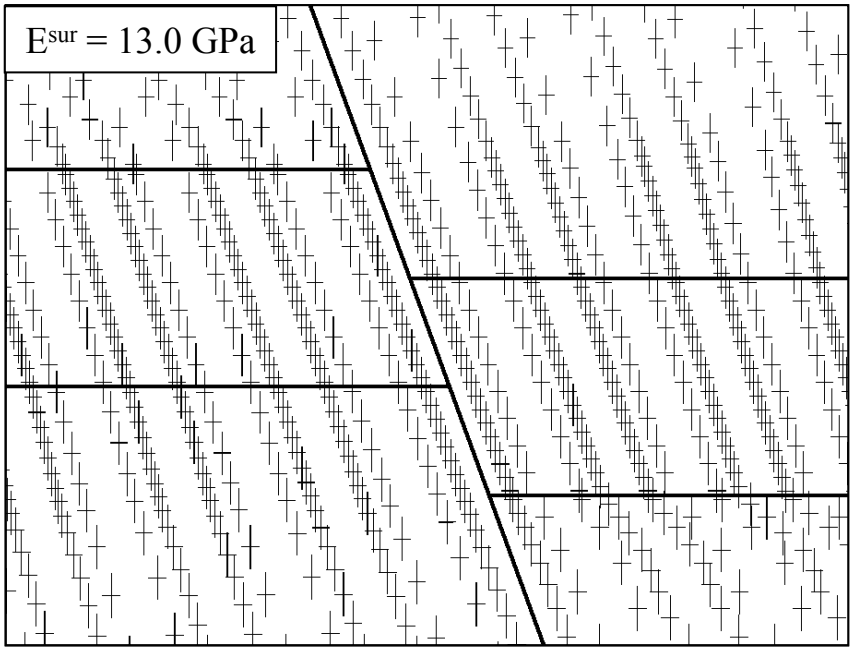

Figure 11.10. Calculated effective principal stress vectors for the initial state of stress in model '2D_throw_½D' with rock properties and initial pore pressure in the surrounding rock being the same as in the reservoir rock ($E^{res} = E^{sur} = 13.0$ GPa, $\nu^{sur} = \nu^{res} = 0.2$ and initial hydrostatic reservoir pore pressure).

For $E^{sur} < E^{res}$, things become the other way around (see Figure 11.11a). Originally vertical effective principal stress vectors around the observation points 4 and 7 are now turned into subvertical directions, more parallel to the fault, thus increasing the angle between the fault and the smallest principal stress direction. Furthermore, the magnitude of the subvertical effective principal stress became somewhat smaller whereas the magnitude of the subhorizontal effective principal stress remained more or less equal. Similar to the previously given explanations this leads according to eqs. (3.2a) and (3.2b) to a decrease in both τ and σ'_n.

Consider now the fault zone around points 1 and 2 for $E^{sur} > E^{res}$, at the top of the footwall reservoir compartment. Effective principal stress vectors near observation point 2 inside of the reservoir, both subvertical and subhorizontal, show relatively low magnitudes when compared to the standard case (see Figures 11.10 and 11.11b). The originally vertical effective principal stress vectors are slightly turned into subvertical directions, more perpendicular to the fault. At the opposite side of the fault, in the surrounding rock, effective principal stress vectors are relatively large in magnitude and show a slight turning of the originally vertical effective principal stress vectors into subvertical directions, more parallel to the fault. Apparently the stresses are attracted to the stiffer surrounding rock and are arched away from the weaker reservoir rock, resulting in smaller values of τ and σ'_n in the fault zone around points 1 and 2. For $E^{sur} < E^{res}$, the situation is reversed (Figure 11.11a): the stiffer reservoir rock attracts now the stresses, leading to larger effective stresses inside of the reservoir and smaller effective stresses outside and an effective principal stress pattern as shown in Figure 11.11a. This leads to larger values of τ and σ'_n in the fault zone

around points 1 and 2. The above explanations for the fault zone at the top of the footwall reservoir compartment apply for reasons of symmetry also the fault zone at the bottom of the hanging wall reservoir compartment.

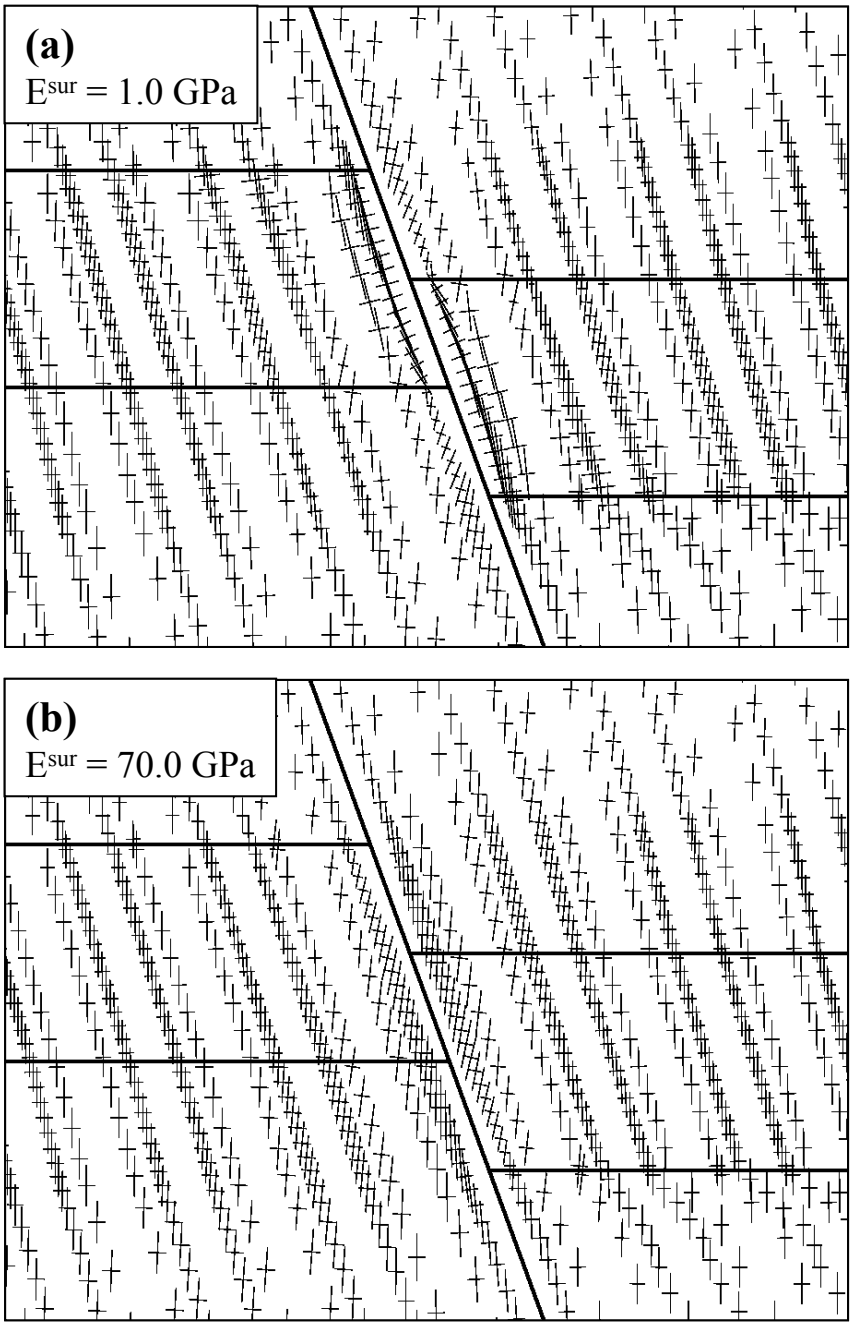

Figure 11.11. Calculated effective principal stress vectors for the initial state of stress in model '2D_throw_½D' for (a) E^{sur} = 1.0 GPa and (b) E^{sur} = 70.0 GPa. E^{res} = 13.0 GPa and ν^{res} = ν^{sur} = 0.2 in both calculations. The initial pore pressure is hydrostatic in both reservoir and surrounding rock.

Calculations showed that stress paths in the fault zone where the two reservoir compartments overlap develop with increasing shear- and effective normal stress, promoting normal fault slip. This is in accordance to the explanations in Chapter 11.1.2. $E^{sur} > E^{res}$ causes the initial shear- and effective normal stress in this fault zone to be larger and closer to failure than in the standard case with no rock property discrepancy. It therefore promotes the reactivation of the normal fault in this zone. $E^{sur} < E^{res}$, on the other hand, causes the initial shear- and effective normal stresses and therefore the maximum fault slip to be less. Calculations indeed show an increasing maximum normal fault slip, located in observation point 7 for all calculations, with increasing values of E^{sur} (Figure 11.12).

Contrarily, the calculations showed that the stress paths in the fault zones near the top of the footwall reservoir compartment and the bottom of the hanging wall reservoir compartment develop with decreasing shear stress, promoting reverse fault slip. $E^{sur} > E^{res}$ causes the initial shear- and effective normal stress in this fault zone to be smaller, shortening the path from the initial state of stress to the failure line compared to the standard case with no rock property discrepancy. It therefore promotes reverse fault slip in these zones. Initial shear stresses in observation point 2 even become negative for high values of E^{sur} (Figure 11.9), suggesting a local field with reverse shear stresses on the fault. It has to be mentioned here that the stresses at the reservoir corner points (2 and 4) have to be considered with care, since these are located at locations with rock property- and pore pressure jumps and large stress concentrations. The numerical calculations results might be exaggerated. $E^{sur} < E^{res}$, on the other hand, causes the initial shear- and effective normal stresses to be larger and therefore the reverse fault slip to be less. Calculations indeed show a larger value of maximum reverse fault slip, located in observation point 2 for all calculations, with increasing values of E^{sur} (Figure 11.12).

For the modelled conditions it can be stated overall, that a surrounding rock Young's modulus higher than the Young's modulus of the reservoir rock promotes the reactivation of a steeply dipping normal fault intersecting a reservoir with a throw of half the reservoir thickness in an extensional tectonic stress regime. Normal fault slip is promoted in the fault zone where the two compartments overlap and reverse fault slip is promoted at the top of the footwall reservoir compartment and at the bottom of the hanging wall reservoir compartment. On the other hand, a surrounding rock Young's modulus smaller than the Young's modulus of the reservoir rock opposes the reactivation of the fault. Note that the explanations given above are valid only for the specific conditions modelled for this dissertation, whereby the fault dips with an angle of 70^{o} and the initial tectonic stress field is extensional ($K_0 = 0.4$). For compressional tectonic stress fields ($K_0 > 1$) and fault dip angles lower than $45^{o} + ½\phi^{f}$, other conditions apply.

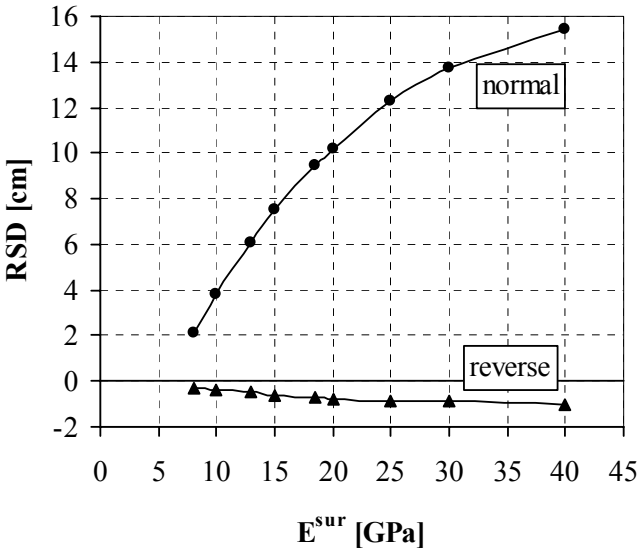

Figure 11.12. Calculated maximum RSD-values (normal fault slip) and minimum RSD-values (reverse fault slip) as a function of the Young's modulus of the surrounding rock (E^{sur}) for model '2D_throw_½D' with E^{res} = 13.0 GPa and $\nu^{res} = \nu^{sur} = 0.2$. The initial pore pressure is hydrostatic in both reservoir and surrounding rock. Maximum values were observed in observation point 7 (see Figure 11.1). Minimum values were observed in observation points 2 and/or 12.

11.2.3 Poisson's ratio

Initial states of stress as a function of ν^{sur} are plotted in Figure 11.13 for five different locations on the fault. Like is the case for the Young's modulus (Chapter 11.2.2), two different fault zones can be basically distinguished: a zone around point 2 (top of the footwall reservoir compartment), where an increasing ν^{sur} leads to decreasing shear- and effective normal stresses on the fault, and a zone marked by the points 4, 6 and 7, where an increasing ν^{sur} leads to increasing values of τ and σ'_n on the fault. In points 1, 4 and 7 only the larger values of ν^{sur} seem to have significant influence on the initial state of stress.

As outlined in Chapter 11.2.2, stress paths in the fault zone where the two reservoir compartments overlap develop with increasing τ and σ'_n, promoting normal fault slip. $\nu^{sur} > \nu^{res}$ causes the initial shear- and effective normal stress in this fault zone to be larger and closer to failure than in the standard case with no rock property discrepancy. It therefore promotes the reactivation of the normal fault in this zone. $\nu^{sur} < \nu^{res}$, on the other hand, causes the initial shear- and effective normal stresses and therefore the maximum fault slip to be less, although its influence seems to be minor. Calculations indeed show an increasing maximum normal fault slip, located in observation point 7 for all calculations, with increasing values of ν^{sur} (Figure 11.14). For the modelled conditions, values of ν^{sur} lower than 0.2 does not have a significant influence on the calculated maximum normal fault slip.

Stress paths in the fault zone around observation point 2 develop with decreasing shear stress, promoting reverse fault slip (see Chapter 11.1.2 for explanation). $\nu^{sur} > \nu^{res}$ causes the initial shear- and effective normal stress in this fault zone to be smaller, shortening the path from the initial state of stress to the failure line compared to the standard case with no rock property discrepancy. It therefore promotes reverse fault slip in this zone. Initial shear stresses in observation point 2 even become negative for high values of ν^{sur} (Figure 11.13), suggesting a local field with reverse shear stresses on the fault. Note that the numerical calculation results at the reservoir corner points (2 and 6) might be somewhat exaggerated due to rock property- and pore pressure jumps and large stress concentrations. $\nu^{sur} < \nu^{res}$, on the other hand, causes the initial shear- and effective normal stresses to be larger and therefore the reverse fault slip to be less. Calculations indeed show a larger value of maximum reverse fault slip, located in observation point 2 and/or 12 for all calculations, with increasing values of ν^{sur} (Figure 11.14), whereby the influence of ν^{sur}-values smaller than 0.2 is minor. Because of symmetry on the fault (see Chapter 11.1), the behaviour around the top of the footwall- and the bottom of the hanging wall reservoir compartment is similar.

For more insight in the influence of the initial state of stress on the fault as a function of the Poisson's ratio of the surrounding rock, the initial effective stress field around the reservoir-intersecting part of the fault is plotted in Figure 11.15 for the two extreme ν^{sur}-values of 0.0 and 0.49. These are most suited for a good visualisation of the perturbations in the principal stress field from the standard case where $\nu^{sur} = 0.2$, which is shown in Figure 11.10. Similar patterns occur for the other values of E^{sur}, but to a lesser extent.

Initial effective principal stress vectors for $\nu^{sur} = 0.49$ show a similar pattern as those for $E^{sur} = 70.0$ GPa (compare Figures 11.15b and 11.11b). This is very reasonable since a high Poisson's ratio means a stiff material: the bulk modulus is high for high values of E and/or ν. The stresses are attracted to the stiffer surrounding rock and are arched away from the weaker reservoir rock, resulting in smaller values of τ and σ'_n in the fault zone around points 1 and 2. Subvertical effective principal stresses concentrate in the zone where the two reservoir compartments overlap. Their magnitudes become somewhat larger when compared to the standard case of Figure 11.10, whereas the subhorizontal effective principal stress magnitudes become somewhat smaller. The description of the initial effective principal stress field and its implications on the initial shear- and effective normal stresses on the fault for $\nu^{sur} > \nu^{res}$ are the same as for $E^{sur} > E^{res}$ and can be read in Chapter 11.2.2.

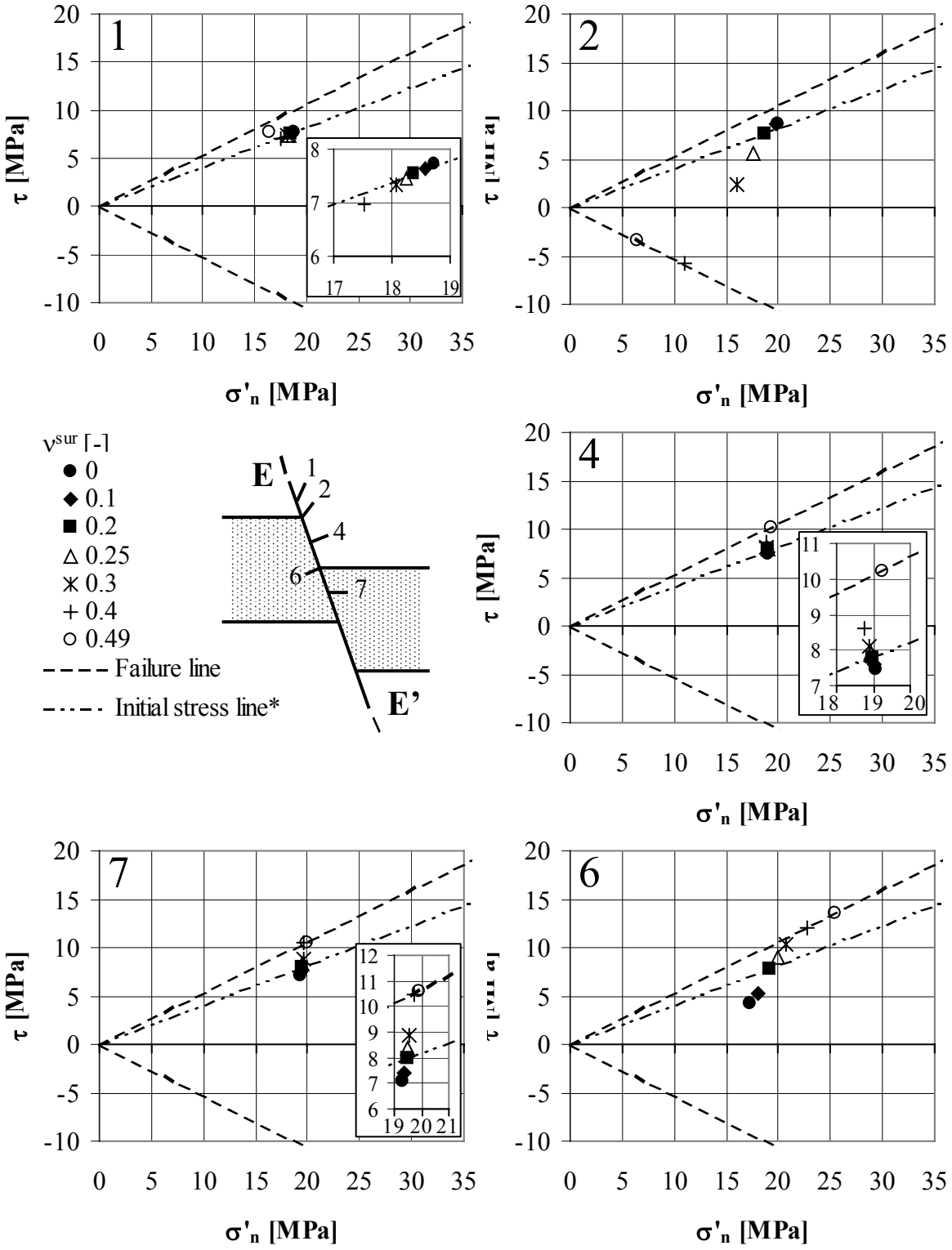

Figure 11.13. Initial states of stress for five different locations on the fault (1, 2, 4, 6 and 7) as a function of the Poisson's ratio of the surrounding rock (ν^{sur}). Calculation results of model '2D_throw_½D' with ν^{res} = 0.2, $E^{sur} = E^{res}$ = 13.0 GPa and initial hydrostatic reservoir pore pressure.
** The 'initial stress line' is calculated according to eqs. (3.2a) and (3.2b), Chapter 3.1.*

Initial effective principal stress vectors for ν^{sur} = 0.0 show minor difference when compared to the standard case (Figures 11.15a and 11.10). Directions are hardly changed. The differences are mainly in the magnitudes, but are not more than approximately 2 MPa (appr. 5% of the subvertical effective principal stress). Effective principal stresses become somewhat larger within the reservoir near the fault and smaller in the reservoir-near surrounding rock near the fault. Apparently, the stiffer reservoir rock attracts the stresses. In the reservoir around observation point 7, (sub)horizontal effective principal stresses are somewhat larger whereas (sub)vertical effective principal stresses remain unchanged. The differential stress (σ'_1 - σ'_3) in eqs. (3.2a) and (3.2b) becomes somewhat smaller, whereas the mean stress (σ'_1 + σ'_3) becomes somewhat larger. The values of τ and σ'_n therefore decrease, whereby τ is more affected than σ'_n. Because of the small changes in magnitude (< 2 MPa), these changes are very small, as indicated in Figure 11.13.

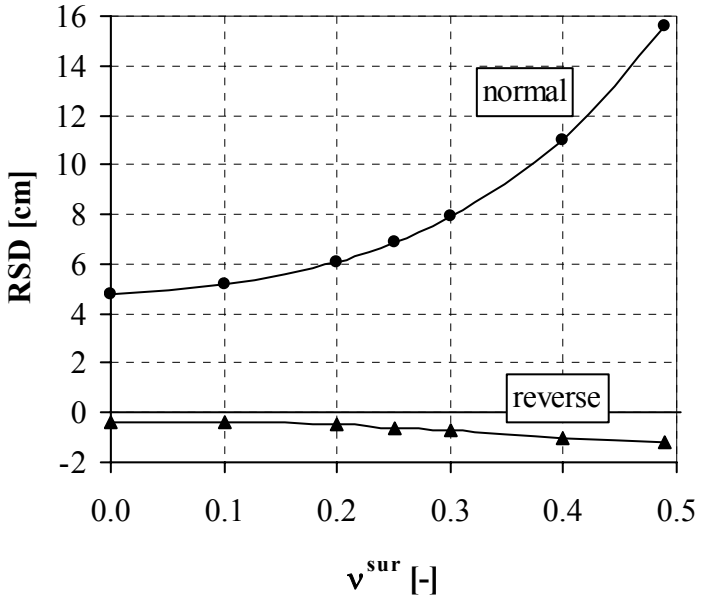

Figure 11.14. Calculated maximum RSD-values (normal fault slip) and minimum RSD-values (reverse fault slip) as a function of the Poisson's ratio of the surrounding rock (ν^{sur}) for model '2D_throw_½D' with ν^{res} = 0.2 and E^{res} = E^{sur} = 13.0 GPa. The initial pore pressure is hydrostatic in both reservoir and surrounding rock. Maximum values were observed in observation point 7 (see Figure 11.1). Minimum values were observed in observation points 2 and/or 12.

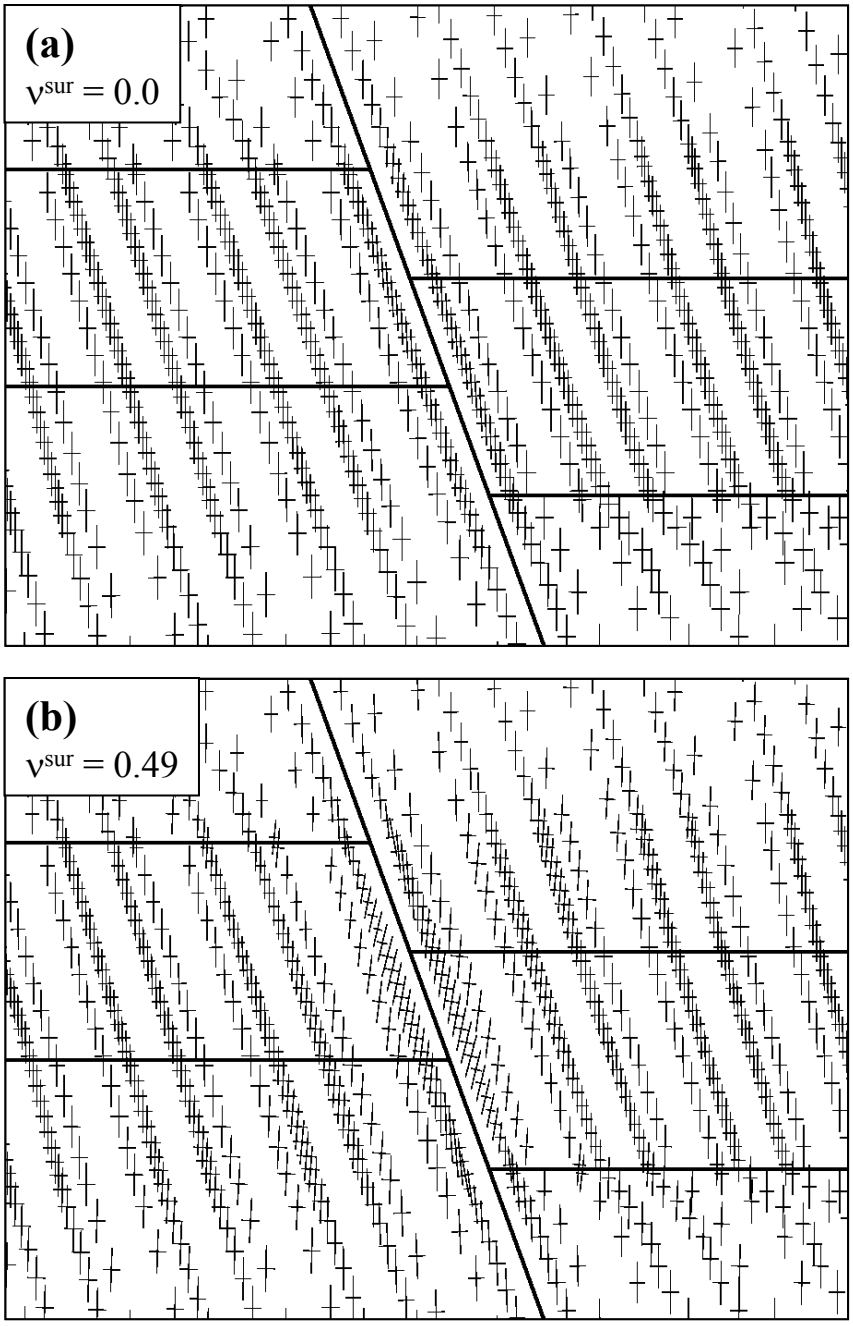

Figure 11.15. Calculated effective principal stress vectors for the initial state of stress in model '2D_throw_½D' for (a) $\nu^{sur} = 0.0$ and (b) $\nu^{sur} = 0.49$. $\nu^{res} = 0.2$ and $E^{res} = E^{sur} = 13.0$ GPa in both calculations. The initial pore pressure is hydrostatic in both reservoir and surrounding rock.

11.2.4 Discussion

Young's moduli for sandstones in general typically range from 0.1 – 30 GPa and Poisson's ratios from 0 – 0.45 (Fjaer *et al.* 1996). For shales these values are 0.4 – 70 GPa and 0 – 0.30. In the northern Netherlands, reservoir Young's moduli and Poisson's ratios are typically around 13.0 GPa and 0.2, respectively (NAM 2000). The reservoir is underlain by stiffer carboniferous rocks (Limburg Formation), consisting of shales and sandstones with Young's moduli around 20 GPa and Poisson's ratios of

about 0.2. Reservoirs are in most cases covered by a shaly cap rock (Ten Boer claystone). E- and ν-values of this cap rock are typically 18.0 – 18.5 GPa and 0.25 (NAM 2000). The calculated RSD-values (Figures 11.12 and 11.14) indicate that for the given ranges the Young's modulus of the surrounding rock is a more important parameter than the Poisson's ratio of the surrounding rock. ν^{sur} only plays a significant role for larger values, say for $\nu^{sur} > 0.3$. Considering the salt layers above the reservoir, this could be the case, since these are commonly modelled with a Poisson's ratio of 0.35.

11.3 Influence initial slight reservoir overpressure

11.3.1 Calculation series

The Groningen and Annerveen gas fields were initially slightly overpressured prior to depletion (Chapter 7.7) with an initial overpressure of approximately 35.0 MPa. This is only slightly larger than a hydrostatic pore pressure at the depth of the reservoirs, which would amount approximately 30.0 MPa. It is studied how this slight overpressure affects the calculated initial state of stress and stress development on the fault plane and fault slip. For this purpose, 2D-model '2D_throw_½D' is used with higher-order elements: 6-noded plane strain triangles for the rock volume (element type CT12E) and 3+3 noded line interface elements for the fault (element type CL12I).

Calculations with an initial pore pressure of 35.0 MPa and an initial hydrostatic pore pressure (appr. 30 MPa) in the reservoir and the parts of the fault plane in contact to the reservoir are performed for two kinds of surrounding rock properties (Table 11.2): equal to reservoir rock ($E^{sur} = E^{res} = 13.0$ GPa, $\nu^{sur} = \nu^{res} = 0.2$ and $\phi^{sur} = \phi^{res} = 30^o$) and stiffer than reservoir rock with default values ($E^{sur} = 18.5$ GPa, $\nu^{sur} = 0.25$ and $\phi^{sur} = 25^o$). For all other geomechanical properties and loading conditions values are used as listed in Table 11.2, except for the fault normal and shear stiffness. They amount 14.4 and 5.4 GPa/m for the entire fault for all calculations, respectively, regardless of the surrounding rock properties. In this way, the calculations can be compared to those of Chapter 11.2 with equal rock properties.

Gas depletion is modelled by decreasing the reservoir pore pressure to 0 MPa in several static depletion steps. In the case of a reservoir with a hydrostatic initial pore pressure, the pore pressure is depleted linearly in ten static depletion steps. Note that since the hydrostatic pressure increases with depth (from 28.4 MPa at the top of the footwall to 30.7 MPa at the bottom of the hanging wall), the depletion at the bottom of the reservoir (3.07 MPa per depletion step) is in this case somewhat higher than at the top of the reservoir (2.84 MPa per depletion step). In the case that the reservoir is initially slightly overpressured (35.0 MPa initial pore pressure in the whole reservoir, see Figure 8.10), the reservoir is depleted to 0 MPa in eleven static depletion steps. The first ten steps are equal to the case of a hydrostatic initial pore pressure: the pore pressure decreases per depletion step with an amount from 2.84 MPa at the top of the reservoir to 3.07 MPa at the bottom. The remaining pore pressure is then depleted in a final eleventh step. Hence, the first ten depletion steps of all calculations incorporate

the same Δp. Stress paths and fault slip after these ten depletion steps are then comparable. The eleventh depletion step in case of an initially overpressured reservoir is performed in order to study the effect of depletion to 0 MPa.

Note that for a Young's modulus and Poisson's ratio of the surrounding rock equal to the reservoir rock ($E^{sur} = E^{res} = 13.0$ GPa and $\nu^{sur} = \nu^{res} = 0.2$), solely the effect of an initial reservoir overpressure and its depletion is modelled. Note also that the effects as presented here are solely the result of a larger initial reservoir pore pressure in the FE-models. Other possible effects related to an initial overpressure which could occur in reality, such as a higher porosity and therefore different geomechanical properties of the reservoir rock, are not taken into account.

11.3.2 Calculation results and discussion

In order to compare the stress paths for various locations along the fault for an initial hydrostatic pore pressure versus an initially overpressured situation, calculations are performed for the case that the surrounding rock properties are equal to the reservoir rock properties. The results are shown in Figure 11.16.

The main difference between the two initial pressure conditions is in the initial state of stress. Furthermore, the eleventh depletion step in case of initial overpressure is absent in the hydrostatic case. A small difference can be observed in the last depletion steps in observation point 4.

Initial states of stress for the initially overpressured reservoir are, for the observation points in contact with the reservoir, characterised by a effective normal stress (σ'_n) which is smaller than for the initially hydrostatically pressured reservoir. σ'_n is hardly affected in points 1 and 2. Furthermore, initial shear stresses are, for the initially overpressured reservoir, smaller in points 6 and 7, larger in point 2 and as good as unaffected in points 1 and 4. For symmetry reasons, similar conditions apply to the lower half of the reservoir, below point 7 (see Chapter 11.1).

For the initially overpressured reservoir, the initial states of stress lead to a way to failure which is longer than for the initially hydrostatically pressured reservoir. Stress paths on the fault around observation points 6 and 7, where the two reservoir compartments overlap, develop towards failure with increasing shear- and effective normal stresses but start with lower values. Stress paths on the fault around point 2, at the top of the footwall reservoir compartment, develop towards the failure line for reverse fault reactivation but have larger initial values. The failure line for the initially overpressured reservoir is, for the case of equal reservoir and surrounding rock properties, generally reached one depletion step after it is reached in the initially hydrostatically pressured reservoir. Calculated fault slip after ten depletion steps is accordingly smaller (Table 11.2 and Figure 11.18). Depletion of the remaining reservoir overpressure to 0 MPa in an eleventh depletion step leads to a larger pore pressure decrease, further stress development and thus more fault slip than for the initially hydrostatically pressured reservoir. Calculated RSD-values are therefore larger in this case.

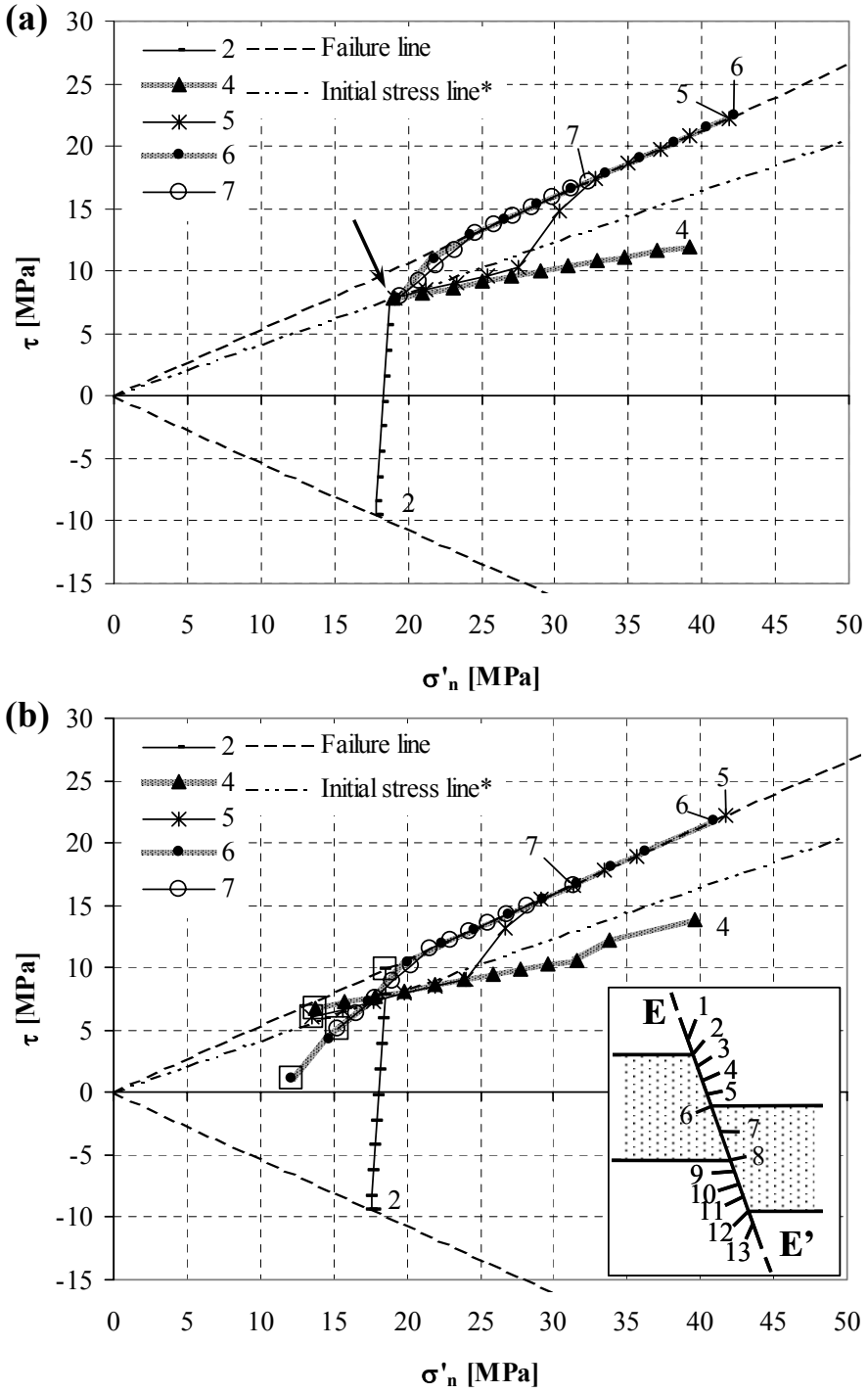

*Figure 11.16. Calculated stress paths for different observation points for model '2D_throw_½D' with surrounding rock properties being the same as reservoir rock properties for (a) initially hydrostatic reservoir pore pressure and (b) initial reservoir overpressure of 35.0 MPa (see Table 11.1). The initial state of stress for (a) is similar for all stress paths and is indicated by an arrow. In (b) it is marked by an open square. The end of the stress paths are marked by the respective observation point number. * The 'initial stress line' is calculated according to eqs. (3.2a) and (3.2b), chapter 3.1.*

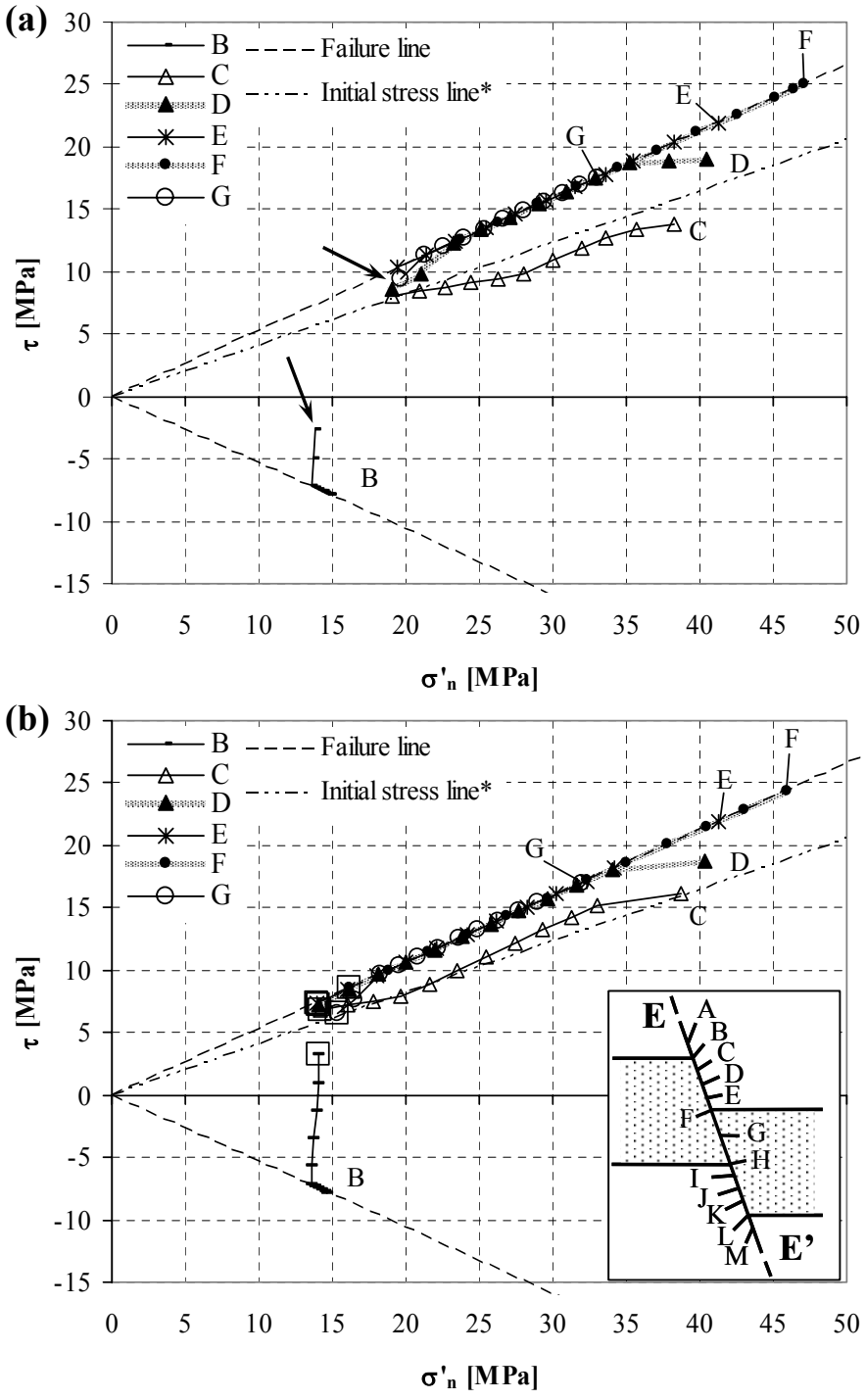

*Figure 11.17. Calculated stress paths for different observation points for model '2D_throw_½D' with surrounding rock properties being stiffer as reservoir rock properties for (a) initially hydrostatic reservoir pore pressure and (b) initial reservoir overpressure of 35.0 MPa (see Table 11.1). The initial state of stress for (a) is similar for all stress paths and is indicated by an arrow. In (b) it is marked by an open square. The end of the stress paths are marked by the respective observation point number. * The 'initial stress line' is calculated according to eqs. (3.2a) and (3.2b), chapter 3.1.*

Similar results as described above apply for calculations with surrounding rock properties stiffer than the reservoir rock (E^{sur}=18.5 GPa, ν^{sur}=0.2, ϕ^{sur}=25°). Comparing the stress paths in Figures 11.16 and 11.17 shows that the calculated initial state of stress forms the main difference between the four different scenarios. The stiffer surrounding rock leads for the initially hydrostatically pressured reservoir to an initial state of stress in observation point 2 which is very close to reverse failure. Failure is in this case already reached after the third depletion step. An initial overpressure in the reservoir stabilises this behaviour largely. In the latter case, failure is only reached in point 2 during the fifth depletion step.

Consider now the stress paths for the following two scenarios: equal surrounding and reservoir rock properties with initial hydrostatic reservoir pore pressure and stiffer surrounding rock properties with initial reservoir overpressure (Figures 11.16a and 11.17b). The stiffer surrounding rock causes the initial state of stress on the fault to be closer to failure than in case of equal surrounding and reservoir rock properties. An initial reservoir overpressure, on the other hand, tends to cause the initial state of stress further away from failure. As is visible from the stress path plots, the stiffer surrounding rock gives for the given conditions the stronger effect: initial states of stress in observation points 4, 5, 6 and 7 are at or very close to failure (Figure 11.17b). The initial state of stress in observation point 2 is, regarding the negative stress path gradient, with a smaller effective normal stress also closer to failure. Failure with reverse plastic fault slip is reached after the fifth depletion step. The reverse reactivation of the fault in observation point 2 causes the stress path of observation point 4, initially developing along the failure line for normal fault reactivation, to stabilise for the last depletion step: it develops away from the failure line. Because of states of stress closer to failure, calculated fault slip is accordingly larger (Figure 11.18 and Table 11.2).

From the foregoing it can be concluded, that a slight initial reservoir overpressure in the geomechanical reservoir models causes the initial state of stress on the fault at reservoir level to be further away from failure than in case of an initially hydrostatically pressured reservoir. An initial reservoir overpressure in the geomechanical models reduces therewith the calculated fault slip at reservoir level, when the same pore pressure reduction applies. However, depletion of the reservoir until the same end pressure provides an additional driving force for fault slip when the reservoir embodies a larger initial pore pressure. Calculated RSD-values are therefore larger in this case. The effects as presented here are solely the result of a larger initial reservoir pore pressure in the reservoir. Other possible effects related to an initial overpressure which could occur in reality, such as a higher porosity and therefore different geomechanical properties of the reservoir rock, are not taken into account.

Table 11.2. Calculated maximum and minimum RSD-values on the fault for different scenario's for model '2D_throw_½D' with higher-order elements CT12E and CL12I.

Scenario no.	*No. of depletion steps*	*Scenario description****			*RSD_{max} [cm]*	*RSD_{min} [cm]*
		*Surrounding rock properties**	*p_{ini}^{res} ***	*Δp^{res}*		
1	10	same	hydrostatic	-hydrostatic	6.1	-0.5
2	10	same	overpressure	-hydrostatic	5.1	-0.4
3	10	stiff	hydrostatic	-hydrostatic	10.2	-0.7
4	10	stiff	overpressure	-hydrostatic	9.6	-0.7
2	11	same	overpressure	-35.0 MPa	7.6	-0.7
4	11	stiff	overpressure	-35.0 MPa	12.1	-0.9

* *relative to reservoir rock properties;*
'same': $E^{sur} = E^{res} = 13.0$ GPa, $\nu^{sur} = \nu^{res} = 0.2$ and $\phi^{sur} = \phi^{res} = 30^o$
'stiff': $E^{sur} = 18.5$ GPa, $\nu^{sur} = 0.25$ and $\phi^{sur} = 25^o$

** *'hydrostatic': p_{ini}^{res} is according to a hydrostatic pore pressure gradient with $\rho_{fluid} = 1000$ kg/m^3*
'overpressure': $p_{ini}^{res} = 35.0$ MPa

*** *Initial pore pressure and pore pressure development in fault regions A and B change accordingly for the overpressured scenarios. Fault normal- and shear stiffness remain the same for all scenarios at 15.4 and 5.4 GPa/m, respectively.*

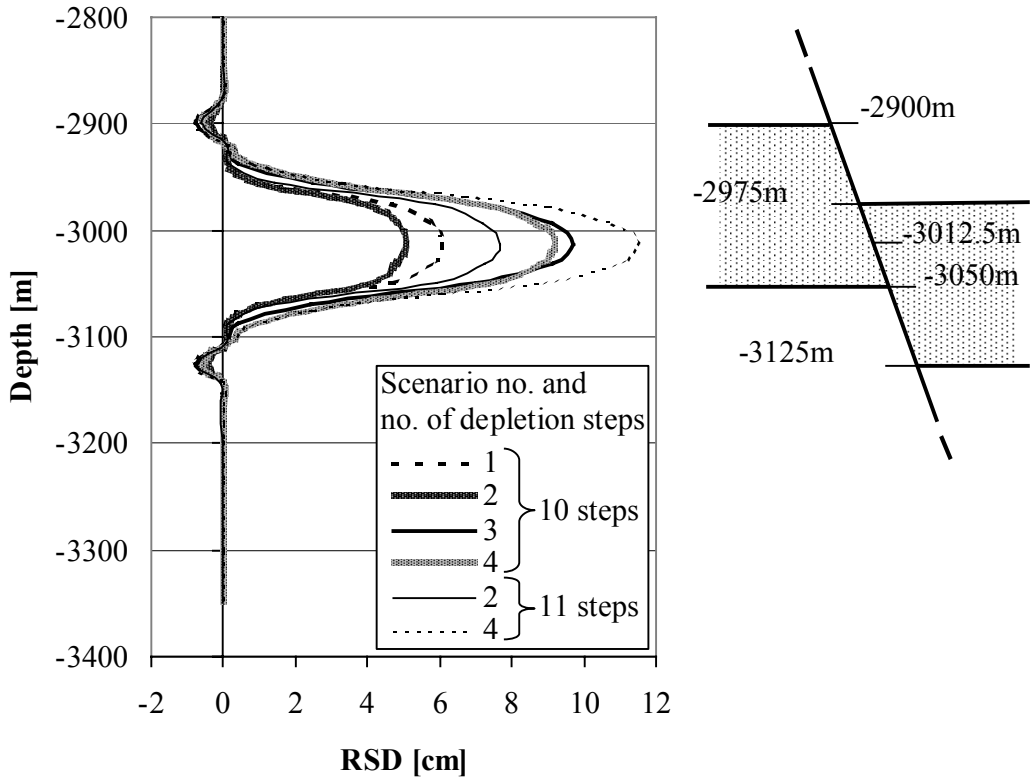

Figure 11.18. Calculated RSD-values on the fault for different scenario's (see Table 11.2) for model '2D_throw_½D' with higher-order elements CT12E and CL12I.

11.4 Influence of throw on calculated fault slip and seismic moment

11.4.1 Calculation series

In this section, the influence of throw along the fault plane on calculated RSD-values and seismic moment is analysed. Several models are used for this purpose (see Figure 11.19 and Chapter 8): model series 'throw_const_...D' with a constant throw along the fault strike, each model with a different amount of throw (Table 11.4), and model 'throw_var', incorporating a varying throw along the strike of the fault. Figure 11.19 shows the geometries of the reservoir and the location of the observation lines used for output in terms of stress paths and RSD-graphs. Two scenarios are considered (see Table 11.1):

- surrounding rock properties equal to the reservoir rock properties ($E^{sur} = E^{res} =$ 13.0 GPa; $\nu^{sur} = \nu^{res} = 0.2$; $\phi^{sur} = \phi^{res} = 30^{o}$) and initial hydrostatic reservoir pore pressure;
- default rock properties ($E^{sur} = 18.5$ GPa; $\nu^{sur} = 0.25$; $\phi^{sur} = 25^{o}$) and initial reservoir pore pressure of 35.0 MPa.

Gas depletion is modelled by reducing the pore pressure in both reservoir compartments and the adjacent fault regions A and B (Figure 11.19) with the same amount. The (hydrostatic) pore pressure in the surrounding rock and remaining part of the fault remains constant at its initial value. The geometry of model 'throw_var' is, with its scissor-like structure, representative for the in situ geometrical structure of gas reservoirs in the northern Netherlands. It has the advantage, that the influence of throw on fault slip can be obtained in one calculation run. Models 'throw_const_...D' are built in the first instance to get a relation between the amount of throw and the seismic moment. The seismic moment can only be calculated for the entire fault plane in the model, resulting in one value for normal fault slip and one value for reverse fault slip. Model 'throw_var' can therefore not distinguish the influence of the throw on the seismic moment. Comparison of the different models will indicate whether the slope of the hanging wall reservoir compartment in model 'throw_var' affects the calculation results.

Table 11.3. Definition of throw for the 3D-models 'throw_const_...D' and 'throw_var'.

Model name	*Throw (m)*	*Throw / D (D=150m)*
throw_const_0D	0	0
throw_const_¼D	37.5	¼
throw_const_½D	75	½
throw_const_¾D	112.5	¾
throw_const_1D	150	1
throw_const_1¼D	187.5	1¼
throw_const_1½D	225	1½
throw_const_2D	300	2
throw_var	0 – 297.95	0 – 1.99

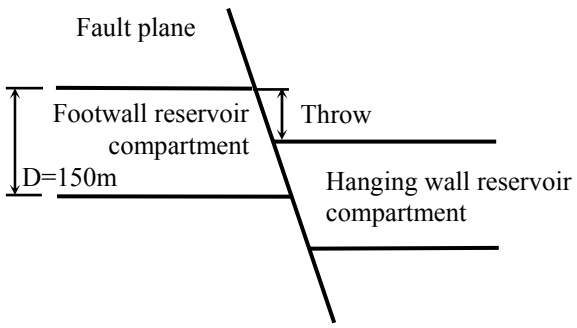

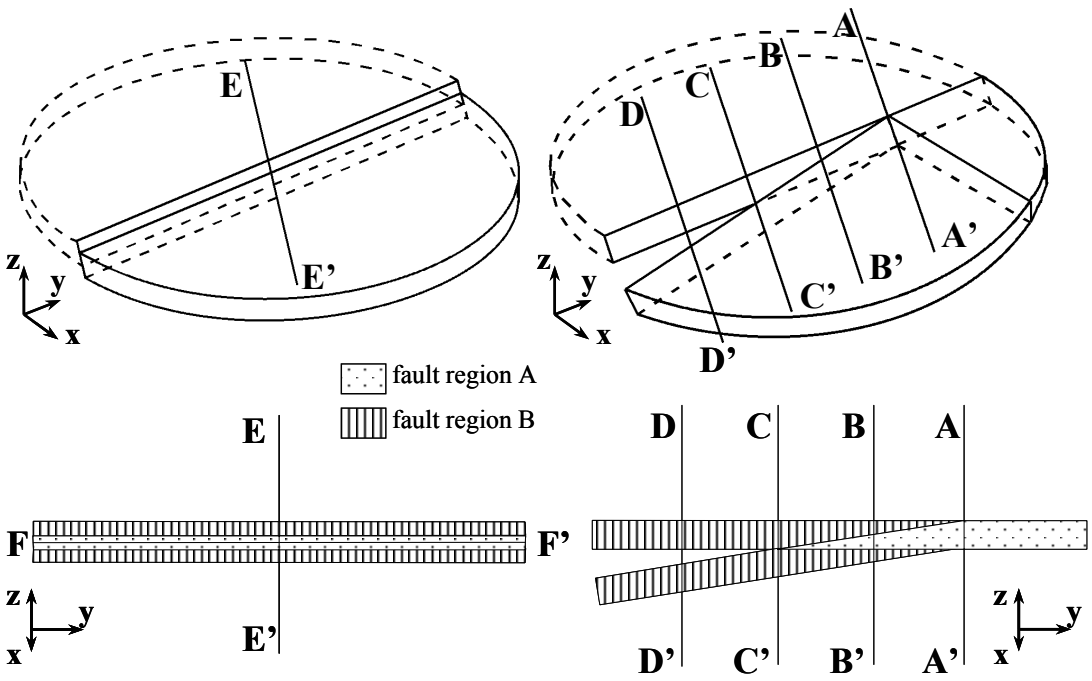

Figure 11.19. Reservoir geometry of models 'throw_const½D' (left) and 'throw_var' (right) with indication of observation lines AA', BB', CC', DD' and EE'. The lower figures show the intersection lines of the two reservoir compartments on the fault plane for a view direction perpendicular to the fault plane with indication of observation line FF' and the three different fault regions (see Chapter 8.1 for a more detailed description).

11.4.2 Calculation results and discussion

Consider first the calculated fault slip in form of RSD-values on the fault plane for model 'throw_var' with equal reservoir and surrounding rock properties and initial hydrostatic reservoir pore pressure (Figure 11.20 and Table 11.4). View direction of the contour plot is normal to the fault plane. Intersection lines of the two reservoir compartments with the fault plane are shown. View direction of the cross sections is in strike direction of the fault. Pointed areas denote the reservoir compartments. The calculated RSD-graph for cross section AA' does not show any significant fault slip. The negligibly small values are within the elastic deformation of the fault. A reservoir setting of type AA' has a low sensitivity to fault reactivation since the two reservoir compartments on either side of the fault are located in the same depth position. They compact with equal amount on both sides of the fault, resulting in negligible amounts of fault slip. Note that this is the case only for equal pore pressure development and rock properties on either sides of the fault.

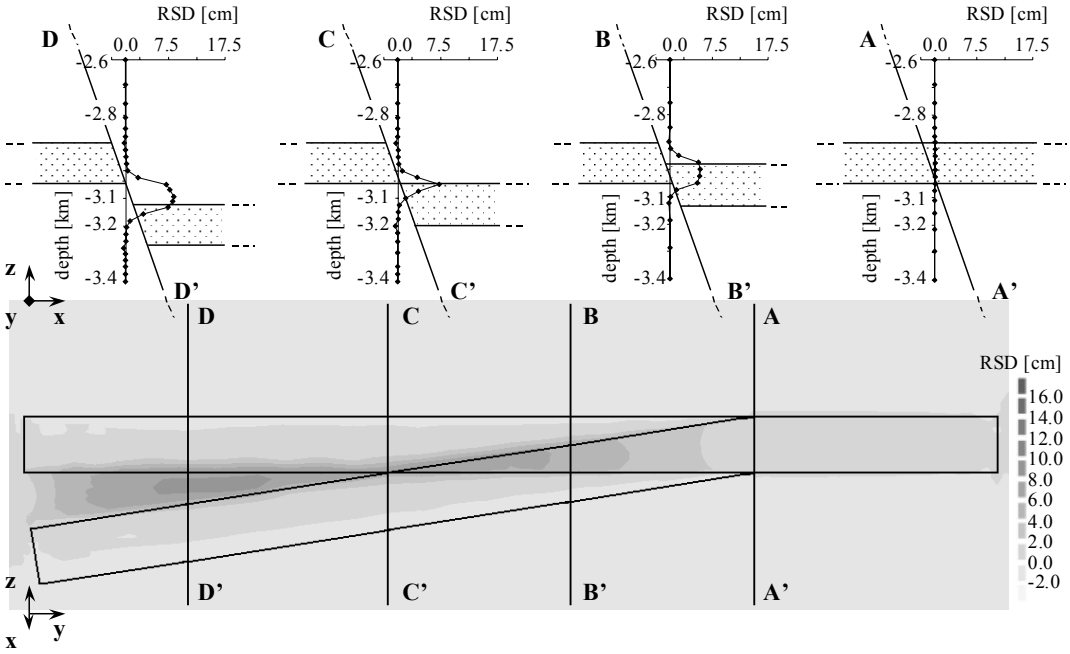

Figure 11.20. Calculated RSD-values on the fault plane for model 'throw_var' with equal reservoir and surrounding rock properties and initial hydrostatic reservoir pore pressure. The maximum value is 8.6 cm. View direction of the contour plot is normal to the fault plane. Intersection lines of the two reservoir compartments with the fault plane are shown. View direction of the cross sections is in strike direction of the fault. Dotted areas denote the reservoir compartments. See Appendix 2 for this figure in colour.

Reservoir configuration BB' is sensitive to fault slip due to differential compaction of the two reservoir compartments: the downward movement of the top of the hanging wall reservoir compartment interacts with the upward movement of the bottom of the footwall reservoir compartment. This interaction is at its maximum in configuration CC', where the top of the hanging wall reservoir compartment is positioned exactly opposite to the bottom of the footwall reservoir compartment. A sharp peak in the RSD-graph is observed here. In configuration DD', this maximum seems to be extended from a single sharp peak to a broad maximum. This result can be explained as follows. Because the throw in configuration DD' is larger than the reservoir thickness, the two reservoir compartments on either side of the fault plane are geometrically separated from each other. Between the two compartments exists a fault region of type C, which' pore pressure remains constant at its initial hydrostatic value during gas depletion. Because of the compaction of the two reservoir compartments, shear stresses increase whereas normal effective stresses show little variation due to the non-depleting and thus relatively high pore pressure in this part of the fault plane. Stress paths develop virtually vertically and reach the failure line during the third depletion step (Figure 11.21).

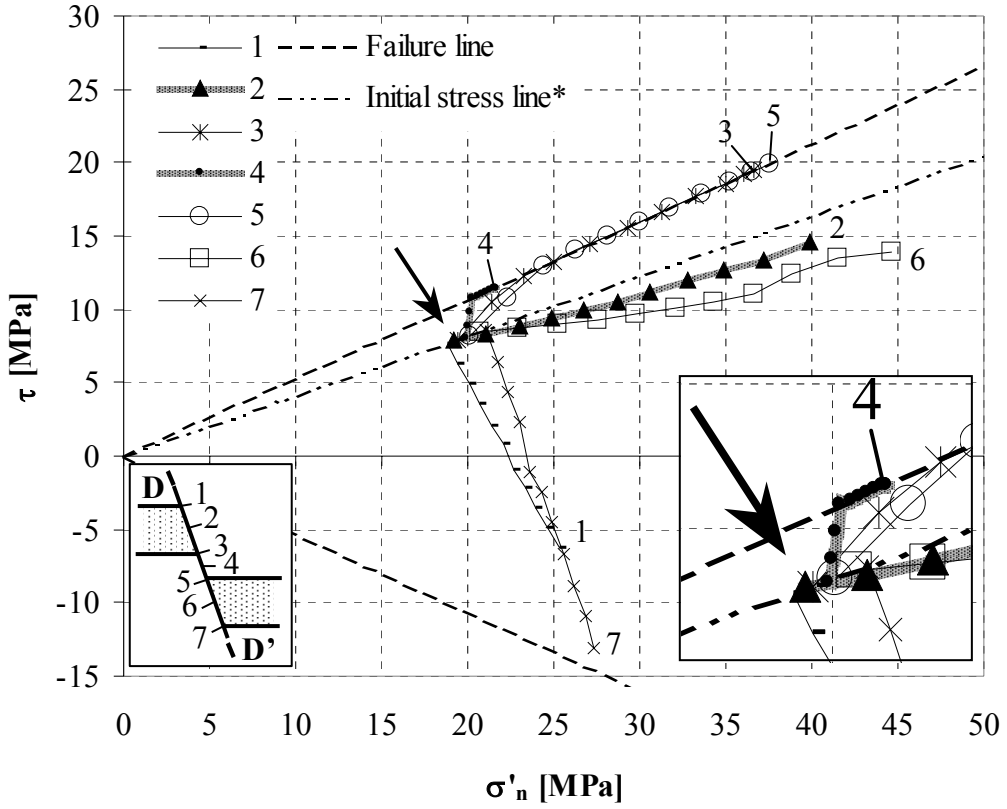

Figure 11.21. Calculated stress paths for different observation points along line DD' for model 'throw_var' with equal surrounding and reservoir rock properties and initial hydrostatic reservoir pore pressure. The initial state of stress is similar for all stress paths and is indicated by an arrow. The end of the stress paths are marked by the respective observation point number. The enlargement in the bottom right corner shows the stress path for observation point 4.
** The 'initial stress line' is calculated according to eqs. (3.2a) and (3.2b), Chapter 3.1.*

Table 11.4. Maximum normal fault slip and integrated normal fault slip over depth for the RSD-graphs in Figure 11.20.

Observation line	*Throw [m]*	*Throw/D (D=150m)*	*RSD_{max} [cm] (largest normal fault slip)*	*Normal fault slip integrated over depth [m^2]*	*(Normal fault slip integrated over depth) x 3000 x D_s [10^{14} Nm]*
AA'	0	0	0.1	0.19	0.03
BB'	75	½	5.4	5.83	0.94
CC'	150	1	7.2	4.19	0.68
DD'	231	1½ + $^1/_{25}$	8.4	9.91	1.61

Faults as represented by cross sections BB', CC' and DD' are all three sensitive for fault slip due to differential reservoir compaction. It has to be noted, that the effect of differential reservoir compaction in configuration DD' is enhanced in the present geomechanical models, due to the constant pore pressure in the part of the fault in between the bottom of the footwall and the top of the hanging wall reservoir compartment. In configuration BB', the maximum RSD-value is somewhat lower than in CC', but according to the RSD-graphs and the contour plot, relatively large values occur over a larger area. Configuration BB' seems in spite of its lower RSD_{max}-value to be more critical than configuration CC' because of the larger area of fault slip.

It is difficult to judge the criticalness of faults for reactivation solely based on the maximum RSD-value. A better approach would be to integrate the RSD-values over the fault plane or cross section lines. This is done for the four cross sections AA', BB', CC' and DD'. The results are listed in Table 11.4 and compared to the RSD_{max}-values of the respective graphs. The comparison indicates indeed that the configuration BB' is for the modelled conditions with equal reservoir and surrounding rock properties and initial hydrostatic reservoir pore pressure more critical than configuration CC'.

In order to come to a more representative quantity as is obtained by the integration of RSD-graphs, the seismic moment (M_0) is introduced in Chapter 9.1.2. The seismic moment is defined by Aki (1966) as the product of the amount of fault slip (RSD), the area of the fault rupture and the shear modulus of the rock formation through which the fault slip takes place. In the DIANA software, the shear modulus is replaced by the fault shear stiffness. This replacement is valid as long as the shear stiffness is calculated according to eq. (9.7).

The calculation of M_0 in DIANA applies only for 3D-models and applies to the entire fault plane. It results in two scalar quantities: a positive value for normal fault slip and a negative value for reverse fault slip. In order to determine M_0 as a function of throw, different models are built, each with a different amount of throw along the fault plane (model series 'throw_const_...D', see Table 11.3 and Chapter 8.1). The four observation lines AA', BB' and CC' in model 'throw_var' represent with a throw of 0, 75 and 150 m the models 'throw_const_0D', '-_½D' and '-_1D', respectively.

Calculated RSD-graphs for the different models of series 'throw_const_...D' along line EE' are similar to the corresponding graphs along observation lines AA', BB', CC' and DD' in model 'throw_var' (see Figures 11.20 and 11.22). The calculated RSD-values are for the graphs of models 'throw_const_...D' somewhat larger than for the corresponding graphs in model 'throw_var' (Table 11.5). The differences are relatively small and are most probably due to the different meshes in the different models and the tilting of the hanging wall reservoir compartment in model 'throw_var'. A larger difference is observed for RSD-values in graph BB' and those from model 'throw_const_½D', which amounts to 1.3 cm. Comparison of the stress paths F and G along observation line EE' of model 'throw_const_½D' with the stress paths 5 and 6 along line BB' of model 'throw_var' (see Figures 11.23 and 11.4a)

shows a more critical development of stress paths for the first case: stress paths are steeper because of a faster shear stress development and reach failure in an earlier stage of depletion. This is most probably the result of a slightly different finite element mesh in the two models, but also the tilting of the hanging wall reservoir compartment in model 'throw_var' might play a role.

No significant fault slip develops in model '0D'. Model '¼D' shows a large area with plastic fault slip, but the RSD-values are relatively low when compared to the other models with larger amounts of throw. When the top of the hanging wall reservoir compartment is located a bit closer to the bottom of the footwall compartment (model '½D'), RSD-values become clearly larger, whereas the area of movement becomes more narrow. Models '¾D' and '1D' show only minor changes in maximum RSD-values in relation to model '½D'. For all the area of movement is affected, which is smallest for model '1D', where the top of the hanging wall reservoir compartment is located exactly opposite to the bottom of the footwall compartment. Because of this specific geometry, one would expect that the maximum RSD-value occurs in model '1D'. However, RSD-graphs for models '1¼D', '1½D' and '2D' show even a slight increase in RSD_{max}. The reason for this behaviour is the combination of differential compaction of the two reservoir compartments, which causes shear stresses to increase, and a relatively small variation of effective normal stresses due to the non-depleting and thus relatively high pore pressure in the part of the fault in between the bottom of the footwall and the top of the hanging wall reservoir compartment. Stress paths develop virtually vertically and reach the failure line during the third depletion step.

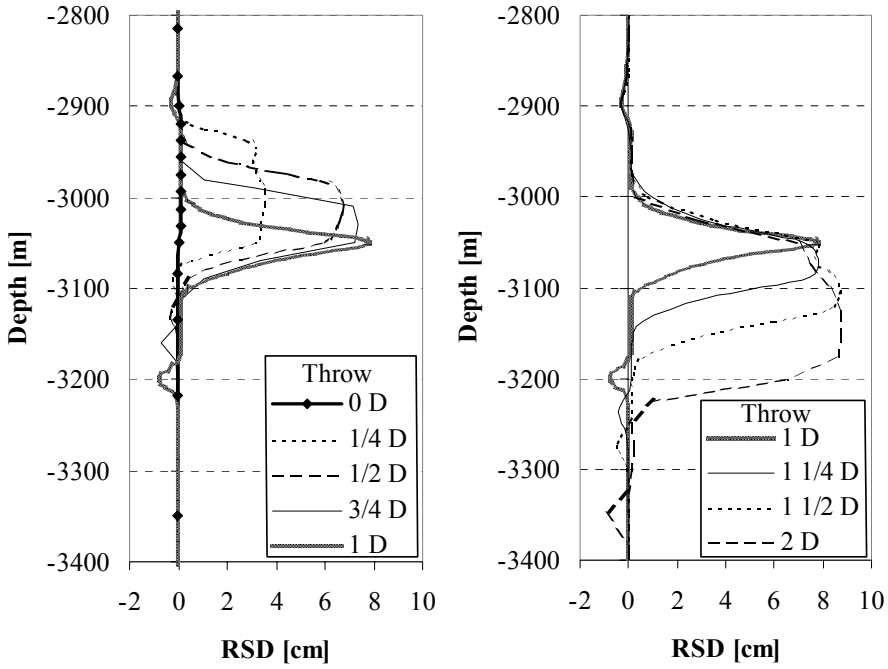

Figure 11.22. Calculated RSD-values along line EE' as a result of reservoir depletion for model series 'throw_const_...D' for with equal surrounding and reservoir rock properties and initial hydrostatic reservoir pore pressure.

Calculated M_0-values for models with a throw smaller than or equal to the reservoir thickness are listed in Table 11.5. According to these values, model 'throw_const_½D' incorporates for the modelled conditions with equal reservoir and surrounding rock properties and initial hydrostatic reservoir pore pressure the most critical configuration: the largest seismic moment is calculated for this configuration. Based on the seismic moment, model 'throw_const_½D' incorporates a configuration which is more critical than that of model 'throw_const_1D', despite the smaller RSD_{max}-value. The results are in good agreement with model 'throw_var'. RSD-graphs such as shown in Figure 11.22 occur because of the model geometry over a width of approximately 3000 m, which is the reservoir width. The products of the integrated RSD-graphs of model 'throw_var' (Figure 11.20), the reservoir width of 3000 m and the shear stiffness of the fault ($D_s = 5.4 \cdot 10^9$ GPa/m) are virtually equal to the calculated seismic moments of corresponding models of calculation series 'throw_const_...D' (see Tables 11.4 and 11.5). It shows the validity of the seismic moment calculations.

Table 11.5. Calculated largest normal and reverse fault slip and seismic moment on the fault as a result of reservoir depletion for different models with equal reservoir and surrounding rock properties and initial hydrostatic reservoir pore pressure. Pore pressure reduction is with a hydrostatic amount until 0 MPa end pressure in 10 depletion steps.

Model name	*Throw [m]*	*Throw/D (D = 150m)*	*RSD_{max} [cm] (largest normal fault slip)*	*RSD_{min} [cm] (largest reverse fault slip)*	*M_0^{normal} [10^{14} Nm]*	*$M_0^{reverse}$ [10^{14} Nm]*
throw_const_0D	0	0	0.1	0.0	0.04	-0.03
throw_var AA'	0	0	0.1	0.0		
throw_const_¼D	37.5	¼	3.5	-0.3	0.75	-0.09
throw_const_½D	75	½	6.7	-0.4	1.10	-0.12
throw_var BB'	75	½	5.4	-0.3		
throw_const_¾D	112.5	¾	7.4	-0.7	1.02	-0.13
throw_const_1D	150	1	7.8	-0.8	0.69	-0.14
throw_var CC'	150	1	7.2	-0.5		
throw_const_1¼D	187.5	1¼	7.9	-0.4		
throw_const_1½D	225	1½	8.7	-0.5		
throw_var DD'	231	1½ + $^1/_{25}$	8.4	-0.4		
throw_const_2D	300	2	8.7	-0.9		

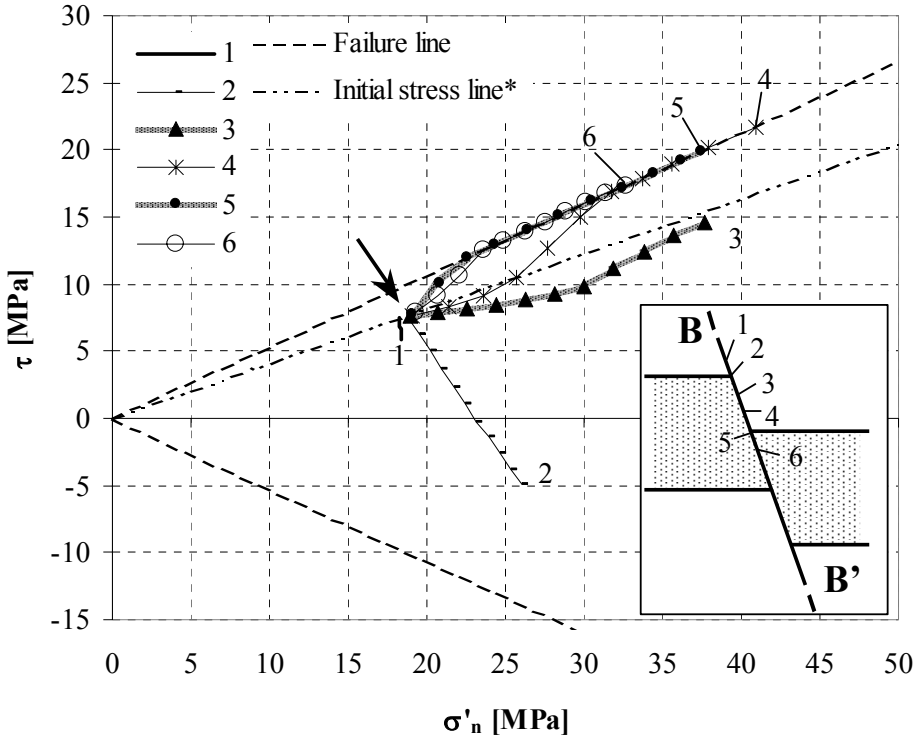

*Figure 11.23. Calculated stress paths for different observation points along line BB' for model 'throw_var' with equal surrounding and reservoir rock properties and initial hydrostatic reservoir pore pressure. The initial state of stress is similar for all stress paths and is indicated by an arrow. The end of the stress paths are marked by the respective observation point number. * The 'initial stress line' is calculated according to eqs. (3.2a) and (3.2b), Chapter 3.1.*

The influence of throw on calculated fault slip is analysed so far for an idealised situation: equal reservoir and surrounding rock properties and an initially hydrostatic reservoir pore pressure. In order to analyse the influence of throw for surrounding rock property values and initial reservoir pore pressure representative for field conditions in the northern Netherlands, calculations of model 'throw_var' and model series 'throw_const_...D' have been performed with default rock properties (surrounding rock stiffer than the reservoir rock, see Table 11.1) and an initially slightly overpressured reservoir (p_{ini}^{res} = 35.0 MPa).

The calculated fault slip is shown in Figure 11.24. RSD-contour plots and -graphs along the observation lines AA', BB', CC' and DD' incorporate the same trend as in Figure 11.20 (equal reservoir and surrounding rock properties and initial hydrostatic reservoir pore pressure): no significant fault slip for reservoir configuration AA'. Fault slip increases towards configuration BB', which concentrates to a single sharp peak for configuration CC' and extends to a broad maximum in configuration DD'. Note that the calculated seismic moments indicate, that configuration CC' (corresponding to model 'throw_const_1D') is more critical than configuration BB' (corresponding to model 'throw_const_½D') for the modelled conditions of default

rock properties and an initially slightly overpressured reservoir (Table 11.6). For equal reservoir and surrounding rock properties and initial hydrostatic reservoir pore pressure, configuration BB' is more critical than configuration CC' (Tables 11.4 and 11.5). Beside this qualitative difference, calculated fault slip is mainly affected in a quantitative manner by the different rock properties and initial pore pressure (Figures 11.20 and 11.24 and Tables 11.5 and 11.6).

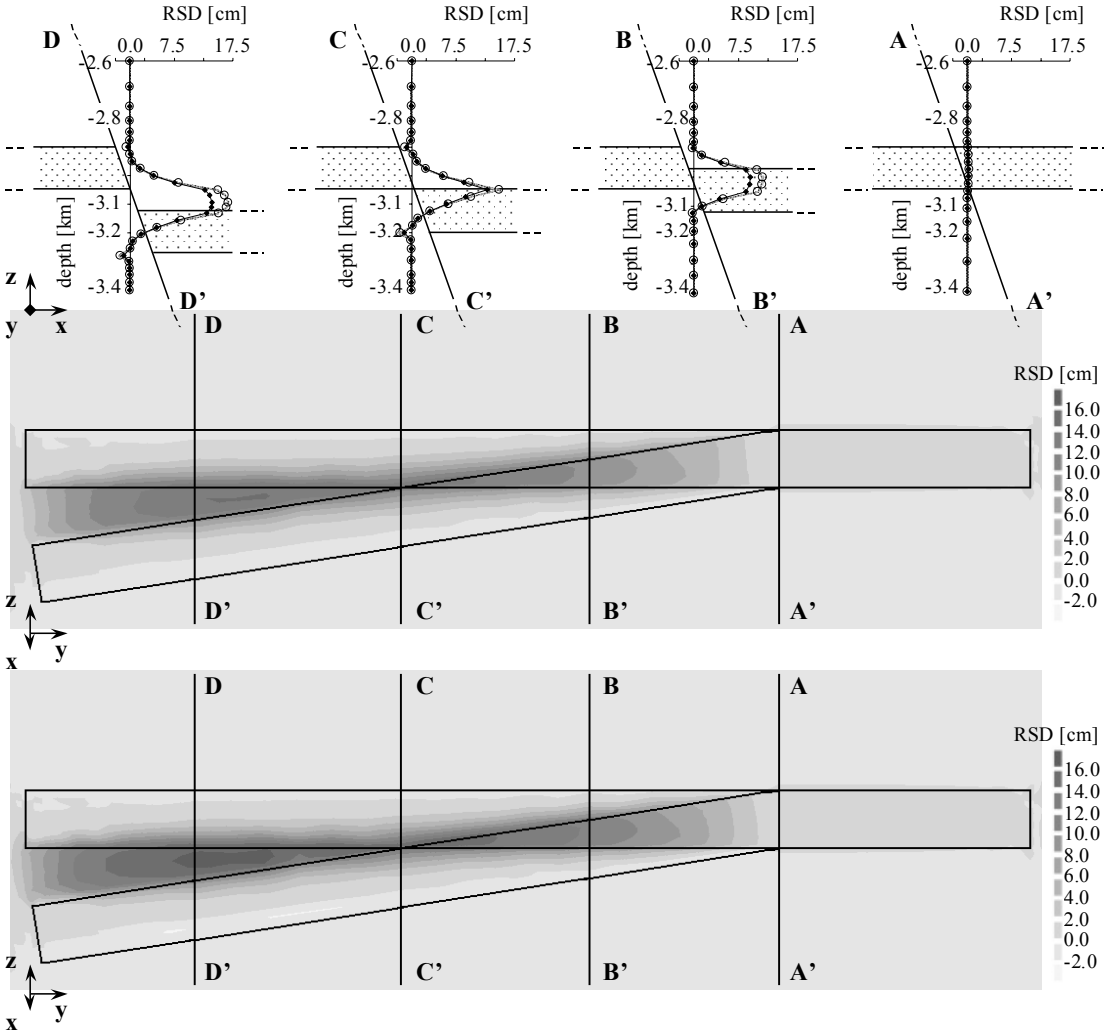

Figure 11.24. Calculated RSD-values on the fault plane for model 'throw_var' with surrounding rock being stiffer than the reservoir rock and initial reservoir overpressure (see Table 11.1). The upper and lower contour plots are for a hydrostatic (10 depletion steps) and full (11 steps) pore pressure reduction, respectively. Hydrostatic and full depletion is marked in the RSD-graphs by solid and open dots, respectively. Maximum normal fault slip amounts 14.2 and 16.7 cm, respectively, and maximum reverse fault slip 1.6 and 2.3 cm, respectively. View direction of the contour plots is normal to the fault plane. Intersection lines of the two reservoir compartments with the fault plane are shown. View direction of the cross sections is in strike direction of the fault. Dotted areas denote the reservoir compartments. See Appendix 2 for this figure in colour.

Table 11.6. Calculated largest normal and reverse fault slip and seismic moment on the fault as a result of reservoir depletion for different models with surrounding rock being stiffer than the reservoir rock and initial reservoir overpressure (see Table 11.1). Pore pressure reduction is with a hydrostatic amount in 10 depletion steps. The calculation results as presented in Tables 11.5 and 11.6 incorporate the same Δp during depletion and are comparable.

Model name	*Throw [m]*	*Throw/D (D= 150m)*	*RSD_{max} [cm] (largest normal fault slip)*	*RSD_{min} [cm] (largest reverse fault slip)*	*M_0^{normal} [10^{14} Nm]*	*$M_0^{reverse}$ [10^{14} Nm]*
throw_const_0D	0	0	0.1	0.0	0.04	-0.04
throw_var AA'	0	0	0.1	0.0		
throw_const_¼D	37.5	¼	6.1	-0.1	1.47	-0.10
throw_const_½D	75	½	10.3	-0.7	2.25	-0.19
throw_var BB'	75	½	9.5	-0.2		
throw_const_¾D	112.5	¾	11.6	-1.2	2.43	-0.21
throw_const_1D	150	1	12.5	-1.4	2.47	-0.25
throw_var CC'	150	1	12.8	-1.3		
throw_const_1¼D	187.5	1¼	13.2	-1.2		
throw_const_1½D	225	1½	13.7	-1.5		
throw_var DD'	231	1½ + $^1/_{25}$	14.0	-1.1		
throw_const_2D	300	2	13.2	-2.0		

Both normal and reverse fault slip are enhanced by the stiffer surrounding rock. This enhancement is illustrated in Figures 11.25 and 11.26, where the development of fault slip with depletion of the reservoir is shown for the two different scenario's (equal and stiffer surrounding rock). For the scenario with equal surrounding and reservoir rock properties (Figure 11.25), fault slip develops very slowly at the beginning of depletion for all observation lines. These steps represent stress paths that are not at failure (see Figures 11.21 and 11.23 for reference). In the first depletion steps, stress paths develop towards the failure line and the fault deforms elastically. When the stress paths reach failure, (plastic) fault slip develops faster. This is marked by an increase of the gradient of the RSD-graphs. Such an increase can be observed in an earlier stage of depletion along observation line CC' than for the lines BB' and DD'. Line CC' corresponds to a reservoir configuration where the top of the hanging wall reservoir compartment is exactly opposite to the bottom of the footwall reservoir compartment (see Figure 11.24). Fault slip develops fastest along observation line DD', due to the almost vertical stress paths in the fault zone in between the two reservoir compartments. The stress path in observation point 4 (Figure 11.21) is an example of this. Development of reverse fault slip and strike slip on the fault are negligible small for the current scenario with equal reservoir and surrounding rock properties. Surrounding rock stiffer than the reservoir rock can enhance both normal and reverse fault slip (Chapter 11.2). For the modelled conditions (E^{sur} = 18.5 GPa, ν^{sur} = 0.25), plastic normal fault slip develops relatively fast from the first depletion step onwards for all three reservoir configurations (Figure 11.26). This is due to the fact that the initial state of stress is at failure for the modelled conditions (see Figure

11.17b for reference), in spite of the initial reservoir overpressure of 35.0 MPa. The steepening of the graphs in the last depletion step results from the fact that the eleventh depletion step incorporates a larger pore pressure drop than the previous ten steps (see Chapter 8.3.4 for a description of the modelling of gas depletion). The siffer surrounding rock causes also plastic reverse fault slip to develop in a later stage of depletion.

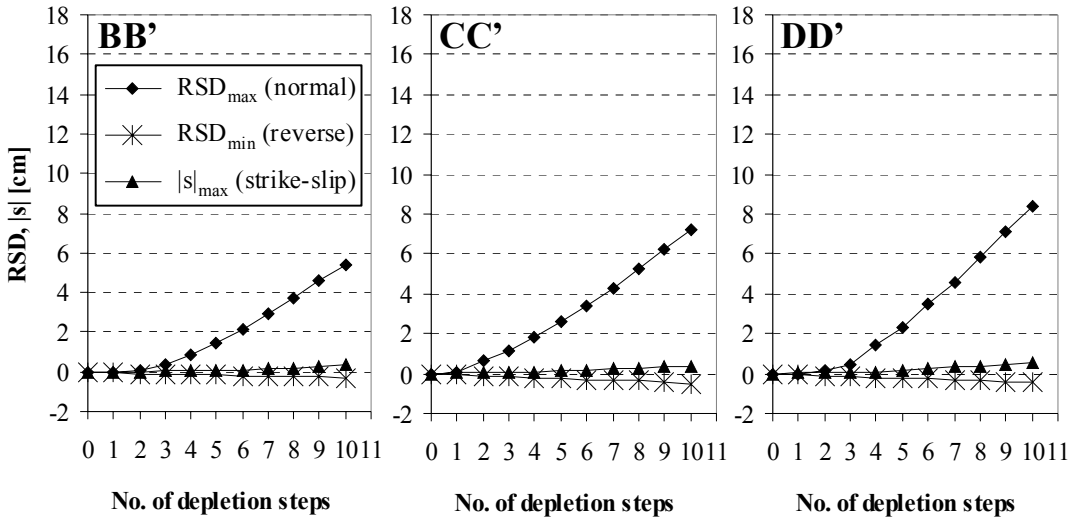

Figure 11.25. Development of fault slip with reservoir depletion for three different observation lines in model 'throw_var' with equal reservoir and surrounding rock properties and initial hydrostatic reservoir pore pressure. Absolute s-values are plotted since these are actually negative at reservoir level (dextral movements), but contribute in the calculations to normal fault slip.

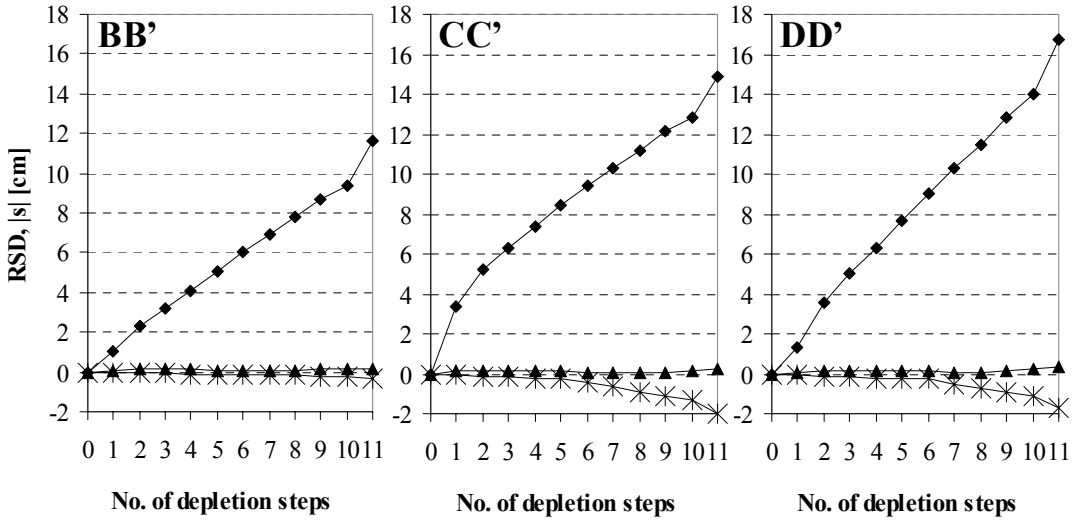

Figure 11.26. Development of fault slip with reservoir depletion for three different observation lines in model 'throw_var' with surrounding rock being stiffer than the reservoir rock and initial reservoir overpressure (see Table 11.1). For legend see Figure 11.25. Absolute s-values are plotted since these are actually negative at reservoir level (dextral movements), but contribute in the calculations to normal fault slip.

Very small values for strike slip are calculated for model 'throw_var' (maximum value: 0.6 cm, see Figures 11.26 and 11.27). They occur along the top of the hanging wall reservoir compartment. They are not observed in the calculations of series 'throw_const_...D' and must therefore be the result of the slope of the hanging wall reservoir compartment. They are not enhanced by the stiffer surrounding rock properties and/or initial reservoir overpresure.

In general the following can be concluded for the given geometry of a steeply dipping normal fault (dip angle 70^{o}) in an extensional stress regime:

- Stiffer surrounding rock (E^{sur} = 18.5 GPa, ν^{sur} = 0.25) enhances both normal and reverse fault slip. This is the case in spite of an initial reservoir overpressure of 35.0 MPa, which basically causes the initial state of stress on the fault plane to be further away from failure.
- Significant reverse fault slip does for the given conditions not develop when the surrounding and reservoir rock properties are equal.
- In terms of seismic moment, configuration BB' is more critical than configuration CC' when the surrounding and reservoir rock properties are equal and the initial pore pressure in both reservoir and surrounding rock is hydrostatic. For the scenario with default rock properties (stiffer surrounding rock and initially slightly overpressured reservoir), configuration CC' is more critical than configuration BB'.
- Configuration CC' is most critical for fault slip at the beginning of gas depletion. In a later stage of depletion, configuration BB' becomes eventually more critical.
- The inclination of the hanging wall reservoir compartment in model 'throw_var' does not cause significant strike slip to develop during depletion.

11.5 Influence of differential pore pressure development due to compartmentalisation on calculated fault slip

11.5.1 Calculation series

In this section, the influence of compartmentalisation on calculated fault slip is analysed. Compartmentalisation occurs when the pore pressure in different reservoir compartments develops differentially. Model 'throw_const_½D' (Figure 11.19a) is used for this purpose. Three different depletion scenario's are considered:

- depletion of both footwall and hanging wall reservoir compartments and fault regions A and B;
- depletion of the footwall reservoir compartment, fault region A and fault region B in contact to the footwall reservoir compartment;
- depletion of the hanging wall reservoir compartment, fault region A and fault region B in contact to the hanging wall reservoir compartment.

During depletion, the pore pressures in the remaining parts are kept at their initial value. Regarding the rock properties and initial reservoir pore pressure, two scenarios are considered (see Table 11.1):

- surrounding rock properties equal to the reservoir rock properties ($E^{sur} = E^{res} =$ 13.0GPa; $\nu^{sur} = \nu^{res} = 0.2$; $\phi^{sur} = \phi^{res} = 30^{o}$) and initial hydrostatic reservoir pore pressure;
- default rock properties ($E^{sur} = 18.5$GPa; $\nu^{sur} = 0.25$; $\phi^{sur} = 25^{o}$) and initial reservoir pore pressure of 35.0 MPa.

11.5.2 Calculation results and discussion

The calculation results are analysed in terms of maximum normal fault slip (RSD_{max}) and reverse fault slip (RSD_{min}). RSD_{max}- and RSD_{min}-values are listed in Table 11.7 for each calculated scenario.

From the calculation results it follows for the given geometrical setting, that normal fault slip is supported by the simultaneous depletion of the two reservoir compartments. Maximum normal fault slip is larger for this case as when only the footwall or the hanging wall compartment is depleted (see Table 11.7 and Figure 11.27). This result is understandable when considering, that downward movement of the top of the hanging wall reservoir compartment and upward movement of the bottom of the footwall compartment both cause normal fault slip. Both movements enhance each other when both reservoir compartments are depleted. Such enhancement is absent in the case of compartmentalisation.

Beside a larger RSD_{max}-value, the normal fault slip occurs over a larger area along the fault plane in case of simultaneous depletion of both reservoir compartments (Figure 11.27). RSD-graphs in the left column, valid for depletion of both reservoir compartments, are much broader than RSD-graphs in the central and right columns (valid for depletion of only the footwall and hanging wall compartment, respectively).

Remarkable is the fact, that in case of footwall depletion only (central column in Figure 11.27), normal fault slip is observed mainly on the part of the fault below the bottom of the footwall reservoir compartment. A similar but reversed observation can be made for the case of hanging wall depletion only (right column in Figure 11.27): normal fault slip is observed mainly above the top of the hanging wall reservoir compartment. For an explanation of these observations, consider the location at the fault corresponding to the top of the hanging wall reservoir compartment for the case that only the hanging wall compartment is depleted. Due to the compaction of the depleting hanging wall reservoir compartment, this is the location where most of the normal fault slip is initiated. The overburden rock at the hanging wall side of the fault follows the reservoir compaction and moves downwards as well. Since the footwall reservoir compartment does not deplete for the considered case, the overburden rock at the footwall side hardly moves vertically. Such differential movement between footwall and hanging wall at the level of the overburden rock causes significant normal fault slip to occur above the reservoir (Figure 11.27, right column). A similar but reversed mechanism occurs at the bottom of the footwall reservoir compartment for the case that only the footwall compartment is depleted. The mechanism is enhanced by a larger pore pressure in the non-depleting part of the fault (compare

Figures 11.27b and c), as could be for instance the case for sealing faults. A larger pore pressure means a lower effective normal stress and an unaltered shear stress on the fault, thus creating more favourable conditions for frictional sliding.

Reverse fault slip is, for the given geometrical setting, supported by reservoir compartmentalisation (see Table 11.7). Consider for instance the cases that the footwall reservoir compartment is depleted. The depletion and reservoir compaction cause the rocks at the top of this compartment to move downwards, leading to reverse fault reactivation at this location. When the hanging wall reservoir compartment is depleted as well, a vertical downward movement of the overburden rocks occurs at the hanging wall side of the fault. This reduces the differential (downward) movement between footwall and hanging wall side of the fault at the level of the top of the footwall reservoir compartment and reduces thus the reverse fault slip. When the hanging wall reservoir compartment is not depleted, the overburden rocks at the hanging wall side of the fault hardly move vertically, enhancing reverse fault slip.

Both normal and reverse fault slip are enhanced by a surrounding rock which is relatively stiff in comparison to the reservoir rock. More explanations on this behaviour can be found in Chapters 11.3 and 11.2. The combination of a relatively stiff surrounding and compartmentalisation can result in relatively large amounts of reverse fault slip. According to the values in Table 11.7, this is the case especially at the top of the footwall reservoir compartment.

Reverse fault slip remains restricted to relatively small zones around the top of the footwall and/or bottom of the hanging wall reservoir compartments. Reverse fault slip along the fault intersecting the overburden/underburden rocks as is the case for normal fault slip in case of compartmentalisation, is for the given geometrical setting not observed.

For the modelled reservoir geometry in an extensional stress regime it can generally be concluded that:

- normal fault slip is supported by the depletion of both reservoir compartments;
- reverse fault slip is supported by reservoir compartmentalisation (differential depletion of foot- and hanging wall);
- in case of depletion of both reservoir compartments, normal fault slip is restricted to the level of the reservoir and does not extend beyond; in case of compartmentalisation, significant normal fault slip can occur along the fault above and below the reservoir; the mechanism is enhanced by a larger pore pressure in the non-depleting part of the fault; the location of reverse fault slip is unaffected by reservoir compartmentalisation and remains restricted to relatively small zones around the top of the footwall and/or bottom of the hanging wall reservoir compartments;
- both normal and reverse fault slip are enhanced by a surrounding rock which is relatively stiff in comparison to the reservoir rock; the combination of a relatively stiff surrounding and compartmentalisation can result in relatively large amounts of reverse fault slip.

Table 11.7. Comparison of calculated RSD-values for different (compartmentalisation) scenario's for the 3D-model 'throw_const_½D'. Observations along line EE'.

Depletion scenario	*Surrounding rock properties**	p_{ini}^{res} **	Δp^{res}	RSD_{max} *[cm] (normal)*	RSD_{min} *[cm] (reverse)*
Footwall and hanging wall	same	hydrostatic	- hydrostatic	6.7	0.4
		overpressure	- hydrostatic	5.2	0.3
			- 35.0 MPa	7.8	0.6
	stiff	hydrostatic	- hydrostatic	11.5	1.1
		overpressure	- hydrostatic	10.3	0.6
			- 35.0 MPa	12.9	1.0
Footwall	same	hydrostatic	- hydrostatic	3.4	0.7
		overpressure	- hydrostatic	4.3	0.5
			- 35.0 MPa	6.0	1.2
	stiff	hydrostatic	- hydrostatic	5.4	2.2
		overpressure	- hydrostatic	5.3	1.7
			- 35.0 MPa	6.6	2.4
Hanging wall	same	hydrostatic	- hydrostatic	3.4	0.6
		overpressure	- hydrostatic	4.2	0.7
			- 35.0 MPa	6.1	1.3
	stiff	hydrostatic	- hydrostatic	5.4	1.7
		overpressure	- hydrostatic	5.3	1.3
			- 35.0 MPa	6.7	1.8

* *relative to reservoir rock properties;*
'same': $E^{sur}=E^{res}=13.0$ GPa, $\nu^{sur}=\nu^{res}=0.2$ and $\phi^{sur}=\phi^{res}=30^o$
'stiff': $E^{sur}=18.5$ GPa, $\nu^{sur}=0.25$ and $\phi^{sur}=25^o$

** *'hydrostatic': p_{ini}^{res} is according to a hydrostatic pore pressure gradient with ρ_{fluid} = 1000 kg/m^3*
'overpressure': p_{ini}^{res} = 35.0 MPa

Initial pore pressure and pore pressure development in fault regions A and B and fault normal- and shear stiffness change accordingly for the different scenarios.

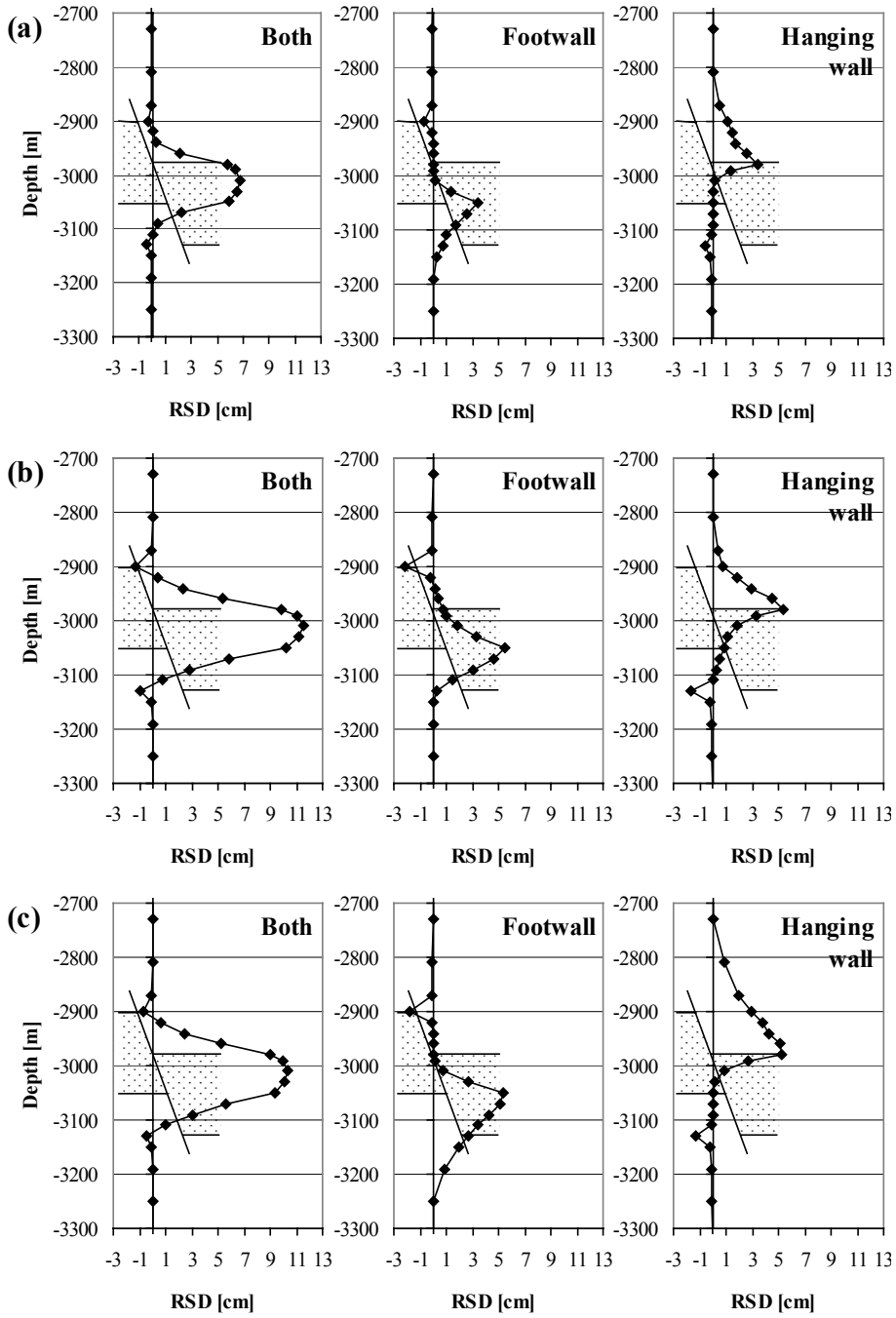

Figure 11.27. Calculated RSD-values along observation line EE' in model 'throw_const_½D' with indication of the depth position of the reservoir for different scenario's (see Table 11.1): (a) equal reservoir and surrounding rock properties and initial hydrostatic reservoir pore pressure; (b) surrounding rock being stiffer than the reservoir rock and initial hydrostatic reservoir pore pressure and (c) surrounding rock being stiffer than the reservoir rock and initial reservoir overpressure. 'Both' indicates depletion of both footwall and hanging wall reservoir compartments, 'Footwall' and 'Hanging wall' indicate depletion of the respective reservoir compartments and adjacent fault regions only. Pore pressure reduction is for all three cases with a hydrostatic amount (10 depletion steps).

11.6 Influence of a 3D (an)isotropic initial tectonic stress field

In this section, the influence of a 3D anisotropic initial tectonic stress field on the stress development and slip on a normal fault intersecting a disk-shaped gas reservoir is analysed.

As outlined in Chapter 3.2, a 3-dimensional stress field in the subsurface can be described by the three stress components σ'_v, σ'_H and σ'_h, where σ'_v is the vertical effective stress, σ'_H is the maximum horizontal effective stress and σ'_h is the minimum horizontal effective stress. Horizontal and vertical stresses are related via the effective stress ratio's K_{0H} and K_{0h} according to eqs. (3.8) and (3.9).

The current tectonic stress field in the northern Netherlands is not directly measured, but can be assumed to result mainly from the Tertiary Alpine Orogeny (see Chapter 7.5). Although still under discussion, it is generally assumed that the present-day direction of the largest horizontal stresses in the Netherlands is NW-SE. The vertical stress is generally assumed to be a principal stress as the result of the weight of the rock mass. The magnitude of the two principal horizontal stresses is not known. Based on previous research on geomechanical modelling of gas reservoirs in the northern Netherlands and personal communication with TNO-NITG (2000), the following values are reasonable estimations: $K_{0H} = 1.0$ and $K_{0h} = 0.4$ (see also Chapter 7.5). It has to be mentioned here that the horizontal stress magnitudes are very difficult to estimate and that they are very sensitive to local variations due to geological structures in the subsurface.

First, the influence of K_0 on stress development and fault slip is studied in Chapter 11.6.1 for an isotropic tectonic stress field with $K_0 = K_{0H} = K_{0h}$. Model 'throw_var' is used for this purpose since this model incorporates a varying throw between the two reservoir compartments and is very representative for existing reservoir geometries occurring in the northern Netherlands. The subsequent chapters deal with 3D anisotropic initial tectonic stress fields. A theoretical description of initial stress field parameters in relation to the 3D-finite element models is given in Chapter 11.6.2. Based on this theoretical description, the influence of anisotropic initial tectonic stress fields is analysed in Chapters 11.6.3 and 11.6.4. Chapter 11.6.3 deals with the relatively simple model 'throw_const_½D' with simplifying assumptions on rock properties and initial reservoir pore pressure, in order to obtain good insight in the implications of anisotropic initial tectonic stress fields on stress development and fault slip during reservoir depletion. Model 'throw_var' is more representative for existing reservoir geometries occurring in the northern Netherlands. This model is used for calculations with realistic rock property- and initial pore pressure values as a kind of case study in Chapter 11.6.4.

11.6.1 Influence of an isotropic initial tectonic stress field

In order to obtain insight in the influence of K_0 on stress development and fault slip, a calculation series is performed for an isotropic tectonic stress field with $K_0 = K_{0H} = K_{0h}$. Model 'throw_var' is used for this purpose since this model is very representative for existing reservoir geometries occurring in the northern Netherlands. Rock properties and initial pore pressure are chosen to represent the situation in the field and are as listed in Table 11.1 for default values (E^{sur} = 18.5 GPa; ν^{sur} = 0.25; ϕ^{sur} = 25^o) and initial reservoir pore pressure of 35.0 MPa. Four calculations are performed with K_0 = 0.40, 0.60, 1.00 and 1.67.

Stress paths along observation line DD' (see Figure 11.19b for configuration) are plotted in Figure 11.28 for different K_0-values. The failure line of the fault with c^f = 0 Pa and ϕ^f = 28^o is indicated. The dotted lines in Figure 11.28 indicate the theoretically possible combinations of τ and σ'_n on the fault plane according to eqs. (3.2a) and (3.2b), for the case that the vertical stress is principal. As outlined in Chapters 11.2 and 11.3, spatial variation in rock stiffness and pore pressure can cause the principal stress to deviate from a vertical direction. Initial states of stress on the fault plane in Figure 11.28 deviate therefore from the graph representing the analytically calculated initial states of stress.

From the calculation results it follows, that the K_0-values only influence the initial states of stress but not the stress development. Differences between stress paths at the same location for different K_0-values, such as the stress path at the top of the hanging wall reservoir compartment for K_0 = 0.60 and 1.00, result from the fact that failure is reached in one case whereas the other case stays elastic. This affects neighbouring stress paths, for instance the stress path directly above this location. The initial states of stress in different location on the fault plane vary with varying K_0-values, but their position relative to each other remain unchanged, as long as their position is not on the failure line. The same result was found by Glab (2001) for 2D plane strain models.

Calculated RSD-values along the four observation lines AA', BB', CC' and DD' are plotted in Figure 11.29 for different K_0-values. It is obvious that for small values of K_0, RSD-values are relatively large. The initial state of stress on the fault plane is closer to failure. Furthermore, the fault has most freedom to move (extend) since the horizontal effective stresses are relatively low (more extensional).

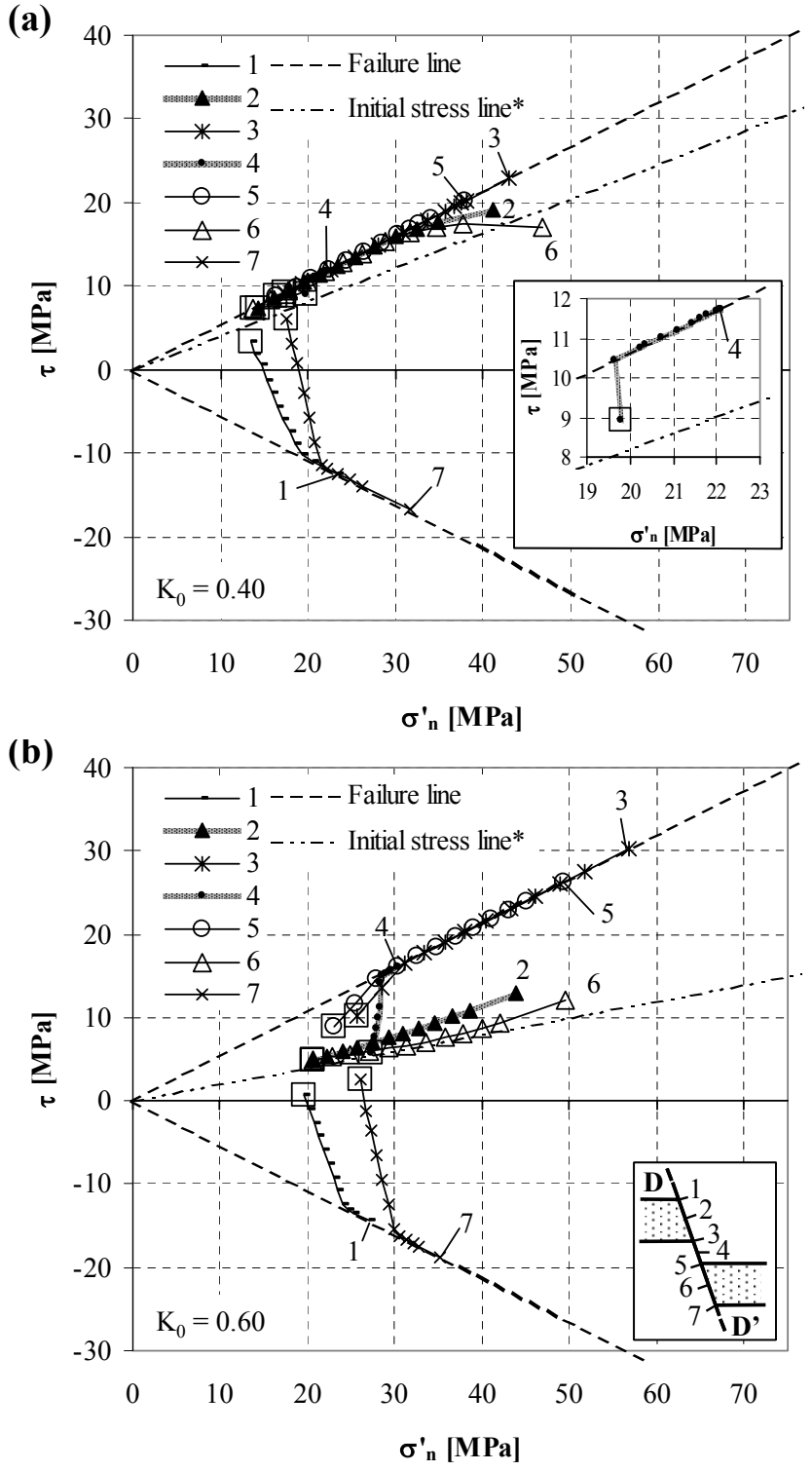

Figure 11.28. Calculated stress paths for (a) K_0 = 0.40 and (b) K_0 = 0.60 for different observation points along line DD' for model 'throw_var' with surrounding rock properties being stiffer as reservoir rock properties and initial reservoir overpressure of 35.0 MPa (see Table 11.1). The initial state of stress is marked by an open square. The end of the stress paths are marked by the respective observation point number.
** The 'initial stress line' is calculated according to eqs. (3.2a) and (3.2b), chapter 3.1.*

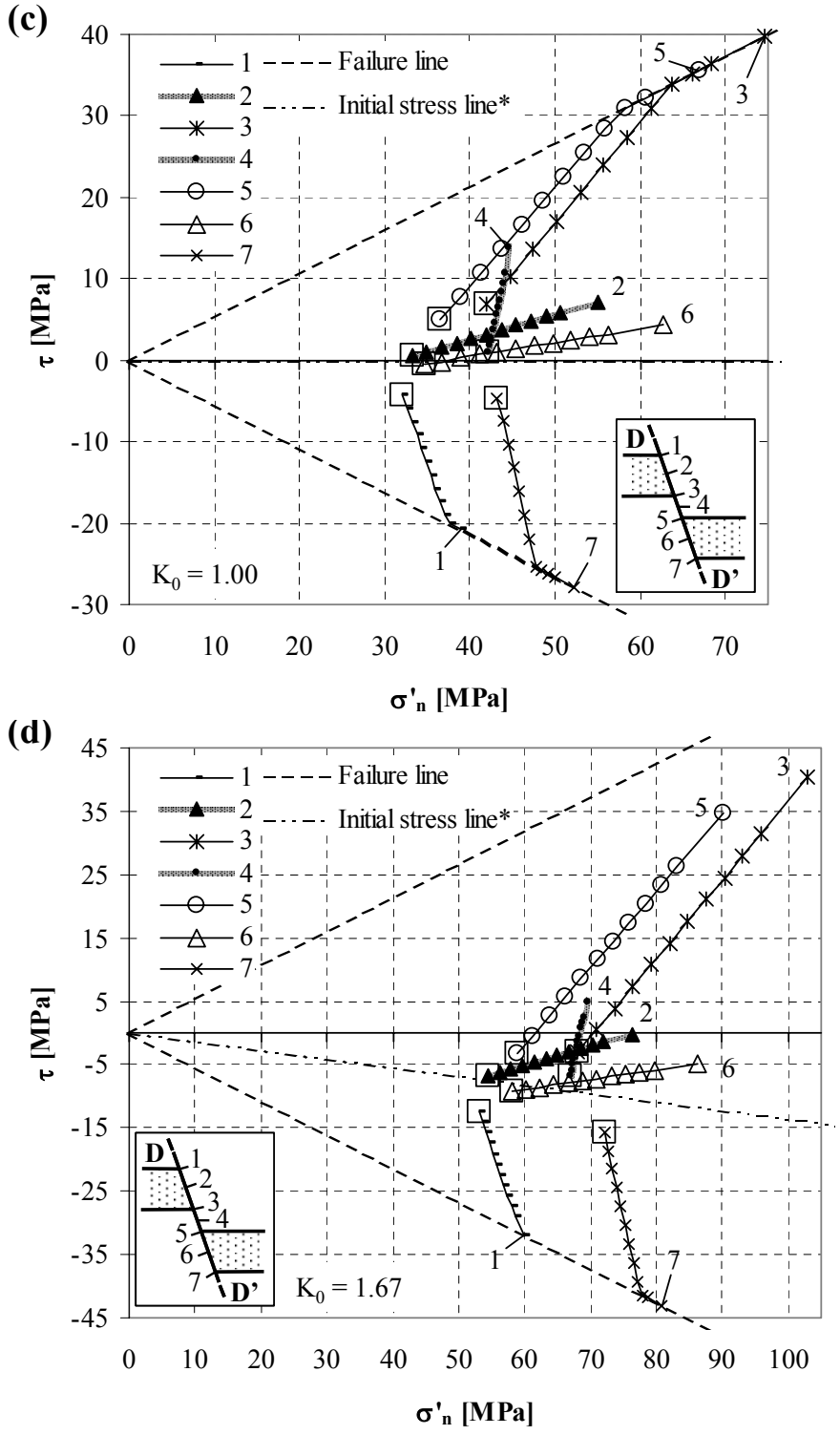

Figure 11.28. Calculated stress paths for (c) K_0 = 1.00 and (b) K_0 = 1.67 for different observation points along line DD' for model 'throw_var'. For further explanations see Figures 11.28 a and b.

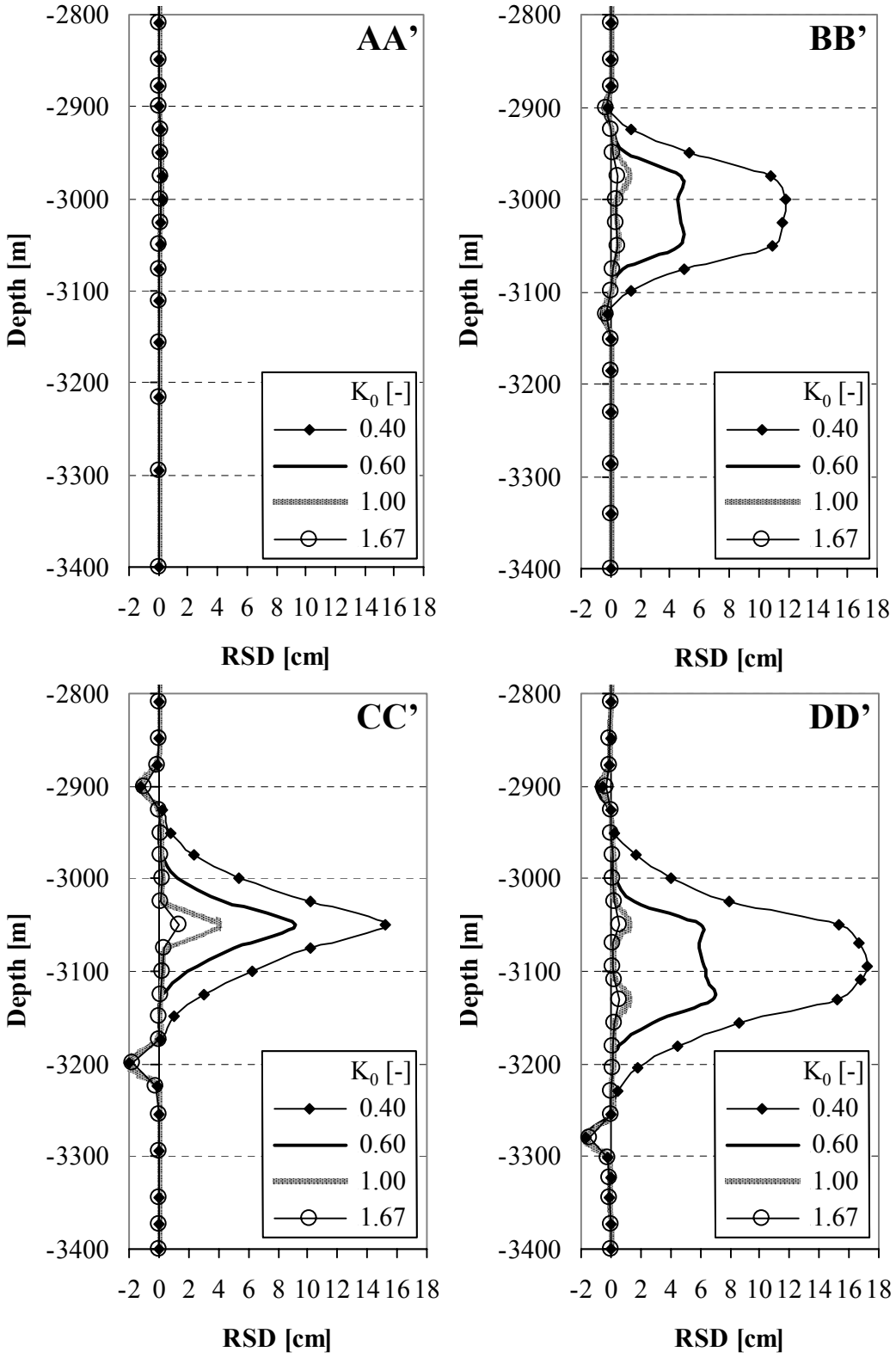

Figure 11.29. Calculated RSD-values along different observation lines in model 'throw_var' for different K_0-values. Surrounding rock is stiffer than reservoir rock and an initial reservoir overpressure of 35.0 MPa is applied (see Table 11.1). Graphs are valid for complete depletion of the reservoir (11 depletion steps).

11.6.2 Theoretical description of initial stress field parameters in relation to the 3D-finite element models

This sections gives a theoretical description of initial stress field parameters in relation to the 3D-finite element models. Based on this theoretical description, the influence of anisotropic initial tectonic stress fields is analysed in the subsequent Chapters 11.6.3 and 11.6.4.

As outlined in Chapter 3.2, a 3-dimensional stress field in the subsurface can be described by the three stress components σ'_v, σ'_H and σ'_h, where σ'_v is the vertical effective stress, σ'_H is the maximum horizontal effective stress and σ'_h is the minimum horizontal effective stress. Horizontal and vertical stresses are related via the effective stress ratio's K_{0H} and K_{0h} according to eqs. (3.8) and (3.9):

$$K_{0H} = \frac{\sigma'_H}{\sigma'_v},$$

$$K_{0h} = \frac{\sigma'_h}{\sigma'_v}.$$

In the case that $K_{0H} \neq K_{0h}$, the stress field is said to be anisotropic. For $K_{0H} = K_{0h} = K_0$, the horizontal stress are equal and an isotropic stress field applies.

Consider the three effective stresses σ'_v, σ'_H and σ'_h in Figure 11.30 and the fault plane with dip angle β in the x,y,z-co-ordinate system as it is defined in the 3D-finite element models in this dissertation. The direction of the two horizontal stress components σ'_H and σ'_h is defined with respect to the fault plane by angle λ. The latter is the clockwise angle between the strike direction of the fault plane and the direction of σ'_H. $\lambda = 0^o$ and 90^o mean a direction of σ'_H parallel and perpendicular to the strike of the fault plane, respectively.

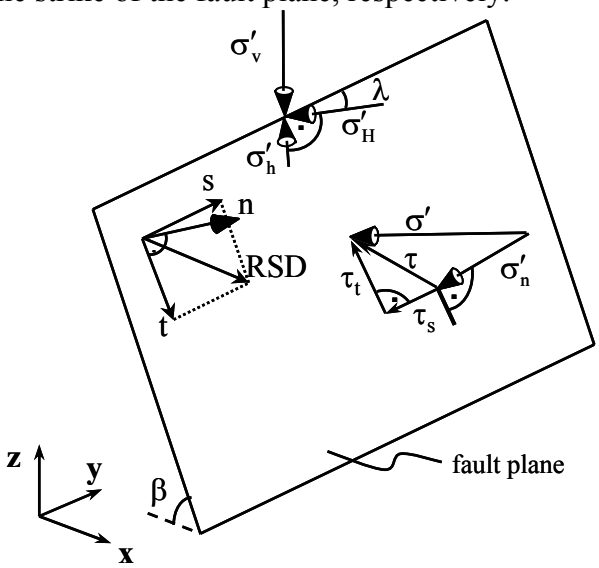

Figure 11.30. Definition of stress directions with respect to the fault plane. For reference, the relative displacement vector components s, t and n are shown.

Assume now that the vertical (effective) stress and thus σ'_H and σ'_h are principal stresses. The effective normal stresses σ'_n and shear stresses τ on the fault plane depend then solely on the magnitude and direction of the three effective principal stress components and are therewith a function of σ'_v, σ'_H, σ'_h and λ. In the following these functions are analytically derived. The initial states of stress on the fault plane calculated in the numerical FE-models can then be compared to the analytical calculated effective normal- and shear stresses.

Vertical stress magnitudes are a function of depth due to the weight of the overburden rock (see Chapter 3.2). Because the initial horizontal effective stresses are a function of the vertical effective stress via K_{0H} and K_{0h}, effective normal- and shear stresses can be normalised and expressed in terms of σ'_v. Hence, the stress variation with depth can be avoided. This is explained in the following.

The global xyz-co-ordinate system in the finite element models is defined with respect to the fault: the x-axis is oriented in the azimuth of the fault, the y-axis is directed in the strike direction of the fault and the z-axis is vertical (Figure 11.30). For reference, the relative displacement vector components s, t and n are shown. n is normal to the fault plane, s is in the strike direction and t is in the down-dip direction of the fault plane (Figure 11.30). Firstly, σ'_x, σ'_y and σ'_z are calculated as a function of σ'_v, σ'_H and σ'_h. Subsequently, the contributions of σ'_x, σ'_y and σ'_z to effective normal stress and shear stress on the fault plane are derived.

Assume now an arbitrary set of two horizontal effective principal stresses in an arbitrary direction defined by λ. From the principal stress components the theoretical stress components for the x- and y-directions can be derived from force equilibrium:

$$\sigma'_x = \tfrac{1}{2}(\sigma'_H + \sigma'_h) - \tfrac{1}{2}(\sigma'_H - \sigma'_h)\cos 2\lambda\,, \tag{11.1}$$

$$\sigma'_y = \tfrac{1}{2}(\sigma'_H + \sigma'_h) + \tfrac{1}{2}(\sigma'_H - \sigma'_h)\cos 2\lambda \quad \text{and} \tag{11.2}$$

$$\tau_s = \tfrac{1}{2}(\sigma'_H - \sigma'_h)\sin 2\lambda\,. \tag{11.3}$$

τ_s represents the part of the shear stress on the fault plane produced by σ'_H and σ'_h and is directed horizontally in the strike direction of the fault plane. It obviously depends on λ and becomes zero in the case that $\sigma'_H = \sigma'_h$. It follows from the assumption that the vertical stress is a principal stress that

$$\sigma'_z = \sigma'_v\,. \tag{11.4}$$

Since σ'_y is directed parallel to the strike of the fault plane, this stress component does theoretically not contribute to the effective normal and shear stress on the fault. σ'_x and σ'_z contribute to a normal effective stress component (σ'_n) and the shear stress component in down-dip direction (τ_t). σ'_n and τ_t depend on σ'_x and σ'_z according to force equilibrium:

$$\sigma'_n = \tfrac{1}{2}(\sigma'_z + \sigma'_x) + \tfrac{1}{2}(\sigma'_z - \sigma'_x)\cos 2\beta \quad \text{and} \tag{11.5}$$

$$\tau_t = \tfrac{1}{2}(\sigma'_z - \sigma'_x)\sin 2\beta\,. \tag{11.6}$$

This is virtually the same as obtained earlier in Chapter 3, eqs. (3.2a) and (3.2b). The total shear stress on the fault plane is then:

$$\tau = \sqrt{\tau_t^{\,2} + \tau_s^{\,2}}\,. \tag{11.7}$$

By implementing the definitions of K_{0H} and K_{0h} into eqs. (11.1) – (11.6), we can normalise the stress tensor in the xyz-co-ordinate system for σ'_v and express it as a function of K_{0H}, K_{0h}, λ and β:

$$\sigma'_x/\sigma'_v = \tfrac{1}{2}(K_{0H} + K_{0h}) - \tfrac{1}{2}(K_{0H} - K_{0h})\cos 2\lambda\,; \tag{11.8}$$

$$\sigma'_y/\sigma'_v = \tfrac{1}{2}(K_{0H} + K_{0h}) + \tfrac{1}{2}(K_{0H} - K_{0h})\cos 2\lambda\,; \tag{11.9}$$

$$\sigma'_z/\sigma'_v = 1\,; \tag{11.10}$$

$$\tau_s/\sigma'_v = \tfrac{1}{2}(K_{0H} - K_{0h})\sin 2\lambda\,; \tag{11.11}$$

$$\tau_t/\sigma'_v = \tfrac{1}{4}[2 - K_{0h}(1 + \cos 2\lambda) - K_{0H}(1 - \cos 2\lambda)]\sin 2\beta\,. \tag{11.12}$$

σ'_n/σ'_v can then be calculated by implementing eqs. (11.8) and (11.10) into (11.5) or according to:

$$\sigma'_n/\sigma'_v = \tfrac{1}{2}(1 + \cos 2\beta) + \tfrac{1}{4}(1 - \cos 2\beta)[K_{0H}(1 - \cos 2\lambda) + K_{0h}(1 + \cos 2\lambda)]. \tag{11.13}$$

τ/σ'_v can be calculated by implementing eqs. (11.11) and (11.12) into (11.7):

$$\tau/\sigma'_v = \sqrt{\left(\tau_t/\sigma'_v\right)^2 + \left(\tau_s/\sigma'_v\right)^2}\,. \tag{11.14}$$

Table 11.8 presents the normalised values of σ'_x, σ'_y, τ_t, τ_s, σ'_n and τ as a function of λ, for $K_{0H} = 1.0$ and $K_{0h} = 0.4$ with $\beta = 70^o$. These values are chosen based on the tectonic stress field analysis (see Chapters 7.5 and 11.6). Figure 11.31 shows the normalised shear stresses τ_t, τ_s and τ versus the normalised effective normal stress on the fault plane for different values of λ for $K_{0H} = 1.00$ and $K_{0h} = 0.40$. A Mohr-Coulomb failure line for $c^f = 0$ Pa and $\phi^f = 28^o$ is plotted for comparison.

Table 11.8. Normalised values of σ'_x, σ'_y, τ_t, τ_s, σ'_n and τ and MSC as a function of λ, for $K_{0H} = 1.00$, $K_{0h} = 0.40$ and $\beta = 70^o$.

λ [^{o}]	σ'_x/σ'_v	σ'_y/σ'_v	τ_s/σ'_v	τ_t/σ'_v	τ/σ'_v	σ'_n/σ'_v	MSC
0	0.400	1.000	0.000	0.193	0.193	0.470	0.814
31	0.559	0.841	0.265	0.142	0.301	0.611	0.942
45	0.700	0.700	0.300	0.096	0.315	0.735	0.842
59	0.841	0.559	0.265	0.051	0.270	0.859	0.650
90	1.000	0.400	0.000	0.000	0.000	1.000	0.000

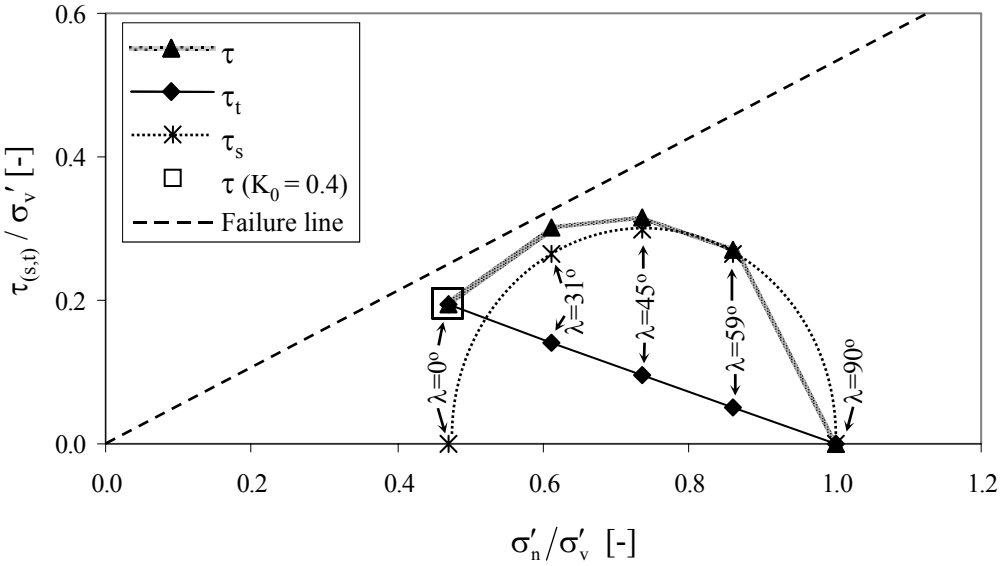

Figure 11.31. Normalised shear stresses τ_t, τ_s and τ versus normalised normal effective stress σ'_n for different values of λ, for $K_{0H} = 1.0$ and $K_{0h} = 0.4$. The open square denotes the initial state of stress for $K_{0H} = K_{0H} = 0.4$, which is independent of λ. A Mohr-Coulomb failure line for $c^f = 0$ Pa and $\phi^f = 28^o$ is plotted for comparison.

In case of isotropic principal horizontal stresses ($\sigma'_H = \sigma'_h$), the term ($K_{0H} - K_{0h}$) in eq. (11.11) vanishes and thus $\tau_s = 0$. Horizontal stresses are equal in all directions and are thus independent of angle λ, which becomes clear when inserting $\sigma'_H = \sigma'_h$ in eqs. (11.1) and (11.2). Inserting $K_{0H} = K_{0h} = K_0$ into eqs. (11.12) and (11.13) leads to a vanishing of all terms with λ. The open square in Figure 11.11 denotes the initial state of stress for $K_{0H} = K_{0h} = 0.4$, which is indeed independent of λ. The normalised values of σ'_x, σ'_y, τ_t, τ_s, σ'_n and τ are the same as for $\lambda = 0^o$ in Table 11.8, with the exception that $\sigma'_y / \sigma'_v = 0.400$.

Consider now the case of anisotropic principal horizontal stresses ($\sigma'_H \neq \sigma'_h$). For $\lambda = 0^o$, σ'_y is equal to σ'_H and σ'_x is equal to σ'_h. This is the other way around for $\lambda = 90^o$: in this case $\sigma'_x = \sigma'_H$. Since the strike direction of the fault is a principal stress direction for these two cases, the horizontal shear stress component τ_s is zero (see Table 11.8 and Figure 11.31). τ_s is at its maximum for $\lambda = 45^o$. As λ increases from 0^o to 90^o, σ'_H becomes directed more perpendicular to the strike direction of the fault and contributes more to the stress component σ'_x. The effective normal stress therefore increases with increasing λ. The dependency of τ_s and σ'_n on λ is given by a 'squeezed' Mohr's circle (Figure 11.31). The combination of τ_s and σ'_n closest to yielding occurs for a value of λ equal to $45^o - \frac{1}{2}\phi^f$, where ϕ^f is the friction angle of the fault. For the chosen value for ϕ^f in our calculations of 28^o, this means for $\lambda = 31^o$.

In the foregoing it is explained that σ'_x and σ'_n increase as λ increases from 0^o to 90^o. Normalised values for σ'_z remain constant at the value of 1.0. Looking at eq. (11.6) indicates that τ_t decreases. From Figure 11.31 it follows that the decrease of τ_t and the

increase of σ'_n are almost linearly proportional. For $\lambda = 90^o$ and $K_{0H} = 1.0$, σ'_x becomes equal to σ'_z and thus $\tau_t = 0$.

Combination of τ_s and τ_t according to eq. (11.7) leads to the τ / σ'_n -graph as shown in Figure 11.31. For the given conditions ($K_{0H} = 1.0$, $K_{0h} = 0.4$, $\beta = 70^o$ and $\phi^f = 28^o$) the initial state of stress is closest to failure for $\lambda = 31^o$ (Figure 11.31). The MSC-value is 0.942 in this case (Table 11.8). The initial states of stress are also rather critical for $\lambda = 45^o$ and 0^o (MSC-values of 0.842 and 0.814, respectively). For $\lambda = 59^o$ and 90^o the criticalness decreases drastically with MSC-values of 0.650 and 0.0, respectively.

For most combinations of K_{0H}, K_{0h} and β, the most critical angle for λ in terms of initial state of stress is $45^o - \frac{1}{2}\phi^f$. However, this is not always the case. For little differences between K_{0H} and K_{0h}, the shear stresses in strike direction of the fault (τ_s) become small and the shear stresses in down-dip direction of the fault (τ_t) play a more dominant role. This is especially the case for large differences between the vertical and horizontal effective stresses (i.e. relatively large or small values of K_{0H} and K_{0h}). An example of such condition is shown in Figure 11.32 for $K_{0H} = 0.60$ and $K_{0h} = 0.33$ ($\beta = 70^o$). Note that the shear stresses as calculated by eq. (11.7) are always positive and that the graphs as given in Figures 11.31 and 11.32 only indicate the magnitude of the shear stresses but not their direction.

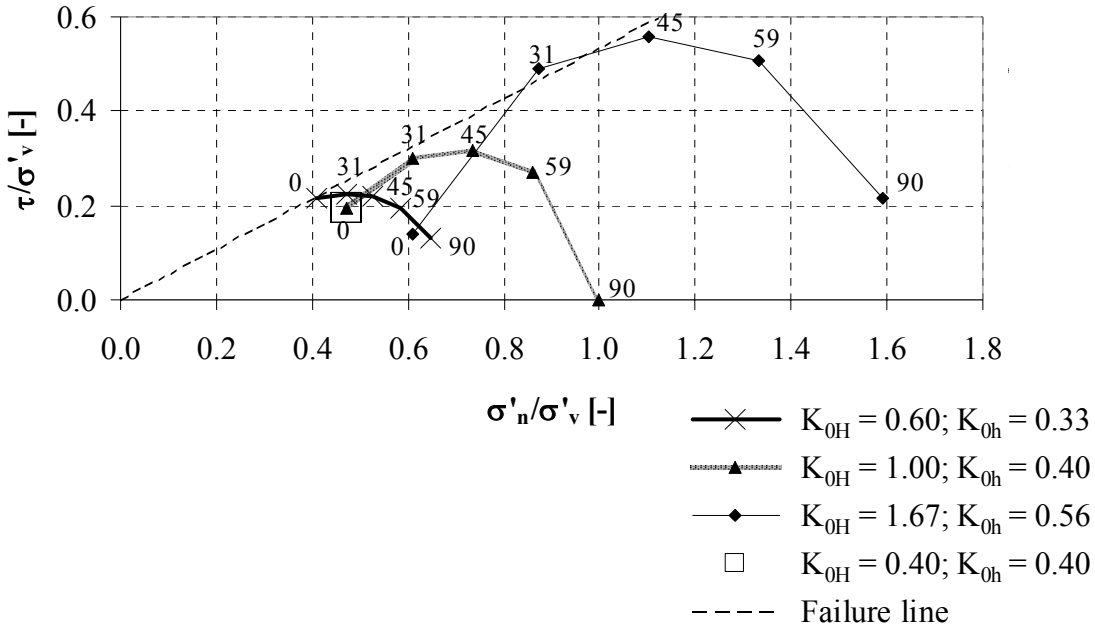

Figure 11.32. Normalised shear stresses τ_t, τ_s and τ versus normalised normal effective stress σ'_n for different values of λ, for different combinations of K_{0H} and K_{0h}. The open square denotes the initial state of stress for $K_{0H} = K_{0H} = 0.4$, which is independent of λ. A Mohr-Coulomb failure line for $c^f = 0$ Pa and $\phi^f = 28^o$ is plotted for comparison. Numbers indicate the values of λ in degrees.

11.6.3 Influence of anisotropic initial tectonic stress field (model 'throw_const_½D')

Based on the theoretical analysis of 3D anisotropic stress fields as described in Chapter 11.6.2, the implications of anisotropic initial tectonic stress fields on stress development and fault slip during reservoir depletion are studied. In order to have no side effects of other parameters, the relatively simple model 'throw_const_½D' is used for this purpose with no discrepancy in rock property values and initial pore pressure between reservoir and surrounding rocks. Rock property values and pore pressures are as listed in Table 11.1 for equal reservoir and surrounding rock properties and initial hydrostatic reservoir pore pressure (appr. 30.0 MPa). For reasons of comparison, calculations with surrounding rock properties stiffer than the reservoir rock and an initially slightly overpressured reservoir (p_{ini}^{res} = 35.0 MPa) are performed as well (see Table 11.1).

A calculation series with K_{0H} = 1.00 and K_{0h} = 0.40 is performed for five different values of λ: 0, 31, 45, 59 and 90°. The values of K_{0H} and K_{0h} are based on the tectonic stress field analysis (see Chapters 7.5 and 11.6). The values of λ are chosen based on the most critical combination of τ_s and σ'_n with $\tau_s = 45^o - ½\phi^f$. For $\phi^f = 28^o$ this results in $\lambda = 31^o$. The value of 59° is equal to $45^o + ½\phi^f$. The Groningen and Annerveen gas fields in the northern Netherlands are characterised by numerous faults at reservoir level with different strike directions, varying from N-S via NW-SE to W-E (see Chapter 7.4). NE-SW trending faults are virtually absent. Assuming that the present-day direction of the largest horizontal stresses in the Netherlands is NW-SE (see Chapters 7.5 and 11.6), this means λ-values ranging from 0° to 45°. Note that not all fault strike directions are present throughout the entire fields. Rather certain parts of the fields are characterised by certain fault patterns.

In Figure 11.33, calculated stress paths for different values of λ are plotted for different locations on the fault plane along observation line EE'. Open squares denote the initial states of stress. The theoretical trend of the initial state of stress state as shown in Figure 11.31 is visible in the stress path plots.

For the given K_{0H}- and K_{0h}-values of 1.00 and 0.40, respectively, the initial states of stress for $\lambda = 0^o$ and 31° are more critical than for the other values of λ: they are relatively close to failure before gas depletion starts. The stress development during gas depletion is most critical for $\lambda = 0^o$. The stress paths for $\lambda = 0^o$ develop in straight lines towards the failure line right from the first depletion step, with relatively large and more or less constant magnitudes per depletion step (Figure 11.33, observation points 6 and 7). The stress paths for $\lambda = 31^o$ show a hesitation in the first depletion steps: smaller or even negative magnitudes per depletion step and smaller stress path gradients, which increase during the progress of depletion. This is also the case for values of λ of 45° and 59°. Stress paths for $\lambda = 90^o$ in turn develop in straight lines as is the case for $\lambda = 0^o$, but further away from failure.

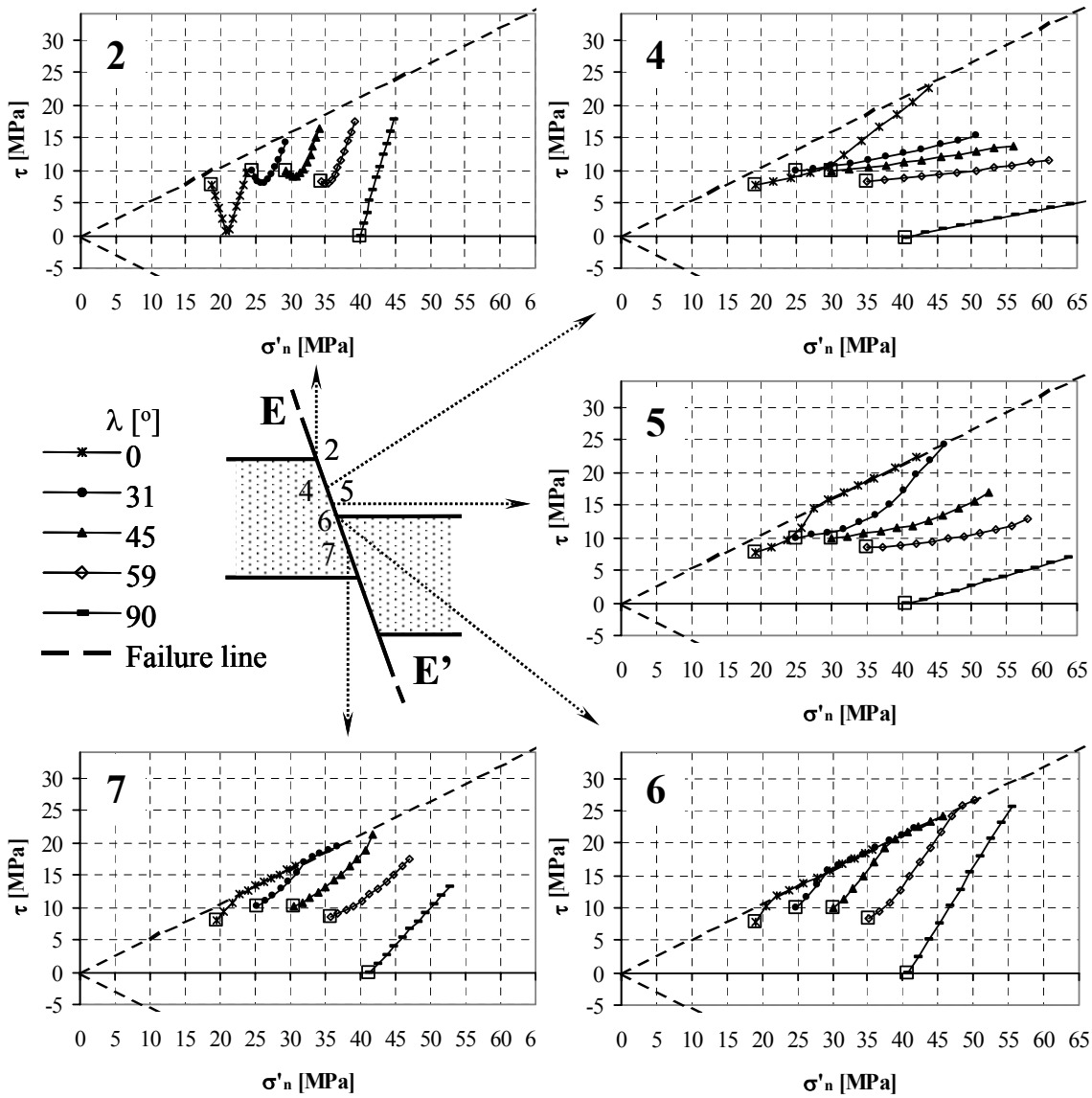

Figure 11.33. Calculated stress paths at different locations on the fault plane along line EE' (see Figure 11.1) for different values of λ with K_{0H} = 1.0 and K_{0h} = 0.4. Model 'throw_var_½D' is used for the calculations with equal surrounding and reservoir rock properties and initial hydrostatic reservoir pore pressure. Open squares denote the initial stress state.

The observation of the smaller stress path magnitudes and gradients in the first depletion steps for $\lambda = 31^o$, 45^o and 59^o and their increase during the progress of depletion can be explained as follows. According to eq. (11.11), initial shear stresses in the strike direction of the fault (τ_s) are zero for $\lambda = 0^o$ and $\lambda = 90^o$. Because of the model geometry, such shear stresses should also not develop during gas production along line EE' since fault movement will be in down dip direction here. This means that for $\lambda = 0^o$ and $\lambda = 90^o$, the initial shear stress vector τ is oriented in the direction of movement initiated by the gas depletion: in the down dip shear direction of the fault. For the other three values of λ (31, 45 and 59^o), the initial shear stress has a relatively large horizontal component τ_s. Consider for example the initial state of stress, as shown in Figure 11.31 for $\lambda = 45^o$. There exists a relatively large initial

shear stress component τ_s in strike direction on the fault plane, whereas the initial shear stress component τ_t in down dip direction of the fault plane is relatively small. The resultant of the two vectors, the initial shear stress τ, is mainly determined by τ_s.

During gas depletion, τ_s hardly changes, whereas τ_t develops relatively fast. This means that during gas depletion, τ_t increasingly determines the size of τ. The stress path shows for the first few depletion steps low gradients and small magnitudes: τ changes initially very little since τ_s mainly determines its magnitude. The stress path represents a curve. In theory, the stress path should run asymptotically towards a straight line with the gradient of the stress path for $\lambda = 0$ or 90^o. The stress paths in Figure 11.33 suggest that this is indeed the case. The described effect of initially slowly developing stress paths should get smaller as the difference between K_{0H} and K_{0h} decreases.

Stress paths for observation point 2 show an initial decrease of shear stresses and an increase in a later stage of depletion. In this location, initial shear stresses in the down-dip direction of the fault (τ_t), which support normal faulting due to the initially extensional stress regime, are built down due to the tendency of reverse fault reactivation in this location (see Chapter 11.1), whereas initial shear stresses in the strike direction of the fault (τ_s) remain more or less constant. When the shear stresses supporting normal faulting are reduced to zero, the minimum in the stress paths for location B corresponds to the shear stress component τ_s. This minimum is indeed located at the σ'_n-axis for $\lambda = 0^o$ ($\tau_s = 0$ MPa). For $\lambda = 90^o$, both τ_s and τ_t are initially zero since $K_{0H} = 1.0$. Further gas depletion causes a shear stress τ_t, supporting reverse faulting, to build up. The magnitude of the total shear stress τ, consisting of the two components τ_s and τ_t, increases again since it is calculated according to eq. (11.7) using a square root. Stress paths could be plotted with negative τ-values after the minimum of the graphs has been reached and shear stress τ_t supporting reverse fault movement start to develop, but this would lead to discontinuous stress paths in Figure 11.33.

In general it can be concluded that failure is reached in a later stage of depletion for larger values of λ. For the chosen reservoir geometry, the initial shear stress component in the strike direction of the fault (τ_s) hardly contributes to a higher sensitivity of the fault plane for reactivation during gas depletion. In fact, the restraining effect of a higher normal stress (σ'_n) on the fault due to a higher horizontal stress in the fault dip direction σ'_x seems to dominate.

This is supported by the RSD-graphs shown in Figure 11.34a and listed in Table 11.9. RSD-values are highest for the case where σ'_H is directed parallel to the strike of the fault plane ($\lambda = 0^o$) and decrease for increasing values of λ. It is obvious that for $\lambda = 0^o$, the fault has most freedom to move: it is a normal fault in a stress regime of triaxial extension, where the axis of extension (smallest horizontal stress direction) is in the fall direction of the fault. Depletion of the reservoir favours extension and thus movement of the fault. For $\lambda = 90^o$, the fault has little freedom to move.

Table 11.9. Calculated maximum and minimum total fault slip (RSD) and strike slip (s) on the fault plane in model 'throw_const_½D' along line EE' (see Figure 11.1) for different values of λ with K_{0H} = 1.0 and K_{0h} = 0.4. Surrounding and reservoir rock properties are equal and the initial reservoir pore pressure is hydrostatic (appr. 30.0 MPa). Pore pressure reduction is with a hydrostatic amount until 0 MPa end pressure in 10 depletion steps.

λ [°]	*RSD_{max} [cm] (normal)*	*$(-s)_{max}$ [cm] (strike slip*)*	*RSD_{min} [cm] (reverse)*	*$(-s)_{min}$ [cm] (strike slip**)*
0	6.8	0.1	-0.4	0.0
31	3.0	1.2	-0.4	0.0
45	1.3	0.3	-0.4	0.0
59	0.7	0.1	-0.4	0.0
90	0.5	0.0	-0.4	0.0

** s-values are listed with the opposite sign, since negative s-values (dextral movements) are observed in regions where normal fault slip is present and positive s-values (sinistral movements) are observed in regions where reverse fault slip is present.*

Table 11.10. Same as Table 11.9, but for surrounding rock stiffer than the reservoir rock with initially slightly overpressured reservoir (35.0 MPa, see Table 11.1). Pore pressure reduction is with a hydrostatic amount in 10 depletion steps. The calculation results as presented in Tables 11.9 and 11.10 incorporate the same Δp during depletion and are comparable.

λ [°]	*RSD_{max} [cm] (normal)*	*$(-s)_{max}$ [cm] (strike slip*)*	*RSD_{min} [cm] (reverse)*	*$(-s)_{min}$ [cm] (strike slip**)*
0	10.4	0.1	-0.7	0.0
31	5.9	2.5	-1.3	-0.6
45	2.8	0.9	-1.3	-0.5
59	1.5	0.3	-1.2	-0.4
90	1.1	0.0	-1.0	0.0

Table 11.11. Same as Table 11.9, but for surrounding rock stiffer than the reservoir rock with initially slightly overpressured reservoir (35.0 MPa, see Table 11.1) and for full reservoir depletion to 0 MPa end pressure (11 depletion steps).

λ [°]	*RSD_{max} [cm] (normal)*	*$(-s)_{max}$ [cm] (strike slip*)*	*RSD_{min} [cm] (reverse)*	*$(-s)_{min}$ [cm] (strike slip**)*
0	13.1	0.1	-1.2	0.0
31	8.2	3.1	-1.8	-0.7
45	4.6	1.6	-1.8	-0.7
59	2.5	0.4	-1.7	-0.4
90	1.6	0.0	-1.5	0.0

For $\lambda = 31^o$, a certain amount of strike-slip is calculated with a maximum value of 1.2 cm (Table 11.9). Strike-slip is also observed to a lesser extent for $\lambda = 45^o$. For all other values of λ, calculated strike-slip is negligible small. In Figure 11.34, the development of maximum fault slip with depletion of the reservoir is shown for $\lambda = 0^o$ and 31^o. As is discussed in Chapter 11.4.2 (Figures 11.25 and 11.26), fault slip develops very slowly at the beginning of depletion since the initial states of stress on the fault plane are not at failure for the modelled conditions. When the stress paths reach failure, fault slip develops faster. For $\lambda = 31^o$, the calculated RSD consists partly of a strike slip component. Since this strike slip component is zero in the first depletion steps it can be concluded that this is not the result of badly consolidated stresses before the start of gas depletion. The relatively large initial shear stresses in the strike direction of the fault plane (τ_s) cause some strike slip to develop during gas depletion.

Calculations with surrounding rock stiffer than the reservoir rock (E^{sur} = 18.5 GPa, ν^{sur} = 0.25, see Table 11.1) and initially slightly overpressured reservoir (p_{ini}^{res} = 35.0 MPa) show similar results for calculated fault slip: normal fault slip is largest for $\lambda = 0^o$ and decreases with increasing values of λ (Figures 11.34b and c and Tables 11.10 and 11.11). The stiffer surrounding rock enhances both normal and reverse fault slip (see Tables 11.9 and 11.10 and Chapter 11.2 for more explanations).

A certain amount of strike slip is calculated for $\lambda = 31^o$, 45^o and 59^o and is largest for $\lambda = 31^o$ (Table 11.10). Strike-slip contributes to both normal and reverse fault slip. Unlike normal fault slip, reverse fault slip is larger for $\lambda = 31^o$, 45^o and 59^o than for $\lambda = 0^o$ and 90^o. This is most probably due to the larger strike slip component.

Based on the calculations in this Chapter 11.6.3 for K_{0H} = 1.00, K_{0h} = 0.40 and $\beta = 70^o$, it can be generally concluded, that:

- the initial state of stress on the fault plane before gas depletion is closest to failure (most critical) for $\lambda = 0^o$ and 31^o; for $\lambda = 31^o$, this is due to a relatively large shear stress component in the strike direction of the fault;
- the stress development on the fault plane is most critical for $\lambda = 0^o$: most fault slip is calculated for this case;
- for some strike slip is observed for $\lambda = 31^o$;
- a relatively stiff surrounding rock enhances both normal and reverse fault slip;
- for a relatively stiff surrounding rock, strike slip could be observed for $\lambda = 31^o$, 45^o and 59^o;
- for a relatively stiff surrounding rock, reverse fault slip is largest for $\lambda = 31^o$, 45^o and 59^o, most probably due to the strike slip component.

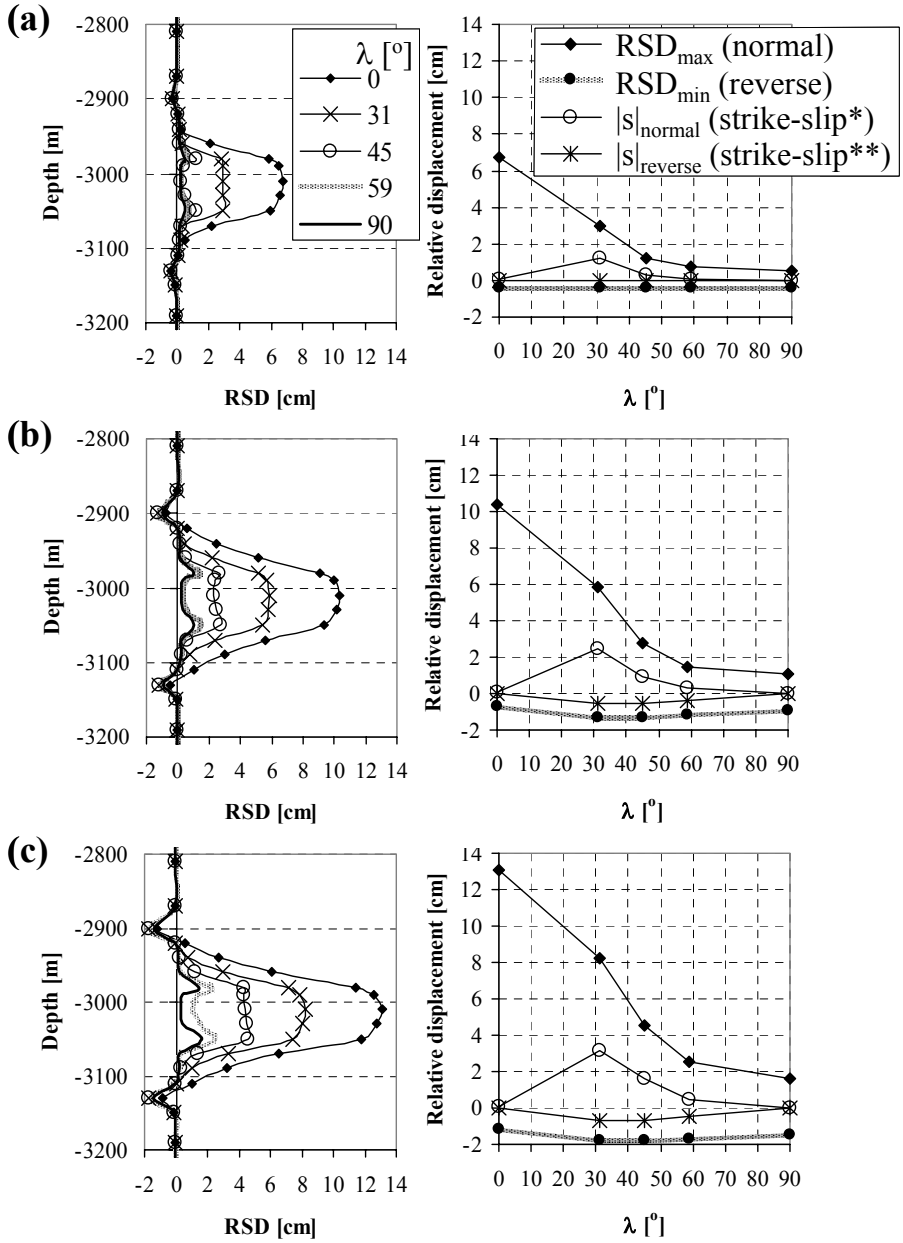

* in the calculations associated to normal fault slip
** in the calculations associated to reverse fault slip

Figure 11.34. Calculated fault slip on the fault plane in model 'throw_const_½D' along line EE' (see Figure 11.1) for different values of λ with K_{0H} = 1.0 and K_{0h} = 0.4. (a) equal surrounding and reservoir rock properties and initial hydrostatic reservoir pore pressure (appr. 30.0 MPa). (b) and (c) same as (a), but for surrounding rock stiffer than the reservoir rock with initially slightly overpressured reservoir (35.0 MPa, see Table 11.1). Pore pressure reduction is for case (b) with a hydrostatic amount (10 depletion steps) and for case (c) for full reservoir depletion to 0 MPa (11 depletion steps). s-values are plotted with the opposite sign since negative s-values (dextral movements) are observed in regions where normal fault slip is present and positive s-values (sinistral movements) are observed in regions where reverse fault slip is present.

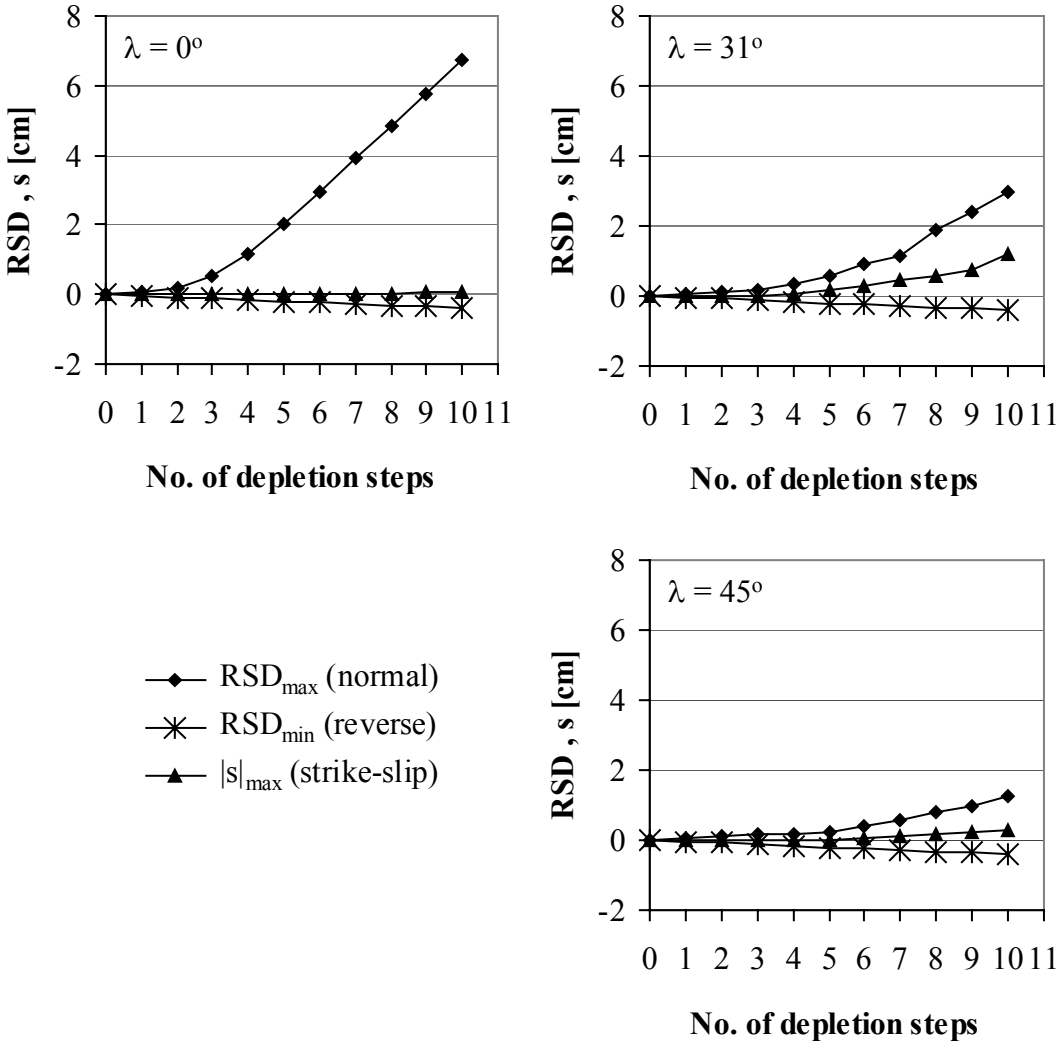

Figure 11.35. Development of fault slip with reservoir depletion for different λ with K_{0H} = 1.0 and K_{0h} = 0.4 for model 'throw_const_½D' with equal reservoir and surrounding rock properties and initial hydrostatic reservoir pore pressure. Absolute s-values are plotted since these are actually negative at reservoir level (dextral movements), but contribute in the calculations to normal fault slip.

11.6.4 Influence of anisotropic initial tectonic stress field (model 'throw_var' with default property and loading conditions)

3D anisotropic stress fields as described in the previous Chapter 11.6.3 are also applied to model 'throw_var' as a kind of case study. Model 'throw_var' is more representative for existing reservoir geometries occurring in the northern Netherlands than model 'throw_const_½D'. Furthermore, it allows an analysis of the effects of a 3D anisotropic stress field on stress development and fault slip for different amounts of throw. The model incorporates surrounding rock properties stiffer than the

reservoir rock and an initially slightly overpressured reservoir (p_{ini}^{res} = 35.0 MPa), see Table 11.1. The reservoir is depleted to an end pressure of 0 MPa (11 depletion steps). A calculation series with K_{0H} = 1.00 and K_{0h} = 0.40 is performed for five different values of λ: 0, 31, 45, 59 and 90°. See Chapter 11.6.3 for the reasons of this choice.
The reservoir geometry and the location of four observation lines AA', BB', CC' and DD' along the fault plane can be seen in Figure 11.19b. Normal fault slip is, for the given reservoir geometry and tectonic stress magnitudes, the dominant mechanism rather than reverse fault slip, especially for lower values of λ (Figure 11.36 and Table 11.12). Normal fault slip decreases for increasing values of λ. This result is similar to the observations for model 'throw_const_½D' in the previous Chapter 11.6.3 (see Figure 11.34) and is due the larger effective stress component in the azimuth of the fault plane for larger values of λ. Normal fault slip generally approaches zero for large values of λ (59° and 90°). An exception occurs for the region along observation line CC' where the top of the hanging wall and the bottom of the footwall reservoir compartments are exactly opposite to each other. Relatively large RSD-values can be observed here also for λ = 90°, but they are concentrated to a relatively sharp peak (Figure 11.36).

Reverse fault slip is observed at the top of the footwall reservoir compartment and the bottom of the hanging wall reservoir compartment, indicated by the negative RSD-values. Unlike normal fault slip, the reverse fault slip does not significantly decrease for increasing values of λ and is present for all values of λ.

For λ = 31°, 45° and 59°, a relatively large strike-slip component (s) contributes to the calculated fault slip (RSD) as well (Table 11.13 and Figure 11.40). Strike-slip contributes to both normal and reverse fault slip. Especially reverse fault slip is affected by strike-slip and is accordingly larger for λ = 31°, 45° and 59°.

Stress paths for different locations on the fault plane are plotted in Figures 11.37 – 11.39. Initial states of stress show patterns similar to the theoretically calculated one as shown in Figure 11.31, Chapter 11.6.2. Deviations are due to the rock property discrepancy between reservoir and surrounding rock and the initially slightly overpressured reservoir. The initial hesitation in stress development as described and explained in Chapter 11.6.3, marked by relatively small stress path gradients and magnitudes per depletion step at the beginning of reservoir depletion, is especially pronounced at location 6 along observation line BB'. The stress path for observation point 2 along observation line CC' develops along the failure line for a large part of the reservoir depletion even for λ = 90°, explaining the relatively large RSD-values observed here even for λ = 90°.

Generally it can be concluded, that the effects as observed for the calculations with model 'throw_const ½ D' in the previous Chapter 11.6.3 also apply for model 'throw_var'. The conclusions as listed at the end of the previous chapter therefore also apply for this chapter.

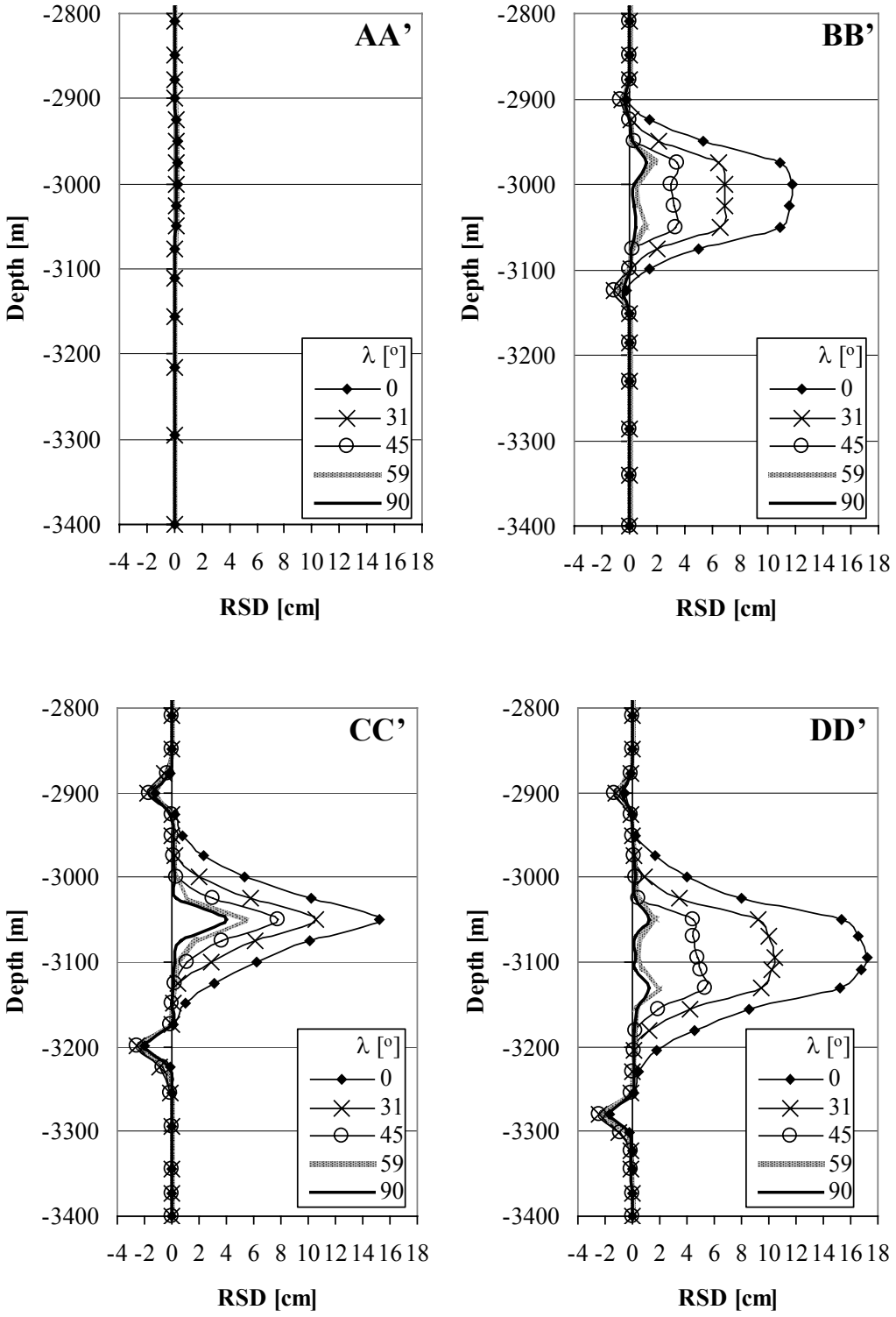

Figure 11.36. Calculated RSD-values along different observation lines in model 'throw_var' for different values for λ with K_{0H} = 1.0 and K_{0h} = 0.4. See Figure 11.19b in Chapter 11.4.1 for reservoir geometry and location of the observation lines on the fault plane. The model incorporates surrounding rock properties stiffer than the reservoir rock and an initially slightly overpressured reservoir, see Table 11.1. The reservoir is depleted to an end pressure of 0 MPa (11 depletion steps).

Table 11.12. Maximum and minimum total fault slip (RSD) in model 'throw_var' as a function of λ with K_{0H} = 1.0 and K_{0h} = 0.4 for surrounding rock properties stiffer than the reservoir rock and an initially slightly overpressured reservoir, see Table 11.1. The reservoir is depleted to an end pressure of 0 MPa (11 depletion steps).

λ [°]	RSD_{max} [cm] (largest normal fault slip) along observation line:				RSD_{min} [cm] (largest reverse fault slip) along observation line:			
	AA'	BB'	CC'	DD'	AA'	BB'	CC'	DD'
0	0.3	11.8	15.2	17.2	0.0	-0.3	-2.0	-1.7
31	0.2	6.9	10.5	10.5	0.0	-1.1	-2.6	-2.4
45	0.2	3.4	7.7	5.3	0.0	-1.1	-2.5	-2.5
59	0.2	1.9	5.5	2.1	0.0	-0.9	-2.2	-2.1
90	0.2	1.2	4.0	1.3	0.0	-0.5	-2.0	-1.7

Table 11.13. Maximum and minimum strike slip (s) in model 'throw_var' as a function of λ with K_{0H} = 1.0 and K_{0h} = 0.4 for surrounding rock properties stiffer than the reservoir rock and an initially slightly overpressured reservoir, see Table 11.1. The reservoir is depleted to an end pressure of 0 MPa (11 depletion steps).

λ [°]	$\|s\|_{max}$ [cm] (largest strike slip associated to normal fault slip) along observation line:				$-\|s\|_{min}$ [cm] (largest strike slip associated to reverse fault slip) along observation line:			
	AA'	BB'	CC'	DD'	AA'	BB'	CC'	DD'
0	0.0	0.4	0.6	0.5	0.0	0.0	-0.1	-0.3
31	0.0	2.3	2.2	4.3	0.0	-0.6	-1.1	-1.3
45	0.0	1.0	1.3	2.0	0.0	-0.6	-1.0	-1.2
59	0.0	0.3	0.6	0.3	0.0	-0.3	-0.7	-0.8
90	0.0	0.1	0.2	0.2	0.0	-0.1	-0.1	-0.2

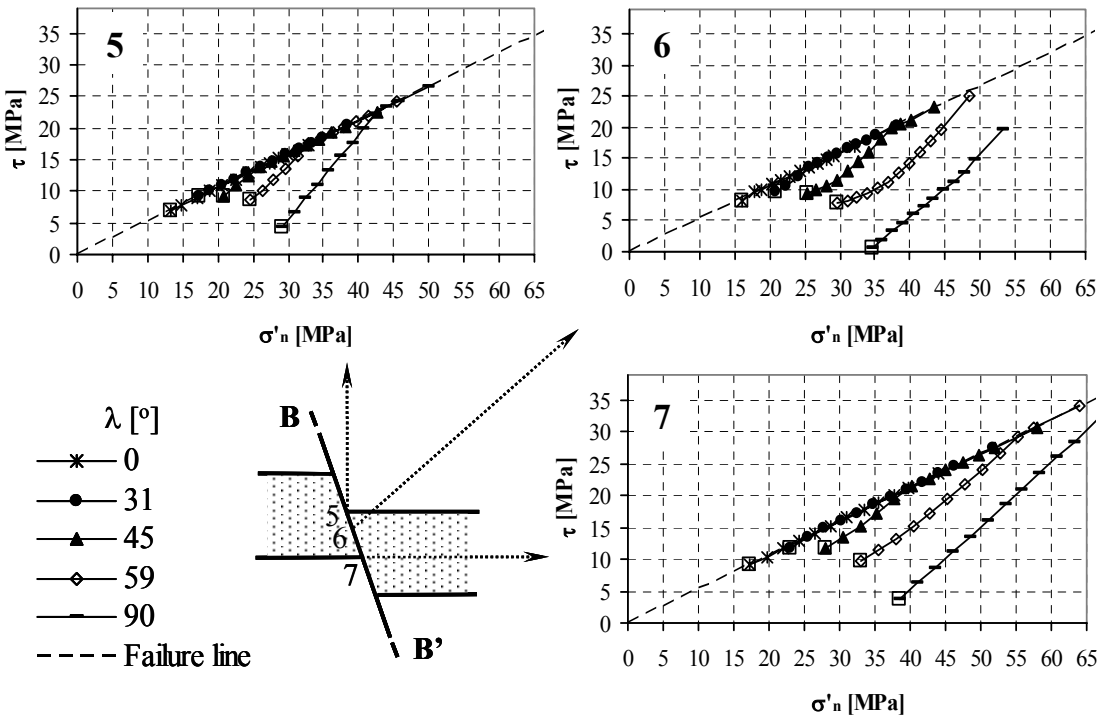

Figure 11.37. Calculated stress paths for model 'throw_var' at different locations on the fault plane along line BB' (see Figure 11.1) for different values of λ with K_{0H} = 1.0 and K_{0h} = 0.4. Calculations are performed with surrounding rock stiffer than the reservoir rock and initial reservoir overpressure (see Table 11.1). Open squares denote the initial stress state.

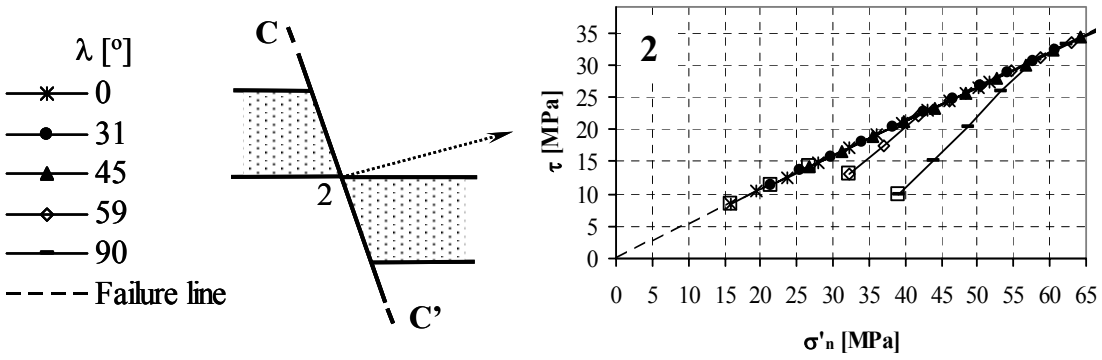

Figure 11.38. Calculated stress paths for model 'throw_var' at different locations on the fault plane along line CC' (see Figure 11.1) for different values of λ with K_{0H} = 1.0 and K_{0h} = 0.4. Calculations are performed with surrounding rock stiffer than the reservoir rock and initial reservoir overpressure (see Table 11.1). Open squares denote the initial stress state.

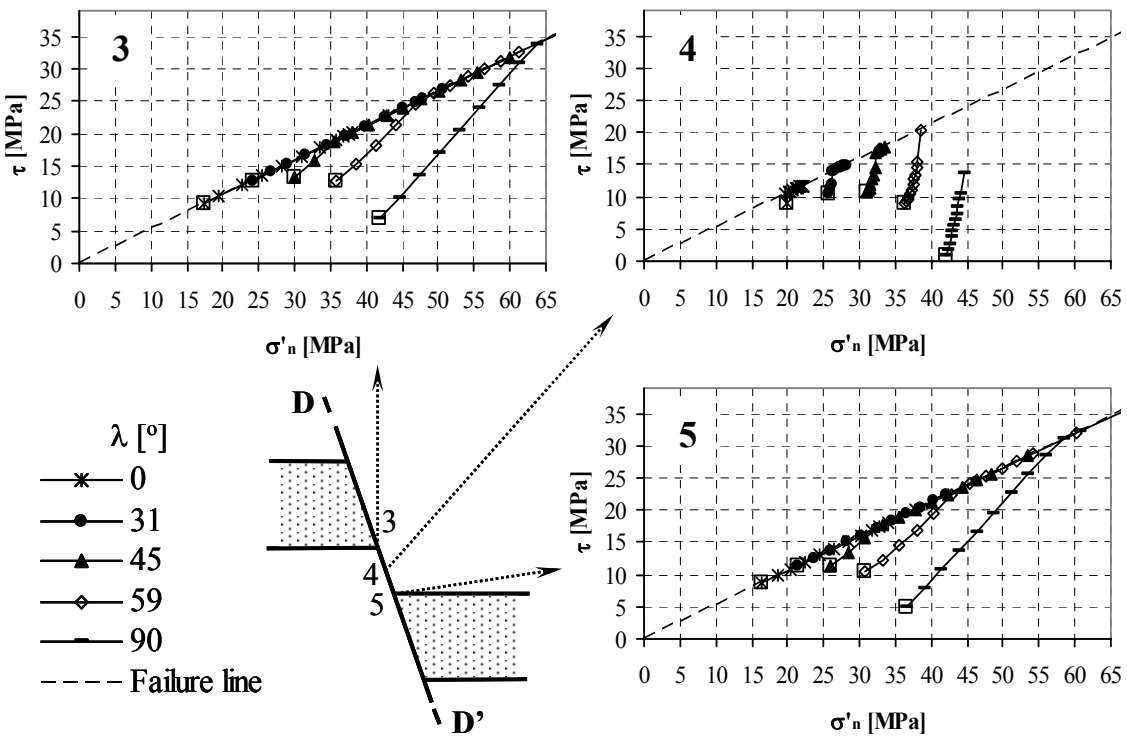

Figure 11.39. Calculated stress paths for model 'throw_var' at different locations on the fault plane along line DD' (see Figure 11.1) for different values of λ with K_{0H} = 1.0 and K_{0h} = 0.4. Calculations are performed with surrounding rock stiffer than the reservoir rock and initial reservoir overpressure (see Table 11.1). Open squares denote the initial stress state.

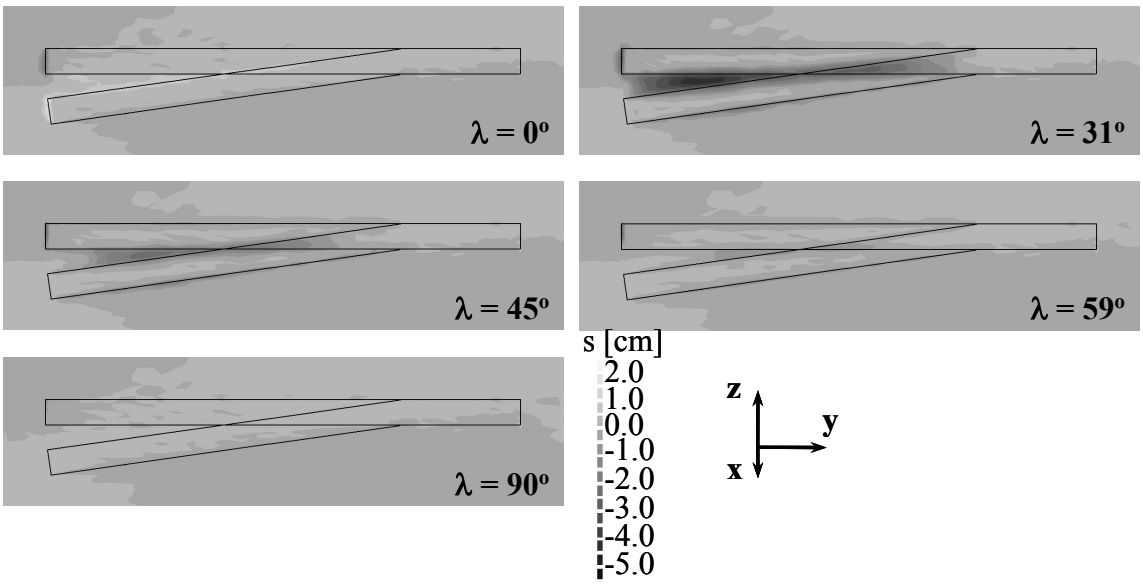

Figure 11.40. Contour plots of relative shear displacement in strike direction of the fault plane (s) for different values of λ with K_{0H} = 1.0 and K_{0h} = 0.4. View direction is normal to the fault plane. Black lines indicate the intersection of the reservoir compartments with the fault plane (see Figure 11.19b). See Appendix 2 for this figure in colour.

12 CONCLUSIONS, DISCUSSION AND RECOMMENDATIONS

12.1 Conclusions

The geomechanical models used for the calculations in this thesis are representative for gas fields in the northern Netherlands. However, their generic character could make the conclusions regarding the calculation results meaningful for other fields in the world as well. Geomechanical calculations incorporate a depleting, mostly disk-shaped reservoir (width larger than thickness) in an extensional stress regime, eventually intersected by a steeply dipping normal fault. The surrounding rock consists of one homogeneous isotropic rock mass without a layered geological structure.

12.1.1 Field data analysis

- To date, a few hundred induced seismic events occurred in the northern Netherlands with magnitudes up to 3.5 on the Richter scale. Magnitudes of most of the induced seismic events fall within the range of 1.5 – 2.0 on the Richter scale. A few larger events, with magnitudes larger than 3.0 on Richter scale, occurred in the Roswinkel and Bergermeer gas fields. The largest induced event in the northern Netherlands to date took place in the Bergermeer field with a magnitude of 3.5 on the Richter scale.
- Seismic events in the Groningen gas field are mainly observed in the western part of the field. They are to a lesser extent observed in the central part of the field. Seismic events are virtually absent in the southeastern and northern parts of the Groningen gas field.
- The spatial distribution of seismic events in the Annerveen gas field is at the time of writing restricted to the western half of the field.
- Seismic cross sections through each seismic event up to January 26 2001 in the Groningen and Annerveen gas fields are studied. The majority of these events is related to the reactivation of steeply dipping (subvertical) normal faults at reservoir level. Even taking into account the uncertainties in the location of the hypocentres, most events occur at reservoir level with a high degree of probability.

12.1.2 Quantification methods

- Several quantitative methods to analyse the sensitivity of a fault for reactivation in numerical calculations are presented and developed for use in the software package DIANA: relative shear displacements (RSD), seismic moment (M_0), stress paths and mobilised shear capacity (MSC). MSC is also applied for rock

volumes (MSC^{3D}). Another quantity used to analyse stress development in and around gas reservoirs is the total stress change per unit depletion (γ).

- Calculations of different model geometries can lead to different magnitudes and distributions of RSD-values over a fault plane. It is therefore difficult to judge the criticalness of faults for reactivation solely based on the maximum RSD-value (RSD_{max}). Integration of the calculated RSD over fault plane and multiplication with the shear modulus of the neighbouring rock formations gives a single scalar quantity for each calculation which is more amenable for comparison purposes: the seismic moment.
- Mobilised shear capacity expresses quantitatively the proximity of a state of stress in a certain location on a fault or in a rock volume to a predefined failure criterion. Analytical expressions are derived in order to calculate MSC and MSC^{3D} for the Mohr-Coulomb failure criterion. The derivation of the formulas does not take into account tension cut-off or a compression failure surface (cap).
- Stress paths in terms of shear- and effective normal stress and relative shear displacements are very convenient for a detailed analysis of the stress development and fault slip at specified locations on the fault plane throughout hydrocarbon extraction. Stress paths and RSD-values should be used in phenomenological analyses for obtaining fundamental and detailed insights in hydrocarbon extraction induced fault reactivation. Seismic moment and mobilised shear capacity are more amenable for parameter studies because of their scalar character.

12.1.3 Calculation results

12.1.3.1 Generic basic reservoir models without fault

The following conclusions are valid for depleting reservoirs (width larger than thickness) in an extensional stress regime, unless stated otherwise.

- Numerically calculated stress changes as a result of hydrocarbon extraction from ellipsoidal reservoirs match very well with analytically calculated graphs as presented in Rudnicki (1999).
- Numerical calculations with different reservoir rock properties and aspect ratios showed, that stress changes are virtually constant throughout an entire ellipsoidal reservoir. This observation is in line with the analytical solutions for ellipsoidal reservoirs.
- Stress changes within disk-shaped reservoirs are not constant throughout the entire reservoir, but show a relatively small $\Delta\sigma'_v$ and a relatively large $\Delta\sigma'_h$ in a zone at the lateral reservoir edge.
- For the modelled reservoir size (1500 m radius and 150 m thickness), calculated stress changes within both ellipsoidal and disk-shaped reservoirs are equal and reflect conditions of uniaxial compaction, except for a zone within the disk-shaped reservoirs at their lateral edge.
- Generally, stress changes just above and below the reservoirs are small. However, stress changes are relatively large in two zones just above and below the lateral

edge of the disk-shaped reservoir. Vertical effective stresses become relatively small during reservoir depletion due to an arching into the sideburden of the reservoir. Horizontal effective stresses increase in these two zones.

- A larger Poisson's ratio of the reservoir rock, a larger reservoir aspect ratio (smaller reservoir width relative to its thickness) and tilting of the reservoir (at least up to a tilt angle of 30^o) lead to smaller values of γ_h (= $\Delta\sigma_h/\Delta p$) and larger values of γ_v (= $\Delta\sigma_v/\Delta p$). They therefore counteract differential stress development at the reservoir centre. Stress paths should become less steep (stabilise).
- Calculations incorporating a tilting reservoir showed large stress concentrations and stress shades around the reservoir corner points (reservoir top and bottom at its lateral edges). Especially at these locations significant differential stress development occurs, indicating a relatively large potential for fault reactivation at these locations.

12.1.3.2 Generic basic disk-shaped reservoir models with fault

The following conclusions are valid for depleting reservoirs (width larger than thickness), intersected by a steeply dipping normal fault in an extensional stress regime, unless stated otherwise.

Characteristics of stress development and fault slip

- During depletion, the main part of the reservoir and the sideburden rock lateral to the reservoir are destabilising (i.e. the stress development converges to the failure surface). The parts inside of the reservoir at its lateral edges and the surrounding rock above and below the reservoir are stabilising (i.e. the stress development diverges from the failure surface). In case of a steeply dipping normal fault intersecting a reservoir with a certain throw, similar zones can be observed in the rocks near the fault plane: Two zones in the surrounding rock near the fault plane above and below the reservoir are destabilising, whereas two zones within the reservoir near the fault plane at the top and bottom of the reservoir stabilise. Note that these conclusions are valid for an extensional stress regime. It is expected that for a compressive stress regime, these conclusions be reversed.
- The stress development in a certain location on the fault plane can be strongly influenced by the stress development in neighbouring locations. Failure in certain locations on the fault can cause gradients of stress paths in neighbouring locations to become steeper. Stress paths, initially diverging from failure, can become converging to and reaching failure in a later stage of depletion.
- Stress development on a fault plane intersecting a producing gas reservoir promotes normal fault reactivation at the bottom of the footwall reservoir compartment and the top of the hanging wall reservoir compartment. It promotes reverse fault reactivation at the top of the footwall reservoir compartment and at the bottom of the hanging wall reservoir compartment.
- Gas depletion can lead to both normal and reverse fault slip on the same fault plane. In the given setting of a steeply dipping normal fault in an extensional

stress regime, normal fault slip due to differential reservoir compaction is the dominant mechanism, rather than reverse fault slip.

Influence of throw on induced fault slip

- The effect of differential reservoir compaction is most pronounced for a configuration, where the top of the hanging wall reservoir compartment is positioned exactly opposite to the bottom of the footwall reservoir compartment. For such configuration, a relatively large amount of fault slip occurs over a narrow area.
- Differential reservoir compaction is absent when the two reservoir compartments on either side of the fault are positioned exactly opposite to each other, so that no throw is present. The resulting fault slip is negligible for this case. Note that this is the case only for equal pore pressure development and rock properties on either sides of the fault.

Differential pore pressure changes due to reservoir compartmentalisation

- In the given setting of a steeply dipping normal fault in an extensional stress regime, intersecting a reservoir and causing a certain amount of throw, normal fault slip is supported by the depletion of both reservoir compartments. In case of depletion of both reservoir compartments, normal fault slip is restricted to the level of the reservoir and does not extend beyond.
- Reverse fault slip is supported by differential pore pressure development due to reservoir compartmentalisation. The location of reverse fault slip is unaffected by reservoir compartmentalisation and remains restricted to relatively small zones around the top of the footwall or bottom of the hanging wall reservoir compartments. Reverse fault slip is also supported by a stiffness of the surrounding rock larger than the stiffness of the reservoir rock (in terms of Young's modulus and Poisson's ratio). Especially the combination of a relatively stiff surrounding and differential pore pressure development due to compartmentalisation can result in relatively large amounts of reverse fault slip.

Young's modulus and Poisson's ratio of the surrounding rock

- A surrounding rock Young's modulus larger than the Young's modulus of the reservoir rock ($E^{sur} > E^{res}$) promotes both normal and reverse reactivation of a steeply dipping normal fault intersecting a reservoir with a throw of half the reservoir thickness in an extensional tectonic stress regime. It shortens the stress path from the initial state of stress to the failure line when compared to the standard case with no rock property discrepancy. $E^{sur} < E^{res}$ opposes the reactivation of the fault.
- The same as in the previous conclusion can be said for the Poisson's ratio: $\nu^{sur} > \nu^{res}$ promotes both normal and reverse fault reactivation. $\nu^{sur} < \nu^{res}$ opposes fault reactivation, although values of ν^{sur} lower than 0.2 seem to have no significant influence on the calculated maximum normal fault slip.
- Calculations indicated that the Young's modulus of the surrounding rock is a more important parameter influencing gas depletion induced fault slip than the Poisson's ratio of the surrounding rock.

Slight initial reservoir overpressure

- Geomechanical calculations with a slight initial reservoir overpressure in the reservoir showed a reduction in calculated fault slip at reservoir level when compared to calculations with an initially hydrostatically pressured reservoir incorporating the same pore pressure reduction (Δp). However, depletion of the reservoir until the same end pressure provides an additional driving force for fault slip when the reservoir embodies a larger initial pore pressure. Calculated RSD-values are therefore larger in this case. The effects as presented here are solely the result of a larger initial reservoir pore pressure in the reservoir. Other possible effects related to an initial overpressure which could occur in reality, such as a higher porosity and therefore different geomechanical properties of the reservoir rock, are not taken into account.

K_0-value of an isotropic initial tectonic stress field

- Calculations with different K_0-values showed, that small values of K_0 result in a relatively large amount of calculated fault slip, because the initial state of stress on the fault plane is closer to failure. Furthermore, the fault has most freedom to move (extend) since the horizontal effective stresses are relatively low (more extensional).

Anisotropic initial tectonic stress field

- In this dissertation, an anisotropic tectonic stress field is described by its maximum and minimum horizontal effective stresses in terms of the effective stress ratios $K_{0H} = \sigma'_H / \sigma'_v$ and $K_{0h} = \sigma'_h / \sigma'_v$ and angle λ, which is the angle between the largest horizontal stress σ'_H and the strike direction of the fault plane.
- Based on the above description, calculations of a reservoir intersected by a steeply dipping normal fault with $K_{0H} = 1.0$ and $K_{0h} = 0.4$ showed, that the initial state of stress on the fault plane before depletion is closest to failure (most critical) for $\lambda = 0^o$ and 31^o. For $\lambda = 31^o$, this is due to a relatively large shear stress component in the strike direction of the fault. This is according to analytical solutions, which indicate that $\lambda = 45^o - \frac{1}{2}\phi^f$ (= 31^o for $\phi^f = 28^o$, ϕ^f being the fault friction angle) incorporates an initial state of stress is closest to failure for most combinations of K_{0H} and K_{0h}, among others for $K_{0H} = 1.0$ and $K_{0h} = 0.4$.
- The stress development on the fault plane is most critical for $\lambda = 0^o$. It reaches the failure line in an earlier stage of depletion than the stress development for larger values of λ. Most normal fault slip is calculated for $\lambda = 0^o$.
- For $\lambda = 31^o$, a certain amount of strike-slip is calculated (16-18% of the total normal fault slip). Strike-slip is also observed to a lesser extent for $\lambda = 45$ and 59^o, but is not calculated for $\lambda = 0$ and 90^o. Strike-slip contributes to both normal and reverse fault slip.
- For surrounding rock stiffer than the reservoir rock, reverse fault slip is largest for $\lambda = 31^o$, 45^o and 59^o. This is most probably due to the strike slip component.
- Stress paths for $\lambda = 0$ and 90^o are, as long as they do not reach the failure line, straight lines. Stress paths for other values of λ show an initial hesitation in development and run asymptotically towards a straight line with the gradient of the stress path for $\lambda = 0$ or 90^o. This initial hesitation is due to an initial shear

stress component in the strike direction of the fault, which hardly changes during gas depletion and which is absent for $\lambda = 0$ and 90^{o}. The initial hesitation should get smaller as the difference between K_{0H} and K_{0h} decreases.

12.2 Discussion

Fault orientation with respect to the anisotropic tectonic stress field in the northern Netherlands

From FE-modelling results it could be concluded, that reactivation of a normal fault at reservoir level in a 3D anisotropic stress field is most pronounced when the strike direction of the fault is parallel to the direction of the maximum horizontal stress. World stress map data (World Stress Map, 2001) indicate that the stress field in the Northern Netherlands is marked by largest principal horizontal stresses oriented NW-SE. In this case, NW-SE striking faults would be most sensitive for fault reactivation.

The largest and most of the seismic events in the Groningen gas field occur in the west part of the field, which is dominated by two major NW-SE trending graben structures, cut by numerous N-S trending grabens, which bound the field on its west side. Another important group of events occurs in the two NW-SE and N-S trending branches of the northernmost major grabenstructure. Seismic events are remarkably absent in the southeastern part of the field, where the rhomboidal fault structure consisting of N-S and E-W trending faults is present. Many seismic events in other gas fields in the Netherlands are also related to NW-SE striking faults. A possible reason could be the favourable orientation of the strike direction of the reactivated faults with respect to the anisotropic tectonic stress field. However, the orientation of a fault is only one out of numerous parameters, which influence the reactivation of faults. For instance, seismic events in the Annerveen gas field are mainly the result of reactivation of N-S trending normal faults. Some seismic events may be related to reactivation of E-W trending reservoir bounding faults.

Normal and reverse fault slip and rock properties of surrounding rocks

The Royal Dutch Meteorological Institute (KNMI) determined for the 1994 and 2001 earthquakes in the Bergermeer gas field near the city of Alkmaar a focal mechanism indicating gas production-induced reverse reactivation of a steeply dipping normal fault (Haak *et al.* 2001). The fault and reservoir have a geometry very similar to the FE-model 'throw_var' of this study. Plastic reverse fault slip along steeply dipping normal faults in an extensional stress regime as a result of gas production is observed in calculations with a stiffness of the surrounding rock larger than the stiffness of the reservoir rock. Differential pore pressure development due to reservoir compartmentalisation promotes such plastic reverse fault slip. Especially the Young's modulus is hereby important. The Poisson's ratio of the surrounding rock becomes only important for very high values.

In the northern Netherlands, reservoir Young's moduli and Poisson's ratios are typically around 13.0 GPa and 0.2, respectively (NAM 2000). The reservoir is underlain by stiffer carboniferous rocks (Limburg Formation), consisting of shales

and sandstones with Young's moduli around 20 GPa and Poisson's ratios of about 0.2. Reservoirs are in most cases covered by a shaly caprock (e.g. Ten Boer Claystone for the Groningen and Annerveen gas fields). E- and ν-values of this caprock are typically 18.0 – 18.5 GPa and 0.25 (NAM 2000). Calculations with rock properties similar to these stiffer units showed enhancement of the reverse reactivation of steeply dipping normal faults at the top of footwall reservoir compartments and/or at the bottom of hanging wall reservoir compartments. A rising gas-water contact during gas production could weaken the fault and support fault slip (Toksöz & Walsh, 1990), a mechanism that would affect the bottom of the hanging wall reservoir compartment.

Calculation results showed the possibility of gas depletion induced reverse fault slip on a steeply dipping normal fault in an extensional stress regime. Note, that according to the same calculations, normal fault slip is the dominant mechanism rather than reverse fault slip.

Salt layers are present above many gas reservoirs in the Netherlands. The long-term viscoelastic behaviour of these salt layers tends to an isotropic state of stress within the salt, in which the horizontal stresses are equal to the vertical stress. Such isotropic state of stress is also present in the theoretical case of a Poisson's ratio of 0.5. According to the calculations for this dissertation, a large Poisson's ratio of the rocks surrounding the reservoir affects the initial state of stress on faults in the reservoir such that it is close to failure. Salt layers in the overburden of the gas reservoirs in the northern Netherlands could have a similar effect.

Seismic moment

The calculated seismic moments in the numerical models represent an upper limit, a maximum seismic potential for the modelled fault(s) under the applied conditions, since it is assumed that 100% of the gas depletion induced fault slip is translated to those seismic moments. The slip, calculated in the model, may in reality occur either aseismically, or as a seismic event or as a combination of the two. Aseismic fault slip does not contribute to a seismic moment. Due to the limitations of the method followed, i.e. elastoplastic modelling, it is impossible to establish if asperities will form during depletion and whether built-up stresses will be released seismically or aseismically. Even if the seismic moment would be known, this seismic energy could be released in one relatively large seismic event or in a series of smaller events. It is therefore not recommendable to translate the calculated seismic moments to magnitudes on Richter scale. The calculations presented in this dissertation can never be a forecast of the magnitude of the events, which are going to occur when a reservoir with the type of modelled setting is produced. The calculated seismic moments are just parameters, which express the criticalness of a fault for reactivation under certain circumstances, and which can be used in subsequent research for a probabilistic approach of the problem of induced seismicity.

Occurrence of induced seismicity in time

Fault slip needs time to develop: the stress needs to develop from an initial state to the failure criterion. Furthermore, a certain amount of fault slip is necessary for a

sufficient stress built-up around an asperity and seismic energy release. Seismic events are therefore expected to occur in a later stage of field production, especially when reverse fault reactivation is involved.

12.3 Recommendations

The present study pays attention to the influence of several parameters on stress development and the sensitivity of a fault for reactivation. Complex key issues occurring in the field, which have a major influence on the development of reservoir production induced seismicity, are still largely unknown. Such key issues are for instance fault properties and pore pressure development in faults, the effects of reservoir overpressure on geomechanical properties of the reservoir, the dynamics of a rising gas-water contact and the tectonic stress field in the subsurface of the northern Netherlands. Future research could concentrate more on measurement or determination and an appropriate geomechanical description of these issues.

The current fault properties, which incorporate Coulomb-friction with a constant friction angle during the whole calculation, could be extended with a displacement-weakening model. This means that after fault movement is initiated, fault sliding takes place more easily. This kind of behaviour is more in line with what happens in reality. Research on this topic could produce more insight in how seismic events and stress concentrations distribute themselves over the fault plane during gas production.

The influence of the salt layer present above the gas reservoirs in the Netherlands on gas depletion induced fault slip should be studied, since it can have a major effect on the local initial tectonic stress field.

Certain gas fields show seismicity during production whereas other gas fields do not. More research on a detailed scale seems necessary in order to explain this behaviour. A suggestion is to search for correlations between the occurrence of seismic events and as much statical and dynamical properties of the studied field(s) as possible, eventually supported by downhole geophone measurements of microseismicity.

It would be useful to set up a stress atlas of simple reservoir/fault geometries, incorporating different geometrical and geomechanical parameters. The criticalness of certain faults for reactivation relative to a reference case could be judged by inserting some parameter values into a spreadsheet.

Geomechanical modelling tools are currently in fast development. Tools allowing complex 3D-models with coupled structural/multi-phase fluid flow/thermal/dynamic and large strain options are currently entering the market, allowing investigation of interesting topics such as a moving gas-water contact, salt deformation and crack formation. In case of sufficient hardware capacity, numerical models incorporating higher order elements should be used.

REFERENCES

Addis, M.A., N.C. Last & N.A. Yassir (1996). *Estimation of horizontal stresses at depth in faulted regions and their relationship to pore pressure variations.* SPE Formation Evaluation, March 1996.

Aki, K. (1966). *Generation and propagation of G waves from the Niigata earthquake of June 16, 1964*: Part 2. Estimation of earthquake moment, released energy and stress drop from the G wave spectra, Bull. Earthq. Res. Inst., Univ. Tokyo, 44, 73-88.

Amadei, B. & O. Stephansson (1997). *Rock stress and its measurement.* Chapman & Hall, London, United Kingdom.

Anderson, E.M. (1951). *The dynamics of faulting and dyke formation with applications to Britain, second edition revised.* Oliver and Boyd, Edinburgh, United Kingdom.

Arthaud, F. & P. Matte (1977). *Late Paleozoic strike-slip faulting in southern Europe and North Africa; results of a right-lateral shear zone between the Appalachians and the Urals.* Geol. Soc. Am. Bull., Vol. 88, p. 1305-1320.

Baldschuhn, R., G. Best & F. Kockel (1991). *Inversion tectonics in the Northwest German Basin.* In: Generation, Accumulation and Production of Europe's Hydrocarbons (Spencer, A.M., ed.), Spec. Publ. E.A.P.G., No. 1, Oxford University Press, United Kingdom.

Bandis, S.C., A.C. Lumsden & N.R. Barton (1983). *Fundamentals of rock joint deformation.* Int. J. Rock Mech. Min. Sci. & Geomech. Abstr. Vol. 20, No. 6, pp. 249-268.

Baranova, V., A. Mustaqeem & S. Bell (1999). *A model for induced seismicity caused by hydrocarbon production in the Western Canada Sedimentary Basin.* Can. J. Earth Sci., Vol. 36, pp. 47-64.

Barends, F.B.J., J.T. van der Poel & J.A.M. Teunissen (1995). *Geomechanical simulation of static and dynamic subsidence by reservoir compaction.* In: Land subsidence, Barends, Brouwer & Schröder (eds.), pp. 237-245, Balkema, Rotterdam Netherlands.

Bell, J.S. & P.F. Lloyd (1989). *Modelling of stress refraction in sediments around the Peace River Arch, western Canada.* In: Current Research, Part D, Geol. Survey of Canada, Paper 89-1D, p. 49-54.

Biot, M.A. (1962). *Mechanics of deformation and acoustic propagation in porous media.* J. Appl. Phys., Vol. 33, pp. 1482-1498.

BOA (Begeleidingscommissie Onderzoek Aardbevingen) (1993). *Final report on a multidisciplinary study of the relationship between gas production and earthquakes in the northern part of the Netherlands.* KNMI (Royal Dutch Meteorological Institute), De Bilt, Netherlands.

Bou-Rabee, F. (1994). *Earthquake recurrence in Kuwait induced by oil and gas extraction.* J. Petrol. Geol., Vol. 17, No. 4, pp. 473-480.

Brady, B.H.G. & E.T. Brown (1993). *Rock mechanics for underground mining, second edition.* Chapman & Hall, London, United Kingdom.

Brignoli, M., A. Pellegrino, F.J. Santarelli, G. Musso & G. Barla (1997). *Continuous and discontinuous deformations above a compacting reservoirs; consequences upon the lateral extension of the subsidence bowl.* Int. J. Rock Mech. & Min. Sci., Vol. 34, No. 3-4.

Bungum, H., A. Alsaker, L.B.Kvamme & R.A. Hansen (1991). *Seismicity and seismotectonics of Norway and nearby continental shelf areas.* J. Geophys. Res., vol. 96, no. B2, pp. 2249-2265.

Calloi, P., M. Depanfilis, D. DiFillipo, I. Marcelli & M.C. Spadea (1956). *Terremoti della val Padana del 15-16 Maggio 1951*. Ann. Geofis., Vol. 9, pp. 63-105.

Charlier, R. (2000). *Personal communication*. University of Liege, Liege, Belgium.

Chen, W.F. & D.J. Han (1988). *Plasticity for structural engineers.* Springer, New York, USA.

Davis, S.D. & W.D. Pennington (1989). *Induced seismic deformation in the Cogdell oil field of west Texas.* Bull. Seismol. Soc. Am., Vol. 79, No. 5, pp. 1477-1494.

De Crook, Th., H.W. Haak & B. Dost (1998). *Seismich risico in Noord-Nederland.* KNMI (Koninklijk Nederlands Meteorologisch Instituut), Techn. Rep., De Bilt, Netherlands.

Doornhof, D. (1992). *Surface subsidence in the Netherlands: the Groningen gas field.* Geologie en Mijnbouw, Vol. 71, p. 119-130.

Doser, D.I., M.R. Baker & D.B. Mason (1991). *Seismicity in the War-Wink gas field, Delaware Basin, West Texas, and its relationship to petroleum production.* Bull. Seismol. Soc. Am., Vol. 81, No. 3, pp. 971-986.

Doser, D.I., M.R. Baker, M. Luo, P. Marroquin, L. Ballesteros, J. Kingwell, H.L. Diaz & G. Kaip (1992). *The not so simple relationship between seismicity and oil production in the Permian Basin, West Texas.* Pageoph, Vol. 139, No. 3/4, pp. 481-506.

Dost, B. (2000). *Geïnduceerde seismiciteit in Noord-Nederland.* In: Report of the Technical Workshop 'Geïnduceerde aardbevingen in Noord-Nederland', 7th November 2000, KNMI (Koninklijk Nederlands Meteorologisch Instituut), De Bilt, Netherlands.

Draxler, J.K. & D.P. Edwards (1984). Formation *evaluation in the Carboniferous of Northern Europe.* Report prepared for Schlumberger.

Engelder, T. & M.P. Fischer (1994). *Influence of poroelastic behavior on the magnitude of minimum horizontal stress, Sh, in overpressured parts of sedimentary basins.* Geology, Vol. 22, pp. 949-952.

Eshelby, J.D. (1957). *The determination of the elastic field of an ellipsoidal inclusion, and related problems.* Proc. of the Royal Soc., London, no. A241, pp. 376-396.

Fjaer, E., R.M. Holt, P. Horsrud, A.M. Raaen & R. Risnes (1992). *Petroleum related rock mechanics.* Developments in Petroleum Science, No. 33. Elsevier, Amsterdam, Netherlands.

Frikken, H.W. (1999). *Reservoir-geological aspects of productivity and connectivity of gasfields in the Netherlands.* Dissertation, Delft University of Technology, Delft, Netherlands.

Frikken, H.W. (2000). *Personal communication*. NAM, Assen, Netherlands.

Galybin, A.N., S.S. Grigoryan & S.A. Mukhamediev (1998): *Model of induced seismicity caused by water injection.* Proc. SPE/ISRM Conf. Eurock'98, Trondheim Norway 1998.

Geertsma, J. (1973). *A basic theory of subsidence due to reservoir compaction: the homogeneous case.* Verhandelingen Kon. Ned. Geol. Mijnbouwk. Gen., Vol. 28, pp. 43-62.

Geertsma, J. & G. Van Opstal (1973). *A numerical technique for predicting subsidence above compacting reservoirs, based on the nucleus of strain concept*. Verhandelingen Kon. Ned. Geol. Mijnbouwk. Gen., Vol. 28, pp. 63-78.

Geluk, M.C. (1999). *Late Permian (Zechstein) rifting in the Netherlands: models and implications for petroleum geology*. Petroleum Geoscience, no. 5, pp. 189-199.

Glab, M. (2001). *Localisation of sensitive reservoir settings for induced seismicity using FEM.* Memoirs of the Centre of Engineering Geology in the Netherlands, No. 206, Delft University of Technology, Delft, Netherlands.

Glennie, K.W. (1986). *Early Permian – Rotliegend.* In: Introduction to the Petroleum Geology of the North Sea (Glennie K.W. ed.), Blackwell Scientific Publ., Oxford, United Kingdom.

Glowacka & Nava (1996). *Major earthquakes in Mexicali Valley, Mexico, and fluid extraction at Cerro Prieto geothermal field.* Bull. Seism. Soc. Am., Vol. 86, No.1, Part A, pp. 93-105.

Goodman, R.E. 1989. *Introduction to rock mechanics*, 2nd edition. John Wiley & Sons, New York, USA.

Grasso, J.R. (1990). *Hydrocarbon extraction and seismic hazard assessment*. EOS Transactions, Amer. Geophys. Union, no. 71, Abstract 1454.

Grasso, J.-R. (1992). *Mechanics of seismic instabilities induced by the recovery of hydrocarbons.* Pageoph, Vol. 139, No. 3 /4, pp. 507-534.

Grasso, J.-R. & C. Wittlinger (1990). *Ten years of seismic monitoring over a gas field.* Bull. Seismol. Soc. Am., Vol. 80, No. 2, pp. 450-473.

Gromberg, J. & L. Wolf (1999). *Possible cause for an improbable earthquake: The 1997 M_w 4.9 southern Alabama earthquake and hydrocarbon recovery.* Geology, Vol. 27, No. 4, pp. 367-370.

Grünthal, G. & D. Stromeyer (1994): *The recent crustal stress field in western Europe sensu lato and its quantitative modelling.* Geol. Mijnbouw 73, p. 173-180.

Haak, H.W., B. Dost & F.H. Goutbeek (2001). *Seismische analyse van de aardbevingen bij Alkmaar op 9 en 10 september en Bergen aan Zee op 10 oktober 2001.* Techn. report no. TR-239, KNMI (Koninklijk Nederlands Meteorologisch Instituut), De Bilt, Netherlands.

Healy, J.H., W.W. Rubey, D.T. Griggs & C.B. Raleigh (1968). *The Denver earthquakes.* Science, vol. 161, pp. 1301-1310.

Hettema, M.H.H., P.M.T.M. Schutjens, B.J.M. Verboom & H.J. Gussinklo (1998). *Production-induced compaction of sandstone reservoirs: The strong influence of field stress.* Proc. SPE Europ. Petrol. Conf., The Hague Netherlands 1998. Publ.: Soc. of Petrol. Eng. (SPE), Richardson TX USA.

Hettema, M.H.H. (1996): *The thermo-mechanical behaviour of sedimentary rock: an experimental study.* Dissertation, Delft University of Technology, Delft, ISBN 90-5651-021-5.

Hillis, R.R. (2001). *Coupled changes in pore pressure and stress in oil fields and sedimentary basins.* Petrol. Geosc., Vol. 7, pp. 419-425.

Itasca Consulting Group Inc. (2001). *Fast Langrangian Analysis of Continua, Version 4.0*. Minneapolis, USA.

Kanamori, H. & E. Hauksson (1991). *A slow earthquake in sediments in the Santa Maria Basin, California.* EOS Transactions, Am. Geophys. Union, Vol. 72, No. 44, pp. 293.

Kenter, C.J., T.L. Blanton, G.M.A. Schreppers, M.N. Baaijens & G.G. Ramos (1998). *Compaction study for Shearwater field.* Proc. SPE/ISRM Conf. Eurock'98, Trondheim Norway 1998.

Khan, M. & L.W. Teufel (2000). *The effect of geological and geomechanical parameters on reservoir stress path and its importance in studying permeability anisotropy.* SPE Reservoir Eval. & Eng., Vol. 3, No. 5, pp. 394-400.

Klein, R.J. & M.V. Barr (1986): *Regional state of stress in western Europe.* Proc. Int. Symp. on Rock Stress and Rock Stress Measurements, Stockholm 1-3 September 1986, p. 33-44.

KNMI (Koninklijk Nederlands Meteorologisch Instituut) (2003a). *Geïnduceerde aardbevingen in Nederland.* Internet link: http://www.knmi.nl/onderzk/seismo/home_n/education/nederland/neder_quake/copyright_akkoord.html.

KNMI (Koninklijk Nederlands Meteorologisch Instituut) (2003b). *Aardbeving bij Hoeksmeer (Noord-Oost Nederland).* Internet link: http://www.knmi.nl/onderzk/seismo/.

Kouznetsov, O., V. Sidorov, S. Katz & G. Chilingarian (1994). *Interrelationships among seismic and short-term tectonic activity, oil and gas production, and gas migration to the surface.* J. Petr. Sci. and Eng., Vol. 13, pp. 57-63.

Kovach, R.L. (1974). *Source mechanisms for Wilmington oil field, California, subsidence earthquakes.* Bull. Seismol. Soc. Am., Vol. 64, pp. 699-711.

Kreyszig, E. (1988). *Advanced engineering mathematics*, 6th ed. Wiley, New York, USA.

Kulhawy, F.H. (1975). *Stress deformation properties of rock and rock discontinuities.* Engineering Geology, No. 9, pp. 327-350.

Leydecker, G. (1992). *The seismological surveillance of Gorbelen site and its surroundings*. Proc. of OECD-NEA Workshop on long-term observation of the geological environment, Helsinki, 9-11 September 1991.

Lorentz, V. & I.A. Nicholls (1976). *Plate and intraplate processes of Hercynian Europe during the Late Paleozoic.* Tectonophysics, Vol. 107, p. 25-56.

Mahi, A. (2003). *Stress development in oil reservoirs*. Ms.C. thesis, Norwegian University of Science and Technology. Trondheim, Norway.

Maillot, B., S. Nielsen & I. Main (1999). *Numerical simulation of seismicity due to fluid injection in a brittle poroelastic medium.* Geophys. J. Int., Vol. 139, No. 2, pp. 263-272.

Maury, V.M.R., J.-R. Grasso & G. Wittlinger (1992). *Monitoring of subsidence and induced seismicity in the Lacq gas field (France); the consequences on gas production and field operation*. Eng. Geol., Vol. 32, No. 3, pp. 123-135.

McGarr, A. (1991). *On a possible connection between three major earthquakes in California and oil production.* Bull. Seosmol. Soc. Am., Vol. 81, pp. 948-970.

Mereu, R.F., J. Brunet, K. Morrissev, B. Price & A. Yapp (1986). *A study of the microearthquakes of the Gobles oil field area of Southwestern Ontario.* Bull. Seismol. Soc. Am., Vol. 76, pp. 1215-1223.

Milne, W.G. (1970). *The Snipe Lake, Alberta, earthquake of March 8, 1970.* Can. J. Earth Sci., Vol. 7, pp. 1564-1567.

Ministry of Economic Affairs (2001). *Oil and gas in the Netherlands – Exploration and production 2001*. Report, Ministry of Economic Affairs, The Hague, Netherlands.

Ministry of Economic Affairs (2003). *Olie en gas in Nederland. – Opsporing en winning in 2002*. Report, Ministry of Economic Affairs, The Hague, Netherlands.

Mobach, E. & H.J. Gussinklo (1994). *In-situ reservoir compaction monitoring in the Groningen field.* Eurock'94, Proc. SPE/ISRM Int. Conf., 29-31 August, Delft, p. 535-547. Elsevier, Amsterdam, Netherlands.

Mura, T. (1982). *Micromechanics of defects in solids*. Martinus Nijhoff, The Hague, Netherlands.

Nagelhout, A.C.G. & J.P.A. Roest (1997). *Investigating fault slip in a model of an underground gas storage facility.* Int. J. R ock Mech. & Min. Sci., Vol. 34, No. 3-4, Paper No. 212.

NAM (Nederlandse Aardolie Maatschappij B.V.) (1998). *Bodemdalingsprognose van Ameland.* Report no. 1998.09.000394, NAM, Assen, Netherlands.

NAM (Nederlands Aardolie Maatschappij B.V.) (2000). *Bodemdaling door aardgaswinning: Groningen veld en randvelden in Groningen, Noord Drenthe en het Oosten van Friesland. Status rapport 2000 en prognose tot het jaar 2050.* Report no. 2000 02 000410, NAM, Assen, Netherlands.

Nicholson & Wesson (1990). *Earthquake hazard associated with deep well injection; a report to the U.S. Environmental Protection Agency. U.S. Geol. Survey* Bull. 1951. U.S. Geol. Survey, Denver CO USA.

Nicholson, C. (1992). *Earthquakes associated with deep well activities: Comments and case histories.* In: Rock Mechanics, Tillerson & Wavesik (eds.), pp. 1079-1086. Publ.: Balkema, Rotterdam Netherlands.

Oertel, G. (1996). *Stress and deformation: A handbook on tensors in geology.* Oxford University Press, Oxford, United Kingdom.

Pande, G.N., G. Beer & J.R. Williams (1990). *Numerical methods in rock mechanics.* Wiley, Chichester, United Kingdom.

Pennington, W.D., S.D. Davis, S.M. Carlson, J. Dupree & T.E. Ewing (1986). *The evolution of seismic barriers and asperities caused by the depressuring of fault planes in oil and gas fields in South Texas.* Bull. Seim. Soc. Am., Vol. 78, pp. 939-948.

Paterson, M.S. (1978). *Experimental rock deformation: The brittle field.* Springer-Verlag, New York, USA.

Pourjavad, M., J.S. Bell & R.K. Bratli (1998). *Stress trajectories in the neighbourhood of fault zones.* Proc. SPE/ISRM Eurock'98 Conf., 7-10 July 1998, Trondheim, Norway.

Raleigh, C.B., J.H. Healy & J.D. Bredehoeft (1972). *Faulting and crustal stress at Rangely, Colorado*. A.G.U., Geophys. Monograph, Vol. 16, pp. 275-284.

Raleigh, C.B., J.H. Healy & J.D. Bredehoeft (1976). *An experiment in earthquake control at Rangely, Colorado.* Science, vol. 191, pp. 1230-1237.

Ranalli, G. (1995). *Rheology of the earth, second edition.* Chapman & Hall, London, United Kingdom.

Reinecker, J., O. Heidbach, & B. Mueller (2003). *The 2003 release of the World Stress Map* (available online at www.world-stress-map.org).

RGD (Rijks Geologische Dienst) (1995). *Geological Atlas of the Subsurface of the Netherlands, Explanation to map sheet III: Rottumeroog – Groningen.* NITG-TNO, Utrecht, Netherlands.

Richter, C.F. (1958). *Elementary Seismology.* W.H. Freeman and Co., San Francisco, USA.

Roest, J.P.A. & W. Kuilman (1993). *Geomechanische analyse van de lichte aardschokken in het Eleveld reservoir.* Report by Delft University of Technology, Dept. of Applied Earth Sciences, Delft, Netherlands.

Roest, J.P.A. & W. Kuilman (1994). *Geomechanical analysis of small earthquakes at the Eleveld gas reservoir.* Proc. Int. Conf. Eurock '94, Delft Netherlands 1994, pp. 573-580. Publ.: Balkema, Rotterdam Netherlands.

Roest, J.P.A. & F.M.M. Mulders (2000). *Overview modelling gas production-induced seismicity mechansims.* Proc. Eurock 2000 Symp., Aachen Germany 2000, pp. 333-338. Publ.: Verlag Glückauf Essen (VGE), Essen Germany.

Rondeel, H.E. & J.S.L. Everaars (1993). *Spanning in noordoost Nederland: een breakoutanalyse.* Report by Vrije Universiteit Amsterdam, Fac. of Earth Sciences, Amsterdam, Netrherlands.

Rondeel, H.E., D.A.J. Batjes & W.H. Nieuwenhuis (1996). *Geology of gas and oil under the Netherlands*: Selection of papers presented at the 1993 Intern. Conf. of the AAPG, The Hague. Kluwer Academic Publishers, Dordrecht, Netherlands.

Rosso, R.S. (1976). *A comparison of joint stiffness measurements in direct shear, triaxial compression, and in situ.* Int. J. Rock Mech. Min. Sci. & Geomech. Abstr. Vol. 13, pp. 167-172.

Rothé, J.-P. (1977). *Seismes artificiels et exploitation pétrolières: L'exemple de Lacq, France*. Annali di Geofisicia, Vol. 30, pp. 369-383.

Rothé, G.H. & C.Y. Lui (1983). *Possibility of induced seismicity in the vicinity of the Sleepy Hollow oil field, SW Nebraska.* Bull. Seismol. Soc. Am., Vol. 73, pp. 1357-1367.

Rudnicki, J.W. (1999). *Alteration of regional stress by reservoirs and other inhomogeneities: Stabilizing or destabilizing?* Proc. 9th Int. Congr. on Rock Mech., Paris France 1999, Vol. 3, pp. 1629-1637. Publ.: Swets & Zeitlinger, Lisse Netherlands.

Rudnicki, J.W. (2003). *Personal communication*. Northwestern University, Evanston, Illinois, USA.

Santarelli, F.J., J.T. Tronvoll, M. Svennekjaer, H. Skeie, R. Henriksen & R.K. Bratli (1998). *Reservoir stress path: The depletion and the rebound*. Proc. SPE/ISRM Conf. Eurock'98, Trondheim Norway 1998.

Segall, P. (1989). *Earthquakes triggered by fluid extraction*. Geology, Vol. 17, pp. 942-946.

Segall, P. (1992*). Induced stresses due to fluid extraction from axisymmetric reservoirs.* Pure and Appl. Geophys., Vol. 139, No. 3-4, pp. 535-560.

Segall, P., J.-R. Grasso & A. Mossop (1994). *Poroelastic stressing and induced seismicity near the Lacq gas field, Southwestern France.* J. Geophys. Res., B, Solid Earth and Planets, Vol. 99, No. 8, pp. 15423-15438.

Segall, P. & S.D. Fitzgerald (1998). *A note on induced stress changes in hydrocarbon and geothermal reservoirs.* Tectonophysics, Vol. 289, pp. 117-128.

Scholtz, C.H. (1990). The *mechanics of earthquakes and faulting.* Cambridge University Press, Cambridge, United Kingdom.

Schreppers, G. (1998). *Compaction and subsidence study of the Ameland gas-field with creep effects.* TNO-report 98-MIT-NM-R/1623, TNO, Delft, Netherlands.

Simpson, D.W. & W. Leith (1985). *The 1976 and 1984 Gasli, USSR, earthquakes – Were the induced? Bull.* Seismol. Soc. Am., Vol. 75, pp. 1465-1468.

Smirnova, M.N. (1977). *Earthquakes induced by hydrocarbon recovery*. In: Seismicity changes induced by human activity (Nauka, Moscow 1977), pp. 128-140.

Stäuble, A.J. & G. Milius (1970). *Geology of the Groningen gas field, Netherlands*. In: Geology of giant petroleum fields (Halbouty, M.T., ed.). AAPG Mem. 14.

Terzaghi, K. (1943*). Theoretical soil mechanics.* Wiley, New York, USA.

Teufel, L.W., D.W. Rhett & H.E. Farrell (1991). *Effect of reservoir depletion and pore pressure drawdown on in situ stress and deformation in the Ekofisk field, North Sea*. Proc. 32nd U.S. Symp. on Rock Mech., Norman OK USA 1991, pp. 63-72. Publ.: Balkema, Rotterdam Netherlands.

TNO Building & Construction Research (1998). DIANA *User's manual, Release 7.* TNO DIANA BV, Delft, Netherlands.

TNO Building & Construction Research (1999). *Personal communication*. TNO-DIANA, Delft, Netherlands.

TNO-NITG (Netherlands Institute of Applied Geoscience TNO – National Geological Survey) (2000). *Personal communication*. TNO-NITG, Utrecht, Netherlands.

Toksöz, M.N. & J.B. Walsh (1990). *Bodemdaling boven het Groningen gasveld, een evaluatie van het bodemdalingsprogramma van de Nederlands Aardolie Maatschappij (NAM)*. NAM, Assen, Netherlands.

Van Wees, J.D., B. Orlic, R. van Eiis, W. Zijl, P. Jongerius, G.J. Sschreppers, M. Hendriks & T. Cornu (2001). *Integrated 3D geomechanical modelling for deep subsurface damage: A case study of tectonic and man induced damages in the eastern Netherlands.* Geol. Soc. of London Spec. Publ.

Van Wijhe, D.H., M. Lutz & J.P.H. Kaasschieter (1980). *The Rotliegend in the Netherlands and its gas accumulations.* Geologie en Mijnbouw, Vol. 59, p. 3-24.

Veenhof, E.N. (1996*). Geological aspects of the Annerveen gas field, the Netherlands*. In: Geology of gas and oil under the Netherlands (Rondeel, H.E. et al., eds.), Kluwer Academic Publishers, Dordrecht, Netherlands.

Watt, J.P., G.F. Davies & R.J. O'Connel (1976). *The elastic properties of composite materials*. Reviews of Geophysics and Space Physics, Vol. 14, pp. 541-563.

Wetmiller, R.J. (1986). *Earthquakes near Rocky Mountain House, Alberta, and relationship to gas production*. Can. J. Earth Sci., Vol. 32, No. 2, pp. 172-181.

Wittke, W. (1990). *Rock mechanics – Theory and applications with case histories*. Springer, Berlin, Germany.

Wu, B., M.A. Addis & N.C. Last (1998). *Stress estimation in faulted regions: The effect of residual friction.* Proc. SPE/ISRM Conf. Eurock'98, Trondheim, Norway.

Ziegler (1982). *Geological Atlas of Western and Central Europe.* Shell Internationale Petroleum Maatschappij B.V. Distributed by Elsevier, Amsterdam, Netherlands.

Ziegler (1989). *Evolution of Laurussia – A study in Late Paleozoic Tectonics.* Kluwer Academic Publishers, Dordrecht, Netherlands.

Zienkiewicz, O.C. (1971). *The finite element method in engineering science*. McGraw-Hill, London, United Kingdom.

Zoback, M. (1992). *First- and second order patterns of stress in the lithosphere: The world stress map project*. J. of Geophys. Res., Vol. 97, No. B8, pp. 11703-11728.

Zoback, M.L., M.D. Zoback *et al.* (1991). *Global patterns of tectonic stress*. Nature, vol. 341, p. 291-298.

APPENDIX 1 INDUCED SEISMIC EVENTS IN THE NETHERLANDS UP TO OCTOBER 23 2003 (SOURCE: KNMI)

YYMMDD	TIME	LOCATION	LAT	LON	X_RD	Y_RD	INT	MAG	DEPTH
19861226	074751.0	Assen	52.992	6.548	232,924	556,587	IV-	2.8	1.0
19871214	204951.0	Hooghalen	52.928	6.552	233,266	549,537	IV	2.5	1.5
19891201	200914.3	Purmerend	52.529	4.971	126,697	504,593	V	2.7	1.2
19910215	021116.5	Emmen	52.771	6.914	257,992	532,491	III-I	2.2	3.0
19910425	102631.5	Geelbroek	52.952	6.575	234,788	552,218	III-I	2.6	3.0
19910808	040114.6	Eleveld	52.965	6.573	234,653	553,624	III-I	2.7	3.0
19911205	002456.7	Middelstum	53.358	6.657	239,503	597,465	III	2.4	3.0
19920523	152911.4	Geelbroek	52.953	6.572	234,563	552,325	III-I	2.6	3.0
19920524	180005.9	Geelbroek	52.957	6.562	233,885	552,685	II	1.6	3.0
19920611	170937.0	Roswinkel	52.831	7.032	265,802	539,341	3.5	2.7	1.5
19920722	232313.2	Eleveld	52.961	6.570	234,437	553,158	III	2.6	3.0
19921206	203432.0	Ten Boer	53.320	6.740	245,107	593,338	1	1.3	3.0
19921211	130050.0	Slochteren	53.210	6.747	245,782	581,126	1	1.4	3.0
19930212	114600.7	Noordbroek	53.295	6.868	253,715	590,669	1	1.0	3.0
19930305	222725.2	Langelo	53.085	6.465	227,177	566,825	2.5	1.5	3.0
19930312	221241.5	Hoogezand	53.160	6.805	249,789	575,582	1	0.9	3.0
19930326	183421.1	Overschild	53.285	6.795	248,848	589,495	1	1.1	3.0
19930505	200832.7	Haren	53.177	6.685	241,729	577,378	1	1.5	3.0
19930514	193942.0	Ten Post	53.305	6.793	248,692	591,773	1	1.1	3.0
19930627	020851.8	Bedum	53.317	6.650	239,118	592,839	1	1.4	3.0
19930627	025710.0	Stedum	53.315	6.660	239,788	592,647	1	1.0	3.0
19930710	002234.5	Appingedam	53.333	6.837	251,518	594,928	1	1.4	3.0
19930727	133918.0	Loppersum	53.336	6.808	249,625	595,169	1	0.8	3.0
19930823	005121.6	Nijenklooster	53.332	6.848	252,297	594,851	1	0.7	3.0
19930904	022450.1	Oldenzijl	53.363	6.765	246,682	598,117	1	1.4	3.0
19930922	173703.8	Middelstum	53.368	6.675	240,682	598,562	2.5	2.0	3.0
19930925	002133.4	Slochteren	53.208	6.812	250,129	580,932	1	0.9	3.0
19931123	123147.6	Slochteren	53.202	6.820	250,699	580,256	2.5	2.2	3.0
19931222	020442.7	Ten Post	53.294	6.753	246,050	590,462	1	1.6	3.0
19940204	213238.9	Winneweer	53.306	6.777	247,581	591,790	1	1.3	3.0
19940205	151005.8	Roswinkel	52.833	7.045	266,672	539,583	4.5	2.9	1.5
19940228	210016.5	Garsthuizen	53.370	6.720	243,671	598,895	1	0.6	3.0
19940302	103638.0	Steendam	53.279	6.807	249,639	588,861	1	1.5	3.0
19940306	200231.2	Eenrum	53.323	6.805	249,431	593,774	1	1.0	3.0
19940314	093101.1	't Zandt	53.345	6.808	249,605	596,207	1	1.3	3.0
19940314	104400.0	Zandeweer	53.390	6.680	240,970	601,053	1	1.6	0.0
19940314	223209.6	Westerbroek	53.170	6.747	245,866	576,693	1	1.1	3.0
19940324	052903.8	Delfzijl	53.316	6.962	259,885	593,193	1	0.8	3.0
19940404	184611.6	Steendam	53.275	6.828	251,094	588,389	1	1.3	3.0
19940507	200853.6	Kolham	53.194	6.798	249,269	579,374	1	1.0	3.0
19940510	013411.9	Hellum	53.226	6.835	251,646	583,021	1	0.8	3.0
19940605	021450.7	Weiwerd	53.295	6.950	259,159	590,784	1	1.0	3.0
19940606	040826.1	Achterdiep	53.156	6.823	251,022	575,217	1	1.0	3.0
19940608	222024.5	Garsthuizen	53.359	6.682	241,142	597,625	1	1.5	3.0
19940626	174438.8	De Klip	53.335	6.852	252,512	595,171	1	1.0	3.0
19940627	205853.8	Uithuizermeeden	53.424	6.770	246,885	604,892	1	1.7	3.0
19940701	062742.6	Stedum	53.332	6.577	234,203	594,462	1	2.7	3.0
19940719	081729.6	't Zandt	53.372	6.743	245,220	599,164	1	2.0	3.0
19940730	091820.7	Middelstum	53.351	6.628	237,609	596,616	4.5	2.7	1.0

YYMMDD	TIME	LOCATION	LAT	LON	X_RD	Y_RD	INT	MAG	DEPTH
19940730	095329.6	Middelstum, naschok	53.365	6.577	234,143	598,134	1	1.3	1.0
19940806	180219.2	Alkmaar	52.654	4.711	109,221	518,630	4.5	3.0	2.5
19940816	143739.8	Annen	53.061	6.698	242,855	564,487	4.5	2.3	3.0
19940907	220604.3	Warffum	53.402	6.575	233,964	602,231	1	1.4	3.0
19940909	155654.3	Emmen	52.714	6.915	258,193	526,189	1	1.7	3.0
19940921	011258.1	Alkmaar	52.658	4.708	109,021	519,047	5	3.2	2.5
19940923	195000.0	Schoonebeek	52.670	6.880	255,931	521,208	2	1.3	3.0
19941026	214101.8	Schildwolde	53.246	6.737	245,039	585,119	1	1.2	3.0
19941213	215000.0	No Name	0.000	0.000	249,947	584,526	1	1.0	0.0
19950124	093839.1	Amsweer	53.316	6.897	255,555	593,044	1	1.3	3.0
19950131	194755.6	Annen	53.063	6.720	244,303	564,737	4	2.0	3.0
19950201	003132.0	Veendam	53.079	6.775	247,956	566,531	2	1.2	3.0
19950321	163744.3	Bierum	53.438	6.913	256,377	606,679	1	1.1	3.0
19950406	080343.4	Loppersum	53.360	6.680	241,030	597,677	1	2.0	3.0
19950426	173549.6	Zuidlaren	53.084	6.668	240,799	566,992	1	0.7	3.0
19950515	095239.3	Weiwerd	53.309	6.945	258,791	592,390	1	1.8	3.0
19950603	220638.5	Zevenhuizen	53.182	6.363	220,220	577,521	1	0.9	3.0
19950620	085940.1	Roswinkel	52.832	7.029	265,598	539,414	3	2.7	2.0
19950715	160539.1	Veenhuizen	53.207	6.823	250,911	580,817		1.0	3.0
19950721	232440.4	Meedhuizen	53.276	6.963	260,095	588,689	1	1.1	3.0
19950913	213436.8	Wirdumerdraai	53.335	6.728	244,299	594,974		1.1	3.0
19951018	003427.3	Altena	53.129	6.492	228,887	571,840		1.3	3.0
19951102	010700.7	Loppersum	53.352	6.718	243,598	596,835	2	1.6	3.0
19951104	055043.2	Uithuizerwad	53.470	6.722	243,577	609,986	1	1.8	3.0
19951120	022054.7	Steendam	53.315	6.762	246,561	592,809	1	1.1	3.0
19951224	132634.1	Polder Wormer	52.511	4.847	118,279	502,595	1	2.3	3.0
19960212	140224.2	Schaaphok	53.256	6.767	247,021	586,231	1	0.9	3.0
19960224	033107.5	Emmen	52.761	6.908	257,635	531,315		1.8	3.0
19960225	135509.3	Roswinkel	52.838	7.062	267,805	540,166	1	0.9	1.5
19960229	080734.4	Eppenhuizen	53.343	6.640	238,401	595,721	1	2.0	3.0
19960306	092050.2	Roswinkel	52.838	7.062	267,805	540,166	2	1.6	1.5
19960312	005144.6	Eexterveen	53.064	6.790	248,994	564,882	2	1.1	3.0
19960312	121348.7	Roswinkel	52.838	7.059	267,631	540,117	4	2.6	2.0
19960312	183412.6	Schuilingsoord	53.072	6.653	239,817	565,676	1	0.8	3.0
19960314	222358.3	Roswinkel	52.838	7.064	267,947	540,136	1	1.1	2.0
19960316	041632.7	Appingedam	53.298	6.848	252,374	591,031	1	1.4	3.0
19960321	181901.8	Roswinkel	52.833	7.054	267,278	539,619	2	1.8	2.0
19960401	185345.1	Amen	52.940	6.608	237,052	550,845	1	0.6	3.0
19960401	232818.3	Nieuw Annerveen	53.067	6.790	248,986	565,289	1	0.1	3.0
19960409	135834.4	Spijkerboor	53.060	6.798	249,561	564,429	1	1.1	3.0
19960415	034131.2	Ten Boer	53.289	6.688	241,727	589,862	1	0.9	3.0
19960417	190512.1	Holwierde	53.357	6.883	254,570	597,680	1	0.9	3.0
19960421	213602.3	Warffum	53.376	6.595	235,342	599,378	1	0.5	3.0
19960425	232220.4	Delfzijl	53.356	6.863	253,242	597,486	1	0.9	3.0
19960607	042056.6	Annerveenschekanaal	53.085	6.780	248,278	567,242	1	1.2	3.0
19960607	083407.0	Garrelsweer	53.309	6.778	247,685	592,143	1	1.3	3.0
19960607	145910.8	Annerveenschekanaal	53.082	6.832	251,744	567,013	1	0.7	3.0
19960616	025327.8	Eleveld	52.947	6.568	234,350	551,598	1	1.7	3.0
19960703	214007.1	Spijkerboor	53.053	6.803	249,911	563,693	1	0.8	3.0
19960804	004217.8	Wachtum	52.724	6.738	246,237	527,063	1	1.6	3.0
19960806	133827.7	Weerdinge	52.756	6.917	258,209	530,771	1	1.6	3.0
19960809	023145.7	Annen	53.057	6.688	242,193	564,031	1	0.3	3.0
19960809	063847.1	Oterdumerwarven	53.287	6.958	259,734	589,942	1	1.6	3.0
19960825	222411.1	Geelbroek	52.945	6.570	234,465	551,451	2	1.7	3.0
19960902	052051.9	Nieuw Roden	53.147	6.422	224,175	573,700	3.5	2.1	3.0
19961016	050900.1	Amen	52.942	6.610	237,160	551,070	1	1.3	3.0
19961116	033349.8	't Zandt	53.355	6.755	246,033	597,251	1	1.3	3.0
19961117	045952.0	Wachtum	52.724	6.732	245,787	527,055	3.5	2.2	3.0

YYMMDD	TIME	LOCATION	LAT	LON	X_RD	Y_RD	INT	MAG	DEPTH
19961130	202657.9	Leek	53.165	6.410	223,365	575,746	1	1.0	3.0
19961206	164648.0	Roswinkel	52.835	7.053	267,220	539,807	1	1.6	1.5
19961216	160115.1	Annerveenschekanaal	53.072	6.815	250,651	565,823	1	0.5	3.0
19961216	160650.2	Annerveenschekanaal	53.078	6.822	251,085	566,481	1	-0.1	3.0
19961226	195205.5	Schaaphok	53.261	6.765	246,898	586,824	1	-0.2	3.0
19961228	005408.5	Winde	53.107	6.505	229,818	569,369	1	1.9	3.0
19961228	181652.7	Roswinkel	52.834	7.043	266,548	539,725	4.5	2.7	2.0
19961228	233946.9	Donderen	53.111	6.502	229,589	569,755	2	1.8	3.0
19970108	012054.4	Westeremden	53.338	6.713	243,294	595,288	1	1.5	3.0
19970114	211340.6	Geelbroek	52.943	6.577	234,917	551,199	1	0.7	3.0
19970116	001246.6	Roswinkel	52.835	7.046	266,708	539,807	4	2.4	2.0
19970124	040004.5	Annen	53.079	6.678	241,478	566,484	1	0.6	3.0
19970217	072055.2	Zijldijk	53.387	6.752	245,743	600,826	1	1.6	3.0
19970217	111600.4	Eleveld	52.948	6.568	234,349	551,691	1	1.2	3.0
19970219	215350.8	Roswinkel	52.832	7.038	266,230	539,495	6	3.4	2.0
19970226	193122.4	Coevorden	52.642	6.803	250,808	517,933	1	1.2	3.0
19970302	152532.5	Kommerzijl	53.289	6.265	213,502	589,361	1	1.3	3.0
19970308	142904.2	Zuidlaarderveen	53.107	6.815	250,575	569,680	1	-0.8	3.0
19970308	142916.9	Zuidlaarderveen	53.109	6.812	250,345	569,990	1	0.0	3.0
19970325	001307.7	Woudbloem	53.252	6.748	245,806	585,726	1	-0.2	3.0
19970401	003419.0	Emmen	52.768	6.873	255,255	532,137	1	1.4	3.0
19970409	222143.9	Noordbroek	53.200	6.865	253,708	580,187	1	0.5	3.0
19970417	202802.9	Roswinkel	52.833	7.055	267,346	539,599	1	0.8	1.5
19970429	181646.3	Schildwolde	53.249	6.803	249,482	585,519	1	1.4	3.0
19970504	024239.7	Weiwerd	53.300	6.930	257,813	591,386	1	1.1	3.0
19970504	042909.8	Kropswolde	53.144	6.737	245,252	573,770	1	0.8	3.0
19970519	154356.2	Roswinkel	52.836	7.053	267,227	539,911	1	1.3	2.0
19970606	193918.8	Opwierde	53.293	6.875	254,165	590,455	1	1.2	3.0
19970619	231925.5	't Zandt	53.364	6.753	245,903	598,231	1	1.8	3.0
19970620	004538.5	Roswinkel	52.834	7.048	266,894	539,718	2	1.8	2.0
19970621	003033.0	Oud-Annerveen	53.094	6.752	246,361	568,207		1.9	3.5
19970709	062312.0	Roswinkel	52.833	7.053	267,234	539,596	1	1.2	2.0
19970717	025629.7	Oud-Annerveen	53.061	6.717	244,085	564,455	1	-0.7	3.0
19970723	064436.0	Lageland	53.247	6.753	246,150	585,195	1	1.2	3.0
19970818	044228.7	Roswinkel	52.834	7.050	267,006	539,739	2	1.6	2.0
19970818	051732.2	Roswinkel	52.834	7.050	267,006	539,721	3	2.1	2.0
19970822	102708.8	Spijkerboor	53.063	6.813	250,558	564,857	1	0.2	3.0
19970823	000156.5	Spijkerboor	53.063	6.813	250,558	564,857	1	0.6	3.0
19970823	193935.0	Lageland	53.239	6.683	241,494	584,256	1	1.6	3.0
19970913	213041.0	Wirdum	53.338	6.747	245,513	595,349	1	1.1	3.0
19970914	193902.6	Annen	53.046	6.740	245,681	562,796	1	0.4	3.0
19971101	225625.8	Zandeweer	53.427	6.705	242,558	605,164	1	1.4	3.0
19971103	181248.7	Donderen	53.108	6.513	230,374	569,489	1	1.4	3.0
19971104	195501.9	Wirdum	53.328	6.793	248,643	594,278	1	1.7	3.0
19971115	162232.1	Oud-Annerveen	53.104	6.822	251,026	569,429	1	0.3	3.0
19971120	173521.0	Slochteren	53.206	6.792	248,796	580,756	1	1.2	3.0
19971126	023537.0	Woudbloem	53.254	6.765	246,913	586,062	1	0.2	3.0
19971203	144719.7	Meedhuizen	53.279	6.897	255,641	588,947	1	1.8	3.0
19971203	150103.6	Siddeburen	53.244	6.858	253,164	585,000	1	1.3	3.0
19971207	070244.4	Zuidlaarderveen	53.075	6.702	243,051	566,012	1	0.3	3.0
19971223	062132.1	Termunterzijl	53.317	7.015	263,437	593,327	1	1.3	3.0
19980108	081145.2	Amen	52.937	6.597	236,272	550,573	1	1.2	3.0
19980122	103155.1	Geelbroek	52.984	6.547	232,828	555,728	1	1.1	3.5
19980128	213303.8	Roswinkel	52.833	7.040	266,336	539,539	5	2.7	2.0
19980128	223404.3	Roswinkel	52.833	7.038	266,201	539,583	3	2.0	2.0
19980131	083939.2	Woudbloem	53.237	6.745	245,615	584,053	1	0.7	3.0
19980205	211149.3	Meedhuizen	53.291	6.935	258,169	590,317	1	1.1	3.0
19980215	072416.4	't Zandt	53.356	6.773	247,251	597,367	3	2.6	3.0

YYMMDD	TIME	LOCATION	LAT	LON	X_RD	Y_RD	INT	MAG	DEPTH
19980329	060640.5	Westeremden	53.345	6.730	244,390	596,070	1	1.3	3.0
19980419	080012.0	Zeerijp	53.339	6.723	243,958	595,412	1	1.5	3.0
19980419	153235.7	Uithuizen	53.425	6.682	241,012	604,894	1	1.6	3.0
19980428	020225.2	Veendam	53.107	6.865	253,920	569,840	1	0.4	3.0
19980430	010841.7	Scharmer	53.197	6.707	243,138	579,574	1	0.9	3.0
19980518	220342.4	Oldenzijl	53.404	6.732	244,378	602,655	1	1.3	3.0
19980530	094315.1	Slochteren	53.204	6.777	247,800	580,422	1	0.9	3.0
19980714	121202.2	Roswinkel	52.833	7.053	267,235	539,540	5	3.3	2.0
19980814	192516.8	Froombosch	53.192	6.803	249,607	579,177		1.1	3.0
19980824	042858.0	Overschild	53.298	6.810	249,820	590,961	1	2.4	3.0
19980905	203611.2	Emmen	52.742	6.875	255,427	529,229	2.5	1.9	3.0
19981004	032832.9	Zeerijp	53.353	6.748	245,593	597,001	1	1.0	3.0
19981020	213205.0	Deurze	52.974	6.607	236,875	554,682	1	0.8	3.0
19981101	174829.5	Geelbroek	52.955	6.572	234,560	552,473	1	1.3	3.0
19981212	075139.5	Oldenzijl	53.392	6.698	242,186	601,261	1	2.0	3.0
19981226	234802.1	Slochteren	53.215	6.830	251,338	581,716	1	1.6	3.0
19990111	083609.1	Roswinkel	52.837	7.057	267,471	540,047	1	1.1	2.0
19990113	193637.0	Zeerijp	53.359	6.777	247,466	597,724	1	2.1	3.0
19990131	045300.5	Siddeburen	53.255	6.825	250,915	586,215	1	0.4	3.0
19990305	190040.2	Borgercompagnie	53.101	6.792	249,024	569,074	1	1.0	3.0
19990306	055639.9	Wirdum	53.325	6.778	247,651	593,906	1	1.6	3.0
19990312	180644.4	Roswinkel	52.833	7.052	267,111	539,571	1-2	1.3	2.0
19990317	231425.4	Roswinkel	52.832	7.052	267,124	539,482	1-2	1.5	2.0
19990421	105956.4	Appingedam	53.312	6.840	251,787	592,577	1	1.4	3.0
19990422	225802.9	Rottevalle	53.112	6.152	206,154	569,561	1	1.0	3.0
19990506	181356.3	Roswinkel	52.836	7.055	267,339	539,896	1-2	1.4	2.0
19990508	204018.9	Stedum	53.325	6.700	242,432	593,845	1	1.6	3.0
19990514	183020.7	Roswinkel	52.834	7.052	267,118	539,741	2	1.7	2.0
19990515	192830.3	Roswinkel	52.834	7.052	267,118	539,741	1-2	1.4	2.0
19990521	000938.8	Sappemeer	53.165	6.815	250,447	576,133	1	0.7	3.0
19990607	202031.3	Steenbergen	53.097	6.402	222,914	568,191	1	1.1	3.0
19990707	090311.3	Amen	52.950	6.627	238,264	552,071	1	1.3	3.0
19990810	232418.3	Garsthuizen	53.382	6.727	244,091	600,201	1	1.4	3.0
19990811	011800.9	Westeremden	53.346	6.702	242,500	596,202	1	0.7	3.0
19990907	171623.5	Eexterveen	53.068	6.795	249,319	565,388	1	1.3	3.0
19990907	194751.0	Eexterveen	53.057	6.813	250,572	564,189	1	0.5	3.0
19991018	185609.5	Schipborg	53.078	6.718	244,162	566,330	1	0.4	3.0
19991018	185755.4	Schuilingsoord	53.061	6.678	241,516	564,389	1	0.3	3.0
19991022	131916.7	Amen	52.941	6.592	235,929	550,994	1	1.7	3.0
19991208	053928.4	Achterdiep	53.179	6.802	249,524	577,729	1	0.2	3.0
19991209	093800.0	Schildwolde	53.247	6.803	249,487	585,241	1	1.1	3.0
19991209	095212.9	Achterdiep	53.184	6.797	249,179	578,242	1	1.0	3.0
19991210	061332.0	Achterdiep	53.175	6.792	248,865	577,215	1	1.4	3.0
19991220	122929.6	Westeremden	53.352	6.710	243,042	596,898	1	1.5	3.0
19991221	045237.7	Kolham	53.190	6.765	247,049	578,905	1	1.0	3.0
19991224	235241.1	Delfzijl	53.320	6.947	258,876	593,616	1	1.8	3.0
19991231	110055.3	Roswinkel	52.835	7.048	266,892	539,830	5	2.8	2.0
20000107	141906.7	Roswinkel	52.834	7.043	266,557	539,711	2	1.1	2.0
20000110	041807.4	Schipborg	53.077	6.655	239,920	566,197	1	0.6	3.0
20000212	194810.6	Appingedam	53.321	6.822	250,546	593,554	1	1.7	3.5
20000319	161336.0	Westeremden	53.343	6.698	242,285	595,827		1.6	3.0
20000327	102322.0	Roswinkel	52.835	7.045	266,667	539,825	1	0.8	2.0
20000401	031351.3	Dalen	52.685	6.750	247,108	522,666		1.3	3.0
20000408	120728.0	Engelbert	53.205	6.632	238,111	580,393		1.2	3.0
20000408	211317.8	Godlinze	53.370	6.845	251,990	599,056		1.1	3.0
20000414	230747.7	Ten Boer	53.308	6.772	247,243	592,006		1.2	3.0
20000516	011114.7	Garsthuizen	53.381	6.710	242,985	600,032		1.9	3.0
20000609	170347.2	Annerveenschekanaal	53.087	6.813	250,506	567,489	1	1.1	3.0

YYMMDD	TIME	LOCATION	LAT	LON	X_RD	Y_RD	INT	MAG	DEPTH
20000611	041220.1	Loppersum	53.348	6.763	246,602	596,483	2	2.0	3.0
20000612	154823.0	Loppersum	53.340	6.742	245,177	595,546	2	2.5	3.0
20000615	014224.9	Siddeburen	53.278	6.830	251,197	588,800	2	2.4	3.0
20000706	230956.7	Loppersum	53.340	6.752	245,843	595,559	1	1.2	3.0
20000710	150549.1	Vries	53.064	6.575	234,583	564,697		1.0	3.0
20000713	084152.4	Vries	53.079	6.565	233,886	566,299		1.1	3.0
20000716	013412.0	't Zandt	53.367	6.782	247,783	598,565		1.5	3.0
20000922	170516.7	Annerveenschekanaal	53.076	6.820	250,978	566,256		1.0	3.0
20000922	205206.5	Annerveenschekanaal	53.081	6.772	247,728	566,786	2	2.2	3.5
20000923	034747.4	Annerveenschekanaal	53.081	6.788	248,845	566,771		1.0	2.7
20001025	181034.7	Roswinkel	52.832	7.052	267,125	539,463	5	3.2	2.3
20001112	021636.2	Deurze	52.977	6.608	236,981	555,054		0.3	3.0
20001223	052006.1	Borgercompagnie	53.108	6.812	250,348	569,842		0.4	3.0
20001226	163357.6	Meedhuizen	53.294	6.910	256,493	590,708		1.4	3.0
20010226	113907.3	Annerveenschekanaal	53.072	6.822	251,097	565,887		0.8	3.0
20010318	031420.7	Lageland	53.244	6.692	242,041	584,766		1.6	3.0
20010428	100008.2	Geelbroek	52.948	6.567	234,236	551,764		1.5	3.0
20010428	100055.5	Eleveld	52.959	6.575	234,776	552,978		1.1	3.0
20010428	230015.8	Roswinkel	52.833	7.053	267,233	539,633	4	2.4	2.1
20010517	074815.9	Hoornsedijk	53.173	6.612	236,835	576,828		1.4	3.0
20010610	033533.2	Annen	53.049	6.753	246,567	563,203		0.5	3.0
20010619	064955.5	Annerveenschekanaal	53.079	6.820	250,971	566,608		1.0	3.0
20010621	035049.0	Overschild	53.295	6.800	249,158	590,670		1.7	3.0
20010807	170901.5	Veendam	53.097	6.845	252,605	568,663		0.3	3.0
20010909	065812.6	Alkmaar	52.651	4.713	109,374	518,265	6	3.5	2.0
20010910	043015.3	Alkmaar	52.653	4.712	109,274	518,445	5	3.2	2.0
20011010	064109.3	Bergen aan Zee	52.682	4.648	105,011	521,739	3	2.7	2.9
20011010	140643.3	Schaaphok	53.239	6.763	246,834	584,355		1.0	3.0
20011010	140657.2	Schaaphok	53.240	6.763	246,832	584,429		0.8	3.0
20011204	190831.0	Woudbloem	53.204	6.785	248,355	580,507		0.2	3.0
20011204	190837.8	Woudbloem	53.204	6.785	248,355	580,507		0.0	3.0
20011204	223337.9	Woudbloem	53.210	6.743	245,560	581,085		1.0	3.0
20011211	151717.6	Slochteren	53.217	6.788	248,551	581,902		0.7	3.0
20011220	012542.9	Veendam	53.081	6.838	252,195	566,818		0.5	3.0
20011225	232809.4	Noordzee	53.487	6.718	243,320	611,874		1.3	0.0
20011226	123653.0	Eexterveen	53.057	6.805	250,015	564,104		-0.2	3.0
20020205	103039.7	Stedum	53.319	6.717	243,555	593,197		2.2	3.0
20020214	170104.7	Roswinkel	52.832	7.037	266,113	539,496	3	2.1	2.0
20020227	035214.0	Appingedam	53.337	6.825	250,732	595,339		1.1	3.0
20020317	011627.9	Donderen	53.094	6.543	232,409	567,908		0.4	3.0
20020414	011144.0	Annen	53.049	6.770	247,686	563,168		1.9	3.0
20020510	103348.9	Bierum	53.378	6.857	252,747	599,980		1.7	3.0
20020511	100723.2	Geelbroek	52.943	6.580	235,141	551,221		1.5	3.0
20020522	133813.0	Eleveld	52.956	6.585	235,453	552,655		1.0	3.0
20020628	030647.3	Smilde	52.968	6.450	226,363	553,848		1.8	3.0
20020718	053116.8	Froombosch	53.188	6.783	248,279	578,687		1.6	3.0
20020727	150108.6	Geelbroek	52.947	6.565	234,126	551,632		1.6	3.0
20020805	192810.1	Oudemolen	53.055	6.657	240,074	563,771		0.9	3.0
20020829	211322.7	Luddeweer	53.247	6.747	245,705	585,205		0.0	3.0
20020905	000021.4	Mariënberg	52.508	6.563	234,809	502,735		0.9	3.0
20020906	060705.5	Veendam	53.112	6.842	252,347	570,365		0.6	3.0
20020922	071333.4	Annen	53.056	6.680	241,636	563,910		0.6	3.0
20020922	073013.8	Annen	53.035	6.638	238,885	561,486		0.5	3.0
20021012	023213.6	Veendam	53.107	6.815	250,575	569,680		0.9	3.0
20021014	234522.5	Roswinkel	52.834	7.045	266,670	539,694	1	0.9	2.0
20021019	180339.4	Spijkerboor	53.071	6.768	247,527	565,633		1.3	3.0
20021214	001324.6	Coevorden	52.677	6.832	252,648	521,865		1.4	3.0
20021216	122339.0	Zuidlaren	53.092	6.718	244,133	567,906		1.4	3.0

YYMMDD	TIME	LOCATION	LAT	LON	X_RD	Y_RD	INT	MAG	DEPTH
20021217	002318.7	Tjuchem	53.291	6.860	253,168	590,249		0.9	3.0
20021218	203109.1	Spitsbergen	53.175	6.847	252,540	577,380		0.8	3.0
20021224	025722.6	Roswinkel	52.833	7.042	266,449	539,522		1.4	2.0
20030101	191615.3	Loppersum	53.338	6.743	245,293	595,289		1.0	3.0
20030113	024545.5	Smilde	52.971	6.413	223,896	554,127		1.7	3.0
20030118	181243.3	Overschild	53.287	6.770	247,176	589,723		1.0	3.0
20030123	074616.6	Winneweer	53.307	6.752	245,912	591,906		1.6	3.0
20030130	002730.2	Leermens	53.342	6.795	248,723	595,875		1.5	3.0
20030131	152047.7	Denemarken	53.232	6.782	248,072	583,618		0.3	3.0
20030202	093223.6	Eleveld	52.950	6.588	235,688	552,009		2.0	3.0
20030206	192524.9	De Paauwen	53.259	6.768	247,124	586,623		0.3	3.0
20030211	192949.5	Zeerijp	53.353	6.773	247,258	596,996		1.3	3.0
20030212	062220.0	De Paauwen	53.262	6.812	250,009	586,995		0.8	3.0
20030214	065424.1	Rottevalle	53.146	6.122	204,107	573,360		1.8	3.0
20030228	215418.19	Westeremden	53.355	6.730	244,369	597,201		0.7	3.0
20030303	205121.89	Middelstum	53.360	6.662	239,809	597,73		2.2	3.0
20030306	201518.67	Hoogezand	53.141	6.753	246,374	573,419		0.9	3.0
20030309	053126.70	Kantens	53.372	6.640	238,344	598,984		1.1	3.0
20030323	160003.03	Emmapolder	53.457	6.783	247,698	608,673		1.5	3.0
20030329	210901.44	Harkstede	53.238	6.682	241,386	584,087		0.4	3.0
20030401	002552.09	Oldenklooster	53.364	6.852	252,448	598,342		0.3	3.0
20030402	201948.74	Loppersum	53.340	6.718	243,623	595,517		1.9	3.0
20030405	164948.33	Engelbert	53.209	6.630	237,991	580,874		0.3	3.0
20030406	000750.70	Overschild	53.272	6.795	248,877	588,012		0.1	3.0
20030406	005727.90	Ruiten	53.205	6.750	246,017	580,499		1.0	3.0
20030406	230204.37	Ruiten	53.206	6.763	246,904	580,683		0.7	3.0
20030416	162042.53	Overschild	53.281	6.775	247,522	589,079		0.7	3.0
20030418	235955.00	Schaaphok	53.238	6.753	246,168	584,25		0.0	3.0
20030420	001939.19	Schaaphok	53.247	6.750	245,928	585,172		0.1	3.0
20030428	215611.33	Ten-Boer	53.284	6.727	244,294	589,26		1.0	3.0
20030429	025504.92	Ten-Boer	53.284	6.730	244,516	589,283		1.3	3.0
20030514	205215.91	Siddeburen	53.254	6.865	253,587	586,121		0.8	3.0
20030514	222346.52	Siddeburen	53.257	6.847	252,357	586,411		0.8	3.0
20030521	045709.24	Annen	53.072	6.765	247,301	565,74		1.1	3.0
20030523	025950.86	Muntendam	53.084	6.823	251,182	567,207		0.6	3.0
20030531	231225.73	Siddeburen	53.247	6.875	254,27	585,374		0.8	3.0
20030603	161538.91	Stedum	53.337	6.683	241,299	595,104		1.5	3.0
20030606	142716.47	Harkstede	53.225	6.682	241,411	582,696		0.7	3.0
20030608	053047.24	Froombosch	53.192	6.788	248,605	579,139		1.0	3.0
20030608	081416.55	Woltersum	53.271	6.737	244,988	587,863		1.5	3.0
20030616	004417.12	Smilde	52.963	6.407	223,46	553,25		2.3	2.6
20030805	184508.49	Assen	52.975	6.558	233,628	554,703		1.1	3.0
20030807	082421.12	Zeerijp	53.350	6.758	246,266	596,643		1.7	3.0
20030807	105639.85	Zeerijp	53.345	6.748	245,611	596,093		1.3	3.0
20030820	084614.99	Veendam	53.106	6.815	250,575	569,661		0.5	3.0
20030825	042455.00	Kiel-Windeweer	53.108	6.792	249,01	569,779		0.7	3.0
20030825	100535.83	Kiel-Windeweer	53.109	6.798	249,454	569,88		0.9	3.0
20030922	175011.50	Uithuizen	53.395	6.688	241,514	601,638		2.4	3.0
20030927	135754.15	Westeremden	53.348	6.697	242,164	596,381		2.7	3.0
20031011	114408.34	Roswinkel	52.835	7.055	267,34	539,858		1.6	2.0

APPENDIX 2 COLOUR FIGURES

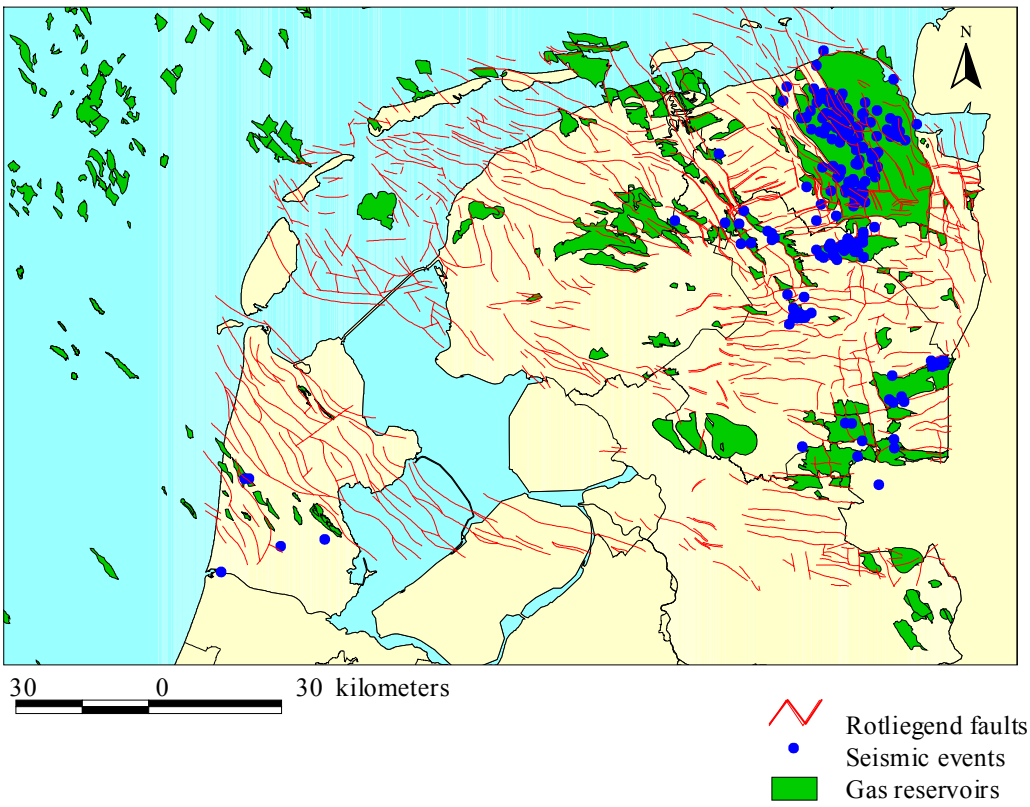

Figure 1.2. Map of the northern Netherlands showing the geographical locations of gas reservoirs, Rotliegend faults (at reservoir level) and seismic events. Source: TNO-NITG, KNMI.

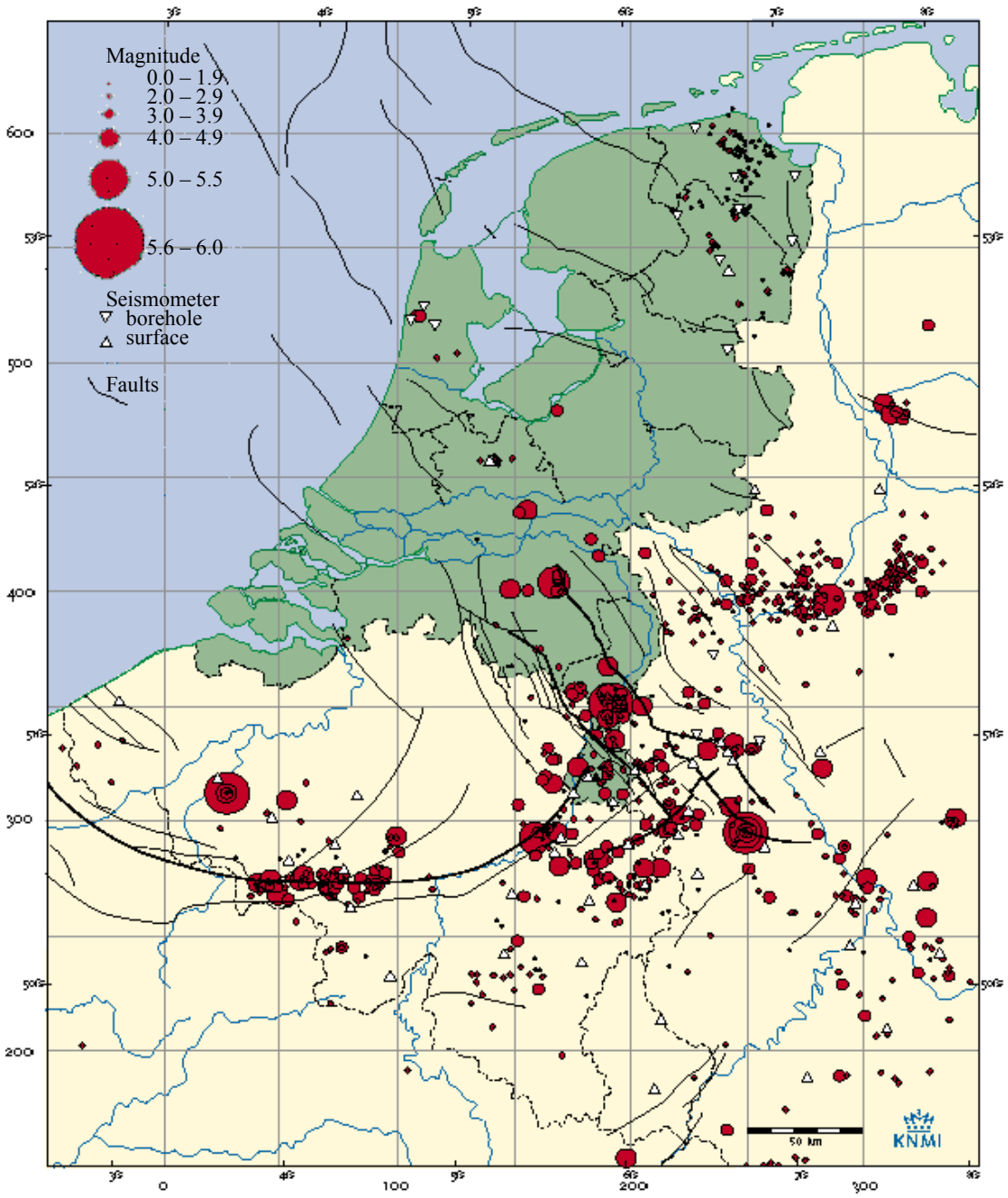

Figure 1.3. Map of the Netherlands and surrounding countries with registered earthquakes from 1905 to 1996. Source: KNMI.

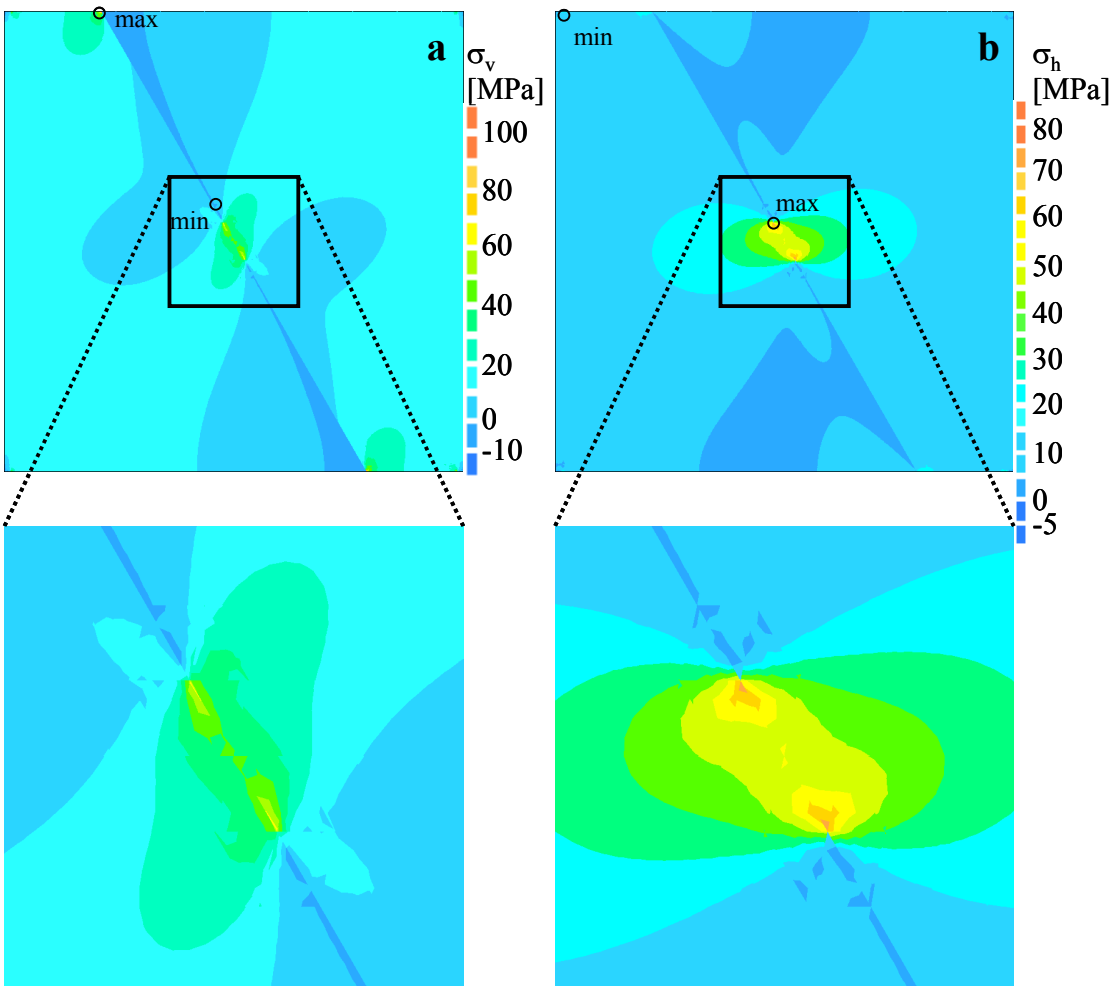

Figure 4.2. *Calculated stresses after loading. (a) Vertical stress; max. value: 115 MPa; min. value: -7.0 MPa. (b) Horizontal stress; max. value: 66.5 MPa; min. value: -6.7 MPa. Positive stress values denote compression. Contour shapes indicate the location of the fault and the asperity. Location of maximum and minimum value is indicated.*

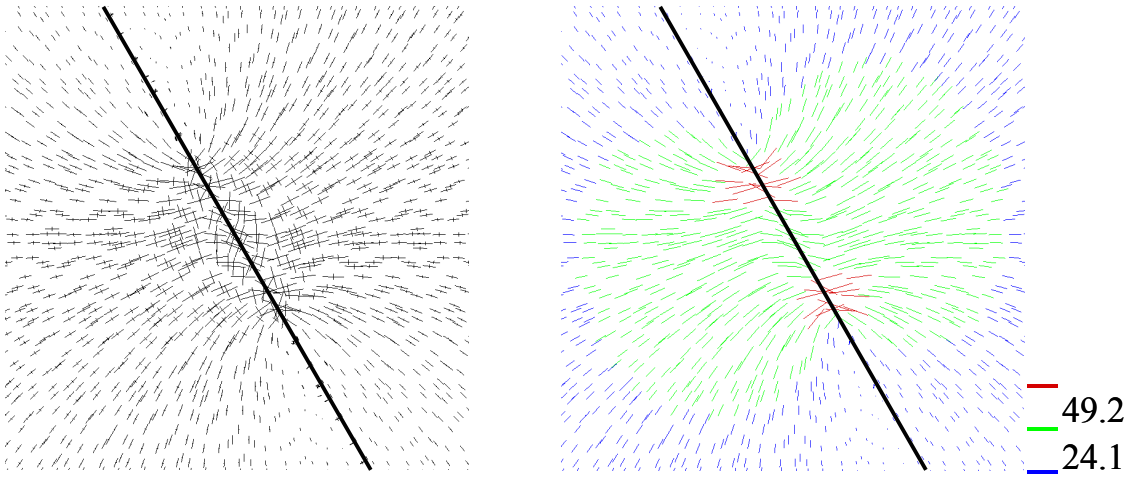

Figure 4.3. *Vector plot of calculated principal stresses after loading. The locations of the fault and the asperity are indicated by the dashed and solid black lines, respectively. The zoom factor is the same as in Figure 4.2.*

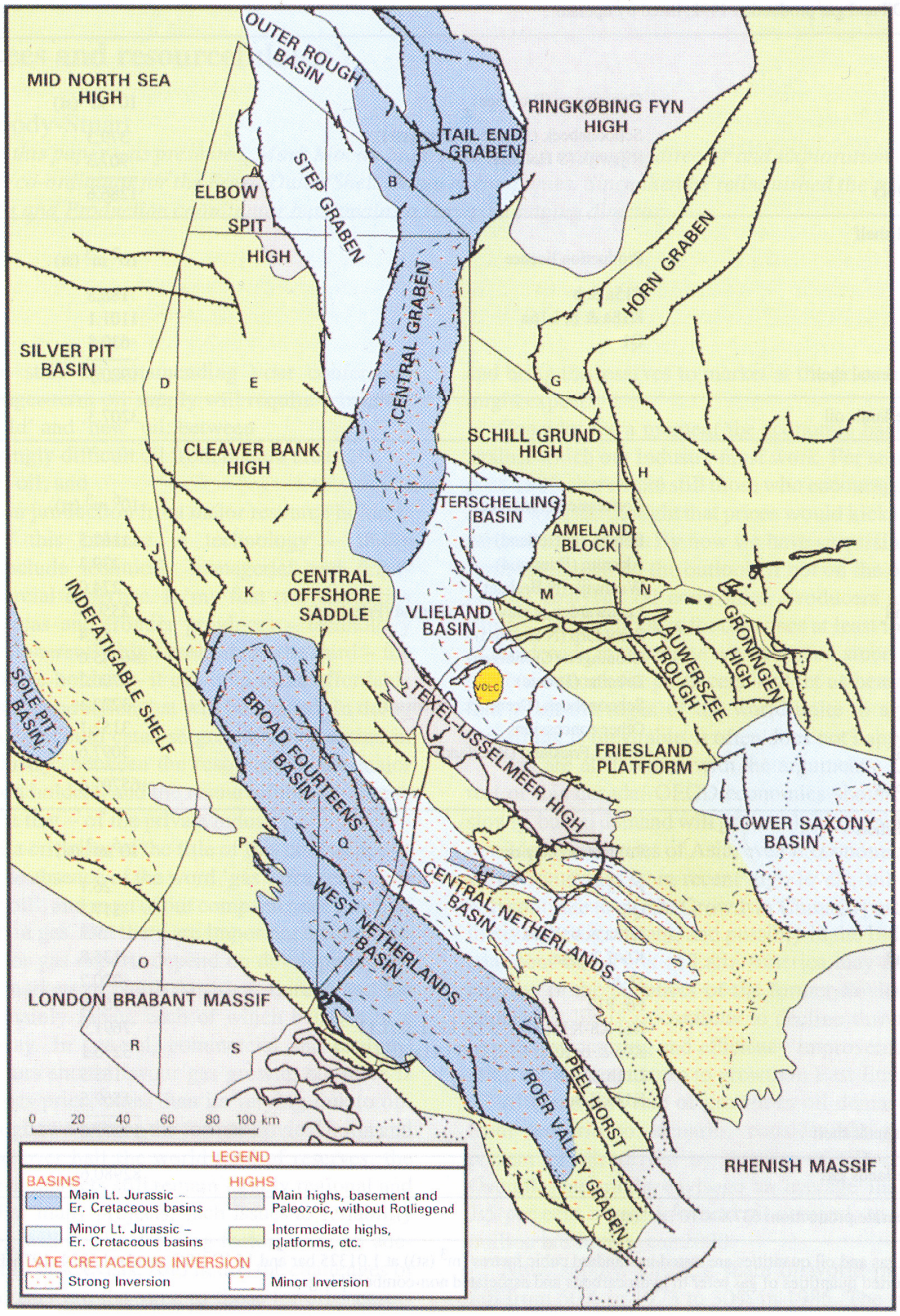

Figure 7.1. Mesozoic structural geology of the on- and offshore Netherlands (from Rondeel et al. 1996).

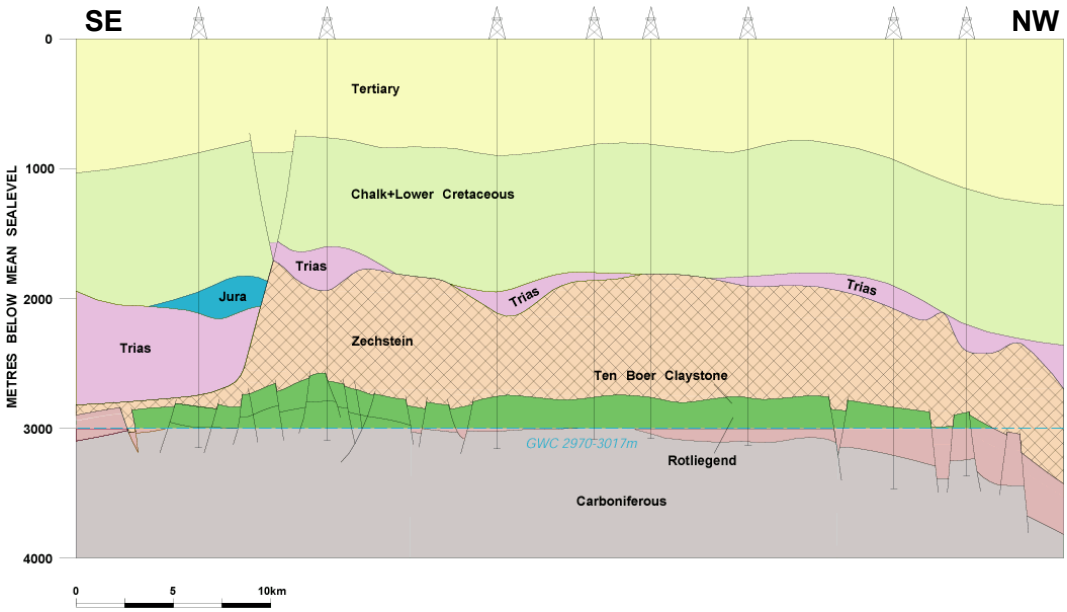

Figure 7.4. Geological cross section through the Groningen gas field (source: NAM).

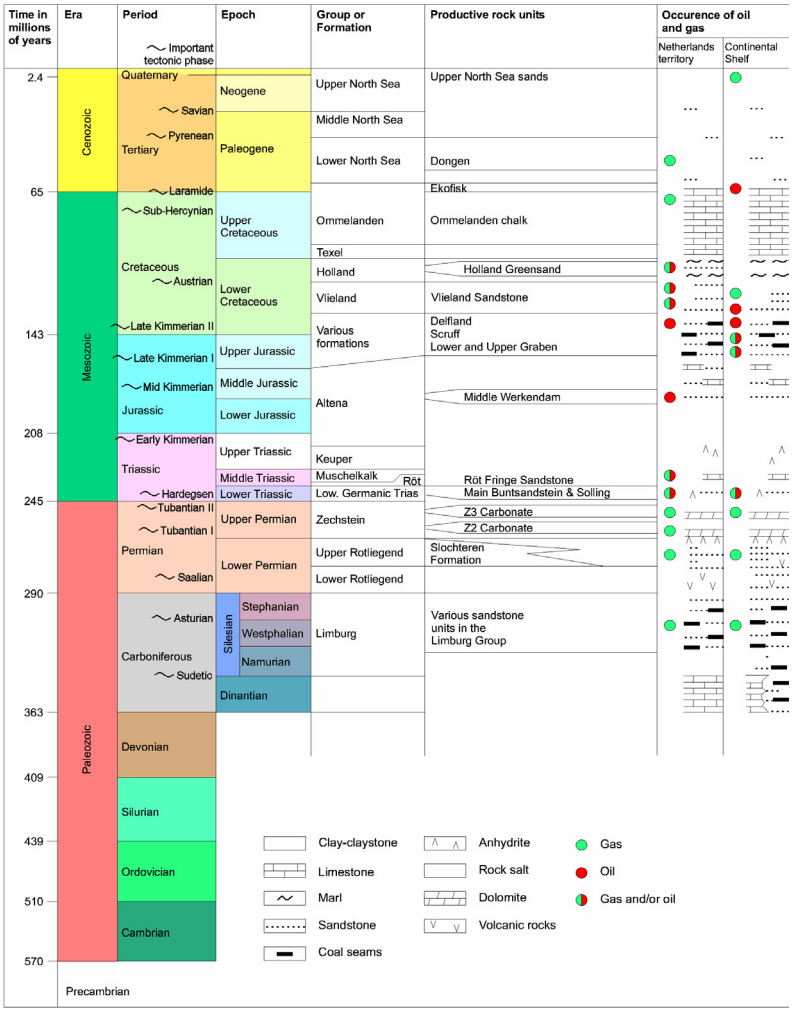

Figure 7.8. Geological time scale with composite stratigraphical column of the Netherlands and the Continental Shelf (after Ministry of Economic Affairs 2001).

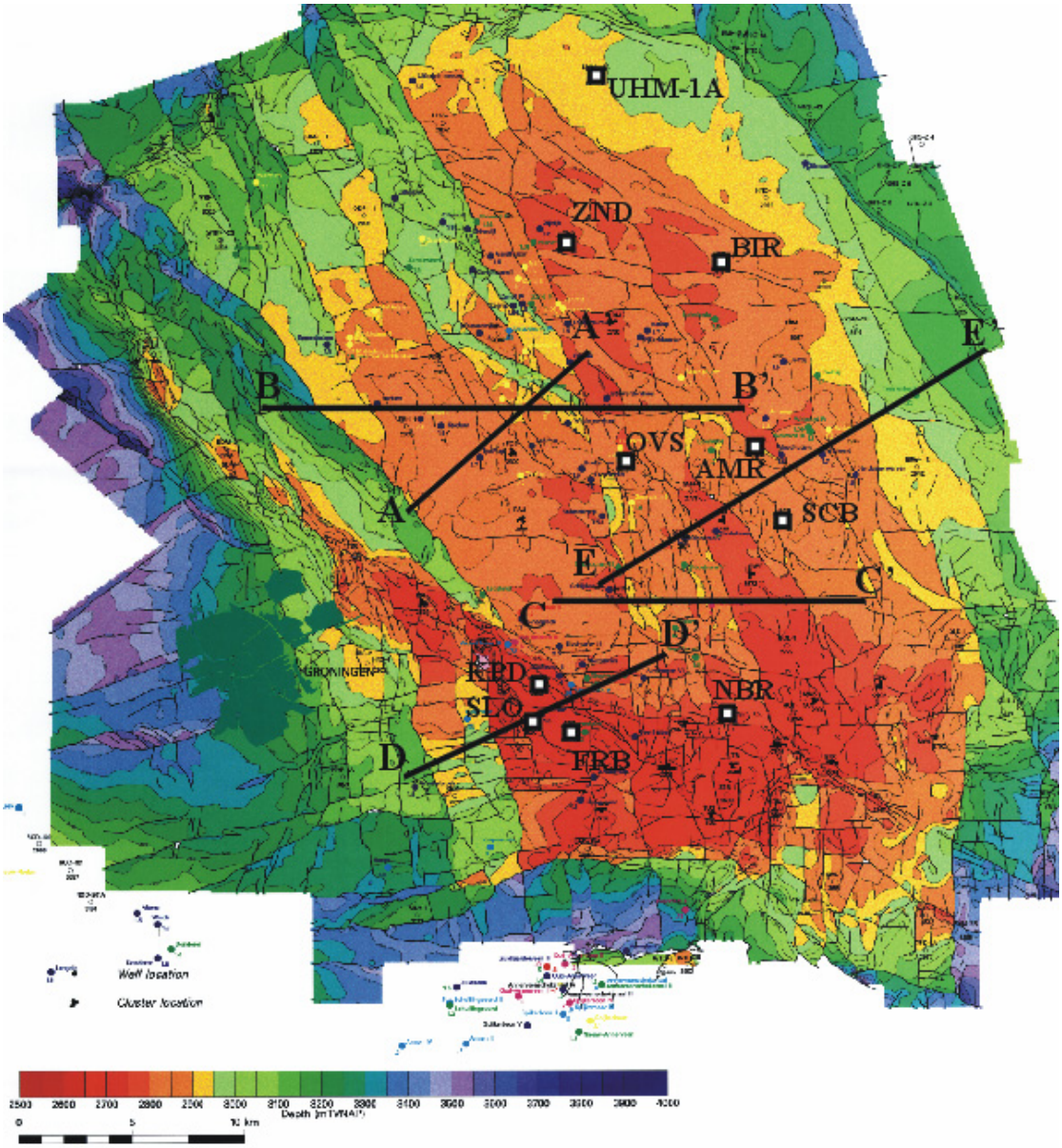

Figure 7.10. Top reservoir depth contour map of the Groningen gas field (source: NAM). White squares denote the location of some well clusters. Coloured dots denote the location of seismic events as determined by KNMI. Profile lines AA', BB', CC', DD' and EE' are shown, corresponding to Figures 7.12 – 7.15 and 7.21.

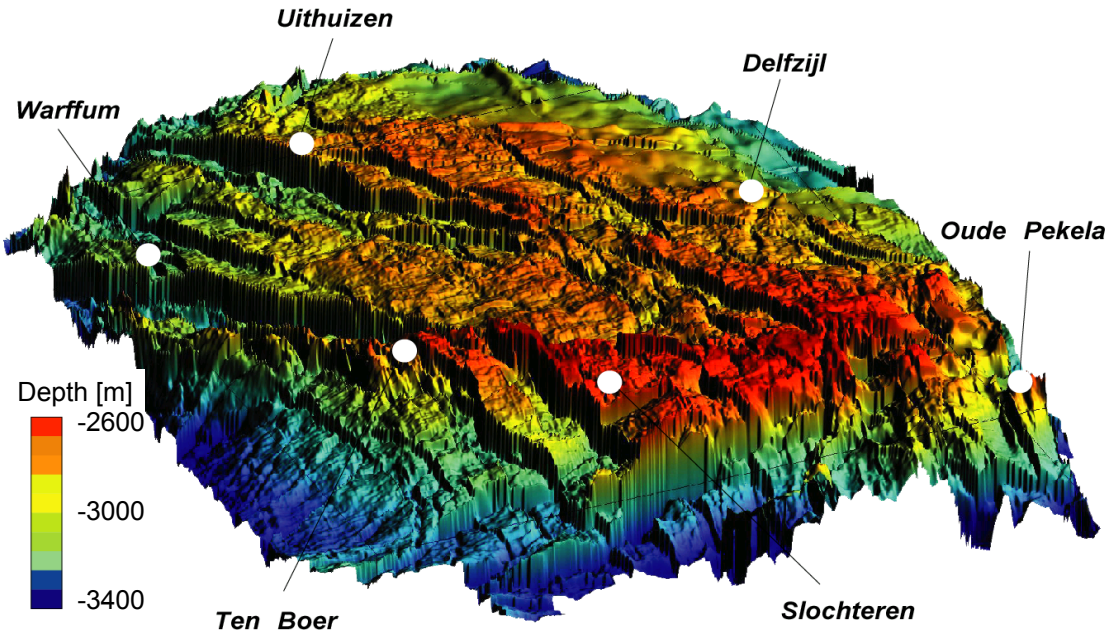

Figure 7.11. Birds-eye view from southwestern direction on the Groningen gas field. Contours indicate the top reservoir depth (source: NAM).

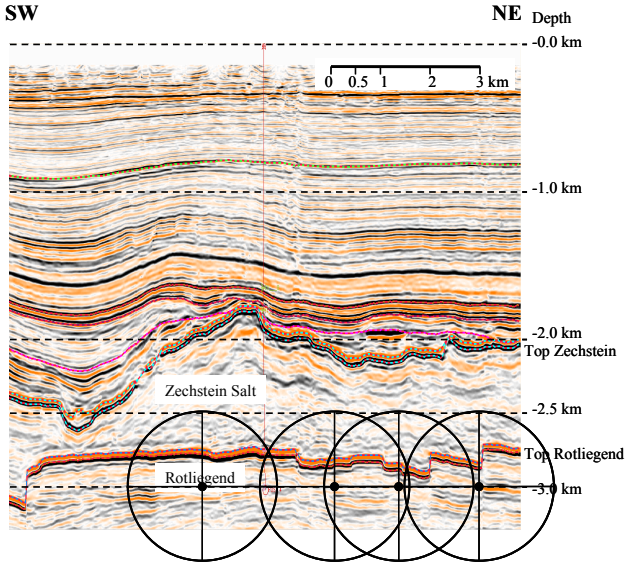

Figure 7.12. Seismic cross section AA' through the Groningen field (for location see Figure 7.10). The vertical scale is three times the horizontal scale. Black dots indicate locations of seismic events as determined by KNMI. A black ellipse around an event denotes the uncertainty in location (source: NAM, KNMI).

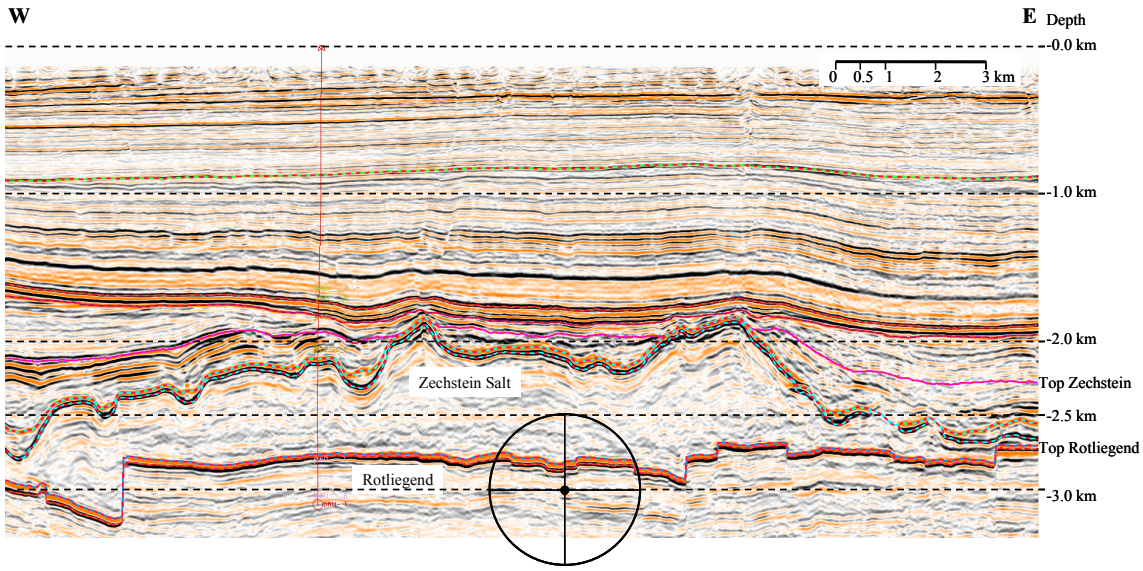

Figure 7.13. Seismic cross section BB' through the Groningen field (for location see Figure 7.10). The vertical scale is three times the horizontal scale. Black dots indicate locations of seismic events as determined by KNMI. A black ellipse around an event denotes the uncertainty in location (source: NAM, KNMI).

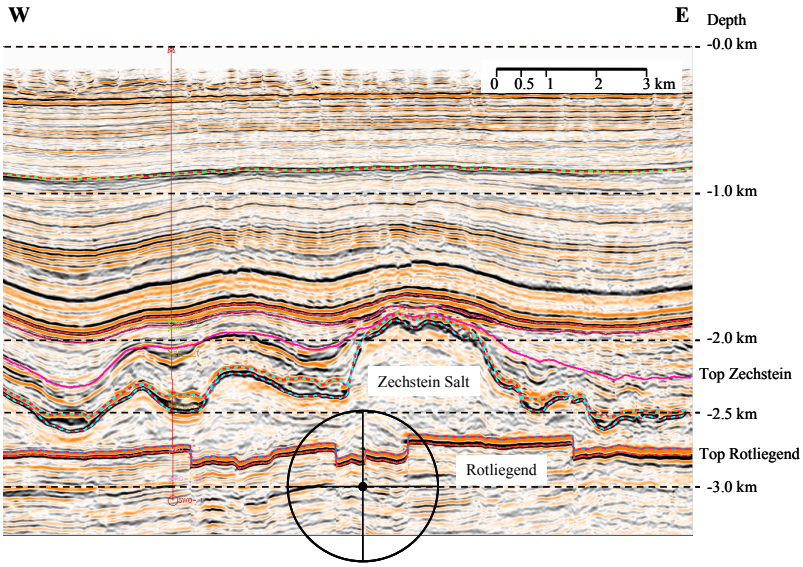

Figure 7.14. Seismic cross section CC' through the Groningen field (for location see Figure 7.10). The vertical scale is three times the horizontal scale. Black dots indicate locations of seismic events as determined by KNMI. A black ellipse around an event denotes the uncertainty in location (source: NAM, KNMI).

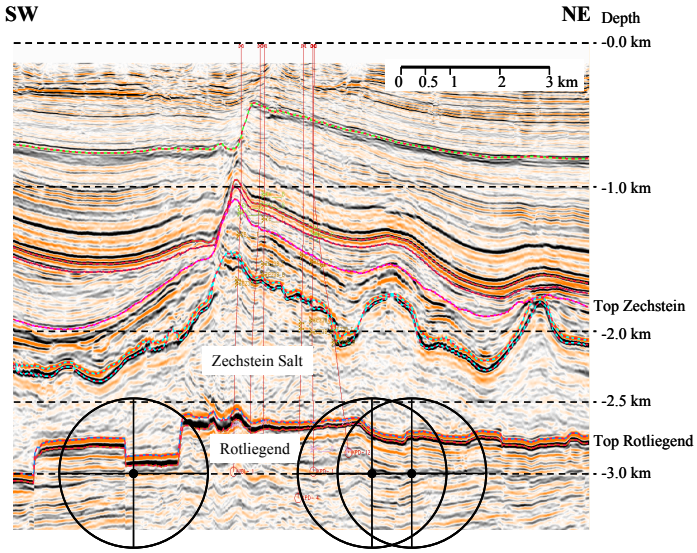

Figure 7.15. Seismic cross section DD' through the Groningen field (for location see Figure 7.10). The vertical scale is three times the horizontal scale. Black dots indicate locations of seismic events as determined by KNMI. A black ellipse around an event denotes the uncertainty in location (source: NAM, KNMI).

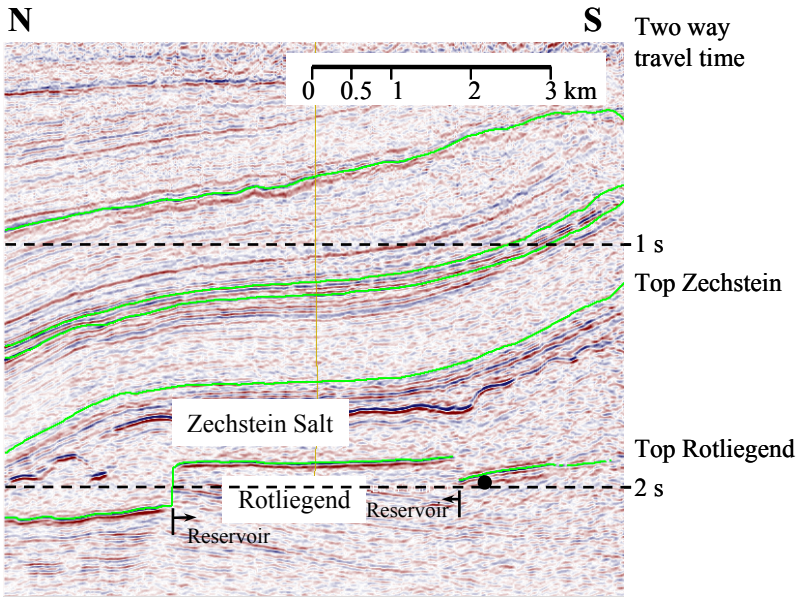

Figure 7.18. Seismic NS cross section through the Annerveen field (for location see Figure 7.16). The vertical scale is in two way travel time in seconds. The black dot indicates the location of a seismic event as determined by KNMI (source: NAM, KNMI).

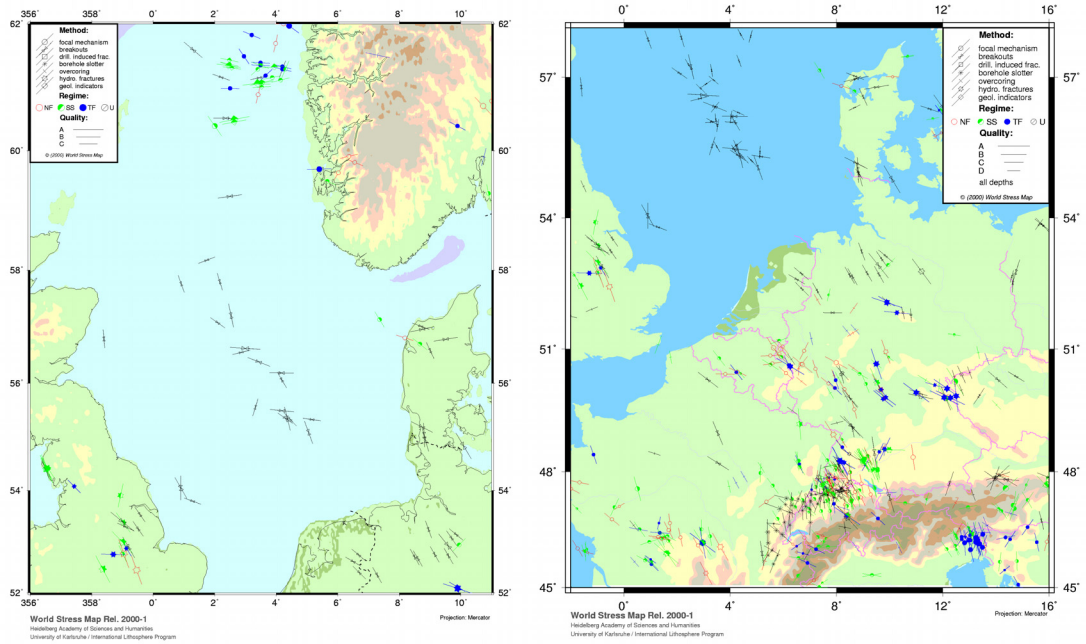

Figure 7.19. Stress maps of the North Sea and central Europe (from Reinecker et al. 2000). Stress symbols display the orientations of the maximum horizontal stress σ_H. The length of the stress symbols represents the data quality, with A as the best quality category. A-quality data are believed to record the orientation of the horizontal tectonic stress field to within $\pm$ 10°-15°, B-quality data to within $\pm$ 15°-20° and C-quality data to within $\pm$ 25°. D-quality data are considered to yield questionable tectonic stress orientations (Zoback 1992). The tectonic regimes are: NF for normal faulting, SS for strike-slip faulting, TF for thrust faulting and U for an unknown regime.

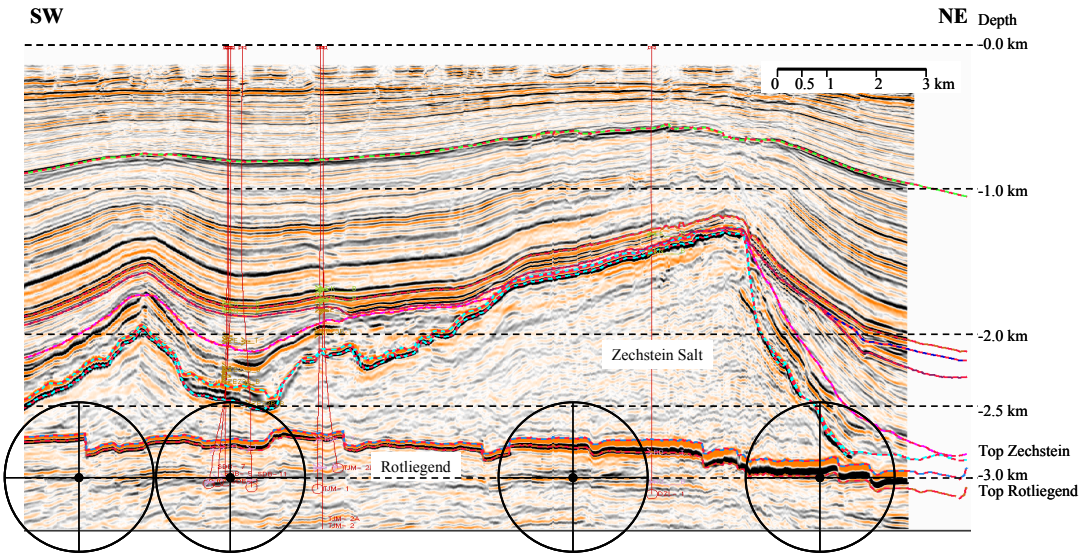

Figure 7.21. Seismic cross section EE' through the Groningen field (for location see Figure 7.10). The vertical scale is three times the horizontal scale. Black dots indicate locations of seismic events as determined by KNMI. A black ellipse around an event denotes the uncertainty in location (source: NAM, KNMI).

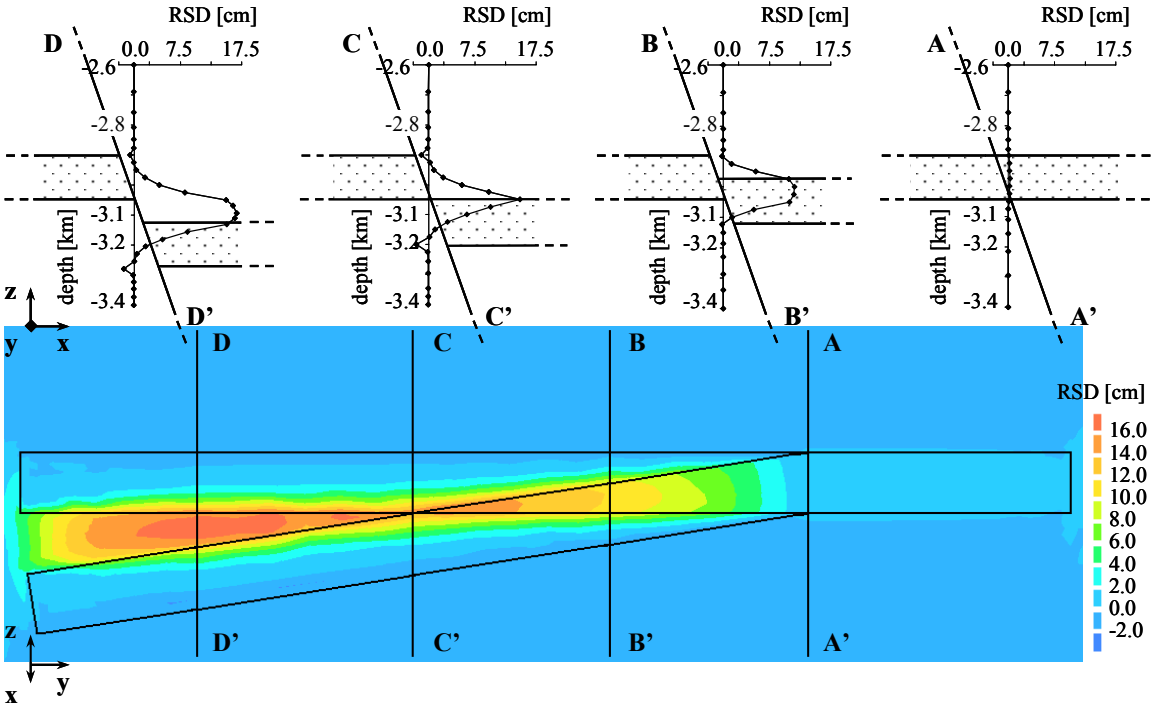

Figure 9.2. Relative shear displacements (RSD) on the fault plane for model 'throw_var' with default properties and loading conditions and full pore pressure reduction (11 depletion steps, see Table 8.6, Chapter 8.3.6). The maximum RSD-value is 16.7 cm, located in between observation lines CC' and DD', close to line DD'. View direction of the contour plot is normal to the fault plane. Intersection lines of the two reservoir compartments with the fault plane are shown. View direction of the cross sections is in strike direction of the fault. Pointed areas denote the reservoir compartments.

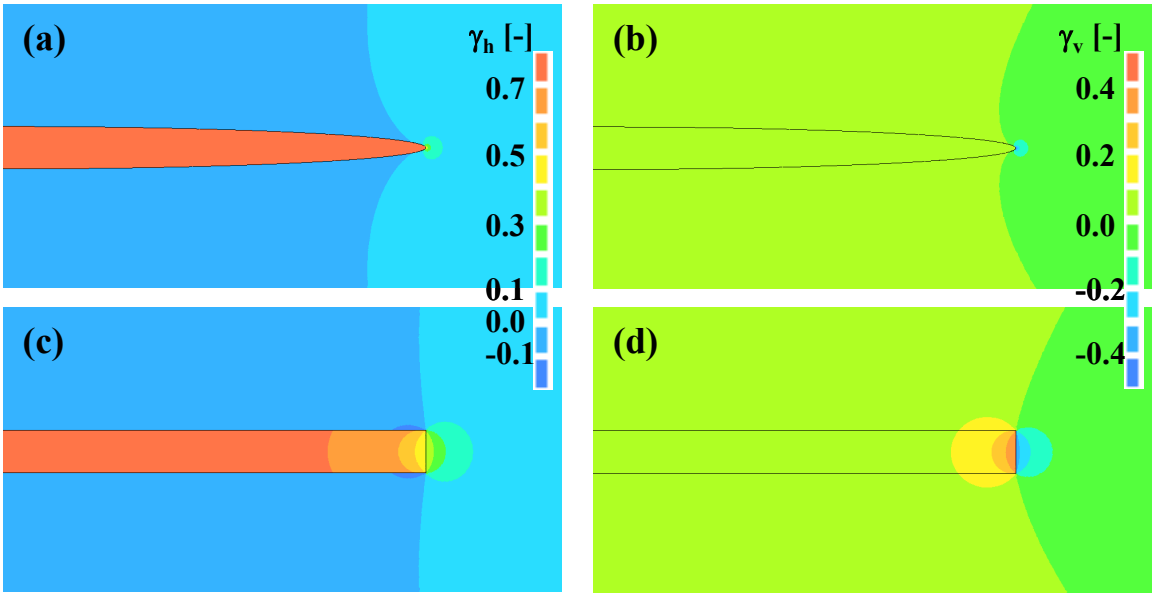

Figure 10.4. Comparison of numerically calculated γ-values in (a) and (b) an ellipsoidal reservoir and (c) and (d) a disk-shaped reservoir. Black lines indicate the circumference of the reservoirs. (a) and (c): γ_h; (b) and (d): γ_v. Reservoir radius: 1500m; reservoir thickness: 150 m (e = 0.05); $\nu^{sur} = \nu^{res} = 0.2$; $E^{sur} = E^{res} = 13.0$ GPa.

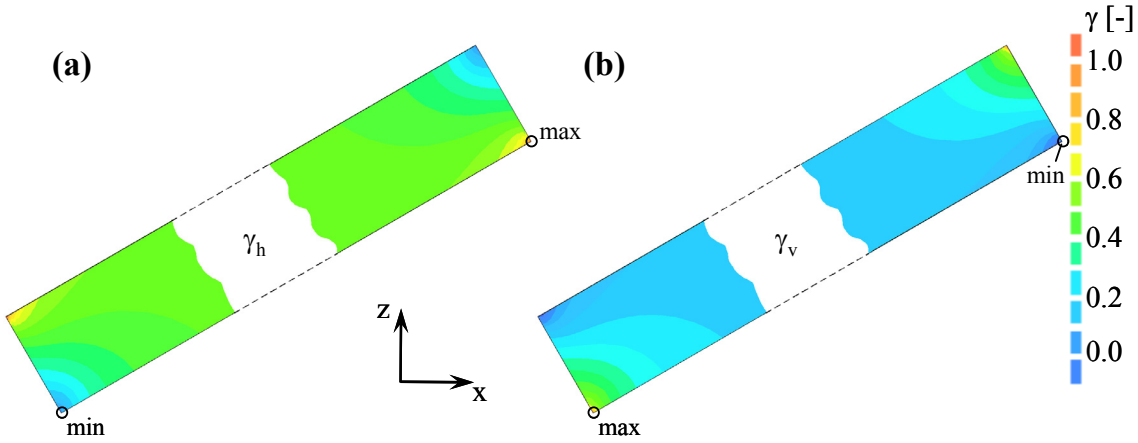

Figure 10.13. Contour plots of calculated (a) γ_h-values and (b) γ_v-values at the reservoir edges for a reservoir tilt angle of 30°. The location of maximum and minimum values for the calculations with a tilt angle $\geq$ 7.6° are indicated.

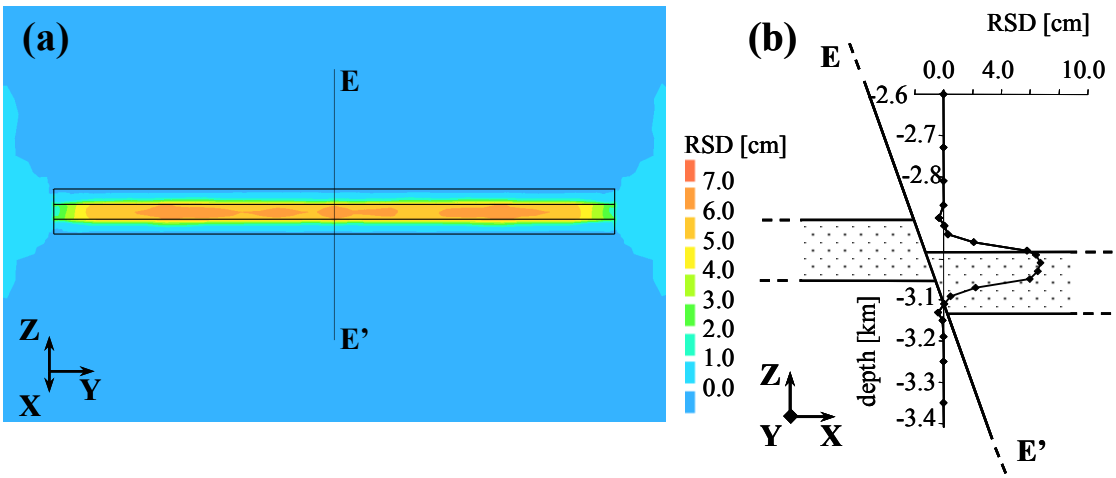

Figure 11.2. Calculated RSD-values as a result of gas depletion for model 'throw_const_½D' with surrounding rock properties being the same as reservoir rock properties and initial hydrostatic reservoir pore pressure. (a) contour plot; view direction is normal to the fault plane. (b) Graphical plot for observation line EE'; dotted areas denote the reservoir compartments.

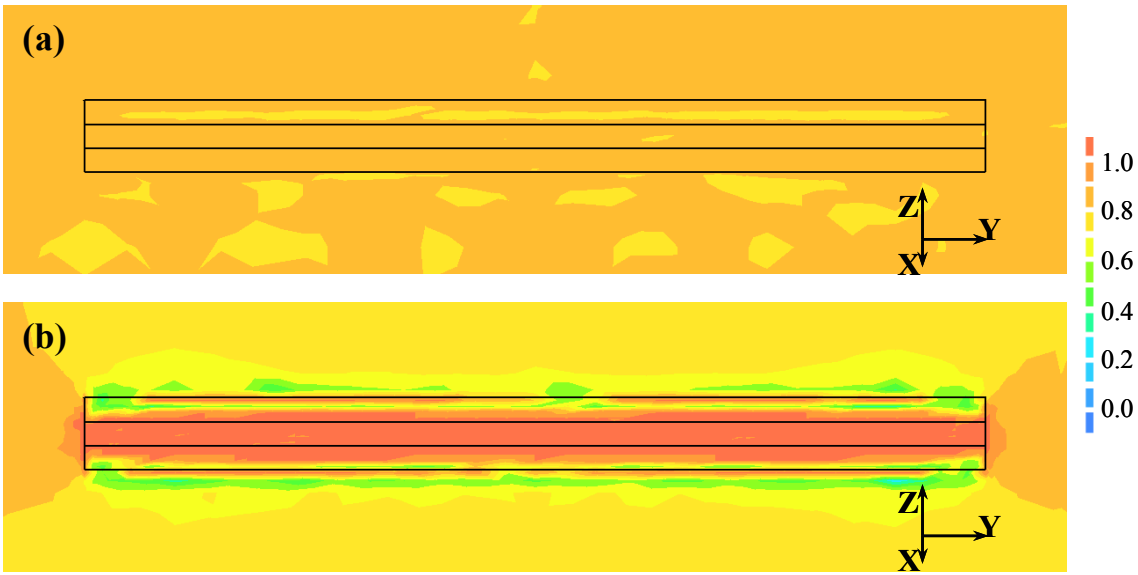

Figure 11.6. Calculated MSC-values on the fault plane, (a) before gas depletion and (b) after gas depletion, for model 'throw_const_½D' with surrounding rock properties being the same as reservoir rock properties and initial hydrostatic reservoir pore pressure. View direction is normal to the fault plane. Black lines indicate the intersection of the reservoir compartments with the fault plane.

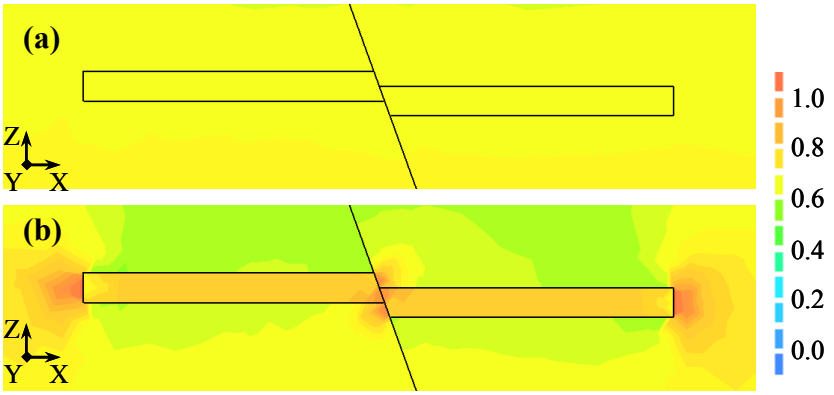

Figure 11.7. Calculated MSC^{3D}-values in the rock volume, (a) before gas depletion and (b) after gas depletion, for model 'throw_const_½D' with surrounding rock properties being the same as reservoir rock properties and initial hydrostatic reservoir pore pressure. View plane is a vertical cross section through the centre of the reservoir, normal to the strike direction of the fault. Black lines indicate the reservoir boundaries and the fault plane.

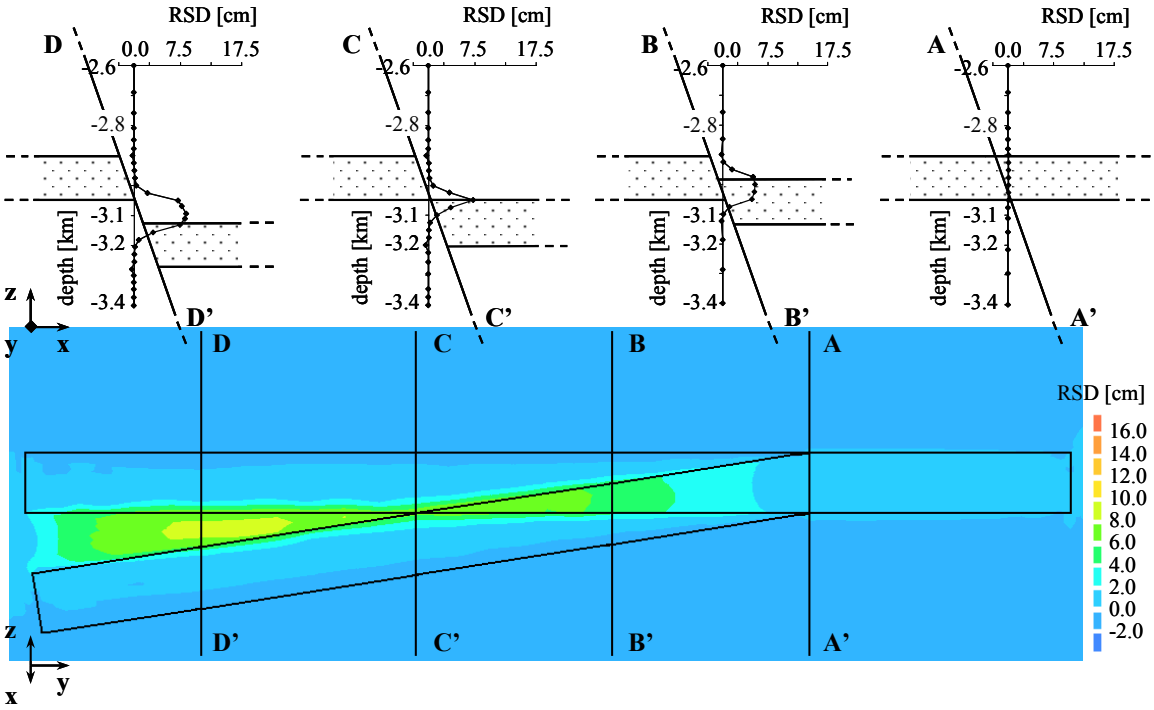

Figure 11.20. Calculated RSD-values on the fault plane for model 'throw_var' with equal reservoir and surrounding rock properties and initial hydrostatic reservoir pore pressure. The maximum value is 8.6 cm, located in between observation lines CC' and DD' close to DD'. View direction of the contour plot is normal to the fault plane. Intersection lines of the two reservoir compartments with the fault plane are shown. View direction of the cross sections is in strike direction of the fault. Dotted areas denote the reservoir compartments.

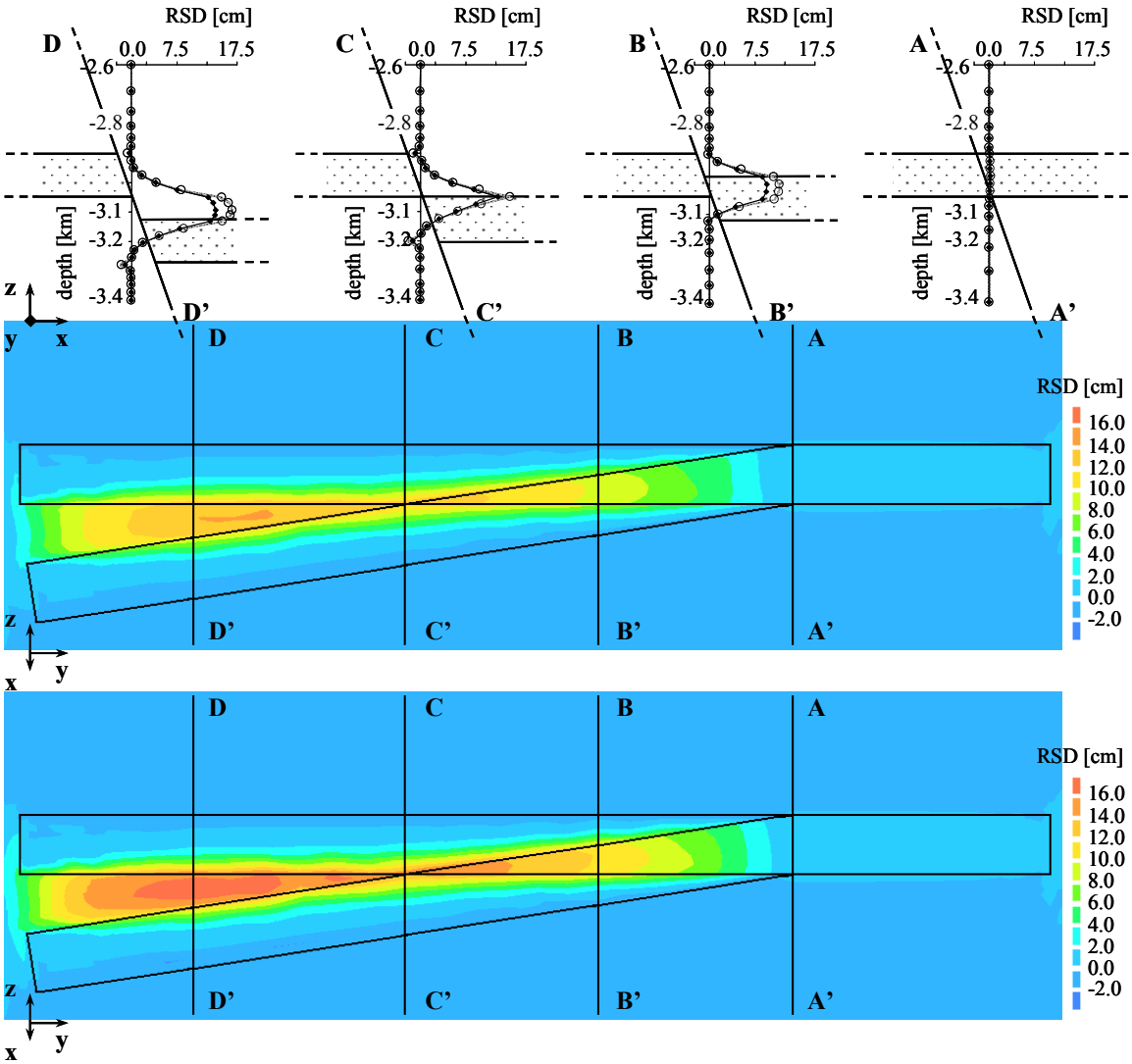

Figure 11.24. Calculated RSD-values on the fault plane for model 'throw_var' with surrounding rock being stiffer than the reservoir rock and initial reservoir overpressure (see Table 11.1). The upper and lower contour plots are for a hydrostatic (10 depletion steps) and full (11 steps) pore pressure reduction, respectively. Hydrostatic and full depletion is marked in the RSD-graphs by solid and open dots, respectively. Maximum normal fault slip amounts 14.2 and 16.7 cm, respectively, and maximum reverse fault slip 1.6 and 2.3 cm, respectively. View direction of the contour plots is normal to the fault plane. Intersection lines of the two reservoir compartments with the fault plane are shown. View direction of the cross sections is in strike direction of the fault. Dotted areas denote the reservoir compartments.

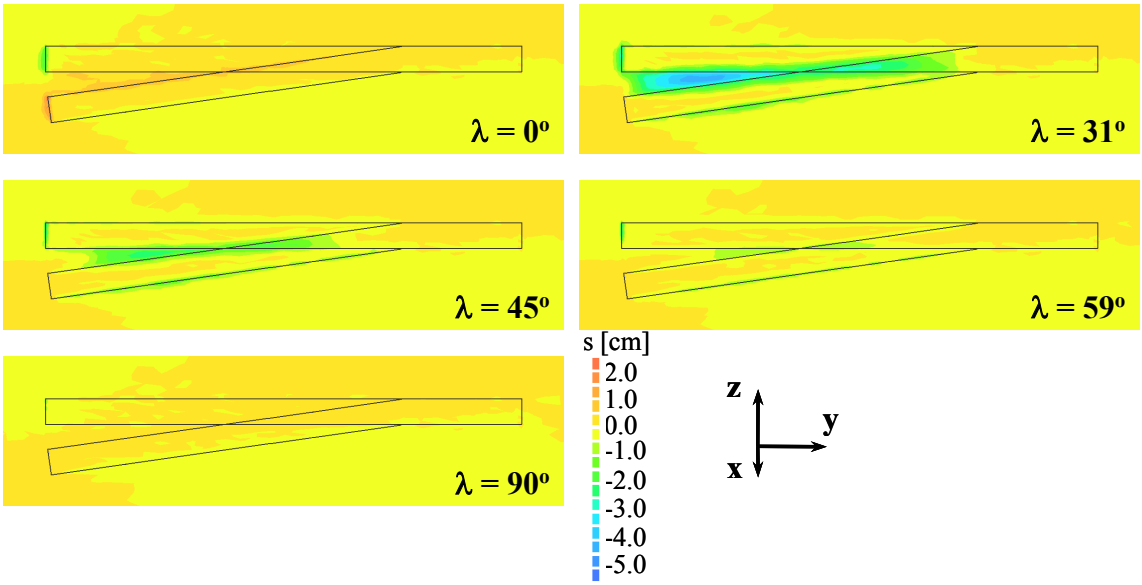

Figure 11.40. Contour plots of relative shear displacement in strike direction of the fault plane (s) for different values of λ with K_{0H} = 1.0 and K_{0h} = 0.4. View direction is normal to the fault plane. Black lines indicate the intersection of the reservoir compartments with the fault plane (see Figure 11.19b).